BEHAVIOR OF HOT ROLLED ASYMMETRIC STEEL I-BEAMS: CONCEPT TO CONSTRUCTION

A Dissertation

by

ERIC ALAN STODDARD

Submitted to the Graduate and Professional School of
Texas A&M University
in partial fulfillment of the requirements for the degree of

DOCTOR OF PHILOSOPHY

Chair of Committee,	Matthew Yarnold
Committee Members,	Peter B. Keating
	Maria Koliou
	Julian Kang
Head of Department,	Zachary Grasley

May 2022

Major Subject: Civil Engineering

Copyright 2022 Eric Alan Stoddard

ABSTRACT

Steel composite floor systems have been commonly used in commercial and residential floor systems. As the push to reduce building heights and increase building construction speed, concrete floor systems with a shallow depth to span ratio have surged ahead of steel composite floor systems. To make steel more competitive in shallow floor systems, multiple unique asymmetric built-up sections have been produced. These built-up sections are labor-intensive and require long lead times to produce. To make steel more competitive in residential floor systems, a hot-roll asymmetric steel I-beam (termed A-shape) was devised.

The overarching goal of this research was to create new knowledge toward the behavior of A-shapes throughout their life, which includes manufacturing, construction, and operation. The research presented herein is divided into five phases. Phase 1 was thermal-mechanical finite element modeling. The modeling approach used nonlinear steel properties and was experimentally validated. The purpose of the modeling was to capture the residual stresses due to the manufacturing cooling process. A parametric study was executed and the controlling flange width-to-thickness ratios were identified for A-shapes. The modeling was also used to study global deformations due to the cooling process, which was found to be manageable for realistic A-shape geometry.

Phase 2 was the development and production of proof-of-concept (POC) beams. The top flange of W-sections was reduced, and the beams were reheated to simulate the cooling of future hot-rolled asymmetric beams. The POC beams were used for further

validation of the simulated global deformations and provided specimens for a full-scale experiment. Phase 2 also incorporated expert feedback from steel mills, which provided guidelines for A-shape dimensions.

Phase 3 was the experimental testing of a full-scale floor system incorporating the POC beams. During all stages of construction and actuator loading, A-shape beam strains and deflections were monitored. The data collected was used to understand the structural behavior of A-shapes as well as validate the theoretical calculations to be used in the next phase.

Phase 4 was a comprehensive analytical study to understand the controlling limits for A-shapes during construction and in-service. The study that was devised evaluated four unique loading scenarios, under 18 limit states, to fully understand the behavior of A-shapes. Phase 5 utilized the understanding of A-shape manufacturing, construction, and in-service behavior to develop recommended A-shape dimensions.

DEDICATION

First and foremost, I would like to thank my wife, Michelle. Your kindness and willingness to help me in every way possible is what has gotten me this far. When I have felt like buckling was inevitable, you increased my Pcr by being by my side and doubling my moment of inertia. Making it this far without you is inconceivable. I would also like to thank my parents and my children. My parents have always been there for me; specifically, I would like to thank my father for always tinkering and teaching me the practical building side of engineering, and my mother for always believing I had and could achieve more. And my six children; my daughter Kylee for always looking out for everyone no matter the adventure, my daughter Alexis for always being better than me at everything pushing me to improve, my son Tristan for always being ready to work on a new project, my daughter Olivia for believing I am no less than a bearded superman, my daughter Hazel for always wanting to hang out and do nerdy stuff, and lastly my son James for showing me how precious life is.

ACKNOWLEDGEMENTS

I would like to personally thank my dissertation committee chair, Dr. Matthew Yarnold, and my committee members, Dr. Peter Keating, Dr. Maria Koliou, and Dr. Julian Kang, for their excitement and support throughout the course of this research. The time and feedback in guiding my graduate research are astonishing.

I would like to give a special thanks to my steel professors for making me care for and wanting to research steel. Dr. Keating, Dr. Yarnold, and Dr. Harris thank you.

In getting to graduate school from Brigham Young University Idaho, I would like to thank my undergraduate advisor and close friend Dr. James Lawrence.

Thanks also go to my friends and colleagues and the department faculty and staff for making my time at Texas A&M University a wonderful experience. With a special thanks to Laura Byrd, Chris Grunkemeyer, Juan Rodriguez, and Terri Taeger for always helping me no matter what I needed, wanted, or could not figure out.

CONTRIBUTORS AND FUNDINGSOURCES

Contributors

This work was supervised by a dissertation committee and an American Institute of Steel Construction (AISC) steering committee. The dissertation committee consisting of Professor Matthew Yarnold [advisor] of the Zachry Department of Civil & Environmental Engineering, Professor Peter Keating of the Zachry Department of Civil & Environmental Engineering, Professor Maria Koliou of the Zachry Department of Civil & Environmental Engineering, and Professor Julian H. Kang of the Department of Construction Science. The author would like to thank the members of the AISC steering committee for their time and guidance consisting of Devin Huber of AISC, Margaret Matthew of AISC, Chris Garrell of AISC, Chia-Ming Uang of the University of California-San Diego, Tom Sabol of Englekirk, Joe Zona of Simpson Gumpertz & Heger, Ronnie Medlock of High Steel, Duff Zimmerman of Cooper Steel, Robert Carter of Steel Dynamics, Tabitha Stine of Nucor, Shane Vernon of Nucor, Christopher Hoyt of Gerdau, Scott Meaney of Gerdau, Rafael Garcia of Gerdau, Drew Seely of Steel Dynamics and Richelle Wilson of Steel Dynamics. Along with the steering committee, the author would like to express gratitude for the information and time given by employees of Gerdau, Nucor, and Steel Dynamics.

The data analysis for Section 4.3 was provided by Sheyenne Davis's Master's Thesis. The phase 3 experimental testing was performed due to help from Sheyenne Davis, Charlie Droddy, Dr. Matthew Yarnold, Dr. Peter Keating, Kirk Martin, and Todd Graham.

Funding Sources

The author would like to express gratitude to AISC for financially supporting this research through the Milek Fellowship. Graduate study was also in part supported by a Graduate Merit Fellowship from Texas A&M University. The author would also like to thank Nucor for believing in our research and donating the material and their services to produce the proof-of-concept A-shapes. Specifically, we would like to acknowledge Mike Thomas, Phil Bischof, and Ross Simmons. The numerical analysis of this research was conducted with high-performance research computing resources provided by Texas A&M University (https://hprc.tamu.edu).

NOMENCLATURE

A-Shape	Asymmetric Hot-roll Steel Beams
AISC	American Institute of Steel construction
ASB	British Steel Asymmetric Beams
AREMA	American Railway Engineering and Maintenance-of-Way Association
CIR	Texas A&M Center for Infrastructural Renewal
W-Shape	ASTM Wide Flange Beam (parallel inner and outer flange surfaces)
M-Shape	ASTM Miscellaneous Beam
S-Shape	ASTM Standard Beam (tapered inner flange surfaces)
HP-Shape	ASTM "H-Pile" Beam (width of the flanges approximately equal to the beam depth)
T-Shape	Tee Beam
IPE	European I Section (parallel flange)
IPN	European I section (taper flange)
HE	European Wide Flange Beam
HD	European Wide Flange Column
HL	European Extra Wide Flange Beam
UPE	European Channel Section (parallel flange)
UC	European Universal Column

UB	European Universal Beam
t_{ft}	Top flange thickness
t_{ftMOD}	Top flange modified thickness
t_{fb}	Bottom flange thickness
b_{ft}	Top flange width or breadth
b_{ftMOD}	Top flange modified width
b_{fb}	Bottom flange width or breadth
F_y	Elastic yield strength of steel
CFY	Compression Flange Yielding
LTB	Lateral-Torsional Buckling
CFLB	Compression Flange Local Buckling
TFY	Tension Flange Yielding
W_{not}	Normalized warping function – top flange
W_{nob}	Normalized warping function – bottom flange
Psf	Pounds per square foot
Plf	Pounds per linear foot
Kip	1000 pounds
Psi	Pounds per square inch
Ksi	Kips per square inch

TABLE OF CONTENTS

Page

ABSTRACT ii

DEDICATION iv

ACKNOWLEDGEMENTS v

CONTRIBUTORS AND FUNDINGSOURCES vi

NOMENCLATURE viii

TABLE OF CONTENTS x

LIST OF FIGURES xii

LIST OF TABLES xxvii

1. INTRODUCTION 1

2. RESEARCH OBJECTIVES 5

3. LITERATURE REVIEW 7

3.1. Composite Floor Systems 7
3.2. Asymmetric Hot-Roll Shapes 10
3.2.1. Current British Steel Shapes 10
3.2.2. Elevator Rail 12
3.2.3. Cross-tie Sections 13
3.2.4. Railway Rails and Splice Bars 14
3.2.5. Hot-roll asymmetric section comparison 15
3.3. Asymmetric Built-Up Sections 15
3.3.1. Standard Plate Girder Section 16
3.3.2. Girder-slab 16
3.3.3. Slim-Floor 17
3.3.4. Kloeckner Westok® Ultra shallow floor beam USFB® 20
3.3.5. Peikko DELTABEAM® 20

4. RESEARCH APPROACH 22

4.1. Phase 1: Manufacturing Behavior – Numerical Modeling 23
4.1.1. Introduction 23
4.1.2. Manufacturing Concerns 24

4.1.3. Thermal-mechanical Modeling 25
4.1.4. Thermal-mechanical Validation Study.....32
4.1.5. Parametric Study 33
4.1.6. Manufacturing Conclusions from Numerical Modeling 45
4.2. Phase 2: Manufacturing Behavior – Proof of Concept Beams and Expert Feedback.....46
4.2.1. Proof-of-Concept Beam Comparison.....46
4.2.2. Expert Feedback 49
4.3. Phase 3: Construction and In-service Behavior - Experimental Testing 51
4.3.1. Introduction – Experimental Testing.....51
4.3.2. Floor System Development 52
4.3.3. Floor System Assembly.....55
4.3.4. Beam Instrumentation 68
4.3.5. Construction Testing 75
4.3.6. Floor System Topping Slab Preparation 81
4.3.7. Topping Slab Pour.....89
4.3.8. In-service and Ultimate Strength Testing.....93
4.3.9. Construction and In-service Loading Results 96
4.4. Phase 4: Construction and In-Service Behavior - Analytical Modeling 105
4.4.1. Introduction 105
4.4.2. Analytical Modeling Outline.....105
4.4.3. Analytical Study - Scenario I: Non-composite eccentric loading 110
4.4.4. Analytical Study - Scenario II: Non-composite concentric loading.....142
4.4.5. Analytical Study – Scenario III: Composite concentric loading.....155
4.4.6. A-shape Flange Area Study.....172
4.5. Phase 5: A-shape Cross-Section Recommendations.....185
4.5.1. Introduction 185
4.5.2. Standard Weight Cross-Sections 187
4.5.3. Heavyweight Cross-Sections.....194

5. CONCLUSIONS AND CONTRIBUTIONS 200

6. RECOMMENDATIONS FOR FUTURE RESEARCH 205

REFERENCES.....207

APPENDIX A ABAQUS PARAMETRIC STUDY MESHES.....212

APPENDIX B ANALYTICAL STUDY PLOTS 242

APPENDIX C ANALYTICAL STUDY MATLAB CODE.....350

APPENDIX D ABAQUS PARAMETRIC STUDY BEAM TABLE 394

APPENDIX E ANALYTICAL STUDY BEAM TABLE 396

LIST OF FIGURES

Figure 1: Typical residential/light commercial flooring systems. (a) Typical cast-in-place concrete floor, (b) Engineered wood flooring system, (c) Steel hot-roll beams with cast-in-place slab, and (d) Steel beams supporting pre-cast concrete panels with a cast-in-place topping slab.....1

Figure 2: Built-up and A-shape cross-sections 3

Figure 3: Double Symmetric I-shape hot-roll steel sections 9

Figure 4: Potential use of A-shapes in-floor systems: (a) pre-cast deck panel composite floor system (b) cast-in-place composite floor systems 10

Figure 5: British Steel ASB sections.....11

Figure 6: Elevator guide rail.....13

Figure 7: Cross-tie section.....13

Figure 8: Railroad rail and splice bar 14

Figure 9: Standard plate girder.....16

Figure 10: Girder-slab D-BEAM® 17

Figure 11: Slim-floor asymmetric beam sections 19

Figure 12:Kloeckner Westok® ultra shallow floor beam USFB® 20

Figure 13: Peikko DELTABEAM®.....21

Figure 14: Typical beam meshing (residual stress analysis).....26

Figure 15: Thermal and material coefficients: (a) specific heat (CEN 2005) (b) thermal conductivity (CEN 2005) (c) film coefficient (Brickstad and Josefson 1998) (d) elastic modulus (Hu et al. 2009) (e) Poisson ratio (Andersson 1978) (f) thermal expansion (AISC 2016) 28

Figure 16: Multilinear kinematic stress (σ_x) vs. strain (ε_x) hardening model adapted from test data 30

Figure 17: Top flange residual stresses for the (a) W8x31 and (b) W16x50. Note FEA indicates the results from this study.....33

Figure 18: Beam modifications for parametric study.....35

Figure 19:(a) FE model W8x31 temperature distribution at 300 seconds (b) FE model W8x31 longitudinal stresses at 300 seconds. Units are in ◦C and Pa, respectively. 37

Figure 20: FE stress profiles for top flange thickness variations of the (a) W8x31 cases and (b) W18x76 cases. 38

Figure 21: FE stress profiles for top flange width variations of the (a) W8x31 cases and (b) W18x76 cases.....38

Figure 22:Web residual stress profiles for width and thickness variations (a) FE stress profiles for top flange W8x31 width variations (b) FE stress profiles for top flange W8x31 thickness variations (c) FE stress profiles for top flange W18x76 width variations.....40

Figure 23: Normalized flange outer fiber residual stress vs. b/t 42

Figure 24: Beam camber sign convention.....43

Figure 25: (a) 9m FE model of a W8x31 with 2.00 b_{ft} (b) 9m FE model of a W8x31 with 0.25 b_{ft}.....43

Figure 26: Global deflections.....45

Figure 27: Process to create Nucor POC beams 47

Figure 28: POC beam plans 47

Figure 29: Reheated POC A-shape beams being removed from the oven.....48

Figure 30: POC W12x65 temperature distribution for physical beams and validated FE model.....49

Figure 31: Full-scale Experimental Floor Set-up 51

Figure 32: CIR floor hold-down grid and tension rods.....52

Figure 33: Initial full-scale floor system layout with CIR grid.....55

Figure 34: A12x53 fabricated A-shape beam delivery 56

Figure 35: W12x65 stub columns with welded base plate.....57

Figure 36: Beam to column shear connection.....58

Figure 37: Beam to column shear tab with slotted holes 59

Figure 38: Beam to column shear connection with slotted holes, installed 60

Figure 39: Center A12x53 connection holes.....61

Figure 40: Center A12x53 beam primed and drilled.....62

Figure 41: Edge W12x65 stub column with connection holes.....63

Figure 42: Edge beam to column ”Fixed” connection, top angle 64

Figure 43: Edge beam to column ”Fixed” connection 65

Figure 44: CIR tension rods basement connection.....66

Figure 45: Stub column connection to CIR strong floor with tension rods 67

Figure 46: Floor system steel frame assembled 68

Figure 47: Plan view of sensor cross-section locations.....69

Figure 48: Beam cross-section sensor location 70

Figure 49: Edge beam top flange sensor installation 71

Figure 50: Edge beam bottom flange sensor installation 72

Figure 51: Center beam top flange sensor installation with protection for encasement ..73

Figure 52: Edge beam top flange string-pot beam attachment.....74

Figure 53: Edge beam bottom flange string-pot rotation and displacement connections 75

Figure 54: Pre-cast hollow core concrete panels.....76

Figure 55: Plan view of panel placement during construction testing 77

Figure 56: Construction loading of the steel frame – first concrete pre-cast panel placement.....78

Figure 57: Construction loading of the steel frame – first concrete pre-cast panel.....79

Figure 58: Construction loading of the steel frame – four of five concrete pre-cast panels placed.....80

Figure 59: Construction loading of the steel frame – all concrete pre-cast panels installed (image by Matthew Yarnold) 81

Figure 60: Pre-cast hollow-core concrete panel foam closure 82

Figure 61: Pre-cast hollow-core concrete panel foam closure after cutting 83

Figure 62: Joint sealing between pre-cast concrete panels 84

Figure 63: Location of silicone beads for the beam to panel sealant 84

Figure 64: Floor system concrete plywood end form, beam scribed 85

Figure 65: Floor system concrete plywood end forms 86

Figure 66: Floor system concrete plywood end form bracing 86

Figure 67: Concrete form wire sealing 87

Figure 68: Steel angle concrete form clamped to edge beams 88

Figure 69: Concrete slab rebar reinforcement tied mat, close up 89

Figure 70: Concrete slab rebar reinforcement tied mat 89

Figure 71: Slab pour, concrete dump bucket 91

Figure 72: Slab pour, the first concrete load placed 91

Figure 73: Slab pour and screeding surface 92

Figure 74: Slab finishing 92

Figure 75: Finished concrete slab 93

Figure 76: Floor system with loading frame and 220 kip actuator 95

Figure 77: Spreader beam and 220 kip actuator 96

Figure 78: Loading scenario 2 center beam strains 99

Figure 79: Loading scenario 2 edge beam strains 100

Figure 80: Theoretical bending and torsional stress with construction loading scenario 2 at the ends of the flanges 102

Figure 81: Theoretical bending and torsional stress with construction loading scenario 2 at the mid-span sensor locations 102

Figure 82: Cross-section of A-shape precast floor system 106

Figure 83: Analytical study outline 109

Figure 84: Analytical study, MATLAB outline 110

Figure 85: Load case 1, precast-concrete panels 111

Figure 86: Load case 2b, precast-concrete panels with a half topping slab 113

Figure 87: Discretization of a beam for constant torsion 117

Figure 88: Torsion in an infinitesimally small section of a beam 117

Figure 89: Superposition of eccentric loading 119

Figure 90: Distribution of normal stresses 121

Figure 91: Normal stresses due to bending and torsion at mid-span. 122

Figure 92: Shear center location 123

Figure 93: Shear stresses due to bending and torsion at the support 127

Figure 94: Scenario I: Normalized tension flange yielding vs. beam cross-sectional area 130

Figure 95: Scenario I: Normalized compression flange yielding vs beam cross-sectional area 131

Figure 96: Scenario I: Normalized tension flange yielding vs. beam flange thickness (tft) 132

Figure 97: Scenario I: Normalized flange shear yielding vs. beam cross-sectional area 133

Figure 98: Scenario I: Normalized flange shear yielding vs. beam web height 134

Figure 99: Scenario I: Normalized web shear yielding vs beam cross-sectional area ... 135

Figure 100: Scenario I: Normalized web shear yielding vs. beam web thickness (tw) 136

Figure 101: Scenario I: Normalized buckling vs. beam cross-sectional area 137

Figure 102: Scenario I: Normalized buckling vs. beam top flange width (bft).....138

Figure 103: Scenario I: Normalized buckling vs. beam top flange thickness (tft) 139

Figure 104: Scenario I: Normalized rotation vs beam cross-sectional area.....140

Figure 105: Scenario I: Normalized rotation vs. beam top flange width (bft) 141

Figure 106: Scenario I: Normalized flange limits vs beam cross-sectional area 142

Figure 107: Loading scenario 2a, precast-concrete panels with a wet topping slab 143

Figure 108: Location of hc and hp on A-shapes 144

Figure 109: Scenario II: Normalized moment capacity vs. beam cross-sectional area..150

Figure 110: Scenario II: Normalized moment capacity vs. beam cross-sectional area (annotated sections) 151

Figure 111: Scenario II: Normalized shear capacity vs. beam cross-sectional area 152

Figure 112: Scenario II: Normalized shear capacity vs. web thickness (tw).....153

Figure 113: Scenario II: Normalized deflection vs. beam cross-sectional area 154

Figure 114: Scenario II: Normalized deflection vs. beam moment of inertia.....155

Figure 115: Loading scenario 3, in-service loading.....156

Figure 116: A-shape dimension nomenclature.....158

Figure 117: Composite section dimensions for elastic analysis.....160

Figure 118: Scenario III: Normalized composite deflection vs. beam cross-sectional area.....169

Figure 119: Scenario III: Normalized composite deflection vs. beam top flange thickness (tft) 170

Figure 120: Scenario III: Normalized vibration vs. beam cross-sectional area 171

Figure 121: Scenario III: Normalized vibration vs. beam top flange thickness (tft)....172

Figure 122: A8-65/35 flange area normalized passing plot 174

Figure 123: A8-60/40 flange area normalized passing plot 175

Figure 124: A8-55/45 flange area normalized passing plot 176

Figure 125: A8-50/50 flange area normalized passing plot 177

Figure 126: A8-45/55 flange area normalized passing plot 178

Figure 127: A8-40/60 flange area normalized passing plot 179

Figure 128: A8-35/65 flange area normalized passing plot 180

Figure 129: Percent of top flange area vs. percent of controlling limit state 183

Figure 130: Percent area of top flange vs. beam weight 184

Figure 131: Percent area of top flange vs beam weight 185

Figure 132: A8 standard weight normalized minimum limit state..... 188

Figure 133: A9 standard weight normalized minimum limit state..... 189

Figure 134: A10 standard weight normalized minimum limit state..... 190

Figure 135: A12 standard weight normalized minimum limit state..... 191

Figure 136: Controlling limit states by percent (standard weight)..... 193

Figure 137: Recommended standard weight beam cross-sections..... 194

Figure 138: A8 heavyweight normalized minimum limit state..... 196

Figure 139: A8 heavyweight normalized minimum limit state..... 197

Figure 140: Controlling limit states by percent (heavyweight)..... 198

Figure 140: Recommended heavyweight beam cross-sections..... 199

Figure 141: A-shape AISC sample table 204

Figure 142: W8x31 0.25 bf ABAQUS tetrahedral model meshing 212

Figure 143: W8x31 0.25 bf ABAQUS stress distribution (Pa) 212

Figure 144: W8x31 0.50 bf ABAQUS tetrahedral model meshing 213

Figure 145: W8x31 0.50 bf ABAQUS stress distribution (Pa) 213

Figure 146: W8x31 0.75 bf ABAQUS tetrahedral model meshing 214

Figure 147: W8x31 0.75 bf ABAQUS stress distribution (Pa) 214
Figure 148: W8x31 1.00 bf ABAQUS tetrahedral model meshing 215
Figure 149: W8x31 1.00 bf ABAQUS stress distribution (Pa) 215
Figure 150: W8x31 1.25 bf ABAQUS tetrahedral model meshing 216
Figure 151: W8x31 1.25 bf ABAQUS stress distribution (Pa) 216
Figure 152: W8x31 1.50 bf ABAQUS tetrahedral model meshing 217
Figure 153: W8x31 1.50 bf ABAQUS stress distribution (Pa) 217
Figure 154: W8x31 1.75 bf ABAQUS tetrahedral model meshing 218
Figure 155: W8x31 1.75 bf ABAQUS stress distribution (Pa) 218
Figure 156: W8x31 2.00 bf ABAQUS tetrahedral model meshing 219
Figure 157: W8x31 2.00 bf ABAQUS stress distribution (Pa) 219
Figure 158: W8x31 0.25 tf ABAQUS tetrahedral model meshing 220
Figure 159: W8x31 0.25 tf ABAQUS stress distribution (Pa) 220
Figure 160: W8x31 0.50 tf ABAQUS tetrahedral model meshing 221
Figure 161: W8x31 0.50 tf ABAQUS stress distribution (Pa) 221
Figure 162: W8x31 0.75 tf ABAQUS tetrahedral model meshing 222
Figure 163: W8x31 0.75 tf ABAQUS stress distribution (Pa) 222
Figure 164: W8x31 1.25 tf ABAQUS tetrahedral model meshing 223
Figure 165: W8x31 1.25 tf ABAQUS stress distribution (Pa) 223
Figure 166: W8x31 1.50 tf ABAQUS tetrahedral model meshing 224
Figure 167: W8x31 1.50 tf ABAQUS stress distribution (Pa) 224
Figure 168: W8x31 1.75 tf ABAQUS tetrahedral model meshing 225
Figure 169: W8x31 1.75 tf ABAQUS stress distribution (Pa) 225

Figure 170: W8x31 2.00 tf ABAQUS tetrahedral model meshing.....226

Figure 171: W8x31 2.00 tf ABAQUS stress distribution (Pa) 226

Figure 172: W18x76 0.25 bf ABAQUS tetrahedral model meshing.....227

Figure 173: W18x76 0.25 bf ABAQUS stress distribution (Pa).....227

Figure 174: W18x76 0.50 bf ABAQUS tetrahedral model meshing.....228

Figure 175: W18x76 0.50 bf ABAQUS stress distribution (Pa).....228

Figure 176: W18x76 0.75 bf ABAQUS tetrahedral model meshing.....229

Figure 177: W18x76 0.75 bf ABAQUS stress distribution (Pa).....229

Figure 178: W18x76 1.00 bf ABAQUS tetrahedral model meshing.....230

Figure 179: W18x76 1.00 bf ABAQUS stress distribution (Pa).....230

Figure 180: W18x76 1.25 bf ABAQUS tetrahedral model meshing.....231

Figure 181: W18x76 1.25 bf ABAQUS stress distribution (Pa).....231

Figure 182: W18x76 1.50 bf ABAQUS tetrahedral model meshing.....232

Figure 183: W18x76 1.50 bf ABAQUS stress distribution (Pa).....232

Figure 184: W18x76 1.75 bf ABAQUS tetrahedral model meshing.....233

Figure 185: W18x76 1.75 bf ABAQUS stress distribution (Pa).....233

Figure 186: W18x76 2.00 bf ABAQUS tetrahedral model meshing.....234

Figure 187: W18x76 2.00 bf ABAQUS stress distribution (Pa).....234

Figure 188: W18x76 0.25 tf ABAQUS tetrahedral model meshing.....235

Figure 189: W18x76 0.25 tf ABAQUS stress distribution (Pa) 235

Figure 190: W18x76 0.50 tf ABAQUS tetrahedral model meshing.....236

Figure 191: W18x76 0.50 tf ABAQUS stress distribution (Pa) 236

Figure 192: W18x76 0.75 tf ABAQUS tetrahedral model meshing.....237

Figure 193: W18x76 0.75 tf ABAQUS stress distribution (Pa) 237

Figure 194: W18x76 1.25 tf ABAQUS tetrahedral model meshing.....238

Figure 195: W18x76 1.25 tf ABAQUS stress distribution (Pa) 238

Figure 196: W18x76 1.50 tf ABAQUS tetrahedral model meshing.....239

Figure 197: W18x76 1.50 tf ABAQUS stress distribution (Pa) 239

Figure 198: W18x76 1.75 tf ABAQUS tetrahedral model meshing.....240

Figure 199: W18x76 1.75 tf ABAQUS stress distribution (Pa) 240

Figure 200: W18x76 2.00 tf ABAQUS tetrahedral model meshing.....241

Figure 201: W18x76 2.00 tf ABAQUS stress distribution (Pa) 241

Figure 202: Scenario I: Normalized tension flange yielding vs top flange thickness (tft) 242

Figure 203: Scenario I: Normalized tension flange yielding vs top flange width (bft) 243

Figure 204: Scenario I: Normalized tension flange yielding vs web thickness (tw).....244

Figure 205: Scenario I: Normalized tension flange yielding vs bottom flange thickness (tfb).....245

Figure 206: Scenario I: Normalized tension flange yielding vs bottom flange width (bfb) 246

Figure 207: Scenario I: Normalized tension flange yielding vs web height 247

Figure 208: Scenario I: Normalized tension flange yielding vs moment of inertia (Ix) 248

Figure 209: Scenario I: Normalized Tension flange yielding vs polar moment of inertia (J).....249

Figure 210: Scenario I: Normalized tension flange yielding vs cross-sectional area 250

Figure 211: Scenario I: Normalized compression flange yielding vs top flange thickness (tft) 251

Figure 212: Scenario I: Normalized compression flange yielding vs top flange width (bft).....252

Figure 213: Scenario I: Normalized compression flange yielding vs web thickness (tw) 253

Figure 214: Scenario I: Normalized compression flange yielding vs bottom flange thickness (tfb) 254

Figure 215: Scenario I: Normalized compression flange yielding vs bottom flange width (bfb) 255

Figure 216: Scenario I: Normalized compression flange yielding vs web height 256

Figure 217: Scenario I: Normalized compression flange yielding vs moment of inertia (Ix) 257

Figure 218: Scenario I: Normalized compression flange yielding vs polar moment of inertia (J) 258

Figure 219: Scenario I: Normalized compression flange yielding vs cross-sectional area 259

Figure 220: Scenario I: Normalized flange shear yielding vs top flange thickness (tft) 260

Figure 221: Scenario I: Normalized flange shear yielding vs top flange width (bft) ... 261

Figure 222: Scenario I: Normalized flange shear yielding vs web thickness (tw) 262

Figure 223: Scenario I: Normalized flange shear yielding vs bottom flange thickness (tfb) 263

Figure 224: Scenario I: Normalized flange shear yielding vs bottom flange width (bfb) 264

Figure 225: Scenario I: Normalized flange shear yielding vs web height 265

Figure 226: Scenario I: Normalized flange shear yielding vs moment of inertia (Ix) ... 266

Figure 227: Scenario I: Normalized flange shear yielding vs polar moment of inertia (J) 267

Figure 228: Scenario I: Normalized flange shear yielding vs cross-sectional area 268

Figure 229: Scenario I: Normalized web shear yielding vs top flange thickness (tft) . 269

Figure 230: Scenario I: Normalized web shear yielding vs top flange width (bft) 270

Figure 231: Scenario I: Normalized web shear yielding vs web thickness (tw) 271

Figure 232: Scenario I: Normalized web shear yielding vs bottom flange thickness (tfb).....272

Figure 233: Scenario I: Normalized web shear yielding vs bottom flange width (bfb)273

Figure 234: Scenario I: Normalized web shear yielding vs web height.....274

Figure 235: Scenario I: Normalized web shear yielding vs moment of inertia (Ix) 275

Figure 236: Scenario I: Normalized web shear yielding vs polar moment of inertia (J)276

Figure 237: Scenario I: Normalized web shear yielding vs cross-sectional area.....277

Figure 238: Scenario I: Normalized buckling vs top flange thickness (tft) 278

Figure 239: Scenario I: Normalized buckling vs top flange width (bft).....279

Figure 240: Scenario I: Normalized buckling vs web thickness (tw).....280

Figure 241: Scenario I: Normalized buckling vs bottom flange thickness (tfb).....281

Figure 242: Scenario I: Normalized buckling vs bottom flange width (bfb).....282

Figure 243: Scenario I: Normalized buckling vs web height.....283

Figure 244: Scenario I: Normalized buckling vs moment of inertia (Ix) 284

Figure 245: Scenario I: Normalized flange shear yielding vs polar moment of inertia (J) 285

Figure 246: Scenario I: Normalized buckling vs cross-sectional area 286

Figure 247: Scenario I: Normalized rotation vs top flange thickness (tft).....287

Figure 248: Scenario I: Normalized rotation vs top flange width (bft) 288

Figure 249: Scenario I: Normalized rotation vs web thickness (tw) 289

Figure 250: Scenario I: Normalized rotation vs bottom flange thickness (tfb) 290

Figure 251: Scenario I: Normalized rotation vs bottom flange width (bfb) 291

Figure 252: Scenario I: Normalized rotation vs web height 292

Figure 253: Scenario I: Normalized rotation vs moment of inertia (Ix) 293

Figure 254: Scenario I: Normalized rotation vs polar moment of inertia (J) 294

Figure 255: Scenario I: Normalized rotation vs cross-sectional area 295

Figure 256: Scenario I: Normalized b/t vs top flange thickness (tft) 296

Figure 257: Scenario I: Normalized b/t vs top flange width (bft) 297

Figure 258: Scenario I: Normalized b/t vs web thickness (tw) 298

Figure 259: Scenario I: Normalized b/t vs bottom flange thickness (tfb) 299

Figure 260: Scenario I: Normalized b/t vs bottom flange width (bfb) 300

Figure 261: Scenario I: Normalized b/t vs web height 301

Figure 262: Scenario I: Normalized flange shear yielding vs moment of inertia (Ix) ... 302

Figure 263: Scenario I: Normalized b/t vs polar moment of inertia (J) 303

Figure 264: Scenario I: Normalized b/t vs cross-sectional area 304

Figure 265: Scenario II: Normalized AISC Moment Capacity vs Top Flange Thickness (tft) 305

Figure 266: Scenario II: Normalized AISC moment capacity vs top flange width (bft) 306

Figure 267: Scenario II: Normalized AISC moment capacity vs web thickness (tw) ... 307

Figure 268: Scenario II: Normalized AISC moment capacity vs bottom flange thickness (tfb) 308

Figure 269: Scenario II: Normalized AISC moment capacity vs bottom flange width (bfb) 309

Figure 270: Scenario II: Normalized AISC moment capacity vs web height 310

Figure 271: Scenario II: Normalized AISC moment capacity vs moment of inertia (Ix) 311

Figure 272: Scenario II: Normalized AISC moment capacity vs polar moment of inertia (J) 312

Figure 273: Scenario II: Normalized AISC moment capacity vs cross-sectional area ..313

Figure 274: Scenario II: Normalized AISC shear capacity vs top flange thickness (tft) 314

Figure 275: Scenario II: Normalized AISC shear capacity vs top flange width (bft) ..315

Figure 276: Scenario II: Normalized AISC shear capacity vs web thickness (tw) 316

Figure 277: Scenario II: Normalized AISC shear capacity vs bottom flange thickness (tfb).....317

Figure 278: Scenario II: Normalized AISC shear capacity vs bottom flange width (bfb) 318

Figure 279: Scenario II: Normalized AISC shear capacity vs web height.....319

Figure 280: Scenario II: Normalized AISC shear capacity vs moment of inertia (Ix) ..320

Figure 281: Scenario II: Normalized AISC shear capacity vs polar moment of inertia (J) 321

Figure 282: Scenario II: Normalized AISC shear capacity vs cross-sectional area.....322

Figure 283: Scenario II: Normalized deflection non-composite vs top flange thickness (tft) 323

Figure 284: Scenario II: Normalized deflection non-composite vs top flange width (bft).....324

Figure 285: Scenario II: Normalized deflection non-composite vs web thickness (tw)325

Figure 286: Scenario II: Normalized deflection non-composite vs bottom flange thickness (tfb).....326

Figure 287: Scenario II: Normalized deflection non-composite vs bottom flange width (bfb) 327

Figure 288: Scenario II: Normalized deflection non-composite vs web height.....328

Figure 289: Scenario II: Normalized deflection non-composite vs moment of inertia (Ix).....329

Figure 290: Scenario II: Normalized deflection non-composite vs polar moment of inertia (J).....330

Figure 291: Scenario II: Normalized deflection non-composite vs cross-sectional area 331

Figure 292: Scenario III: Normalized deflection composite vs top flange thickness (tft) 332

Figure 293: Scenario III: Normalized deflection composite vs top flange width (bft). 333

Figure 294: Scenario III: Normalized deflection composite vs web thickness (tw) 334

Figure 295: Scenario III: Normalized deflection composite vs bottom flange thickness (tfb) 335

Figure 296: Scenario III: Normalized deflection composite vs bottom flange width (bfb) 336

Figure 297: Scenario III: Normalized deflection composite vs web height 337

Figure 298: Scenario III: Normalized deflection composite vs moment of inertia (Ix) 338

Figure 299: Scenario III: Normalized deflection composite vs polar moment of inertia (J) 339

Figure 300: Scenario III: Normalized deflection composite vs cross-sectional area 340

Figure 301: Scenario III: Normalized vibration comfort vs top flange thickness (tft). 341

Figure 302: Scenario III: Normalized vibration comfort vs top flange width (bft) 342

Figure 303: Scenario III: Normalized vibration comfort vs web thickness (tw) 343

Figure 304: Scenario III: Normalized vibration comfort vs bottom flange thickness (tfb) 344

Figure 305: Scenario III: Normalized vibration comfort vs bottom flange width (bfb) 345

Figure 306: Scenario III: Normalized vibration comfort vs web height 346

Figure 307: Scenario III: Normalized vibration comfort vs moment of inertia (Ix) 347

Figure 308: Scenario III: Normalized vibration comfort vs polar moment of inertia (J) 348

Figure 309: Scenario III: Normalized vibration comfort vs cross-sectional area 349

LIST OF TABLES

Page

Table 1: British Steel ASB Shapes Available 12

Table 2: Hot-roll asymmetric comparison 15

Table 3: In-situ concrete compressive strength 94

Table 4: Measured strains, rotations, and stresses 98

Table 5: Comparison of experimental stresses vs. theoretical stresses 104

Table 6: Unbalanced area passing beam cross-sections 181

Table 7: Failure type reference number 182

Table 8: Beam cross-section unique parameters 187

Table 9: Satisfactory standard weight beam cross-section parameters 192

Table 10: Controlling limit state by percent 192

Table 11: Satisfactory heavyweight beam cross-section parameters 198

Table 12: Abaqus Parametric Study Beam Table 394

Table 13: Analytical Study Beam Table 396

1. INTRODUCTION

Building floor systems are a key part of the design and construction of all buildings. The initial selection process has a large determination on the total building height and design. The floor system selection dictates such factors as floor-to-floor height, open span limiting dimensions, speed of construction, and comfort of the floor at open spans. Three main types of floor systems are concrete floors containing cast-in-place or precast systems (Figure 1a), steel-concrete composite floor systems (Figure 1c and Figure 1d), and engineered wood joist systems (Figure 1d). Each floor system has distinct advantages and disadvantages in its application.

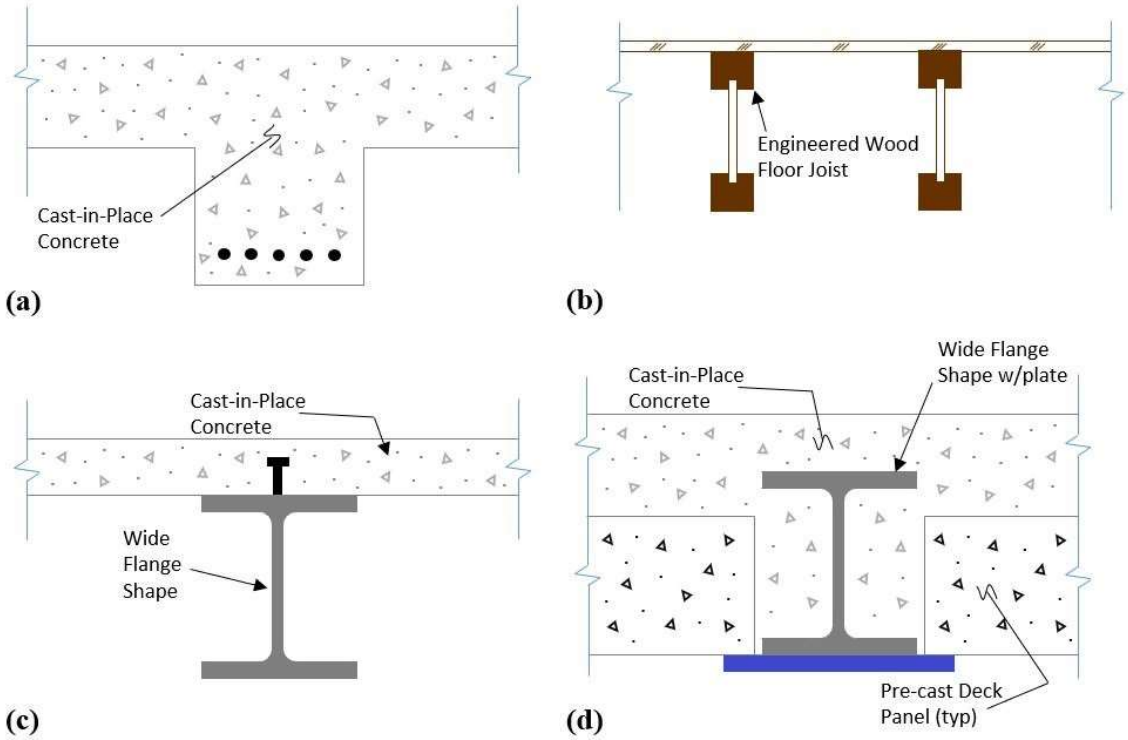

Figure 1: Typical residential/light commercial flooring systems. (a) Typical cast-in-place concrete floor, (b) Engineered wood flooring system, (c) Steel hot-roll beams with cast-in-place slab, and (d) Steel beams supporting pre-cast concrete panels with a cast-in-place topping slab.

Entirely concrete systems (Figure 1a) are very stiff systems, with relatively shallow floor depths. Concrete systems also utilize post-tensioning to maximize span lengths. The downside to a concrete floor system is time. Concrete systems have complex rebar placement, extensive forming, and shoring. Another disadvantage of concrete floor systems is the concrete cure time that must take place before construction can continue. The manpower needed during construction and additional time drive-up building times and costs.

Wood floor systems (Figure 1b) are the most cost-effective solution to elevated building floors. Wood systems are easy to place and take no "set" time for continued construction. Wood floor systems are also light weight reducing overall building weight. The downside to a wood floor system is they are a relatively flexible floor, and to achieve long spans requires very deep floor depths.

The alternative to these two systems is a conventional composite floor constructed of steel beams with a concrete slab (Figure 1c). The advantage to the composite floor systems is they can be constructed quickly, and the steel beams support the concrete decking without expansive shoring or forming. Composite floor systems perform well and can achieve longer required spans. The disadvantage to composite systems is the large floor depths needed to support the concrete deck during construction.

Steel-concrete floor systems have begun to optimize steel beams to reduce the floor system depth by placing the steel beams in the plane with the concrete (Figure 1d). As floor height restrictions and construction, speed has begun to control building design.

The move to shallower systems has risen. These systems have shorter construction schedules, utilizing steel composite systems with custom sections. These custom (or built-up) steel sections accommodate the shallow depth floor systems. As the short to medium-span floor market becomes more competitive with precast concrete systems and engineered lumber, a more efficient steel composite system is needed to compete. Although the custom steel sections achieve the desired result, these sections lack fast production speeds and have extensive manufacturing costs. American Institute of Steel Construction (AISC) is championing this push for faster steel systems to compete with market demand through the implementation of their "Need for Speed" initiative. The goal is to decrease the time for steel structures to go from design to erection by 50% (AISC 2021).

To facilitate AISC's speed goal, and in addition to reducing the cost of shallow floor systems, the concept of a hot-roll asymmetric steel I-beam (termed A-shape) was contrived (Figure 2). These A-shapes shall replace many of the built-up sections commonly utilizing shallow floor systems.

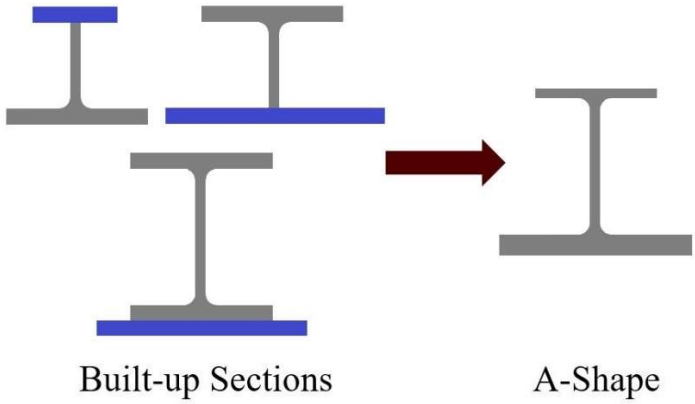

Figure 2: Built-up and A-shape cross-sections

Currently, no major United States steel mills produce an asymmetric I-beam. Internationally, in limited supply, ten asymmetric sections are rolled with minimal variation, minimal testing, or behavioral understanding (further details are provided in the next section). The goal of this research is to understand A-shape behavior from production to service. An understanding of A-shape behavior during manufacturing, construction, and in-service scenarios provide the necessary knowledge to develop proportional limits and other criteria to develop optimized cross-sectional dimensions. This information can then be used to realize the long-term goal of the research, which is for A-shapes to be produced in U.S. steel mills and specified in future AISC manuals for steel construction.

2. RESEARCH OBJECTIVES

The overarching goal of this research is to create new knowledge toward the behavior of hot-roll asymmetric steel I-beams (termed A-shapes). This behavior focuses on the primary stages throughout the life of A-shapes, which includes manufacturing, construction, and in-service operation. From this understanding, A-shape cross-sections can be developed for future steel mill production and construction applications.

The specific objectives of the research were:

1. Manufacturing Behavior
    a. Phase 1: Determine A-shape manufacturing behavior through extensive thermal-mechanical modeling with a focus on the residual stresses and global deformations as a result of the cooling process.
    b. Phase 2: Development proof-of-concept A-shape beams for validation of the thermal-mechanical modeling process and to provide specimens for structural testing. In addition, conduct interviews with the major U.S. steel mills to obtain other manufacturing criteria critical for hot rolling A-shape production.
2. Construction and In-service Behavior
    a. Phase 3: Conduct full-scale experimental construction and in-service testing, along with ultimate strength testing of a floor system utilizing A-shapes.

b. Phase 4: Establish the construction and in-service behavior for an array of floor system geometries using A-shapes through a comprehensive analytical study.

3. Cross-section Recommendations

a. Phase 5: Determine recommended A-shape cross-sectional dimensions at varying depths that are best suited for manufacturing, construction, and in-service buildings.

3. LITERATURE REVIEW

3.1. Composite Floor Systems

Current research on composite floor systems has not focused on hot-roll asymmetric I-beam improvement. Most recent research has been geared toward floor system understanding of ultimate strength, fire, and vibration performance, much of which has been extensive numerical modeling. To better understand the performance of composite floor systems during fire events computer software to aid in the future design of large-scale fire tests and fire protection have been developed (Bailey 1999), a new finite element detailed methodology for evaluating slim floor beams under fire conditions was conceived (Maraveas et al. 2012), slim floor beams have been evaluated on their structural performance during thermal loading (Mäkeläinen and Ma 2000), component fire experiments of composite floor beams with various end support conditions were studied (Choe et al. 2020), effects of load intensity, and restraint on the fire resistance of composite beams (Alfawakhiri et al. 2016). Along with fire testing in-service and ultimate have been studied on current asymmetric systems.

Extensive ultimate testing has been conducted and evaluated to understand the composite behavior of differing asymmetric floor systems. A new design method for the plastic design of the bending capacity at ultimate load (Lam et al. 2015), an investigation into time-dependent creep of two test specimens with independent loading for creep model validation (Baldassino et al. 2019), three test specimens with unique shear reinforcement were tested at ultimate for numerical composite modeling validation (Xia et al. 2021), component push-out tests were performed on composite slim-floor beams to

determine the characteristic load capacity (Braun et al. 2014), design of software consisting of design guides and practical detailing for asymmetric slim floor beams (Rackham et al. 2006), the detailed design and construction using slim floor beams with deep decking was evaluated with a series of full-scale in-service and ultimate testing (Mullett and R.M.Lawson 1993), a numerical investigation into asymmetric slim floor beams and composite slim floor beams to determine stiffness and flexural capacity was perfomed using non-linear models calibrated from preious studies (Borghi et al. 2021), an indepth analysis into the sagging bending momenbts due to cracked concrete under service loading and contributions of the concrete chord to the effective moment of inertia (Hauf and Kuhlmann 2015), a look into the current design philosophy and basic structural elements for modeling technique design approaches and static testing (Ahmed and Tsavdaridis 2019), thecontrol of vibrations induced by people walking on long-span composite floor decks (Varela and Battista 2011), and mitigating footfall-induced vibration in long-span floor systems (Nguyen et al. 2014). Another recent study investigated floor systems spanning up to 9 meters (30 feet) with minimal floor thickness (Huber et al. 2011). However, limited research has been performed on the large-scale production of hot-roll A-shapes to improve composite floor systems. With the increasing demand for asymmetric cross-sections from the steel industry and AISC, a better understating of the behavior and limits of hot-roll asymmetric beams is needed.

The United States (U.S.) market for hot-roll steel beams is limited to double symmetric I-shapes such as W, M, HP, or S shapes (Figure 3) (AISC 2016). These beams are utilized (in some form) in a large percentage of steel building floor systems,

which take advantage of composite construction (precast and cast-in-place). A majority of systems use deep sections with in-situ concrete. In shallow floor systems utilizing precast concrete floor system applications, steel beams are used to support the concrete panels. In precast panels, the top flange can hinder panel installation and requires cutting or modifying a current rolled section or making relatively expensive built-up plate girder sections. Figure 4(a) is a typical built-up section used in shallow composite floor systems. Figure 4(b) is a typical deck on beam composite floor system. Both systems could potentially benefit from an A-shape.

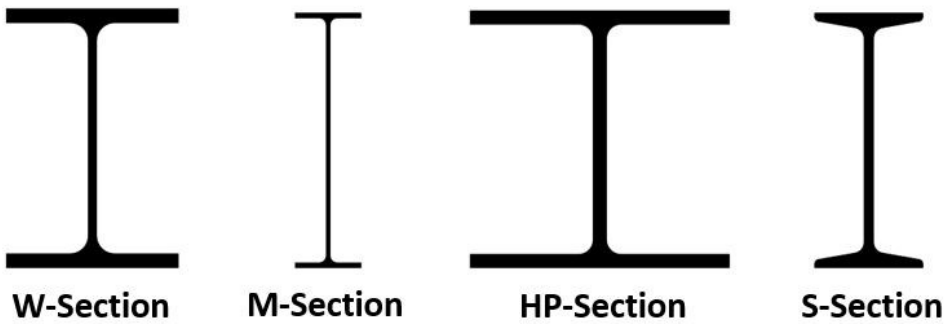

Figure 3: Double Symmetric I-shape hot-roll steel sections

Conventional cast-in-place concrete floor systems are also widely utilized; these systems typically involve a deck slab cast on top of rolled steel beams. The concrete and steel are made composite through the application of welded shear studs. In composite floor systems, the top flange of the steel beam does not have significant contributing strength or stiffness to the final floor system configuration (Figure 4b). However, during construction, it is an important factor. An asymmetric I-beam can be more structurally efficient, although the additional cost of fabrication typically outweighs the efficiency.

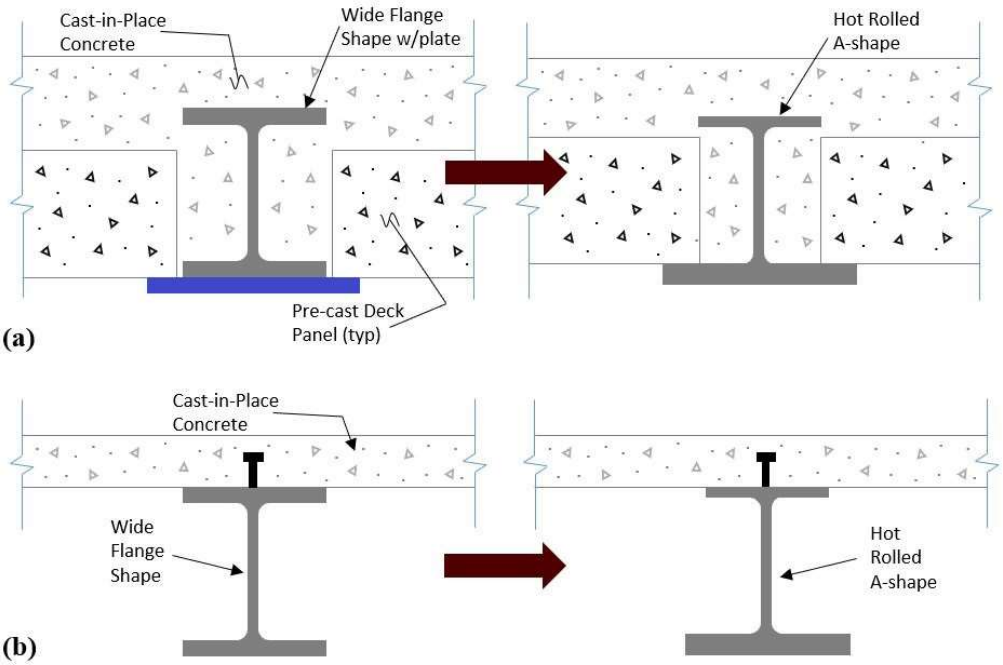

Figure 4: Potential use of A-shapes in-floor systems: (a) pre-cast deck panel composite floor system (b) cast-in-place composite floor systems

3.2. Asymmetric Hot-Roll Shapes

Asymmetric hot-roll sections are not new to the steel industry. Steel members, known as Cross Tie Sections, have been rolled by custom mills and produced in limited shapes going back to the early 1900s (Carnegie Steel Company 1923). British Steel rolls ten different asymmetric I-shapes (British Steel 2018). However, these I-shapes only include a minor reduction to the top flange width. Elevator rail and Railway rail are also asymmetric hot-roll sections. These asymmetric sections are detailed below.

3.2.1. Current British Steel Shapes

British Steel is a subsidiary of the Jingye Group and currently has ten asymmetric section designs that are hot rolled. The sections seem to be rolled by request only. British

Steel refers to their A-sections as Asymmetric Steel Beams (ASB). The sections range in total height from 272 mm (10.7 in.) to 342 mm (13.5 in.). The top flanges (b_{ft}) are 110 mm (4.3 in.) smaller than the bottom flange (b_{fb}) meaning 55 mm (2.16 in.) are taken from each side of the top flange. The top flanges of the beams range from 175 mm (6.9 in.) to 203 mm (8.0 in.), keeping the bottom flange range of 285 mm (11.2 in.) to 313 mm (12.3 in.). The flange thickness (t_f) does not vary from top to bottom flange on each beam. The range of flange thicknesses varies from 14 mm (0.6 in.) to 40 mm (1.6 in.) (British Steel 2018). The British Steel beams are designed to be used with the ComFlor 210 and ComFlor 225 composite floor decks (Tata Steel UK 2017). Figure 5 compares the smallest (280 ASB 74) and largest (300 ASB 249) asymmetric beams in the ten-beam offerings. In addition, Table 1 provides detailed information on each of the ASB sections.

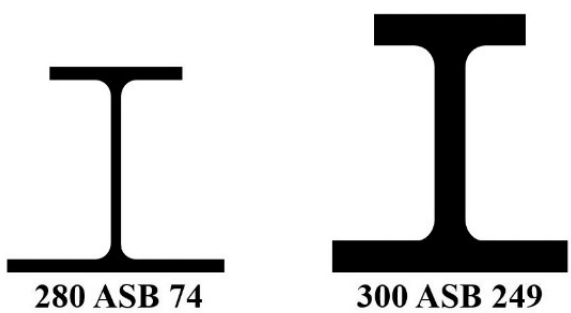

Figure 5: British Steel ASB sections

Table 1: British Steel ASB Shapes Available

Designation:	Section Depth:	Width top flange:	Width bottom flange:	Web thickness:	Flange thickness:		Kg/m and *lbs/ft*
280 ASB 74	272	175	285	10	14	(mm)	73.6
	10.7	6.9	11.2	0.39	0.55	(in.)	*49.5*
280 ASB 100	276	184	294	19	16	(mm)	100.3
	10.9	7.2	11.6	0.75	0.63	(in.)	*67.4*
280 ASB 105	288	176	286	11	22	(mm)	104.7
	11.3	6.9	11.3	0.43	0.86	(in.)	*70.4*
280 ASB 124	296	178	288	13	26	(mm)	123.9
	11.6	7	11.3	0.51	1.02	(in.)	*83.3*
280 ASB 136	288	190	300	25	22	(mm)	136.4
	11.3	7.5	11.8	0.98	0.87	(in.)	*91.7*
300 ASB 153	310	190	300	27	24	(mm)	152.8
	12.2	7.5	11.8	1.06	0.95	(in.)	*102.7*
300 ASB 155	326	179	289	16	32	(mm)	155.4
	12.8	7	11.4	0.63	1.26	(in.)	*104.4*
300 ASB 185	320	195	305	32	29	(mm)	184.6
	12.6	7.7	12	1.26	1.14	(in.)	*124*
300 ASB 196	342	183	293	20	40	(mm)	195.5
	13.5	7.2	11.5	0.79	1.57	(in.)	*131.4*
300 ASB 249	342	203	313	40	40	(mm)	249.2
	13.5	8	12.3	1.57	1.57	(in.)	*167.5*

3.2.2. Elevator Rail

The most asymmetric hot rolled shape found by the author is the elevator guide rail. The elevator guide rail ranges in sizes from the T75 model with a base width of 62 mm (2.44 in.) and height of 75 mm (2.95 in.) to the T127 model with a base width of 127 mm (5 in.) and a height of 89 mm (3.5 in.) (Taicang Xinxing Machinery Factory 2020). Guide rail is rolled by Gerdau and multiple foreign steel manufacturers. Figure 6 illustrates the unique asymmetric guide rail cross-section. The elevator guide rail is not a

hot-roll beam shape but reflects the ability for hot-roll asymmetric cross-sections. The elevator guide rail is used in a vertical application as a track that the elevator rides on.

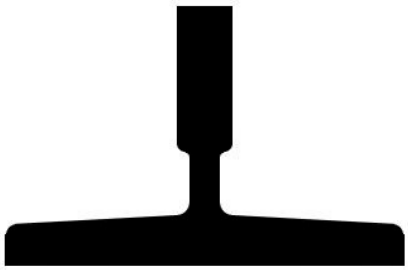

Figure 6: Elevator guide rail

3.2.3. Cross-tie Sections

Cross-tie hot-roll steel sections (Figure 7) were an alternative to timber or steel box railroad track cross-ties. Carnegie Steel in 1923 rolled five unique cross-tie cross-sections, with the smallest section having a height of 76 mm (3 in.) with a bottom flange width of 127 mm (5 in.) up to their largest section with a height of 165 mm (6.5 in.) and a bottom flange width of 254 mm (10 in.) (Carnegie Steel Company 1923). The cross-tie served as a beam resting on the ground, supporting the railroad train rail.

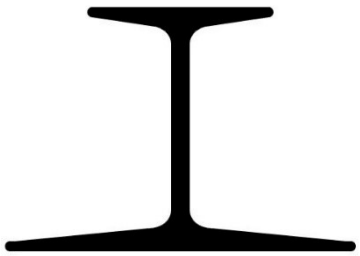

Figure 7: Cross-tie section

3.2.4. Railway Rails and Splice Bars

Railway rail (Figure 8) has been produced for almost a century. Railway rail is one of the most produced hot-roll asymmetric cross-sections. Due to the popularity and early non-standardization, a multitude of rail sizes has been rolled over the last one hundred years. The 1912 Illinois Steel Company manual listed rail sizes from 40 mm (1 9/16 in.) to as tall as 156 mm (6 1/8 in.) with flat base widths of 40 mm (1 9/16 in.) to 156 mm (6 1/8 in.) respectively (Illinois Steel Company 1912). The 1962 United States Steel's manual lists AREMA rail sizes up to 186 mm (7 5/16 in.) with a base of 152 mm (6 in.) (United States Steel 1962). The largest rail researched was the Pennsylvania Standard, with a height of 203 mm (8 in.) and base of 171 mm (6 ¾ in.). Although railroad rail is not typically viewed as a conventional beam spanning between supports, railroad rail is a beam set on an elastic foundation subjected to positive and negative bending moments as the rail is loaded, similar to a continuous beam.

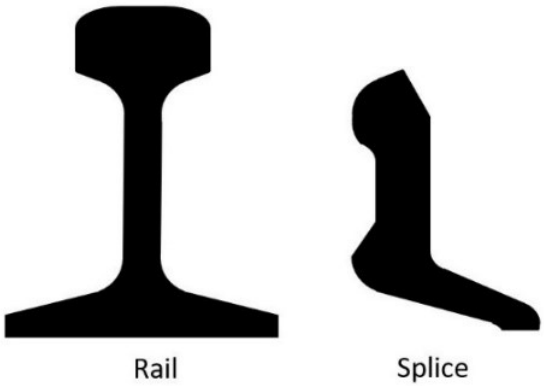

Figure 8: Railroad rail and splice bar

3.2.5. Hot-roll asymmetric section comparison

A limited number of hot-rolled asymmetric sections discussed previously were analyzed for how geometrical the asymmetric sections are. Table 2 is a comparison of a select number of sections from each hot-roll category listed previously. Table 2 shows the percent of beam area above the elastic neutral axis and also a percent of beam area above the mid-height of the section. Table 2 was made to show how asymmetric different hot-roll sections are for an asymmetric comparison.

Table 2: Hot-roll asymmetric comparison

Cross-section analyzed:	Total Section Area:	Area above neutral axis:		Area above mid-height:	
280 ASB 74	9374 mm^2	4129 mm^2	**44%**	3917 mm^2	**42%**
300 ASB 249	31746 mm^2	14510 mm^2	**46%**	13672 mm^2	**43%**
T89 Elevator Guide Rail	1571 mm^2	604 mm^2	**38%**	485 mm^2	**31%**
M21 Cross-Tie	3719 mm^2	1629 mm^2	**44%**	1562 mm^2	**42%**
M28 Cross-Tie	5194 mm^2	2095 mm^2	**40%**	1940 mm^2	**37%**
ASCE 60 Railroad Rail	7670 mm^2	3872 mm^2	**50%**	3788 mm^2	**49%**

3.3. Asymmetric Built-Up Sections

With limited to no availability for hot-roll asymmetric beam sections many manufacturers devised unique methods of producing asymmetric sections. The initial offerings were simple plate girders, but more unique sections utilizing hot-roll sections to increase production in differing rolls were patented and produced. Eight different cross-section designs are presented in this section.

3.3.1. Standard Plate Girder Section

The most common asymmetric cross-section is the built-up plate girder. The relatively simple design incorporates bar stock or cut plates to form the I shape. The cross-section requires a plate for each flange and a plate for the web (Figure 9). For an I-shaped design, welding both the top flange and bottom flange onto the web makes this one of the most time-consuming designs. Plate girders date back to the 1840s and were initially connected using bolts and rivets (Tyrrell 1911). Although labor-intensive, the customization is unmatched, allowing the material dimensions and strength of each section of the beam to be unique.

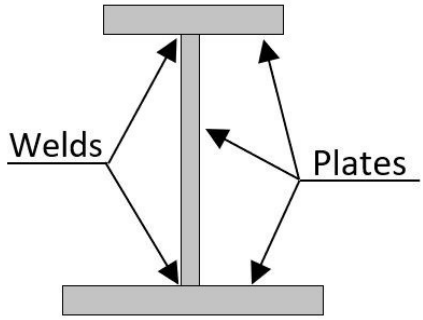

Figure 9: Standard plate girder

3.3.2. Girder-slab

Girder-slab floor systems utilize a semi-built-up section named the D-BEAM®, to achieve the asymmetric beam for their desired shallow floor depths. Currently, Girder-Slab manufactures fourteen D-BEAM variants that range from depths of 203mm (8 in.) to 248 mm (9 ¾ in.)(Girder-Slab Technologies 2016). Girder-Slab D-BEAMS are

manufactured by cutting a larger W-section down the web in a shallow castellated pattern. The two T-section halves of the cut W-section both become the bottom flange of the D-BEAM (Girder-Slab Technologies 2016). A bar is then welded to the cut castellated pattern of the web, becoming the new top flange illustrated in Figure 10. For example, a DB8x45 starts as a W12x58. The web of the W12x58 is cut and a 16 mm x 254 mm (5/8 in. x 10 in.) bar is welded to the cut web producing two DB8x45s. D-BEAMs are designed to be used in shallow flooring systems using precast concrete panels with and without topping slabs (Girder-Slab Technologies 2016). The castellated pattern cut in the web allows additional beam depth to be achieved from the original parent beam depth but requires precise and extensive cutting.

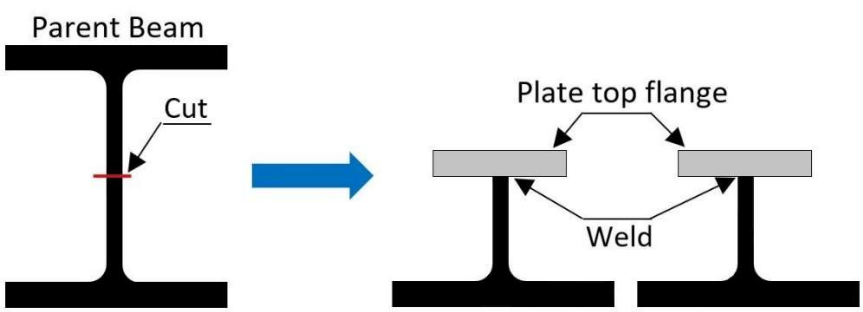

Figure 10: Girder-slab D-BEAM®

3.3.3. Slim-Floor

The Slim-Floor system also utilizes built-up sections to achieve an asymmetric beam section. Slim-Floor has four main asymmetric beam types shown in Figure 11. The four types are the Slim Floor Beams (SFB), H-Beams (HB), and two different Integrated Floor Beams (IFB) sections.

Slim-Floors' first beam type is referred to as Integrated Floor Beams (IFB). Under the IFB there are two distinct types, IFB type A and IFB type B (ArcelorMittal Europe 2017). The IFB type A beam (Figure 11 IFB type A) is made from an HE or IPE rolled section cut longitudinally down the web, which results in two T-sections. Those T-sections become the top flange and web section of the IFB type A beam. A bar wider than the parent beams flange width is then welded onto the web of the remaining T-shape making the IFB type A beam. The IFB type A has a rolled upper section with a welded bottom flange. Slim-Floor lists 44 type A sections ranging from 250 mm (9.84 in.) to 300 mm (11.81 in.)(ArcelorMittal Europe 2017).

The second type of IFB is the type B designation. The IFB type B section (Figure 11 IFB type B) starts with an HE or HP rolled section and is also cut down the web longitudinally, resulting in two T-section beams similar to the IFB type A beam. The difference becomes the assembly of the IFB type B beam. When assembling the type B sections, the rolled parent beam is the lower flange and web of the new section similar to the D-Beams. A bar that is narrower than the parent beams flange width is welded to the top of the T-section completing the IFB type B section (ArcelorMittal Commercial Sections 2019). Slim-Floor lists 18 type B sections that range from 270 mm (10.63in.) to 364 mm (14.33 in.) in depth.

The third type of Slim-Floor asymmetric beam is the Slim Floor Beam (SFB) (Figure 11 SFB). The SFB starts with an HE or IPE rolled section; unlike the previous beams mentioned, there is no cutting done to the SFB parent beam. The section is made asymmetric by welding a bar below the bottom flange. Slim-Floor lists 51 different

sections for their SFBs ranging from 140mm (5.51 in.) to 340 mm (13.39 in.) that are advertised but they can create any custom section from a rolled shape if needed. A slight modification to the SFBs of drilling holes in the web for rebar to pass through making a more secure composite system is referred to as Composite Slim Floor Beams (CoSFB). The cross-sectional design of the SFB and CoSFB are identical.

The fourth and last beam type in the Slim-Floor system is the HB beam (Figure 11 HB). The HB beam is constructed using two UPE hot-roll steel sections and connecting them with threaded rods spaced apart with the web of the UPE sections facing inward (Figure 11 HB). A plate is then connected to the bottom flange of the new section, making it asymmetric, allowing a similar function as the other three beam types (ArcelorMittal Commercial Sections 2019). The voided space between the UPE webs allows concrete to make a composite connection.

The reason for all the different sections is from a weight, price, and composite action standpoint. Slim-Floor recommends the IFB sections when weight is a deciding design factor, where the SFB system is the most cost-effective. The HB is a fully composite system with concrete encasing the in and around the beam. The range of Slim-Floor beams is used with cast-in-place flooring systems and pre-cast panels.

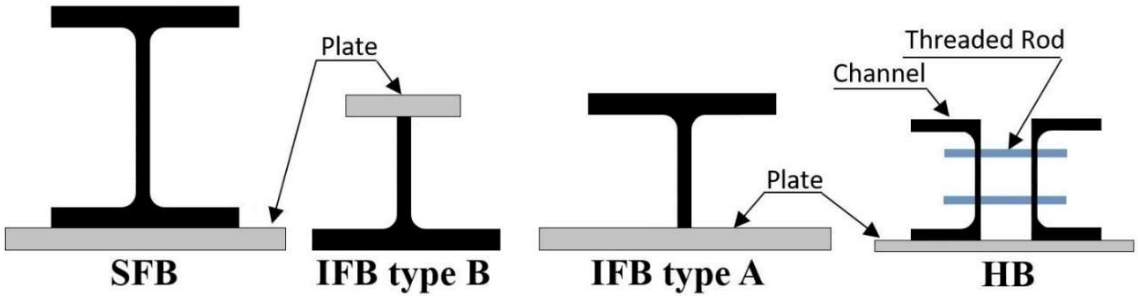

Figure 11: Slim-floor asymmetric beam sections

3.3.4. Kloeckner Westok® Ultra shallow floor beam USFB®

The Kloeckner Ultra Shallow Floor Beams (USFB) cross-sections are achieved without the use of a plate or bar stock. The USFBs are constructed using two hot-roll sections that are cut down the web longitudinally in a castellated pattern. The pattern allows for the new beam to have a taller profile than the parent beams. Kloeckner claims a 40-60% height increase (Kloeckner Metals 2020). After the parent beams are cut, the larger beam sections web is welded to the smaller sections web (Figure 12), creating an asymmetric profile. Since the process is so custom and the options for top and bottom beams so extensive, allowing the use of UB, UC, IPE, HE, HD, HL, and ASTM beams, there are not a set number of USFBs. Due to the popularity of the British Steel ASB Kloeckner supplies a geometric equivalent to the hot-roll ASBs (Kloeckner Metals 2020).

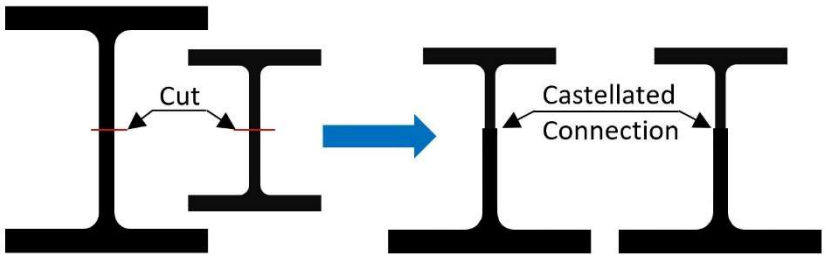

Figure 12:Kloeckner Westok® ultra shallow floor beam USFB®

3.3.5. Peikko DELTABEAM®

The Peikko DELTABEAM® is a buildup welded trapezoidal boxed beam Figure 13. The construction consists of top and bottom flange plates that are welded to two separate web plates making the boxed beam. The DELTABEAM® utilizes a bottom

plate (flange) 2.37-4.5 times larger than its top plate. The web is then placed at an angle of approximately 17°-21°, leaving a bearing surface on each side of the beam for decking. Peikko makes 19 standard D-type or main span sections up to 44 feet in length. The DELTABEAM® ranges in depth from 230 mm-530 mm (9.06 in.-20.87 in.) and has a bottom plate width from 395 mm-860 mm (15.55 in.-33.86 in.). One of the main advantages of the DELTABEAM® is the hollow section construction that allows the beam to be filled with concrete, making the beam a composite beam with confined concrete. The DELTABEAM® also utilized pre-manufactured holes into the webs that allow rebar to pass transversely through the beam, tying the flooring system to the beam.

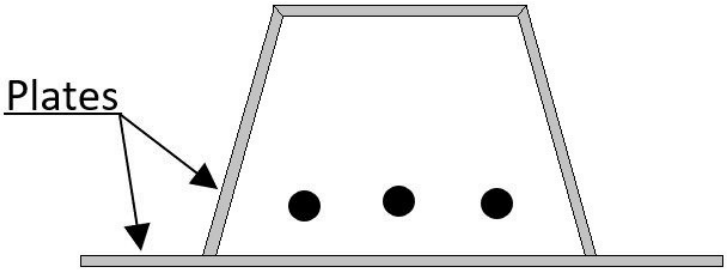

Figure 13: Peikko DELTABEAM®

4. RESEARCH APPROACH

The research approach was to break the study into five separate phases. The five phases are laid out to understand hot-roll asymmetric steel I-beam (A-shape) behavior from production to in-service.

Phase 1 performed thermal-mechanical modeling to evaluate the manufacturing behavior of hot-roll asymmetric beams. Specifically, Phase 1 aimed to understand the residual stress patterns and global deformations that resulted from the cooling after the hot-rolling process. A parametric study was set up in ABAQUS CAE and executed to determine any cross-sectional limits in geometry for asymmetric beams. The modeling process and resulting conclusions from the thermal-mechanical modeling are explained in detail in Phase 1.

Phase 2 was the development of proof-of-concept beams to provide physical insight into the behavior of asymmetric beam cooling and for experimental testing. Standard hot-roll W-sections were modified and reheated to simulate the heating and cooling during the rolling process. The proof-of-concept beams were manufactured to simulate residual stresses and deformation for Phase 3 testing.

Phase 3 was the full-scale experimental testing of a composite floor system utilizing A-shapes, partially using beams from Phase 2. Phase 3 was led by Texas A&M Masters Student, Sheyenne Davis (Davis 2022). The tests consisted of a three-beam composite floor system with precast concrete panels and a cast-in-place topping slab. The beams were monitored during all aspects of construction. After completing the

construction of the floor system, service-level loading was applied and then incremented up to failure.

Phase 4 was an analytical study on the construction and in-service behavior of A-shapes. To evaluate A-shape behavior at critical construction and in-service loading stages, a MATLAB program was written and executed. Phase 4 incorporated limits based on building codes, industry-accepted design guides, Phase 1 study limits, and additional sources as needed to model behavior.

Phase 5 is the recommended A-shape cross-sections that result from a greater understanding of the total A-shape behavior. Phase 5 uses all the asymmetric beam behavioral information gained in Phases 1-4 to make a recommendation on four unique cross-sections to cover 8.0 in. (203 mm), 9.0 in. (228 mm), 10.0 in. (254 mm), and 12.0 in. (305 mm) beam cross-section depths.

4.1. Phase 1: Manufacturing Behavior – Numerical Modeling[1]

4.1.1. Introduction

Early talks with roll mills expressed concern over the global deformations from an asymmetric hot-roll steel beam. Along with the global deformations, another concern structurally is the residual stress patterns present in hot-roll beam sections. An extensive numerical analysis was undertaken to understand any geometric limits due to global

---

[1] Reprinted with permission from "Residual Stress and Global Deflection Limits for Future Hot-Rolled Steel Asymmetric I-Beams" by Eric Stoddard, Matthew Yarnold Ph.D. P.E., 2021, J. Struct. Eng., Copyright 2021 by American Society of Civil Engineers. https://doi.org/10.1061/(ASCE)ST.1943-541X.0003204

deformations and residual stresses. Due to the extreme cost of manufacturing a new rolled shape, numerical research was preferred.

4.1.2. Manufacturing Concerns

The primary contribution of the numerical analysis is the manufacturing limits for hot-roll A-shape cross-sectional geometries. After conversations with the three major US steel mills (Nucor, Gerdau, and Steel Dynamics) and steel industry professionals, some concerns were expressed. Two main manufacturing concerns expressed are due to the cooling of an asymmetric beam cross-section. The first concern is excessive residual compressive stresses, which will impact the lateral-torsional buckling resistance during construction. The second concern (expressed by the steel mills) is global deformations (or curvature). As a result, a comprehensive thermal-mechanical finite element (FE) modeling approach was developed to simulate the behavior of rolled shapes during the cooling process. This included heat-transfer analysis to identify the thermal behavior combined with stress analysis. The general analysis approach was applied to conventional doubly symmetric I-shapes for validation of the methodology. This was performed through a comparison of the results with several accepted stress distributions along with physical experiments and validated FE results. A wide range of A-shape cross-sectional configurations was analyzed to identify the residual stresses and global deformations. The main finding is a recommended flange width-to-thickness limit to satisfy the compressive stress limit. This limit will be used with Phase 4, along with

evaluating other limit states to establish the specific A-shape cross-sections for Phase 5. The other finding was that despite concerns, global deformations are not a concern for realistic proportions of future A-shapes. Further details on the methodology, validation, and parametric study are presented below.

4.1.3. Thermal-mechanical Modeling

3D thermal-mechanical FE analysis was selected for identification of the residual stresses and deformations imposed on hot-rolled A-shapes as a result of cooling. ABAQUS/CAE software was chosen because of its robust nonlinear transient thermal and stress analysis capabilities. The FE modeling was performed with accepted and validated material properties along with FE methods (Quayyum and Hassan 2017) (described in detail in the Material Properties section). A coupled temperature-displacement analysis was chosen, which utilized a 10-node thermally coupled tetrahedral element with second-order accuracy, trilinear displacement, and temperature. The additional information for the modeling process is described in the following sections.

4.1.3.1. Geometry and Boundary Conditions

The cross-sectional geometry of the residual stress FE models was consistent throughout the study. A single tetrahedral element was used through the thickness of the flanges and web. Then the aspect ratio of the elements was set as close to unity as possible. Tetrahedral elements allowed for the fillets to be modeled, which improved the temperature distributions and resulting residual stress distributions. A typical meshing can be seen in Figure 14.

A sensitivity study was performed, which varied the mesh type and seed size. The mesh selected produces accurate results along with sufficient data resolution (validation shown below) while maintaining reasonable processing times. Sensitivity models, implementing hexahedral elements and tetrahedral elements, were studied with varying seed sizes up to 25 percent of the validation flange thickness. Longitudinal stress measurements were compared in all cases. The sensitivity study also considered the stress variation through the flange thickness. Flange stresses were compared between the average and the outer fiber. A resulting difference of less than 1.8% was found acceptable, and the outer fiber stresses were used for the remainder of the study. With processing times on the Texas A&M supercomputer of over 150 hours per model and negligible stress profile differences, the single element meshing was chosen.

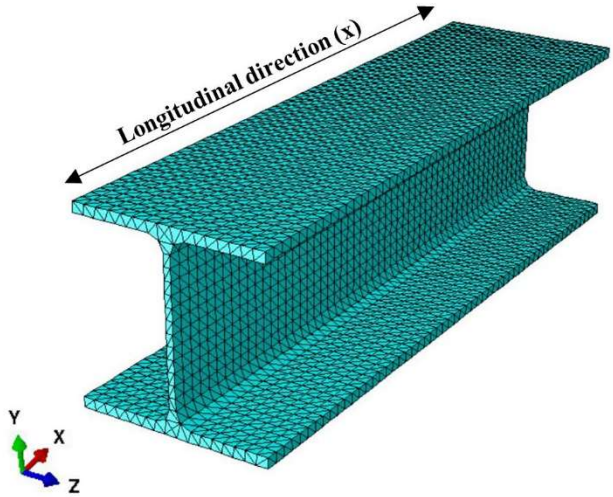

Figure 14: Typical beam meshing (residual stress analysis)

The length of the beams analyzed varied based on the objective of the analysis and the depth of the cross-section. The residual stress models incorporated a length three

times the depth, which has been shown in testing and theory (St. Venant Principle) to allow sufficient stresses to fully develop (Huber 1956). The reason for using a reduced length is to minimize the processing time while still maintaining a sufficient number of nodes for adequate data resolution. For the deformation analysis, 9m (30ft) beams were analyzed. This was considered a reasonable length for hot-rolled beam production based on tours of two different steel mills. A similar sensitivity study was performed for deformation analysis. An appropriate meshing was selected, resulting in processing times of full-length beams up to 50 hours per model.

The beam boundary conditions were pinned or rolled in each corner to allow rotation and beam movement. The beams were not supported between corner conditions, and gravitation effects were not applied. The modeled boundary conditions allowed the beams the ability to "shrink" when cooled without constraint. This was done to eliminate stresses induced by physical constraints.

4.1.3.2. Material Properties

A significant number of material properties needed to be identified and defined in the program to accurately perform the analysis. This included constant properties such as the steel density and temperature-dependent properties such as thermal conductivity, elastic modulus, Poisson's ratio, thermal expansion, film coefficient, latent heat, specific heat, and plastic modulus Figure 15. Past research on residual stress analysis resulting from uneven cooling has shown that many temperature-dependent steel properties are needed for accurate results (Quayyum and Hassan 2017). Many properties of steel are

consistent for different grades of steel. The properties used were to model ASTM A992 steel, with 345 MPa (50 ksi) yield strength.

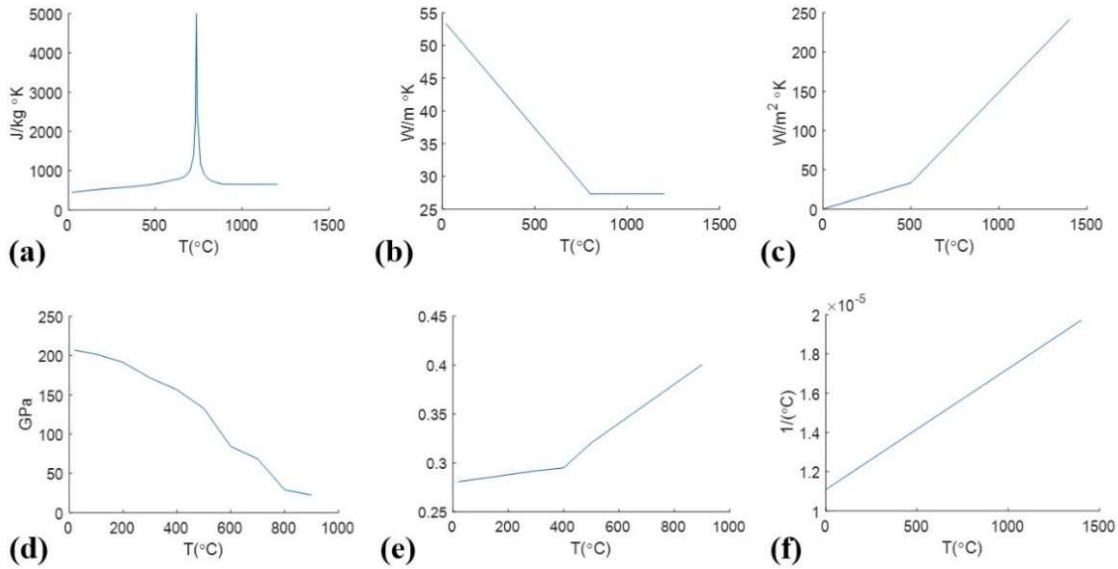

Figure 15: Thermal and material coefficients: (a) specific heat (CEN 2005) (b) thermal conductivity (CEN 2005) (c) film coefficient (Brickstad and Josefson 1998) (d) elastic modulus (Hu et al. 2009) (e) Poisson ratio (Andersson 1978) (f) thermal expansion (AISC 2016)

The thermal and mechanical analyses were coupled; however, the coefficients can mostly be grouped separately. The thermal modeling coefficients needed to solve Fourier's heat equation are density, specific heat, thermal conductivity, surface coefficient, and latent heat (Quayyum and Hassan 2017). The material was assumed to be isotropic and homogeneous. The density of the steel was modeled as constant with temperature and having a magnitude of 7870 kg/m3 (490 lb/ft3) (AISC 2016). The specific heat (shown in Figure 15(a)) was modeled with temperature (CEN (European Committee for Standardization) 2005), where the significant spike at approximately 725 °C (1340 °F) indicates the phase change of the steel. Thermal conductivity also varies

with temperature. Illustrated Figure 15(b) is the bi-linear relationship utilized (CEN (European Committee for Standardization) 2005). The surface coefficient (shown in Figure 15(c)) is also a bi-linear relationship and can be explained as the temperature "loading" (Brickstad and Josefson 1998), which is expanded upon further in 4.1.3.3. Latent heat in this case is the energy released during the liquid to solid phase change. This was derived from the specific volumetric enthalpy (Wickström 1979) and was modeled over the phase change.

The mechanical coefficients needed for the coupled analysis were elastic modulus, Poisson's ratio, thermal expansion, latent heat, and plastic yield. The elastic modulus was varied with temperature, as shown in Figure 15(d). This relationship was taken from tests performed on coupons that were heated to different elevated temperatures and loaded at those elevated temperatures until fracture (Hu et al. 2009). Poisson's ratio was modeled as a bi-linear relationship (shown in Figure 15(e)) (Andersson 1978). The linear coefficient of thermal expansion is provided in Figure 15(f) (AISC 2016).

The plastic yield response is modeled with multiple stress-strain curves at different temperatures (Figure 16). The plastic response was adapted for ABAQUS from past test values from the steel test (Harmathy and Stanzak 2009).

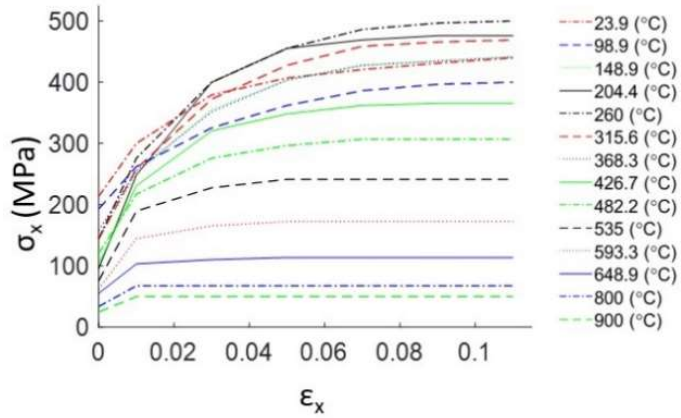

Figure 16: Multilinear kinematic stress (σ_x) vs. strain (ε_x) hardening model adapted from test data

The plastic hardening is modeled as multilinear-kinematic hardening, where the surface is defined by equivalent von Mises stresses. Eq. (1) illustrates the calculations, which include the second-order stress tensor (σ), kinematic shift (α), deviatoric stress tensor (S), and deviatoric part of the back stress (α^{dev}).

$$f(\boldsymbol{\sigma} - \boldsymbol{\alpha}) = \sqrt{\frac{3}{2}(\boldsymbol{S} - \boldsymbol{\alpha}^{dev}) \ : \ (\boldsymbol{S} - \boldsymbol{\alpha}^{dev})} \tag{1}$$

The model assumes the associated plastic flow shown in Eq. (2). In this equation $\dot{\boldsymbol{\epsilon}}^{pl}$ represents the rate of plastic flow and $\dot{\bar{\epsilon}}^{pl}$ represents the equivalent plastic strain rate,

which is provided in Eq. (3).

$$\dot{\boldsymbol{\epsilon}}^{pl} = \frac{\partial f(\boldsymbol{\sigma} - \boldsymbol{\alpha})}{\partial \boldsymbol{\sigma}} \dot{\bar{\epsilon}}^{pl} \tag{2}$$

$$\dot{\bar{\epsilon}}^{pl} = \sqrt{\frac{2}{3} \dot{\boldsymbol{\epsilon}}^{pl} : \dot{\boldsymbol{\epsilon}}^{pl}} \tag{3}$$

The total strain rate ($\dot{\epsilon}$) equation includes the elastic strain rate ($\dot{\epsilon}^{el}$) and the plastic strain rate, as shown in Eq. (4).

$$\dot{\epsilon} = \dot{\epsilon}^{el} + \dot{\epsilon}^{pl} \tag{4}$$

4.1.3.3. Temperature "Loading"

The FE modeling initial conditions were 1300° C (2372° F) (Quayyum and Hassan 2017) to remove any appreciable stress. A temperature below the melting point was chosen to mimic the pre-rolling temperatures of steel beams. To cool the beam to an ambient air temperature of 20° C (68° F) an accepted film coefficient (Figure 15 (c)) for steel was modeled (Brickstad and Josefson 1998). The film coefficient was modeling simple cooling in still air. During the cooling, conduction, convection, and radiation all play a role in cooling the section. The rate at which conduction, convection, and radiation cool the beam is not constant and varies with temperature. To simplify modeling, since all three coefficients vary the speed at which the beam cools, the separate coefficients are combined into a single coefficient. The bi-linear film coefficient takes those cooling parameters into account in one modeled coefficient.

4.1.4. Thermal-mechanical Validation Study

4.1.4.1. Literature Comparison

The thermal-mechanical modeling process, described in the prior section, was used to analyze two separate beam cross-sections, and the results were compared with experimental (and accepted numerical) results from the literature to validate the modeling process. The two cross-sections chosen were the AISC W8x31 and W16x50. These two beam sections were selected because of the ample residual stress test data available in the literature. The FE results for longitudinal residual stresses were compared to physically measured stresses along with accepted stress distributions. The finite element analysis (FEA) results were compared with sectioning results from Lehigh University (Huber 1958) for the W8x31 and sectioning results from Alpsten (Alpsten 1972) for the W16x50. Along with physically measured results, accepted stress patterns from Young (Young 1975), ECCS (ECCS 1984), Galambos & Ketter (Galambos and Ketter 1959), and BSK99 (BSK (Blekinge Studentkar) 2003) were plotted. Accepted numerical results from Quayyan (Quayyum and Hassan 2017) were also presented for the W16x50. The plotted W8x31 stress comparison (Figure 17 (a)) and W16x50 (Figure 17 (b)) illustrates the comparison. The FEA results are within the accepted distributions. In addition, the outer fiber compressive stresses are relatively close to the literature values. Overall, the authors are confident that the FE modeling process produces reasonable results.

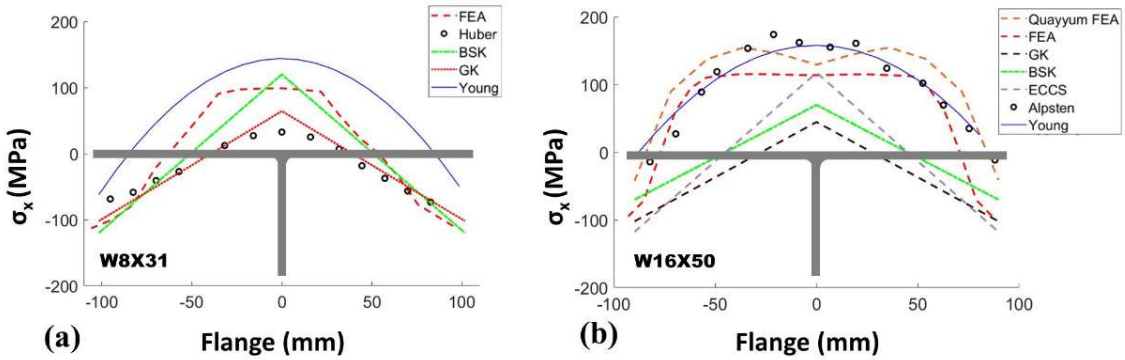

Figure 17: Top flange residual stresses for the (a) W8x31 and (b) W16x50. Note FEA indicates the results from this study.

4.1.5. Parametric Study

A parametric study was devised to determine the cross-sectional limits for manufacturing hot rolled A-shapes. These limits were based on the residual stresses and deformations of the beams after simulated cooling from manufacturing. The general approach was to perform thermal-mechanical FE modeling (described earlier) for different A-shape cross-sectional geometries. The specific geometries investigated and the overall findings are provided below.

4.1.5.1. Cross-Section Geometry

The method for selecting the A-shape cross-sectional dimensions to be analyzed started with a selection of two standard wide flange sections. The selection of the beam cross-sections was based on realistic shapes used for composite building floor systems. It was also desired to include two different depths. The beams chosen were the AISC W8x31 and W18x76. Next, the approach was to vary the width or thickness of the top flange while holding all other dimensions constant. The resulting 30 unique cross-sections are shown in Figure 18. The specific cross-section dimensions were linearly

varied, the flange width and thickness were individually varied from 25% to 200% of the original flange dimensions. Note that the limits produce unrealistic extreme cases that were included to determine the full spectrum of behavior. This included the standard W8x31 along with (7) W8x31 modified top flange width sections (b_{ftMOD}) (1st row of Figure 18) and (7) W8x31 modified top flange thickness sections (t_{ftMOD}) (3rd row of Figure 18). The remaining 15 sections include the standard W18x76 along with (7) W18x76 modified top flange width sections (b_{ftMOD}) (2nd row of Figure 18) and (7) W18x76 modified top flange thickness sections (t_{ftMOD}) (4th row of Figure 18). Note 1.00 b_f and 1.00 t_f are identical and original (non-altered) shapes.

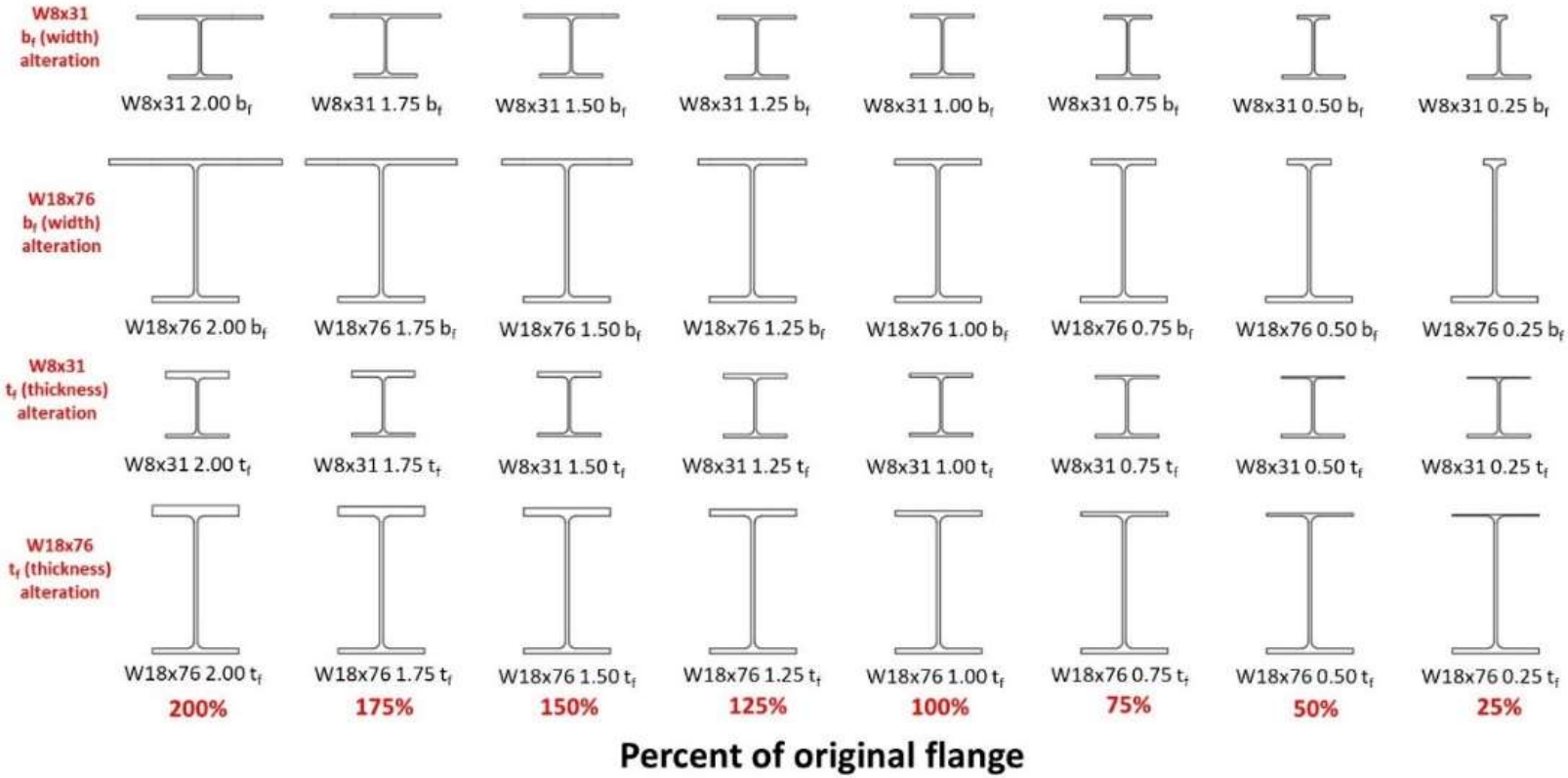

Figure 18: Beam modifications for parametric study

4.1.5.2. Finite Element Analysis

The thermal-mechanical FE analysis was performed for each A-shape cross-section mentioned in the prior section. In total, 30 unique cross-sections were analyzed. The FE analysis began with the standard sections (W8x31 and W18x76). As expected, the uneven temperature variations in the flange during cooling cause a residual stress pattern to form. The temperature variation and resulting residual stress pattern for the W8x31 beam are illustrated in Figure 19. It can be observed how the outer fiber of the flanges cool faster than the middle of the flange, where it meets the web. This typically produces compressive stress at the outer fibers of the flange where the flange is rapidly cooling, and tensile stress in the flange middle where there is more steel and cooling is slowed. These temperature and stress distributions for doubly symmetric beams can be of significant magnitude. Altering a flange increases or decreases the flange's ability to cool, affecting the residual stress pattern. In addition, changes to only one flange produce unsymmetrical temperature variations along with the height of the section, which induces global deformations (results presented below). The entire parametric study beam meshes and stress distributions are presented in Appendix A.

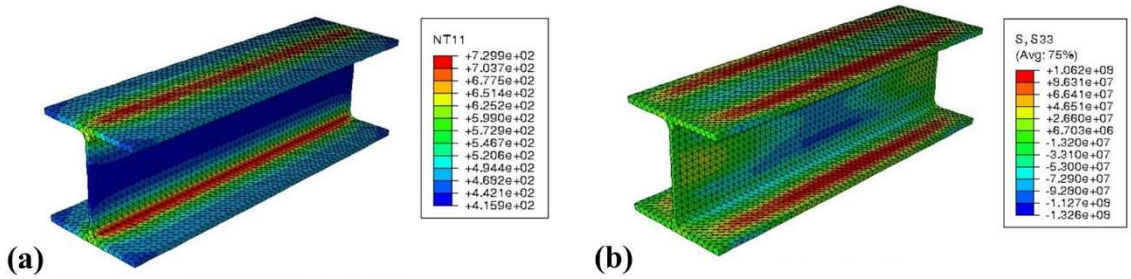

Figure 19:(a) FE model W8x31 temperature distribution at 300 seconds (b) FE model W8x31 longitudinal stresses at 300 seconds. Units are in ◦C and Pa, respectively.

The FE residual stress results for the flange thickness changes are provided in Figure 20. In both the W8x31 (Figure 20 (a)) and W18x76 (Figure 20 (b)) cases, the highest compressive stresses at the flange outer fiber were seen in the very thin cases ($0.25t_{ft}$). This is due to the high width-to-thickness ratio of the flange, producing high-temperature variations across the flange during cooling. The W8x31 altered beams showed a very consistent outer fiber stress of around 100 MPa (14.5 ksi). Even doubling of the flange thickness ($2.00t_{ft}$) did not affect the compressive outer fiber. The outer fiber of the $0.25t_{ft}$ W18x76 dipped below the 200MPa (29 ksi) of compression (Figure 20 (b)), again due to the relatively high ratio. For both the W8x31 and W18x76 cases, the tensile stress at the web connection lowered (or stayed consistent) with increasing flange thickness (t_f).

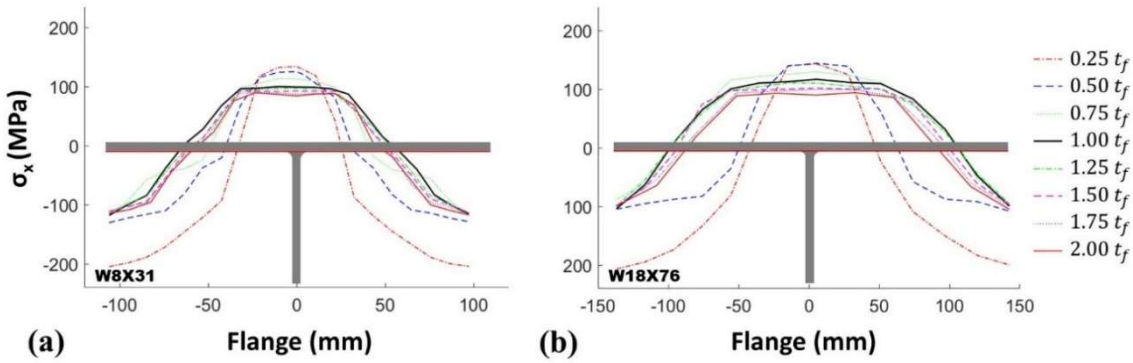

Figure 20: FE stress profiles for top flange thickness variations of the (a) W8x31 cases and (b) W18x76 cases.

The FE results for the flange width changes are provided in Figure 21. The modification of width did not show extreme compression stresses forming as with the thickness changes. This is due to the relatively low width-to-thickness ratio's (and resulting temperature variations during cooling), even for the 2.00 b_{ft} case. Residual stresses stayed relatively consistent through the thickness of the flange. The thickest flange modeled was the W18x76 2.00b_f which had a b/t of 4 and thickness of 34.5 mm (1.36 in.).

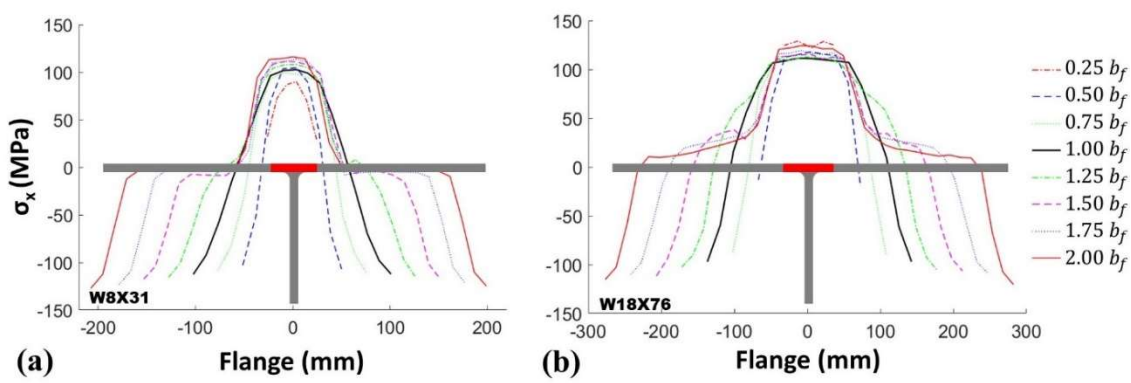

Figure 21: FE stress profiles for top flange width variations of the (a) W8x31 cases and (b) W18x76 cases

The W8x31 (Figure 21(a)) and W18x76 (Figure 21 (b)) both show maximum compressive stresses of approximately 120MPa (17.4 ksi) at the outer fiber. A reduction in flange width ($0.25b_{fi}$) has a very low width-to-thickness resulting in tension at the outer fiber of the flange.

Web residual stress profiles (Figure 22) share interesting insight into how flange alterations influence residual stress profiles in the web. The changing of flange thickness (t_{ftMOD}) had the largest impact in the web, causing a decrease in web compressive stresses at the thinnest profiles in both the W8x31 and W18x76.

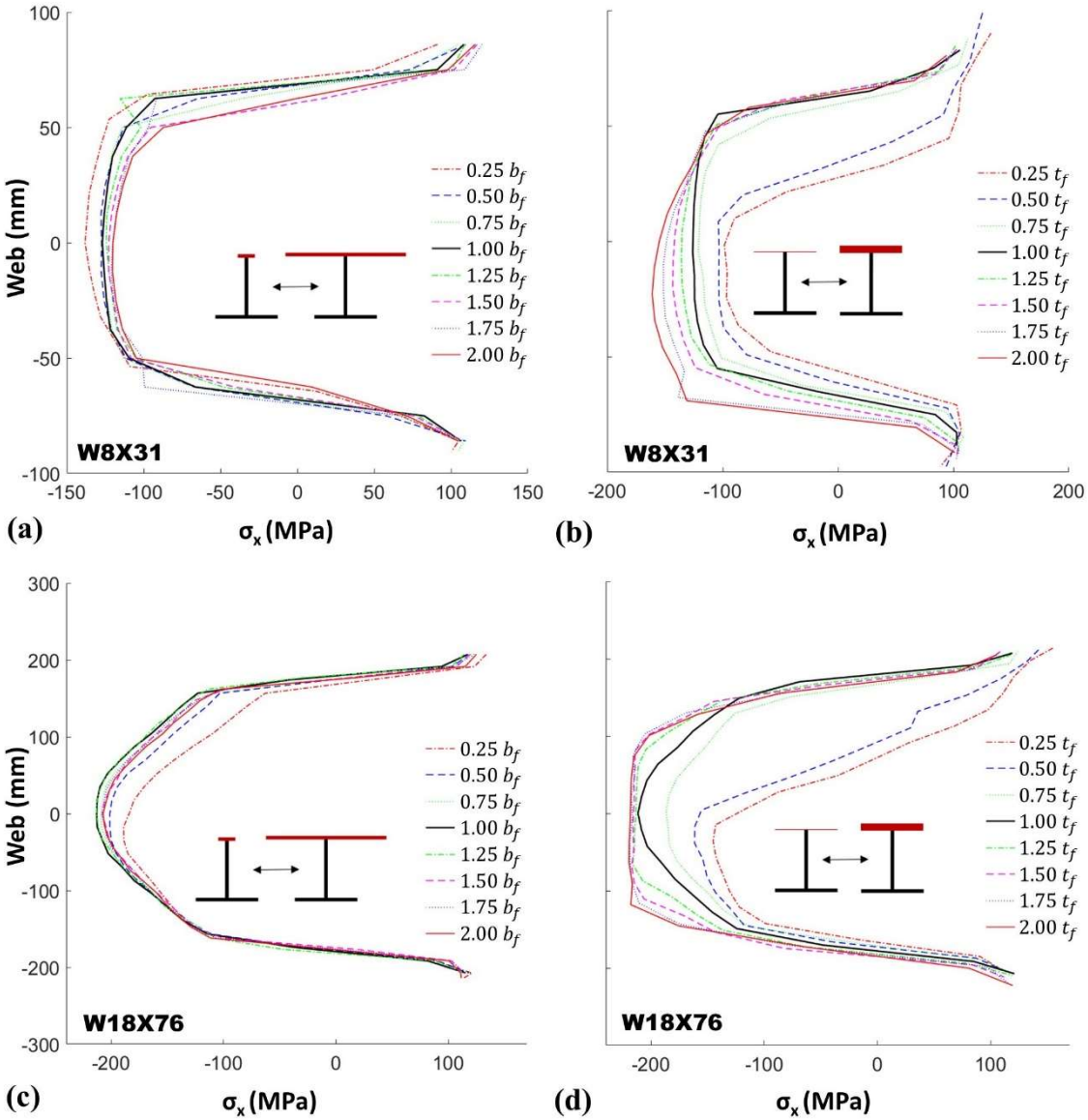

Figure 22:Web residual stress profiles for width and thickness variations (a) FE stress profiles for top flange W8x31 width variations (b) FE stress profiles for top flange W8x31 thickness variations (c) FE stress profiles for top flange W18x76 width variations

4.1.5.3. Findings

4.1.5.3.1. Residual Stresses

The goal of the parametric thermal-mechanical FE modeling study was to better understand A-shape residual stresses and deformations so that cross-sectional manufacturing limits could be established. Using the residual stress data obtained in the parametric study, many standard geometric properties were studied to find a correlation with the residual stress at the flange outer fiber. The outer fiber stresses were the focus because, as shown above, this is the location with the highest compressive stress. It is anticipated that most A-shapes will be utilized in composite floor systems where the top (reduced) flange is in compression. As a result, global stability is a concern. Residual stresses are a critical parameter for stability analysis. Note detailed stability analysis is identified as future research and explained below.

The geometric relationship that best correlates with flange outer fiber residual stress is the width-to-thickness (*b/t*) ratio of the flange, where the projected width (*b*) is defined as half the total width of the flange (consistent with AISC). Figure 23 plots the normalized outer fiber stress (residual stress divided by yield stress) from each beam vs. the *b/t* ratio of the modified flange. A 30% yield stress limit was also plotted on the graph, showing the current quantity used by AISC in many specification equations (AISC 2016). Using Figure 23 for reference, a *b/t* limit of 17 was selected by the research team as the cross-sectional limit for manufacturing A-shapes.

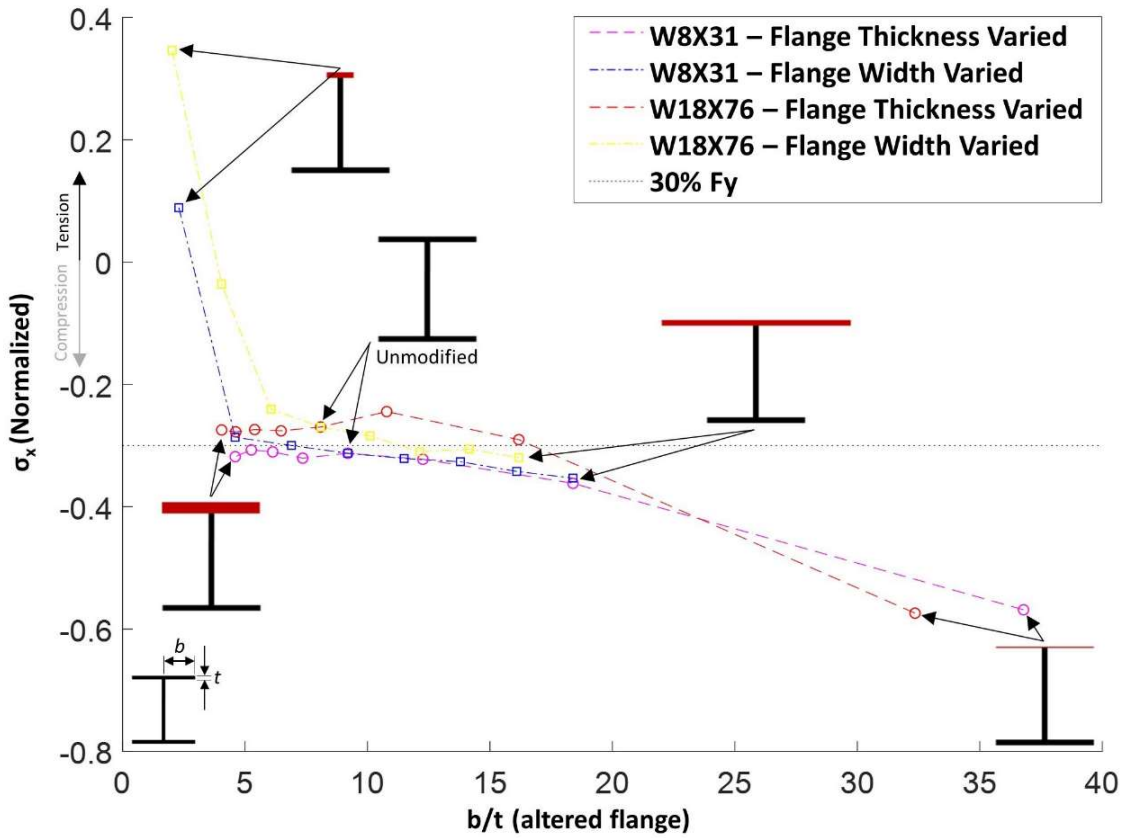

Figure 23: Normalized flange outer fiber residual stress vs. b/t

4.1.5.3.2. Global Deformations

Global deformations were evaluated to anticipate potential future manufacturing issues. These deformations have been expressed as a concern by some in the steel industry. Manufacturing deformations can be fixed with rotary straightening. However, excessive deformations could make the beams more difficult to handle throughout the mill. In addition, the more severely deformed the beam, the more straightening is required, which can impact the cost and resulting future use.

To evaluate global deformations, 9m (30ft) length beams were analyzed to mimic realistic manufactured lengths. The 9m (30ft) A-shapes were modeled using the

parameters and boundary conditions presented previously. Figure 24 illustrates positive and negative camber definitions.

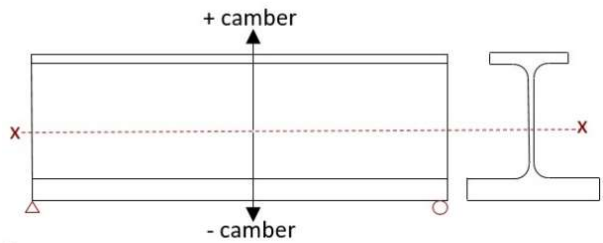

Figure 24: Beam camber sign convention

The global deformations (camber) were the primary focus and determined for all A-shapes. As a visual reference, the modified W8x31 with 2.00 b_{ft} and 0.25 b_{ft} deflected shapes are provided in Figure 25(a) and Figure 25(b), respectively. Figure 25(a) illustrates positive camber as defined by Figure 24. The reason for the positive camber is the vertical temperature profile during cooling. The bottom of the beam cools faster, causing greater contraction of this portion of the beam. The opposite situation (negative camber) arises for cases similar to Figure 25(b).

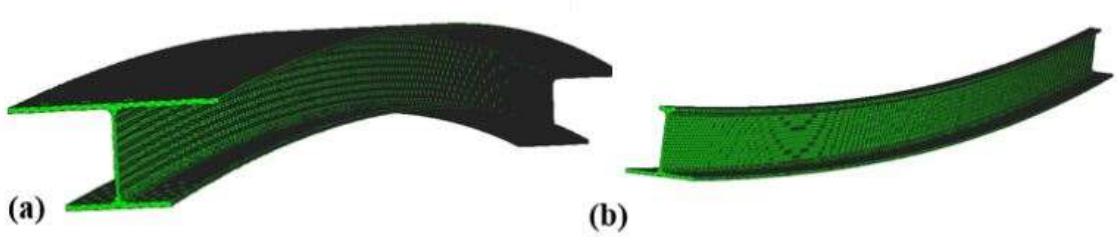

Figure 25: (a) 9m FE model of a W8x31 with 2.00 b_{ft} (b) 9m FE model of a W8x31 with 0.25 b_{ft}

The 9m (30ft) beams were first modeled without initial imperfections. This provided an understanding of deflection behavior for each case. Then, initial

imperfections of L/125 or 7.32 cm (2.88 in) were extensively explored. The nodal input locations were altered, creating a parabolic curvature. An extreme value of L/125 was imposed in the direction the beam tended to deflect due to the geometry. Worse case models of W8x31 0.25 b_f and W8x31 2.00 t_f were analyzed. The results showed that initial imperfections produced nearly the same cooling deformation as those without initial imperfections. As a result, all the displacement data shown is without initial imperfections and only represents the deformations as a result of cooling. Figure 26 provides the camber results for all cases. These results were compared to the ASTM A6 (ASTM A6 / A6M-19 2019) camber limit for channels since they are also asymmetric hot rolled sections. For 9m (30ft) beam lengths, the limit is approximately 1.91 cm (0.75 in). In total, nine of the modeled sections did exceed the ASTM A6 channel limits. However, in all but one case, the exceedance was relatively small. The largest global beam center displacement from the study was the W8x31 with 0.25 b_{ft}, which is an extreme case primarily included to capture the full range of behavior. Note for comparison, Figure 26 also provides the ASTM A6 camber limit for W sections, which is equal to 0.95 cm (0.375 in). This limit would be overly stringent for a hot-rolled asymmetric section and provided for context.

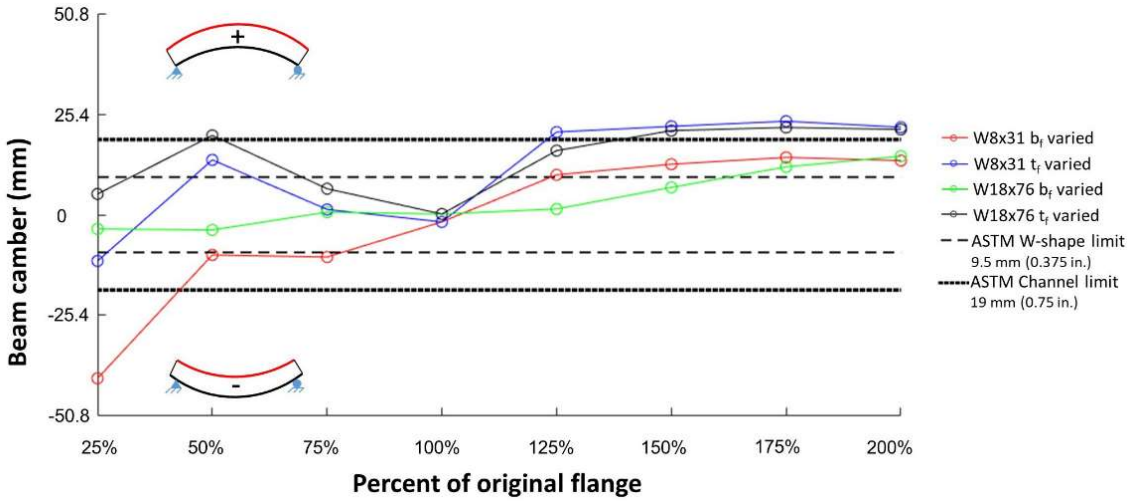

Figure 26: Global deflections

4.1.6. Manufacturing Conclusions from Numerical Modeling

This phase quantitatively determined manufacturing limits that are required for hot-rolled A-shapes. The investigation focused on the induced residual stresses and deformations as a result of the cooling process. A comprehensive thermal-mechanical FE modeling procedure was developed to simulate the behavior of hot-roll shapes after the rolling process. This included heat-transfer analysis to identify the thermal behavior combined with stress analysis. Validation of the methodology was performed through a comparison of the numerical results with accepted physical experiments from the literature and proof-of-concept beams (discussed in the next section). Then, using the validated methodology, a wide range of A-shape cross-sectional configurations were analyzed to identify the residual stresses and global deformations. The primary findings include the following:

- A flange *b/t* limit of around 17 is recommended to manufacture A-shapes with compressive residual stresses below 30% of the yield stress.

- No cross-sectional limit is recommended to satisfy the global deformation (camber) of A-shapes. Some cases exceeded the ASTM A6 camber criteria utilized. However, the magnitude of exceedance was sufficiently small enough to be corrected with rotary straightening.

4.2. Phase 2: Manufacturing Behavior – Proof of Concept Beams and Expert Feedback

4.2.1. Proof-of-Concept Beam Comparison

Proof-of-concept (POC) A-shape beams were devised by the author and produced by Nucor to replicate a hot-roll A-shape. The primary purpose for creating POC beams is for future full-scale laboratory testing. However, a secondary purpose was to utilize their cooling rates to further validate the thermal-mechanical modeling process.

The high cost of retooling rolling mill stands along with the lack of understanding for A-shape behavior, necessitated a creative solution to develop POC beams. Therefore, the general approach was to cut down (or narrow) the top flange of a W-shape, reheat the beam, and then let it cool in a similar manner to conventional rolled shapes (Figure 27). This approach does not capture the correct grain structure but was still considered sufficient for research purposes.

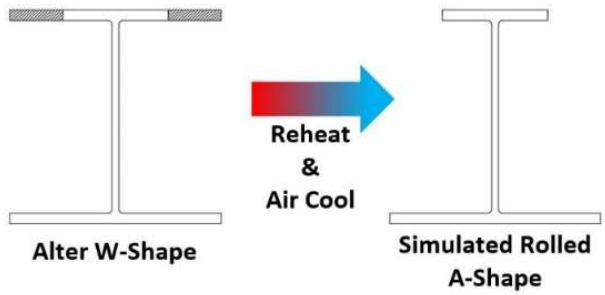

Figure 27: Process to create Nucor POC beams

The specific process to produce the POC beams was initiated with donated W12x65 beams from the Nucor-Yamato Steel facility in Blytheville, Arkansas. The beams were then shipped to the Nucor facility in Longview, Texas. In the Longview facility, the top flange of the W12x65 beams was cut longitudinally, removing 7.62 cm (3 in) from each side of the flange Figure 28. This resulting asymmetric beam was labeled as an A12x53 or W12x65 0.50 b_f beam.

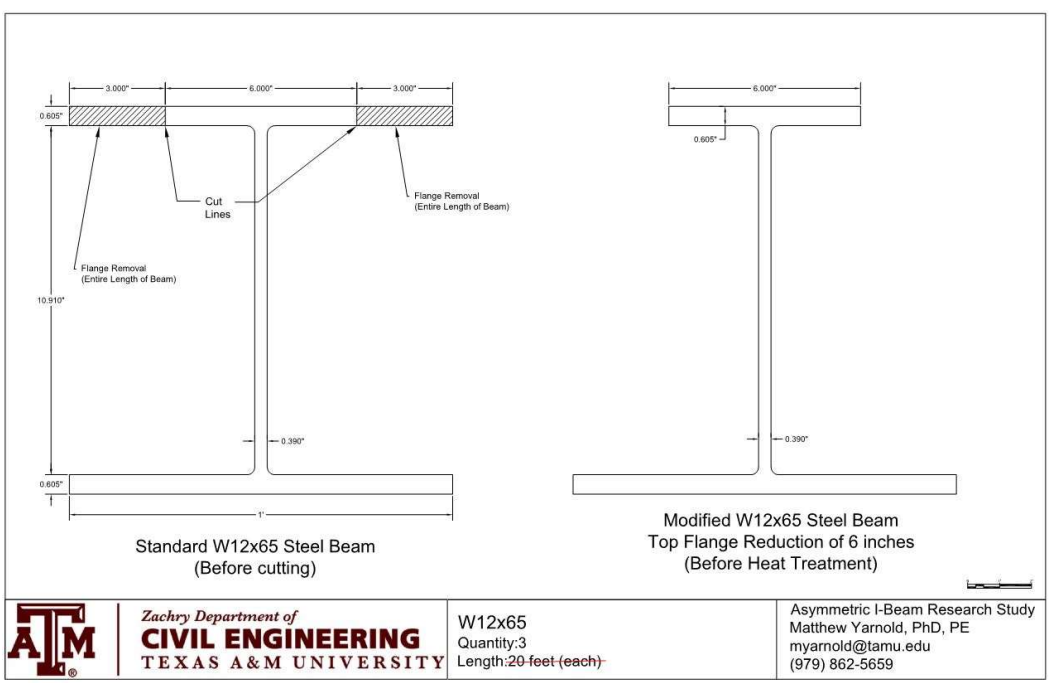

Figure 28: POC beam plans

Longview also had the required ovens for heating the beams once cut. The beams were heated to approximately 950ºC (1740 ºF). The reheated beam removal from the oven can be seen in Figure 29. Again, the POC beams were produced to mimic rolled shapes without the extensive cost of having to retool an entire roll line.

Figure 29: Reheated POC A-shape beams being removed from the oven

During the cooling process of the POC beams, non-contact temperature measurements were taken by the research team. These measured temperatures were compared to the FE model temperature distribution, as shown in Figure 30. The percent differences ranged from 1.9% to 15.8%. The differences were attributed to challenges with conducting accurate temperature measurements along with aspects of the cooling process not included in the model (e.g., convective heat transfer from a slight wind and beams cooling in groups). Overall, the research team believes the POC beam thermal behavior further validates the FE modeling approach.

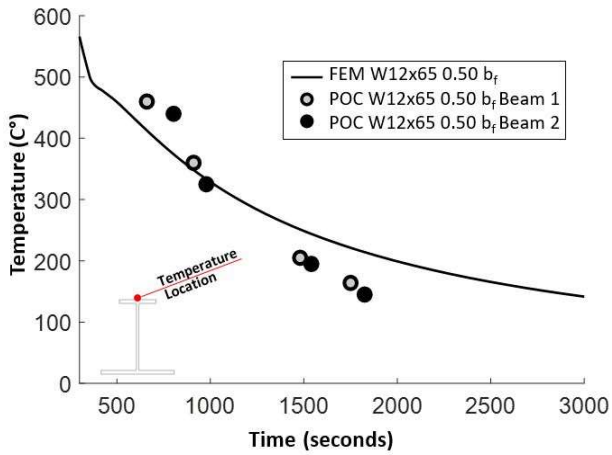

Figure 30: POC W12x65 temperature distribution for physical beams and validated FE model

4.2.2. Expert Feedback

The author obtained expert feedback from interviews/meetings with the three major US steel producers. Expert feedback came in the form of zoom meetings with industry roll-pass engineers, roll pass designers, metallurgical engineers, roll mill supervisors, and product developers from Nucor, Steel Dynamics, and Gerdau. In total, four separate meetings were held with the three steel producers. A summarized version of the information provided for increasing the feasibility for rolling an A-shape is listed below.

- Moving material due to unbalanced areas can cause steel to be overworked (Nucor Corporation 2020)
- Thicken top flange to balance flange areas (Steel Dynamics 2020)
- Roll lengths of beams up to 240 feet (Steel Dynamics 2020)
- Utilize water spray to control beam warping (Steel Dynamics 2020)

- Matching flanges to currently rolled shapes would reduce cost (Steel Dynamics 2020)
- Balance work ratios between top and bottom flanges (Steel Dynamics 2020)
- Use A992 grade 50 steel (Steel Dynamics 2020)
- Balance mass or weight in the top and bottom flanges (Gerdau 2021a)
- Using enlarged fillets for reduced cracking at flange-web connection due to asymmetry (Gerdau 2021a)
- Keep dimensions within a wide flange family (Gerdau 2021a)
- Workability would depend on the closest near-net shape (Gerdau 2021a)
- Up to a 12-inch flange on an 8-inch section should be achievable (Gerdau 2021b)
- 10 inch or narrower would be preferred on the bottom flange (Gerdau 2021b)
- Equal flange areas are preferred (Gerdau 2021b)
- Use A992 grade 50 steel (Gerdau 2021b)
- Thin webs are difficult to roll with thick flanges (Gerdau 2021b)
- Minimum web thickness of 0.5 inches with a flange thickness to web thickness of no more than a 1.5-2 ratio (Gerdau 2021b)
- An additional A-shape challenge is the beam is asymmetric on a different axis than most asymmetric sections. The A-shape is rolled in the H

position making the asymmetry side to side. Most asymmetric cross-sections are symmetric side to side. (Gerdau 2021b)

4.3. Phase 3: Construction and In-service Behavior - Experimental Testing

4.3.1. Introduction – Experimental Testing

The experimental testing in phase 3 was a physical test of A-shape beams within a shallow precast panel floor system. The floor system steel framing consisted of six stub columns and three A-shape beams. The full-scale floor system utilized fabricated A-shape beams supporting pre-cast concrete panels on the top of the bottom flange (Figure 31). The floor system was finished with a concrete topping slab for composite in-service performance. The floor system was developed, built, instrumented, and tested by the research team. This phase of the research was achieved in part with Texas A&M Master's student Sheyenne Davis (Davis 2022).

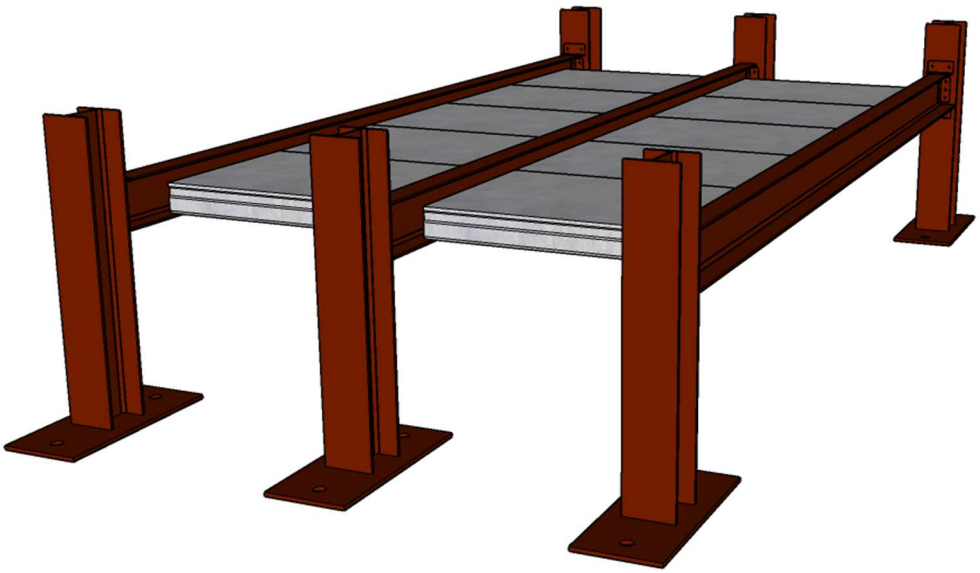

Figure 31: Full-scale Experimental Floor Set-up

4.3.2. Floor System Development

The development of the full-scale floor system started with the POC beams produced by Nucor (section 4.2). The decision was made to use one of the POC A12x53 beams and design the floor system around that beam. Three large constraints helped guide the floor system design. The first was the length of the POC beam. The POC beams were 30 feet in total length. The two other constraints on the floor system came directly from the Center for Infrastructural Renewal (CIR). The CIR houses the structural high bay laboratory where the construction and in-service testing was performed. The CIR has a grid of hold-down locations spaced on the strong floor in a 3-foot grid pattern, illustrated in Figure 32. Figure 32 also shows the hold-down rods used to anchor all the test equipment to the CIR strong floor. Those hold-down rods anchor through the floor by attaching a washer and nut to the top and bottom of a 4-foot steel rod 2.5 inches in diameter. The underneath floor attachment is shown in the floor assembly section below. The unique aspects of the design were to accommodate the 3-foot grid system with the loading frame and the test floor specimen.

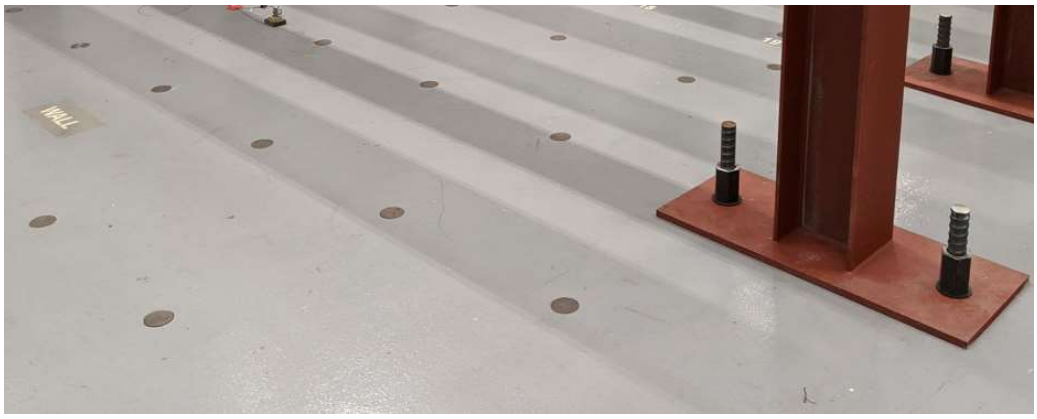

Figure 32: CIR floor hold-down grid and tension rods

The last constraint was due to the width of the loading frames. The maximum width of the floor system was governed by the header beam. The loading frame width is dictated by the header beam used. The header beam spans between the two columns, essentially completing the loading frame assembly. The header beam is what supports the hydraulic actuator during in-service and ultimate loading. The CIR has header beams in 3-foot length increments. The loading frame and the differing header beam spacings were drawn in AutoCAD for reference. To keep the floor systems symmetric, a three-beam set-up was chosen, as shown in Figure 33.

To keep a symmetric three-beam configuration, a beam spacing of 3-foot, 6-foot, or 9-foot was considered. A 6-foot beam spacing was selected, which required the use of an 18-foot header beam. With the header selected, the constraints on the width of the floor system were set. The reason the header beam was 6 feet wider than the floor systems was to allow the loading frame to anchor in the strong floor mounting holes on each side of the test specimen (Figure 33). The loading frame header beam was constructed out of two W24x103 sections bolted together, and the two columns were W12x106 with welded baseplates. The header beam spanned between the tension columns.

With the floor system specimen beam spacing set, the length of the system could be determined. The length of the floor system was constrained by the length of the POC beams, the CIR strong floor hold-down 3-foot grid, and beam cross-section. To keep the loading frame centered over the floor system, the spacing between the test specimen

columns required an odd number between base plate attachment points (Figure 33). The spacing needed to be between 5-3 foot grid spaces and 9-3 foot grid spaces. The five grid spaces or 15 feet required a beam length of approximately 17 feet to span between specimen stub columns. Due to larger beam depths, the 17 feet span was not as long as needed for the test. The seven grid spaces required a beam length of approximately 23 feet. The nine spaces put a beam length at our specimen length of 29 feet. Due to the method of POC beam production, the smaller top flange thickness placed the 29 feet beam length beyond acceptable for the proposed loading, so the 7-3 foot spacing was selected. Drawing the 7-3 foot spaces resulted in column center to center spacing of 24 feet and a beam length of 22 feet-10 inches.

The specimen columns to support the floor system were constructed of 6.5-foot lengths of W12x65 sections, which were welded to a one-inch base plate. The 1-inch thick base plate was sized with two holes spaced 3-feet apart to accommodate the CIR floor hold-down pattern with the column welded in the center of the base plate. The base plate dimensions were 48 inches by 20 inches.

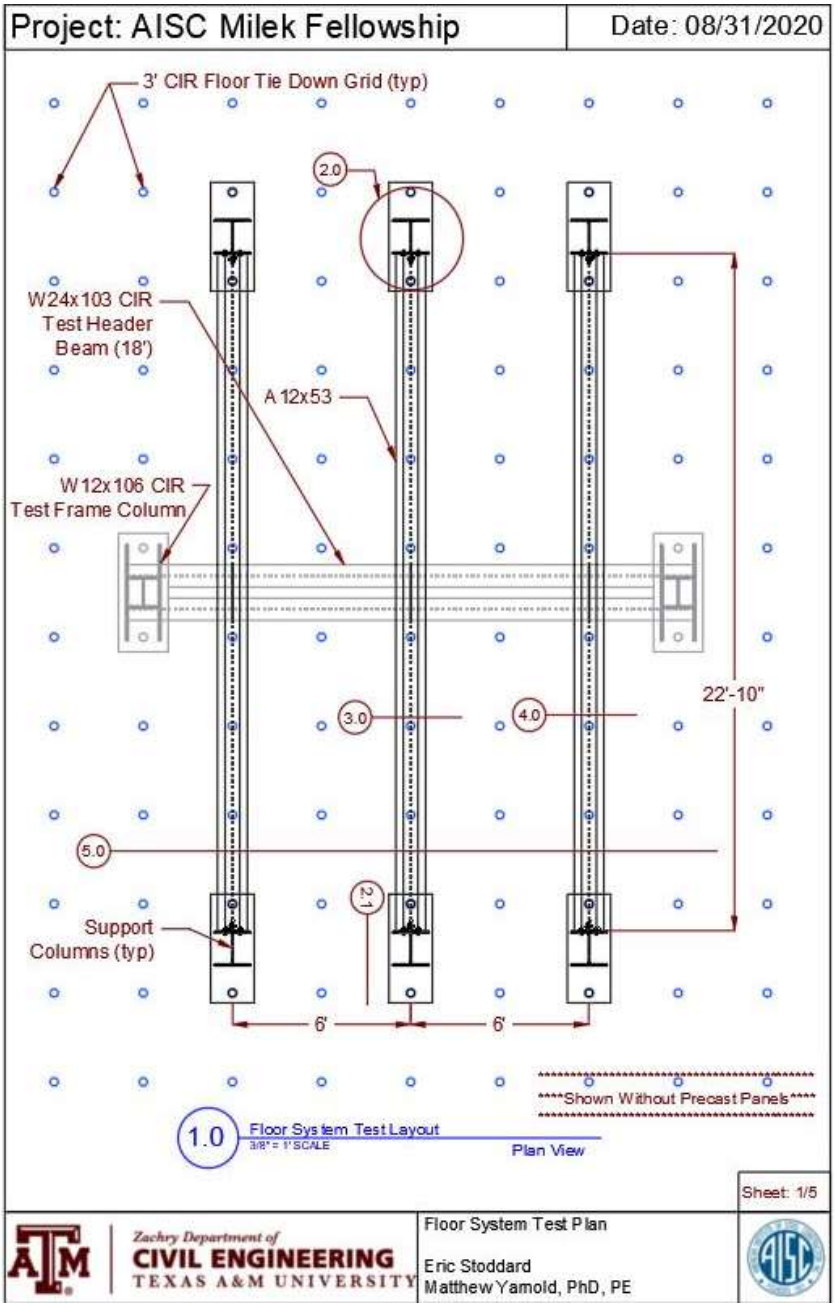

Figure 33: Initial full-scale floor system layout with CIR grid

4.3.3. Floor System Assembly

The floor system framing was comprised of three A-shape fabricated beams, six stub columns, and shear tabs for the beam to column connection. The edge beams and

the columns were fabricated by Davis Iron Works. The edge beams were W12x65 beams that had a reduced top flange of six inches, renamed A12x53. The top flanges were cut by Davis Iron Works. Figure 34 shows the delivery of the Davis fabricated beams. The beams came with web punched bolt holes for shear tab connections.

Figure 34: A12x53 fabricated A-shape beam delivery
(image by Matthew Yarnold)

The second part of the framing fabricated by Davis Iron Works was the stub columns. The stub columns were fabricated from six and a half foot lengths of W12x65 sections with a one-inch thick base plate welded to the W-section. The 20-inch x 48-inch base plate was for connection to the CIR hold-down system. Figure 35 shows how the columns were delivered. Each column was punched with six 13/16 inch holes for connection with the beam shear tabs. The placement of shear tab holes placed the centerline of the beam at four and a half feet off the floor. In total, six identical stub columns were fabricated for the test specimen.

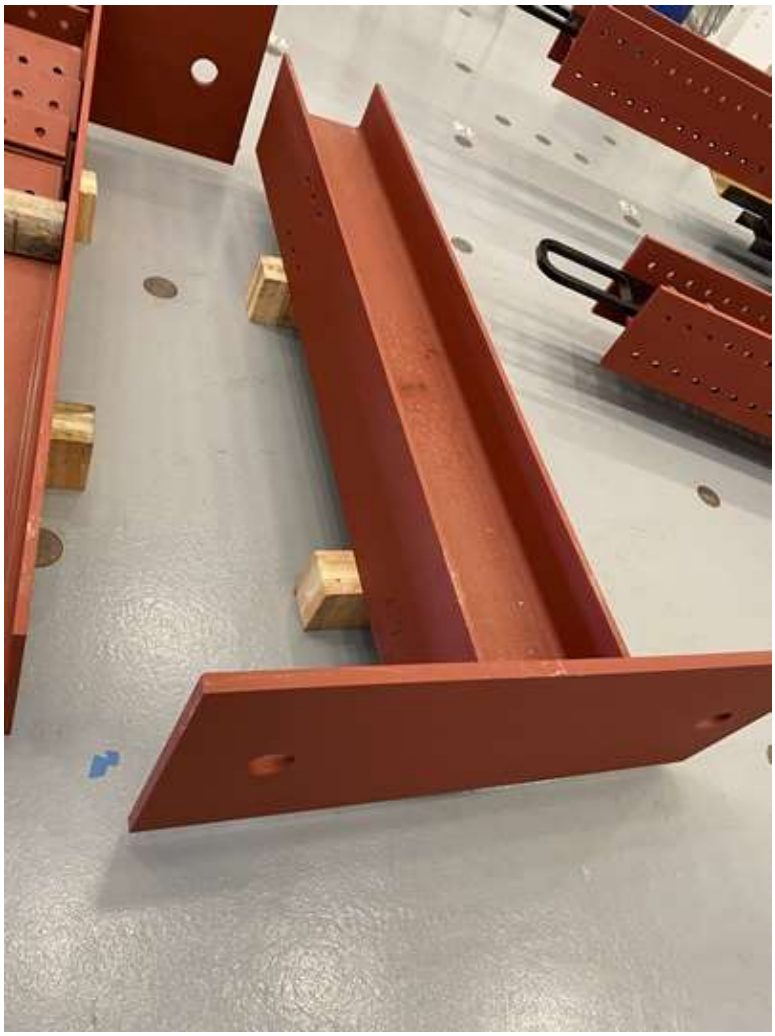

Figure 35: W12x65 stub columns with welded base plate

The final part that was fabricated off-site by Davis Iron Works was the shear tab connections. These shear connections (Figure 36) were cut and punched from a 5 inch by 3½ inch by 3/8 inch angle. In total, twelve shear tabs were fabricated. The same 13/16 inch hole size was punched in each leg of the angle. Each beam to column connection originally consisted of two shear tab connections, one on each side of the beam web.

Figure 36: Beam to column shear connection
(image by Matthew Yarnold)

Along with the off-site fabricated elements discussed previously, in-house components were fabricated to change the connection for erection purposes and to stiffen the edge beam-column connection. The center beam was also fabricated from the Nucor POC beams 4.2. The CIR facility and personnel were instrumental in the alterations and fabrication needed. With the change to the edge beam to column connection, additional alterations to the stub columns were necessary.

To alleviate alignment issues, new shear tabs were fabricated with slotted holes in the 5-inch leg that connected to the column face. The snug fit of the old shear connections without slotted holes did not allow any movement in the connection which would make squaring the steel frame after erection impossible. Figure 37 shows the slotted holes that were punched in the longer leg of the angle and the same 13/16 inch hole punched for connection to the beam web. Figure 38 is the angle fabricated in Figure 37 attaching the A-shape beam to the stub column.

Figure 37: Beam to column shear tab with slotted holes

Figure 38: Beam to column shear connection with slotted holes, installed

The second component that was produced in-house by the CIR was the center A12x53 beam. This beam was previously cut and heated by NUCOR to simulate a hot rolled beam section 4.2.1. This beam had to be cut to length, mill scale removed, and holes drilled for attachment to the fabricated columns. This work was done by Eric Stoddard and Sheyenne Davis, with guidance from Charlie Droddy and the CIR staff. Figure 39 is the POC beam after being cut to length and having the web drilled from the shear tab connection to the stub columns. Figure 40 is the finished and primed beam.

The beam was primed to have the same finish as the beams produced by Davis Iron Works. The large difference between this center beam and the edge beams was the heating process the center beam was fabricated with (to achieve realistic residual stresses), and the edge beams did not undergo heating and subsequent cooling after top flange reduction.

Figure 39: Center A12x53 connection holes

Figure 40: Center A12x53 beam primed and drilled

With no previous testing on A-shapes from cut W-shape sections, it was decided to stiffen the connection on the outer beam to column connection to reduce rotation induced by eccentric loading on the edge beams during the concrete topping slab placement. The connection was stiffened by adding an angle to the top and bottom flange of the edge beams. The four edge stub columns had additional holes drilled to accommodate the more fixed connection design. Figure 41 shows the six holes that were punched for the shear tab connection and the additional two sets of holes above and below the shear tab holes. Those additional four holes were for the addition of the aforementioned angles. The angle was bolted to the stub column and welded to the beam flange Figure 42. The bolting to the stub column was two-fold, it would simplify the disassembly after the testing by not having to cut welds between the beam and column,

and it would also allow the connection to be unbolted, allowing only the shear tab to handle the rotation. The additional fixity at the connection was not a concern during panel-loading but was implemented for the topping slab pour later in the construction testing. Since the middle beam would not be subjected to appreciable eccentric loading during the concrete pour, only the edge beam connection was modified. Figure 43 represents the typical edge beam connection with shear tabs, top angle, and bottom angle installed.

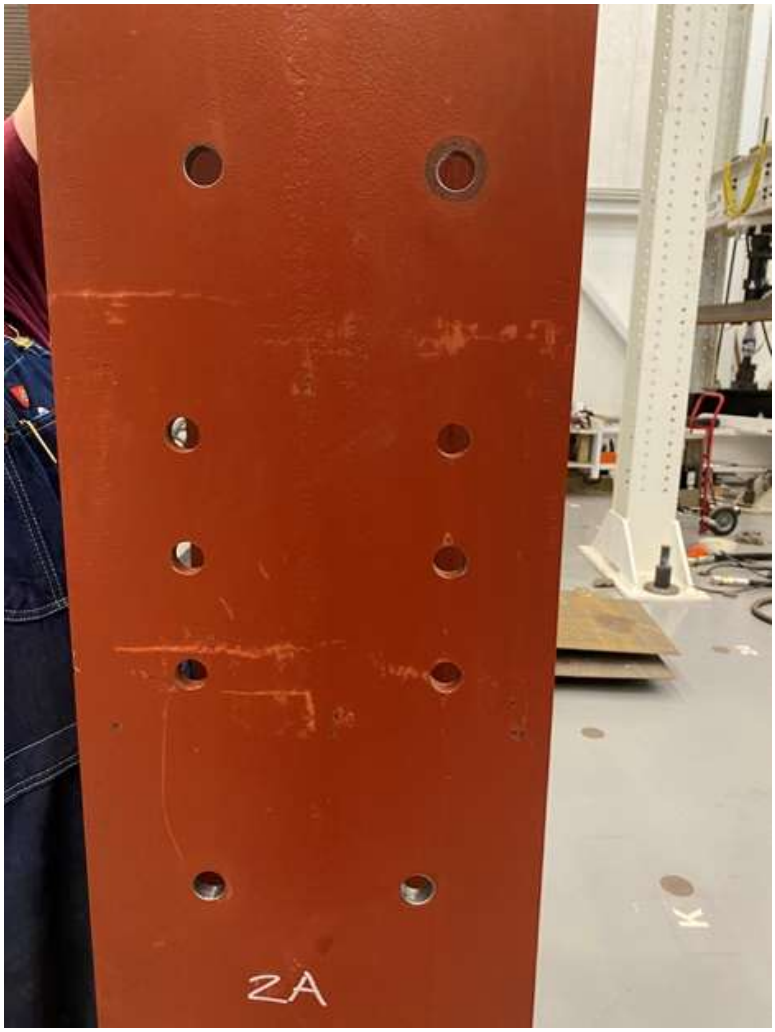

Figure 41: Edge W12x65 stub column with connection holes

Figure 42: Edge beam to column ”Fixed” connection, top angle

Figure 43: Edge beam to column ”Fixed” connection
(image by Matthew Yarnold)

After fabrication of all the steel framing components, the system could be assembled and was ready for instrumentation and testing. With the assistance of the CIR staff, the beams were craned into place and connected to the stub columns with shear tab connections. The bolts were tightened with a spud wrench. The tension rods that penetrated through the strong floor into the basement had washers and nuts installed (Figure 44). A fully tensioned tie-down rod was not required for the floor specimen.

After alignment and squaring of the beams and columns, the tie-down rods were tightened with a wrench and sledgehammer (Figure 45). Figure 46 is a photograph of the complete steel framing.

Figure 44: CIR tension rods basement connection

Figure 45: Stub column connection to CIR strong floor with tension rods

Figure 46: Floor system steel frame assembled

4.3.4. Beam Instrumentation

The beams were instrumented with electrical resistance strain sensors as well as string potentiometers (or pots) to record displacement and rotations. A total of 39 strain gauges were installed in three cross-sections, with five total string pots in the center cross-section. Figure 47 shows the location of the sensor cross-sections. In total, three-beam cross-sections had strain sensors installed. The location of the cross-sections is shown in Figure 47, with cross-section 2 located in the center of the floor system. The location of strain sensors and string pots is shown in Figure 48. Note that only cross-section 2 had string pots for vertical deflection and rotation. The center beam in the floor

system had additional strain sensors located in the middle of the top flange (Figure 48). The 39 strain sensors were distributed equally, with 13 sensors in each cross-section, as shown in Figure 48.

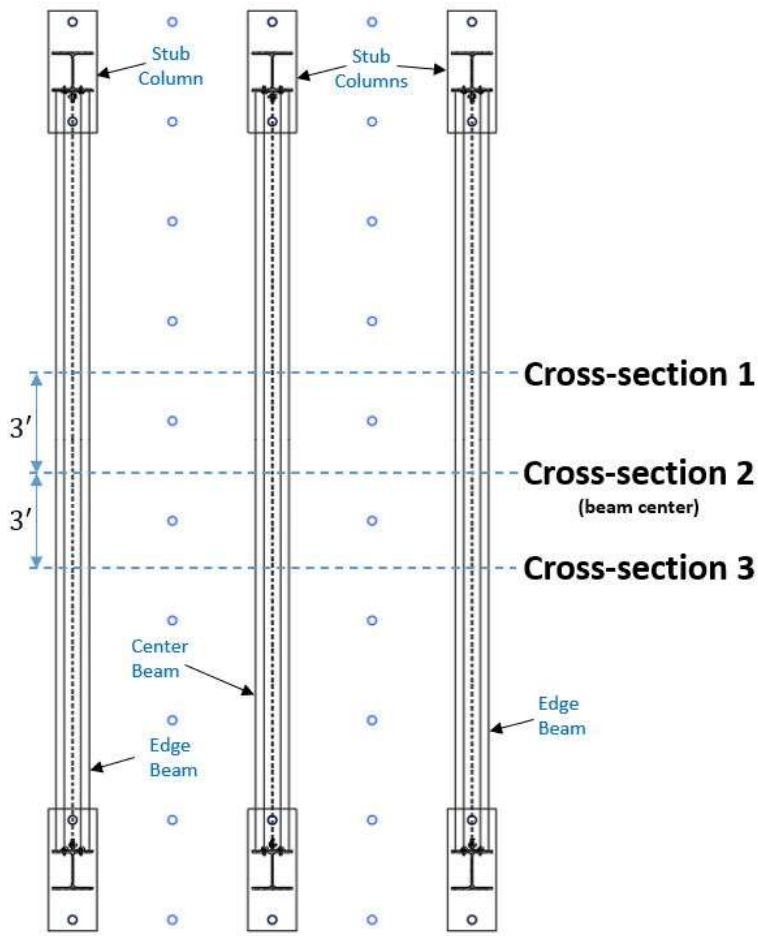

Figure 47: Plan view of sensor cross-section locations

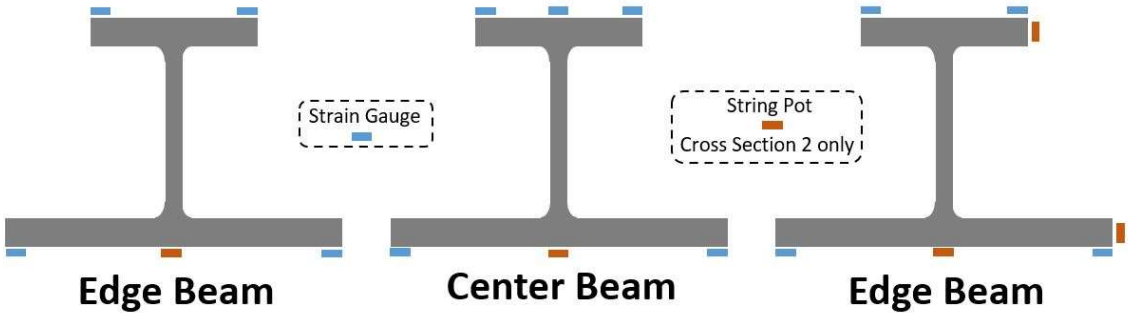

Figure 48: Beam cross-section sensor location

The 0.25-inch electrical resistance strain sensors adhered to the beam flanges were 0.5 inches from the flange edge. After the sensor locations were prepared for installation, the sensors were installed, and the lead wires were then soldered to the strain sensors. The installed strain sensors and attached leads can be viewed in Figure 49. Figure 49 shows the top flange sensors located on an edge beam consisting of two sensors. Figure 50 shows the beam rotated 180 degrees with the bottom flange up for sensor installation. All six bottom flange sensors can be seen in Figure 50 installed. Figure 51, as mentioned earlier, is the three sensors located on the top flange of the center beam. The sensors in Figure 51 were also coated due to encasement in the topping slab.

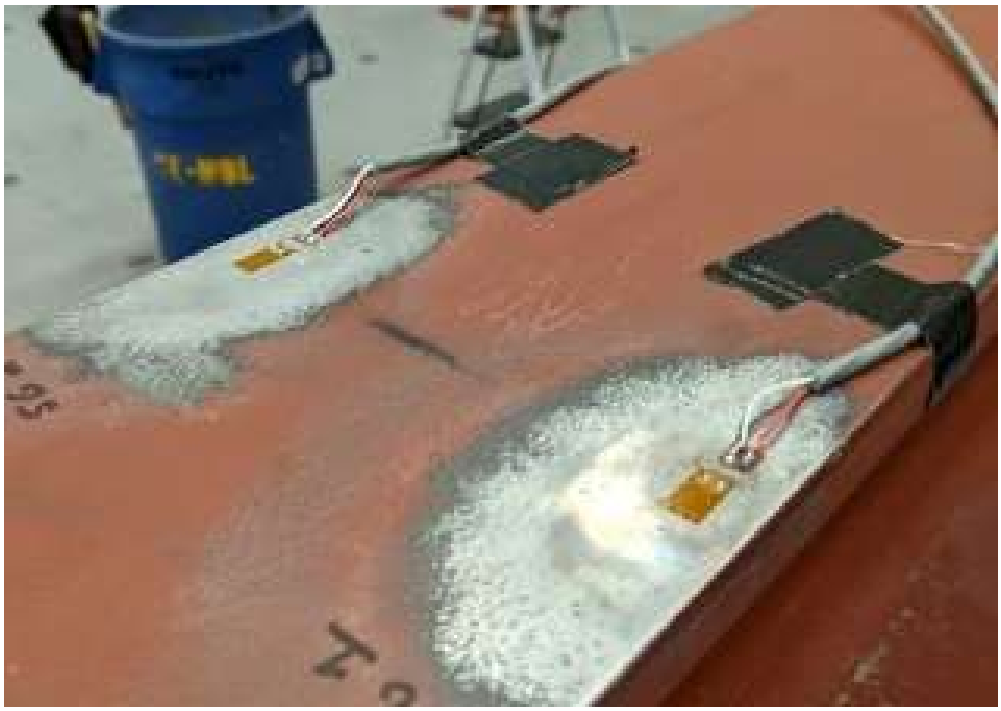

Figure 49: Edge beam top flange sensor installation

(image by Matthew Yarnold)

Figure 50: Edge beam bottom flange sensor installation

(image by Matthew Yarnold)

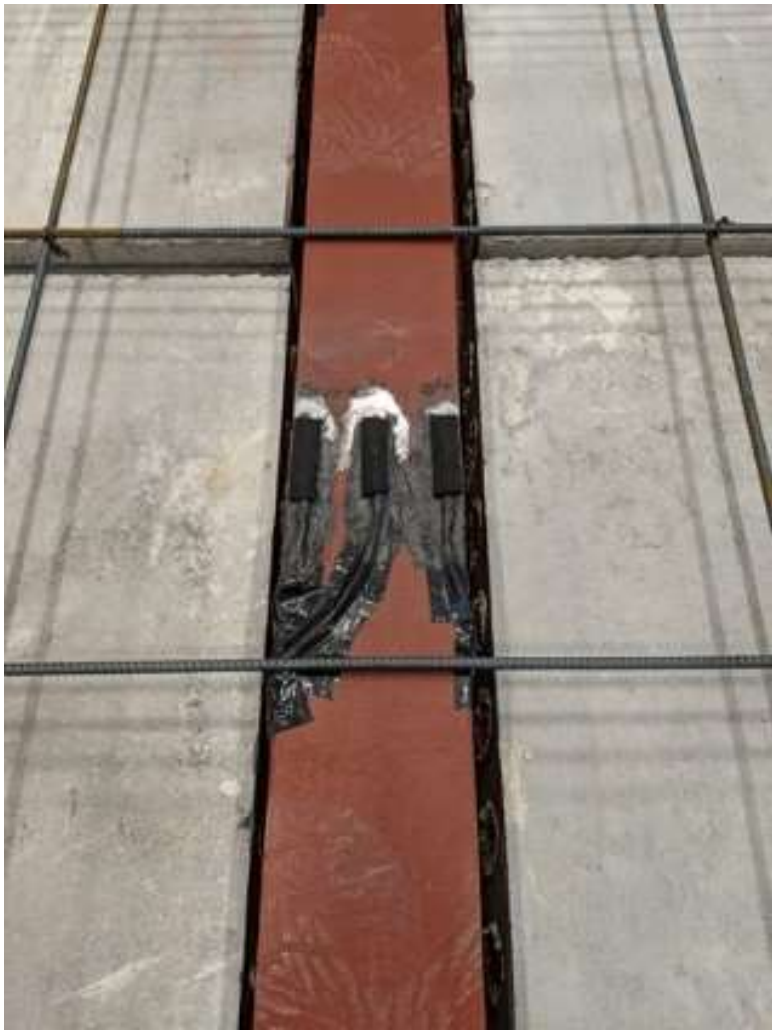

Figure 51: Center beam top flange sensor installation with protection for encasement

The second set of sensors installed on the floor system was the string pots. The string pots were only located in the center of the floor system on cross-section 2. In total, five-string pots were employed, with three measuring vertical displacements and two measuring beam rotations on an edge beam. Figure 52 is the attachment of the string pot to the top flange of the beam to capture rotation. The string pot was connected to a steel angle, increasing the distance from the flanges of the beam, helping magnify rotation

sensitivity. The angle was attached to the beam with magnets. Figure 53 is the bottom flange of an edge beam. The figure shows two angles, with one for the vertical deflection string pot and the second for beam rotation. To capture the beam rotation, not just lateral displacement, two string pots were used, with one on the top flange and the second on the bottom flange.

Figure 52: Edge beam top flange string-pot beam attachment

Figure 53: Edge beam bottom flange string-pot rotation and displacement connections

4.3.5. Construction Testing

The first test upon completion of the sensor installation and steel floor framing assembly is referred to as construction testing. During this stage of testing, 4-foot x 6-foot precast concrete panels (Figure 54) were placed between beams resting on the bottom flange of the beams.

Figure 54: Pre-cast hollow core concrete panels

Each beamline required the placement of 5 panels, with 10 panels completing the entire test floor system. The panels were placed and removed several times to mimic different construction scenarios (Figure 55). A total of three different scenarios were tested.

The three unique panel-loading scenarios consisted of a boundary condition change and a different sequence of panel loading. Figure 55 shows all three scenarios along with the panel-loading sequences. Loading scenario 1 incorporated the fixed edge

beams and loaded each bay individually. Loading scenario 2 used pinned connections on the center and edge beams, this was achieved by removing the bolts from the angle welded to the top and bottom flanges of the edge beam. After boundary changes for loading scenario 2, only one bay was tested. For the final loading scenario, the bolts were replaced in the edge beam welded angles and the panels were placed one at a time in every other bay. Essentially this loading balanced the load on the center beam with every even number panel placed.

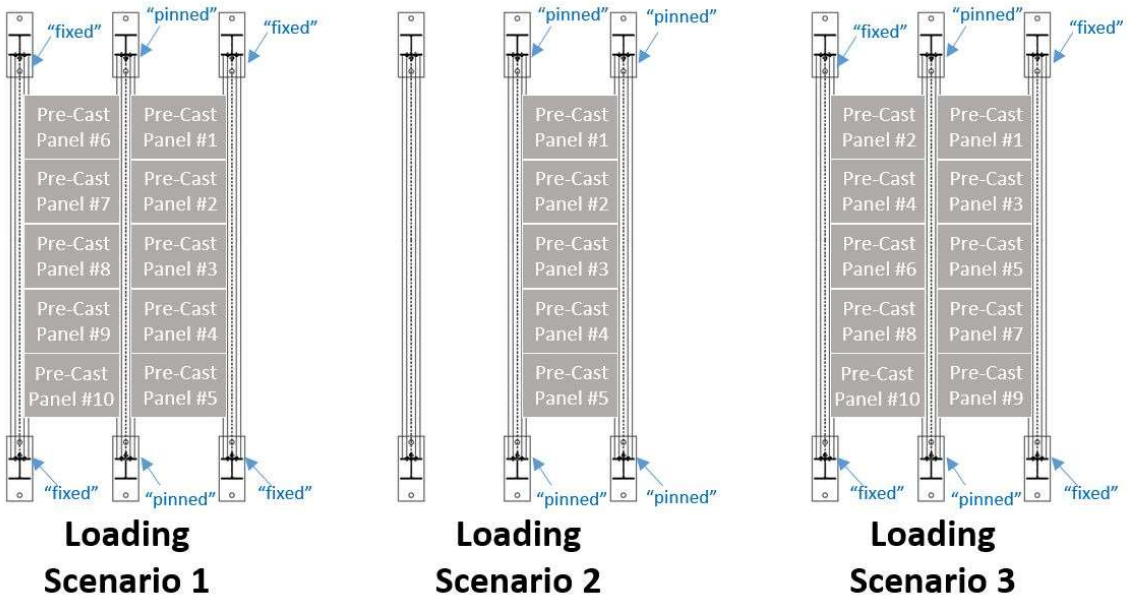

Figure 55: Plan view of panel placement during construction testing

The previous loading scenarios were concrete pre-cast panels placed on the bottom flange of the beams using a forklift (Figure 56). In future construction applications, a crane can be utilized in the same manner. The panels were squared with the beams and set in place (Figure 57). Figure 58 shows four panels placed in one bay. Each bay held a maximum of five panels. Figure 59 shows the floor system with all ten

panels or both bays filled after loading scenario 3. Strain and displacement measurements were recorded through all three loading scenarios.

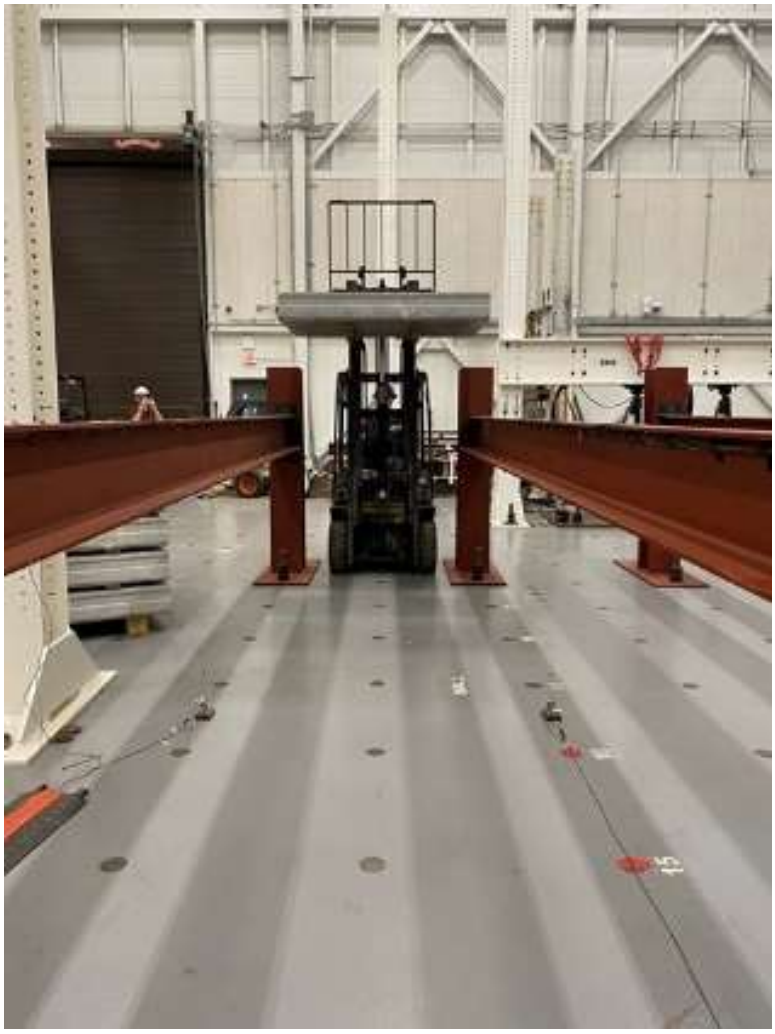

Figure 56: Construction loading of the steel frame – first concrete pre-cast panel placement

Figure 57: Construction loading of the steel frame – first concrete pre-cast panel

Figure 58: Construction loading of the steel frame – four of five concrete pre-cast panels placed

Figure 59: Construction loading of the steel frame – all concrete pre-cast panels installed (image by Matthew Yarnold)

4.3.6. Floor System Topping Slab Preparation

The concrete topping slab preparation was the next stage in the floor system test after completion of the construction loading. The topping slab preparation consisted of preparing the ends of the pre-cast hollow core slabs, sealing between the pre-cast hollow core slabs, plywood forming the ends of the floor system, steel forming above the edge beams, and tying a rebar mat. The first step was to prepare the ends of the pre-cast concrete slabs.

The pre-cast concrete hollow core slabs were manufactured with a hollow core to reduce the weight of the slab (Figure 60). Before the slab could be poured, the hollow

voids needed to be blocked, or they would fill with concrete and defeat the purpose of casting the weight-reducing voids. The most cost-effective and easiest solution was to place a piece of paper in the void and spray expanding foam in the void (Figure 60). Pre-manufactured covers are available for faster applications. Upon hardening of the expanding foam, the excess that protruded past the outer face of the pre-cast slab could be removed (Figure 61). This step was in preparation for the slab pour but was complete before the pre-cast slabs were placed during the construction test. With the pre-cast slab ends sealed, the next step was to prepare the joint between slabs in the assembled floor system.

Figure 60: Pre-cast hollow-core concrete panel foam closure

Figure 61: Pre-cast hollow-core concrete panel foam closure after cutting

With the pre-cast slab voids sealed and installed in the floor system, the next step was to seal the joints between slabs and the beam flanges. The fitment of the pre-cast to pre-cast was tighter than expected. The worry was any concrete spillage onto the CIR floor. Due to this concern, extra protection was taken to contain any leakage of concrete. Between each pre-cast panel, the same expanding foam was used Figure 62. The foam was sprayed between each panel, sealing the joint from any concrete spillage. The fitment between the pre-cast panels and the A12x53 beam bottom flanges was very tight. Due to the need to vibrate concrete around the beams, it was decided to seal the joint to ensure no leakage. A bead of silicone caulk was run the length of the pre-cast to steel

beam joint Figure 63. The bead was hand-applied under the pre-cast slabs. With the pre-cast slabs sealed the forming for the in-situ concrete needed to be completed.

Figure 62: Joint sealing between pre-cast concrete panels

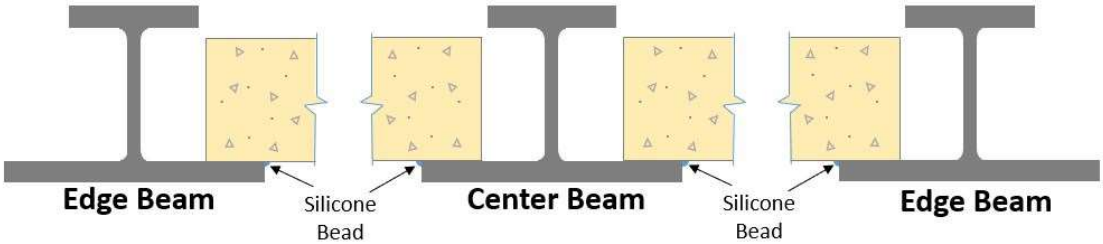

Figure 63: Location of silicone beads for the beam to panel sealant

With the pre-cast panel connection sealed, the forming for the slab could be completed—two unique areas needed to be formed. The first area was the ends of the

floor system. The decision was made not to encase the connection so it could be viewed during the in-service and ultimate load testing. The forming was achieved by cutting plywood to fit the profile of the beam (Figure 64). The plywood extended 1½ inch above the beams to allow sufficient concrete cover. The plywood end form extended between beam webs (Figure 65). The plywood forming was reinforced with 2 inches x 4 inches (Figure 66). The forms were also braced to the stub columns at the ends and center of the forms (Figure 66). The same silicone and expanding foam was used on the forms to assure all penetrations were sealed and would not leak onto the CIR floor (Figure 67). The second portion of forming the floor system was to form over the edge beams.

Figure 64: Floor system concrete plywood end form, beam scribed

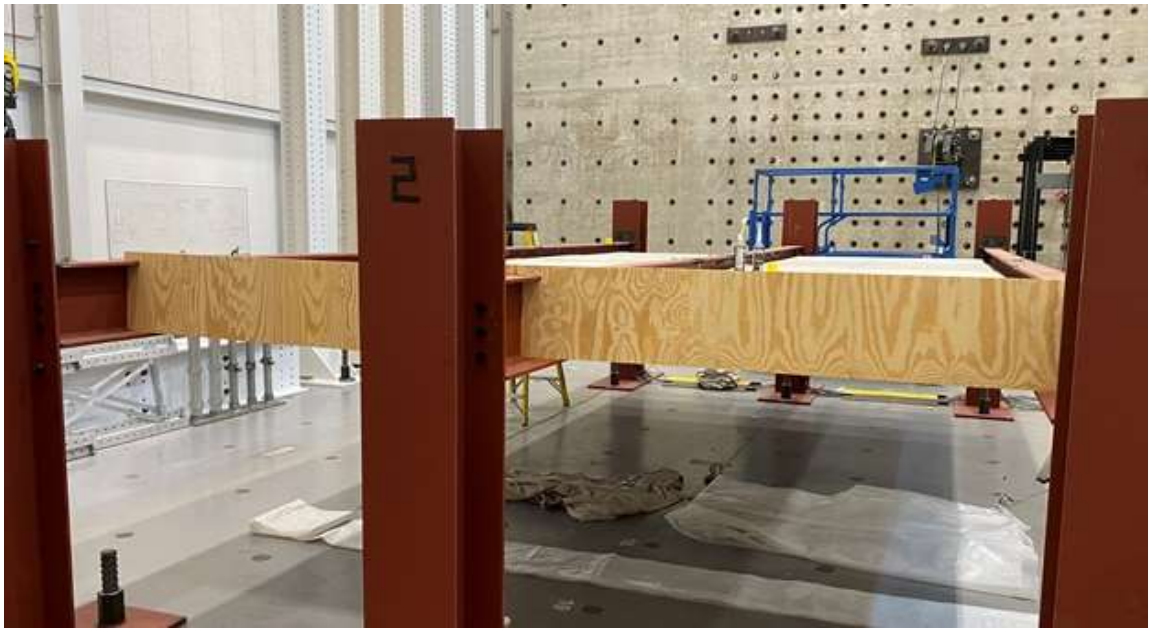

Figure 65: Floor system concrete plywood end forms

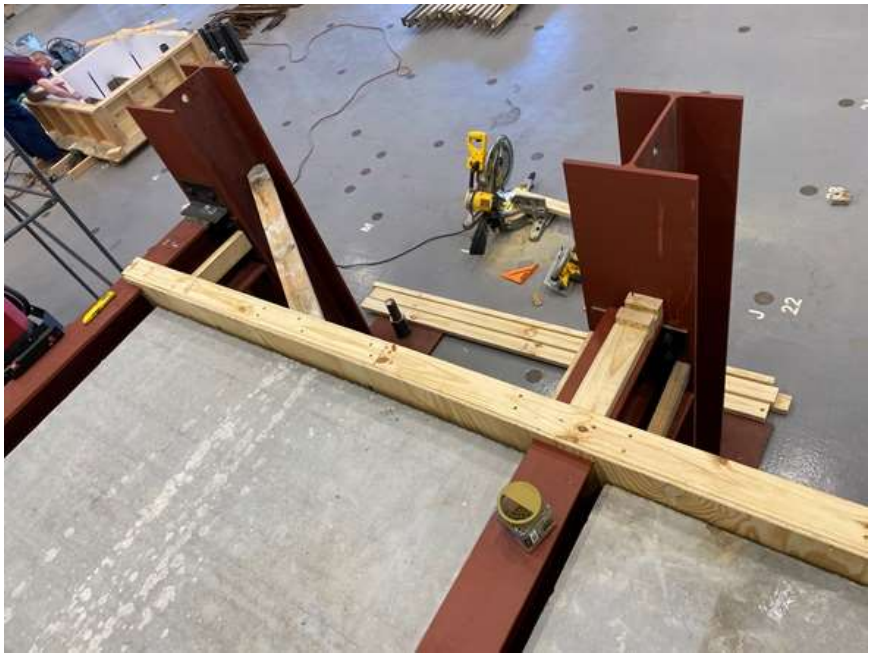

Figure 66: Floor system concrete plywood end form bracing

Figure 67: Concrete form wire sealing

The completion of the plywood end forms left only the edges over the edge beams that needed to be formed. The simplest solution to form over the beams and have an edge to screed the concrete from was angle iron. With 1½ inch of cover over the top of beam flanges, the decision was made to purchase 1½ inch pieces of angle iron and clamp them to the middle top flange of the edge beams (Figure 68). Low-profile c-clamps and hand clamps were used to hold the angle iron to the beam flange. The clamps were kept under the top plane of the angle iron, allowing a screed board to ride on the angle iron making a level topping slab. The final step in preparing the floor system for the topping slab was constructing a rebar mat.

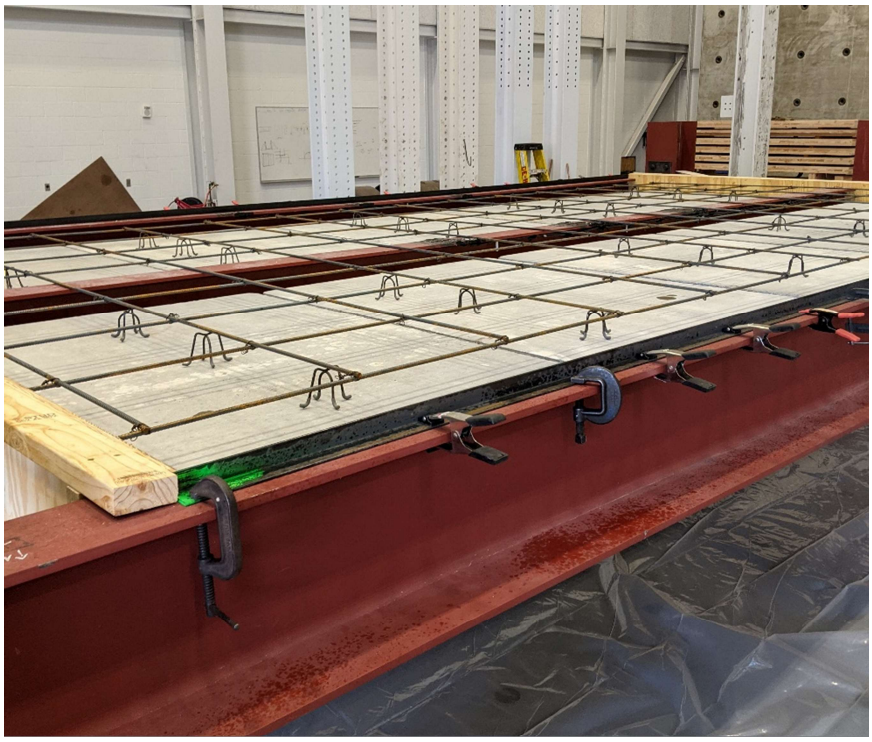

Figure 68: Steel angle concrete form clamped to edge beams
(image by Matthew Yarnold)

The final step before pouring the topping slab was placing a rebar mat. The mat was constructed with #4 rebar (grade 60). The rebar was spaced at 16 inches on center each way. The rebar mat was continuous length with no lap splices needed. The rebar was continuous over the center beam and stopped short of the edge beams (Figure 69). The rebar mat was hand-tied and supported on 3-inch rebar chairs and the top flange of the center beam. With the completion of the rebar reinforcement, the floor system was ready for the topping slab Figure 70.

Figure 69: Concrete slab rebar reinforcement tied mat, close up

Figure 70: Concrete slab rebar reinforcement tied mat

4.3.7. Topping Slab Pour

The topping slab pour was the final construction testing done. The cross-sectional area of the floor system needing concrete was calculated at 839.8 in^2. With

concrete only being placed over the panels making the length of the concrete section of 5-4 foot panels or 20 feet. That volume was calculated to be 4.32 cubic yards of concrete. The top of the floor system being over 5½ feet required a dump bucket attached to the CIR overhead crane (Figure 71). The concrete was placed by the dump bucket and vibrated in place (Figure 72). The screed board can also be seen in Figure 72 next to the floor system columns. With concrete being placed and vibrated, the screed board was used to smooth and level the surface. Figure 73 shows the screed board in use. Upon completion of the placement, vibration, and screeding of the concrete, the slab was then finished Figure 74. After the slab was floated, a texture was added with a broom finish, and the edges of the slab were hand troweled, smooth finishing the slab Figure 75. Due to the slab curing in a temperature-controlled environment, the slab was not covered but was sprayed with water every six hours. Four-inch concrete cylinders were also taken during the pour for compressive strength testing.

Figure 71: Slab pour, concrete dump bucket

(image by CIR Staff)

12

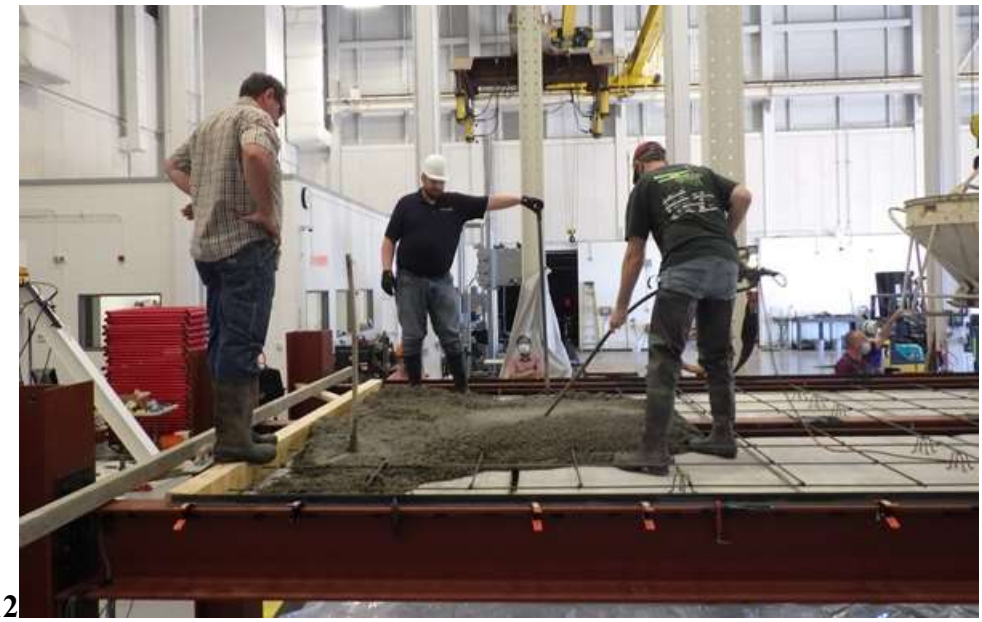

Figure 72: Slab pour, the first concrete load placed

(image by CIR Staff)

Figure 73: Slab pour and screeding surface

(image by CIR Staff)

Figure 74: Slab finishing

(image by Matthew Yarnold)

Figure 75: Finished concrete slab

4.3.8. In-service and Ultimate Strength Testing

The construction testing stages of the floor testing resulted in a greater understanding of behavior in a non-composite state. With the floor system then being fully composite, in-service and ultimate testing could take place. The floor system was tested 54 days after the in-situ concrete was poured. Test compressive strengths from cylinders prepared during the concrete pour were tested at 28 days and the day of the test at 54 days. Table 3 summarized the results from all seven compressive strength tests and also calculated the average for each set of tests.

Table 3: In-situ concrete compressive strength

Time:	Peak Force:		4x8 Cylinder Peak Stress:	
28 day	66.1	kips	5260	psi
28 day	72.3	kips	5753	psi
28 day	66.1	kips	5260	psi
28 day	61.7	kips	4910	psi
Average	***66.55***	***kips***	***5296***	***psi***
54 day	67.5	kips	5155	psi
54 day	64.5	kips	5120	psi
54 day	71.3	kips	5191	psi
Average	***67.8***	***kips***	***5155***	***psi***

The test setup for the in-service and ultimate testing consisted of the completed floor system, test frame including the hydraulic cylinder, and a spread beam assembly. The test frame was constructed of two W12x106 columns with base plates secured to the CIR strong floor. The test frame is the white steel frame in Figure 76. Bolted between the columns was an 18-foot double W24x103 header. The W24x103 header utilized five diaphragms to secure the doubleheader assembly together. The 220kip actuator was connected to the header assembly (Figure 76). The actuator applied the compressive force directly to a 9-foot spread beam that was a double W24x103. The spreader beam distributed the load into two steel pin assemblies spaced 6 feet apart or 3 feet off of the center longitudinally. The loading was a four-point bending test with a constant moment region. The floor system was loaded at 2 kips per min until failure was achieved.

Figure 76: Floor system with loading frame and 220 kip actuator

(image by Matthew Yarnold)

Figure 77: Spreader beam and 220 kip actuator
(image by Matthew Yarnold)

4.3.9. Construction and In-service Loading Results

The construction and in-service testing on the full-scale floor system yielded very interesting findings. Those findings are fully detailed in Sheyenne Davis's Master's Thesis (Davis 2022). Of all the results from the full-scale test, two particular findings are disseminated and discussed herein. The first set of data, referred to as the construction loading, compares the torsional stresses and strains to the analytical study scenario I (4.4.3) calculations. The second finding is the ultimate strength of the floor system.

The construction loading part of the experiment consisted of loading the precast panels on the lower flange of the A12x53 beams. The full construction test consisted of

different boundary conditions along with unique loading patterns. Although three separate tests were conducted during the construction loading, the most applicable to this study was the heavy torsional loads induced during loading scenario 2 shown in Figure 55. During loading scenario 2 one bay of the floor system was loaded, causing eccentric loading on both the edge and center beam. During loading scenario 2 both beams were only connected with shear tabs making the modeling of pinned connections applicable (and conservative). The strain sensors at the locations shown in Figure 48 recorded strains during the loading test.

The strains recorded in cross-section 2 (Figure 47) during loading scenario 2 (Figure 55) are shown given in Figure 78 and Figure 79. Figure 78 shows the strains from the center beam, which had five strain sensors installed in cross-section 2. Figure 79 shows the strains from the edge beam, which had four strain sensors installed in cross-section 2. The steps in both data sets indicate the placement of each panel. With five panels being placed, there were five steps in the strain plots. The positive strains indicate tension in the member, and the negative strains indicate compression. The maximum strains with all five panels loaded were averaged from the plots and listed in Table 4. Along with the strains, the stresses computed from the strains are listed in Table 4. The strains were well below plastic deformation, which allowed a simple conversion using Young's elastic modulus of steel (29,000 ksi). During the test, two string pots recorded the top and bottom translation of the edge beam. The two displacement measurements were used to find the rotation of the edge beam. The recorded edge beam rotation is also listed in Table 4. The stress data calculated from the recorded strains

were used to check the code equations and, ultimately, the scenario I code (part of Phase 4). Along with stress comparison between measured and theory, the data was also used to understand the distribution of forces during torsion.

Table 4: Measured strains, rotations, and stresses

Sensor	Strain (με)	Stress (ksi)	Rotation (degrees)
Edge Beam:			---
SS-1	-172.7	-5.0	
SS-2	10.2	0.3	---
SS-3	58.6	1.7	---
SS-4	38.2	1.1	---
rotation	---	---	1.62
Center Beam:			
SS-5	3.1	0.1	---
SS-6	-60.2	-1.7	---
SS-7	-132.1	-3.8	---
SS-8	24.3	0.7	---
SS-9	53.5	1.6	---

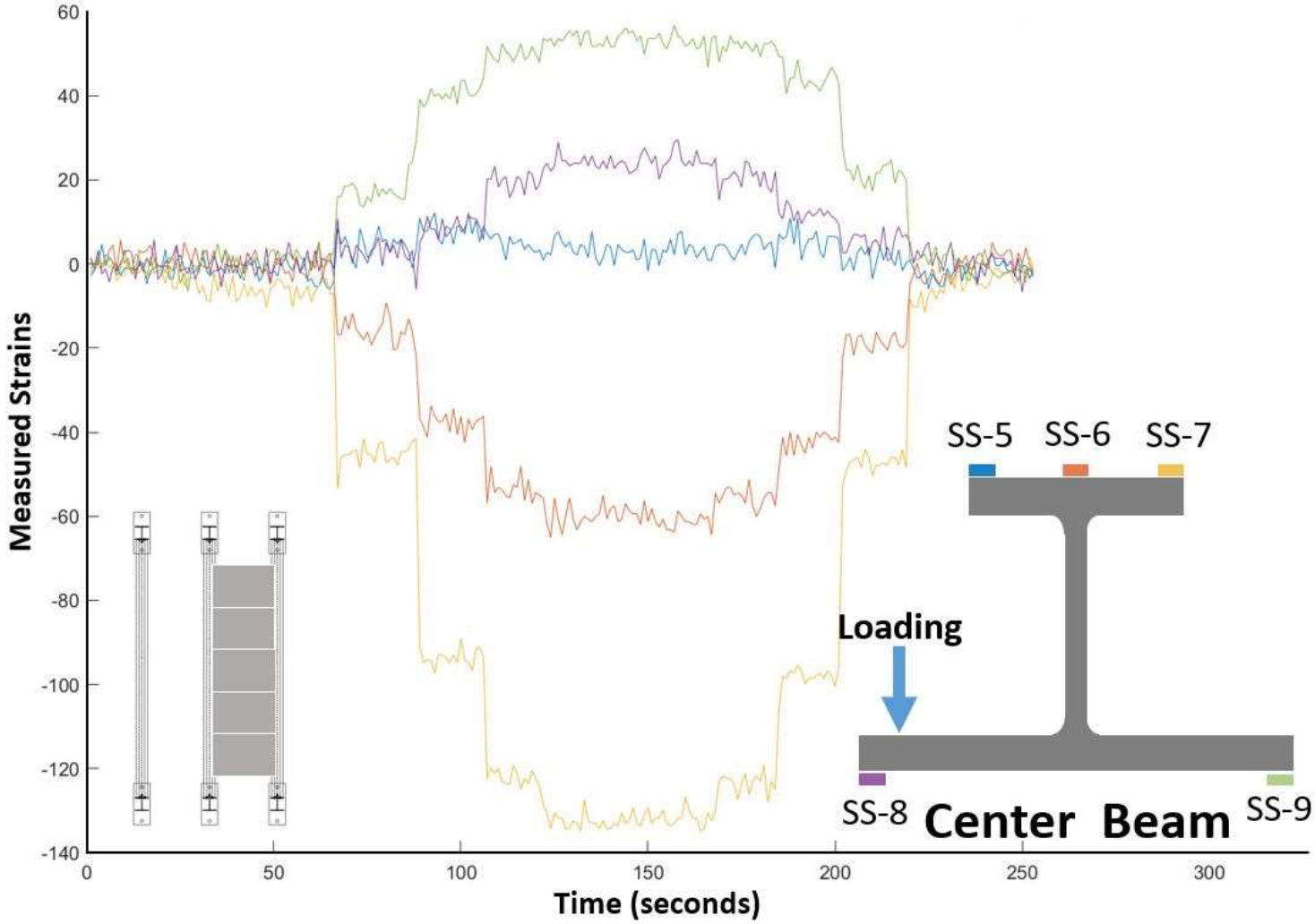

Figure 78: Loading scenario 2 center beam strains

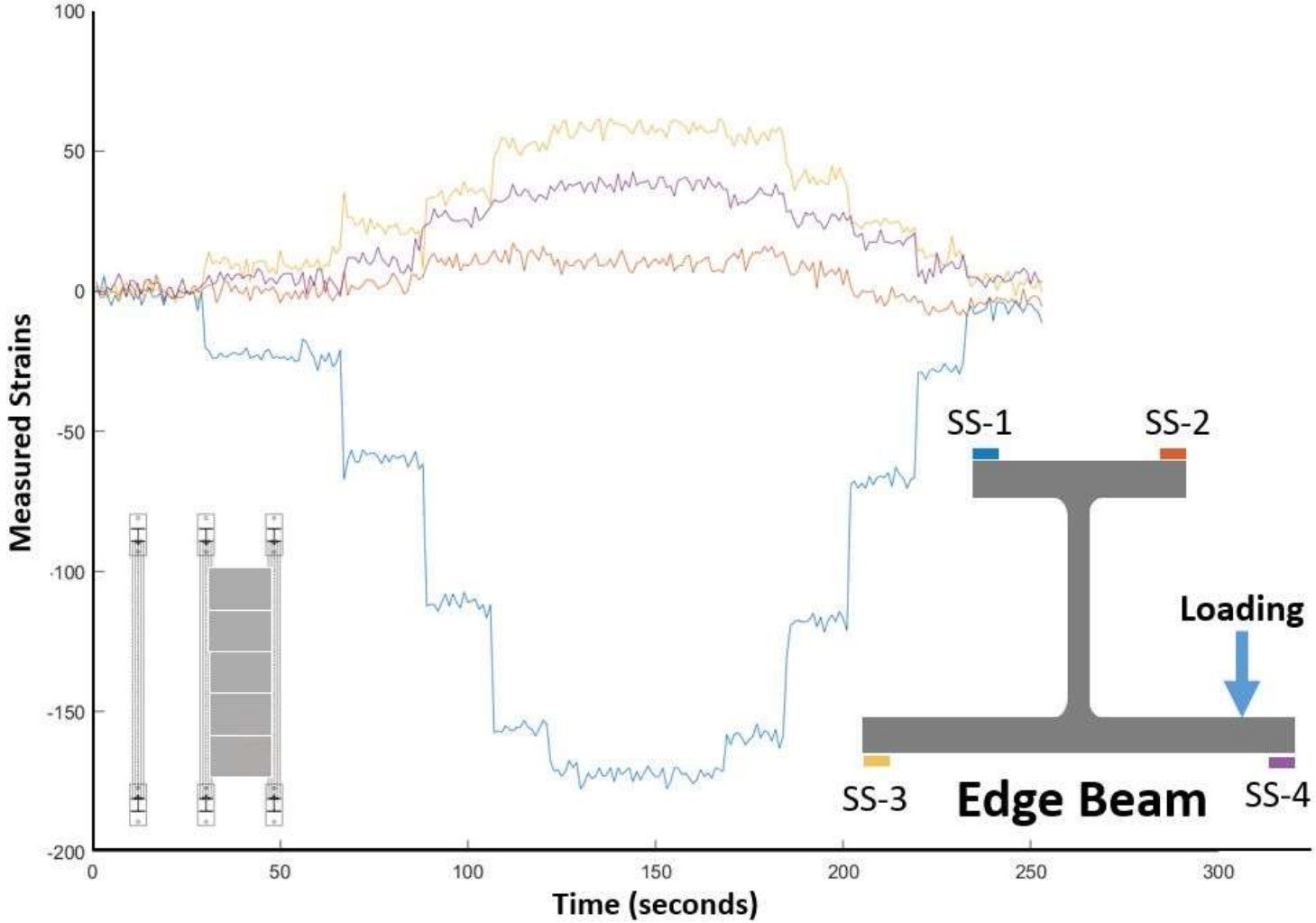

Figure 79: Loading scenario 2 edge beam strains

The theoretical torsional and bending stresses were calculated with the same loading that was used in the test. A 65 psf panel weight was multiplied by half the panel width of 5 foot 4 inches. That distributed load was then applied to the theoretical beam at an eccentricity of 5 inches. A detailed explanation of the theoretical calculation approach is provided below in Phase 4.

The results from calculating the theoretical torsional and bending stresses are shown modeled on the beam cross-section in Figure 80. The combined theoretical stresses were calculated at the extreme flange end and needed to be transformed at a location similar to where the strain measurements were taken during the test. The center of the strain sensors was located 0.5 inches from the outside edge of the flanges. The theoretical stresses are linear stress distributions orthogonal to the length of the beam. The linearity assumption allowed the stresses to be corrected to the strain sensor locations. The transformed stresses are shown in Figure 81.

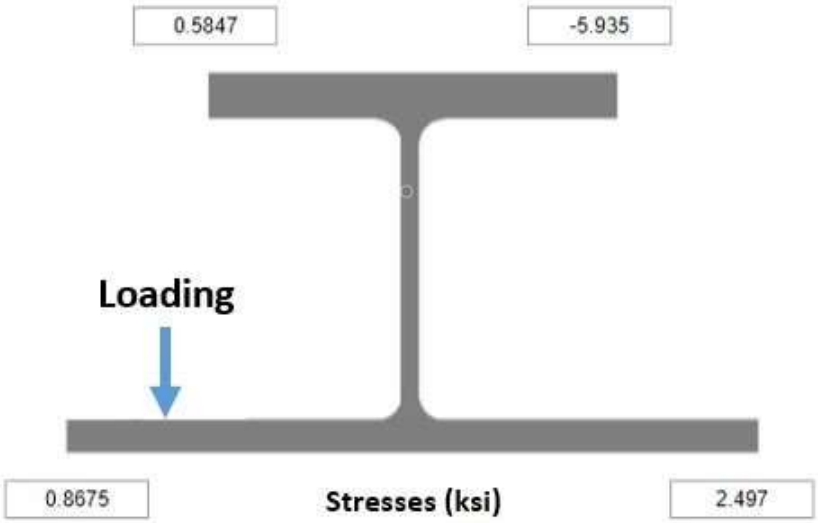

Figure 80: Theoretical bending and torsional stress with construction loading scenario 2 at the ends of the flanges

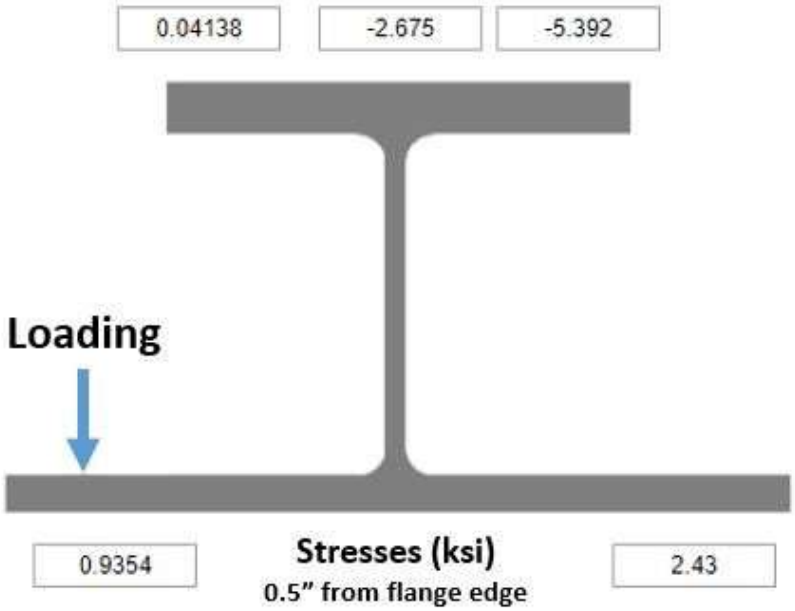

Figure 81: Theoretical bending and torsional stress with construction loading scenario 2 at the mid-span sensor locations

Due to symmetric loading, the edge beam and center beam theoretically have identical stresses. Allowing only one theoretical set of values to be compared to both

measured cross-sectional stresses. With symmetric loading, the stress distributions from the beams were also compared.

Table 5 is the comparison of each stress distribution from the experimental beams to the theoretical. The larger percent errors between beams and between the theory were on the lower stresses. The issue with any form of conservative assumptions with torsional stresses and bending stresses is that being conservative in one location can cause the opposite effect in other locations. Phase 4 further explains the relationship between torsional and bending stresses. Across the cross-section, bending and torsional stresses have either a canceling effect or a combined effect depending on the location on the flange. The largest stresses occur in the flange edges away from the loading, with combined compressive forces from bending and torsional in the top flange and combined tensile forces from bending and torsion in the bottom flange. The main areas of focus on beams subjected to torsion are those two locations. In symmetric beams, the max compressive forces in the top flange are identical in magnitude to the max tensile forces in the bottom flange. With an asymmetric cross-section, the top flange compressive forces have a higher magnitude than the bottom flange tensile forces, making the compressive combination top flange forces the worst case in the cross-section. Comparing the test to the theoretical compressive stresses, the percent error from the center beam of 8% and the edge beam of 41% shows the differences between beams and how relatively close the theoretical stresses are to measurable values. In addition, the theoretical calculations were proved to be conservative compared to the experimental results.

The rotations from the experiment and the theory were also compared. The rotation of the edge beam from the experiment was 1.62 degrees. The theoretical rotation theta was calculated at 1.76 degrees, only a difference of 9%. Again, the theoretical calculations proved to be conservative compared to the experimental results.

Table 5: Comparison of experimental stresses vs. theoretical stresses

Location on cross-section	Edge Beam Stresses (ksi)	Center Beam Stresses (ksi)	Beam Comparison Percent Error	Theoretical Stresses (ksi)	Theorectial Percent Error Edge Beam	Theorectial Percent Error Center Beam
1 & 7	-5.01	-3.83	23%	-5.39	8%	41%
6	---	-1.75	---	-2.68	---	53%
2 & 5	0.30	0.09	70%	0.04	86%	53%
3 & 9	1.70	1.55	9%	2.43	43%	57%
4 & 8	1.11	0.71	36%	0.94	16%	33%

The floor system was also subjected to in-service loading up to failure. Loads equal to 100 psf up to ultimate were applied to the floor system. The resulting deflections due to 100 psf equivalent loading was L/3000 and a deflection at ultimate was L/270. The floor system failed at a load of 94 kips which equates to a load of approximately 500 psf. Due to the high composite strength from the experimental test, ultimate strength checks were not included in the analytical study as part of Phase 4 below. The entire composite behavior can be accessed in Sheyenne Davis's Master's Thesis (Davis 2022).

4.4. Phase 4: Construction and In-Service Behavior - Analytical Modeling

4.4.1. Introduction

Phase 4 consists of an analytical study to understand the behavior of A-shapes during construction and in-service conditions. Phase 4 was set up to analyze a single beamline and plot its behavior through a multitude of loading scenarios: during construction and in-service conditions. The approach to modeling the beams was to devise different loading cases during construction and after final assembly and apply numerical calculations to understand the limits during those loading scenarios. The shallow precast panel floor system under investigation was divided into four unique loading cases with three unique methodologies to evaluate each loading case. A more detailed outline of the analytical modeling approach is detailed in 4.4.2.

4.4.2. Analytical Modeling Outline

Phase 4 was the modeling of A-shapes during construction and in-service loading in a beamline analysis. The floor system under investigation utilized a precast concrete panel placed on the bottom flange of the A-shape with a topping slab encasing the A-shape Figure 82. During construction, three separate load cases were identified.

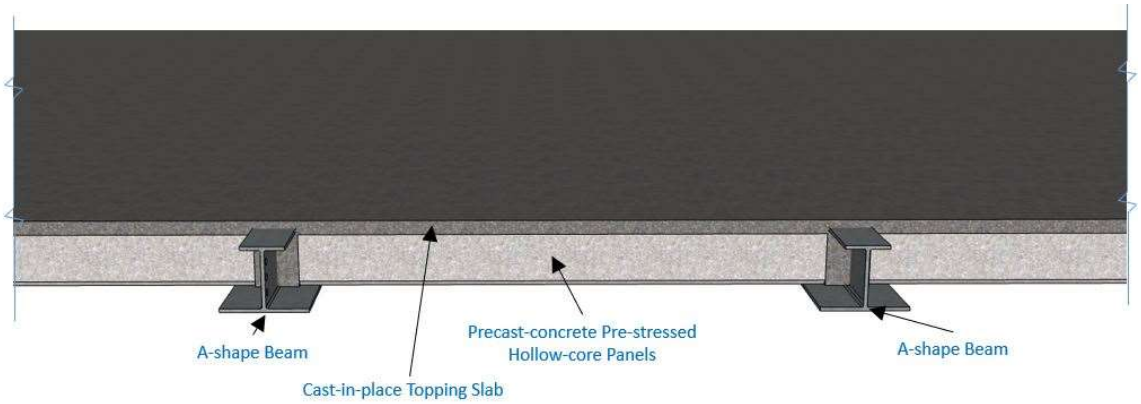

Figure 82: Cross-section of A-shape precast floor system

The first of the loading cases were Load Case 1. Load Case 1 (Figure 83) was the loading on the beam due to panel placement with a construction live loading. This load case is a non-composite case. Essentially this case is the pre-cast panels set on the bottom flange with workers walking on the panels during placement. The analysis of loading case 1 falls under scenario I, which is an analysis of A-shapes subjected to torsion. Boundary conditions included pinned for torsional and flexural analysis. This was shown to be conservative based on the experimental test results in Phase 3 of the study.

The second load case is identified as Load Case 2a (Figure 83). This load case is also due to construction load and is in the non-composite state. This load case was loading on the beam after panels were placed, and the additional weight of the wet topping slab with construction live loading was applied to the beam. Load case 2a was a concentric load causing the analysis of this load case to fall under scenario II. Scenario II investigates the A-shapes flexure under the concentric loading with pinned end conditions.

The third and final construction load case was Load Case 2b (Figure 83). Load Case 2b is an in-depth look at the effects of only placing the concrete topping slab in individual bays at a time. This non-composite load case has the additional weight of the concrete, causing a torsional load with a high concentric loading from the pre-cast panels. Load Case 2b utilized scenario I for analysis due to the torsional demand. Similar to Load Case 1, the torsional and flexural supports conditions were modeled as pinned.

The final load case is an in-service loading, Load Case 3 (Figure 83). Load Case 3 was an examination of the floor system after the concrete topping slab had cured. Load Case 3 focused on floor comfort more than floor ultimate strength. Ultimate strength was not investigated after experimental testing results (see the Phase 3 results). Load Case 3 studied the composite deflection and vibration due to different live loading scenarios.

With a general understating of how the A-shapes were analyzed, a more detailed explanation of what beams were analyzed is necessary. To reduce the number of beams analyzed, certain criteria from roll-pass experts and AISC beam sizing limits were implemented. The depth of the A-shape was set to 8 inches. The top flange thickness (t_{ft}) was set with a minimum thickness of 1/8" to a maximum thickness of 2 inches with 16 iterations in 1/8 inch increments. The top flange width (b_{ft}) was set to a minimum breath of 2 inches and maximum width of the section depth of 8 inches with ½ inch increments. The web (t_w) was constrained to a minimum of half the top flange thickness or ½ inch, whichever was larger (Equation (5)).

$$t_w = \max\left(\frac{t_{ft}}{2}, \frac{1''}{2}\right) \tag{5}$$

Minimum seat width of 2 inches was implemented for the bottom flange width. In other words, the bottom flange (b_{fb}) was set to be 4 inches larger than the top flange (b_{ft}) iterated width as shown in Equation (6).

$$b_{fb} = b_{ft} + 4'' \tag{6}$$

The bottom flange thickness (t_{fb}) was calculated to balance the areas between the top and bottom flange (Equation (7)). As stated earlier, this criteria is to improve the ability of the shape to be manufactured. The A-shapes were modeled as pin-pin for flexure and torsion. The length of the beams was set to 20 feet with a beam spacing of 10 feet. Applying these criteria supplied 208 unique cross-sections to be analyzed.

$$t_{fb} = \frac{b_{ft}\, t_{ft}}{b_{fb}} \tag{7}$$

The outline of the analytical study is mapped out in Figure 83. Each of the load cases discussed previously was analyzed using the appropriate scenario described after the load case in the methodology section. After the load cases were analyzed through the scenarios using the described methodology, the plots of those results were given in the results of each scenario. An overall results section combines the controlling results from each scenario for what could be described as a master plot. Those results shown in Figure 83 are minimum controlling results are the controlling factor for each A-shape

analyzed. All load cases and scenarios were modeled in MATLAB and followed the analysis shown in Figure 84. Figure 84 represents the methodologies and codes used between the loading scenarios and the results of Figure 83. The entire MATLAB code is provided in Appendix C.

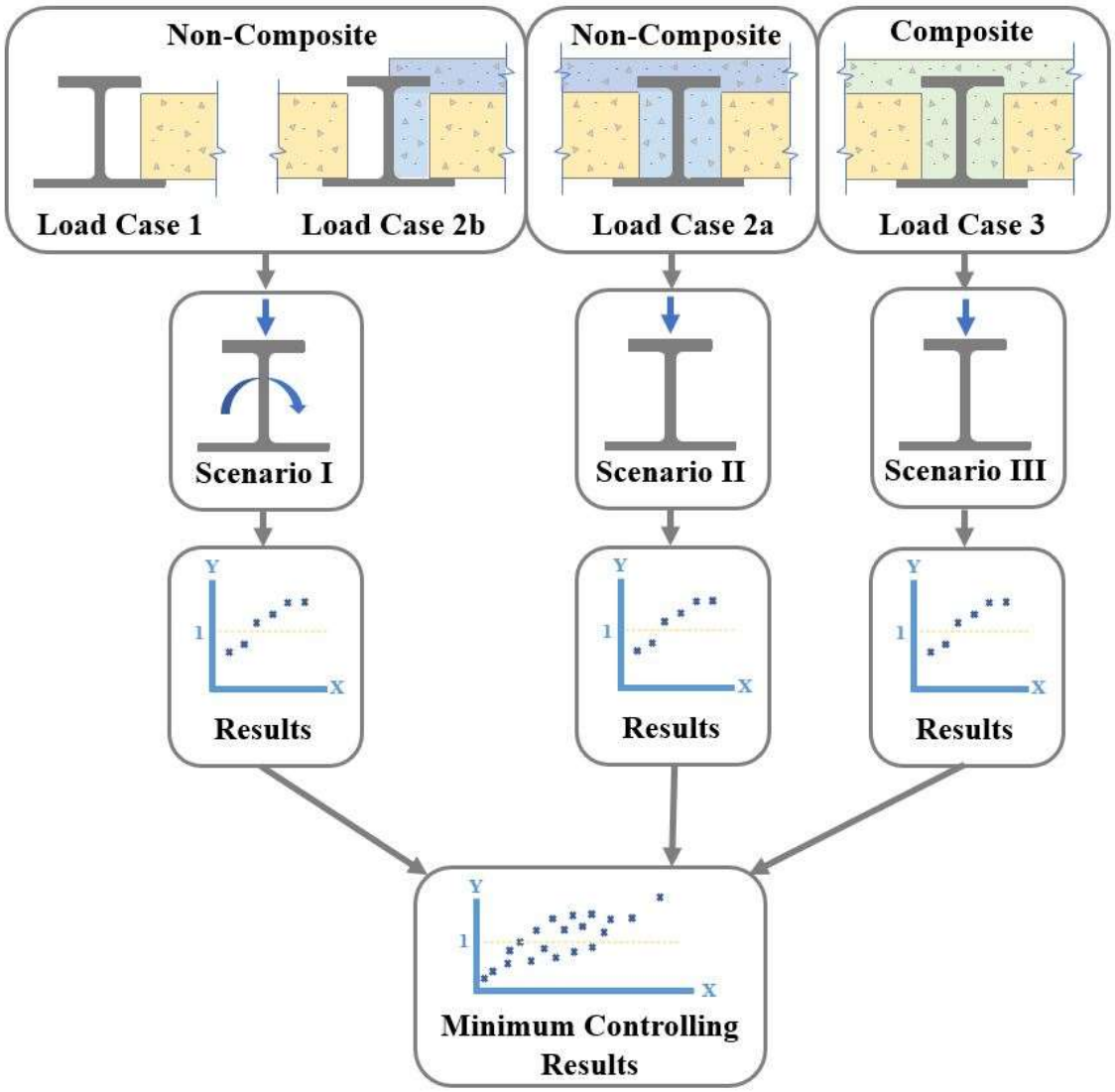

Figure 83: Analytical study outline

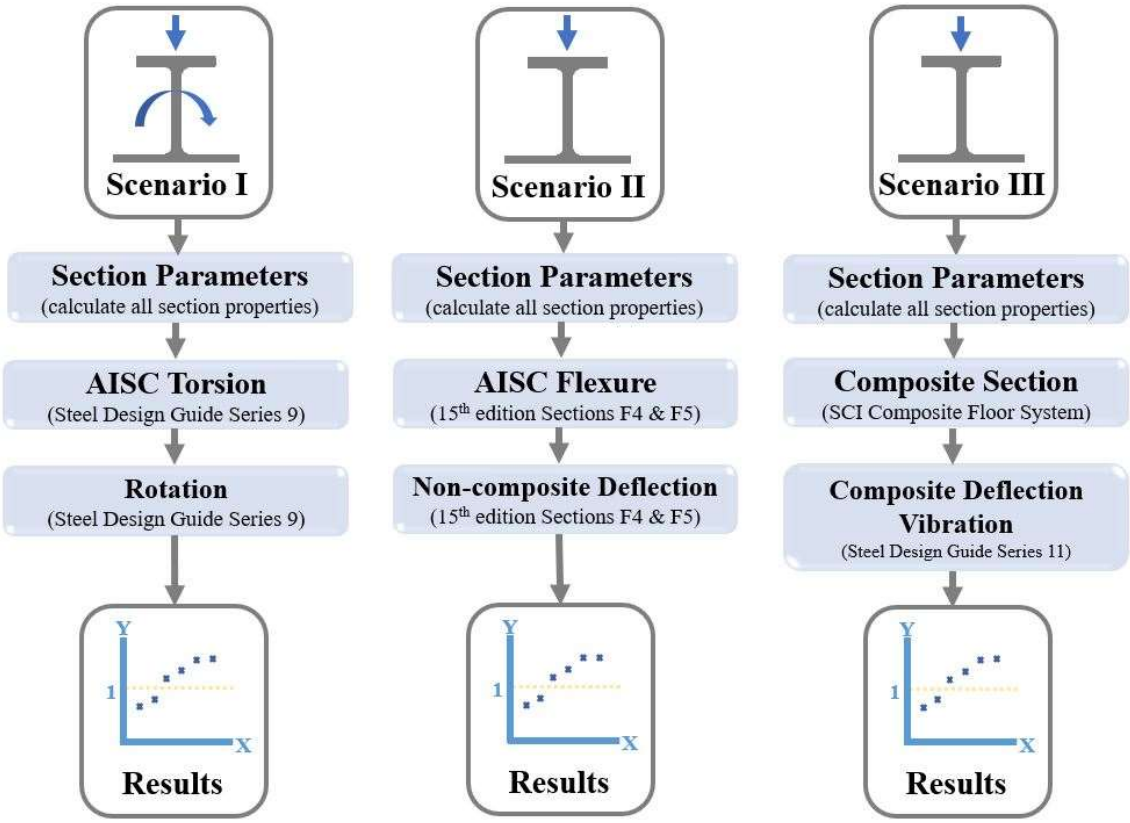

Figure 84: Analytical study, MATLAB outline

4.4.3. Analytical Study - Scenario I: Non-composite eccentric loading

4.4.3.1. Scenario I Model: Load Case 1

Load Case 1 utilized Scenario I: non-composite eccentric loading. Load case 1 was the construction loading during pre-cast panel placement (Figure 85). During panel placement, the beam loading is unique, with each panel being placed.

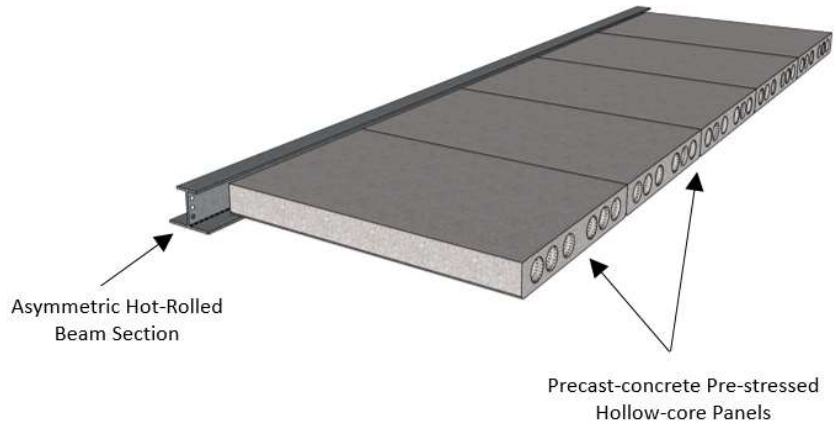

Figure 85: Load case 1, precast-concrete panels

With multiple ways of panel placement, there is no set standard to how panels are placed during construction. The panels could be placed along a beamline making the loading highly eccentric, or with every other panel balancing the load on the beam. Installing panels along a beamline is less efficient structurally since it induces a significant torsional moment. However, assuming this construction approach was utilized since it is conservative. Subsequently, the loading of the more torsion-heavy method was chosen for analysis. The parameters needed for Load Case 1 are:

- Construction live load of 20 psf (ASCE/SEI 2015)
- Construction live load factor of 1.6 (ASCE/SEI 2015)
- Panel dead load of 57 psf (Flood Precast 2019)
- Dead load factor of 1.4 (ASCE/SEI 2015)
- Tributary width of the panel of 5 feet
- Beam length of 20 feet
- Eccentricity of load of $\frac{b_{fb}}{2}$ - 1 inch

- Rotational limit of 4 degrees

4.4.3.2. Scenario I Model: Load Case 2b

Load Case 2b also utilized Scenario I: non-composite eccentric load modeling. This construction loading case was chosen as a worst-case scenario during the topping slab pour. Load Case 2b could either be viewed as only finishing the topping slab up to a beamline or concrete placement in a single bay during the topping slab pour. The loading from the pre-cast panels induces a high concentric load, with the additional weight of the wet concrete topping slab adding a torsional component. Figure 86 illustrates the loading orientation graphically. Note the difference between Load Case 1 and Load Case 2b is an increased imbalance between the concentric and eccentric loading. Ideally, Load Case 1 is a high magnitude of eccentric loading, with Load Case 2b having high concentric loading with an eccentric component. Both Load Cases are considered, to model high eccentricity with low concentric load (Load Case 1) and low eccentricity with high concentric loading (Load Case 2b). Load Case 2a is fully concentric loading discussed in loading Scenario II modeling.

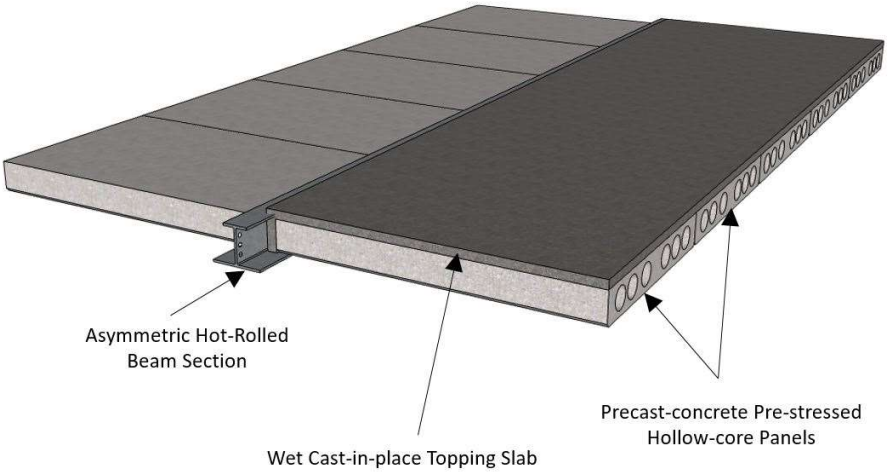

Figure 86: Load case 2b, precast-concrete panels with a half topping slab

The modeling of Load Case 2b is similar to Load Case 1 with an eccentric scenario I modeling and unique demands. The parameters needed for Load Case 2b are:

- Construction live load of 20 psf (ASCE/SEI 2015)
- Construction live load factor of 1.6 (ASCE/SEI 2015)
- Panel dead load of 57 psf (Flood Precast 2019)
- Panel dead load factor of 1.4 (ASCE/SEI 2015)
- Tributary width of the panel of 10 feet
- Topping slab thickness of 3 inches
- Tributary width of topping slab of 5 feet
- Beam length of 20 feet
- Eccentricity of load of $\frac{b_{fb}}{2}$ - 1 inch
- Rotational limit of 4 degrees

4.4.3.3. Scenario I Model: Methodology

The single-bay loading of precast panels (Load Case 1) or single bay topping slab (Load Case 2b) causes extreme eccentricity. The eccentric loading causes a torsional moment to be applied to the cross-section. With no lateral bracing of the section's top (compression) flange and when dealing with an open cross-section, lateral-torsional buckling can be a failure mode of concern. Scenario I modeling lays out the methodology for analyzing torsion in open section A-shapes.

The torsion causes a rotation or a twisting transverse to the horizontal bending. The cross-section with no end restraints would rotate out of plane due to the loading. Subsequently, the cross-section with end constraints resists the rotation causing torsional stresses to develop in the cross-section. An understanding of torsion in open web sections is necessary to analyze the eccentric loading on an A-shape. Physical testing provided insight and guidance into the calculations needed to numerically model the A-shape cross-sections. Similar to industry design, a pin-pin condition was chosen to be conservative and for consistency with design criteria.

Base knowledge of torsion was necessary to understand the location and relationship of stresses. Torsion is unique in the aspect that stresses reduce or accumulate depending on the location in the cross-section. A quick understanding of torsion follows. Two separate torsional moments develop in the cross-section. Equation (8) is the torsional moment due to rotation of the section, also referred to as St. Venant Torsion or pure torsion (Chajes 1974). The first derivative of the angle of twist per unit length (θ') is related to the torsion using the shear modulus of elasticity (G) and the

torsional constant (J). For non-circular cross-sections, if axial deformation would be unrestrained or allowed to rotate freely only pure torsion exists.

$$T_{twisting} = GJ\theta' \tag{8}$$

However, if longitudinal displacements due to torsion (termed warping) are restrained, the cross-section will experience longitudinal warping stress (Chajes 1974). Equation (9) is the

$$T_{warping} = -EC_w\theta''' \tag{9}$$

torsion due to warping resistance (Seaburg and Carter 2003). During warping, a shear force in the flanges form a couple that resists the applied torque. Combining Young's modulus (E) with a warping constant (C_w) gives us the warping rigidity of the section (EC_w). Equation (10) is a combination of both the resistance to the cross-section twisting and resistance to the cross-section warping (Seaburg and Carter 2003). Ultimately the angle of twist (θ) in the beam

$$T = GJ\theta' - EC_w\theta''' \tag{10}$$

needs computed allowing for the derivatives of twist to also be computed. The first step is to rearrange Equation (10) by dividing by the warping rigidity (EC_w) of the cross-section, resulting in Equation (11).

$$\frac{T}{EC_w} = \frac{GJ\theta'}{EC_w} - \theta''' \tag{11}$$

This effectively removes the constant from the θ''' term. To remove the constants from

the θ' term, a new definition shown in Equation (12) can be implemented to remove the

$$a^2 = \frac{EC_w}{GJ} \tag{12}$$

warping rigidity (EC_w) and the pure torsional rigidity (GJ) from the right-hand side of Equation (11). Substituting Equation (12) results in Equation (13). Equation (13) is for a constant torsional moment applied to the beam (Seaburg and Carter 2003).

$$\frac{T}{EC_w} = \frac{\theta'}{a^2} - \theta''' \tag{13}$$

To better model the design scenario listed above, the constant torsional moment needs to be changed to a uniformly distributed torsional moment. To alter Equation (13), an understanding of the relationship between the constant torsional moment and uniformly distributed torsional moment must be established. Figure 87 represents the applied distributed moment on a cross-section. By removing a thin slice (dz) of the

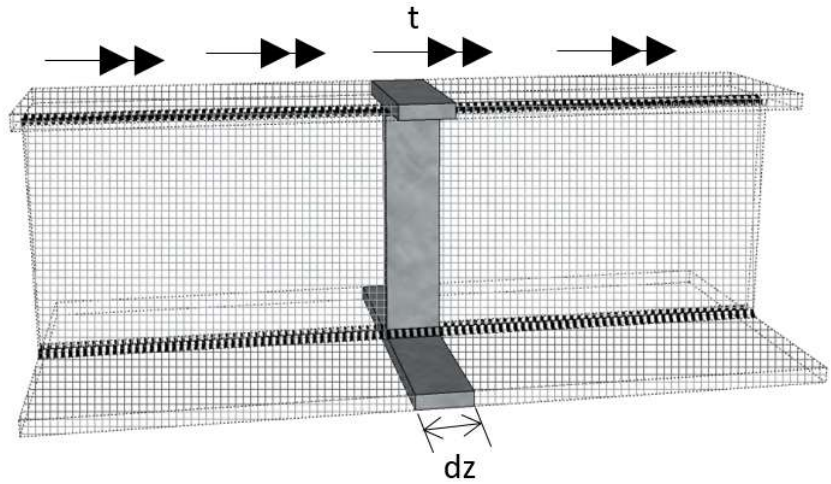

Figure 87: Discretization of a beam for constant torsion

cross-section, we can fully visualize the relationship. Figure 88 show the torsion in the cross-section, due to the applied distributed moment on an infinitesimally

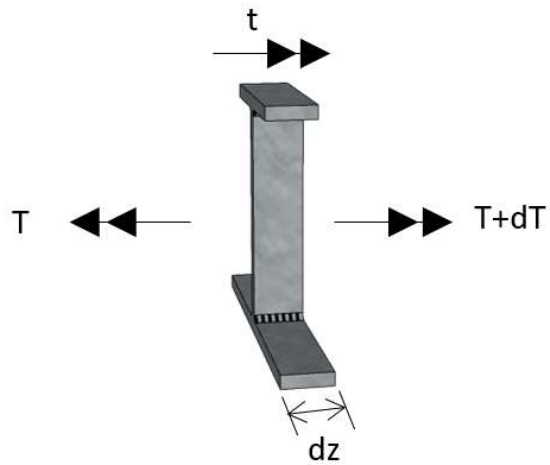

Figure 88: Torsion in an infinitesimally small section of a beam

small section of the beam. The addition or change is torsion on the right hand of the section is (dT). Summing the torsional moments in Figure 88 results in Equation (14).

$$T + dT + t\,dz - T = 0 \tag{14}$$

A further simplification of Equation (14) is represented in Equation (15). Substituting Equation (15) into Equation (13) and differentiating results in the

$$\frac{dT}{dz} = -t \tag{15}$$

equation for a uniformly distributed torsional moment Equation (16) (Seaburg and Carter 2003). The differential

$$\frac{-t}{EC_w} = \frac{\theta''}{a^2} - \theta'''' \tag{16}$$

equation can then be solved for θ. Equation (17) is the solution to the differential

$$\theta = A + Bz + Ccosh\frac{z}{a} + Dsinh\frac{z}{a} - \frac{tz^2}{2GJ} \tag{17}$$

Equation (16) (Seaburg and Carter 2003). A further simplification can be made by applying pinned boundary conditions and solving the arbitrary constants ($A, B, C\ and\ D$), where l is the beam length and z is the location on the beam were θ is evaluated. With the solution for $\theta, \theta', \theta''and\ \theta''''$ Equations (18) to (21) normal stresses

and shear stresses due to torsion can then be calculated (Seaburg and Carter 2003).

$$\theta = \frac{ta^2}{GJ}\left[\frac{l^2}{2a^2}\left(\frac{z}{l} - \frac{z^2}{l^2}\right) + cosh\frac{z}{a} - tanh\frac{l}{2a} \times sinh\frac{z}{a} - 1.0\right] \tag{18}$$

$$\theta' = \frac{-a^2t}{GJ}\left[\frac{l^2}{2a^2}\left(\frac{2z}{l^2} - \frac{1}{l}\right) - \left(\frac{sinh\frac{z}{a}}{a}\right) + \frac{\tanh\left(\frac{l}{2a}\right)\cosh\left(\frac{z}{a}\right)}{a}\right] \tag{19}$$

$$\theta'' = \frac{-a^2t}{GJ}\left[\frac{1}{a^2} - \frac{\cosh\left(\frac{z}{a}\right)}{a^2} + \frac{\sinh\left(\frac{z}{a}\right)\tanh\left(\frac{l}{2a}\right)}{a^2}\right] \tag{20}$$

$$\theta''' = \frac{a^2t}{GJ}\left[\frac{\sinh\left(\frac{z}{a}\right)}{a^3} - \frac{\tanh\left(\frac{l}{2a}\right)\cosh\left(\frac{z}{a}\right)}{a^3}\right] \tag{21}$$

The evaluation of total stress can then be evaluated. The maximum normal stress for a simply supported beam subjected to torsion is found at the mid-span. Two separate normal stresses are present and can be evaluated individually and combined using superposition. Figure 89 is the graphical representation of an eccentric load beam

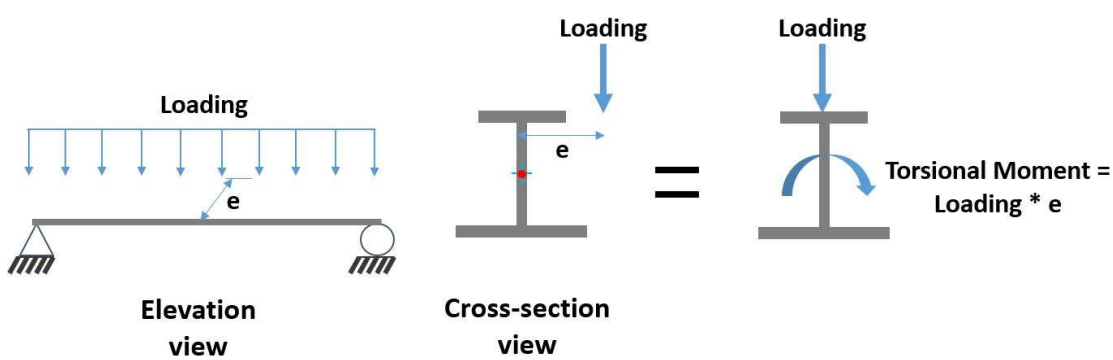

Figure 89: Superposition of eccentric loading

modeled as a concentric load with a torsional moment. The reason for this separation is to then evaluate the bending stresses calculated using Equation (22) which required the moment (M_u) and section modulus (S_x)and the torsional stresses from Equation (23), separately.

$$\sigma_{bending} = \frac{M_u}{S_x} \tag{22}$$

$$\sigma_{warping} = E\, W_{no}\, \theta'' \tag{23}$$

The normal stresses due to bending (Equation (22)) from the applied load and normal stresses due to the torsional warping restraint from the applied torsional moment (Equation (23)) are the two normal stresses calculated (Seaburg and Carter 2003). The distribution of the bending and torsional stresses in the cross-section can be seen in Figure 90. The bending stress (Figure 90a) is a linear distribution varying through the depth of the cross-section. The bending stress distribution is maximum at the top and bottom flanges of the cross-section. During positive bending, the maximum compressive bending stress is in the top flange, and a maximum bending tensile stress is in the bottom flange (Figure 90a). The torsional stresses vary linearly through the flange width. Both the top and bottom flange have compressive and tensile forces. Figure 90b plots the stress distribution across the flanges due to a clock-wise loading. The flange stresses would be opposite with a counter clock-wise loading.

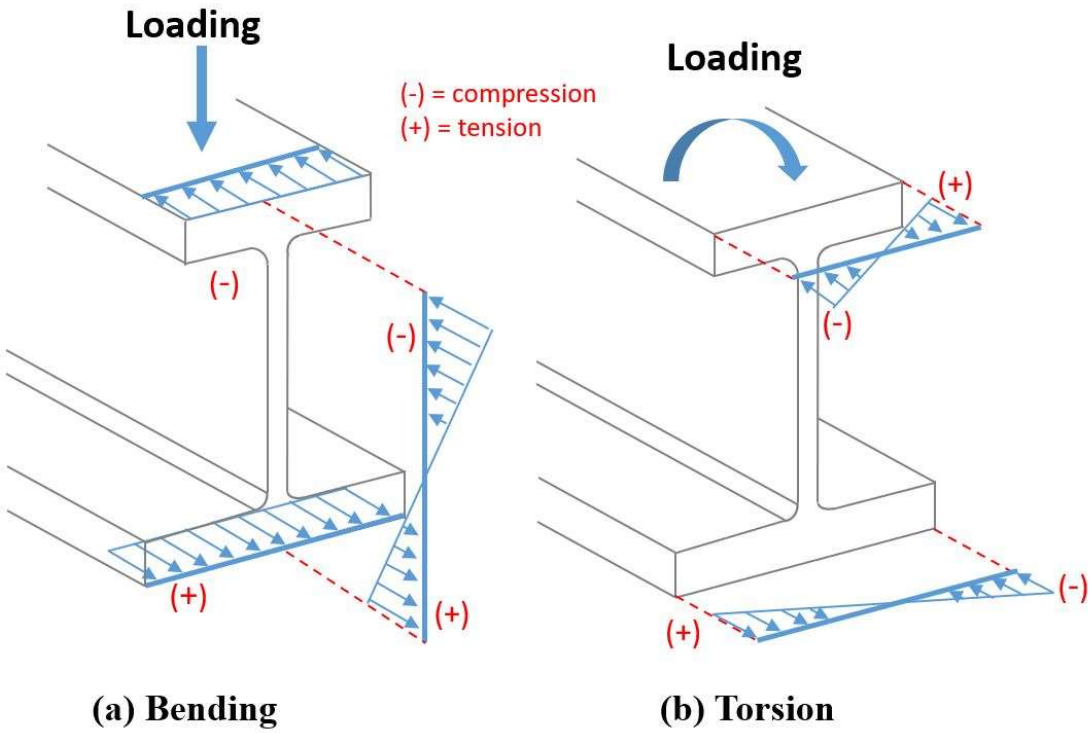

Figure 90: Distribution of normal stresses

The normal stresses are either in tension (+) or compression (-), depending on the location in the cross-section and direction of the applied torsional moment. Figure 91 represents the location of the maximum tension and compression bending stress and warping stresses in the cross-section. Note at separate corners of the cross-section, the warping and bending stresses can be opposite signs causing a reduction in total stress at those locations or acting in the same direction, causing an accumulation of maximum stress.

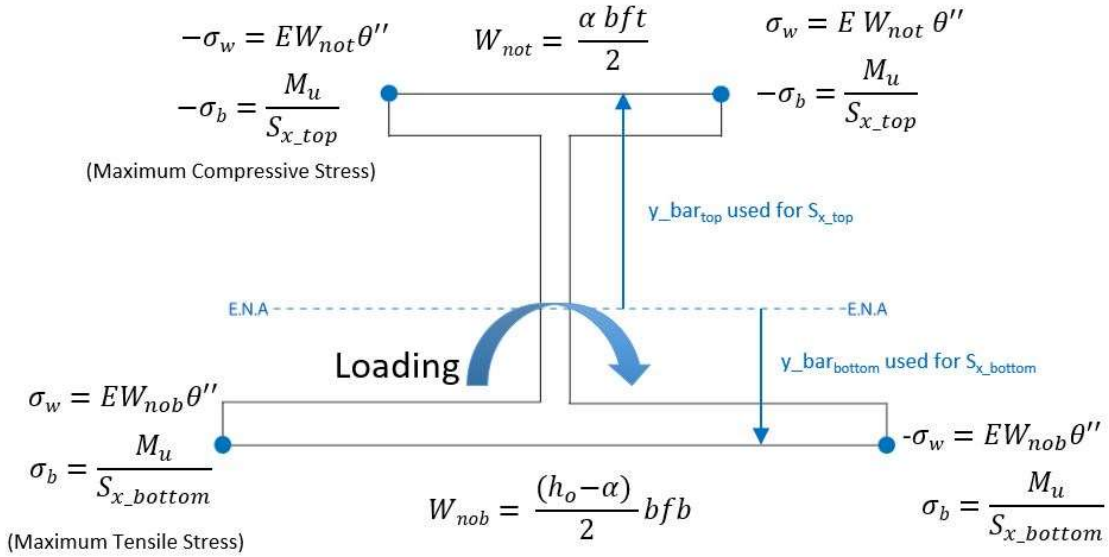

Figure 91: Normal stresses due to bending and torsion at mid-span.

Figure 91 is the combined effects of the bending and torsional stresses at each corner of the cross-section. Note the upper right corner, and lower right corner of the cross-section have different signs causing the forces to help cancel out or reduce. Where in the upper left and lower left the forces are in the same direction causing the stresses to be at a maximum. Due to the loss of double symmetry of an A-shape, separate warping constants and section moduli are needed for the top and bottom flange stress analysis. The unique warping constants and section moduli correlate to different stress results for each flange utilizing Equations (11) and (12). The needed section modulus can be computed using the y_bar_{top} or y_bar_{bottom} from the elastic neutral axis. No alteration needs to be made to the moment of inertia in Equation (11) calculations. The location of the shear center (α) of the section is found by forming the flange couple (Equation (24)). Simplifying Equation (24) results in Equation (25). Further simflication and division to

solve for the shear center (α) (Equation (26)). Figure 92 is a defines all geometric dimensions needed for calculation of the shear center.

$$\frac{t_{ft}b_{ft}^3}{12}(h_o - \alpha) = \frac{t_{fb}b_{fb}^3}{12}(\alpha) \tag{24}$$

$$t_{ft}b_{ft}^3 h_o - t_{ft}b_{ft}^3\alpha = t_{fb}b_{fb}^3\alpha \tag{25}$$

$$\alpha = \frac{b_{fb}^3 t_{fb}}{(b_{ft}^3 t_{ft} + b_{fb}^3 t_{fb})} h_o \tag{26}$$

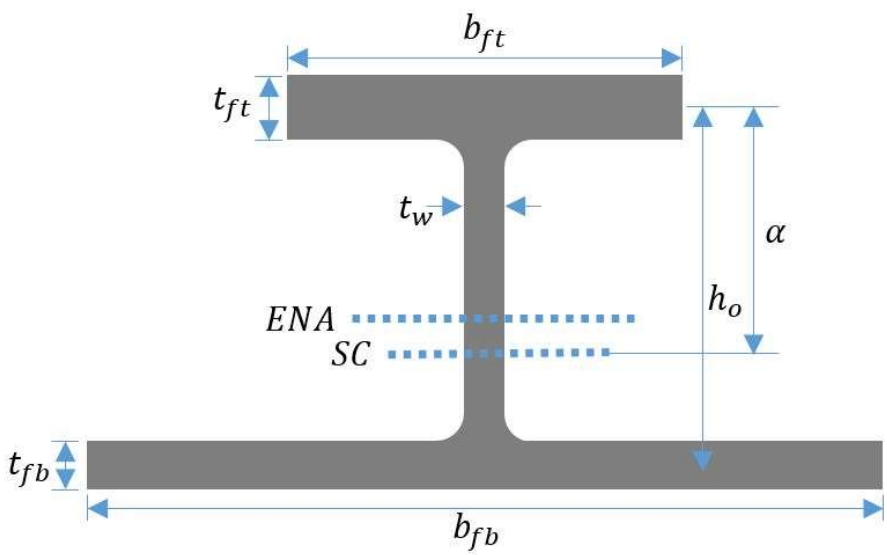

Figure 92: Shear center location

The warping constant W_{not} in Equation (27) and W_{nob} in Equation (28) are taken after locating the shear center (α) (Heins 1975).

$$W_{not} = \frac{\alpha \ b_{ft}}{2} \tag{27}$$

$$W_{nob} = \frac{(h_o - \alpha)}{2} b_{fb} \tag{28}$$

Maximum compressive stresses ($fun_{compression}$) and maximum tensile stresses ($fun_{tension}$) are two parameters checked for failure compliance. In doubly symmetric shapes the $fun_{compression}$ and $fun_{tension}$ stresses are the same value. In A-shapes, the different warping constants require a check of both stresses individually.

Along with checking normal stresses (fun) at the mid-span of the beam, shear stresses (fuv) at the beam end also must be calculated and checked. The three shear stresses that develop at the support in the beam flange are due to bending, pure torsion, and warping stresses. Similar to the normal stresses the shear stresses vary in the top and bottom flange due to the loss of double symmetry. The web also develops shear stresses due to bending and pure torsion. Unlike the flanges, there are no shear stresses in the web due to warping.

Evaluation of the flange shear stresses requires three equations. Equation (29) is the shear stresses due to bending. Four variables are needed to compute bending shear stress ($\tau_{bending_flange}$). Those include the shear from the applied load (V_u), the statical moment of the flange (Q_f), the moment of inertia (I_x) and the flange thickness (t_f). The flange thickness and statical moment are unique per flange. The statical moment of the flange is calculated by multiplying the flange area with the distance from the flange centroid to the elastic neutral axis. Equation (30) computes the shear stress due to pure torsion in the flange ($\tau_{pure\ torsion_flange}$) using the shear modulus (G), flange thickness

(t_f) and the first derivative of twist (θ'). Unique to each calculation for pure torsion is the flange thickness. The final shear stress in the flange at the support is due to the warping restraint of the cross-section. Equation (31) list the four parameters needed to calculate the shear stress due to warping restraint ($\tau_{warpi\quad_flange}$) those include Youngs modulus of steel (E), the flange thickness (t_f), warping statical moment (S_w)

$$\tau_{bending_flange} = \frac{V_u\, Q_f}{I_x\, t_f} \tag{29}$$

$$\tau_{pure\ torsion_flange} = G\ t_f \theta' \tag{30}$$

$$\tau_{warping_flange} = \frac{E\, S_w\, \theta'''}{t_f} \tag{31}$$

and the third derivative of twist (θ''') (Seaburg and Carter 2003). The warping statical moment (S_{wt}) in Equation (32) is used for the top flange. The warping statical moment (S_{wb}) in Equation (33) is used for the bottom flange. Both equations are derived from the normalized warping function (W_{no}) as shown in Equations (27) and (28), and flange properties. Due to the asymmetric nature of the proposed cross-sections, shear in the top flange ($fuv_{top\ flange}$) and bottom flange ($fuv_{bottom\ flange}$) have to be check separately with the corresponding flange parameters.

$$S_{wt} = \frac{W_{not}\, t_{ft}\, b_{ft}}{4} \tag{32}$$

$$S_{wb} = \frac{W_{nob}\, t_{fb}\, b_{fb}}{4} \tag{33}$$

Corrected parameter locations and shear force direction are shown in Figure 93. Due to a sign change on pure torsion and warping shear stresses, a summation of forces at the flange is achieved for maximum shear stress.

Web shear stresses (fuv_{web}) at the support location also needed to be computed and checked. The web shear stresses include pure torsion and bending. The warping that is present in the flanges is not propagated into the web. Four variables are needed to compute bending shear stress ($\tau_{bending_web}$) as shown in Equation (34). Those include the shear from the applied load (V_u), the statical moment of the web (Q_w), the moment of inertia (I_x), and the web thickness (t_w). Equation (35) computes the shear stress due to pure torsion

$$\tau_{bending_web} = \frac{V_u \ Q_w}{I_x \ t_w} \tag{34}$$

$$\tau_{pure\ torsion_web} = G\ t_w \theta' \tag{35}$$

in the web ($\tau_{pure\ torsion_web}$) using the shear modulus (G), web thickness (t_w), and the first derivative of twist (θ'). Maximum values for web shear are taken at the elastic neutral axis. Shear direction and location on the web can be viewed in Figure 93.

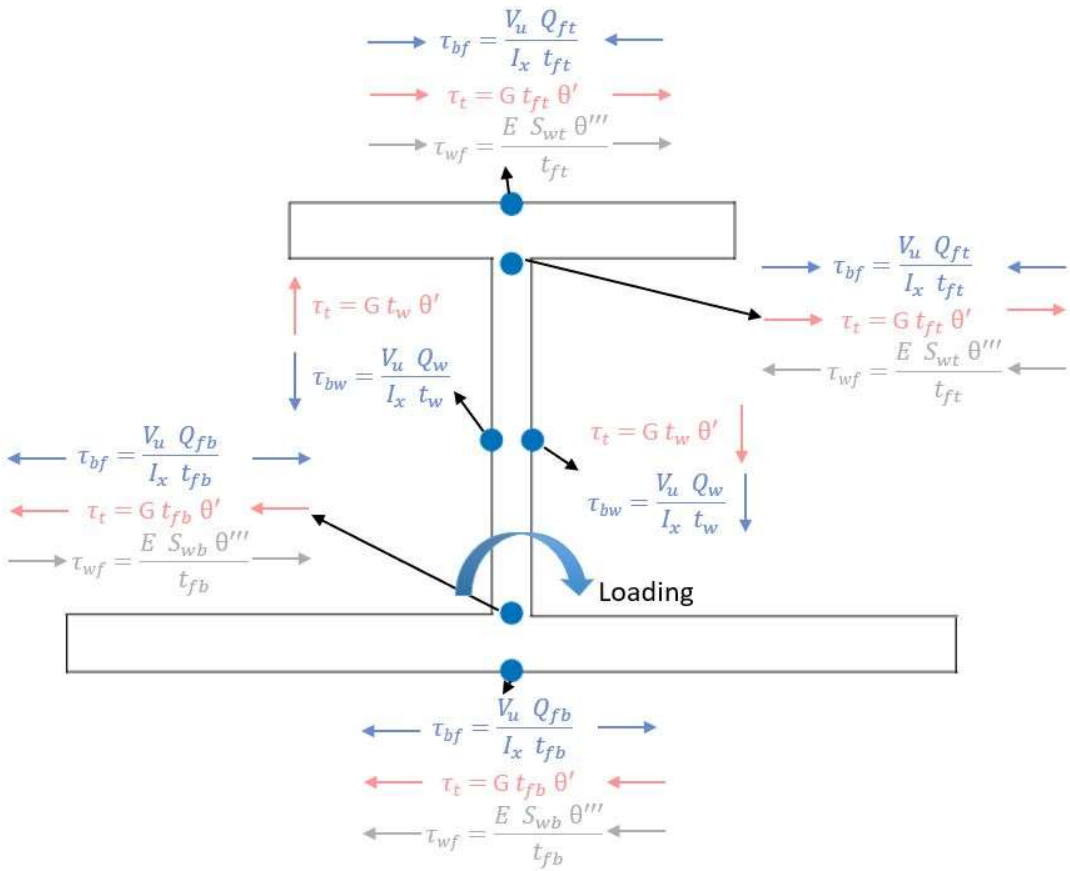

Figure 93: Shear stresses due to bending and torsion at the support.

The parametric study performed all seven stress checks described previously. Those stresses were checked against different limit states depending on code allowance. The maximum compression and maximum tensile normal stresses are checked under Equation (36) or Equation (37) (Seaburg and Carter 2003).

$$\frac{\emptyset F_y}{fun_{tension}} \geq 1 \tag{36}$$

$$\frac{\emptyset F_{cr}}{fun_{compression}} \geq 1 \tag{37}$$

Shear stresses were checked in the web and both top and bottom flanges. The flanges were checked using Equation (38) (Seaburg and Carter 2003). The final shear stress check was on the web, as shown in Equation (39) (Seaburg and Carter 2003). The stability of the section is checked in Equation (40) (Seaburg and Carter 2003). Along with the normal and shear stress checks, the cross-section rotation at midspan was checked with Equation (41) and maximum (b/t) residual check Equation (42) from the previous numerical study (Figure 23).

$$\frac{\emptyset 0.6F_y}{\max(fuv_{top\ flange}, fuv_{bottom\ flange})} \geq 1 \tag{38}$$

$$\frac{\emptyset 0.6F_y}{fuv_{web}} \geq 1 \tag{39}$$

$$\frac{\emptyset F_{cr}}{fun_{compression}} \geq 1 \tag{40}$$

$$\frac{\theta_{allow}}{\theta} \geq 1 \tag{41}$$

$$\frac{b}{t} \geq 17 \tag{42}$$

4.4.3.4. Scenario I Model: Results

The results from each limit state listed above in Equation (36) – Equation (42) are presented in this section. The forthcoming plots are the normalized results (capacity/demand) on the ordinate with the beam parameter plotted on the abscissa. Each limit state is presented with the area being the first beam parameter, when other plots are needed for clarity, they are provided in this section. Appendix A has all plotted results

containing relationships between the normalized results and t_{ft}, t_{fb}, b_{ft}, b_{fb}, t_w, $Web\ height$, I_x, and J.

The first normalized parameter plot in Figure 94 is the tension flange yielding limit state, calculated with Equation (36). Discussed at the same time is the normalized compression flange yielding limit state (Figure 95) from Equation (37). Both the tension flange and compression flange yielding are similar plots with a slight reduction in capacity to the compression flange yielding. The overall trends associated with the two plots are similar. Flange area is the major controlling factor in both situations. Figure 94 has the smallest 0.125 inch t_{ft} in beam number 193 at the bottom of the plot and beam number 208 with a 2 inch t_{ft} having the most capacity. The interesting part of the plots is the bands that are shown. Each band represents a group of flange thicknesses (t_{ft}) with the changing flange width (b_{ft}) causing the change in capacity. Plotting the flange thicknesses (t_{ft}) (Figure 96) groups the same flanges thicknesses together. Figure 96 represents the capacity increase with additional flange thincknesses (t_{ft}) and the lesser strength increase with flange width (b_{ft}) changes . Each vertical grouping shares a flange thickness (t_{ft}) with a flange width (b_{ft}) that increases as the strength increases vertically. Overall, it was found that tension and compression flange yielding is not a concern for common A-shape proportions, with most cross-sections normalized values exceeding 1.

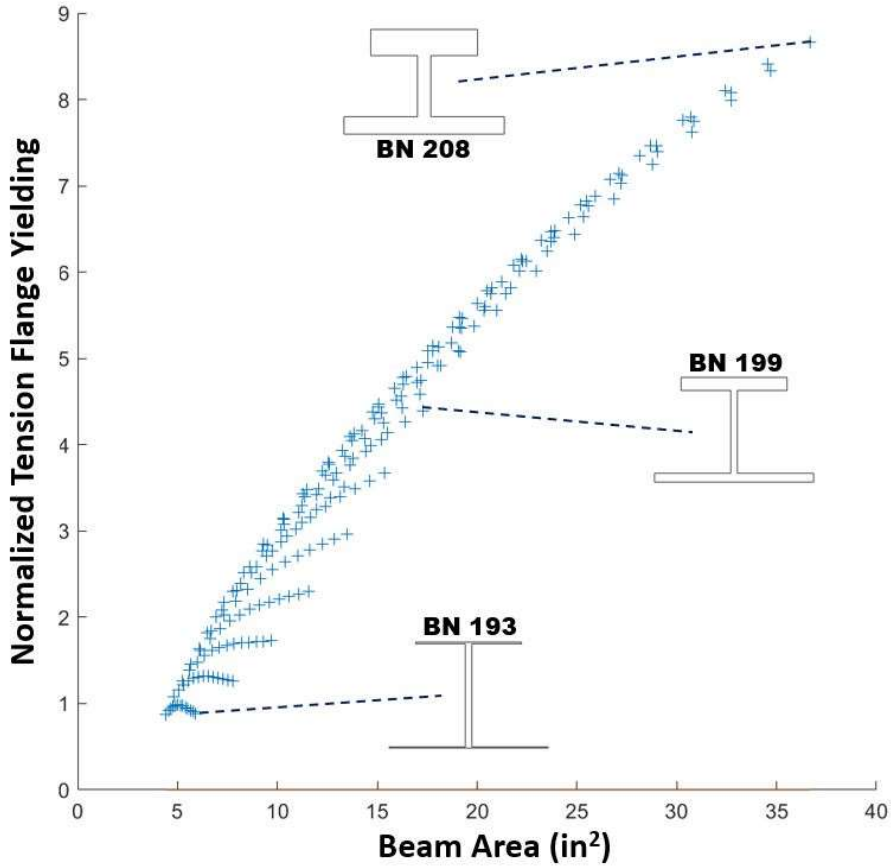

Figure 94: Scenario I: Normalized tension flange yielding vs. beam cross-sectional area

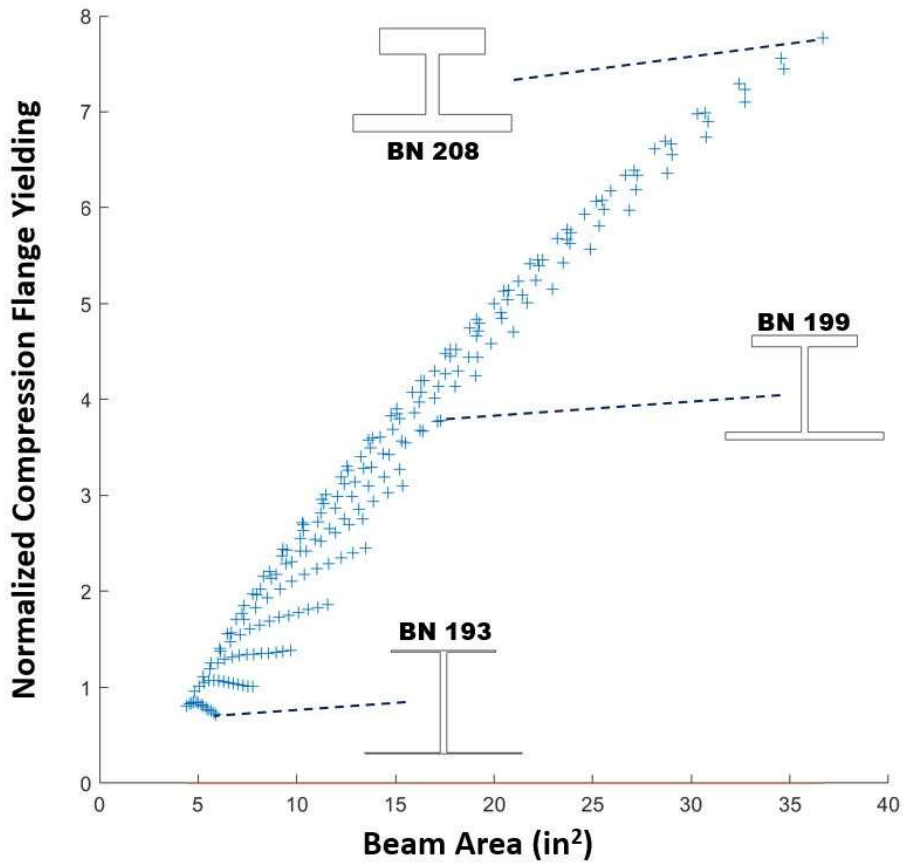

Figure 95: Scenario I: Normalized compression flange yielding vs beam cross-sectional area

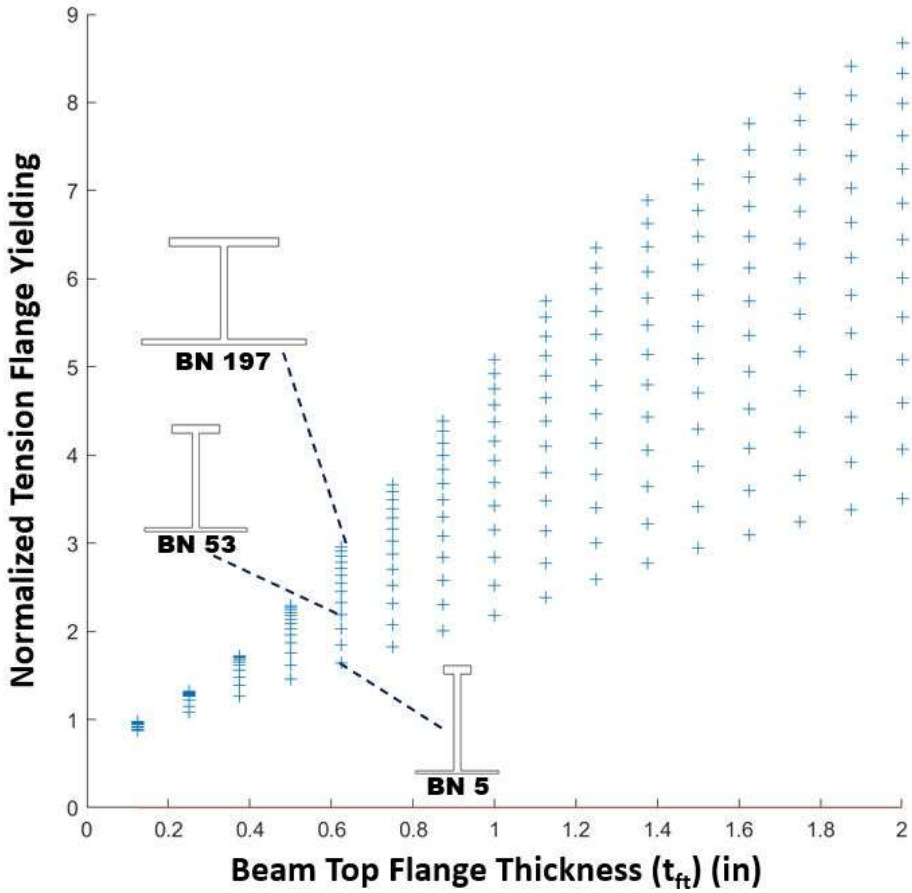

Figure 96: Scenario I: Normalized tension flange yielding vs. beam flange thickness (t_{ft})

The second equation analyzed was Equation (38). Equation (38) is the limit state for flange shear yielding in the top flange and bottom flange. To reduce outputs, and due to the limiting control flange shear yielding presents, the maximum stress between the two flanges was plotted in Figure 97. The top and bottom flange shear stresses were checked by the code but only outputted for the maximum stress. Due to the bottom flange being held as the larger flange the controlling flange was the top flange. A closer look at the warping statistical moment (S_w) (Equation (32)) shows the governing factor is the warping constant (W_n) (Equation (27)). Due to geometric constrains (α) is always

going to be a larger value than $(h_o - \alpha)$ causing the top flange to control. Altering the plotted area to web height in Figure 98 shows the dominating effect web height has on the flange shear yielding strength. However, the substantially high normalized results show that this limit state is not a concern for A-shape beams under these loading conditions.

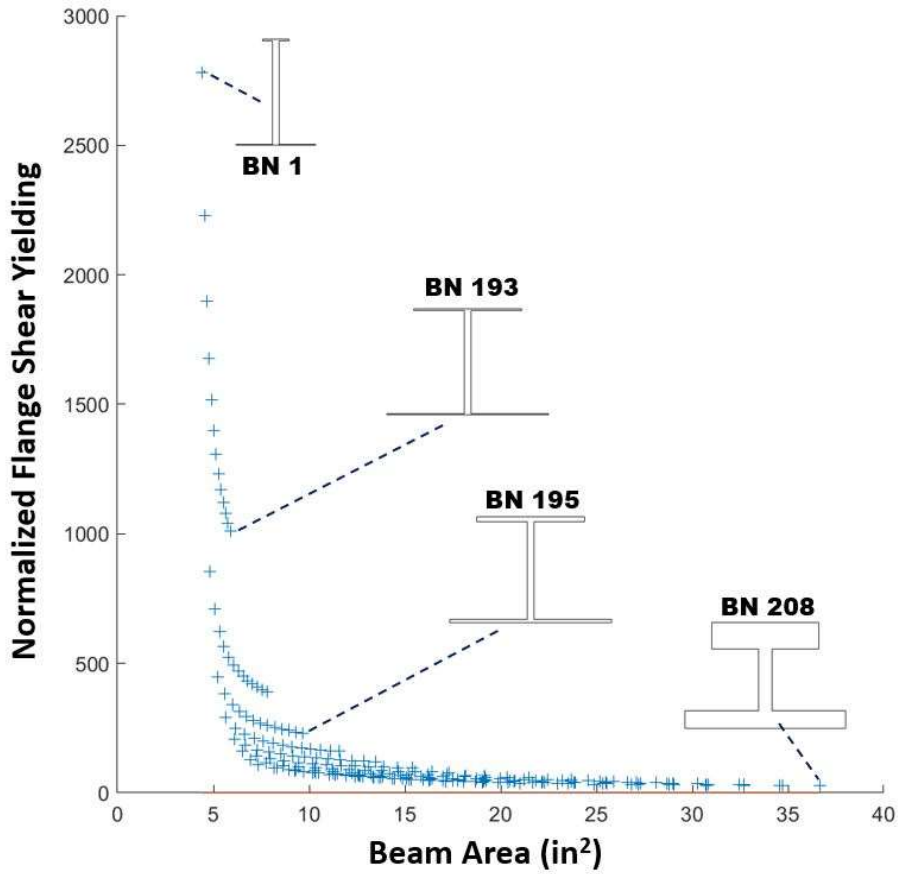

Figure 97: Scenario I: Normalized flange shear yielding vs. beam cross-sectional area

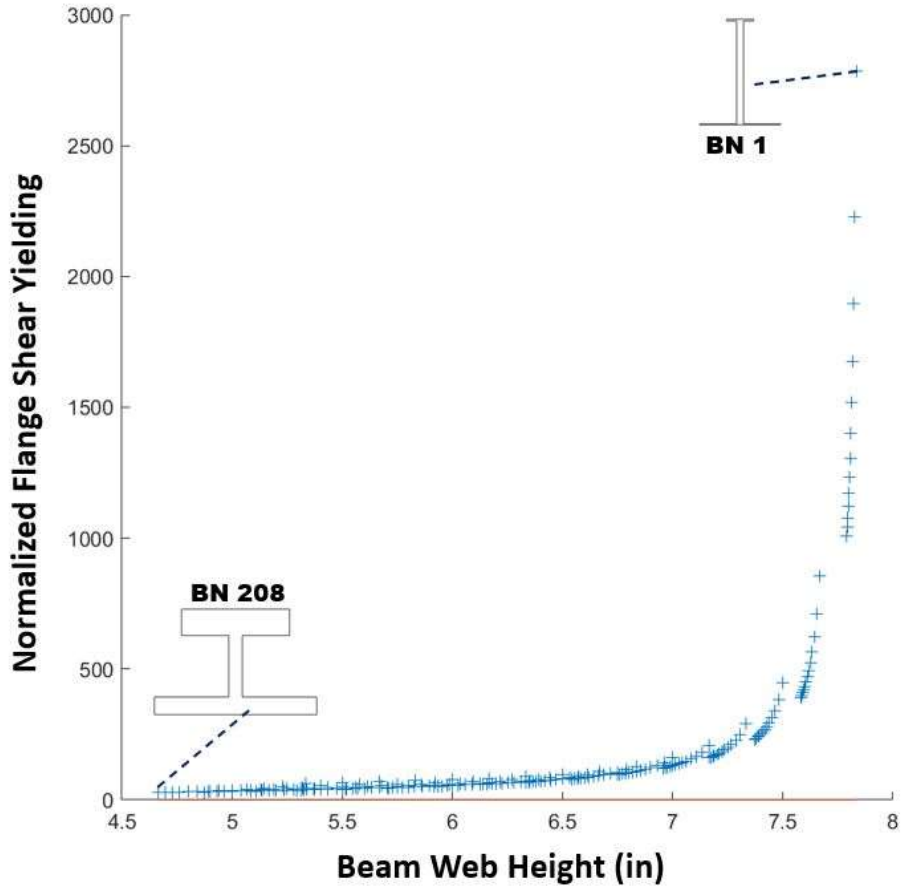

Figure 98: Scenario I: Normalized flange shear yielding vs. beam web height

The normalized web shear yielding plot vs. the cross-sectional area of the beam shown in Figure 99 is the result of Equation (39). The area plot has two unique attributes to point out. The first is that as the web gets shorter and thicker, the strength is decreased. The second is the large cluster at the top of the plot is due to a constrained web thickness not being able to fall below 0.5 inches. Altering the area for web thickness in Figure 100 illustrates the web height and thickness's control on web shear yielding. Figure 100 has separate bands that represent beams with the same flange thicknesses and the same web thicknesses; for example, beam numbers 41 and 201 have a 1.125 inch t_{ft}

with only a change in the flange width causing the local reduction in capacity. The overall trend of capacity loss between bands is evident, with the largest beam number 208 shown as the smallest web shear yielding capacity. Web shear yielding under these loading conditions was not a design concern.

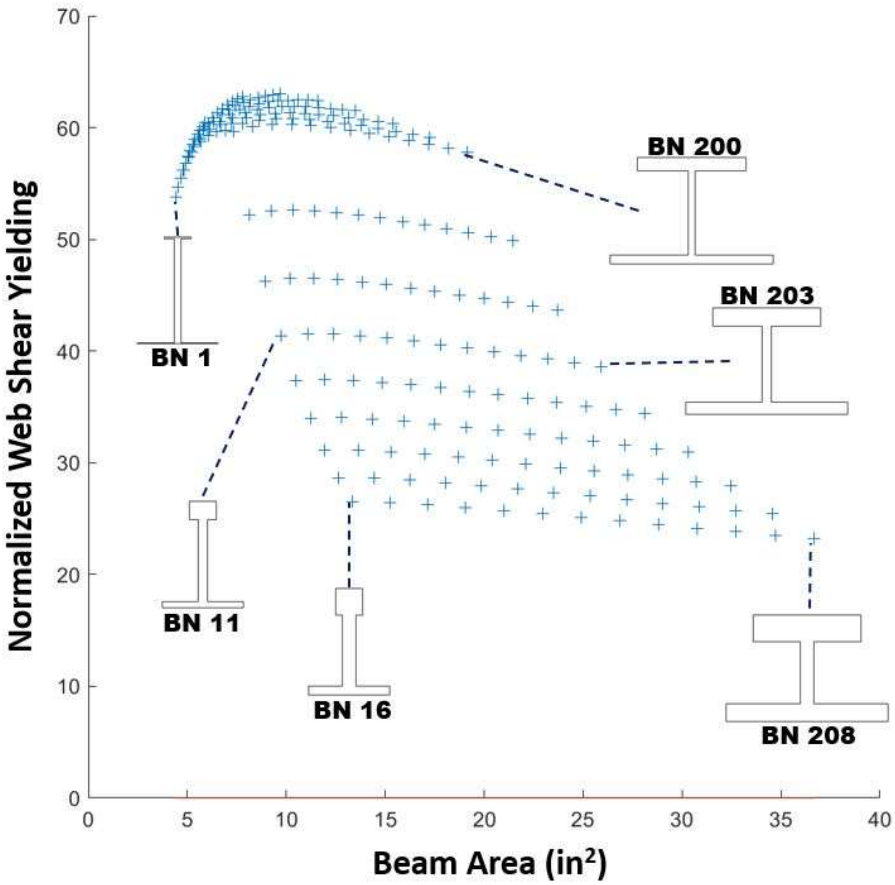

Figure 99: Scenario I: Normalized web shear yielding vs beam cross-sectional area

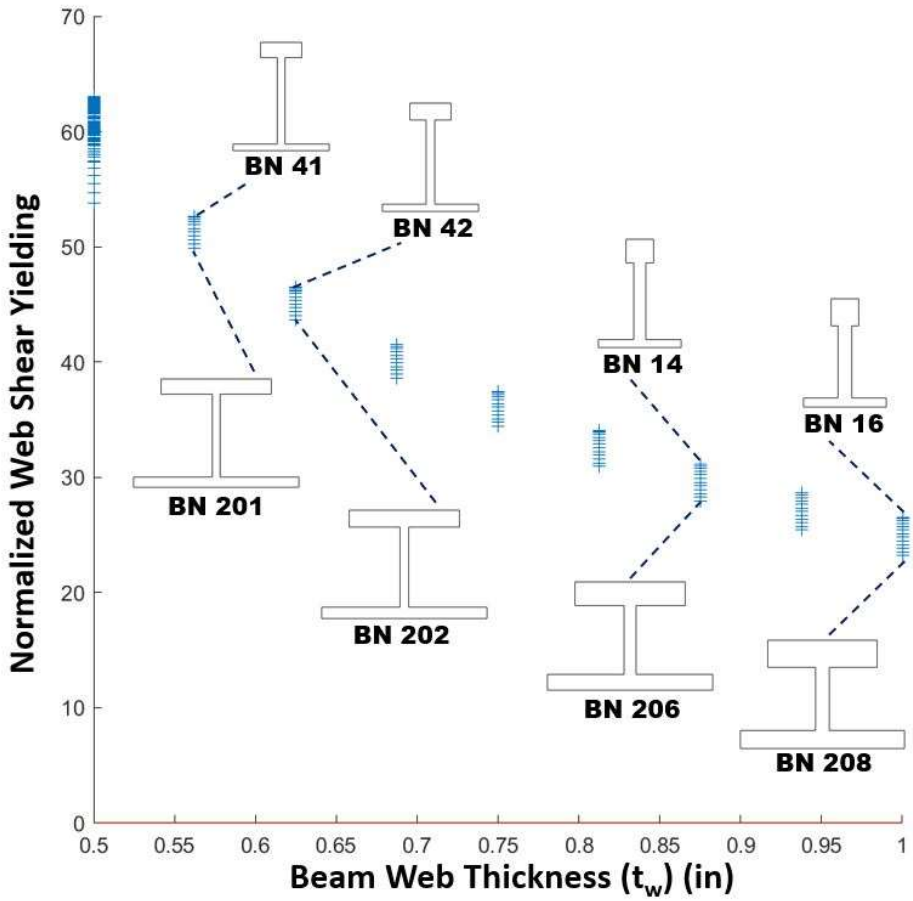

Figure 100: Scenario I: Normalized web shear yielding vs. beam web thickness (t_w)

The next normalized parameter to discuss is one of the most important due to the way torsional loads affect an open cross-section. Buckling of the section is evaluated using Equation (40), which later was shown to control many of the cross-sections geometries. Figure 101 is the plot of normalized buckling and the cross-sectional area. By inspection of the plot, the top flange width (b_{ft}) and top flange thickness (t_{ft}) both play a roll in the capacity of the cross-section due to buckling. Figure 102 plots the normalized buckling results against the top flange width (b_{ft}). Figure 103 plots the normalized buckling results vs. the top flange thickness (t_{ft}). The unique aspect of

analyzing Figure 102 and Figure 103 together is the relationship that the flange width and flange thickness play in capacity. In the top flange width (b_{ft}) plot (Figure 102) the changes in thickness (t_{ft}) can be observed. The increse in thickness (t_{ft}) increases the buckling resistance on a linear increase. The change in flange thickness (t_{ft}) plot (Figure 103) shows the increased buckling resistance due to flange width (b_{ft}) changes. With a changing flange width (b_{ft}) the resistance to buckling increases at a faster rate. These two increases show that both flange thickness (t_{ft}) and flange width (b_{ft}) play a role in buckling resistance, although the flange width (b_{ft}) has a greater influence.

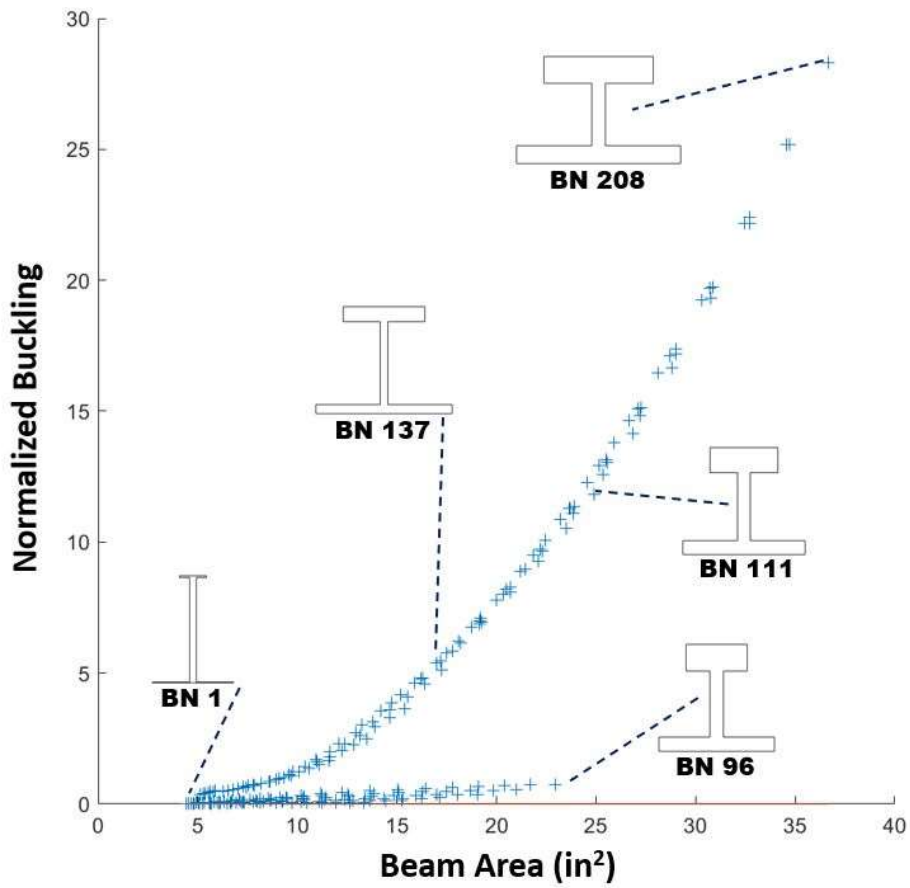

Figure 101: Scenario I: Normalized buckling vs. beam cross-sectional area

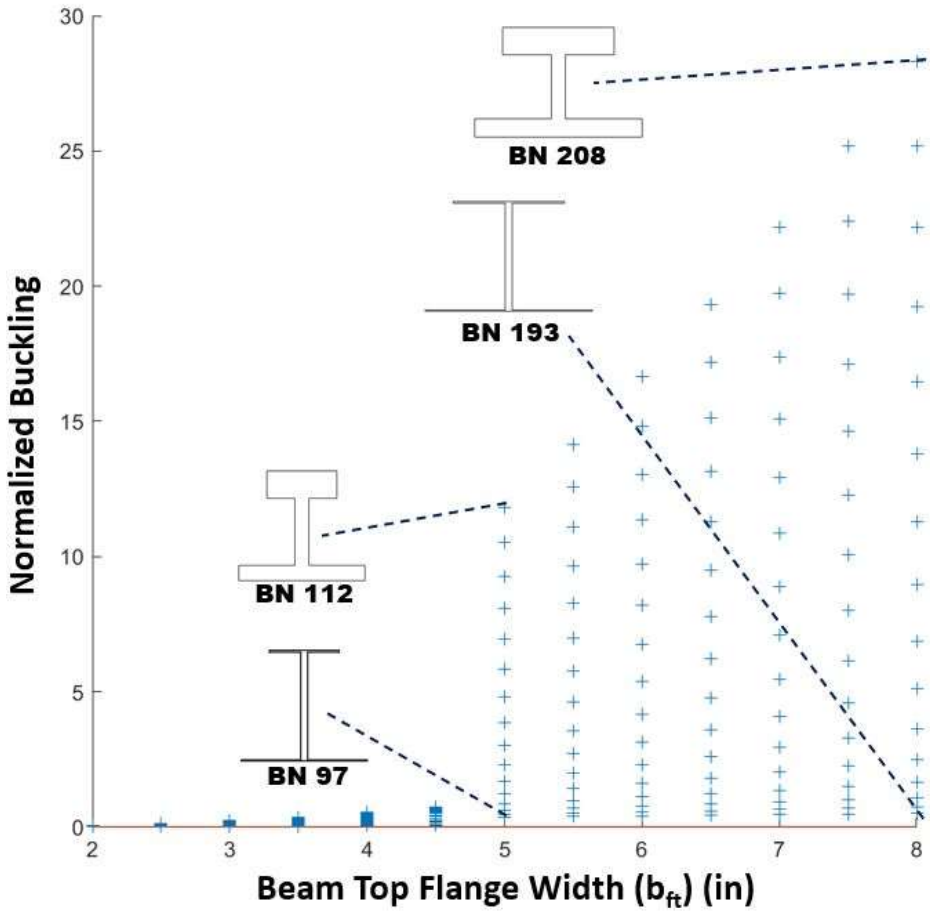

Figure 102: Scenario I: Normalized buckling vs. beam top flange width (b_{ft})

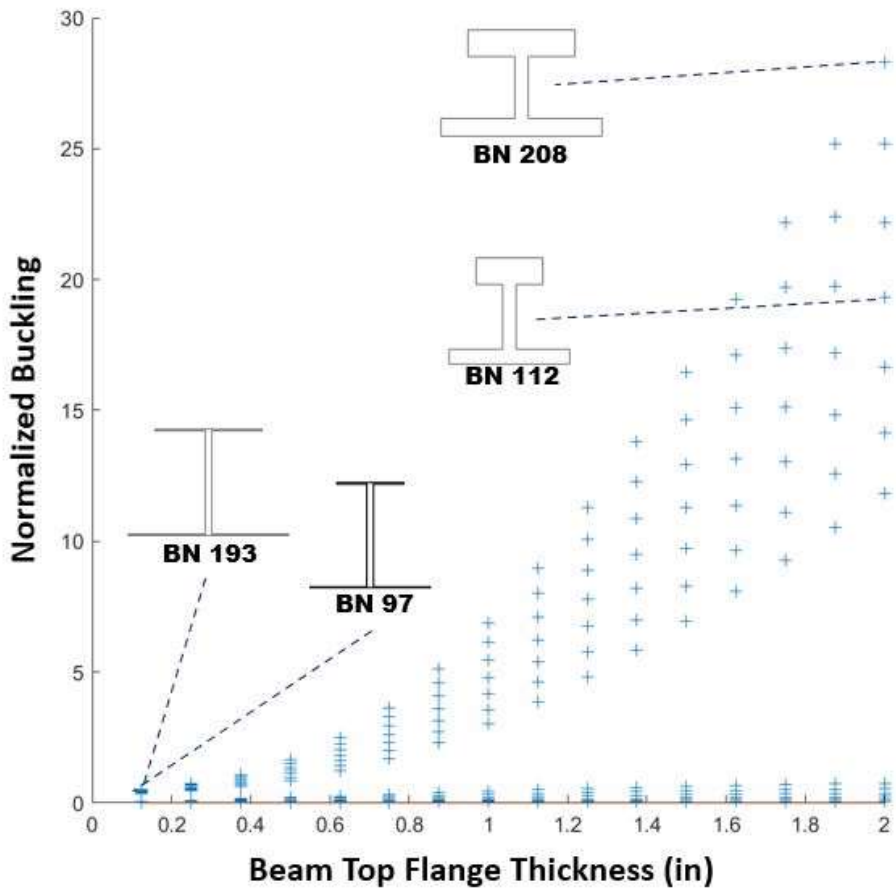

Figure 103: Scenario I: Normalized buckling vs. beam top flange thickness (t_{ft})

The rotation of the cross-section (Equation (41)) is presented in Figure 104. The rotation plot is similar to the buckling plot. A combination of the top flange thickness (t_{ft}) and top flange width (b_{ft}) affect the beam rotation due to changes in torsional stiffness. Figure 105 is the normalized rotation vs. the top flange width (b_{ft}). Showing the results for normalized rotation in Figure 105, the relationship between the flange thickness (t_{ft}) and flange width (b_{ft}) can be better understood. The rotation limit state did control some of the A-shape cross-sectional geometry (discussed later).

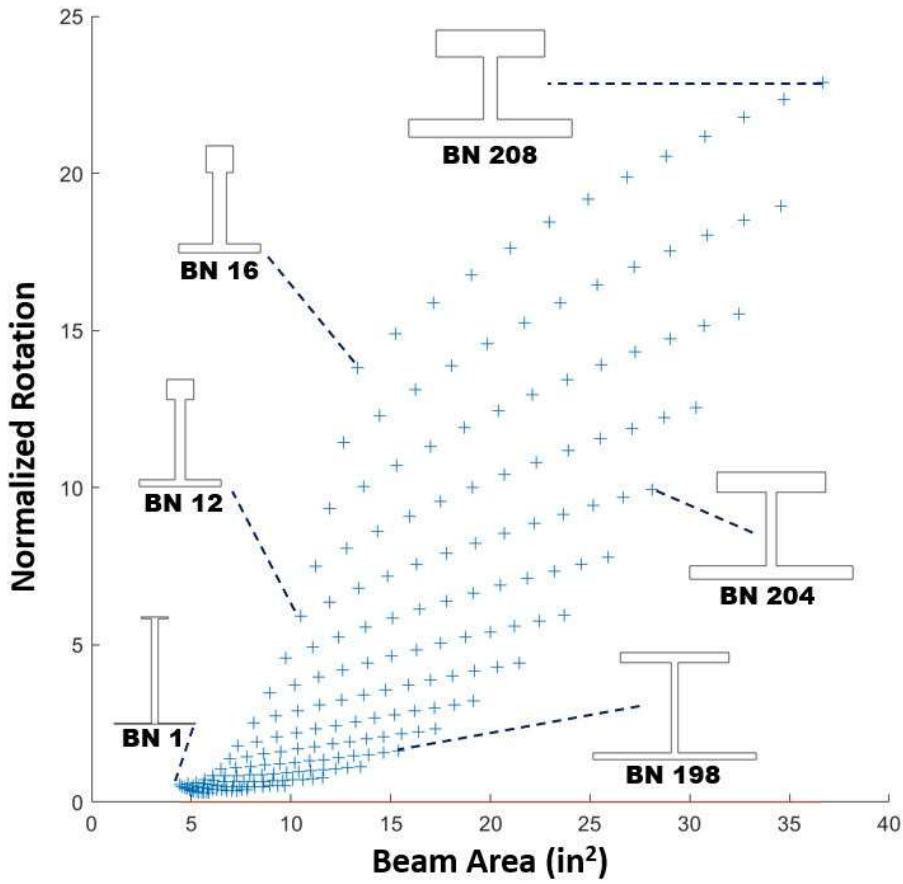

Figure 104: Scenario I: Normalized rotation vs beam cross-sectional area

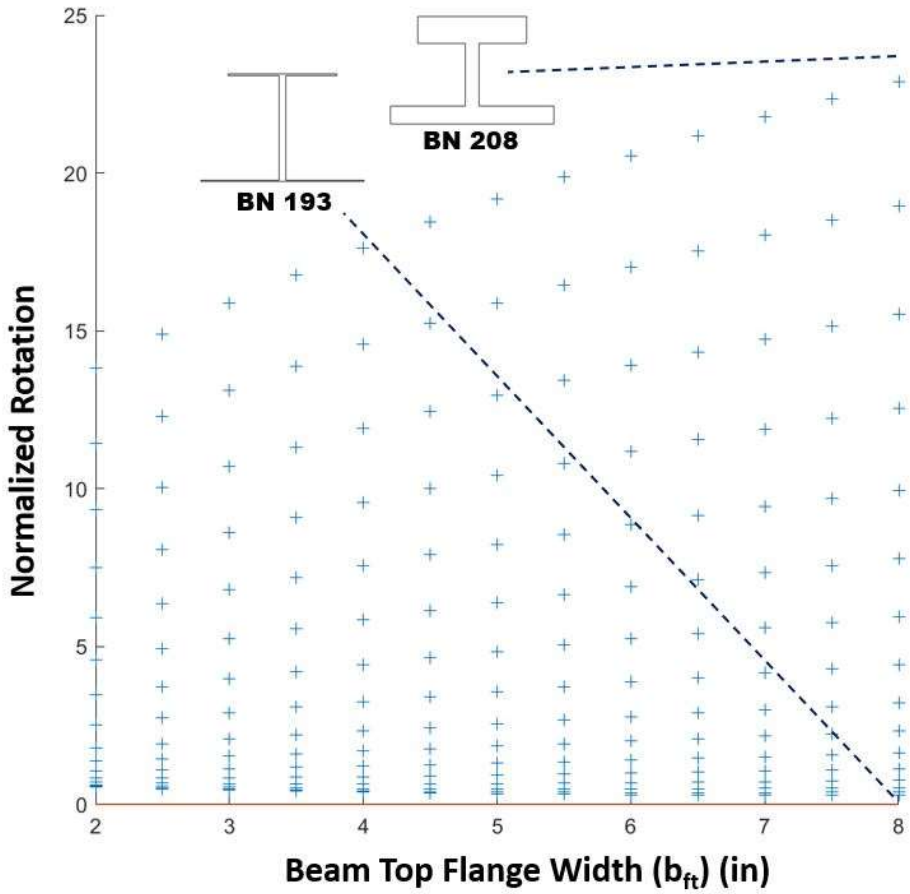

Figure 105: Scenario I: Normalized rotation vs. beam top flange width (b_{ft})

The final normalized condition for Scenario I is Equation (42), the b/t flange limit determined from section 4.1.5.3. Figure 113 is the plot of normalized b/t vs. the cross-sectional area. Simular as the name implies, the top flange thickness (t_{ft}) and top flange width (b_{ft}) both affect the b/t of the cross-section. Overall, this was not found to have a significant impact on the future A-shape geometry.

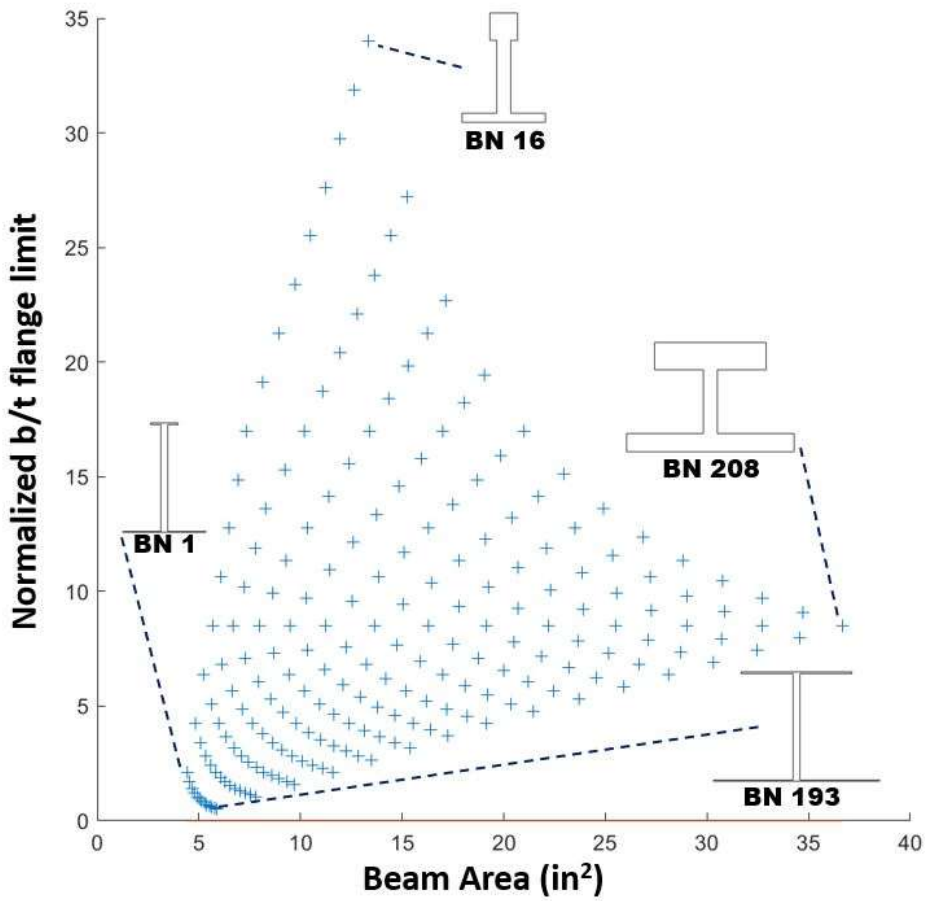

Figure 106: Scenario I: Normalized flange limits vs beam cross-sectional area

4.4.4. Analytical Study - Scenario II: Non-composite concentric loading

4.4.4.1. Scenario II Model: Load Case 2a

Load Case 2a utilized Scenario II: non-composite concentric loading analysis. The construction load (Figure 107) takes place after the topping slab has been placed and before that topping slab has cured.

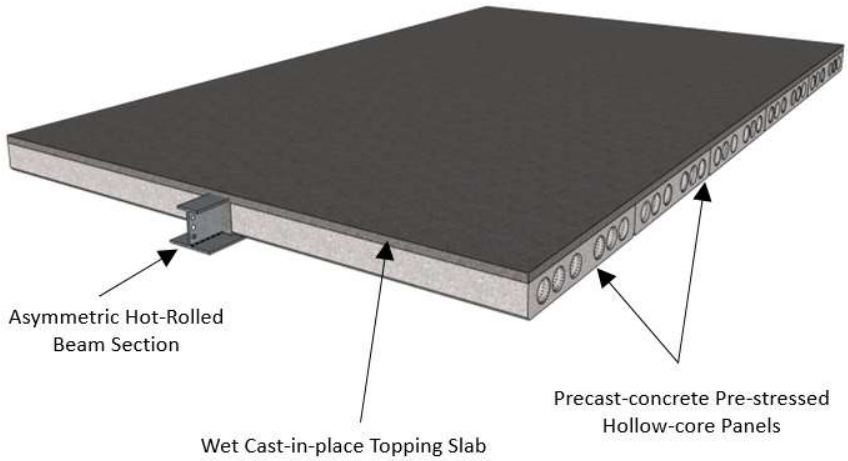

Figure 107: Loading scenario 2a, precast-concrete panels with a wet topping slab

Loading Case 2a is symmetric loading, unlike Loading Cases 1 and 2b. Loading Case 2a is the highest load on the A-shape in a non-composite configuration. The loading is the highest total weight but without the increased demand for torsion. The beams were evaluated for several limit states that included compression flange yielding, lateral-torsional buckling, compression flange local buckling, and tension flange yielding. Along with these checks, shear and deflection checks were completed.

The parameters needed for Load Case 2a are:

- Construction live load of 20 psf (ASCE/SEI 2015)
- Construction live load factor of 1.6 (ASCE/SEI 2015)
- Panel dead load of 57 psf (Flood Precast 2019)
- Dead load factor of 1.4 (ASCE/SEI 2015)
- Tributary width of the panel of 10 feet
- Topping slab thickness of 3 inches
- Tributary width of topping slab of 10 feet

- Beam length of 20 feet
- Service deal + live deflection limit of L/240 (Council 2017)

4.4.4.2. Scenario II Model: Methodology

The first step to analyze the asymmetric cross-section is to calculate the web slenderness (λ_{web}) and compare that to the limiting slenderness for non-compact webs (λ_{rw}) as shown in Equation (43) (AISC 2016).

$$\lambda_{rw} = 5.70\sqrt{\frac{E}{F_y}} \tag{43}$$

To compute the web slenderness (λ_{web}), twice the distance from the bottom of the top flange to the elastic neutral axis (h_c) (shown in Figure 108) is divided by the web thickness (t_w) as shown in Equation (44) (AISC 2016).

$$\lambda_{web} = \frac{h_c}{t_w} \tag{44}$$

If the web slenderness (λ_{web}) is larger than (λ_{rw}) the section is categorized as having a slender web. If this is the case, local buckling needs to be considered.

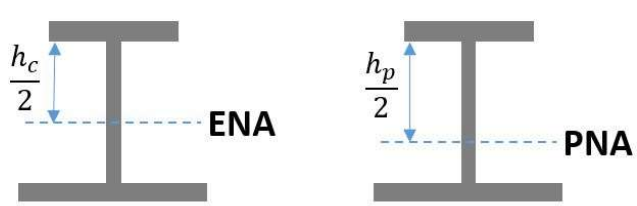

Figure 108: Location of h_c and h_p on A-shapes

Cross-sections without a slender web were categorized as either compact or non-compact, and the four limit states were analyzed. The first limit state analyzed is compression flange yielding using Equation (45) (AISC 2016).

$$M_n = R_{pc} M_{yc} \tag{45}$$

Compression flange yielding is the product of the web plastification factor (R_{pc}) and the compression flange yield moment (M_{yc}). The second limit state is lateral-torsional buckling. Depending on the unbraced limiting factors (L_p & L_r) one of two equations control buckling. When the unbraced length is greater than the inelastic limit (L_r) ($L_b > L_r$) Equation (46) controls, which represents elastic lateral-torsional buckling (AISC 2016).

$$M_n = F_{cr} S_{xc} \leq R_{pc} M_{yc} \tag{46}$$

The product of the section modulus (S_{xc}) and the flexural local critical buckling stress (F_{cr}), which is cacluated as shown in Equation (47) (AISC 2016).

$$F_{cr} = \frac{C_b \pi^2 E}{\left(\frac{L_b}{r_t}\right)^2} \sqrt{1 + 0.078 \frac{J}{S_{xc} h_0} \left(\frac{L_b}{r_t}\right)^2} \tag{47}$$

An unbraced length (L_b) that is between the inelastic limit state (L_r) and the yielding limit state (L_p)($L_p < L_b \leq L_r$) utilized Equation (48) controls, which represents inelastic lateral-torsional buckling (AISC 2016).

$$M_n = C_b \left[R_{pc} M_{yc} - \left(R_{pc} M_{yc} - F_L S_{xc} \right) \left(\frac{L_b - L_p}{L_r - L_p} \right) \right] \leq R_{pc} M_{yc} \tag{48}$$

The third limit state to analyze is compression flange local buckling. Compression flange local buckling is divided by slender flanges and non-compact flanges. Non-compact flanges use Equation (49) for the controlling moment (AISC 2016).

$$M_n = R_{pc} M_{yc} - \left(R_{pc} M_{yc} - F_L S_{xc} \right) \left(\frac{\lambda - \lambda_{pf}}{\lambda_{rf} - \lambda_{pf}} \right) \tag{49}$$

Slender flanges implement Equation (50) for the controlling moment (AISC 2016).

$$M_n = \frac{0.9 E k_c S_{xc}}{(\lambda)^2} \tag{50}$$

The final limit state for non-slender webs is tension flange yielding. Tension flange yielding employs Equation (51) utilizing the yield moment in the tension flange (M_{yt}) (AISC 2016).

$$M_n = R_{pt} M_{yt} \tag{51}$$

The cross-sections that have web slenderness (λ_{web}) which falls above the web limiting slenderness (λ_{rw}) or slender webs, the same checks are performed. The checks use differing equations for the four limit states mentioned previously. The equations that control slender web cross-sections are listed below. Compression flange yielding implements Equation (52) by using the product of the bending strength reduction factor (R_{pg}), steel yield strength (F_y) and section modulus (S_{xc}) (AISC 2016).

$$M_n = R_{pg} F_y S_{xc} \tag{52}$$

The lateral torsional buckling, similar to compact and noncompact webs, is broken into two separate cases due to unbraced length. The two cases incorporate a different critical stress (F_{cr}) into the same controlling moment Equation (53) (AISC 2016).

$$M_n = R_{pg} F_{cr} S_{xc} \tag{53}$$

When the unbraced length is greater than the inelastic limit (L_r) ($L_b > L_r$) Equation (54) controls the critical stress (F_{cr}) (AISC 2016).

$$F_{cr} = \frac{C_b \pi^2 E}{\left(\frac{L_b}{r_t}\right)^2} \leq F_y \tag{54}$$

An unbraced length (L_b) that is between the inelastic limit state (L_r) and the yielding limit state (L_p)($L_p < L_b \leq L_r$), Equation (55) controls the critical stress (F_{cr}) (AISC 2016).

$$F_{cr} = C_b \left[F_y - \left(0.3 F_y\right) \left(\frac{L_b - L_p}{L_r - L_p} \right) \right] \leq F_y \tag{55}$$

Compression flange local buckling is divided into two separate critical stress equations very similar to lateral-torsional buckling. The governing moment Equation (53) is also used in compression flange local buckling. The two separate critical stress equations are divided between non-compact flanges and slender flanges. Equation (56) is the code critical stress equation to satisfy non-compact flange compression flange local buckling (AISC 2016).

$$F_{cr} = \left[F_y - \left(0.3F_y\right)\left(\frac{\lambda - \lambda_{pf}}{\lambda_{rf} - \lambda_{pf}}\right)\right] \tag{56}$$

The slender flange critical stress Equation (57) is used in Equation (53) to satisfy compression flange local buckling with a slender web and flange (AISC 2016).

$$F_{cr} = \frac{0.9Ek_c}{\left(\frac{b_f}{2t_f}\right)^2} \tag{57}$$

The final limit state for slender webs is tension flange yielding Equation (58) (AISC 2016).

$$M_n = F_y S_{xt} \tag{58}$$

The cross-sections were also checked for shear and service deflection. The shear check utilized Equation (59) using the web area (A_w) and web shear strength coefficient (C_{v1}) to account for web buckling (AISC 2016).

$$V_n = 0.6F_y A_w C_{v1} \tag{59}$$

The deflection (Δ) was evaluated using Equation (60), which is the closed-form solution for mid-span deflection of a simply supported beam subjected to a uniform distributed load.

$$\Delta = \frac{5wl^4}{384EI} \tag{60}$$

The parametric study compared the controlling moment and shear against the demand to determine if the cross-section had adequate strength. The way the Matlab code is set up is to output only the controlling moment reducing the Scenario 2 check to three equations. Those checks are Equation (61), Equation (62), and Equation (63) (AISC 2016).

$$\frac{\emptyset M_n}{M_u} \geq 1 \tag{61}$$

$$\frac{\emptyset V_n}{V_u} \geq 1 \tag{62}$$

$$\frac{L/limit}{\Delta} \geq 1 \tag{63}$$

4.4.4.3. Scenario II Model: Results

The first plot for scenario II utilizes Equation (61). The normalized moment capacity vs. the cross-sectional area is illustrated in Figure 109. The plot is as expected, with smaller cross-sectional areas having a lower moment capacity. Three distinct bands can be seen in Figure 109. Those three bands and one additional area are highlighted in Figure 110. Four beam cross-sections failed under compression flange local buckling and are highlighted as CFLB in Figure 110. All other cross-sections failed in either elastic or inelastic lateral-torsional buckling, labeled in Figure 110. Two distinctions between the inelastic lateral-torsional buckling are in the web plastification factor (R_{PC}). With the higher capacity curve having a web plastification factor greater than one. Moment capacity of the beam has a large influence on beam cross-section design.

Although this analysis does not load the beam in torsion the unbraced length with no composite action still allows lateral-torsional buckling to be a controlling factor.

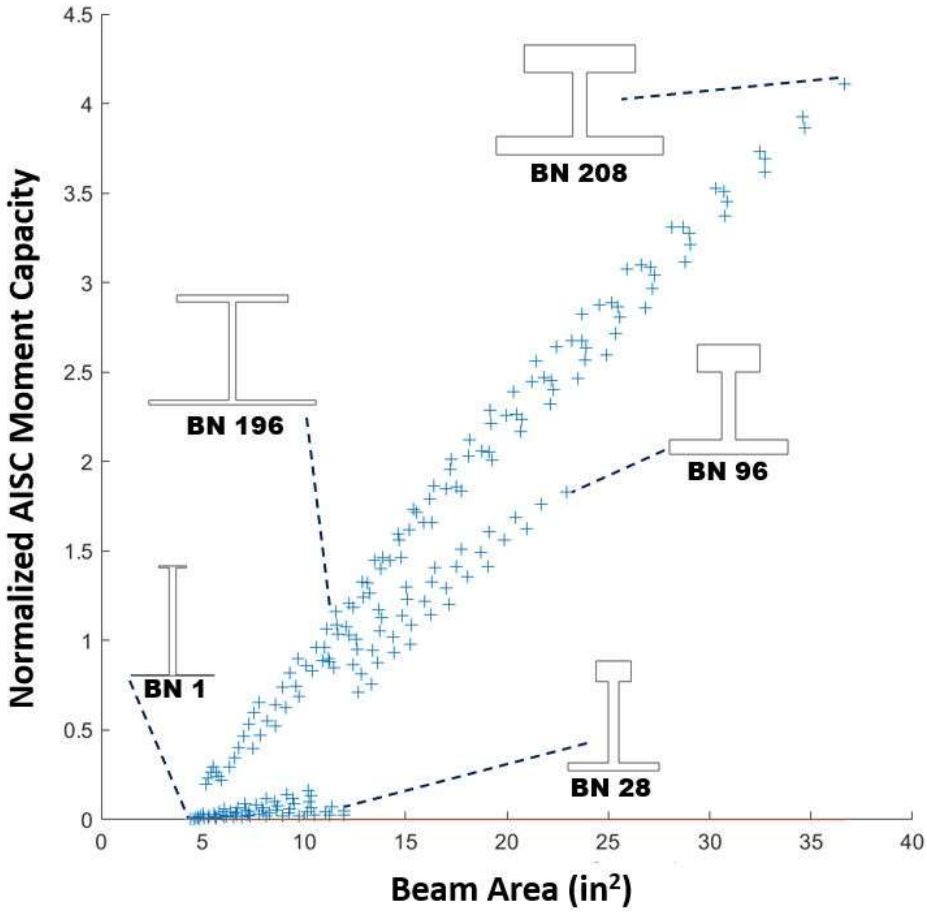

Figure 109: Scenario II: Normalized moment capacity vs. beam cross-sectional area

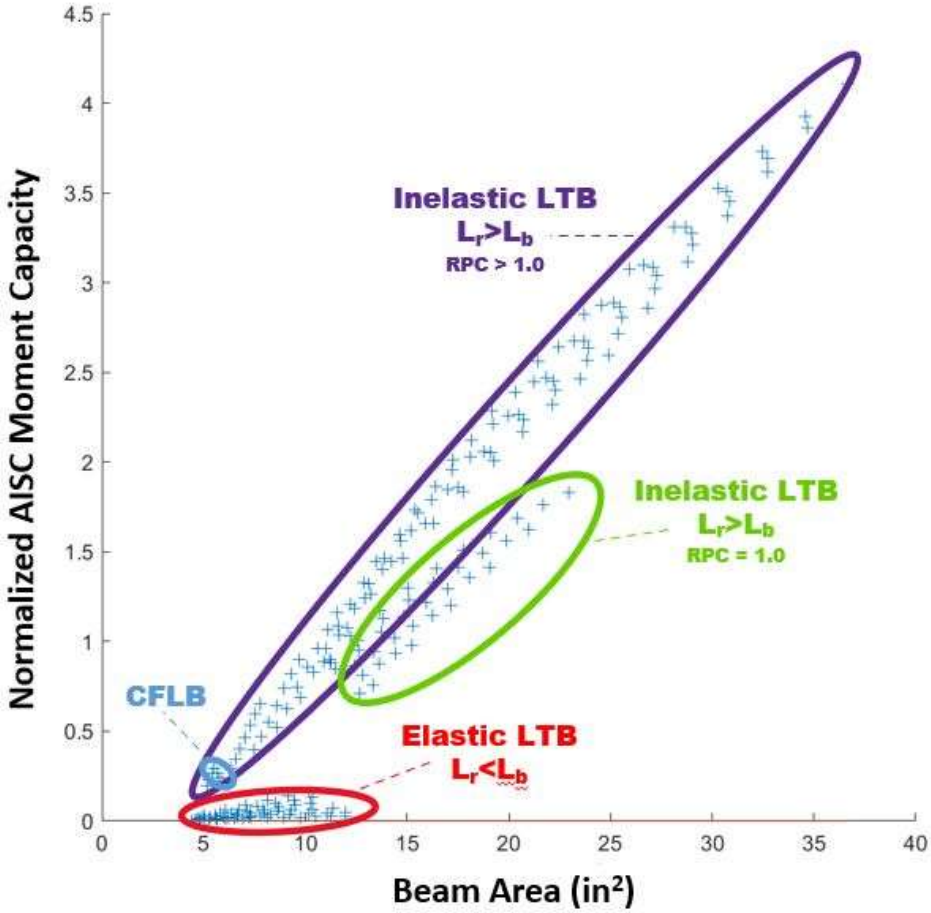

Figure 110: Scenario II: Normalized moment capacity vs. beam cross-sectional area (annotated sections)

The second normalized design criterion in scenario II is the shear capacity Equation (62). Figure 111 plots the normalized shear capacity vs. the cross-sectional area. The area plot shows larger web thickness (t_w) and top flange thickness (t_{ft}) tend to produce more capacity for shear. Plotting the normalized shear capacity vs. the web thickness (t_w) reveals the flange thickness (t_{ft}) only affects the capacity due to the height constraint (8 inches) imposed on the cross-section and the area balance of the flanges. In other words, as the top flange width (b_{ft}) reduces, the bottom flange

thickness (t_{fb}) reduces, making the web effectively taller between flanges. Figure 112 shows an increase in the shear capacity as the web thickness (t_w) increases in small bands. Each vertical band in Figure 112 show the slight capacity increase due to a reduced bottom flange thickness (t_{fb}). Shear capacity of the different cross-section for this load case did not have any control on cross-section design, although the values for the thinner webs cross-sections would require a check for other loading cases.

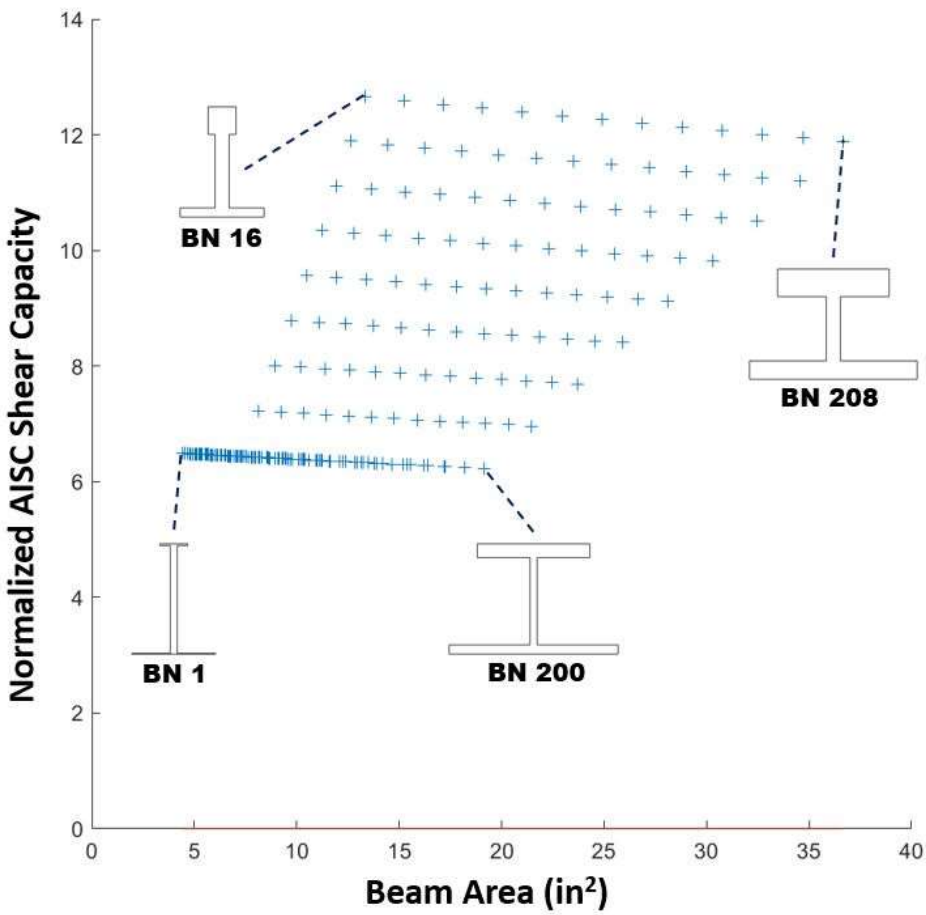

Figure 111: Scenario II: Normalized shear capacity vs. beam cross-sectional area

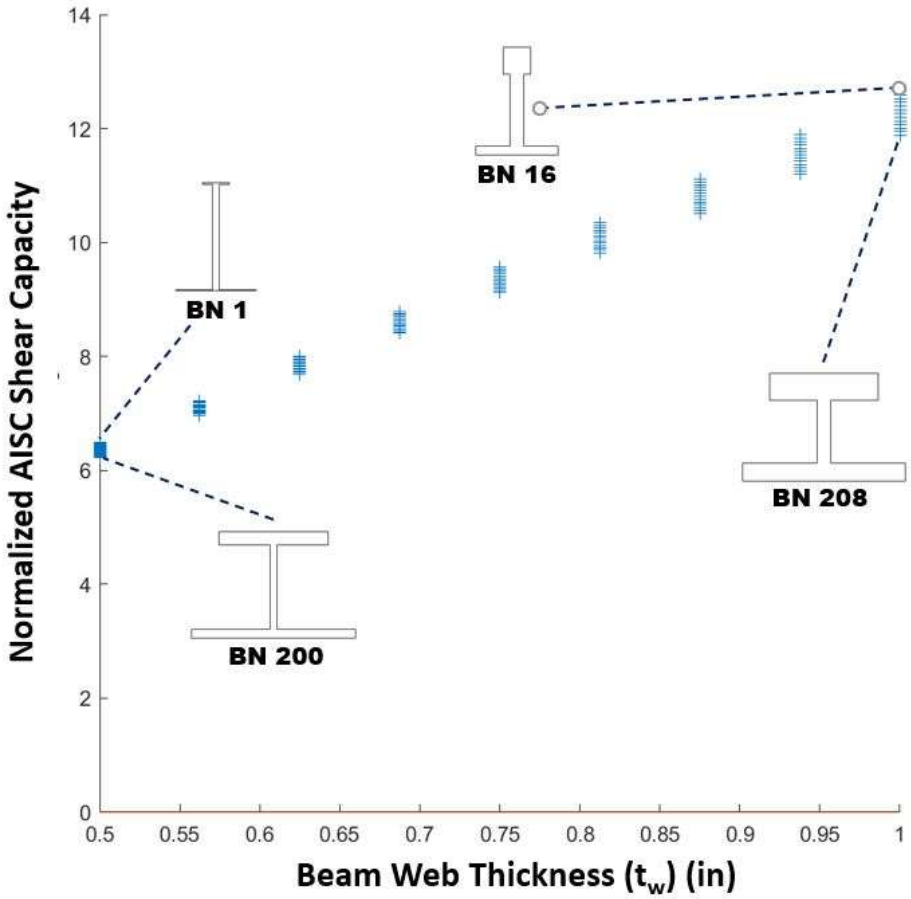

Figure 112: Scenario II: Normalized shear capacity vs. web thickness (t_w)

The final normalized capacity in scenario II was the non-composite deflection utilizing Equation (63). Figure 113 is the normalized defection vs. the cross-sectional area. The cross-sectional area, specifically the flange area increasing, causes a reduced deflection or an increase in normalized deflection. By plotting the moment of inertia on the abscissa, the true relationship between the cross-section and deflection can be viewed. Figure 114 represents the relationship between the moment of inertia of the cross-section and the decrease in deflections as the moment of inertia increased, in a

linear relationship. The non-composite deflection was a controlling limit state in A-shape selection and behavior, with many of the smaller area cross-sections not passing.

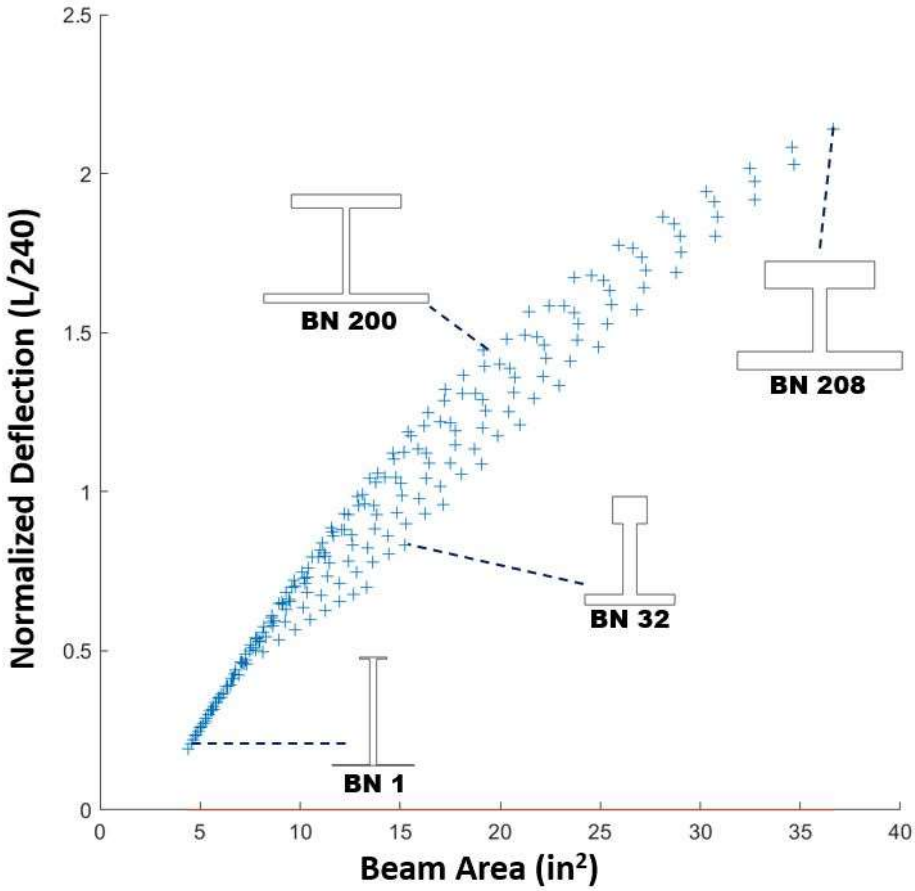

Figure 113: Scenario II: Normalized deflection vs. beam cross-sectional area

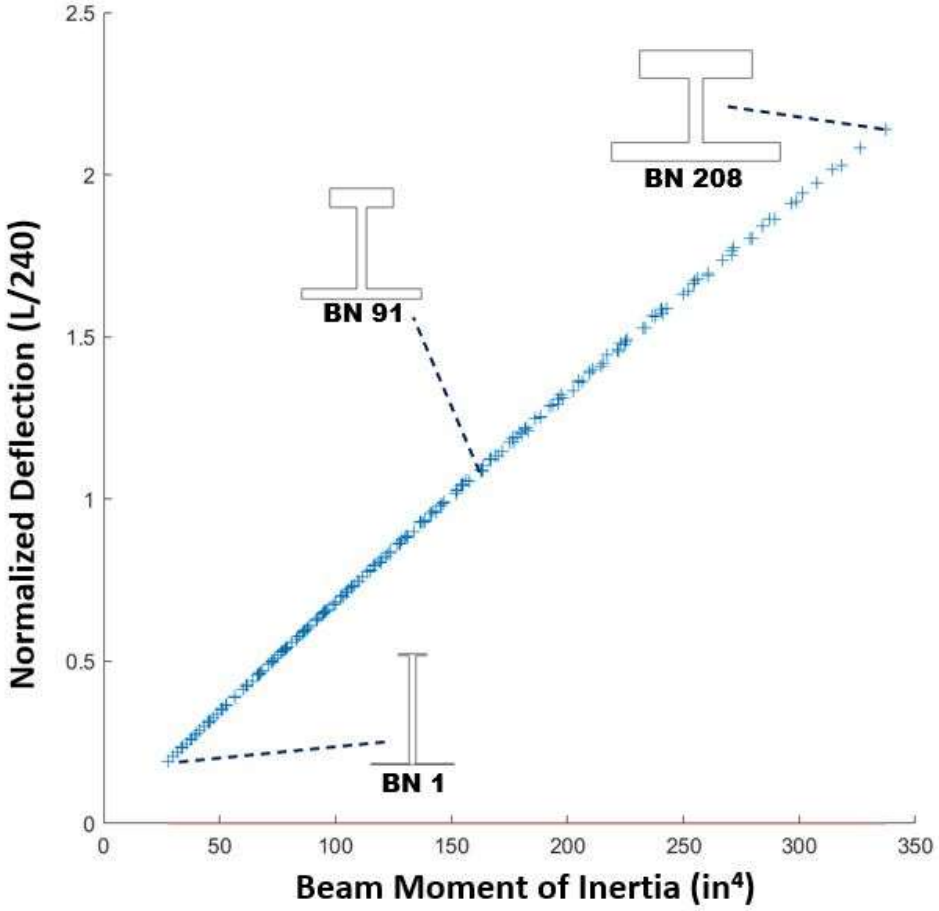

Figure 114: Scenario II: Normalized deflection vs. beam moment of inertia

4.4.5. Analytical Study – Scenario III: Composite concentric loading

4.4.5.1. Scenario III Model: Load Case 3

The final loading was fully composite in-service loading (Figure 115). This scenario was after the concrete topping slab had fully cured, creating the full composite flexural strength and stiffness of the floor system. Due to the increased strength of the system after full composite action, the floor checks focused on the service conditions. Due to the full-scale testing findings, the ultimate strength was not of concern at this

stage. The two service conditions checks are deflections and vibrations from in-service conditions. The methodology for these calculations is presented below.

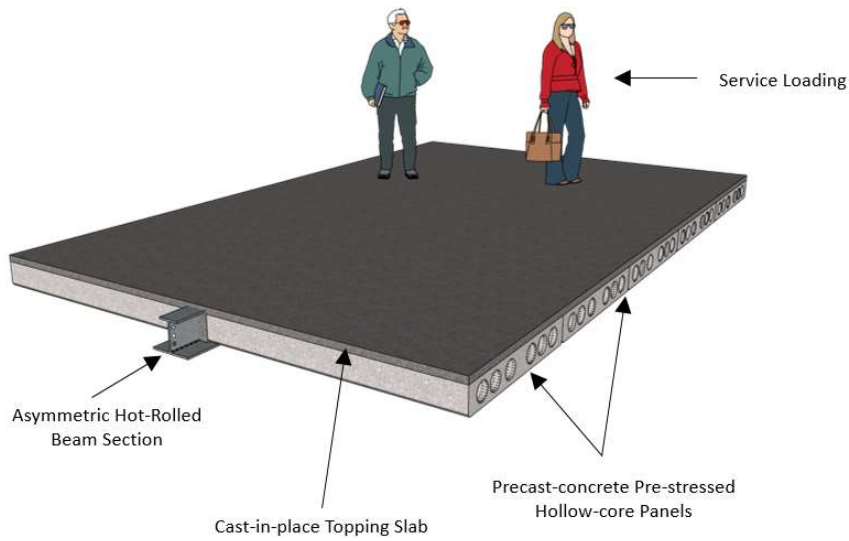

Figure 115: Loading scenario 3, in-service loading

The parameters needed for Load Case 3 are:

- In-service live load of 100 psf (ASCE 2013)
- In-service live load factor of 1.0 (ASCE 2013)
- Deflection limit of L/360 (Council 2017)
- Beam spacing of 10 feet
- Concrete 28-day compressive strength of 4000 psi
- Topping slab thickness of 3 inches
- Beam length, weight, and depth of 30 feet, 65 plf, 12 inches respectively
- Cross-sectional area, and moment of inertia of 17 in^2, and 833 in^4
- Damping (β) of 0.03 (Murry et al. 2016)
- Beam panel mode constant (C_j) of 2.0 (Murry et al. 2016)

- Beam panel mode constant (C_g) of 1.8 (Murry et al. 2016)
- Walking excitation loading of 65 lbs (Murry et al. 2016)
- Vibration live loading of 8 psf (Murry et al. 2016)
- Superimposed dead loading of 4 psf (Murry et al. 2016)
- Acceleration limit of 0.5% gravity (Murry et al. 2016)

4.4.5.2. Scenario III Model: Methodology

The first step to completing a composite analysis of the floor systems is to compute the elastic section properties. Using the elastic properties, the deflection and natural frequency of the floor system can be analyzed and compared to acceptable levels. Finding the elastic properties of the composite section starts with the A-shape definition and properties. Figure 116 defines the unique nomenclature of an A-shape graphically. Using the defined flange naming, the elastic centroid (y_e) and moment of inertia (I_x) can be computed.

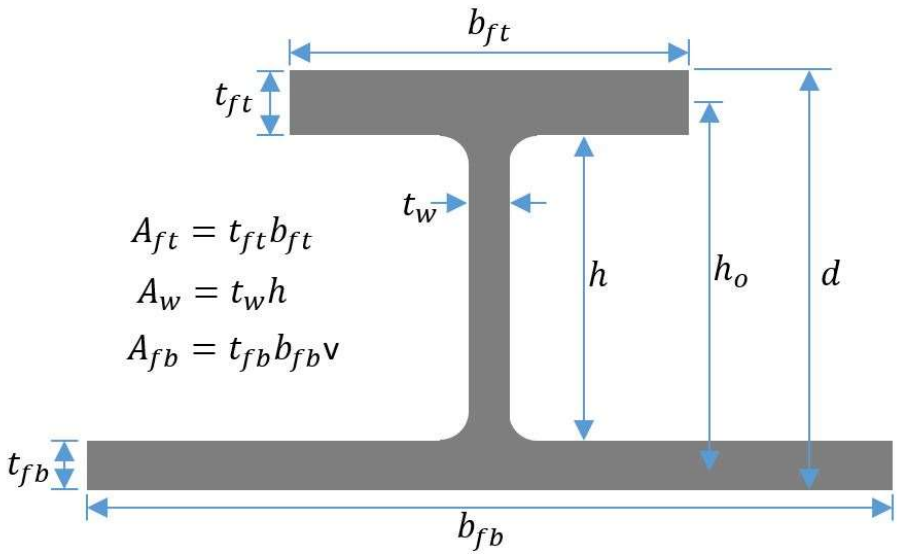

Figure 116: A-shape dimension nomenclature

With an understanding of the flange dimension naming, the equation for the section elastic neutral axis (y_e) can be written as Equation (64) or a more simplified version of the elastic neutral axis (y_e) in Equation (65) (Mullett 1998).

$$y_e = \frac{(t_{ft}b_{ft})\left(\frac{t_{ft}}{2}\right)+(t_{fb}b_{fb})\left(d-\frac{t_{fb}}{2}\right)+(t_w h)\left(\frac{h}{2}+t_{ft}\right)}{(t_{ft}b_{ft})+(t_{fb}b_{fb})+(t_w h)} \tag{64}$$

$$y_e = \frac{A_{ft}\left(\frac{t_{ft}}{2}\right)+A_{fb}\left(d-\frac{t_{fb}}{2}\right)+A_w\left(\frac{h}{2}+t_{ft}\right)}{(A_{ft}+A_{fb}+A_w)} \tag{65}$$

With the y-bar of the section computed the moment of inertia can be calculated. Equation (68) is the moment of inertia of an A-shape. The simplified version utilizing flange and web areas is Equation (67) (Mullett 1998).

$$I_x = \left(\frac{b_{ft}{t_{ft}}^3}{12}\right) + \left(t_{ft}b_{ft}\right)\left(y_e - \frac{t_{ft}}{2}\right)^2 + \left(\frac{b_{fb}{t_{fb}}^3}{12}\right) + \left(t_{fb}b_{fb}\right)\left(d - y_e - \frac{t_{fb}}{2}\right)^2 + \left(\frac{t_w h^3}{12}\right) + \left(t_w h\right)\left(y_e - t_{ft} - \frac{h}{2}\right)^2 \tag{66}$$

$$I_x = \left(A_{ft}\frac{{t_{ft}}^2}{12}\right) + \left(A_{ft}\right)\left(y_e - \frac{t_{ft}}{2}\right)^2 + \left(A_{fb}\frac{{t_{fb}}^2}{12}\right) + \left(A_{fb}\right)\left(d - y_e - \frac{t_{fb}}{2}\right)^2 + \left(A_w\frac{h^2}{12}\right) + \left(A_w\right)\left(y_e - t_{ft} - \frac{h}{2}\right)^2 \tag{67}$$

A similar approach to finding the A-shape section properties can be taken to acquire the composite section properties. The composite section can be divided into three separate areas for analysis similar to the A-shape. Figure 117 illustrates the separation of the areas into the top slab area (A_{c1}), the beam encasing concrete (A_{c2}), and the A-shape section (A_B). First the elastic neutral axis of the cross-section needs to be computed. Equation (68) uses the section areas and centroids to compute the composite elastic neutral axis. One difference between the A-shape calculation in Equation (67) and the composite calculations Equation (68) is the difference in materials (Mullett 1998). To accommodate separate materials, one material has to be converted into the other material. In this case, the concrete was modeled as steel using a modular ratio (n). Equation (69) is the ratio of the modulus of steel (E_s) divided by the modulus of concrete (E_c).

$$y_{ec} = \frac{A_B\, y_e + \frac{A_{c2}}{n}\left(d - \frac{d_d}{2} - t_{fb}\right) + \frac{A_{c1}}{n}\left(\frac{d_s}{2} - d_c\right)}{\left(A + \frac{A_{c2}}{n} + \frac{A_{c1}}{n}\right)} \tag{68}$$

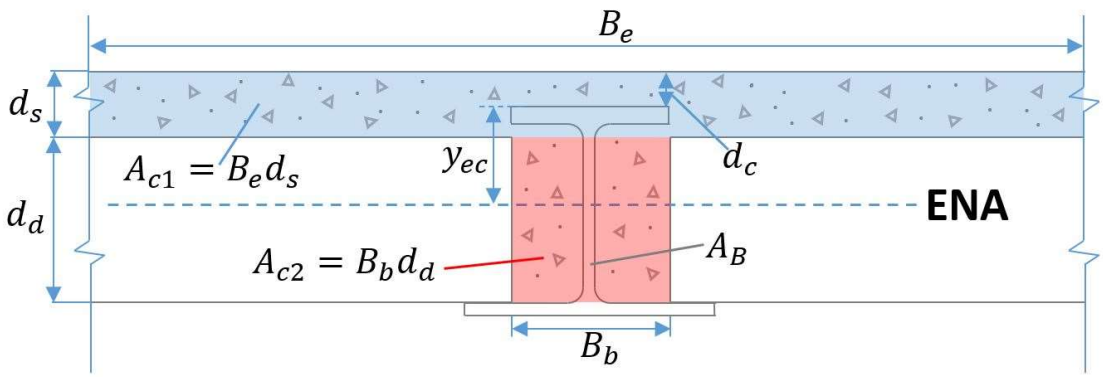

Figure 117: Composite section dimensions for elastic analysis

$$n = \frac{E_s}{E_c} \tag{69}$$

With the elastic neutral axis of the composite section located, the moment of inertia of the composite section (I_c) could be calculated using Equation (70)(Mullett 1998). Again with using the modular ratio (n) the moment of inertia of each concrete area along with the parallel axis (Ad^2) component of each concrete area can be computed.

$$I_c = I_x + A_B\,(y_e - y_{ec})^{\,2} + \frac{A_{c1}}{n}(0.5d_s - d_c - y_{ec})^2 + \frac{A_{c1}\,d_s^2}{n\,12} + \frac{A_{c2}}{n}(d - 0.5d_d - t_{fb} - y_{ec})^2 + \frac{A_{c2}\,d_d^2}{n\,12} \tag{70}$$

The live load deflection of the composite section can be computed with the composite section moment of inertia using Equation (71) (AISC 2016). One small caveat to point out with the deflection, the modulus of elasticity is the modulus of steel (E_s) since our section was converted to steel for the moment of inertia calculation. The

modulus of steel (E_s) could be replaced with the product of the modulus of concrete (E_c) and the modular ratio (n) found earlier.

$$\Delta = \frac{5\, w\, l^4}{384\, E_s\, I_c} \tag{71}$$

The parameters of Equation (71) also contain the service live loading (w) on the floor and the length of the beam (l). Along with an IBC in-service deflection check, the floor vibration was also a composite parameter that was analyzed.

The floor vibration check ultimately compares the peak acceleration to gravity and determines the predicted floor comfort. The first large difference between vibration and other composite calculations is the 35% increase to the concrete modulus (E_c) (Murry et al. 2016). This alteration is done when calculating the dynamic modular ratio for vibration (n_v) as shown in Equation (72) (Murry et al. 2016). The increase in concrete modulus (E_c) plays a role in the composite calculations for elastic neutral axis (y_j) and moment of inertia of the composite beam (I_j). Equation (73) is the vibration altered composite elastic neutral axis (y_j) and Equation (74) is the vibration altered composite moment on inertia (I_j) (Mullett 1998).

$$n_v = \frac{E_s}{1.35\, E_c} \tag{72}$$

$$y_j = \frac{A_B\, y_e + \frac{A_{c2}}{n_v}\left(d - \frac{d_d}{2} - t_{fb}\right) + \frac{A_{c1}}{n_v}\left(\frac{d_s}{2} - d_c\right)}{(A + \frac{A_{c2}}{n_v} + \frac{A_{c1}}{n_v})} \tag{73}$$

$$\begin{aligned} I_j = I_x + A_B\,(y_e - y_j)^{\,2} + \frac{A_{c1}}{n_v}(0.5d_s - d_c - y_j)^2 + \frac{A_{c1}\, d_s^2}{n_v\, 12} \\ + \frac{A_{c2}}{n_v}(d - 0.5d_d - t_{fb} - y_j)^2 + \frac{A_{c2}\, d_d^2}{n_v\, 12} \end{aligned} \tag{74}$$

Upon completion of altering the composite section properties for dynamic effects, the beam defection (Δ_j) and the fundamental frequency of the beam (f_i) can be calculated. Equation (75) is the defection under dynamic loading (w_j) as shown in Equation (76) with a beam length given as (L_j) (Murry et al. 2016). Equation (76) combines loading of the beam self-weight (w_{joist}), precast panel dead load (DL), live loading (LL), weight of the concrete slab (w_{slab}), and the beam spacing (S) for the tributary width of the loadings listed previously. With the equation for deflection, the frequency of the beam can be computed with Equation (77), adding gravity (g) to the list of variables (Murry et al. 2016).

$$\Delta_j = \frac{5\, w_j\, L_j^4}{384\, E_s\, I_j} \tag{75}$$

$$w_j = S\,(LL + DL + w_{slab}) + w_{joist} \tag{76}$$

$$f_j = 0.18\sqrt{\frac{g}{\Delta_j}} \tag{77}$$

With beam deflections calculated, the next step is to compute the deflection of the girder and floor system transverse to the beamline. Equation (78) is the transformed moment of inertia per unit width in the direction of the slab span (Murry et al. 2016). Equation (79) is the transformed moment of inertia per unit width beam span direction (Murry et al. 2016). Equation (80) is the effective beam panel width and must be less or equal to two-thirds of the overall floor width. Equation (80) introduces a new variable for adjustment for beam location (C_j), for beams not parallel to a free edge the value is 2 (Murry et al. 2016).

$$D_s = \frac{(12\frac{in}{ft})\,d_{slab}^3}{12\,n_v} \tag{78}$$

$$D_j = \frac{I_j}{S} \tag{79}$$

$$B_j = C_j\left(\frac{D_s}{D_j}\right)^{0.25}(\,L_j) \tag{80}$$

The weight of the beam panel is calculated using Equation (81) (Murry et al. 2016). To compute the girder transformed composite moment of inertia, the effective slab width

(Eff_{TcswG}) is determined using Equation (82) (Murry et al. 2016). The transformed concrete slab width (Eff_{TCSW}) is calculated in Equation (83), the effective width of the slab in the deck (Eff_{WSD}) is calculated in Equation (84), and the transformed concrete slab area (Eff_{TCSA}) is calculated in Equation (85) (Murry et al. 2016).

$$W_j = \left(\frac{w_j}{S}\right) B_j \, L_j \tag{81}$$

$$Eff_{TcswG} = min\left[0.2\ L_g, 0.5L_{j_left}\right] + min\left[0.2\ L_g, 0.5L_{j_right}\right] \tag{82}$$

$$Eff_{TCSW} = \frac{Eff_{TcswG}}{n_v} \tag{83}$$

$$Eff_{WSD} = \frac{S}{n_v} \tag{84}$$

$$Eff_{TCSA} = Eff_{TCSW}(d_{slab}) \tag{85}$$

With the completion of the effective width of the slab, the elastic neutral axis in the girder direction (y_g) and the composite moment of inertia transverse to the beam (I_g). Equation (86) computes the elastic centroid, adding the variable for the area of the girder (A_g) and Equation (87) includes the moment of inertia of the girder (I_{xg}) (Murry et al. 2016).

$$y_g = \frac{Eff_{TCSA}\left(\frac{d}{2} + \frac{d_{slab}}{2}\right)}{Eff_{TCSA} + A_g} \tag{86}$$

$$I_g = I_{xg} + A_g y_g^2 + \frac{Eff_{TCSW} * d_{slab}^3}{12} + Eff_{TCSA}\left(\frac{d}{2} + \frac{d_{slab}}{2} - y_g\right)^2 \tag{87}$$

With the computed composite moment of inertia for the girder, the girder frequency (f_g) and girder deflection (Δ_g) can be calculated. Equation (88) calculates the weight per linear foot on the girder (Murry et al. 2016). Equation (89) defines the girder defection (Δ_g) and is used to compute Equation (90) for girder frequency (f_g) (Murry et al. 2016).

$$w_g = L_j\left(\frac{w_j}{S}\right) + w_{girder} \tag{88}$$

$$\Delta_g = \frac{5\, w_g\, L_g^4}{384\, E_s\, I_g} \tag{89}$$

$$f_g = 0.18\sqrt{\frac{g}{\Delta_g}} \tag{90}$$

With the beam and girder deflection calculations, the floor system frequency and peak acceleration from walking excitation can be calculated. The transformed moment of inertia per unit width in the girder span direction (D_g) is given in Equation (91) (Murry et al. 2016). The effective girder panel width (B_g) is less than or equal to two-thirds of the floor-length Equation (92) (Murry et al. 2016). The effective girder panel

width adds a constant variable C_g that allows for either beam girder connection on the flange or web. Calculating the girder weight (W_g) is provided in Equation (93) (Murry et al. 2016). The fundamental frequency (f_n) is calculated in Equation (94) (Murry et al. 2016). If the girder span is less than the effective beam panel width (B_j), a reduction in the girder deflection can be taken. The reduced girder deflection (Δ'_g) is calculated in Equation (95) (Murry et al. 2016). With the new reduced girder deflectgion (Δ'_g) the equivalent panel mode weight (W) can be calculated. Equation (96) uses the girder and beam deflection to calculate the equivalent panel mode (W) (Murry et al. 2016).

$$D_g = \frac{I_g}{L_g} \tag{91}$$

$$B_g = C_g \left(\frac{D_j}{D_g}\right)^{0.25} * L_g \tag{92}$$

$$W_g = \left(\frac{w_g}{L_j}\right) B_g L_g \tag{93}$$

$$f_n = 0.18 \sqrt{\frac{g}{\Delta_g + \Delta_j}} \tag{94}$$

$$\Delta_g' = \frac{L_g}{B_j}(\Delta_g) \tag{95}$$

$$W = \frac{\Delta_j}{\Delta_j + \Delta_g'} W_j + \frac{\Delta_g'}{\Delta_j + \Delta_g'} W_g \tag{96}$$

With the equivalent panel mode weight (W), the peak acceleration (a_p) of the floor can be computed. To compute peak acceleration (a_p), the natural frequency of the floor (f_n), the walking excitation (P_o), and the damping estimate (β) is needed. Equation (97) combine these parameters to compute the peak floor acceleration (a_p) (Murry et al. 2016). Note the peak acceleration is normalized with gravity to compare the percent of acceptable floor acceleration to tolerances deemed satisfactory or non-satisfactory. The limit imposed on the peak acceleration is 0.5% for peak acceleration divided by gravity $\left(\frac{a_p}{g}\right)$.

$$\frac{a_p}{g} = \frac{P_o e^{-.035\, f_n}}{\beta\, W} \tag{97}$$

Upon completion of the composite deflection calculations and the peak acceleration of the floor system, a determination of satisfactory results must be determined. For the defection limit Equation (98), a simple limit was set and compared to each result. The floor peak acceleration limiting Equation (99) allowed for all peak accelerations below 0.5% as passing (Murry et al. 2016).

$$\frac{L/limit}{\Delta} \geq 1 \tag{98}$$

$$\frac{0.5\%}{\frac{a_p}{g}} \geq 1 \tag{99}$$

The limit states from each section were assigned a number for reference. Table 7 lists those limit states and their assigned number.

4.4.5.3. Scenario III Model: Results

The two limit states presented in scenario III are composite deflection as calculated in Equation (98) and excessive floor vibrations, which are calculated in Equation (99). Both area plots (Figure 118 and Figure 120) are similar due to their dependency on the composite moment of inertia. With the slab tributary area and topping slab thickness unchanging, a look into the composite moment of inertia did not shed much light on the relationship to the cross-section. The normalized composite deflection was plotted vs. the top flange beam thickness (t_{ft}) in Figure 119. The normalized vibration comfort was plotted vs. the top flange beam thickness (t_{ft}) in Figure 121. In Figure 119 and Figure 121 the beam top flange thickness (t_{ft}) and beam top flange beam width (b_{ft}) can be better understood. As the thickness increases the capacity of the composite section is increased slightly. As the thickness and the width of the top flange are increased the capacity is increased at a sharper rate. Composite

deflection did influence the beam behavior in this load case. The composite deflection in other loading case geometries could easily be a controlling limit state. The vibration limit state was more controlling only allowing about half of the cross-sections a passing score. The vibration was a controlling limit state.

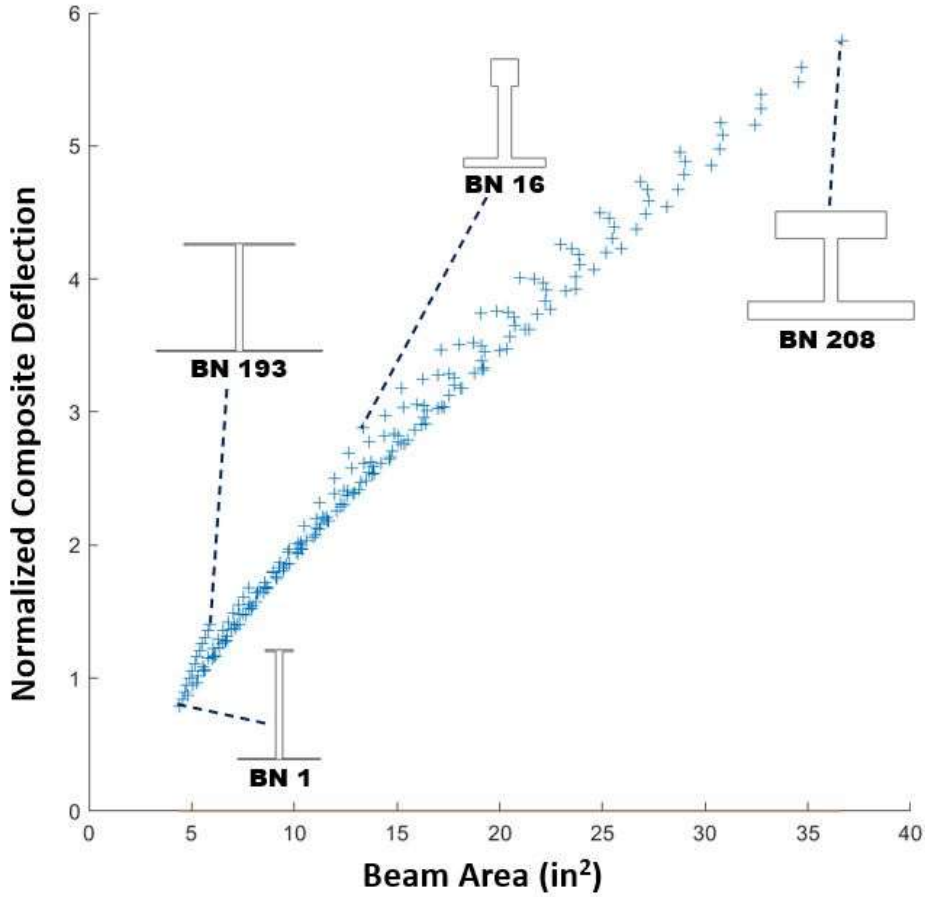

Figure 118: Scenario III: Normalized composite deflection vs. beam cross-sectional area

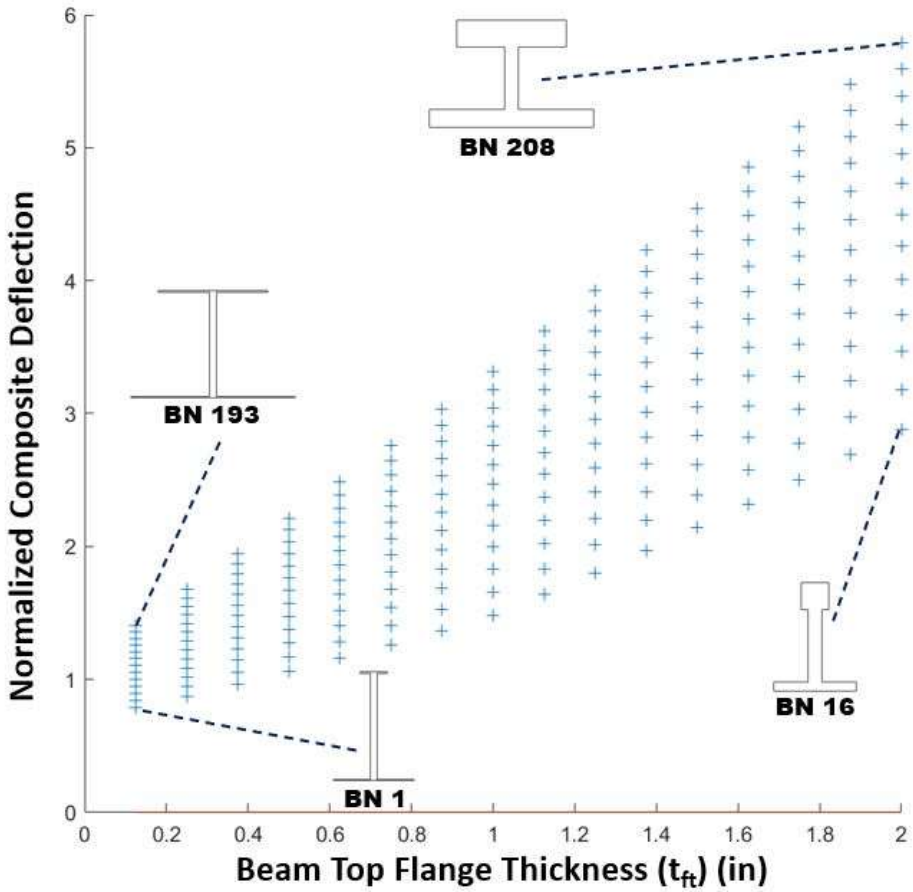

Figure 119: Scenario III: Normalized composite deflection vs. beam top flange thickness (t_{ft})

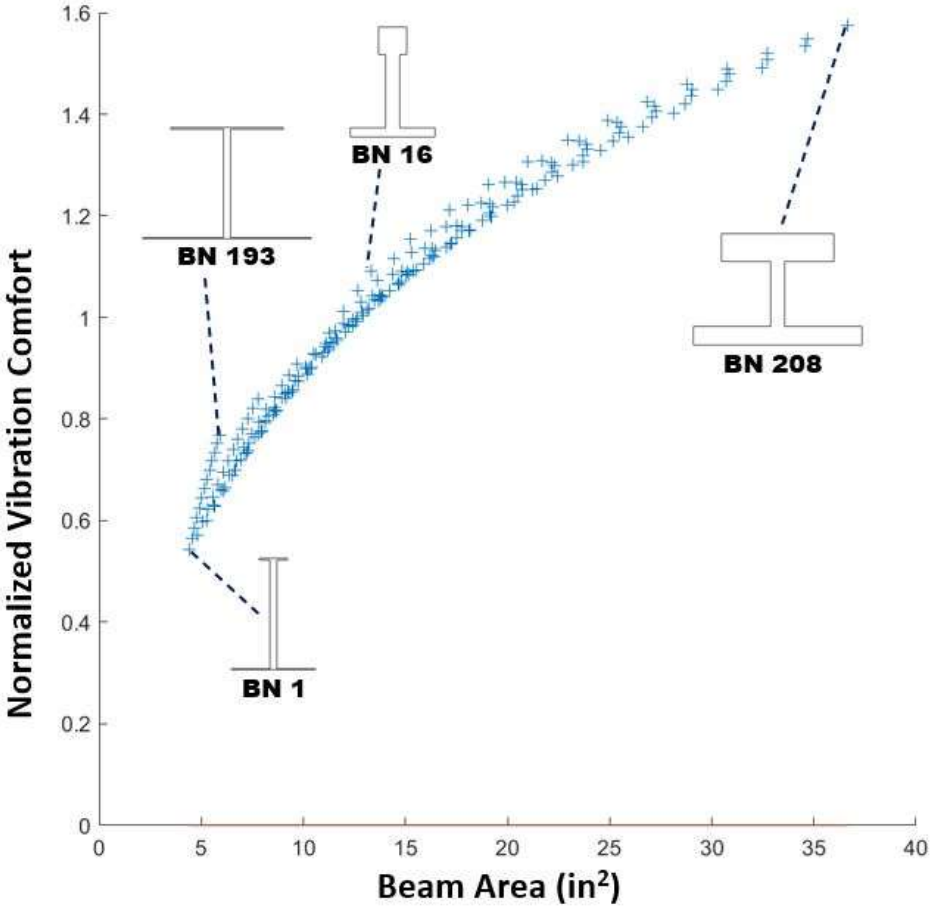

Figure 120: Scenario III: Normalized vibration vs. beam cross-sectional area

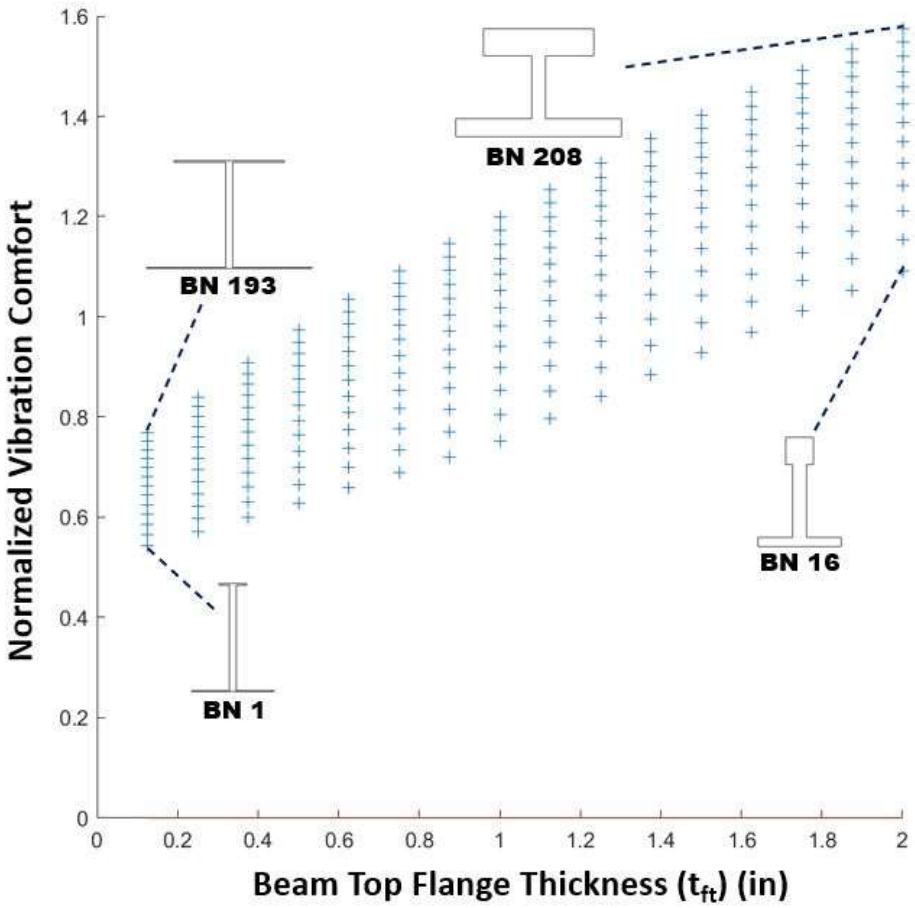

Figure 121: Scenario III: Normalized vibration vs. beam top flange thickness (t_{ft})

4.4.6. A-shape Flange Area Study

The top flange to bottom flange areas was initially kept the same due to feedback from multiple U.S. steel manufacturers 4.2.2. With equal areas controlling the final shape, an in-depth study into the performance of unequal areas was performed. The study consisted of changing the balance between the flange areas. The equal-area beam model was indicated with a 50% / 50% representing the percent area of the top flange vs. the total flange area and the percent of the bottom flange vs. total area. The study compared the normalized minimum controlling limit state for different area balance

approaches. The normalized minimum controlling limit state was a plot of the controlling criteria for any beam cross-section with its normalized results vs. the area of the cross-section. Simply put, the plot took the smallest normalized value from all the checks of the analytical study and plotted them vs. the area that the cross-section produced. With this approach, any cross-section plotted above 1.0 was an overall passing cross-section. Six unique flange area proportions were analyzed with the analytical study. The areas stared at a larger top flange area of 65%/35% and changed by increments of 5% down to the larger bottom flange area of 35%/65%. The minimum area beam from each normalized plot was found. Note that beam numbers from the area change plots are unique from this section but are still provided.

The first criteria analyzed was the larger top flange area, which was the plot of 65%/35%, as shown in Figure 122. The passing beam cross-section had a top flange area of 7.00 in^2 and a bottom flange area of 3.77 in^2. The next criteria analyzed was the 60%/40% cross-sections, as shown in Figure 123. The passing beam cross-section had a top flange area of 6.13 in^2 and a bottom flange area of 4.08 in^2. The next criteria analyzed was the 55%/45% cross-section, as shown in Figure 124. The passing beam cross-section had a top flange area of 5.69 in^2 and a bottom flange area of 4.65 in^2. The next criteria analyzed was the 50%/50% cross-sections, as shown in Figure 125. The passing beam cross-section had a top flange area of 5.25 in^2 and a bottom flange area of 5.25 in^2. The next criteria analyzed was the 45%/55% cross-sections, as shown in Figure 126. The passing beam cross-section had a top flange area of 4.69 in^2 and a bottom flange area of 5.73 in^2. The next criteria analyzed was the 40%/60% cross-sections, as

shown in Figure 127. The passing beam cross-section had a top flange area of 6.00 in^2 and a bottom flange area of 9.00 in^2. The final set of cross-sections analyzed was the 35%/65% cross-sections, as shown in Figure 128. The passing beam cross-section had a top flange area of 6.00 in^2 and a bottom flange area of 11.14 in^2. Table 6 lists all geometric data per passing cross-section discussed previously.

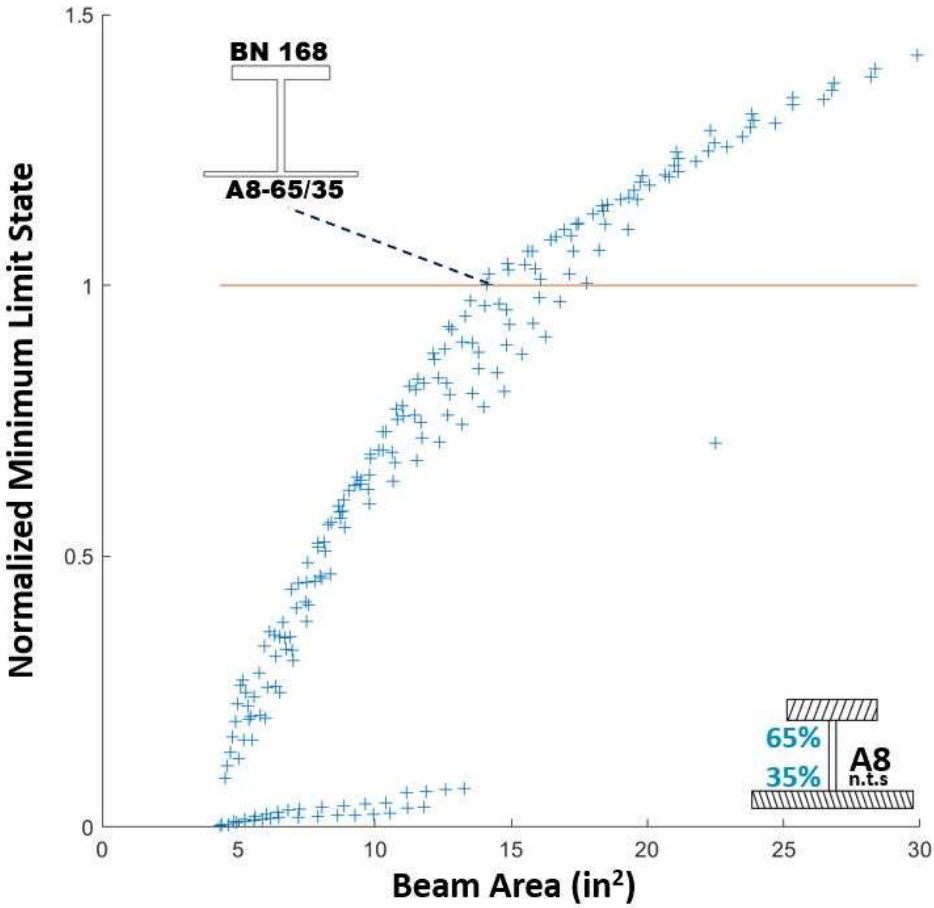

Figure 122: A8-65/35 flange area normalized passing plot

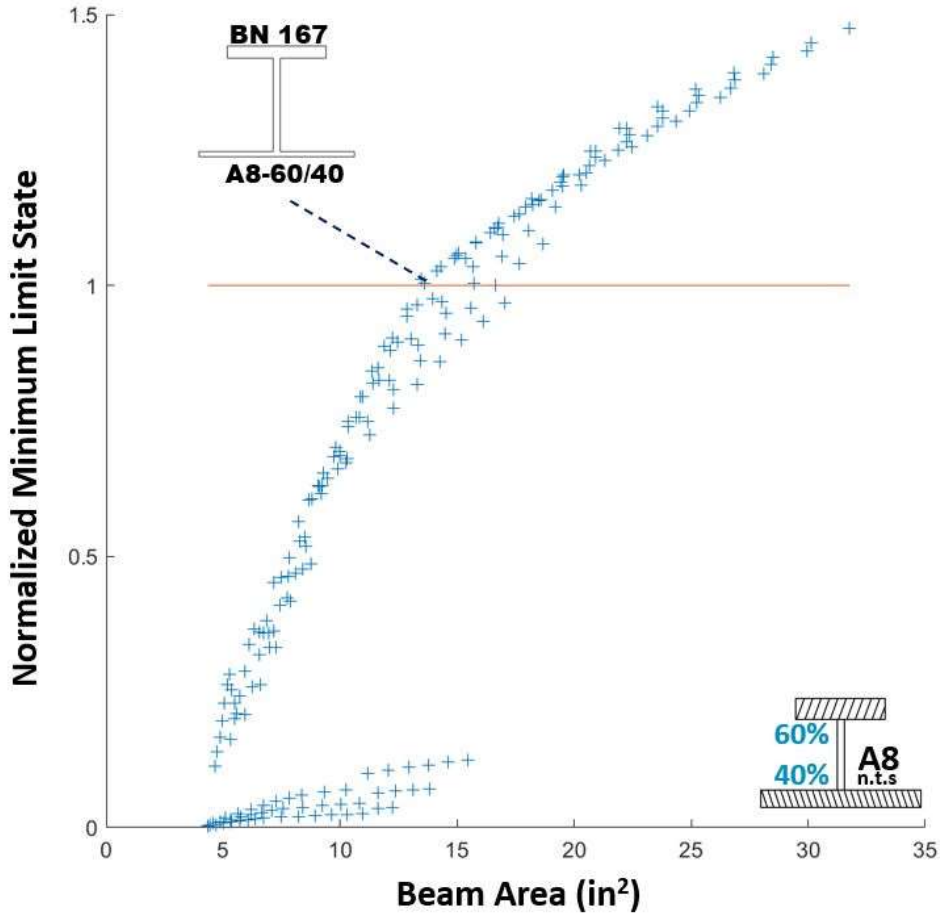

Figure 123: A8-60/40 flange area normalized passing plot

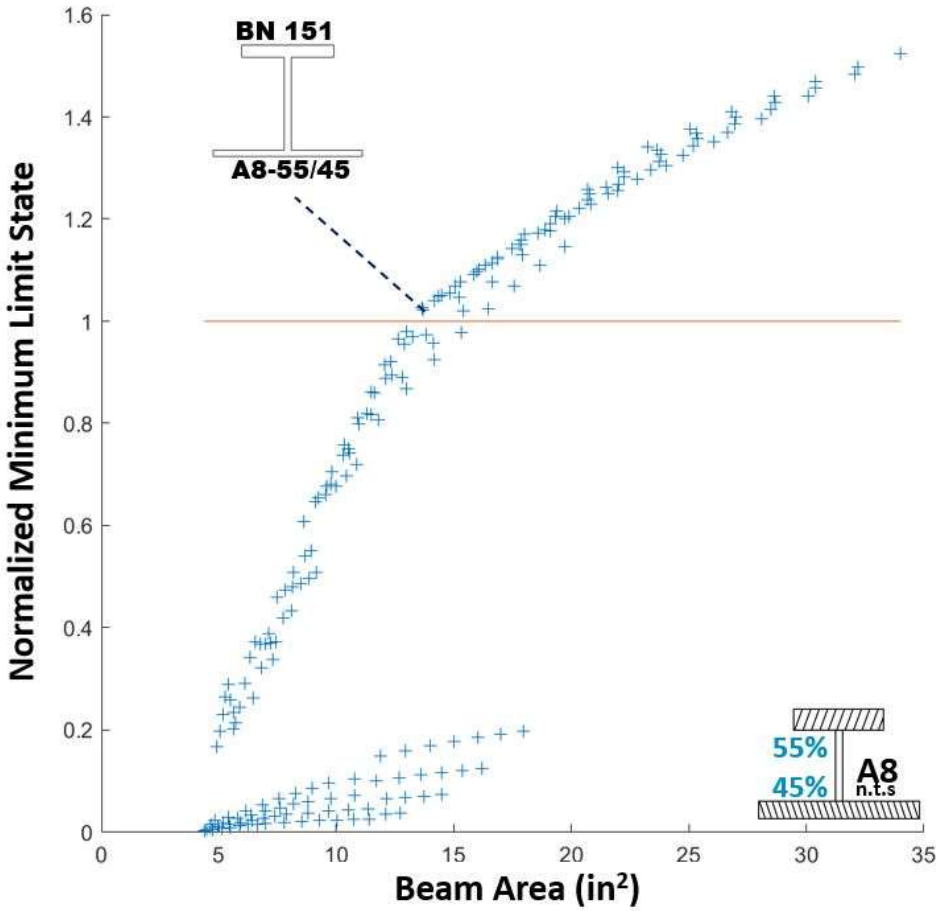

Figure 124: A8-55/45 flange area normalized passing plot

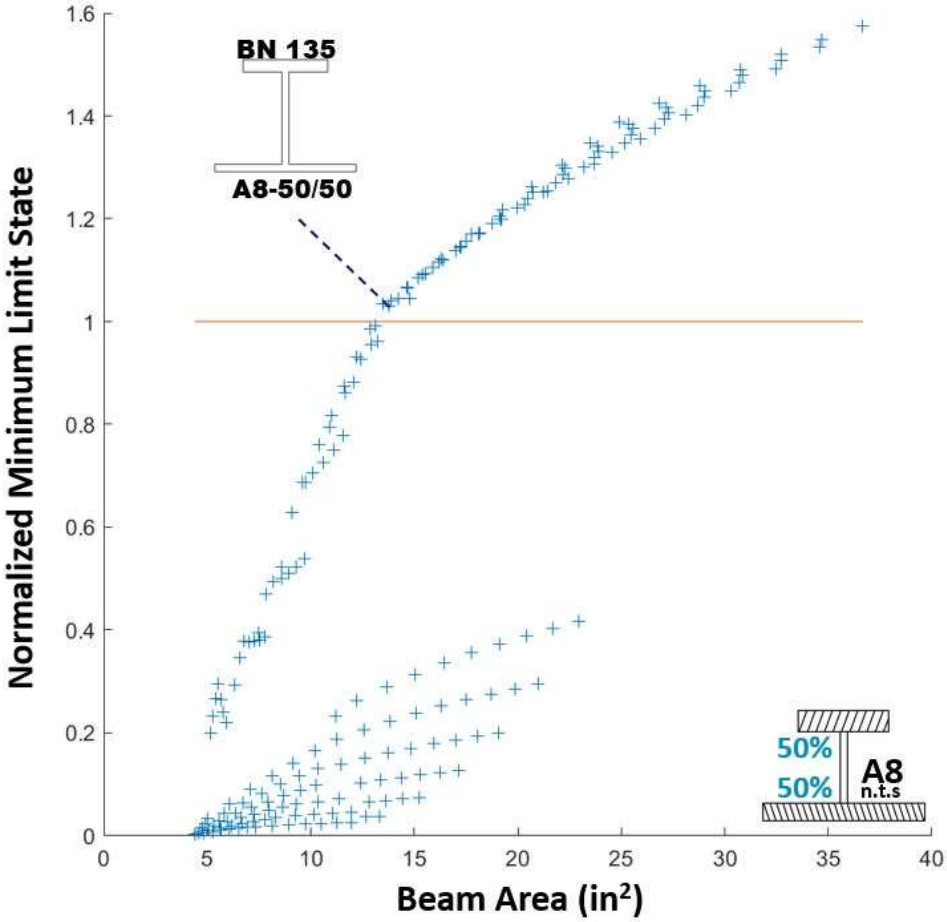

Figure 125: A8-50/50 flange area normalized passing plot

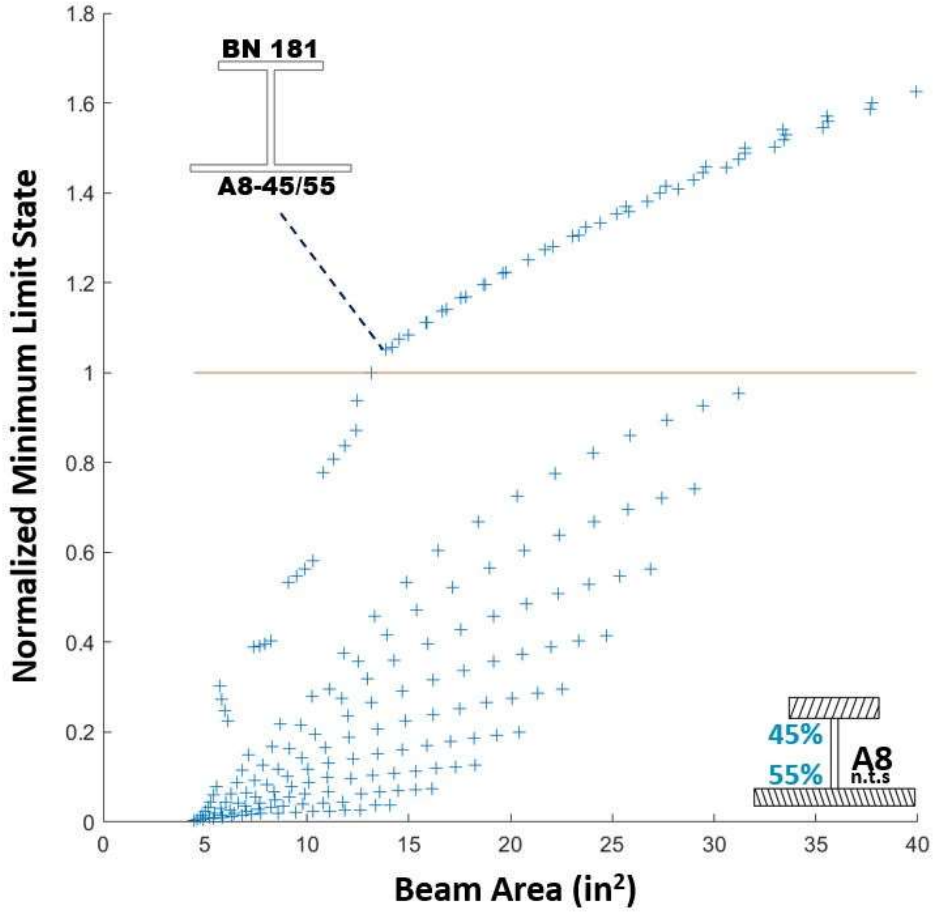

Figure 126: A8-45/55 flange area normalized passing plot

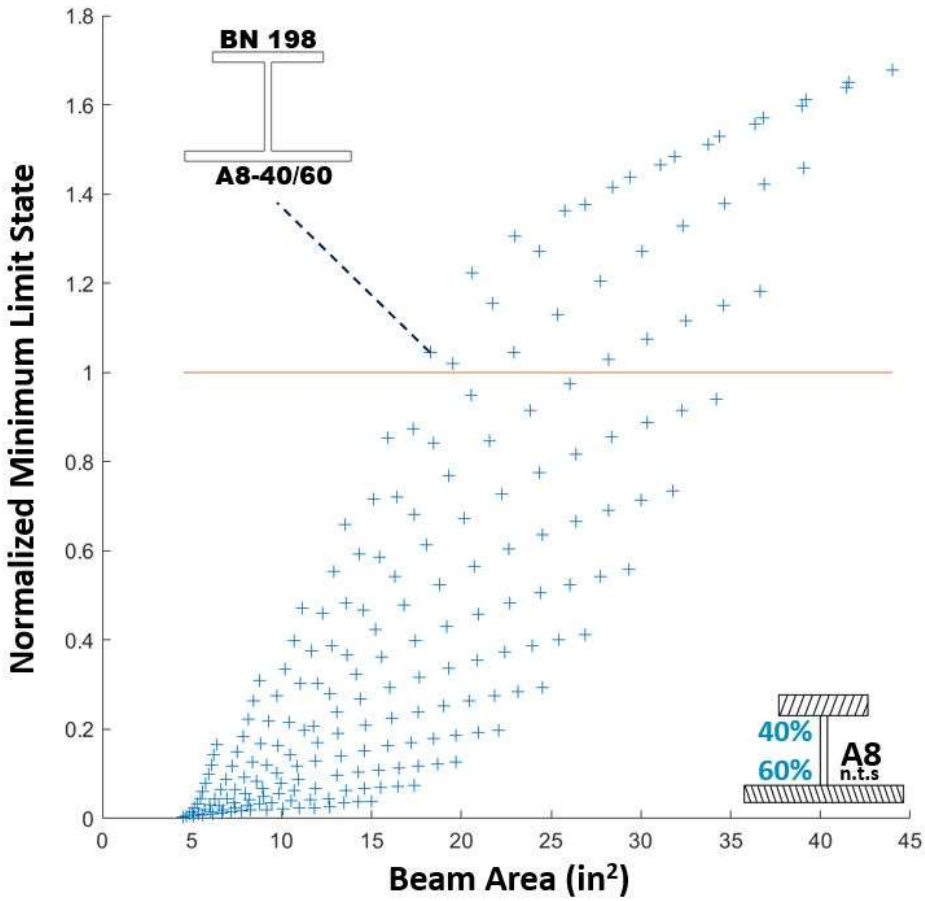

Figure 127: A8-40/60 flange area normalized passing plot

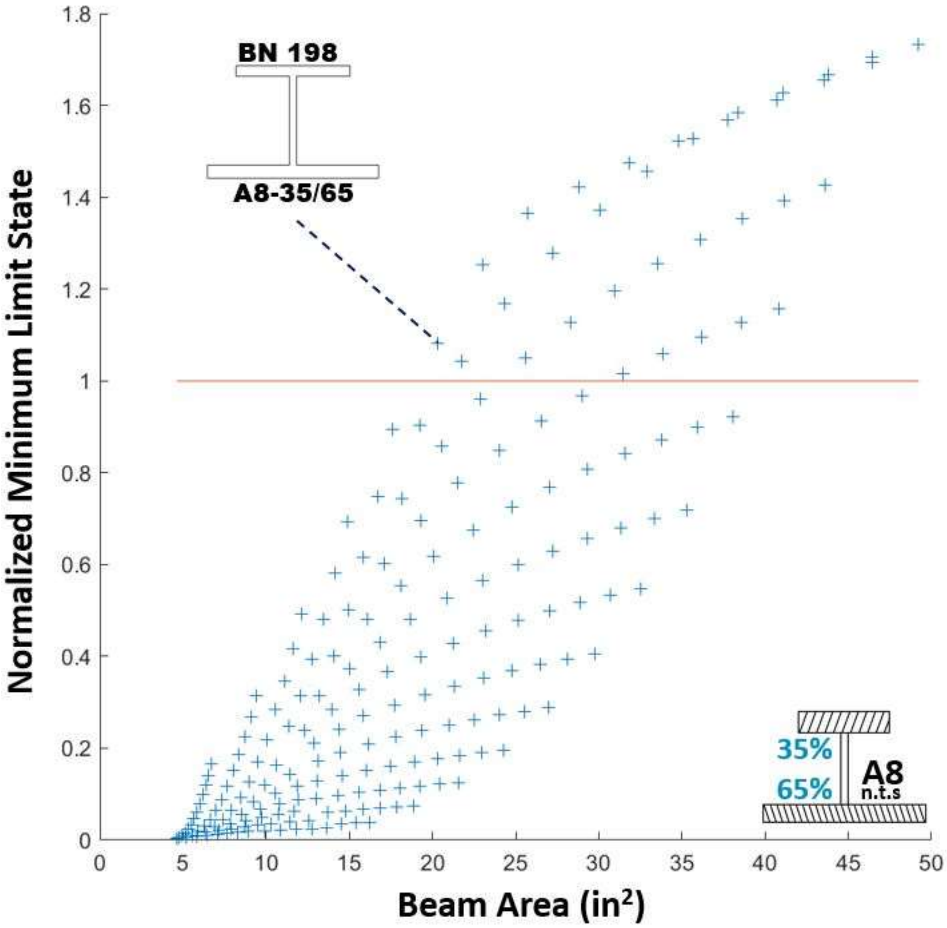

Figure 128: A8-35/65 flange area normalized passing plot

Table 6: Unbalanced area passing beam cross-sections

Section:	A8 65/35	A8 60/40	A8 55/45	A8 50/50	A8 45/55	A8 40/60	A8 35/65
Beam Number	168	167	151	135	181	198	198
Top Flange Thickness (t_{ft})(in)	1.000	0.875	0.875	0.875	0.625	0.750	0.750
Top Flange Width (b_{ft})(in)	7.000	7.000	6.500	6.000	7.500	8.000	8.000
Web (t_w)(in)	0.500	0.500	0.500	0.500	0.500	0.500	0.500
Bottom Flange Thickness (t_{fb})(in)	0.343	0.371	0.443	0.525	0.498	0.750	0.929
Bottom Flange Width (b_{fb})(in)	11.000	11.000	10.500	10.000	11.500	12.000	12.000
Section Area (in^2)	14.1	13.6	13.7	13.8	13.9	18.3	20.3
Moment of Inertia (in^4)	148.6	148.5	151.4	152.3	156.8	202.8	214.9
Weight per Foot (plf)	48	46	47	47	47	62	69
Controling Failure Number	13	13	25	13	25	18	18
Top Flange Area (in^2)	7.00	6.13	5.69	5.25	4.69	6.00	6.00
Bottom Flange Area (in^2)	3.77	4.08	4.65	5.25	5.73	9.00	11.14
Total Flange Area area (in^2)	10.77	10.21	10.34	10.50	10.42	15.00	17.14

The results with each area change completed allowed an in-depth assessment of the controlling limit states. Each set of cross-sections was checked against the 18 limit states discussed in each analytical study scenario Table 7. Out of the 18 limit-states checked, all beam cross-sections were governed by five of the limit-states. The five limit states are Scenario I Load Case 1 rotation (failure number 6), Scenario II Load Case 2a moment capacity (failure number 11), Scenario II Load Case 2a deflection (failure number 13), Scenario I Load Case 2b buckling (failure number 18), and Scenario III Load Case 3 vibration (failure number 25). Figure 129 plots the percent from each case vs. the top flange area. Note that with a smaller top flange area (35%), buckling controls over 66% of all beam cross-sections. With an increase of the top flange area, buckling is no longer an issue with deflection increasing in the controlling limit state.

Table 7: Failure type reference number

Failure Type:	Failure Number:
Scenario I: Load Case 1	
Tension Flange Yielding	1
Compression Flange Yielding	2
Flange Shear Yielding	3
Web Shear Yielding	4
Buckling	5
Rotation	6
b\t	7
Scenario II: Load Case 2a	
AISC Moment	11
AISC Shear	12
Deflection (L/240)	13
Scenario I: Load Case 2b	
Tension Flange Yielding	14
Compression Flange Yielding	15
Flange Shear Yielding	16
Web Shear Yielding	17
Buckling	18
Rotation	19
Scenario III: Load Case 3	
Composite Deflection (L/360)	24
Vibration	25

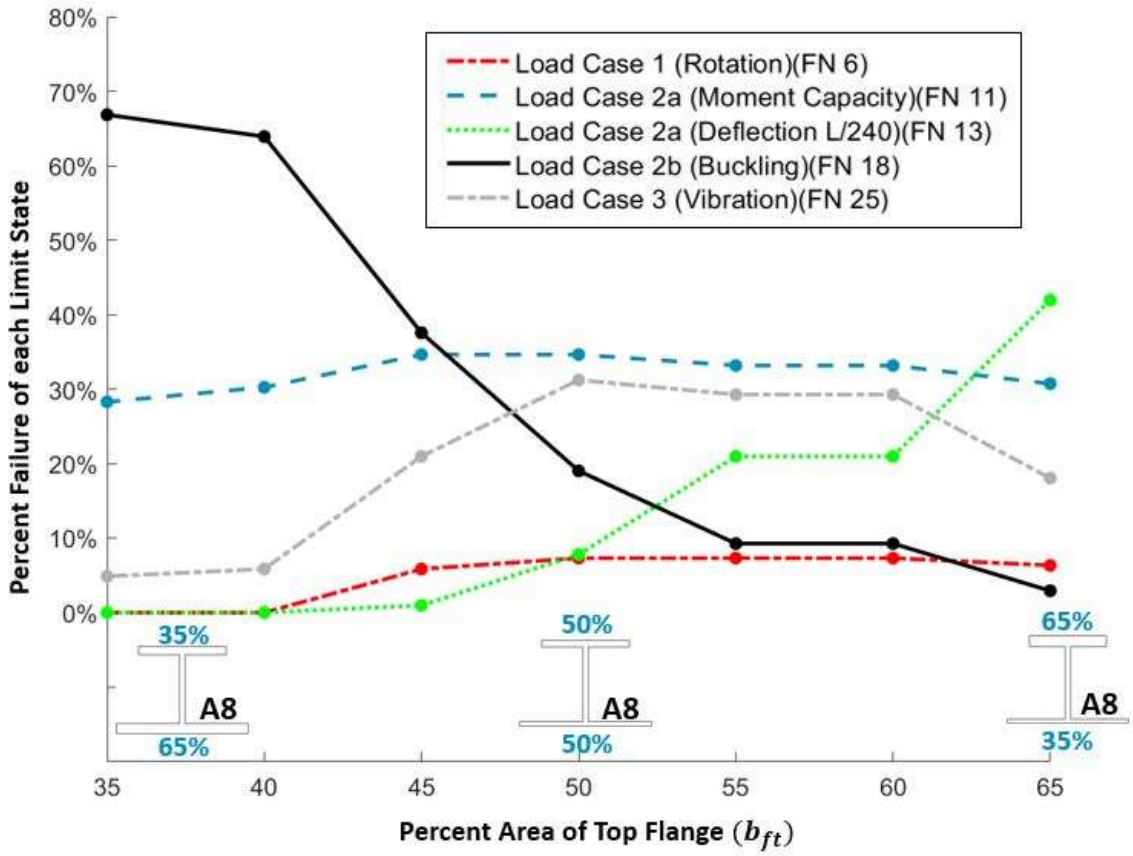

Figure 129: Percent of top flange area vs. percent of controlling limit state

The two largest findings found with the area change are plotted in Figure 130 and Figure 131. Figure 130 plots the weight of each passing cross-section vs. the top flange percent area. Figure 130 illustrates the increased cross-sectional area needed for the structural demand on minimum area top flanges. With a reduced top flange (35%), the beam cross-section to satisfy design criteria required a 69 plf beam while dropping down to the 50% top flange section required only a 47 plf cross-section to satisfy the same structural demand. Figure 131 is the width of the needed bottom flange (b_{fb}) plotted vs the percent area of the top flange. An increase or decreseas in the top flange area requires a larger bottom flange width (b_{fb}) than the balanced case of 50% top flange

area. The initial reason for using a 50%/50% beam was to satisfy the workabilinty when hot rolling a section. This flange area study also illuminates the advantages in weight and width to selecting a beam with balanced flange areas.

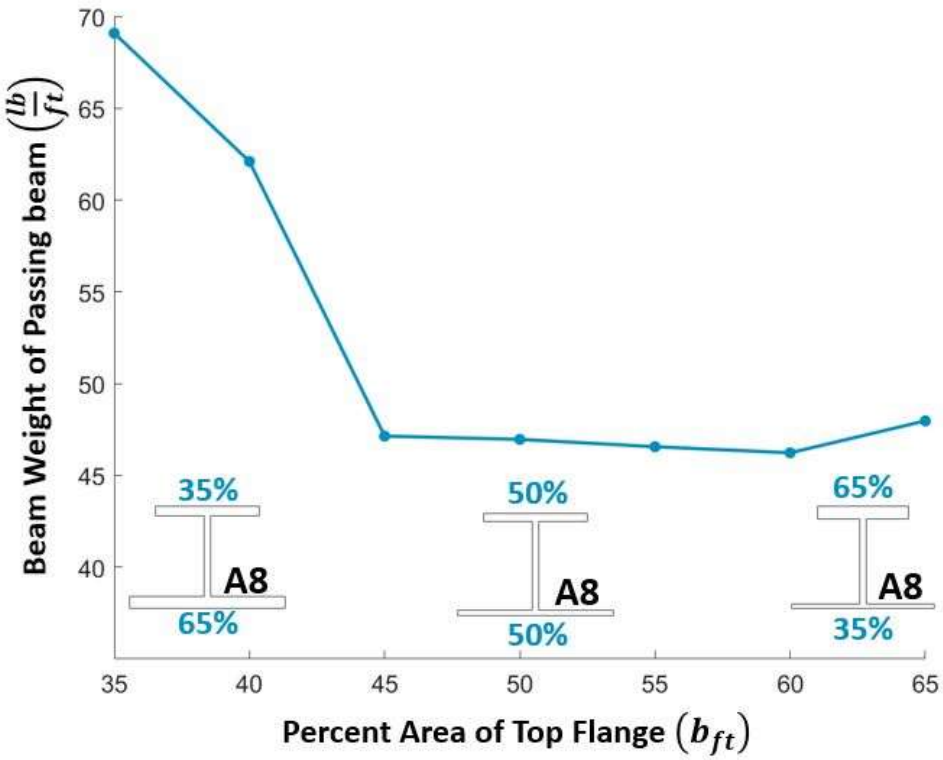

Figure 130: Percent area of top flange vs. beam weight

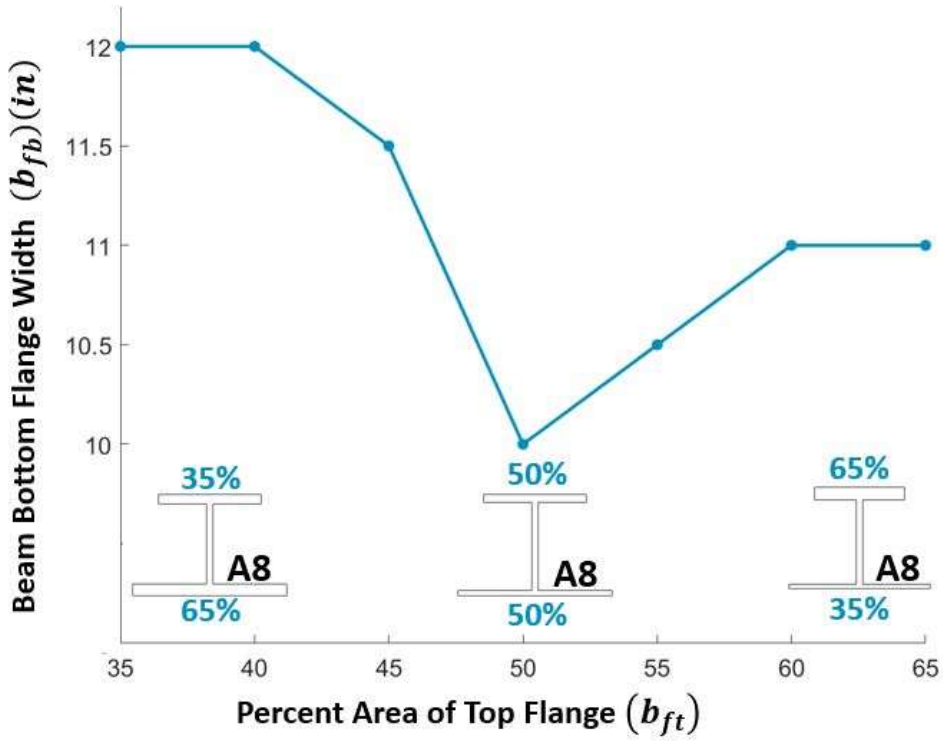

Figure 131: Percent area of top flange vs beam weight

4.5. Phase 5: A-shape Cross-Section Recommendations

4.5.1. Introduction

Phase 5 is a culmination of the previous four phases. After A-shape behavior was generally understood, a recommendation of six cross-sections was made. Four cross-sections with varying depth were recommended for girder framing systems referred to as standard weight sections and two cross-sections for larger beam spacings eliminating the girders and framing directly into columns referred to as heavyweight sections. The steel mills and AISC requested recommendations for 8 in., 9 in., 10 in., and 12 in. deep sections for the standard weight sections along with 8 in. and 9 in. deep sections for the

heavyweight sections. This was due to the limited floor system depth for competing systems.

The different loading criteria for each depth section were input into the MATLAB program, initially developed for the A8 analytical study. Beam spacing was held at 10 feet for all standard weight depths. Beam spacing to determine heavyweight sections was modeled at 20 and 25 feet for the 8 in. and 9 in beams, respectively. The unique aspect of recommending a cross-section for each depth was the separate loading per depth as illustrated in Table 8. A minimum controlling limit state plot was created for each standard depth section. The minimum controlling plots combine all the normalized limit states, used the minimum for each cross-section, and compare those values to the cross-sectional area. Every cross-section shown above the 1.0 value is deemed passing. The normalized minimum limit state plots ascending cross-sectional area on the abscissa. Therefore every cross-section above 1.0, which is shown on the passing plots, was a passing cross-section with the minimum area cross-section falling above the 1.0 line and the furthest left cross-section. Each of the depths analyzed used the balanced area flanges following mill recommendation and flange area study results (4.4.6).

Table 8: Beam cross-section unique parameters

Section:	A8 (s)	A8 (H)	A9 (s)	A9 (H)	A10 (s)	A12 (s)
Beam depth	8"	8"	9"	9"	10"	12"
Precast panel depth	6"	6"	7"	6"	8"	10"
Precast panel weight	57 psf	47 psf	60 psf	47 psf	62 psf	77 psf
Topping slab thickness	3"	3"	3"	4"	3"	3"
b_{ft} minimum	2"	2"	3"	3"	4"	6"
b_{ft} maximum	8"	8"	9"	9"	10"	12"
Beam Length	20'	20'	22.5'	20'	25'	30'
Beam Spacing	10'	20'	10'	26	10'	10'

4.5.2. Standard Weight Cross-Sections

The first beam analyzed with the analytical study was the 8-inch deep standard section (A8). The analytical study focused on individual limit state results, combining the individual limit states to form a controlling overall limit state plot this was done in the MATLAB code. The A8 plot (Figure 132) shows all A8 beam cross-sections and labels the most efficient (minimum area) passing cross-section. Table 9 lists the cross-section dimensions for the four passing beams, including the A8. Figure 133 illustrates the minimum passing cross-sections for the 9 inches deep (A9) sections. The span length, depth, and other loading parameters (Table 8) were changed for the increased depth. The resulting A9x55 dimensions are included in Table 9. The next depth of cross-sections analyzed was the 10 inches deep beams (A10). Figure 134 is the minimum passing cross-sections for the 10inchs depth cross-sections. The minimum passing cross-section was the A10x62, which is included in Table 9. The final depth analyzed was the 12 inches beam (A12). Figure 135 is the minimum cross-sections for the A12 beam depth. The minimum area beam A12x81 beam parameters are included in Table 9. A list

of the failures per normalized minimum limit state by percent is given in Table 10. Noting from Table 10, A8 beams were controlled by the AISC Scenario II Load Case 2a moment and Scenario III Load Case 3 vibration, whereas the A12 beams were controlled more by the beam Scenario I Load Case 1 rotation and Scenario II Load Case 2a deflection. Figure 136 plots the results from Table 10. Figure 136 shows the shift in limit states between each cross-section depth.

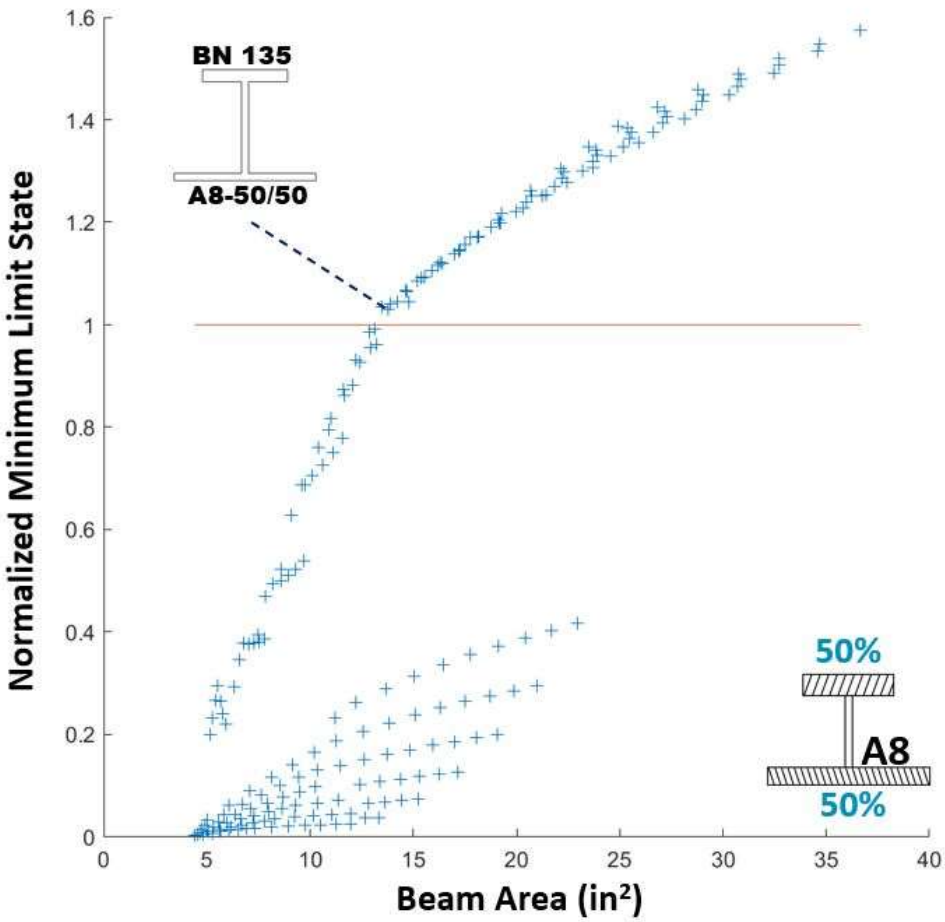

Figure 132: A8 standard weight normalized minimum limit state

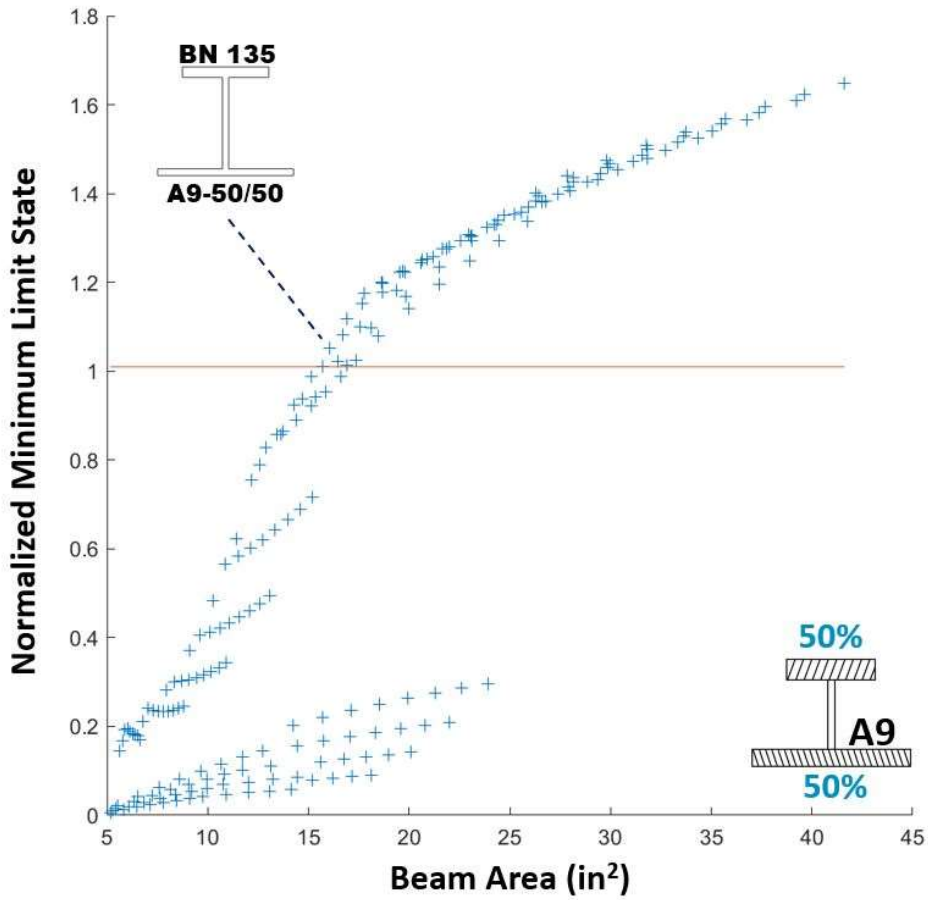

Figure 133: A9 standard weight normalized minimum limit state

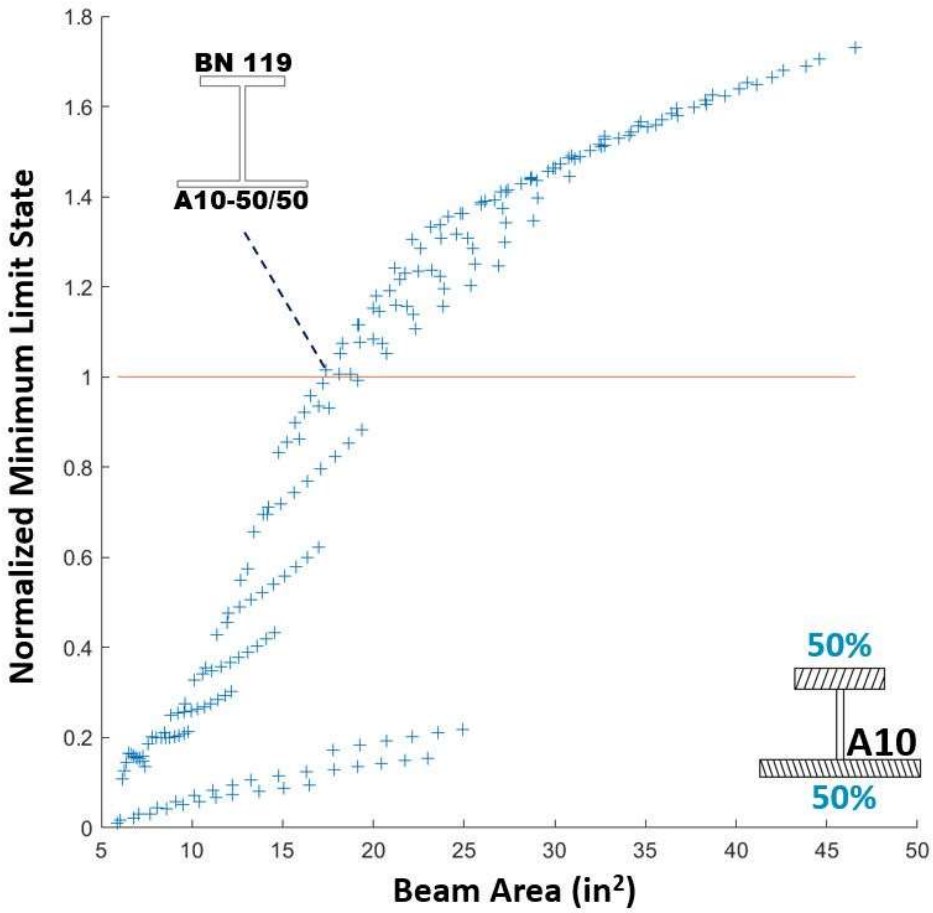

Figure 134: A10 standard weight normalized minimum limit state

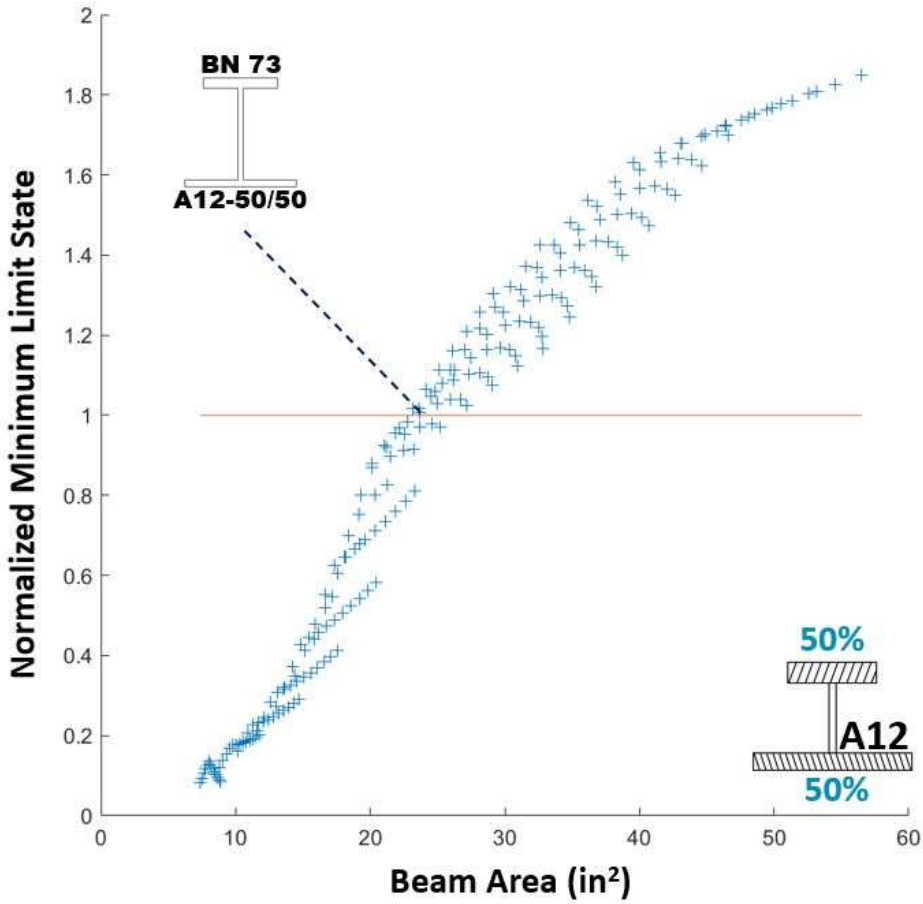

Figure 135: A12 standard weight normalized minimum limit state

Table 9: Satisfactory standard weight beam cross-section parameters

Section:	A8x47	A9x55	A10x59	A12x81
Top Flange Thickness (tft)(in)	0.875	0.875	0.875	1.125
Top Flange Width (bft)(in)	6.000	7.000	7.500	8.000
Web (tw)(in)	0.500	0.500	0.500	0.563
Bottom Flange Thickness (tfb)(in)	0.525	0.557	0.571	0.750
Bottom Flange Width (bfb)(in)	10.000	11.000	11.500	12.000
Section Area (in2)	13.8	16.4	17.4	23.7
Moment of Inertia (in4)	152.3	228.8	309.1	600.8
Weight per Foot (plf)	47	55	59	81
Controlling Limit State	13	13	13	13

Table 10: Controlling limit state by percent

Section:	A8	A9	A10	A12
Load Case 1: Rotation	7%	21%	27%	26%
Load Case 2a: Moment Capacity	35%	25%	20%	17%
Load Case 2a: Deflection L/240	8%	17%	31%	45%
Load Case 2b: Buckling	19%	12%	5%	4%
Load Case 3: Vibration	31%	25%	17%	8%

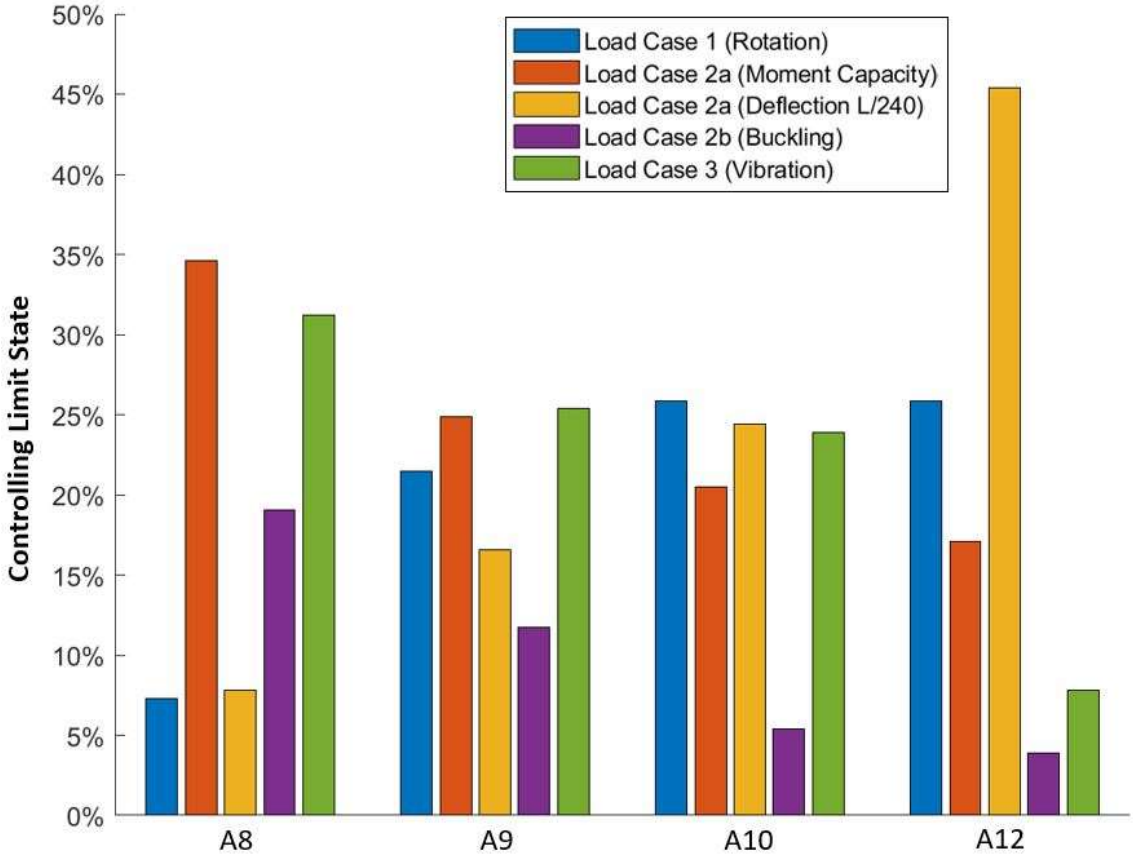

Figure 136: Controlling limit states by percent (standard weight)

The recommended beam sections for each depth are graphically illustrated to scale in Figure 137[2]. The cross-sections range from the A8x47 to the larger A12x81. For all recommended beam dimensions, consult Table 9. Note that these beams were created based on the parameters selected within the analytical study (e.g., beam length, beam spacing, etc.).

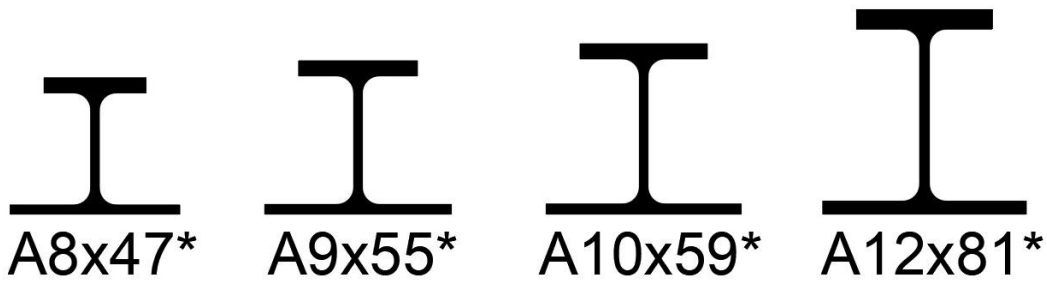

Figure 137: Recommended standard weight beam cross-sections

4.5.3. Heavyweight Cross-Sections

The heavyweight cross-sections were modeled using the same technique discussed for the standard weight cross-sections. The unique aspect of the heavyweight sections is the removal of a girder spanning between columns. This girder removal requires larger beam spacings but reduced deflection and vibration induced from the girder. The heavyweight sections created a second option for hot-rolled thin floor systems. The 8 in. and 9 in. depths were used for the heavyweight sections (Table 8).

The first beam analyzed with the analytical study heavyweight cross-sections was the 8-inch deep section (A8). The analytical study focused on individual limit state

[2] *Beam cross-section weight and designations are given without fillet weights to stay consistent with analytical study results.

results, combining the individual limit states to form a controlling overall limit state plot this was done in the MATLAB code. The A8 plot (Figure 138) shows all A8 heavyweight beam cross-sections and labels the most efficient (minimum area) passing cross-section. Table 11 lists the cross-section dimensions for the heavyweight passing beams. Figure 139 illustrates the minimum passing cross-sections for the 9 inches deep (A9) heavyweight sections. Both the A8 heavyweight and A9 heavyweight cross-sections selected were governed by Scenario II load case 2a limit state noncomposite deflection. Figure 140 displays the failure limit states for all heavyweight A8 and A9 sections. Note one additional failure limit state for heavyweight cross-sections of the beam rotation 2b limit state. The 2b rotation limit state is due to utilizing a six-inch pre-cast panel and requiring an additional one inch of topping slab cover on the A9 heavyweight beam.

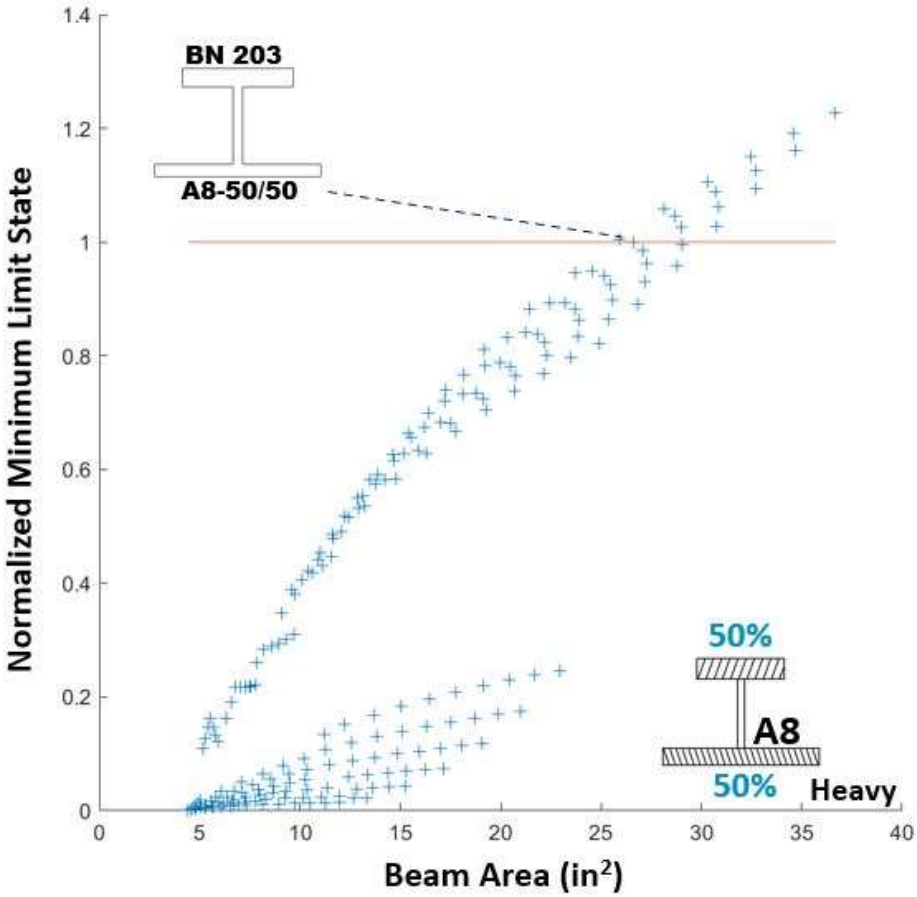

Figure 138: A8 heavyweight normalized minimum limit state

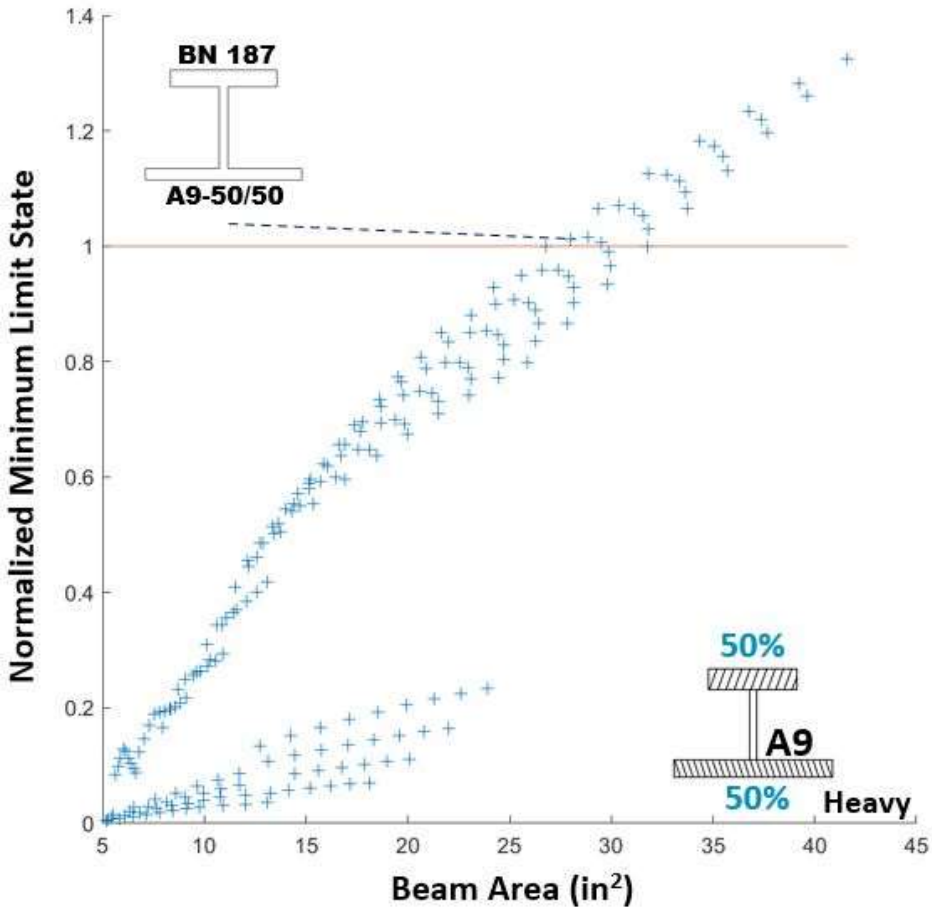

Figure 139: A8 heavyweight normalized minimum limit state

Table 11: Satisfactory heavyweight beam cross-section parameters

Section:	A8x88	A9x95
Top Flange Thickness (tft)(in)	1.375	1.375
Top Flange Width (bft)(in)	8.000	8.500
Web (tw)(in)	0.688	0.688
Bottom Flange Thickness (tfb)(in)	0.917	0.935
Bottom Flange Width (bfb)(in)	12.000	12.500
Section Area (in2)	25.9	28.0
Moment of Inertia (in4)	271.6	379.5
Weight per Foot (plf)	88	95
Controlling Limit State	13	13

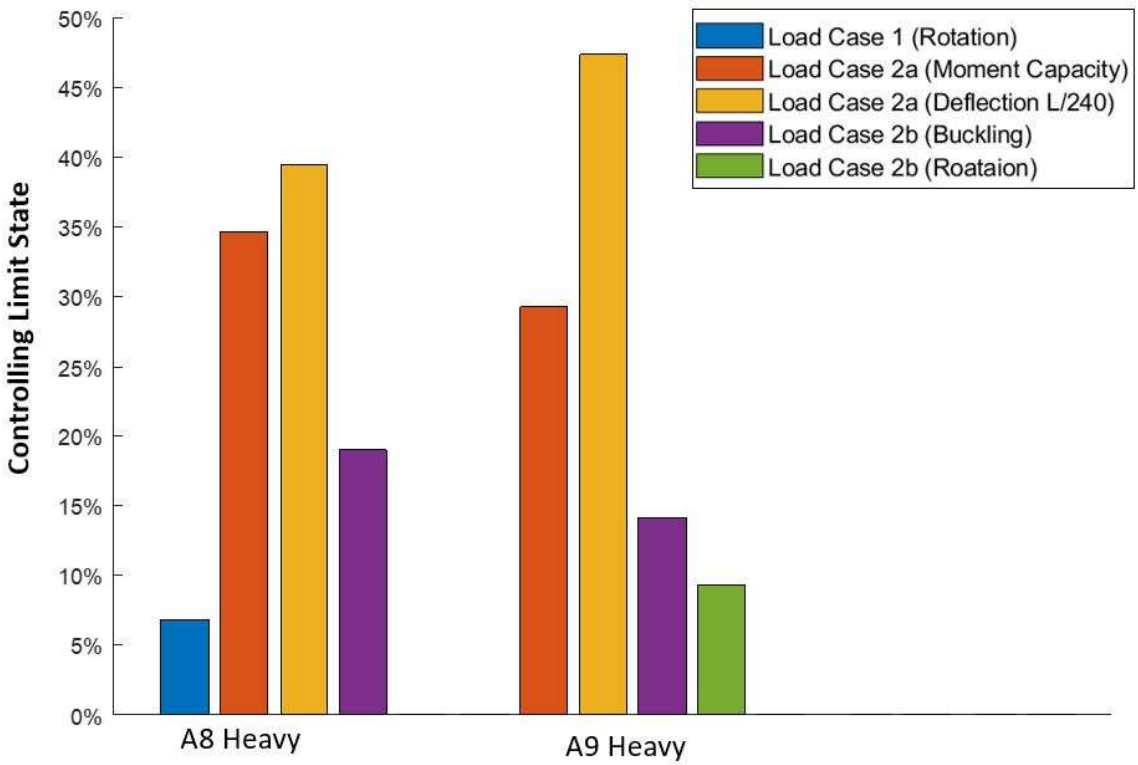

Figure 140: Controlling limit states by percent (heavyweight)

The recommended beam sections for the two heavyweight depths are graphically illustrated to scale in Figure 141[3]. The cross-sections are the A8x88 to the larger A9x95. For all recommended beam dimensions, consult Table 11.

Figure 141: Recommended heavyweight beam cross-sections

[3] *Beam cross-section weight and designations are given without fillet weights to stay consistent with analytical study results.

5. CONCLUSIONS AND CONTRIBUTIONS

The overarching goal of this research was to create new knowledge toward the behavior of hot-roll asymmetric steel I-beams (termed A-shapes). This behavior focuses on the primary stages throughout the life of A-shapes, which includes manufacturing, construction, and in-service operation. From this understanding, A-shape cross-sections were developed for future steel mill production and construction applications. To achieve this goal, the research was divided into five phases that focused on: (1) manufacturing behavior through numerical modeling, (2) manufacturing behavior through the development of proof-of-concept beams and expert feedback, (3) construction and in-service behavior through experimental testing, (4) construction and in-service behavior through analytical modeling, and (5) final A-shape cross-section recommendations. The primary achievements, contributions, and conclusions for each research phase are provided below.

Phase 1: Manufacturing Behavior – Numerical Modeling:

- A comprehensive thermal-mechanical FE modeling procedure was developed to simulate the behavior of hot-roll shapes after the rolling process. This included heat-transfer analysis to identify the thermal behavior combined with stress analysis. Validation of the methodology was performed through comparison of the numerical results with accepted physical experiments from the literature and proof-of-concept beams (performed in Phase 2) and accepted stress distributions.

- The thermal-mechanical modeling parametric study identified a recommended flange *b/t* limit of 17 to manufacture A-shapes with compressive residual stresses below 30% of the yield stress.
- The thermal-mechanical modeling parametric study concluded that global deformations due to uneven cooling were outside of typical ASTM limits for wide flange beams but were still manageable since they were relatively close to ASTM channel limits.

Phase 2: Manufacturing Behavior – Proof of Concept Beams and Expert Feedback:

- A simplified method for the development of proof-of-concept A-shape beams was created, which involved reducing one flange of standard W-shapes, reheating the beams to roughly 950ºC (1740 ºF), and then allowing them to cool in a similar fashion to conventional rolled shapes.
- The proof-of-concept A-shape beams were developed through the support of Nucor. Non-contact temperature measurements were recorded during the cooling process. These measurements were utilized for further validation of the thermal-mechanical modeling performed in Phase 1 of the research.
- Global deformation measurements (camber) of the proof-of-concept beams confirmed the relatively low magnitude expected from the cooling of A-shape beams.

Phase 3: Construction and In-Service Behavior – Experimental Testing:

- A full-scale floor system utilizing A-shape beams with precast panels and a cast-in-place topping slab was designed, fabricated, constructed, instrumented, and tested to experimentally evaluate the behavior. This work was performed in collaboration with Texas A&M University Master's student Sheyenne Davis.
- Construction of the floor system was relatively easy and fast to assemble. However, the true reduction in construction time would be the limited fabrication required if the A-shape was hot rolled vs. built-up.
- The experimental results during construction pre-cast panel placement (non-composite state) found the controlling A-shape stresses to be less than theoretical calculations due to conventional assumptions, such as support condition fixity.
- The experimental in-service composite behavior was better than anticipated, with a 100 psf equivalent live load deflection equal to L/3000.
- The experimental ultimate strength was more than sufficient, with the floor system failing at a vertical load equivalent to 500 psf loading.
- The experimental results overall found the controlling loading stage to be during deck casting due to the eccentric loading and lack of compression flange lateral bracing.

Phase 4: Construction and In-Service Behavior – Analytical Modeling:

- A comprehensive analytical modeling methodology was developed for sizing hot-rolled A-shape beams. The methodology incorporated manufacturing guidelines and evaluated the structural behavior during the critical stages of construction and the in-service states. This methodology can be applied to future A-shape or similar sizing studies.
- The analytical study yielded insight into the behavior of A-shape beams under a multitude of scenarios. This behavior was illustrated graphically through an array of plots and graphs. One of the main conclusions was the sensitivity of the top flange on the controlling limit states such as lateral-torsional buckling (during construction), deflection, and vibration.
- The analytical study identified five controlling limit states for all feasible A-shape cross-sections. The first is rotation during precast panel placement. The next three are flexural capacity (concentric loading), deflection (dead and live load), and flexural buckling (eccentric loading), all during the slab casting. The final limit state is in-service vibration.
- A supplemental study on the balance of flange areas for A-shapes indicated that a 50/50 balance is structurally efficient. This coincides with the desire by the steel mills to have balanced flange areas for roll mill workability. It is recommended that all future A-shapes utilize these proportions.

Phase 5: A-Shape Cross-Section Recommendations:

- The prior four phases of research were utilized to size A-shape cross-sections. This includes an 8-inch, 9-inch, 10-inch, and 12-inch deep section. These shapes satisfy all the manufacturing, construction, and in-service performance required, based on the assumptions within this study.
- Six A-shape cross-sections were developed and recommended, as shown in Figure 142. The controlling limit states for each of the sections were identified for future evaluation of these beams.

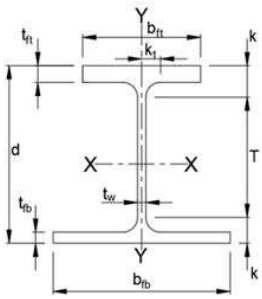

Table 1-5

A-Shapes

Dimensions

Shape	Area, A	Depth, d		Web Thickness, t_w		Web $\frac{t_w}{2}$	Top Flange Width, b_{ft}		Top Flange Thickness, t_{ft}		Bottom Flange Width, b_{fb}		Bottom Flange Thickness, t_{fb}		Nominal wt.
	in.^{2}	in.		in.		in.	in.		in.		in.		in.		lb/ft
A12x81	23.7	12.0	12	0.563	9/16	5/16	8.00	8	1.125	1 1/8	12.0	12	0.750	3/4	81
A10x59	17.4	10.0	10	0.500	1/2	1/4	7.5	7 1/2	0.875	7/8	11.5	11 1/2	0.571	9/16	59
A9x95	28.0	9.0	9	0.688	11/16	3/8	8.5	8 1/2	1.375	1 3/8	12.5	12 1/2	0.935	15/16	95
A9x55	16.4	9.0	9	0.500	1/2	1/4	7.00	7	0.875	7/8	11.0	11	0.557	9/16	55
A8x88	26.0	8.0	8	0.688	11/16	3/8	8.00	8	1.375	1 3/8	12.0	12	0.917	15/16	88
A8x47	13.8	8.0	8	0.500	1/2	1/4	6.00	6	0.875	7/8	10.0	10	0.525	1/2	47

Figure 142: A-shape AISC sample table

6. RECOMMENDATIONS FOR FUTURE RESEARCH

The following recommendations for future research could further improve the identification of future hot-rolled steel A-shapes.

- Future research should consider a further investigation into the five controlling limit states identified in the analytical modeling. For example, the investigation into the load-height effect and lateral-torsional buckling modification factor (C_b) may improve the efficiency of A-shape beams.
- Due to the influence that deflections and vibrations had on the analytical model, a more rotationally fixed connection to the girders/columns could be evaluated and tested to improve is-service conditions.
- Along with limit states, beam spacing was held at 10 feet for framing into girder sections. Removing the girders and opening the beam spacing to connect directly into columns would remove girder displacements and additional vibrations due to the girders that could improve the overall system performance. This improvement would also simplify the floor system's erection. With a wider beam spacing, larger torsional forces would be applied to the A-shapes causing the flexural behavior to need to be evaluated by full-scale testing.
- The beams in the study for A8 sections were held at a length of 20 feet. A longer beam should be studied, and a theoretical maximum length found and possibly tested. This investigation could include the use of lightweight concrete to reduce the dead load demands.

- The current recommended A-shapes were sized for pre-cast panel construction. Slim-floor and other systems also use deep decking with asymmetric beam sections. The evaluation of a unique floor system utilizing A-shapes with deep decking could be numerically evaluated and experimentally tested at full-scale.
- The current research only evaluated pre-cast concrete panels. With the market expansion into mass timber options such as cross-laminated timber (CLT), dowel laminated timber (DLT), nail laminated timber (NLT), or glue-laminated timber (GLT), floor panels should be researched and, if viable, would be a great candidate for full-scale testing. The systems could still incorporate a concrete topping slab or new connection type at the steel beams.

REFERENCES

Ahmed, I. M., and Tsavdaridis, K. D. (2019). "The evolution of composite flooring systems: applications, testing, modelling and eurocode design approaches." *Journal of Constructional Steel Research*, The Authors, 155, 286–300.

AISC (American Institute of Steel Construction). (2016). *Specification for Structural Steel Buildings, ANSI / AISC 360-16*. *American Institute of Steel Construction*.

AISC (American Institute of Steel Construction). (2021). "Need for Speed." <https://www.aisc.org/why-steel/innovative-systems/need-for-speed/>.

Alfawakhiri, F., Carter, C. J., Berhinig, R. M., Zeeveld, P., Hervey, F. E., and Woods, L. C. (2016). "The effects of load intensity and restraint on the fire resistance of steel and composite beams." *Int. Conf. Structures in Fire.*, 9th, 484–491.

Alpsten, G. A. (1972). "Prediction of thermal residual stresses in hot- rolled plates and shapes of structural steel." *IABSE Ninth Congress*.

Andersson, B. A. B. (1978). "Thermal stresses in a submerged-arc welded joint considering phase transformations." *Journal of Engineering Materials and Technology, Transactions of the ASME*, 100(4), 356–362.

ArcelorMittal Commercial Sections. (2019). *Electric arc furnace Rolling process Quenching and Self-Tempering (QST) process for HISTAR® steel*.

ArcelorMittal Europe. (2017). "Slim-Floor An innovative concept for floors." 4–45.

ASCE/SEI. (2015). *Design Loads on Structures during Construction*. Reston, Virginia.

ASCE. (2013). *Minimum Design Loads for Buildings and Other Structures*. Reston, VA.

ASTM A6 / A6M-19. (2019). *Standard Specification for General Requirements for Rolled Structural Steel Bars, Plates, Shapes, and Sheet Piling*. West Conshohocken, PA.

Bailey, C. G. (1999). "The behaviour of asymmetric slim floor steel beams in fire." *Journal of Constructional Steel Research*, 50(3), 235–257.

Baldassino, N., Roverso, G., Ranzi, G., and Zandonini, R. (2019). “Service and Ultimate Behaviour of Slim Floor Beams: An Experimental Study.” *Structures*, Elsevier, 17(October 2018), 74–86.

Borghi, T. M., Oliveira, L. A. M., and El Debs, A. L. H. de C. (2021). “Numerical investigation on slim floors: comparative analysis of ASB and CoSFB typologies.” *Revista IBRACON de Estruturas e Materiais*, 14(4), 1–19.

Braun, M., Hechler, O., Obiala, R., Kuhlmann, U., Eggert, F., Hauf, G., and Konrad, M. (2014). “Experimental investigation of Composite Slim-Floor Beams-Application of concrete dowels.” *Stahlbau*, 83(10), 741–749.

Brickstad, B., and Josefson, B. L. (1998). “A parametric study of residual stresses in multi-pass butt-welded stainless steel pipes.” *International Journal of Pressure Vessels and Piping*, 75(1), 11–25.

British Steel. (2018). “Sections: Asymmetric Beams (ASB).”

BSK (Blekinge Studentkar). (2003). “Swedish design rules for steel structures.”

Carnegie Steel Company. (1923). *Pocket Companion*. Pittsburgh.

CEN (European Committee for Standardization). (2005). “Design of steel structures. Part 1-2 General rules - Structural fire design.” *Eurocode 3, EN1993-1-2,Brussels, Belgium*.

Chajes, A. (1974). “Principles of structural stability theory.” *Civil engineering and engineering mechanics series*, xii, 336 p.

Choe, L., Ramesh, S., Grosshandler, W., Hoehler, M., Seif, M., Gross, J., and Bundy, M. (2020). “Behavior and Limit States of Long-Span Composite Floor Beams with Simple Shear Connections Subject to Compartment Fires: Experimental Evaluation.” *Journal of Structural Engineering (United States)*, 146(6), 1–14.

Council, I. C. (2017). “International Building Code.”

Davis, S. (2022). “Full–Scale Floor System Testing of Hot-Rolled Asymmetric Steel I-Beams.” Texas A&M University.

ECCS. (1984). “Ultimate Limit State Calculations of Sway Frames with Rigid Joints.” 33.

Flood Precast. (2019). *Hollowcore Slab*. Birmingham, United Kingdom.

Galambos, T., and Ketter, R. (1959). “Columns Under Combined Bending and Thrust.” *Transactions of the American Society of Civil Engineers*, 126(1), 1–23.

Gerdau. (2021a). “Asymmetric I-Beam Zoom Meeting.” (March 24, 2021).

Gerdau. (2021b). “A-shape Zoom Meeting.” (November 10, 2021).

Girder-Slab Technologies, L. (2016). *THE GIRDER-SLAB ® SYSTEM DESIGN GUIDE v3.3 ASSOCIATE The GIRDER-SLAB® System Design Guide v3.3 @GIRDERSLAB*.

Harmathy, T. Z., and Stanzak, W. W. (2009). “Elevated-Temperature Tensile and Creep Properties of Some Structural and Prestressing Steels.” *Fire Test Performance*, 186-186–23.

Hauf, G., and Kuhlmann, U. (2015). “Deformation calculation methods for slim floors.” *Steel Construction*, 8(2), 96–101.

Heins, C. P. (1975). *Bending and Torsional Design in Structural Members*. Lexington Books.

Hu, G., Morovat, M. A., Lee, J., Schell, E., and Engelhardt, M. (2009). “Elevated temperature properties of ASTM A992 steel.” *Proceedings of the 2009 Structures Congress - Don’t Mess with Structural Engineers: Expanding Our Role*, 1067–1076.

Huber, A. W. (1956). “Residual stresses in wide-flange beams and columns.” *Fritz Engineering Laboratory Report*, Paper 1498.

Huber, A. W. (1958). “Residual stresses in wide flange beams and columns . Lehigh University , (July 1956), revised.” (July 1956).

Huber, D., Varma, A. H., Bowman, M. D., Connor, R. J., Liu, J., and Adams, D. E. (2011). "DEVELOPMENT AND VALIDATION OF LONG SPAN FLOOR SYSTEMS FOR MULTI-STORY RESIDENTIAL STRUCTURES." *Purdue University*.

Illinois Steel Company. (1912). *Illinois Steel Company Manual*.

Kloeckner Metals. (2020). *THE CELLULAR BEAM POCKET GUIDE ENTRUSTED TO DESIGN AND DELIVER METAL SOLUTIONS*.

Lam, D., Dai, X., Kuhlmann, U., Raichle, J., and Braun, M. (2015). "Slim-floor construction - design for ultimate limit state." *Steel Construction*, 8(2), 79–84.

Mäkeläinen, P., and Ma, Z. (2000). "Fire resistance of composite slim floor beams." *Journal of Constructional Steel Research*, 54(3), 345–363.

Maraveas, C., Swailes, T., and Wang, Y. (2012). "A detailed methodology for the finite element analysis of asymmetric slim floor beams in fire." *Steel Construction*, 5(3), 191–198.

Mullett, D. L. (1998). *Composite Floor Systems*.

Mullett, D. L., and R.M.Lawson. (1993). *Slim floor Construction using Deep Decking (SCI Publication P127)*. The Steel Construction Institute, Ascot, UK.

Murry, T. M., Allen, D. E., Ungar, E. E., and Davis, D. B. (2016). *Vibrations of Steel-Framed Structural Systems Due to Human Activity, Design Guide 11*. AISC, Chicago, IL.

Nguyen, T., Gad, E., Wilson, J., and Haritos, N. (2014). "Mitigating footfall-induced vibration in long-span fl oors *." 15(1).

Nucor Corporation. (2020). "Asymmetric I-Beam Zoom Meeting." (July 28, 2020).

Quayyum, S., and Hassan, T. (2017). "Initial Residual Stresses in Hot-Rolled Wide-Flange Shapes: A Computational Technique and Influence on Structural Performances." *Journal of Structural Engineering (United States)*, 143(5), 1–15.

Rackham, J. W., Hicks, S. J., and Newman, G. M. (Gerald M. . (2006). "Design of asymmetric slimflor beams with precast concrete slabs." 101.

Seaburg, P. A., and Carter, C. J. (2003). “AISC Design Guide 9: Torsional Analysis of Structural Steel Members.” *Steel Design Guide Series*.

Steel Dynamics, I. (2020). “Asymmetric I-Beam Meeting.” (July 29, 2020).

Taicang Xinxing Machinery Factory. (n.d.). “Elevator Guide Rail Dimensions.” <http://www.tcxinxing.com/index.php/technialparameters/Elevator Guide Rail Dimensions/17.html>.

Tata Steel UK. (2017). “ComFlor manual.”

Tyrrell, H. G. (1911). *History of Bridge Engineering*. The G.B. Williams Co., Printers, Evanston, Illinois.

United States Steel. (1962). *United States Steel Manual*.

Varela, W. D., and Battista, R. C. (2011). “Control of vibrations induced by people walking on large span composite floor decks.” *Engineering Structures*, 33(9), 2485–2494.

Wainman, D. E. (1996). “BS476: Part 21 Fire Resistance Tests Summary of Data Obtained During a Test on Composite Slim Floor Beam.”

Wickström, U. (1979). “TASEF-2 - a computer program for temperature analysis of structures exposed to fire.” (2).

Xia, Y., Han, C., Zhou, D., Wang, Y., and Wang, P. (2021). “Ultimate flexural strength analysis of composite slim floor beam.” *Advances in Structural Engineering*, 24(10), 2214–2226.

Young, B. W. (1975). “Residual stresses in hot rolled members.” *Proceedings IABSE Colloquium: On Column Strength.*, 23, 25–38.

APPENDIX A

ABAQUS PARAMETRIC STUDY MESHES

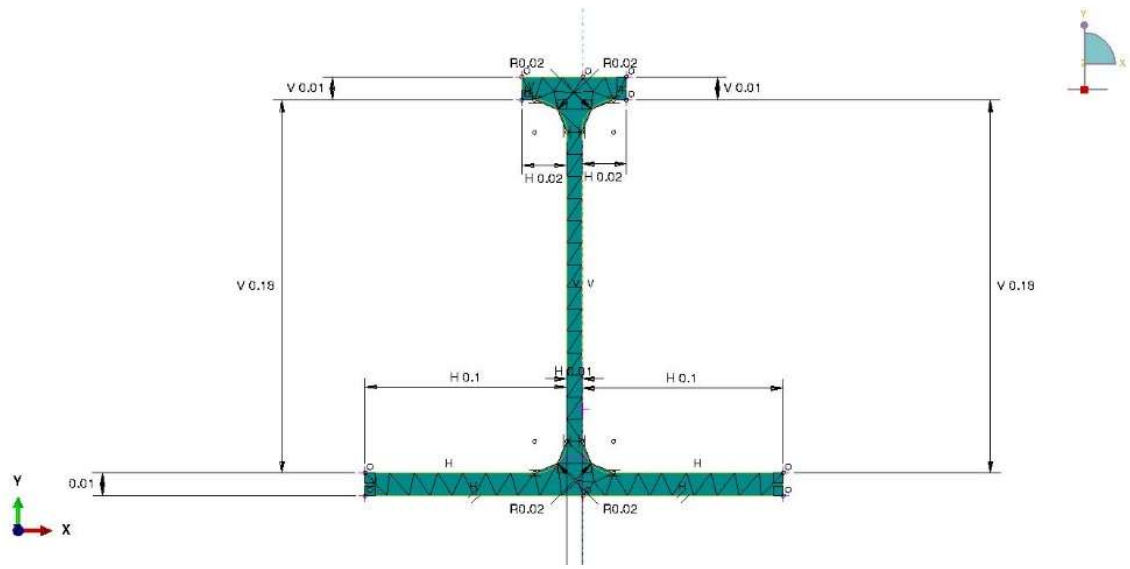

Figure 143: W8x31 0.25 b_f ABAQUS tetrahedral model meshing

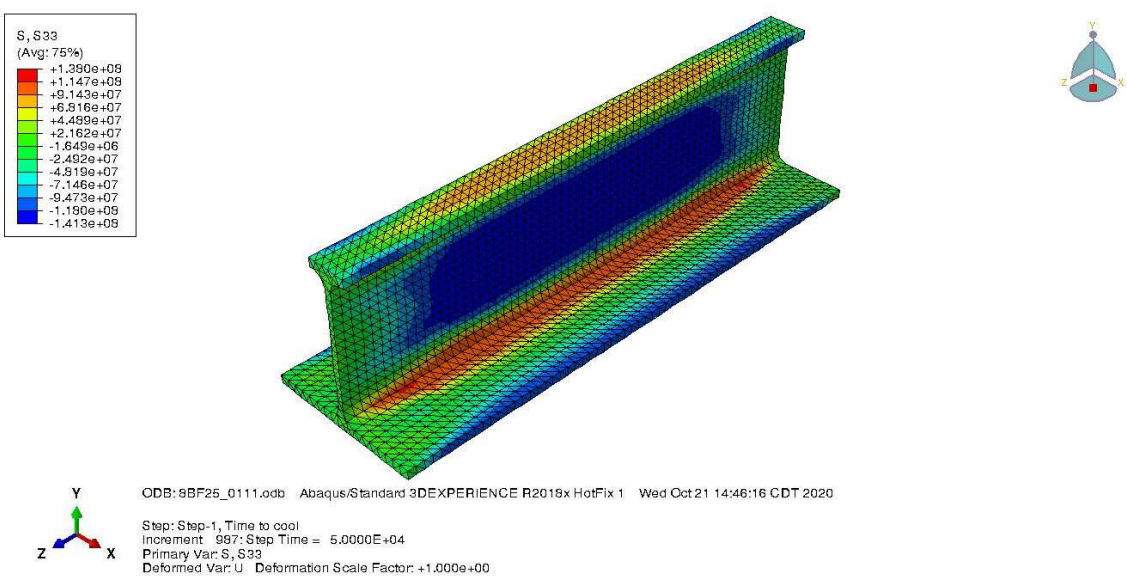

Figure 144: W8x31 0.25 b_f ABAQUS stress distribution (Pa)

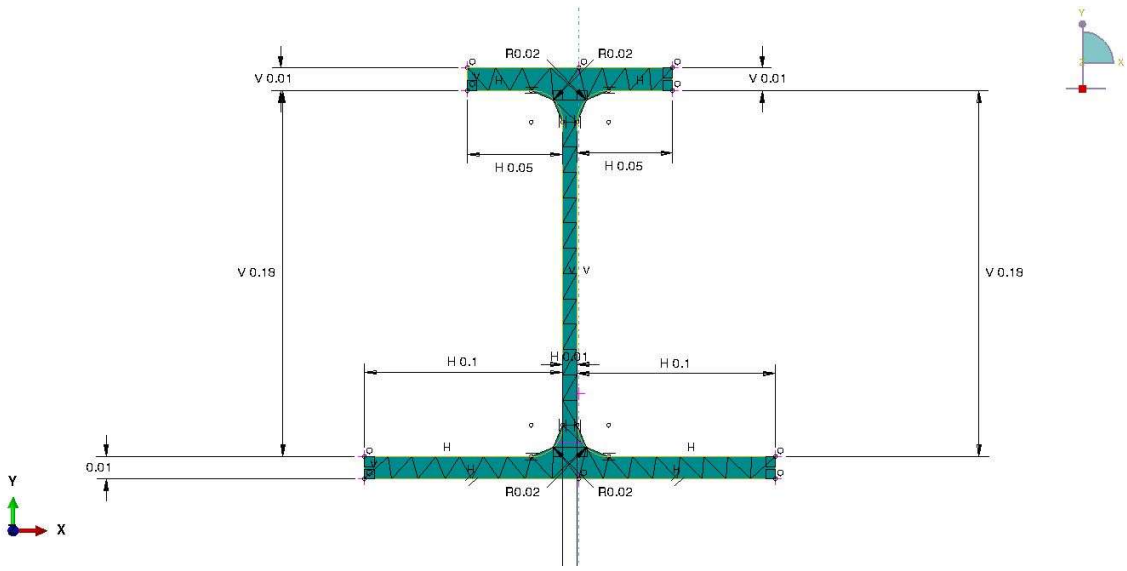

Figure 145: W8x31 0.50 b_f ABAQUS tetrahedral model meshing

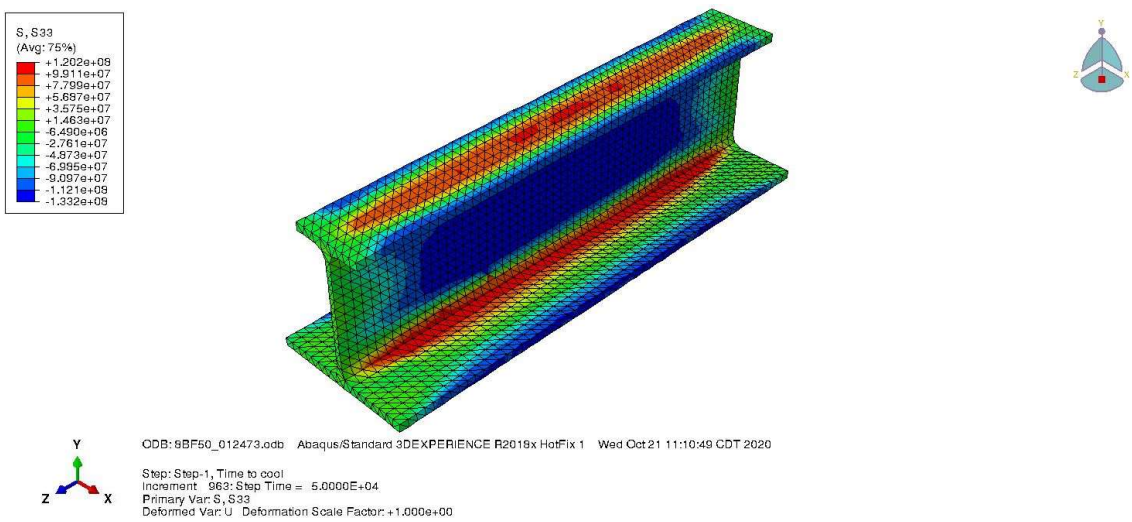

Figure 146: W8x31 0.50 b_f ABAQUS stress distribution (Pa)

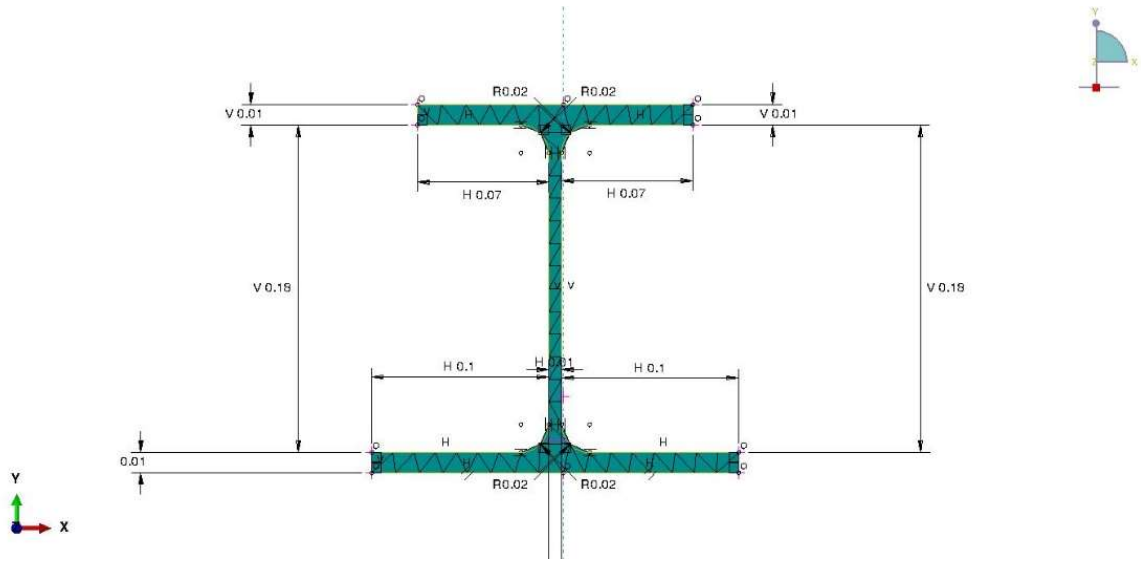

Figure 147: W8x31 0.75 b_f ABAQUS tetrahedral model meshing

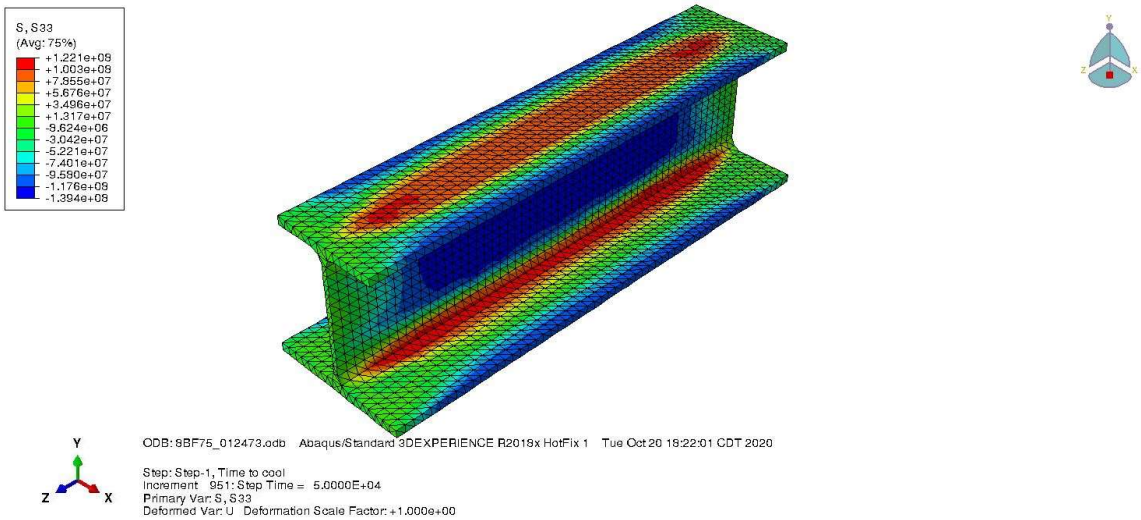

Figure 148: W8x31 0.75 b_f ABAQUS stress distribution (Pa)

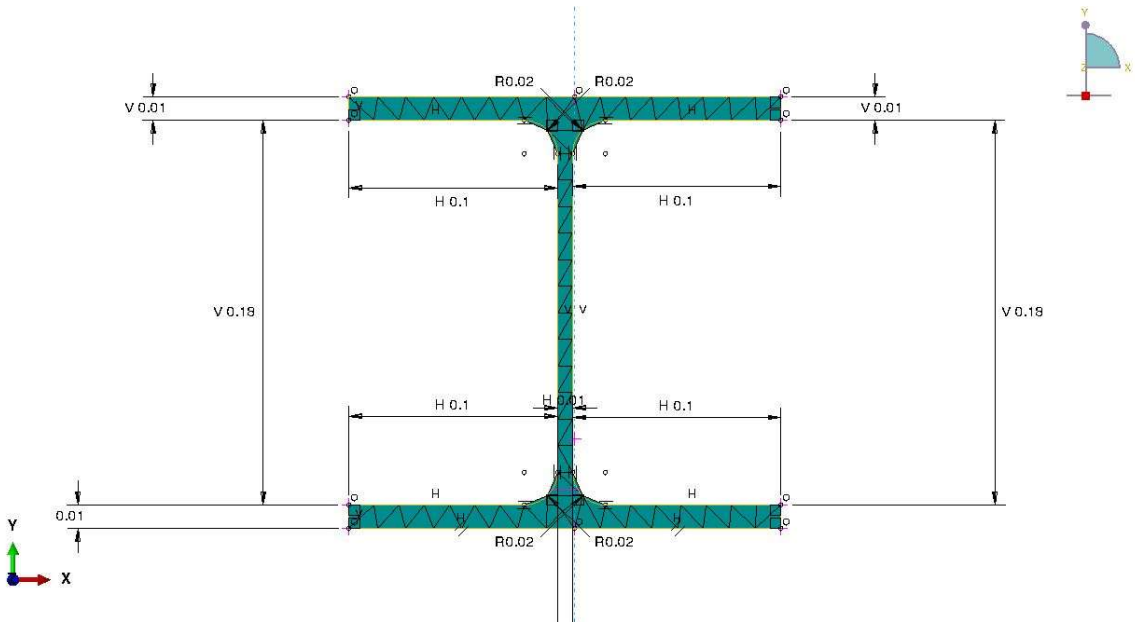

Figure 149: W8x31 1.00 b_f ABAQUS tetrahedral model meshing

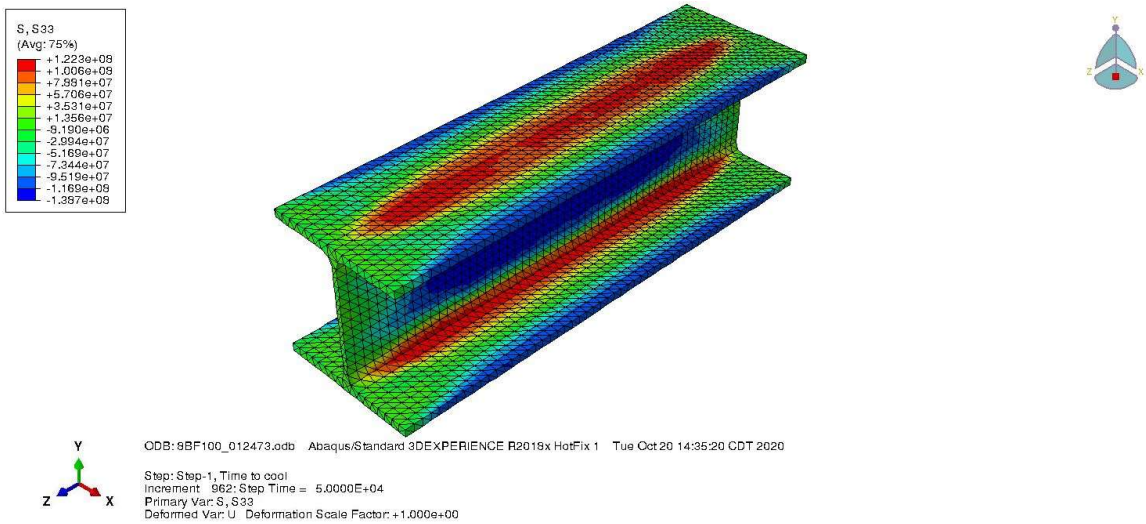

Figure 150: W8x31 1.00 b_f ABAQUS stress distribution (Pa)

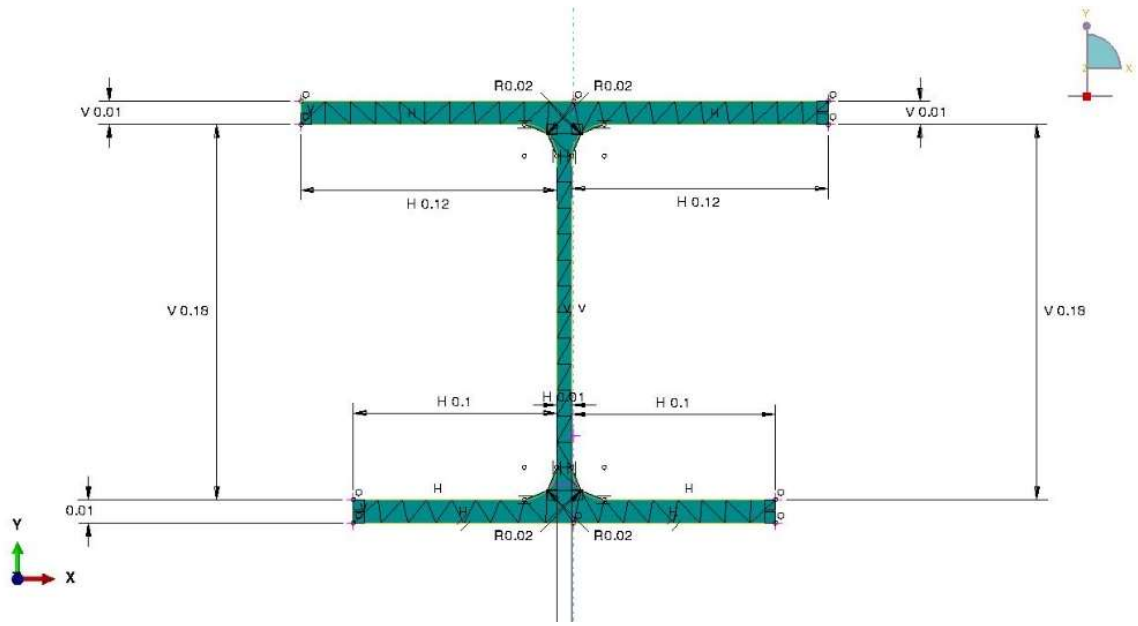

Figure 151: W8x31 1.25 b_f ABAQUS tetrahedral model meshing

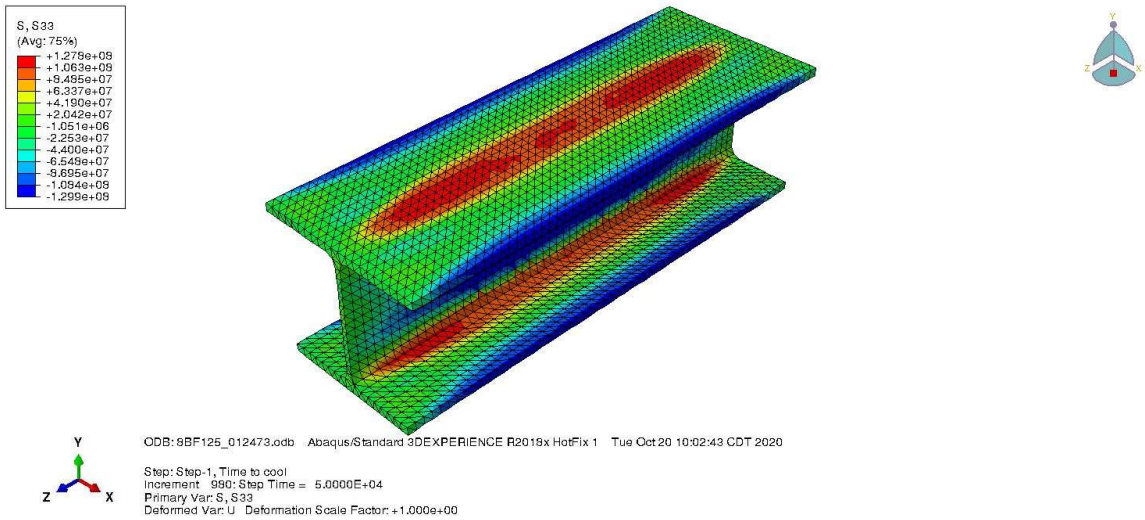

Figure 152: W8x31 1.25 b_f ABAQUS stress distribution (Pa)

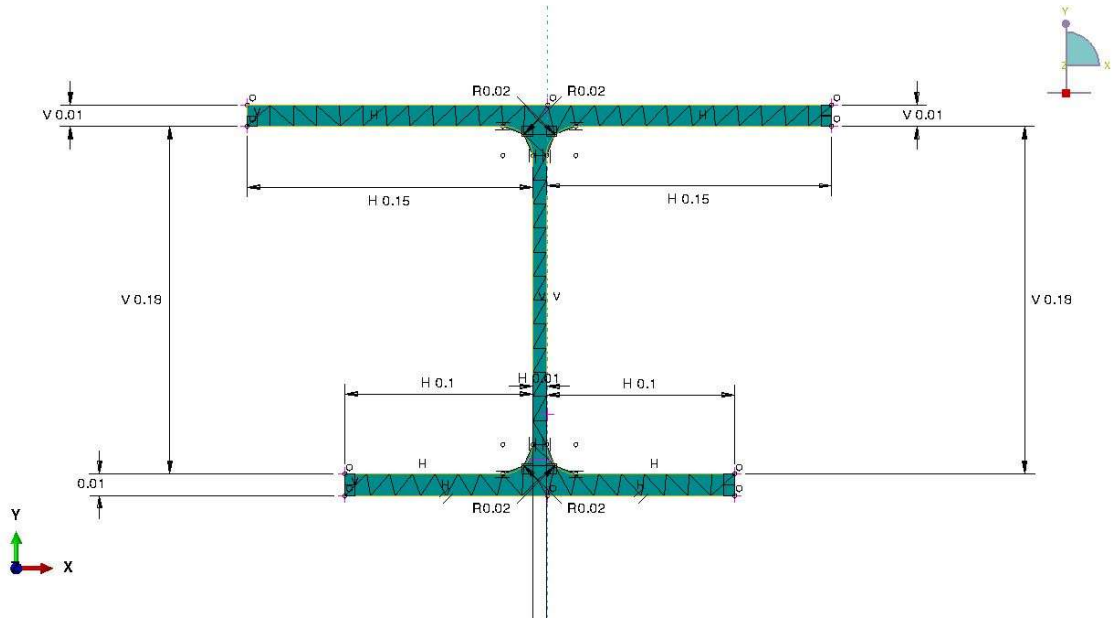

Figure 153: W8x31 1.50 b_f ABAQUS tetrahedral model meshing

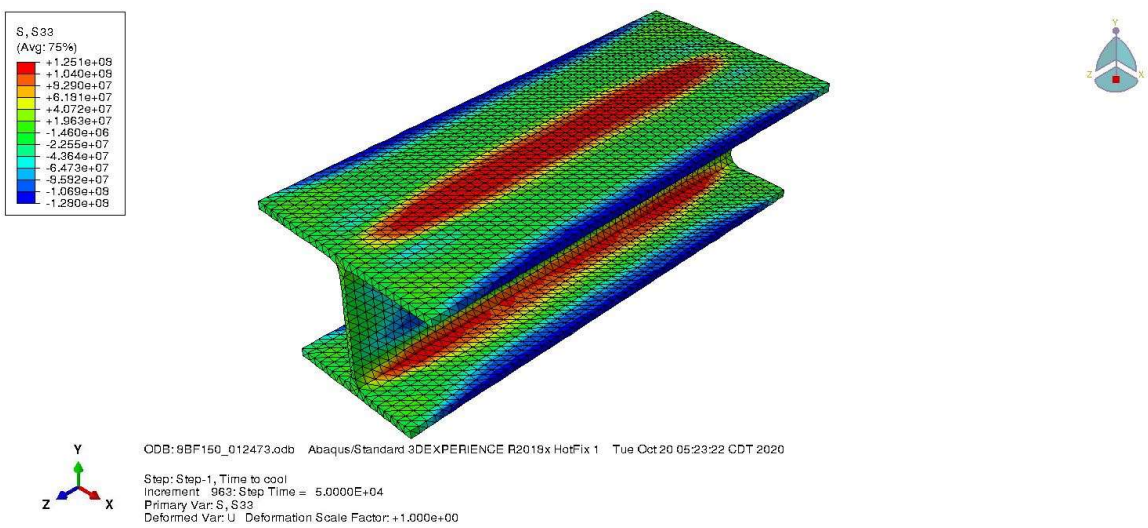

Figure 154: W8x31 1.50 b_f ABAQUS stress distribution (Pa)

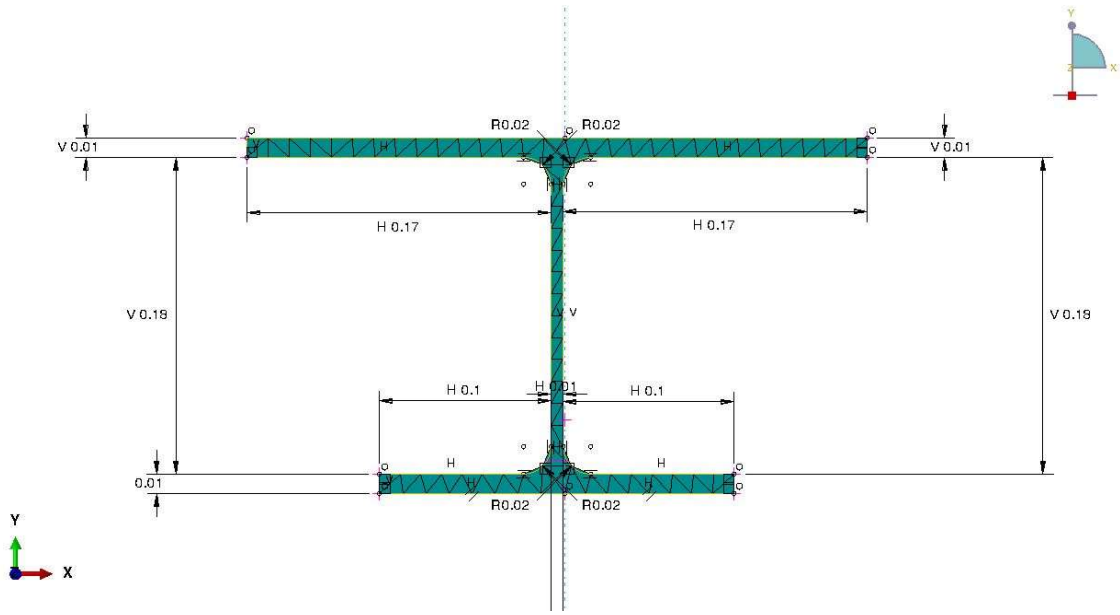

Figure 155: W8x31 1.75 b_f ABAQUS tetrahedral model meshing

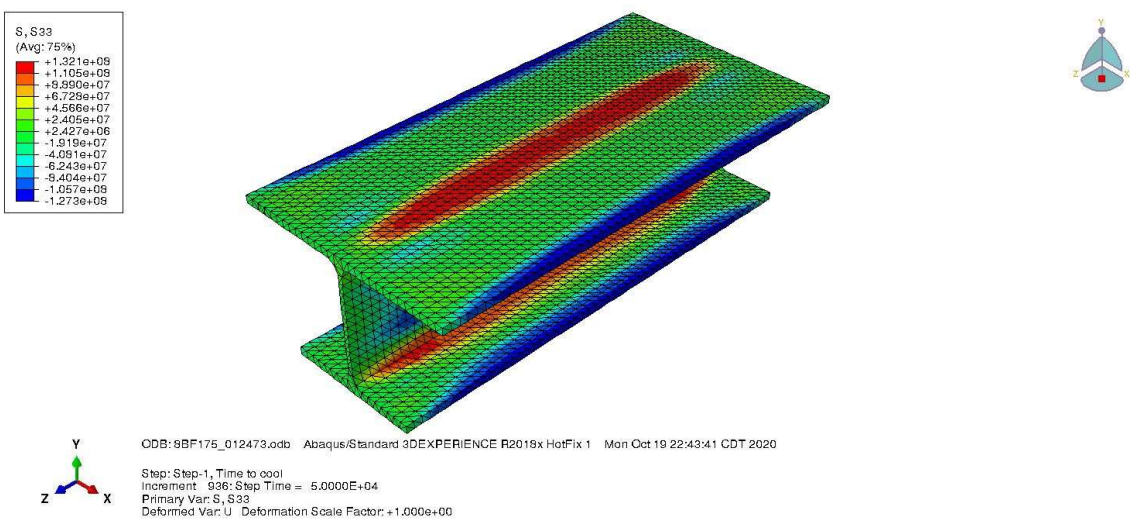

Figure 156: W8x31 1.75 b_f ABAQUS stress distribution (Pa)

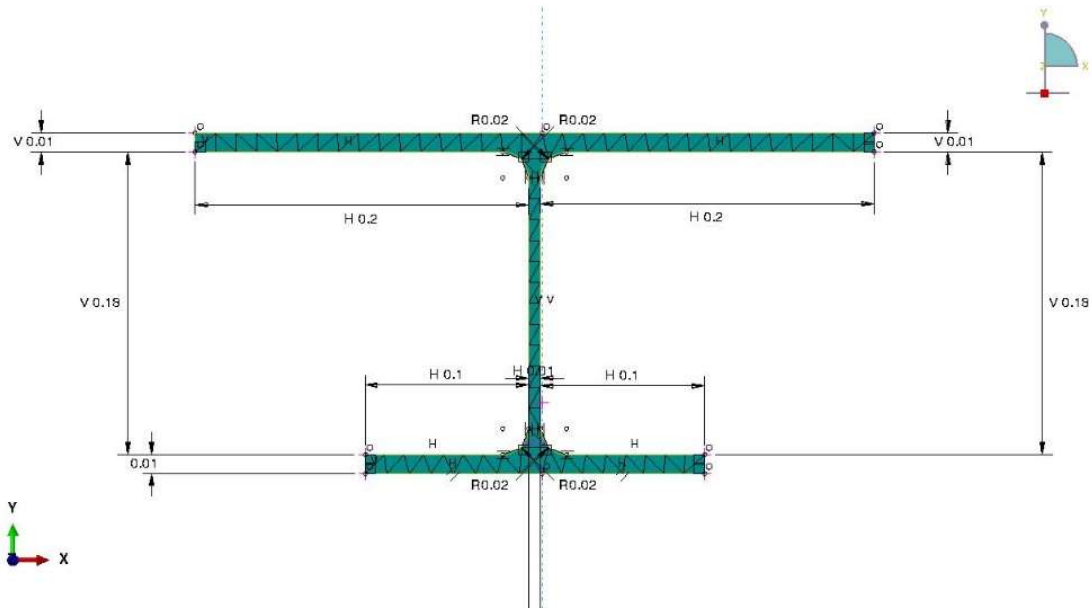

Figure 157: W8x31 2.00 b_f ABAQUS tetrahedral model meshing

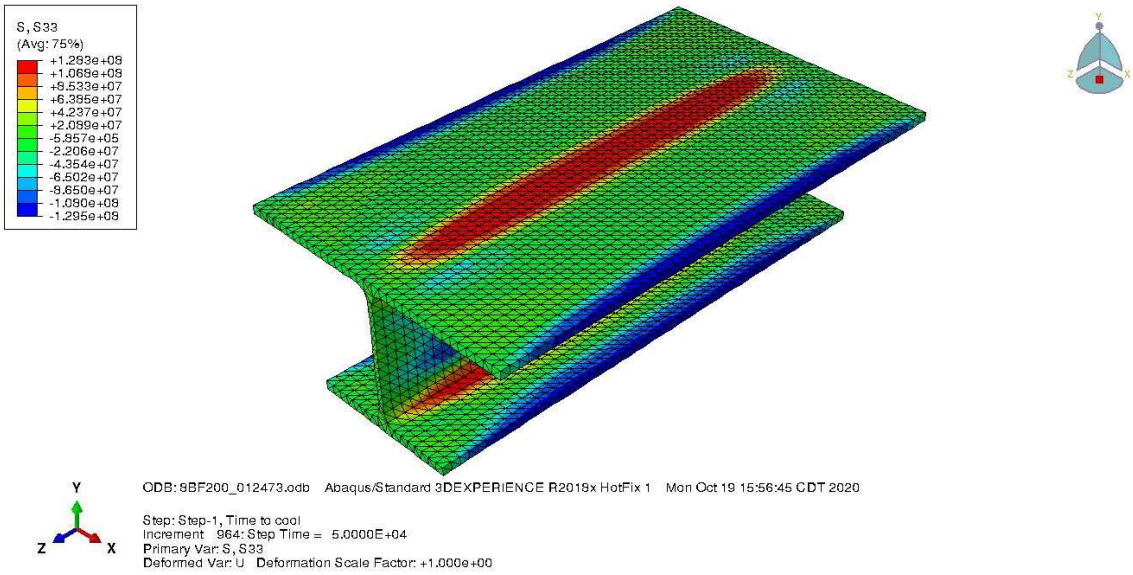

Figure 158: W8x31 2.00 b_f ABAQUS stress distribution (Pa)

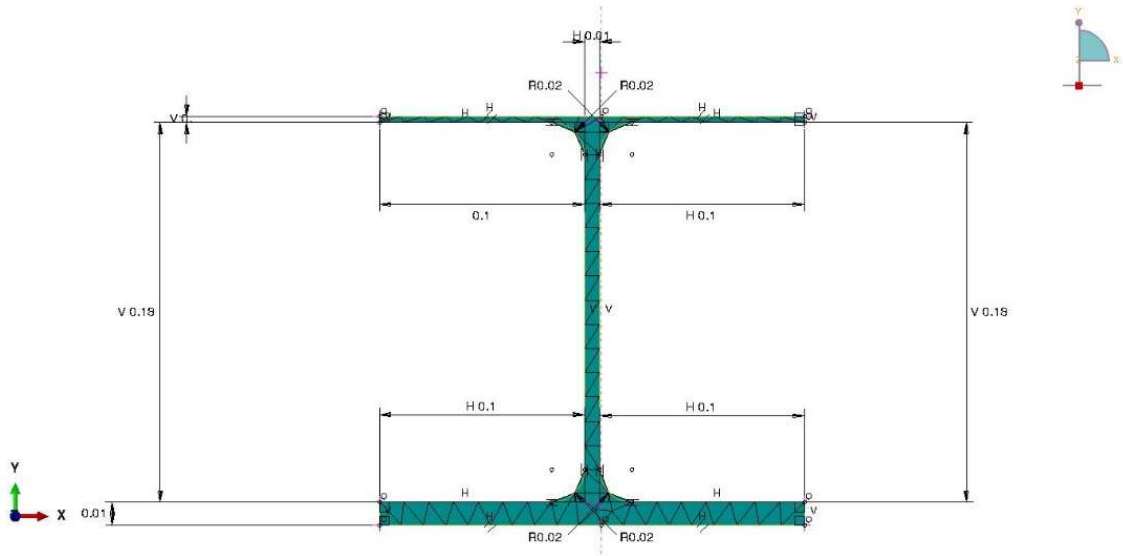

Figure 159: W8x31 0.25 t_f ABAQUS tetrahedral model meshing

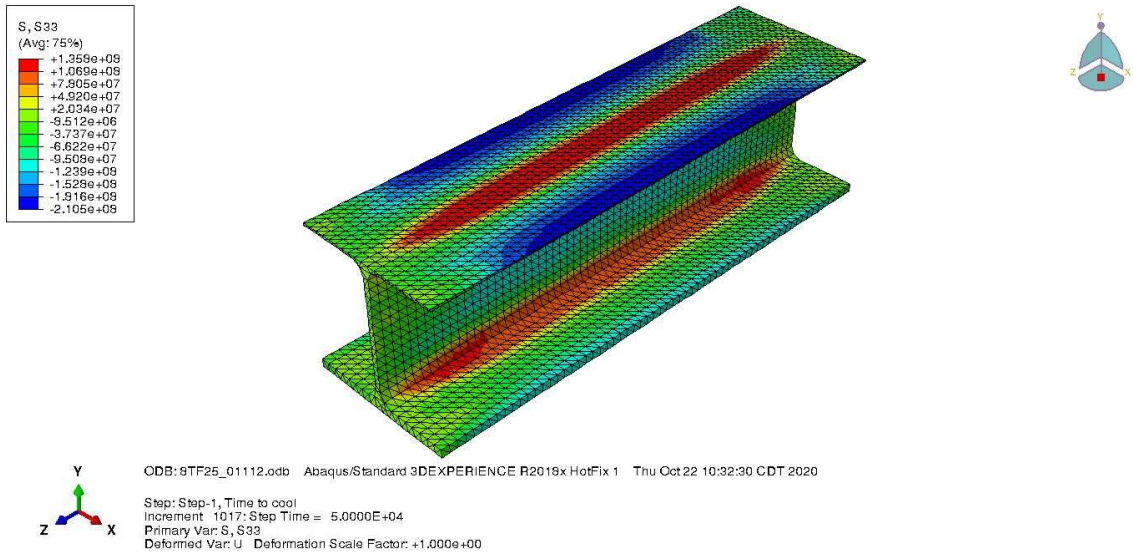

Figure 160: W8x31 0.25 t_f ABAQUS stress distribution (Pa)

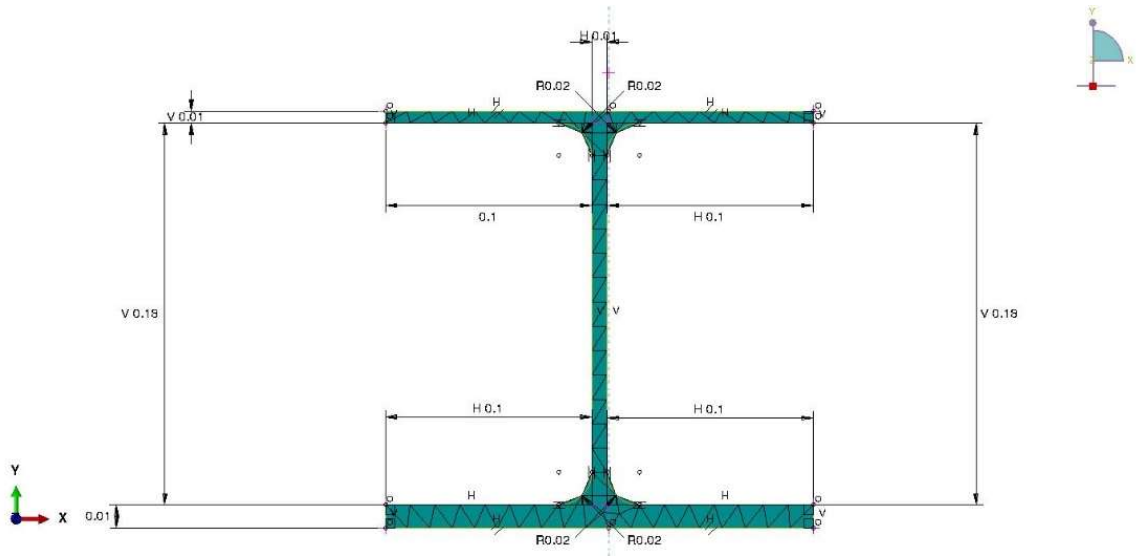

Figure 161: W8x31 0.50 t_f ABAQUS tetrahedral model meshing

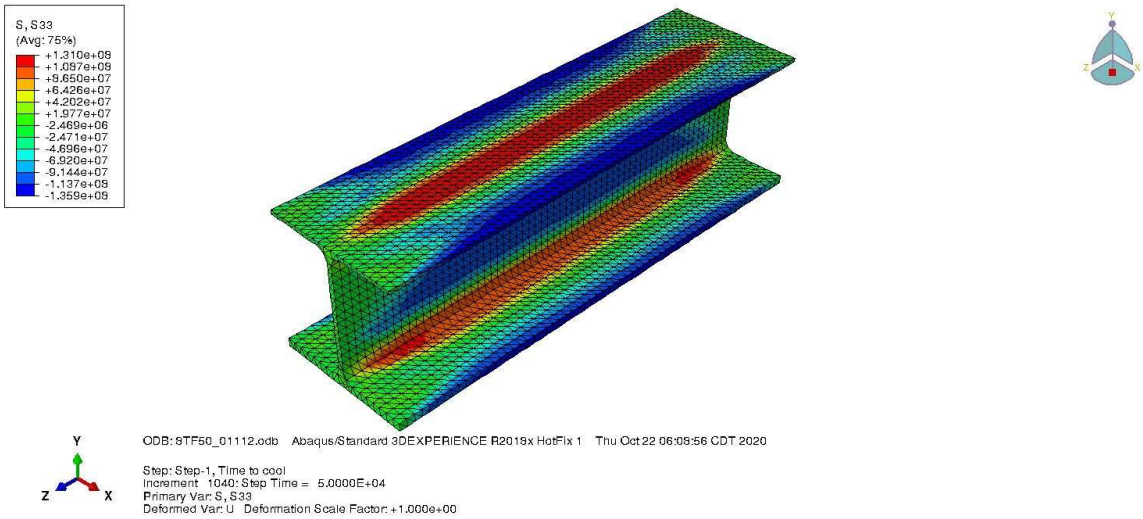

Figure 162: W8x31 0.50 t_f ABAQUS stress distribution (Pa)

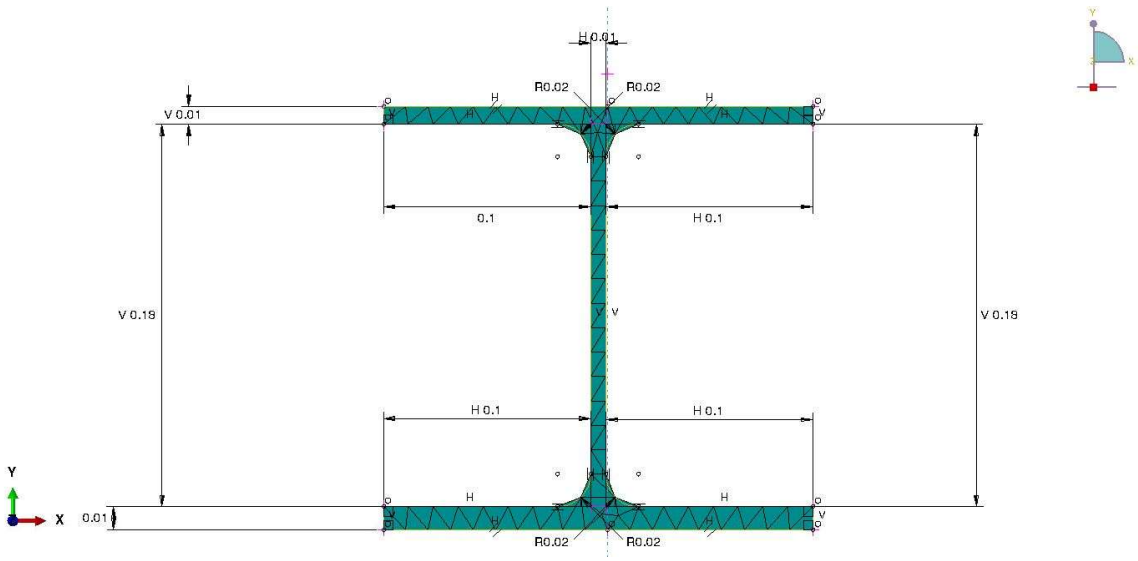

Figure 163: W8x31 0.75 t_f ABAQUS tetrahedral model meshing

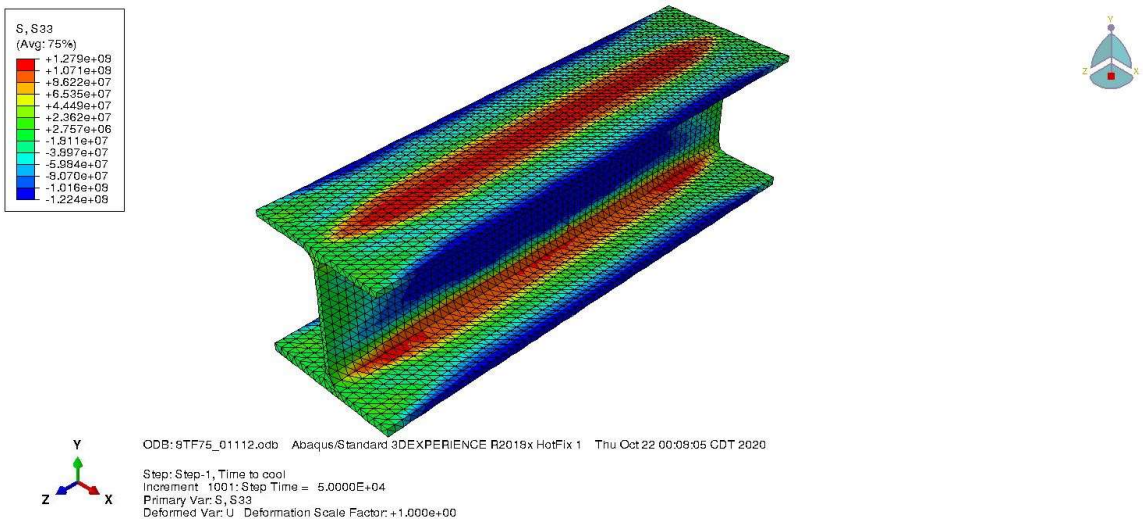

Figure 164: W8x31 0.75 t_f ABAQUS stress distribution (Pa)

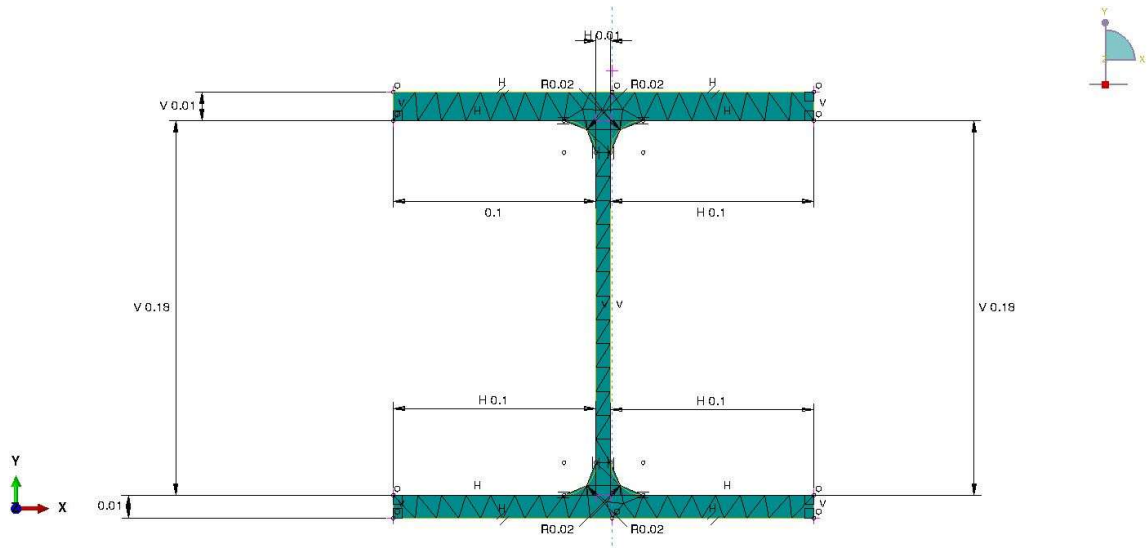

Figure 165: W8x31 1.25 t_f ABAQUS tetrahedral model meshing

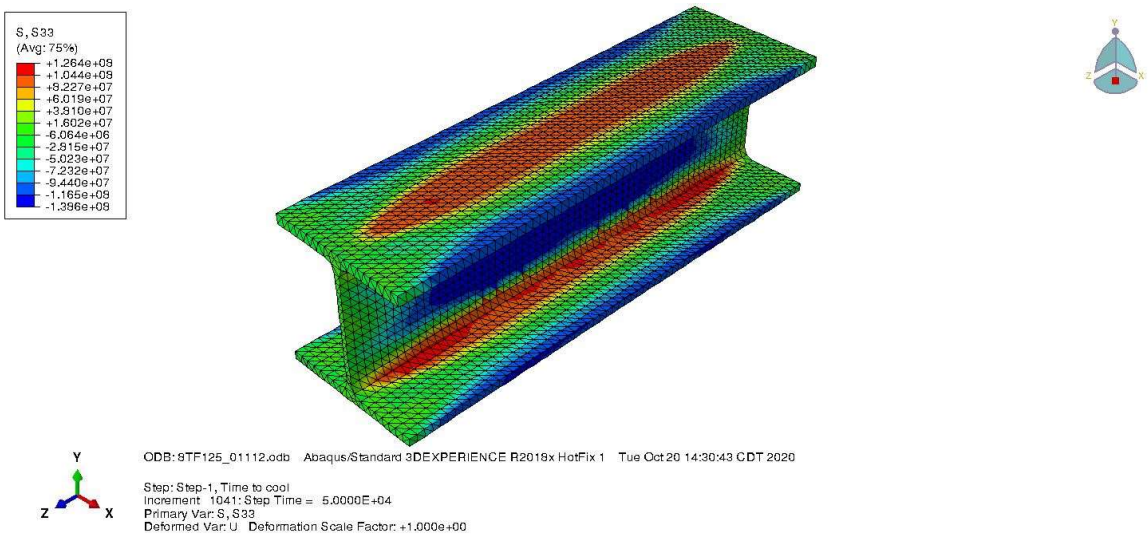

Figure 166: W8x31 1.25 t_f ABAQUS stress distribution (Pa)

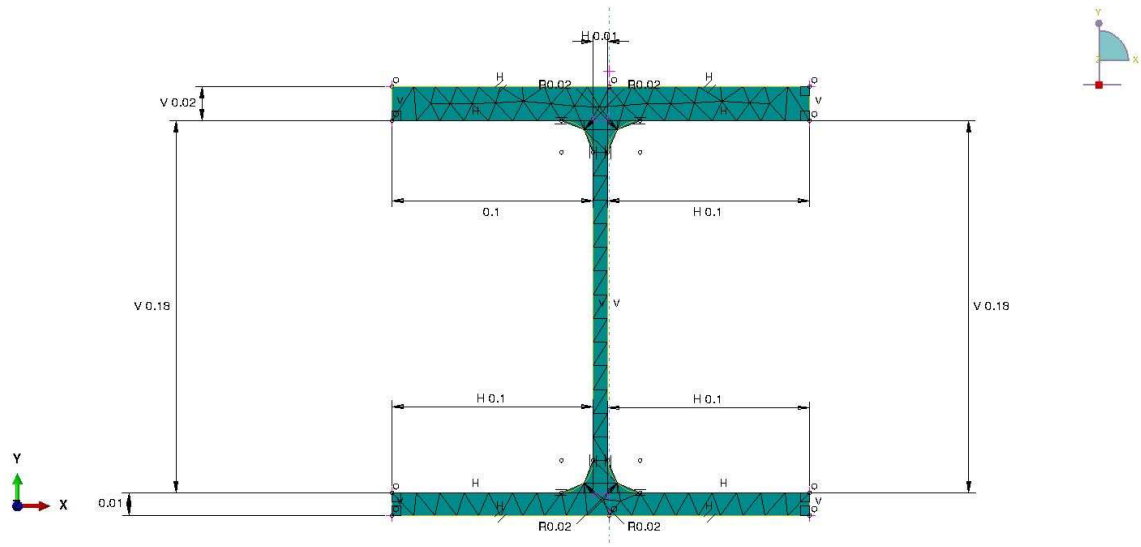

Figure 167: W8x31 1.50 t_f ABAQUS tetrahedral model meshing

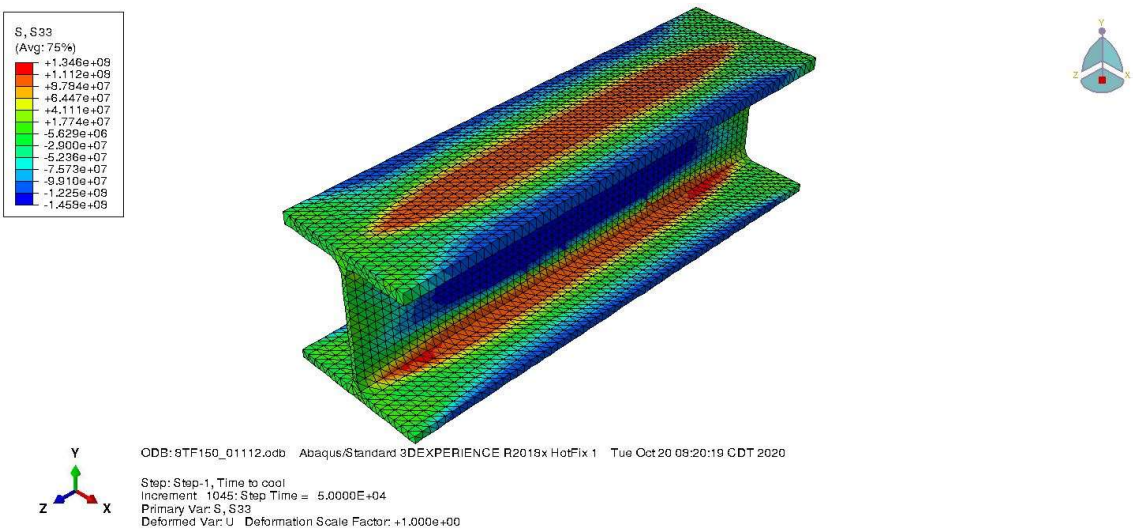

Figure 168: W8x31 1.50 t_f ABAQUS stress distribution (Pa)

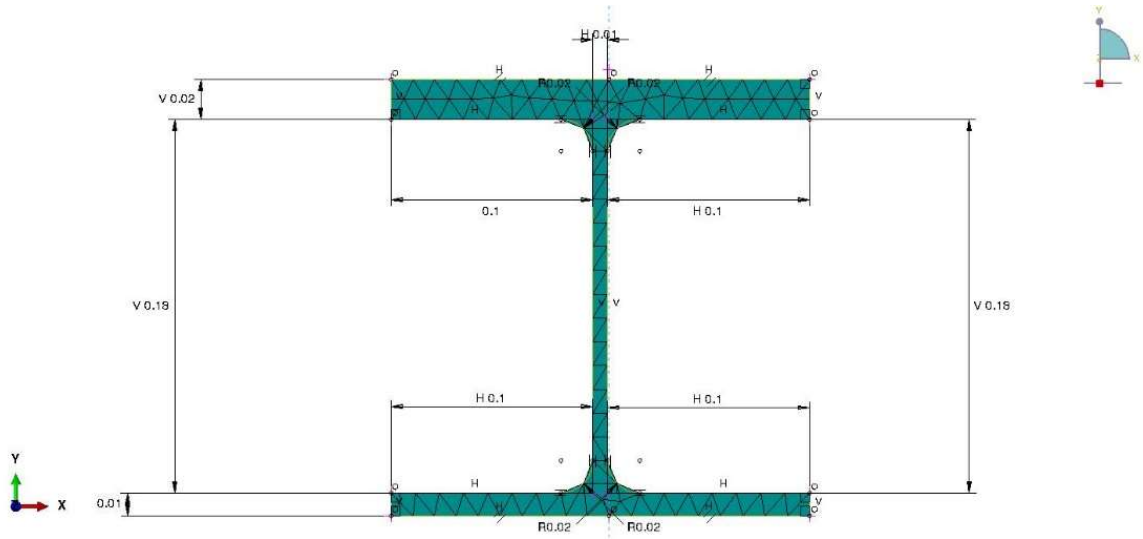

Figure 169: W8x31 1.75 t_f ABAQUS tetrahedral model meshing

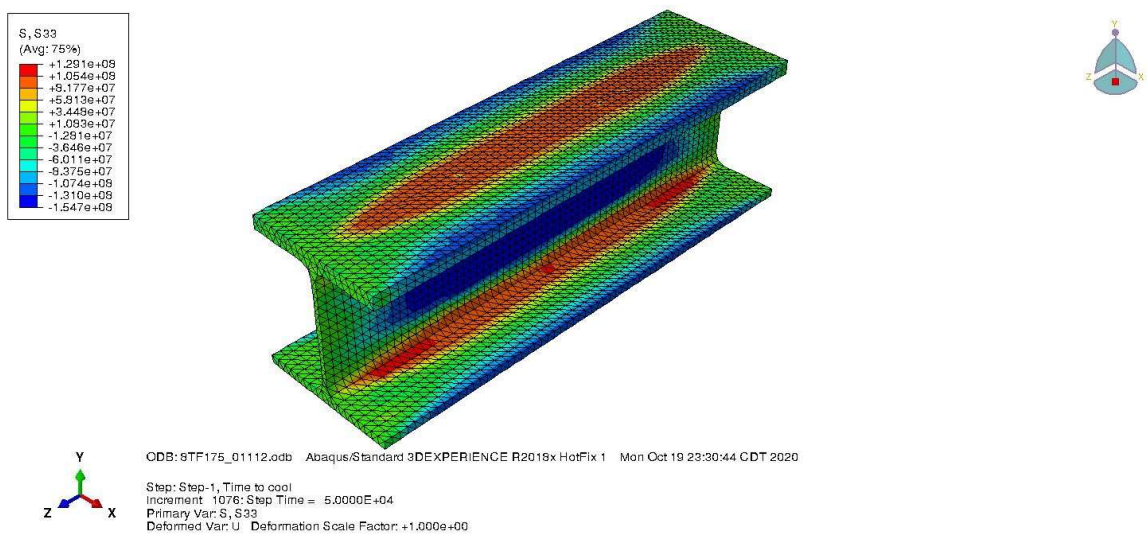

Figure 170: W8x31 1.75 t_f ABAQUS stress distribution (Pa)

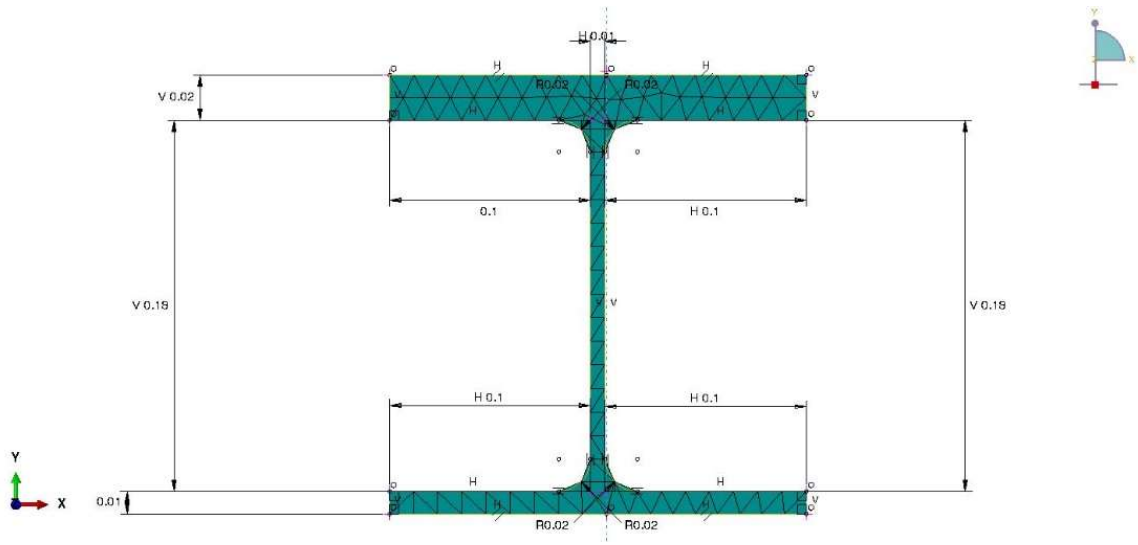

Figure 171: W8x31 2.00 t_f ABAQUS tetrahedral model meshing

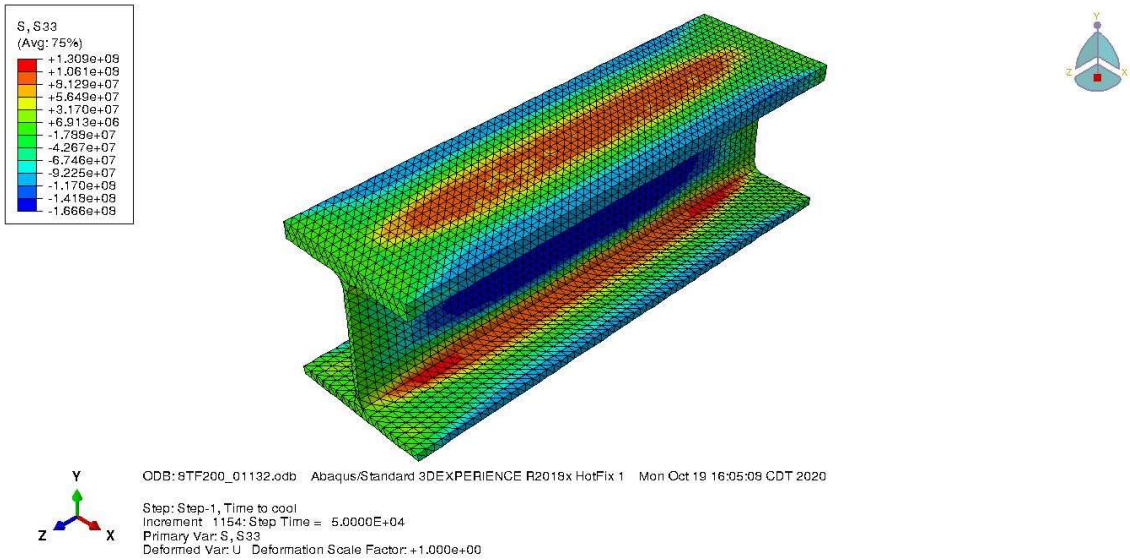

Figure 172: W8x31 2.00 t_f ABAQUS stress distribution (Pa)

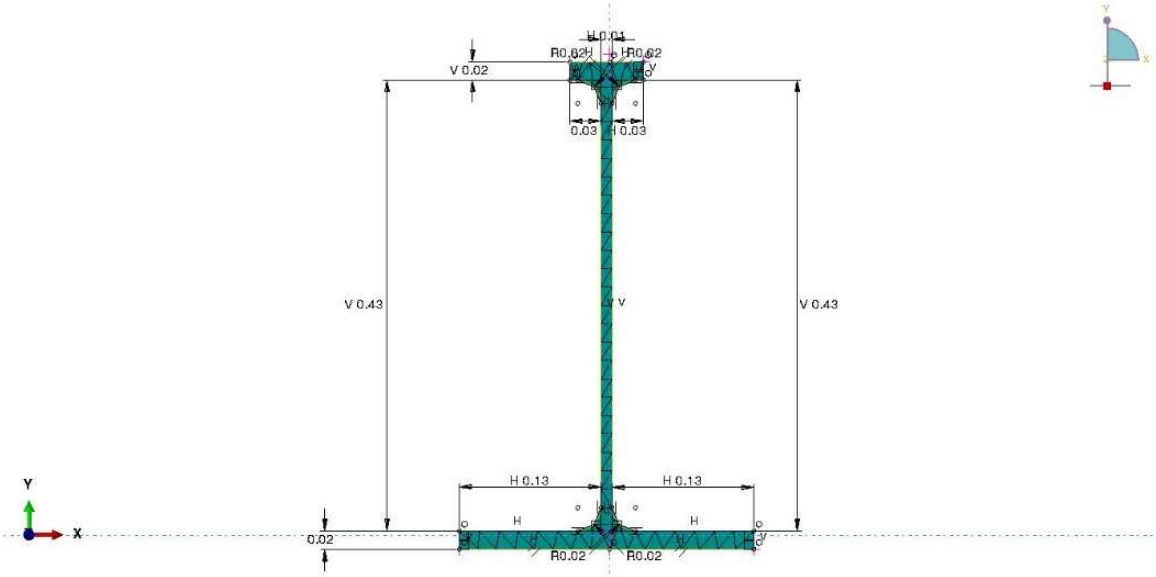

Figure 173: W18x76 0.25 b_f ABAQUS tetrahedral model meshing

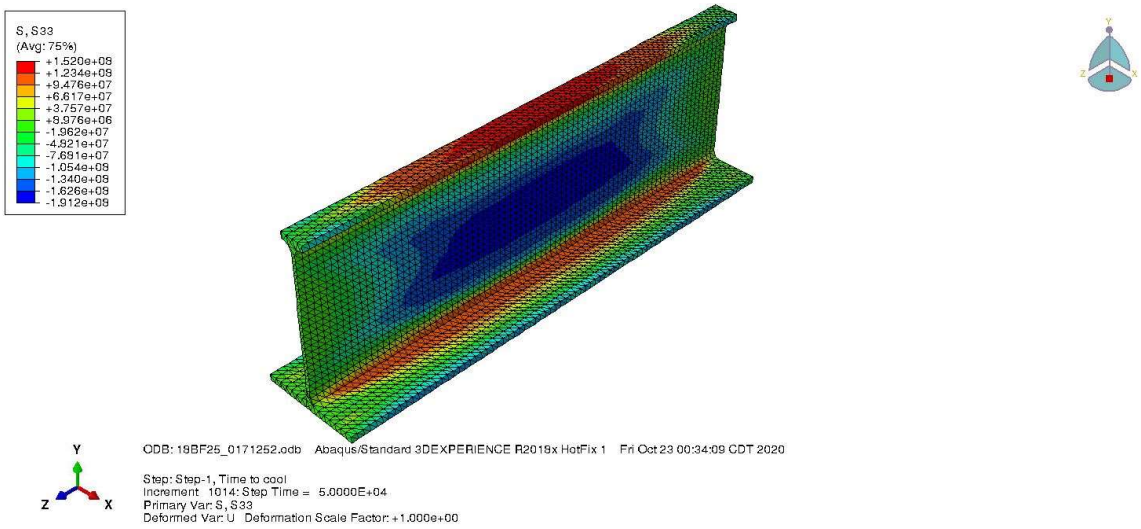

Figure 174: W18x76 0.25 b_f ABAQUS stress distribution (Pa)

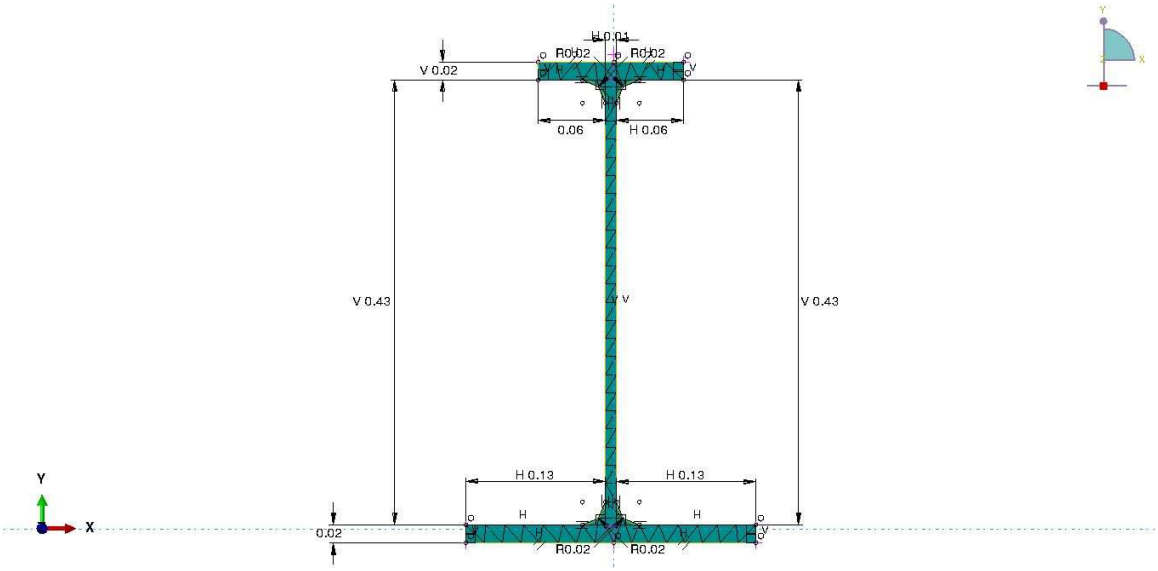

Figure 175: W18x76 0.50 b_f ABAQUS tetrahedral model meshing

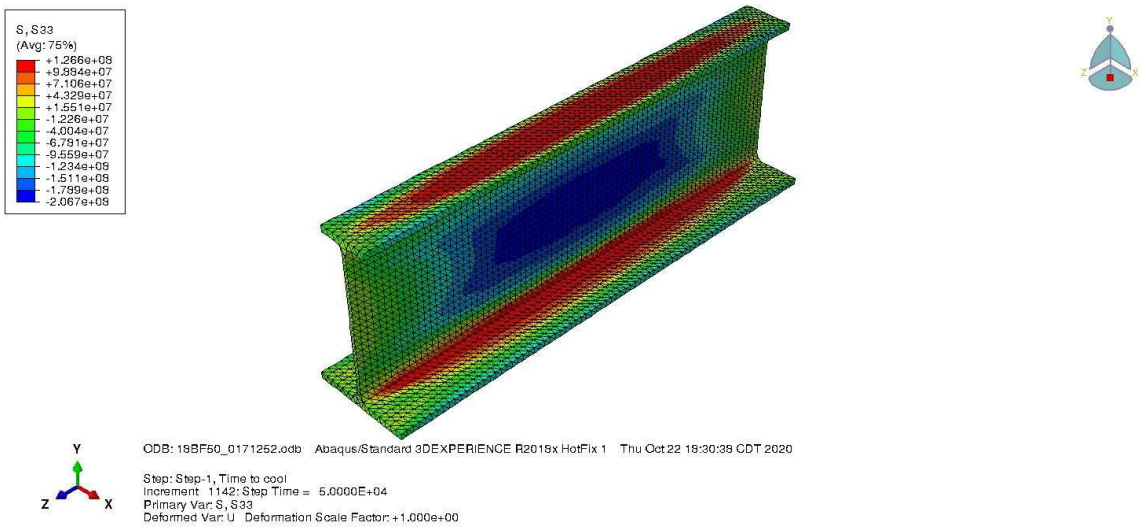

Figure 176: W18x76 0.50 b_f ABAQUS stress distribution (Pa)

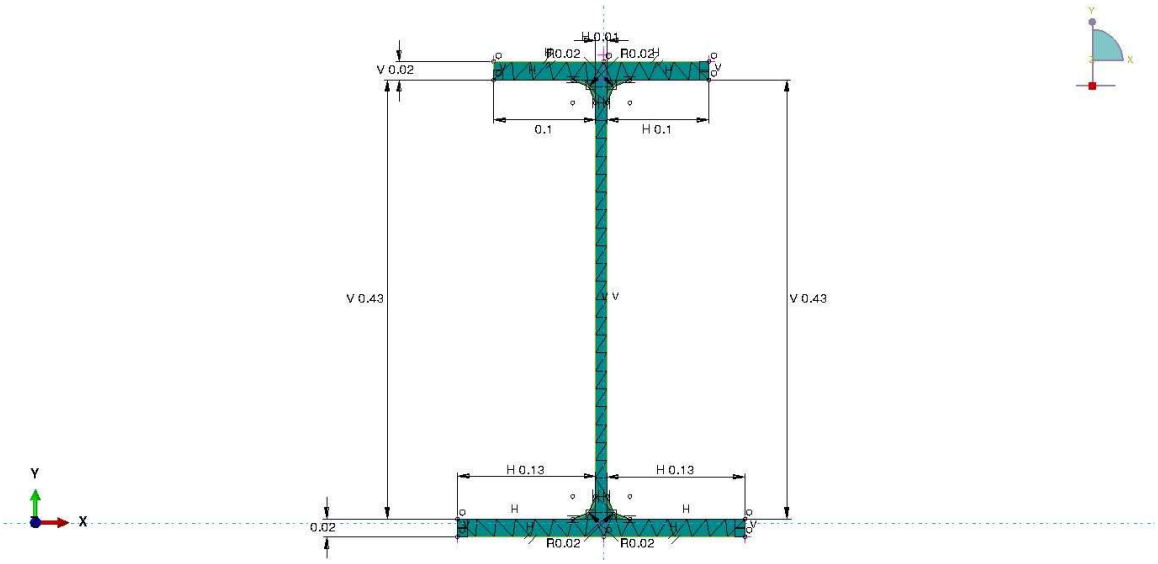

Figure 177: W18x76 0.75 b_f ABAQUS tetrahedral model meshing

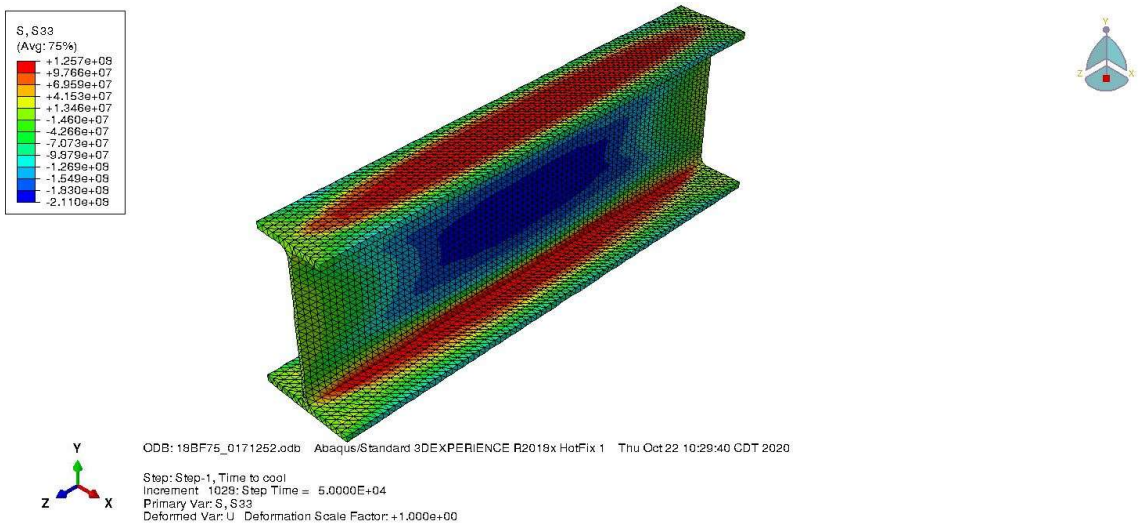

Figure 178: W18x76 0.75 b_f ABAQUS stress distribution (Pa)

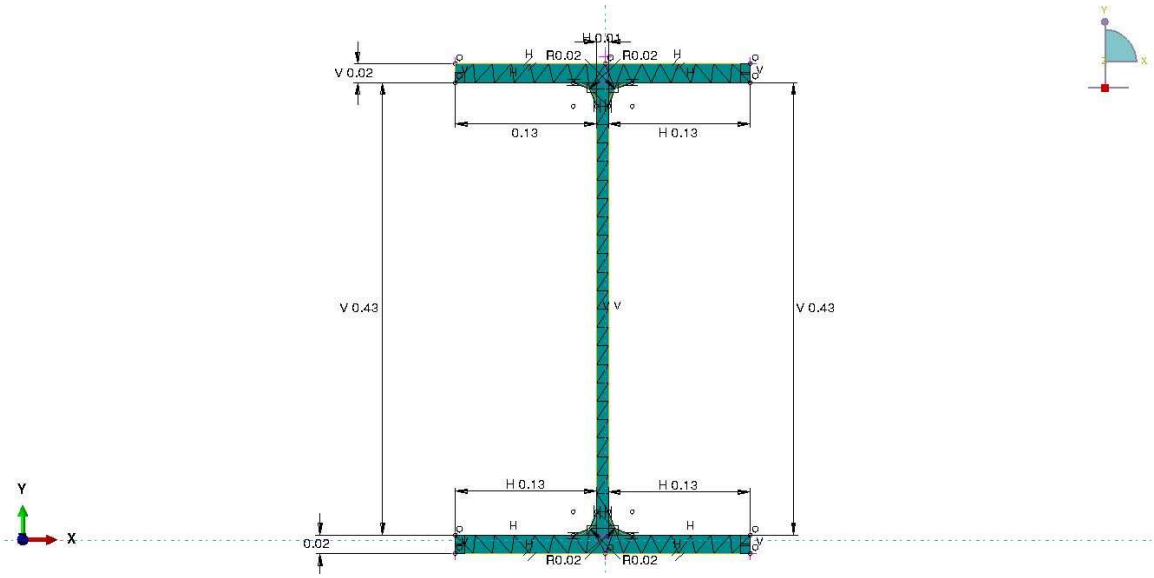

Figure 179: W18x76 1.00 b_f ABAQUS tetrahedral model meshing

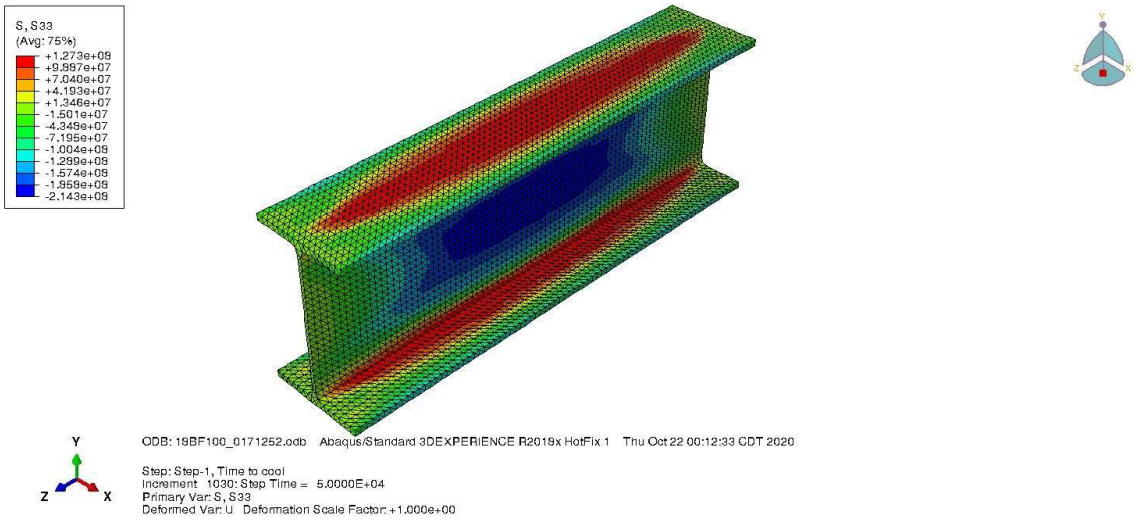

Figure 180: W18x76 1.00 b_f ABAQUS stress distribution (Pa)

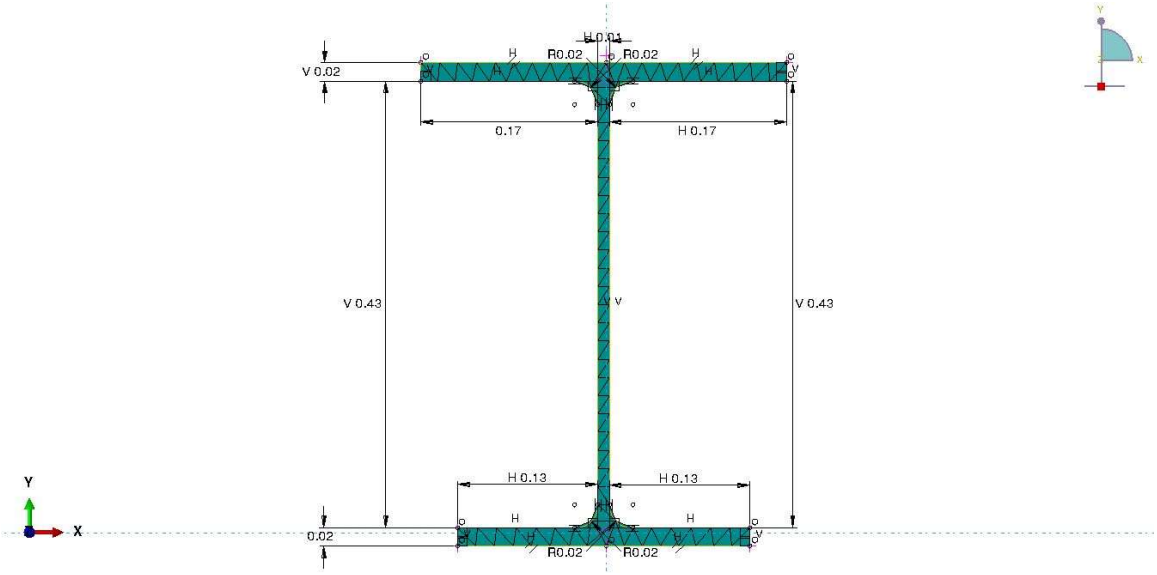

Figure 181: W18x76 1.25 b_f ABAQUS tetrahedral model meshing

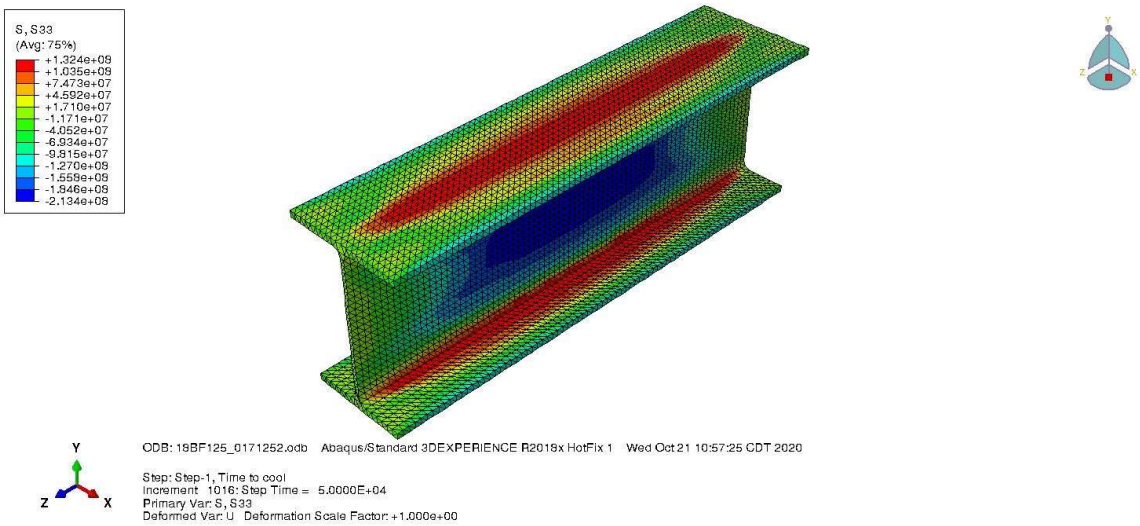

Figure 182: W18x76 1.25 b_f ABAQUS stress distribution (Pa)

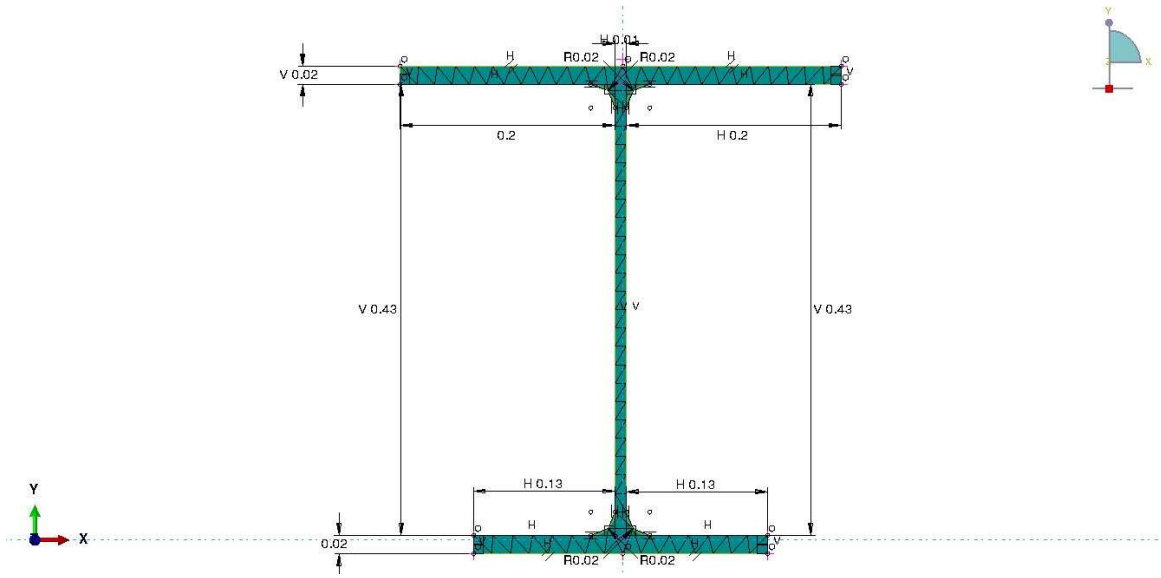

Figure 183: W18x76 1.50 b_f ABAQUS tetrahedral model meshing

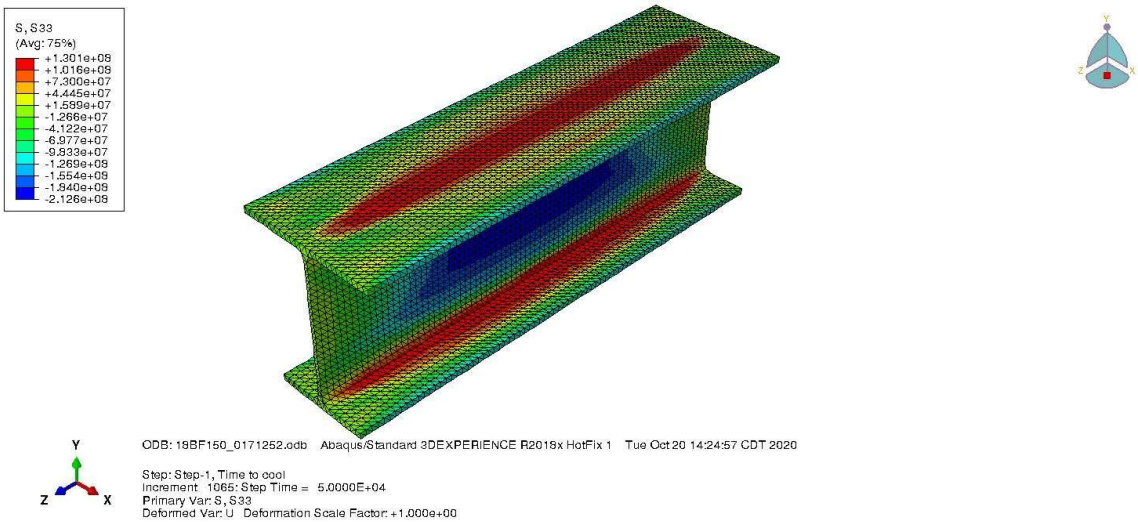

Figure 184: W18x76 1.50 b_f ABAQUS stress distribution (Pa)

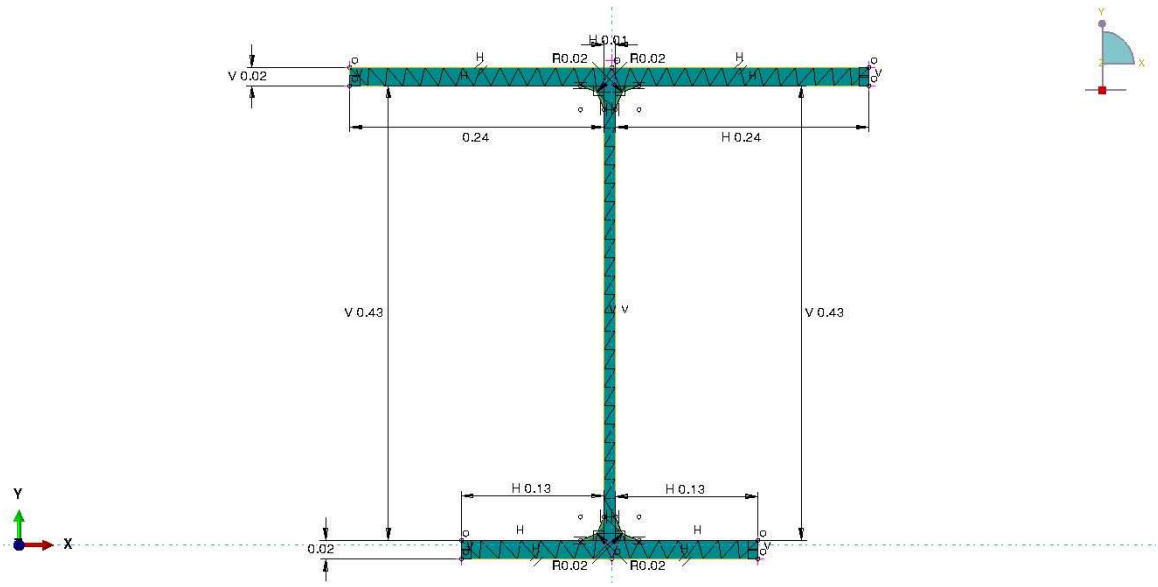

Figure 185: W18x76 1.75 b_f ABAQUS tetrahedral model meshing

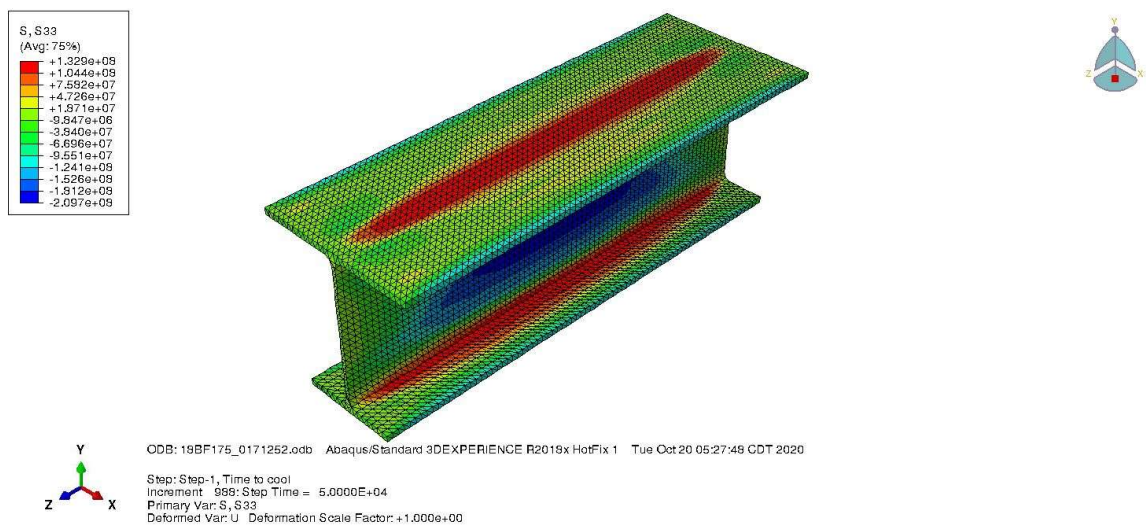

Figure 186: W18x76 1.75 b_f ABAQUS stress distribution (Pa)

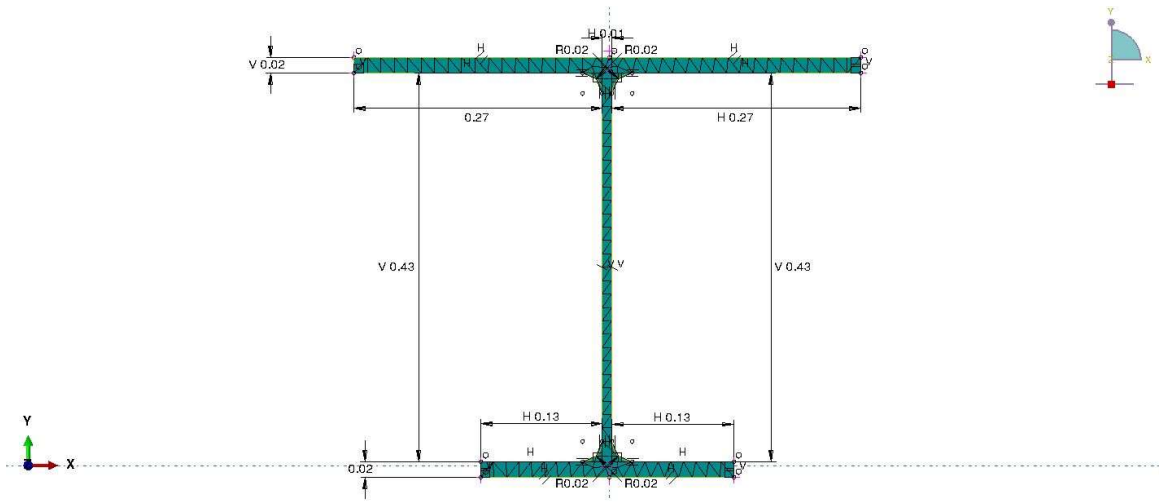

Figure 187: W18x76 2.00 b_f ABAQUS tetrahedral model meshing

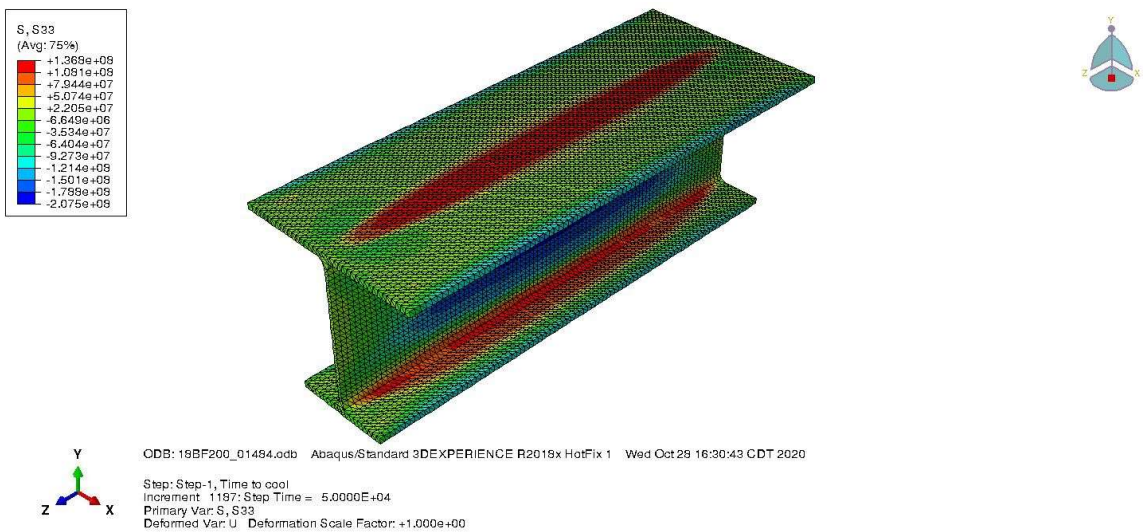

Figure 188: W18x76 2.00 b_f ABAQUS stress distribution (Pa)

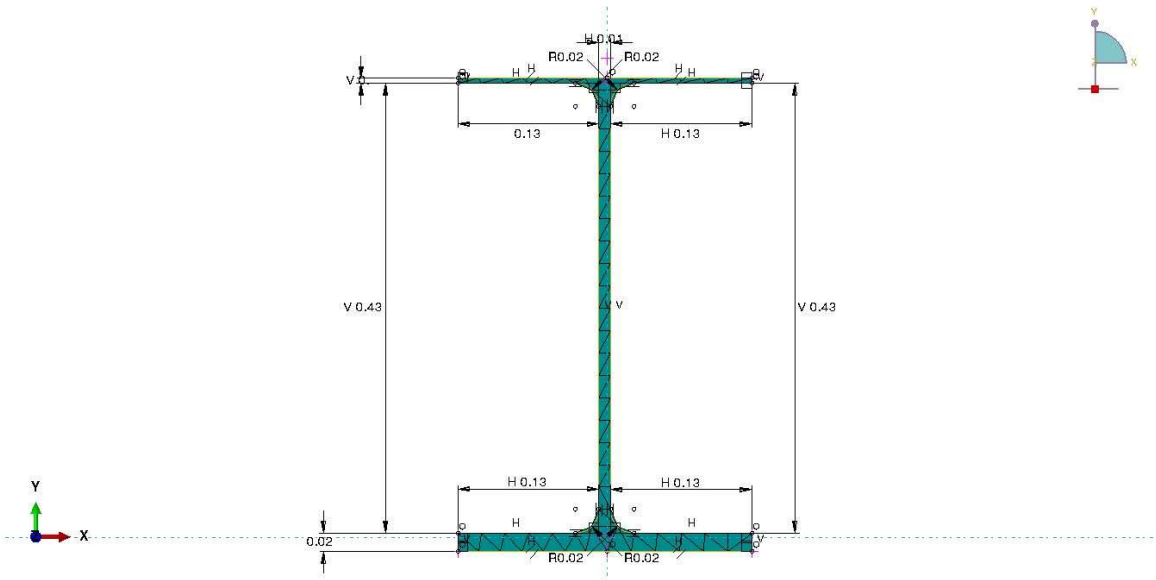

Figure 189: W18x76 0.25 t_f ABAQUS tetrahedral model meshing

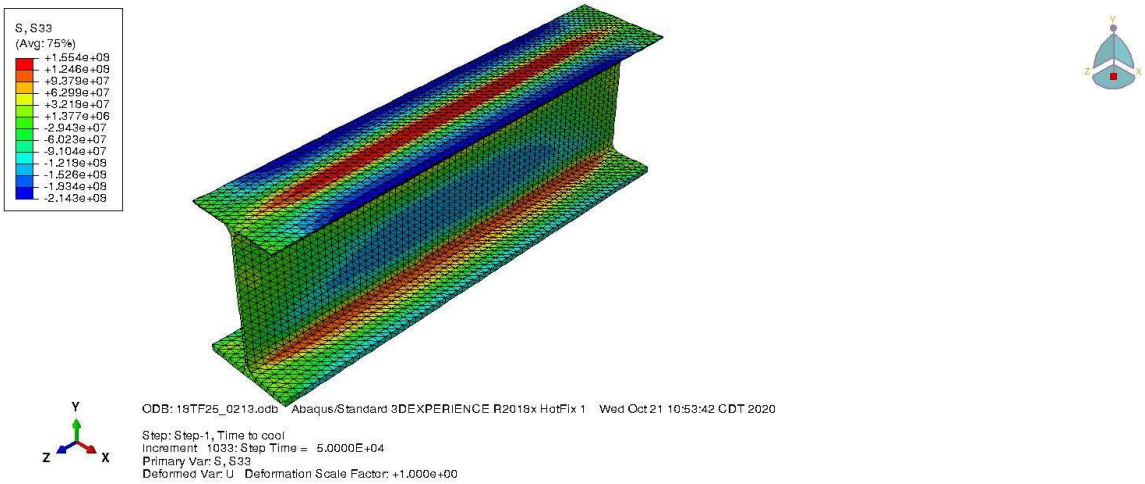

Figure 190: W18x76 0.25 t_f ABAQUS stress distribution (Pa)

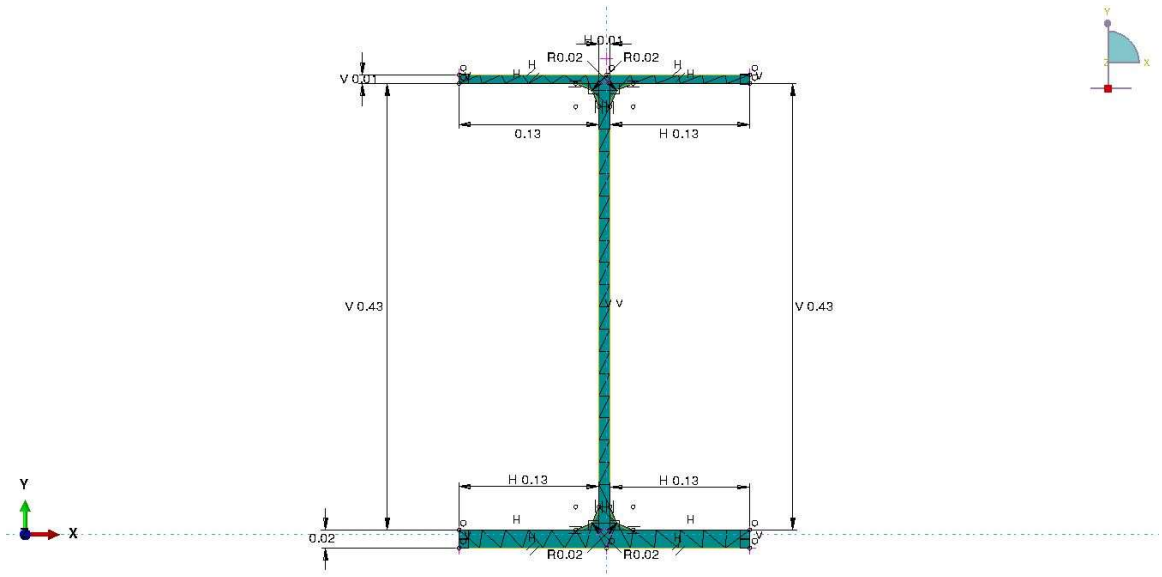

Figure 191: W18x76 0.50 t_f ABAQUS tetrahedral model meshing

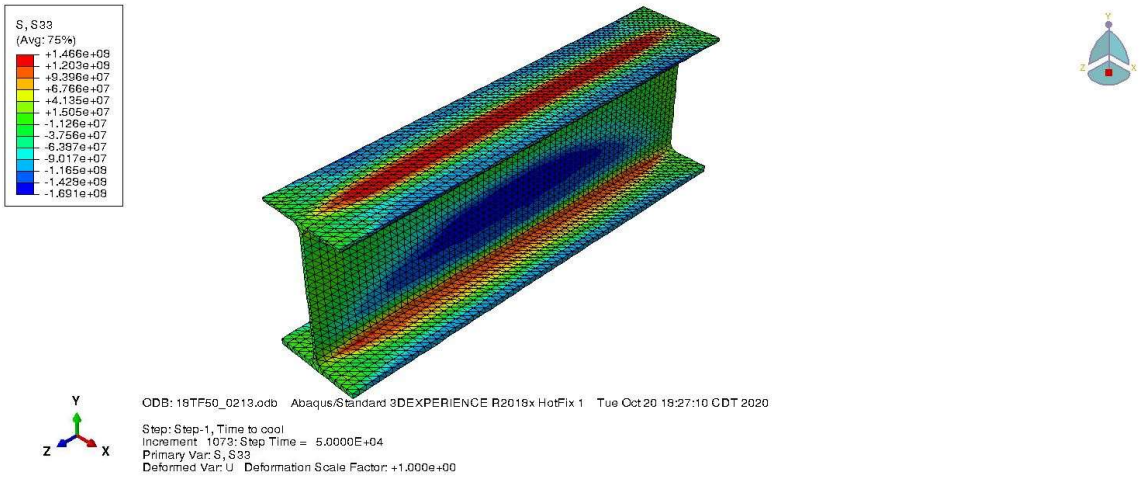

Figure 192: W18x76 0.50 t_f ABAQUS stress distribution (Pa)

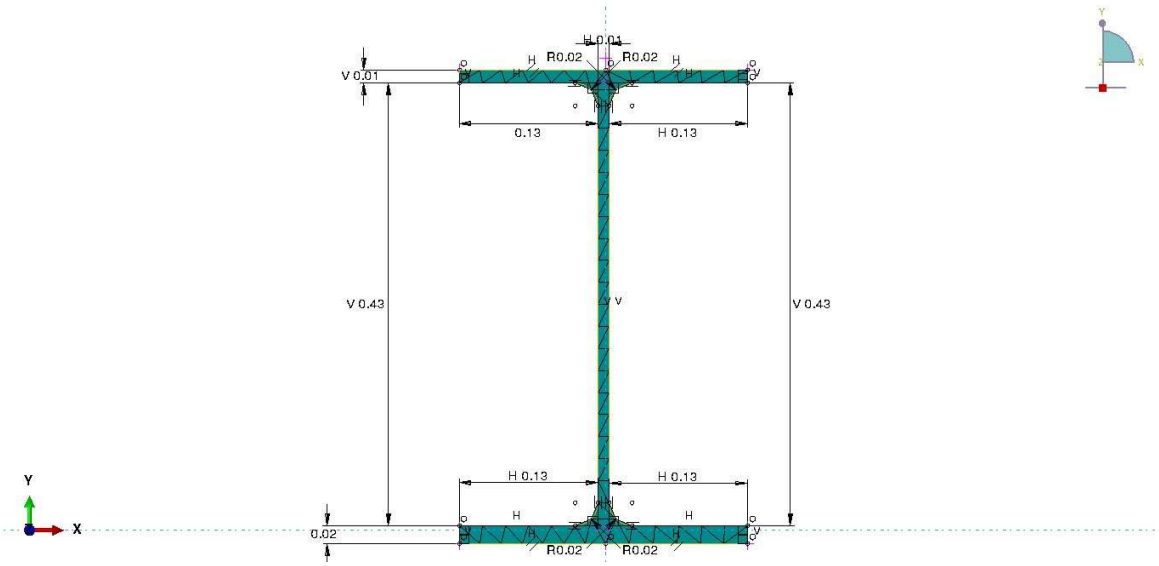

Figure 193: W18x76 0.75 t_f ABAQUS tetrahedral model meshing

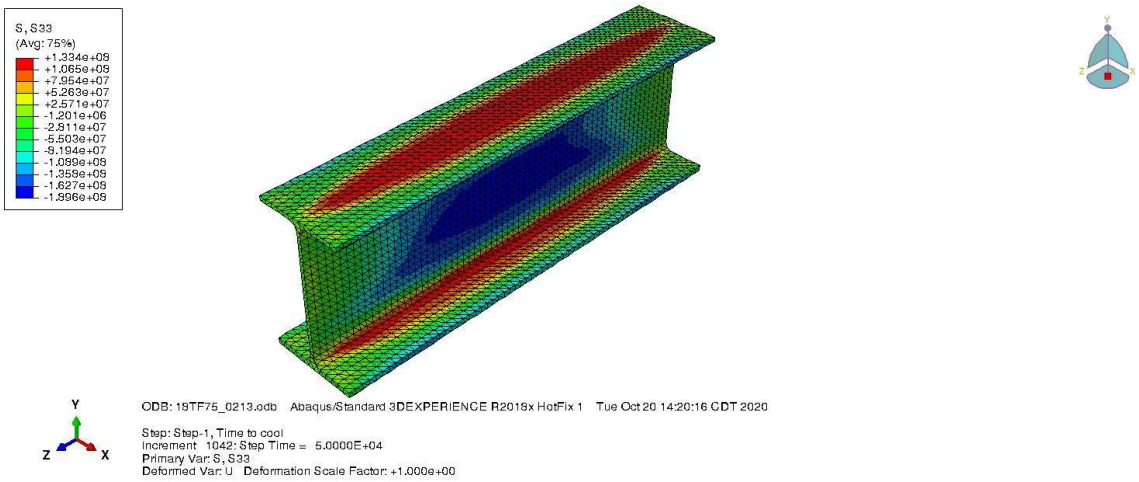

Figure 194: W18x76 0.75 t_f ABAQUS stress distribution (Pa)

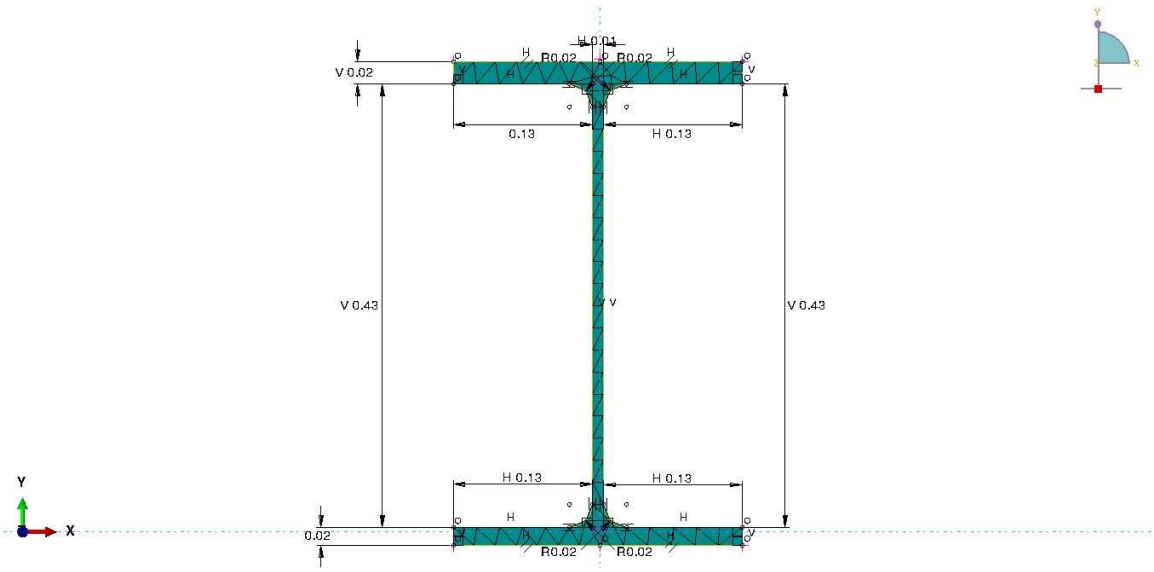

Figure 195: W18x76 1.25 t_f ABAQUS tetrahedral model meshing

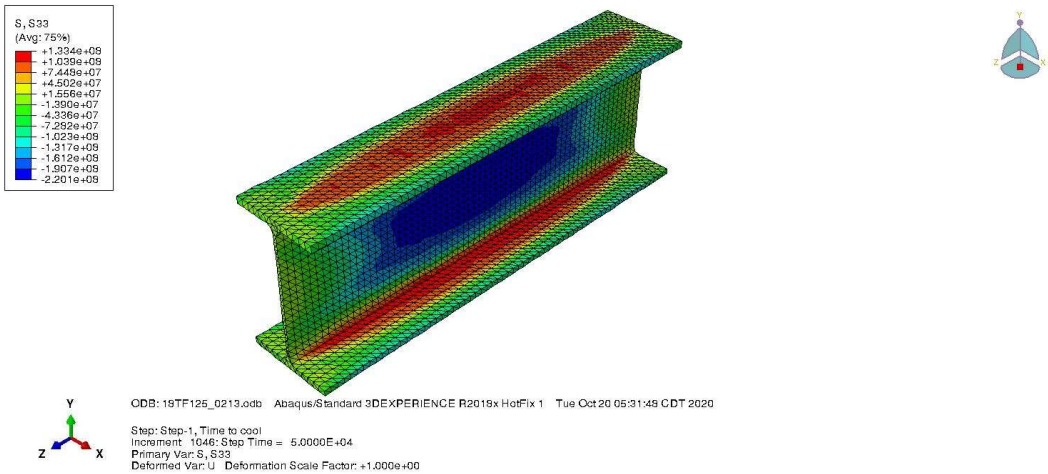

Figure 196: W18x76 1.25 t_f ABAQUS stress distribution (Pa)

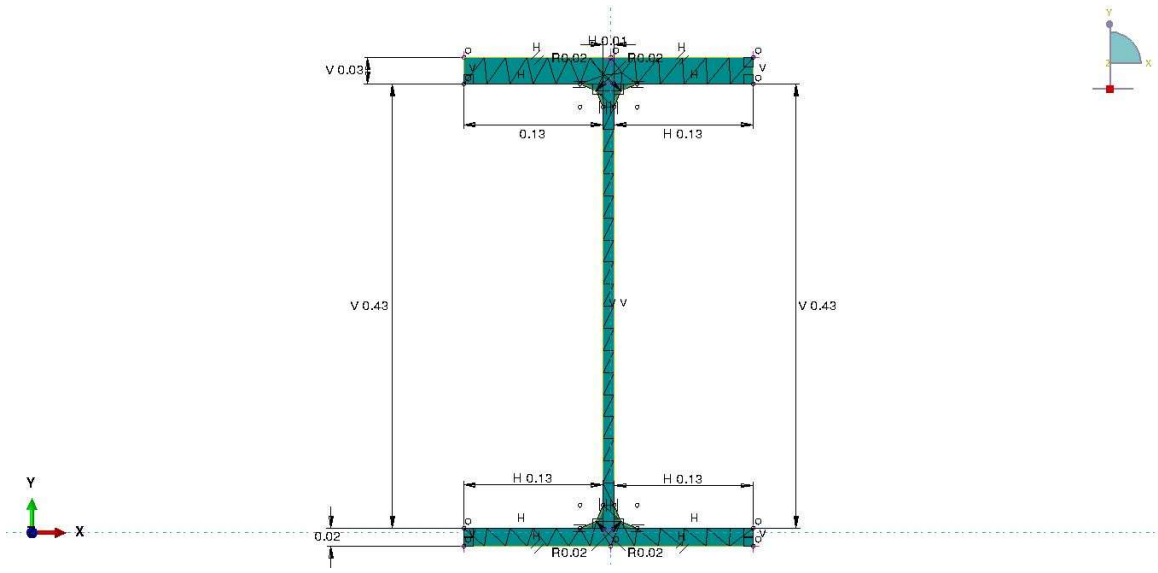

Figure 197: W18x76 1.50 t_f ABAQUS tetrahedral model meshing

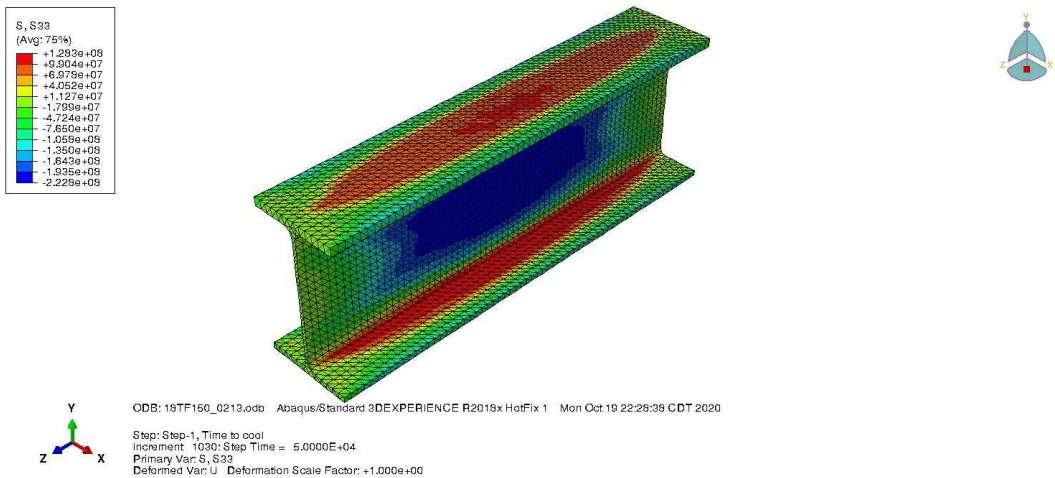

Figure 198: W18x76 1.50 t_f ABAQUS stress distribution (Pa)

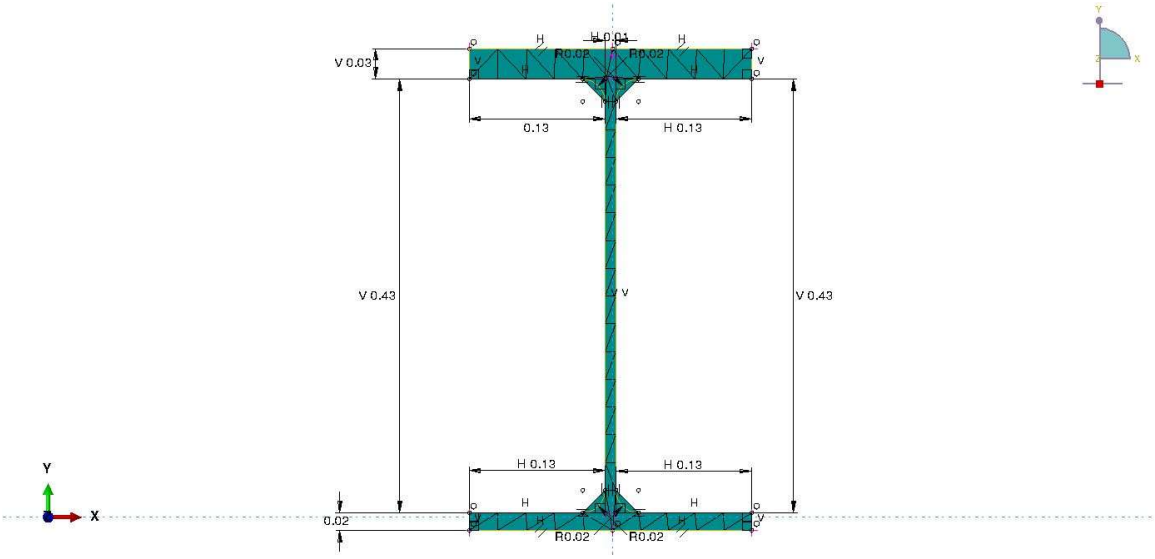

Figure 199: W18x76 1.75 t_f ABAQUS tetrahedral model meshing

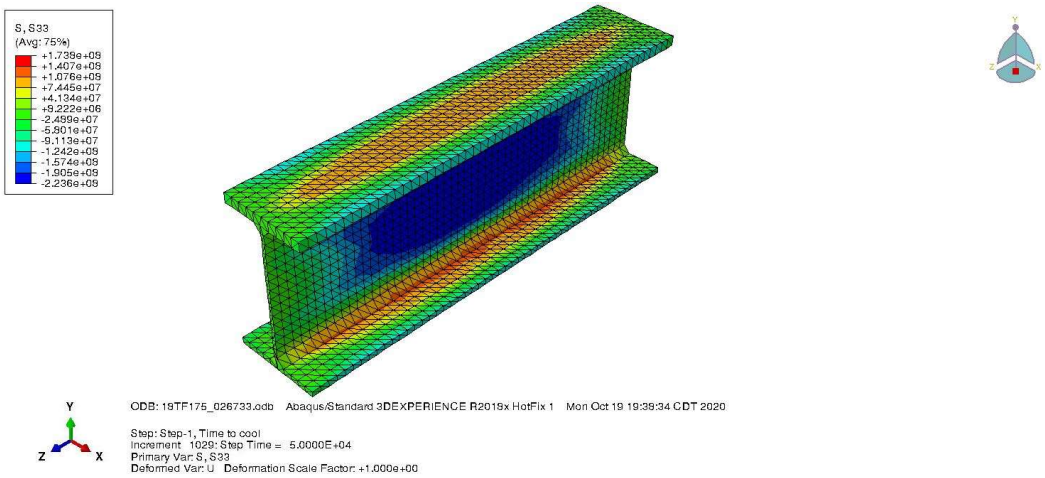

Figure 200: W18x76 1.75 t_f ABAQUS stress distribution (Pa)

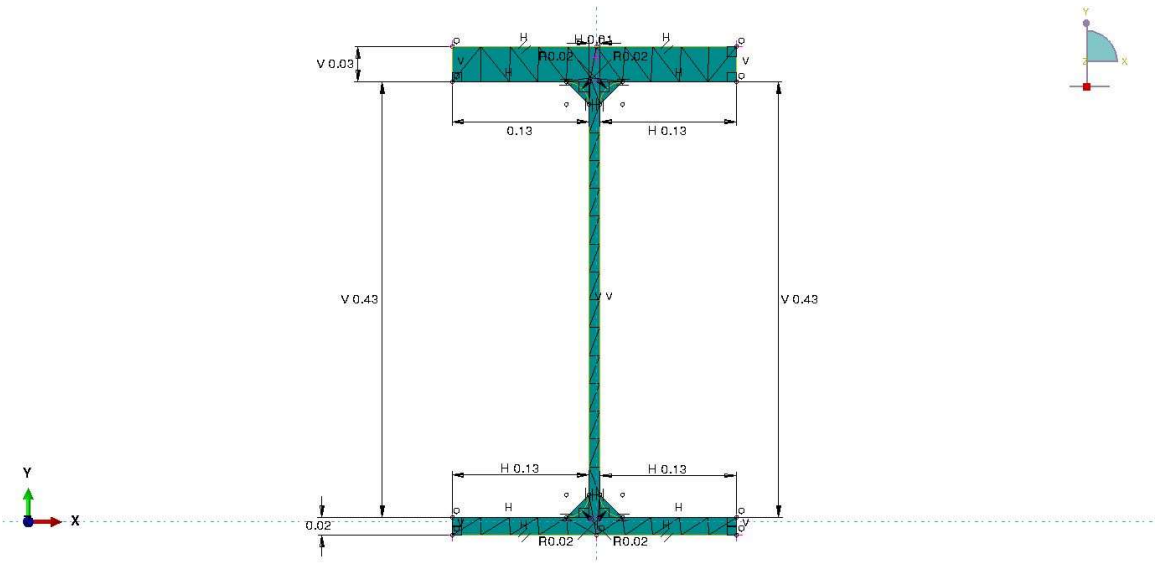

Figure 201: W18x76 2.00 t_f ABAQUS tetrahedral model meshing

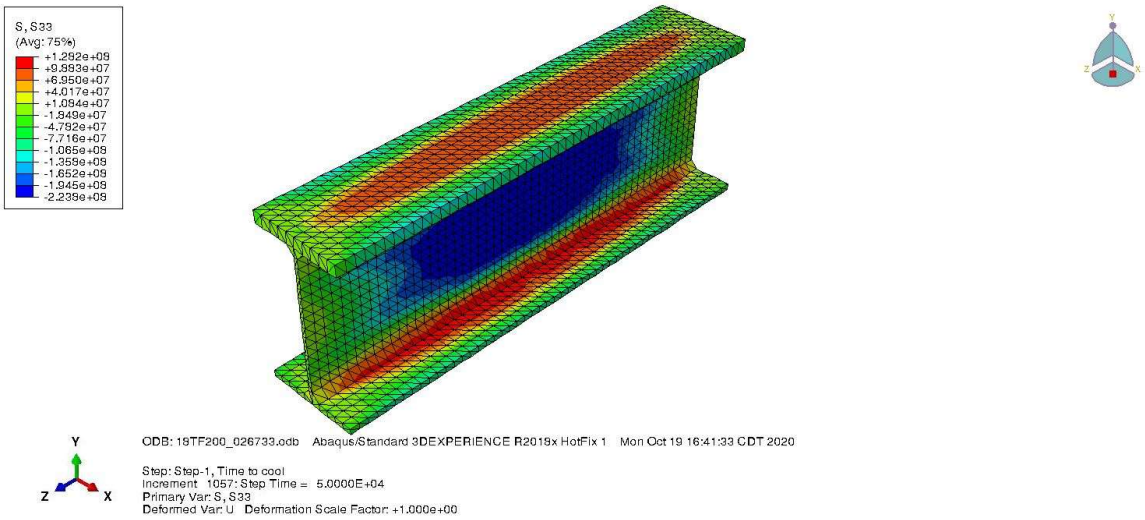

Figure 202: W18x76 2.00 t_f ABAQUS stress distribution (Pa)

APPENDIX B

ANALYTICAL STUDY PLOTS

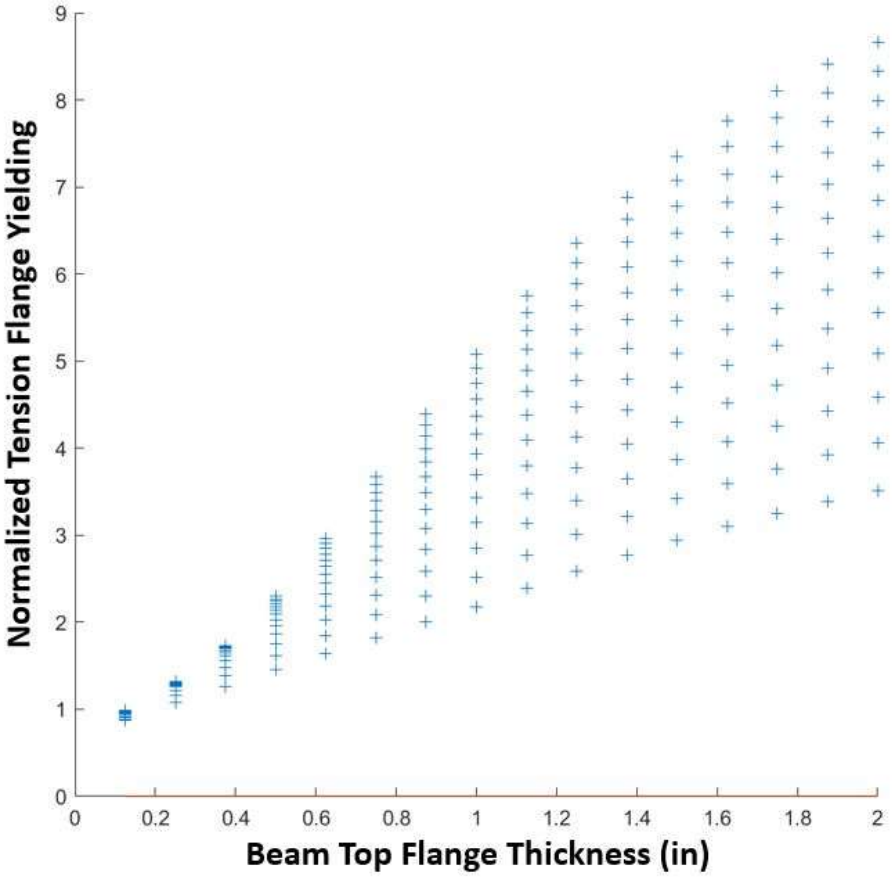

Figure 203: Scenario I: Normalized tension flange yielding vs top flange thickness (t_{ft})

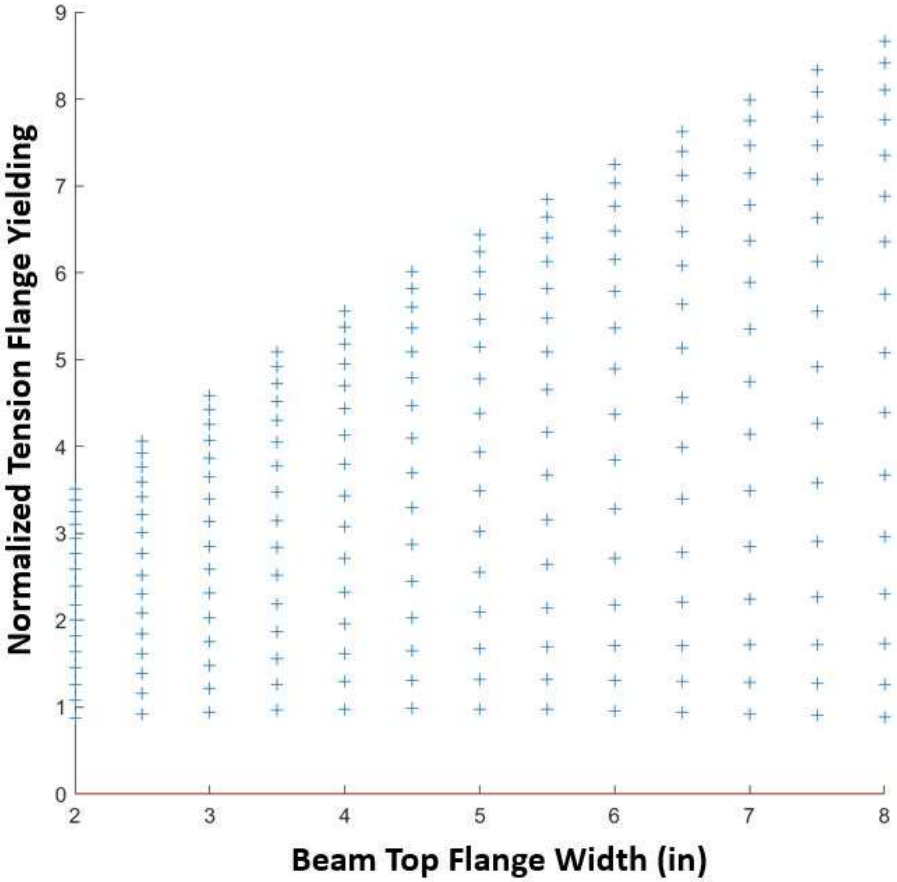

Figure 204: Scenario I: Normalized tension flange yielding vs top flange width (b_{ft})

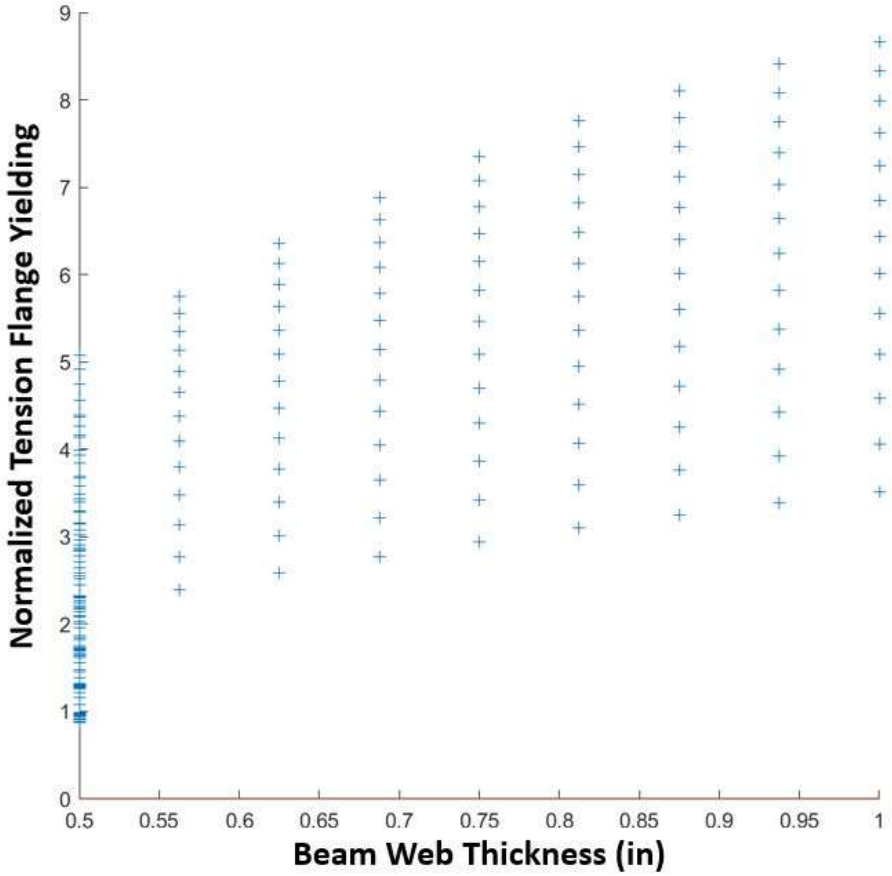

Figure 205: Scenario I: Normalized tension flange yielding vs web thickness (t_w)

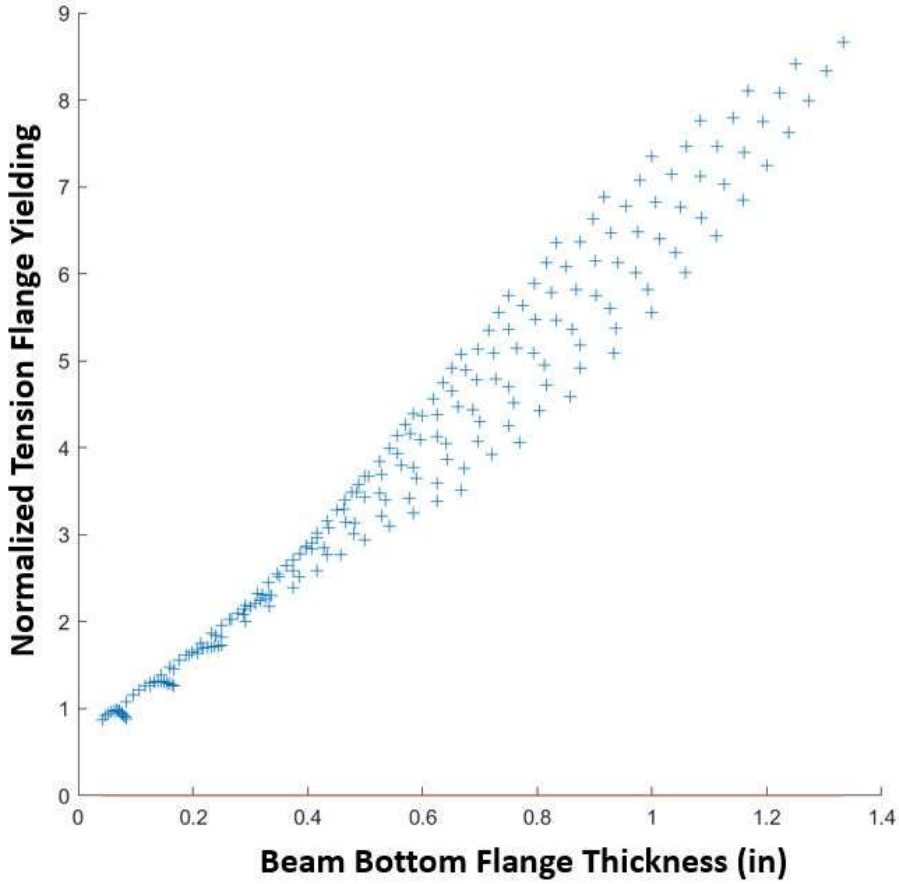

Figure 206: Scenario I: Normalized tension flange yielding vs bottom flange thickness (t_{fb})

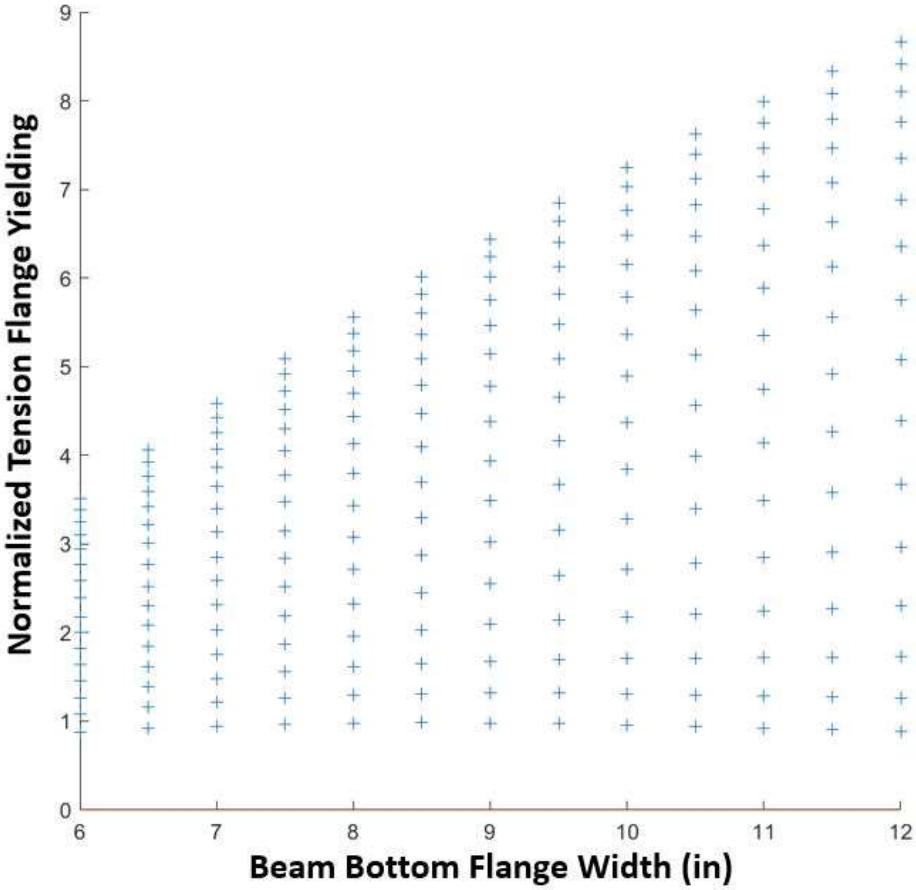

Figure 207: Scenario I: Normalized tension flange yielding vs bottom flange width (b_{fb})

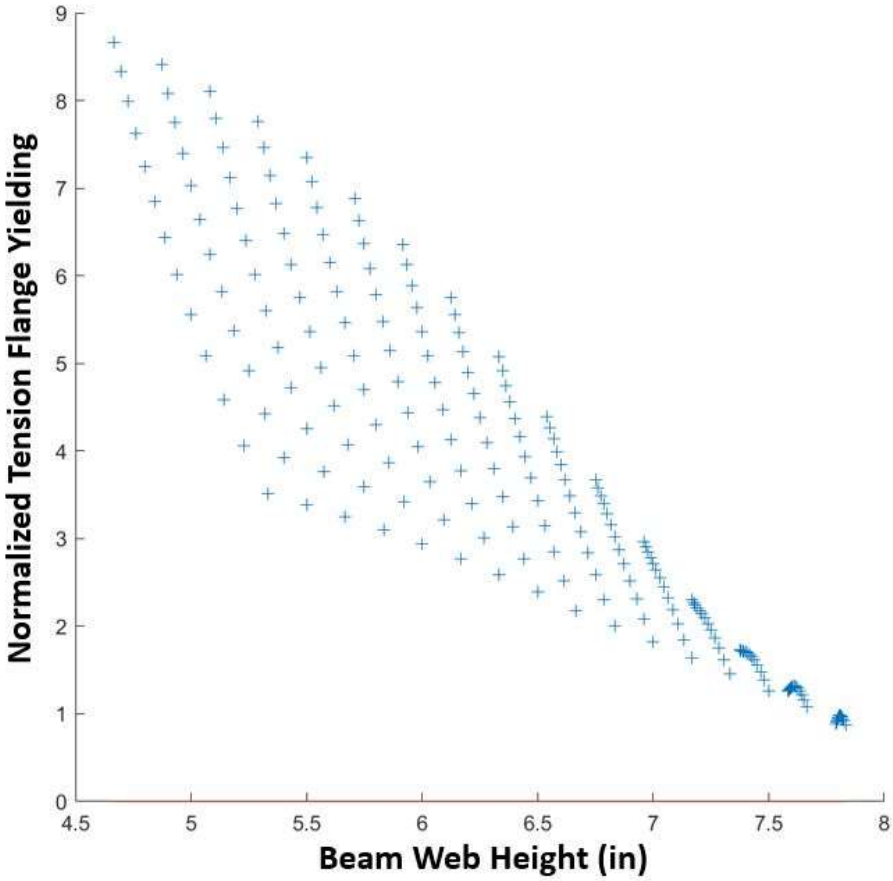

Figure 208: Scenario I: Normalized tension flange yielding vs web height

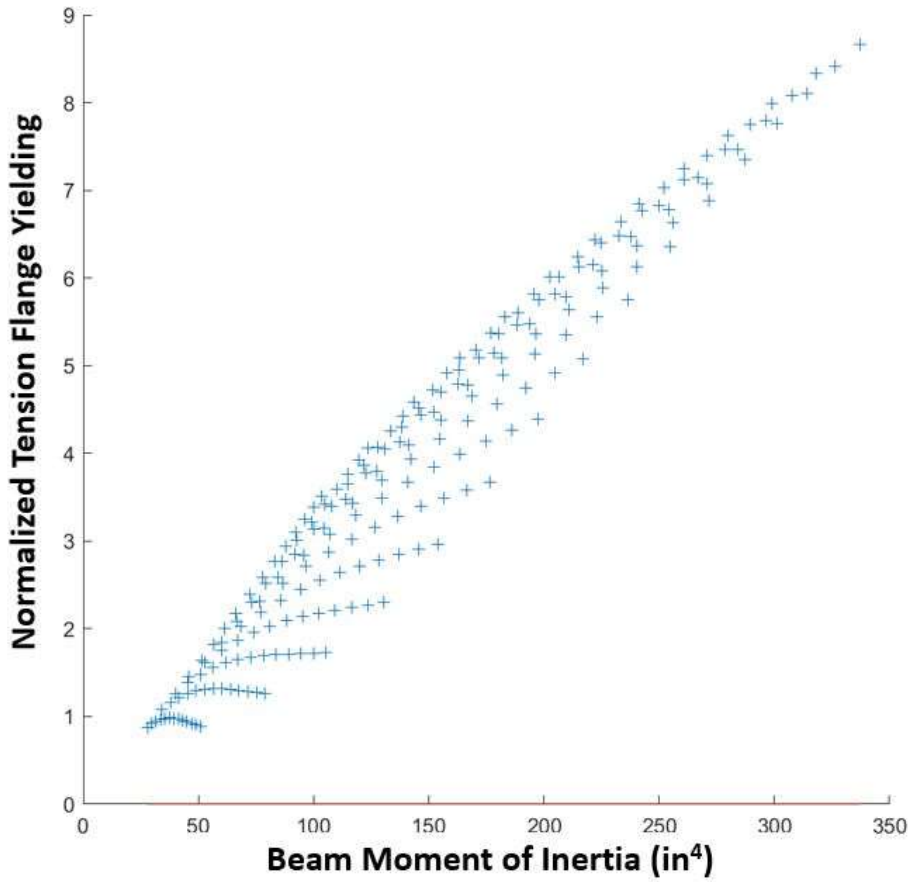

Figure 209: Scenario I: Normalized tension flange yielding vs moment of inertia (I_x)

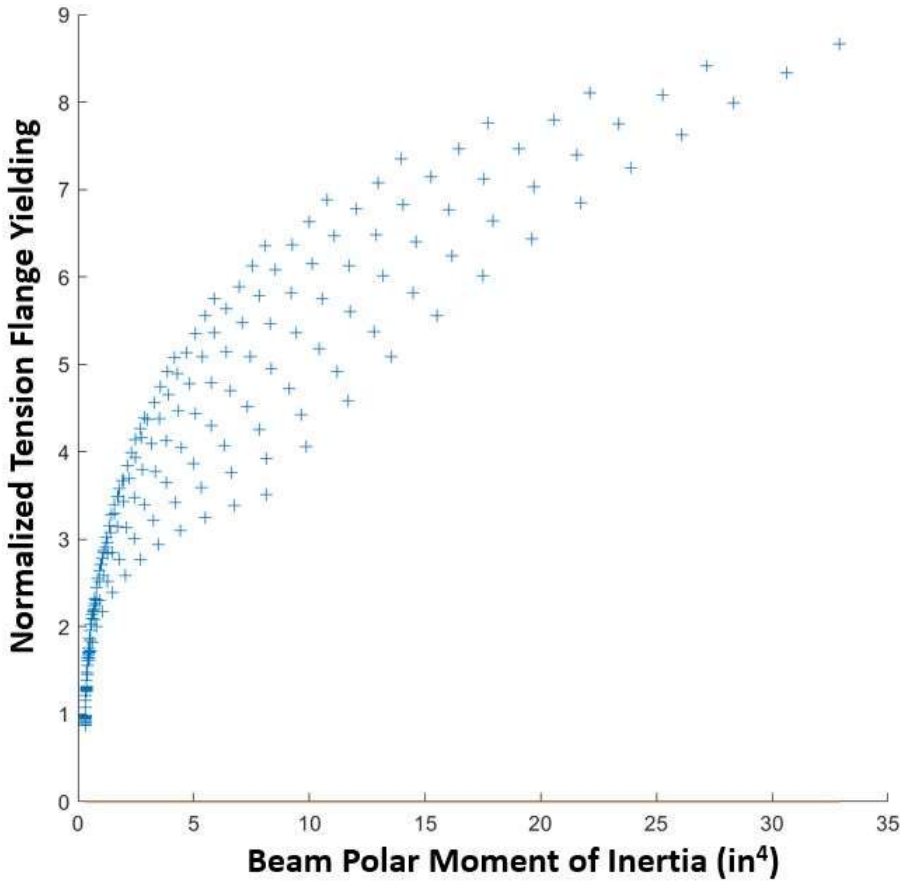

Figure 210: Scenario I: Normalized Tension flange yielding vs polar moment of inertia (*J*)

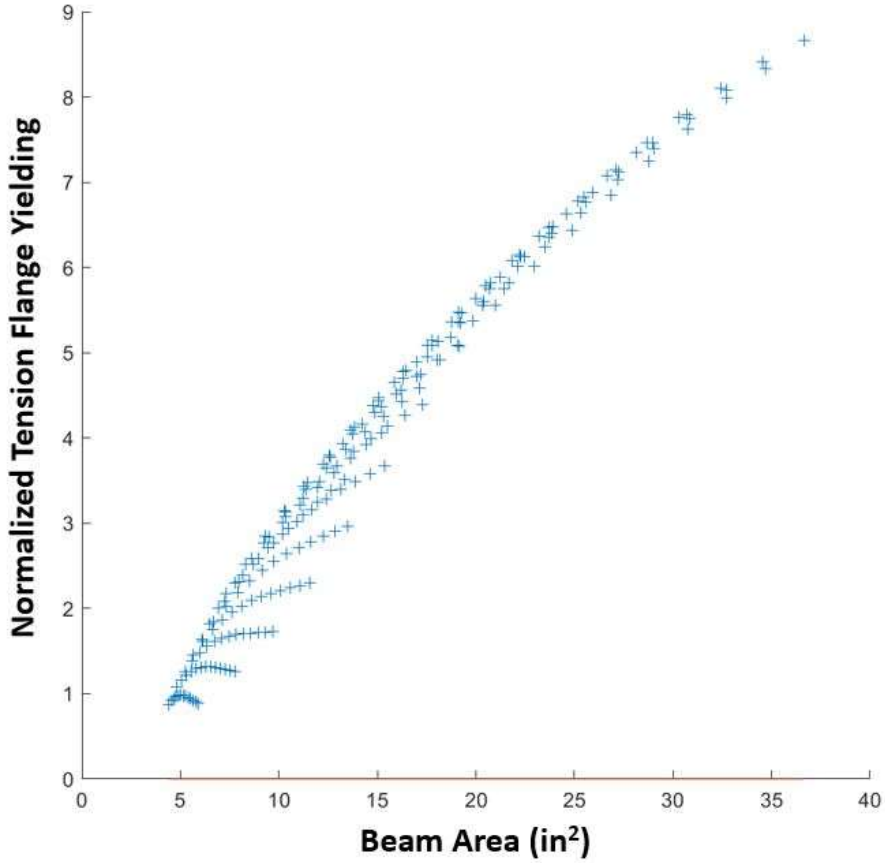

Figure 211: Scenario I: Normalized tension flange yielding vs cross-sectional area

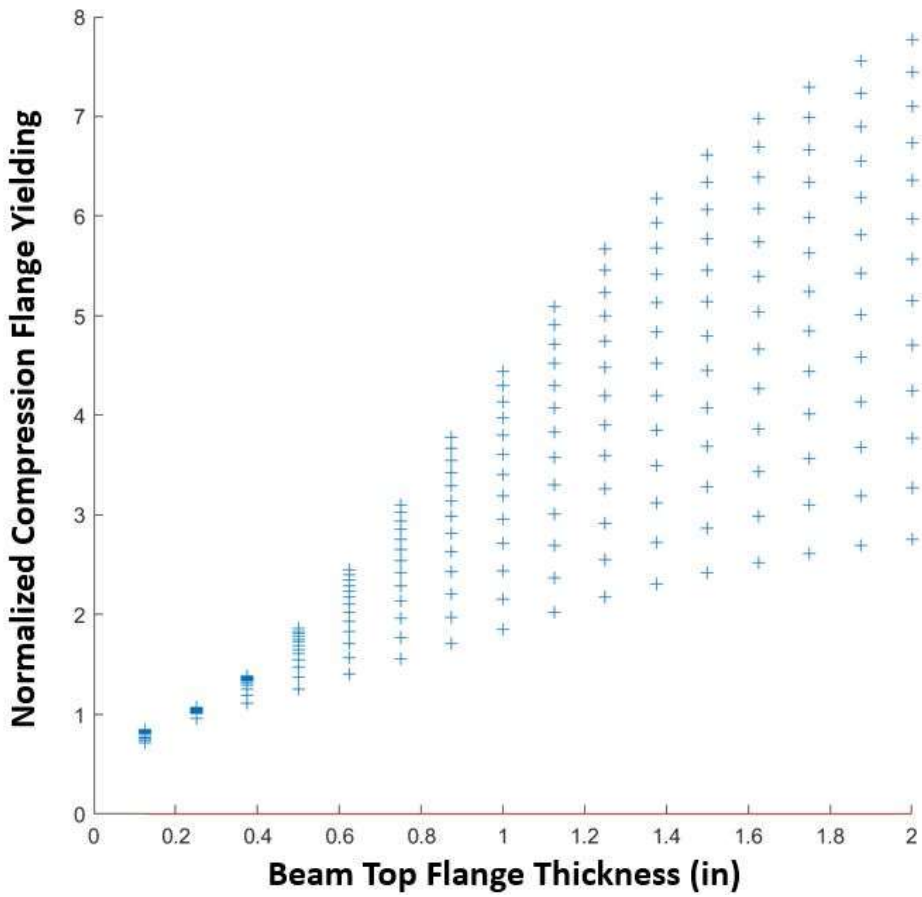

Figure 212: Scenario I: Normalized compression flange yielding vs top flange thickness (t_{ft})

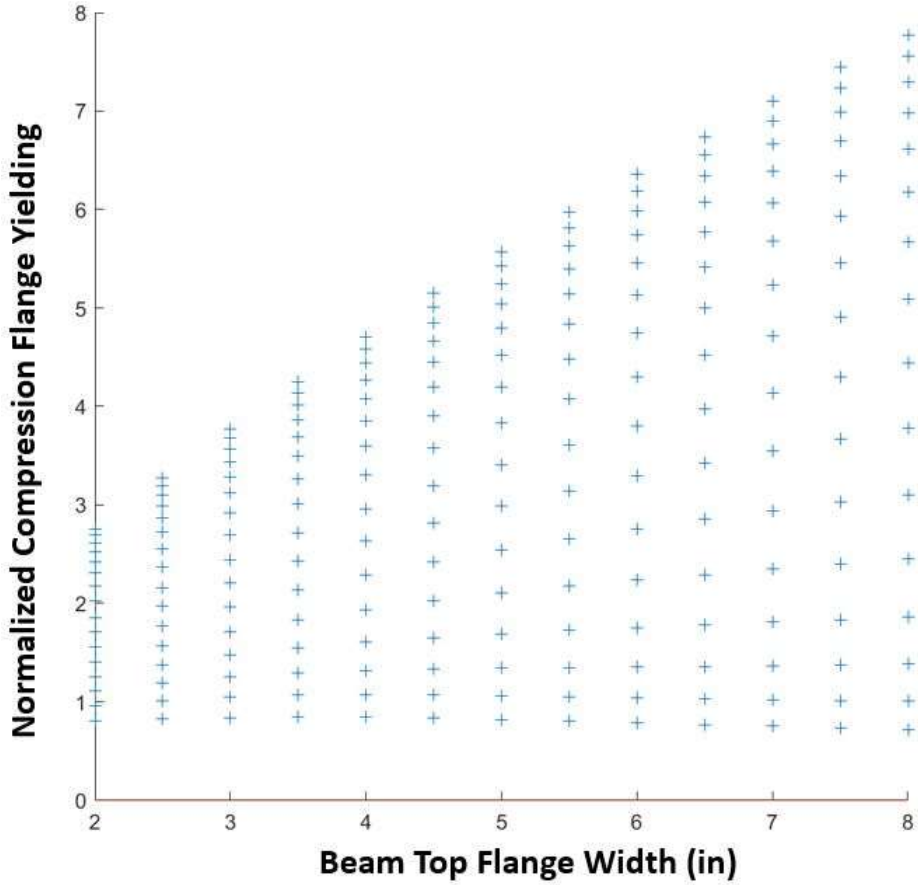

Figure 213: Scenario I: Normalized compression flange yielding vs top flange width (b_{ft})

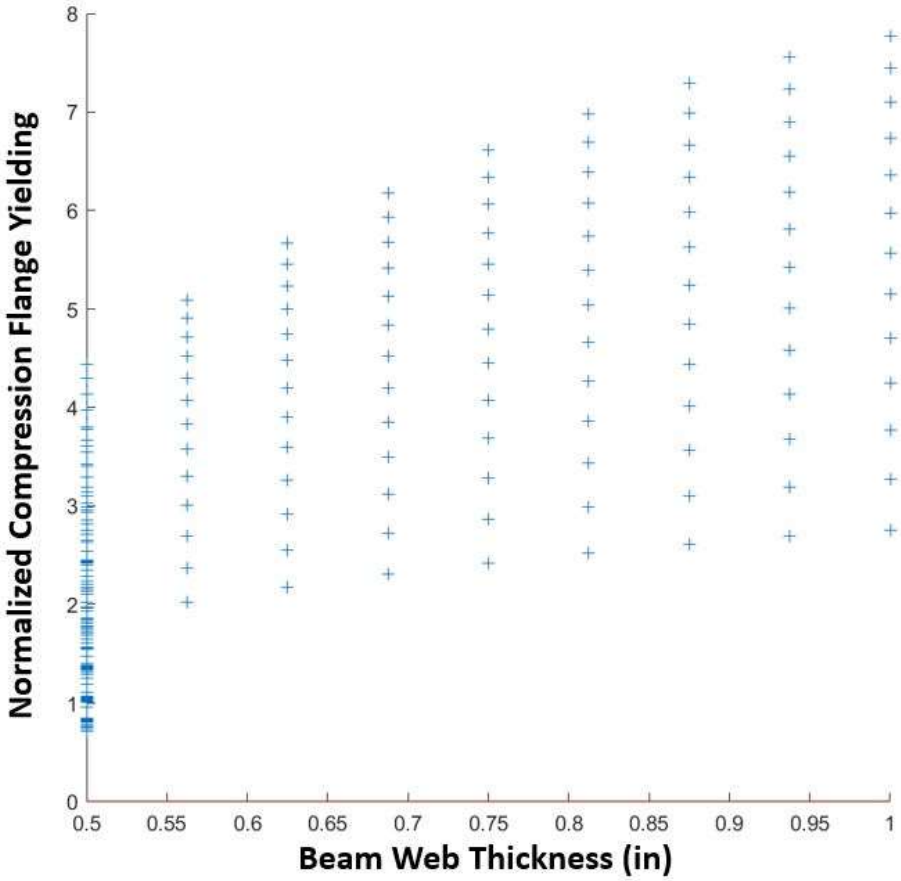

Figure 214: Scenario I: Normalized compression flange yielding vs web thickness (t_w)

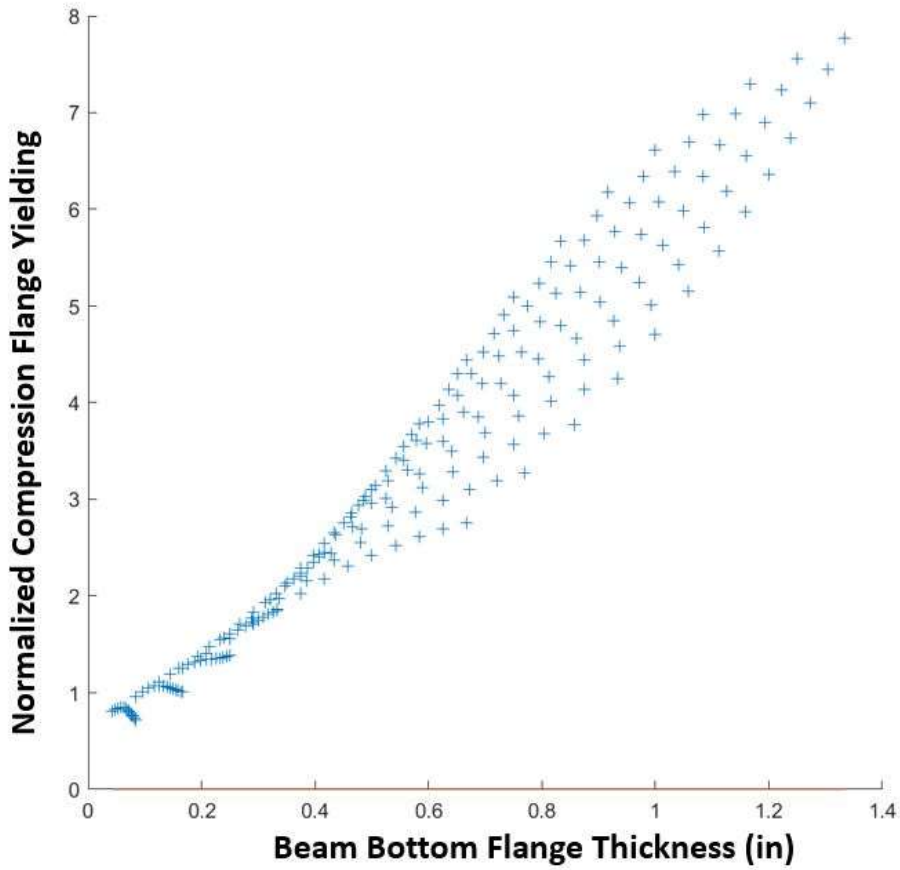

Figure 215: Scenario I: Normalized compression flange yielding vs bottom flange thickness (t_{fb})

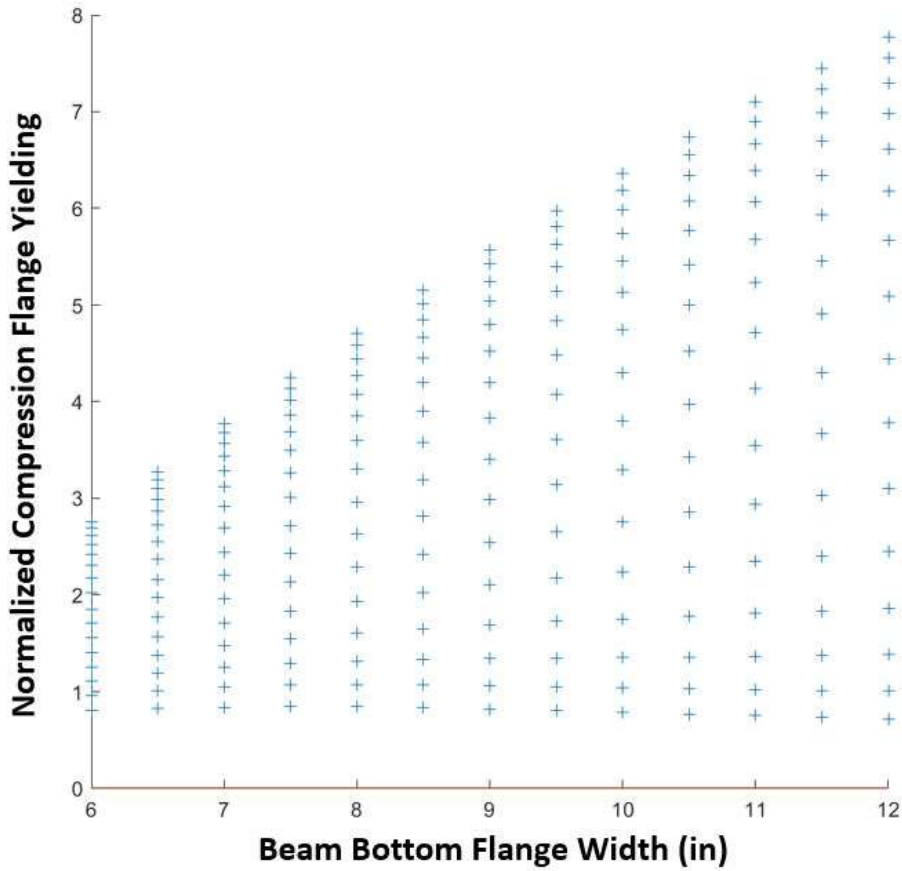

Figure 216: Scenario I: Normalized compression flange yielding vs bottom flange width (b_{fb})

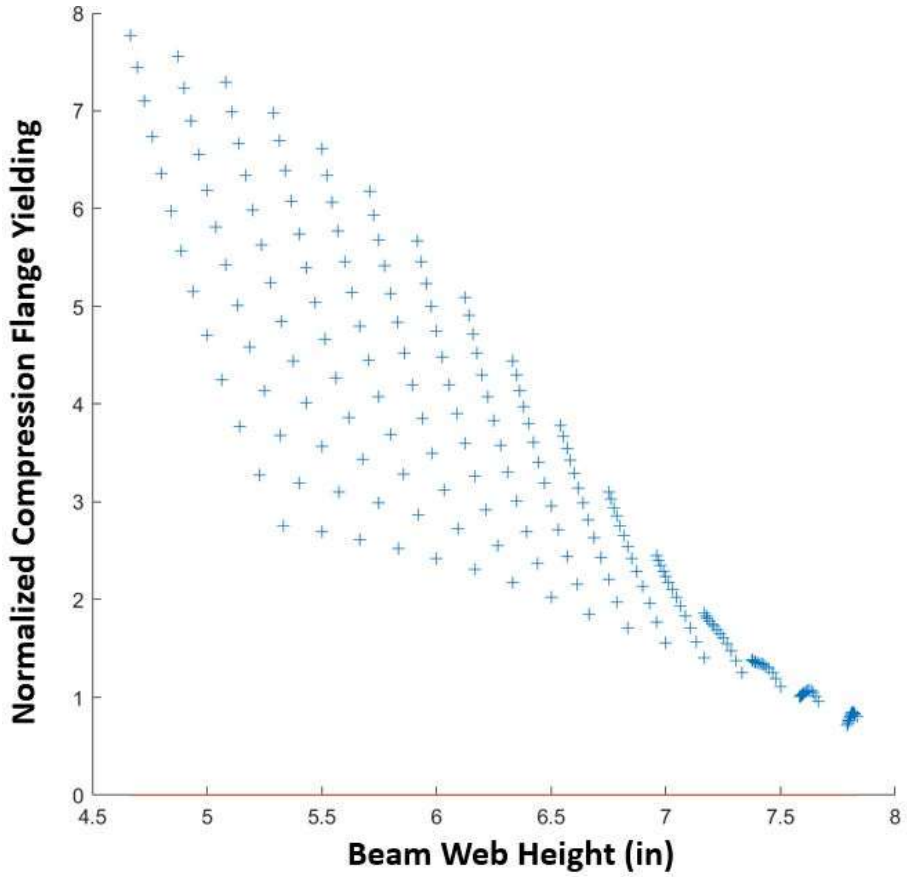

Figure 217: Scenario I: Normalized compression flange yielding vs web height

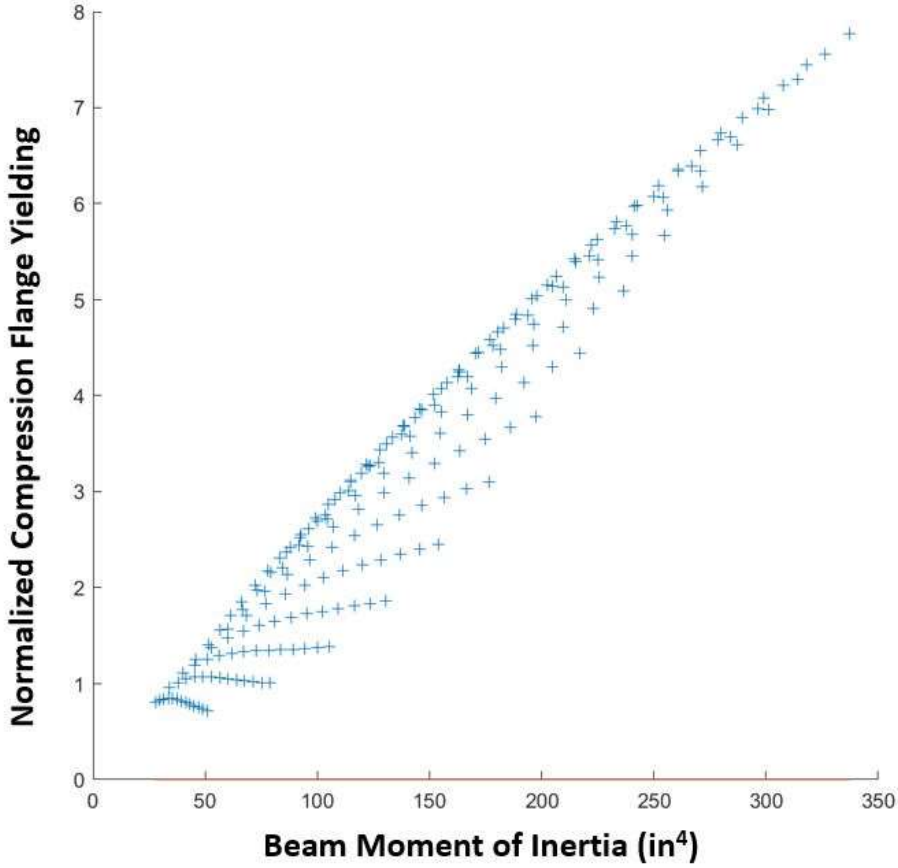

Figure 218: Scenario I: Normalized compression flange yielding vs moment of inertia (I_x)

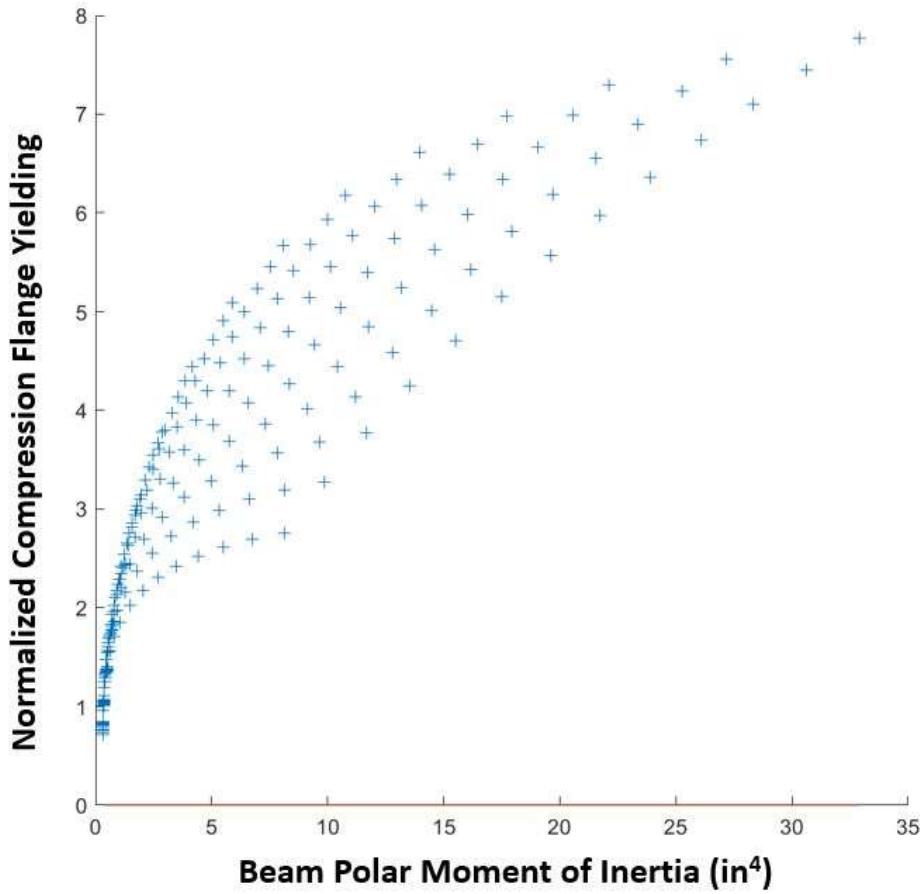

Figure 219: Scenario I: Normalized compression flange yielding vs polar moment of inertia (*J*)

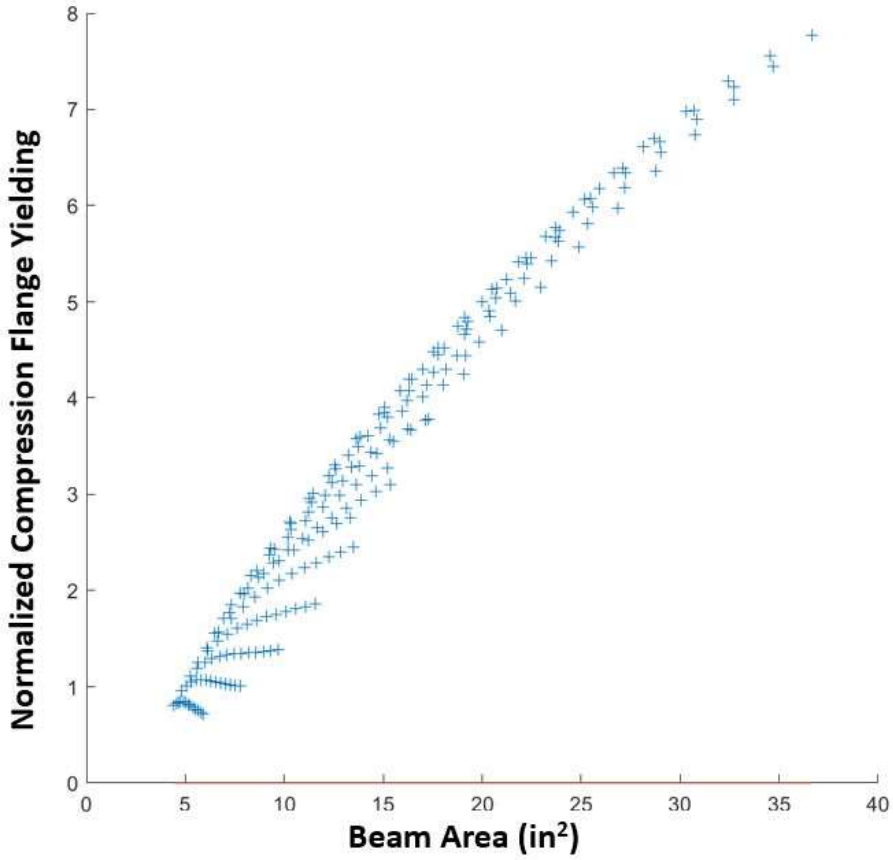

Figure 220: Scenario I: Normalized compression flange yielding vs cross-sectional area

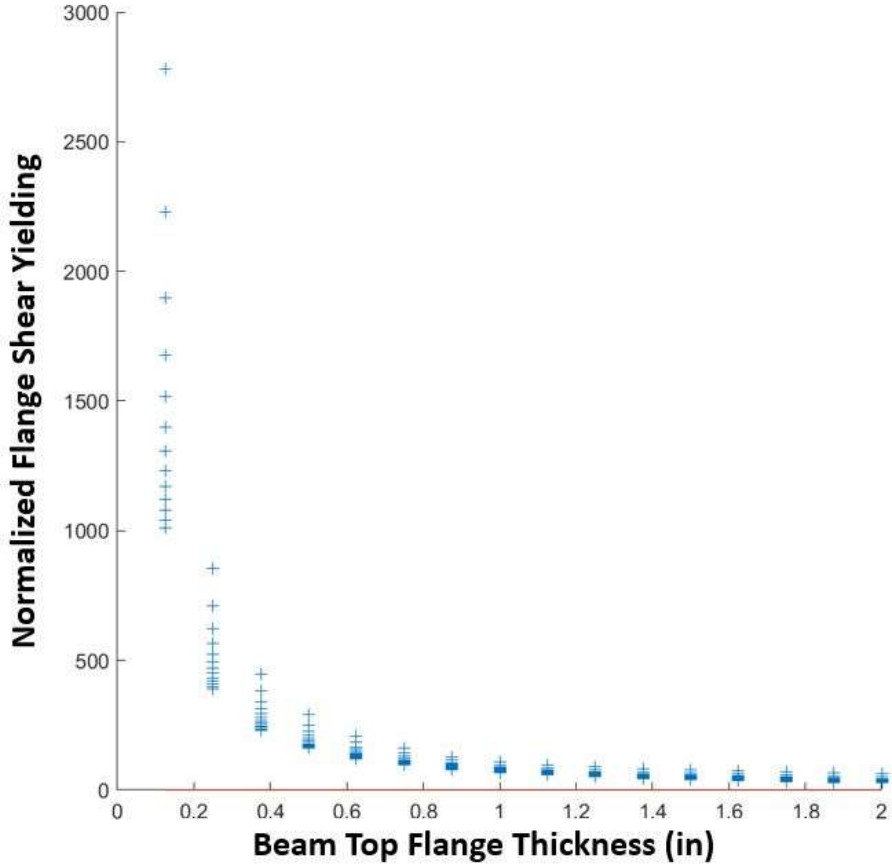

Figure 221: Scenario I: Normalized flange shear yielding vs top flange thickness (t_{ft})

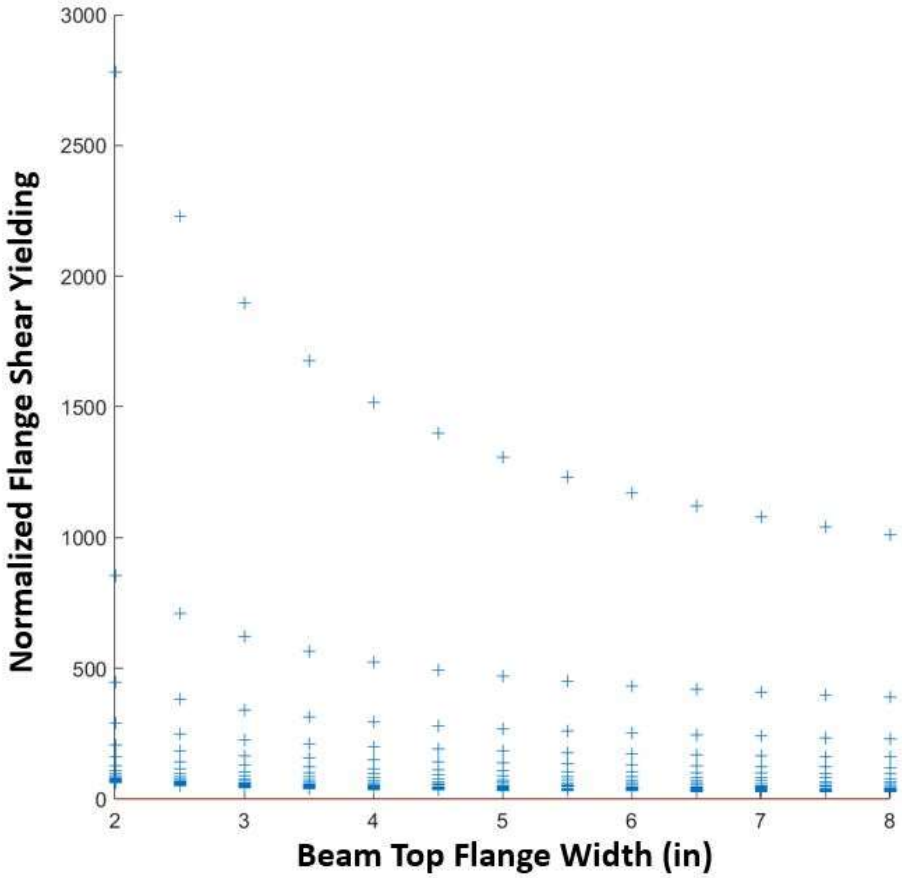

Figure 222: Scenario I: Normalized flange shear yielding vs top flange width (b_{ft})

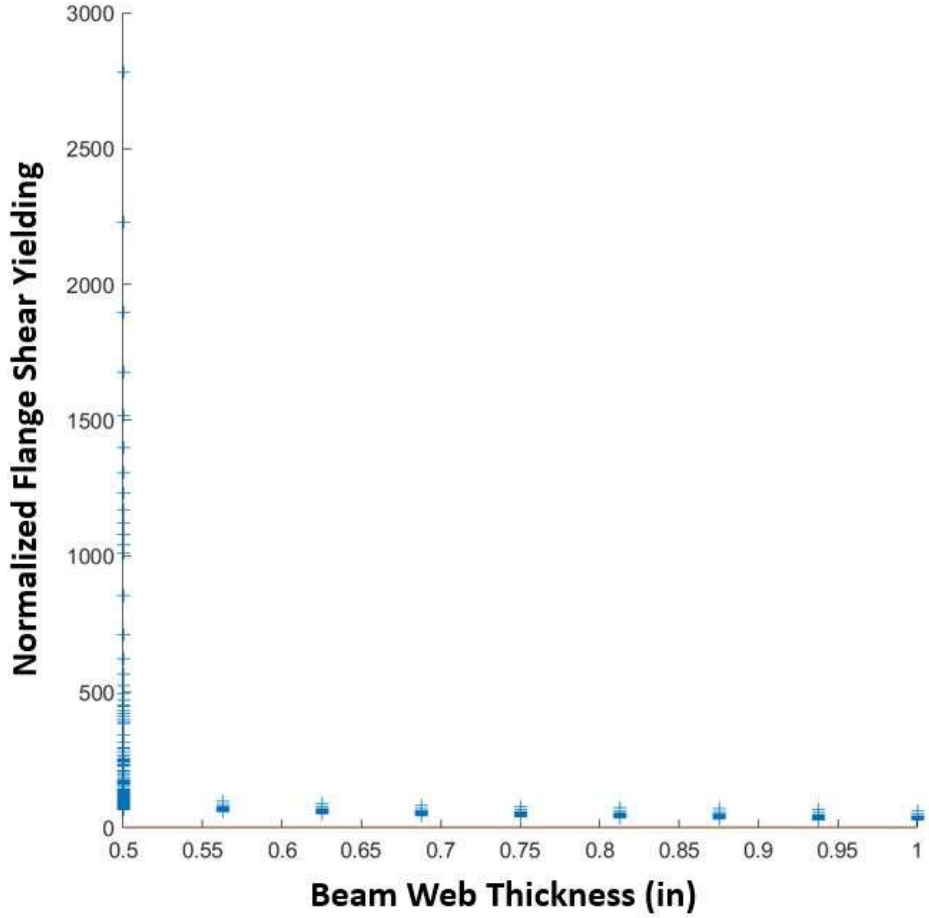

Figure 223: Scenario I: Normalized flange shear yielding vs web thickness (t_w)

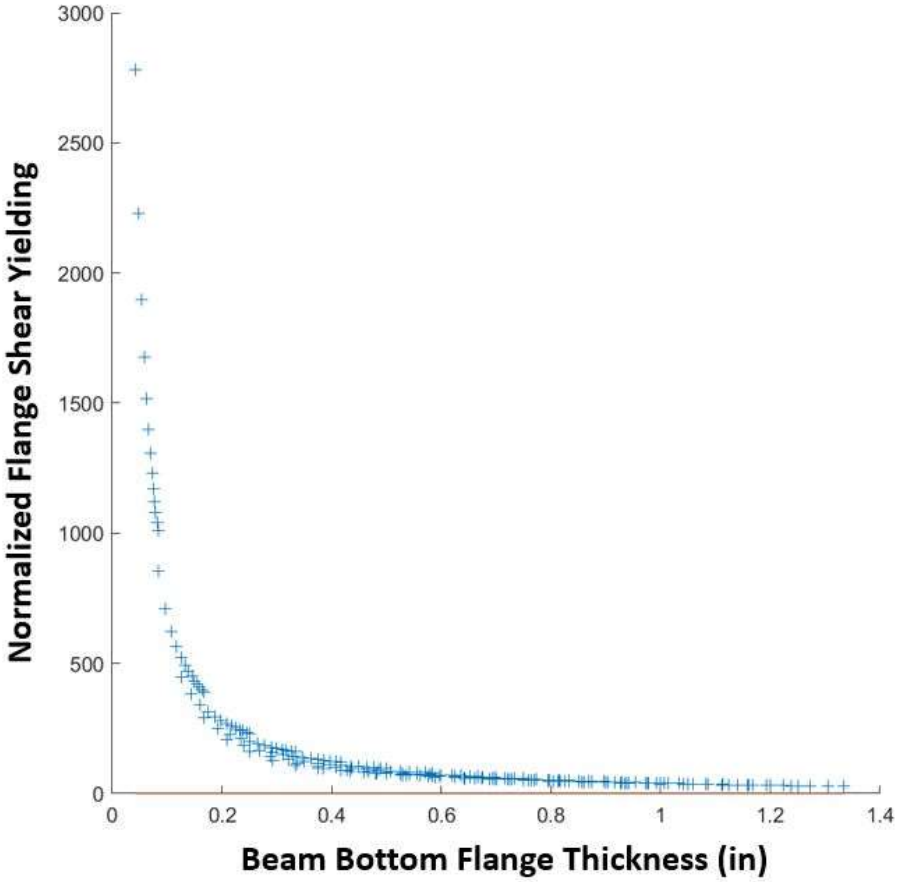

Figure 224: Scenario I: Normalized flange shear yielding vs bottom flange thickness (t_{fb})

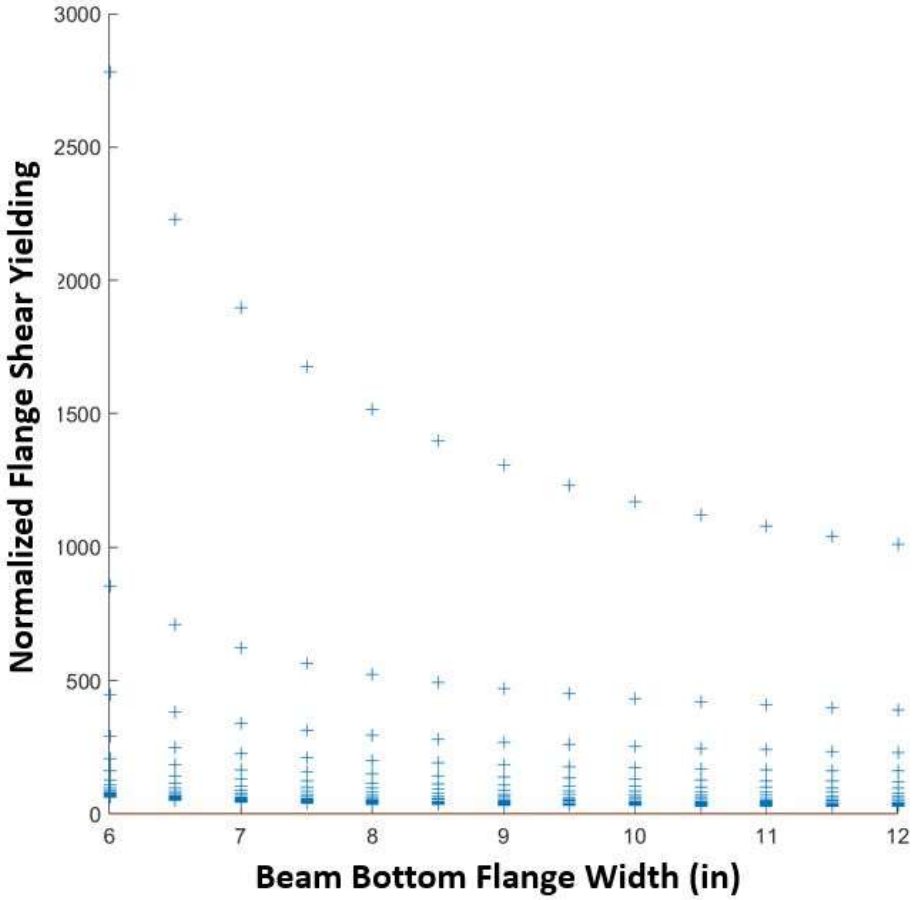

Figure 225: Scenario I: Normalized flange shear yielding vs bottom flange width (b_{fb})

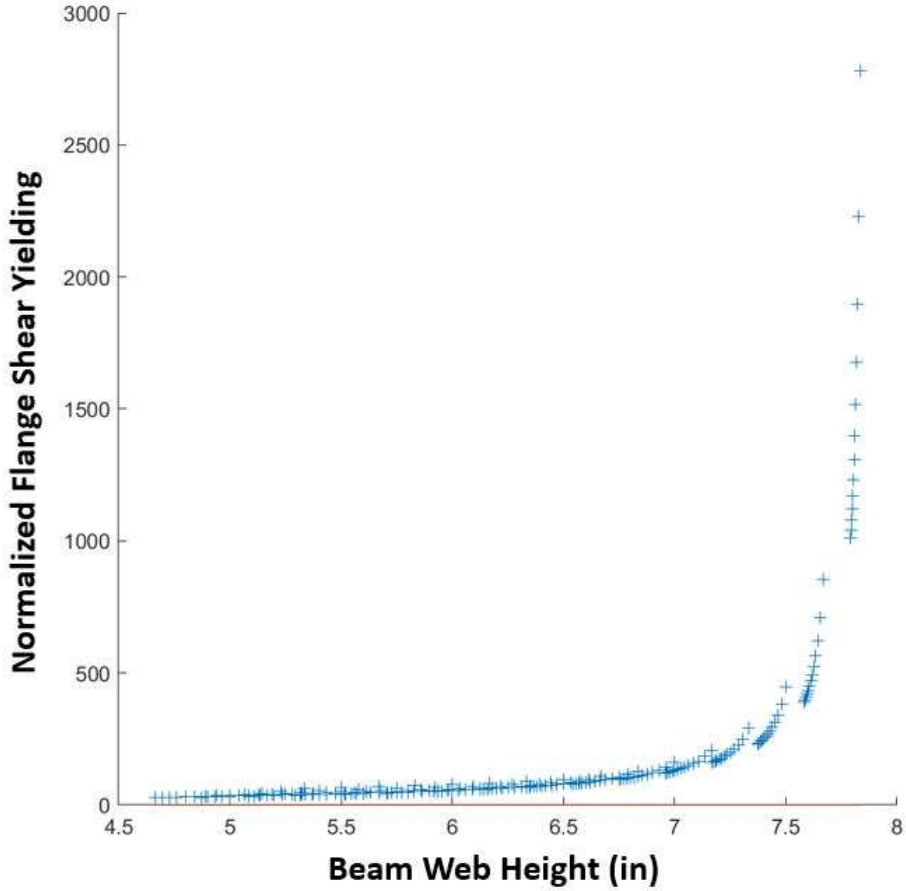

Figure 226: Scenario I: Normalized flange shear yielding vs web height

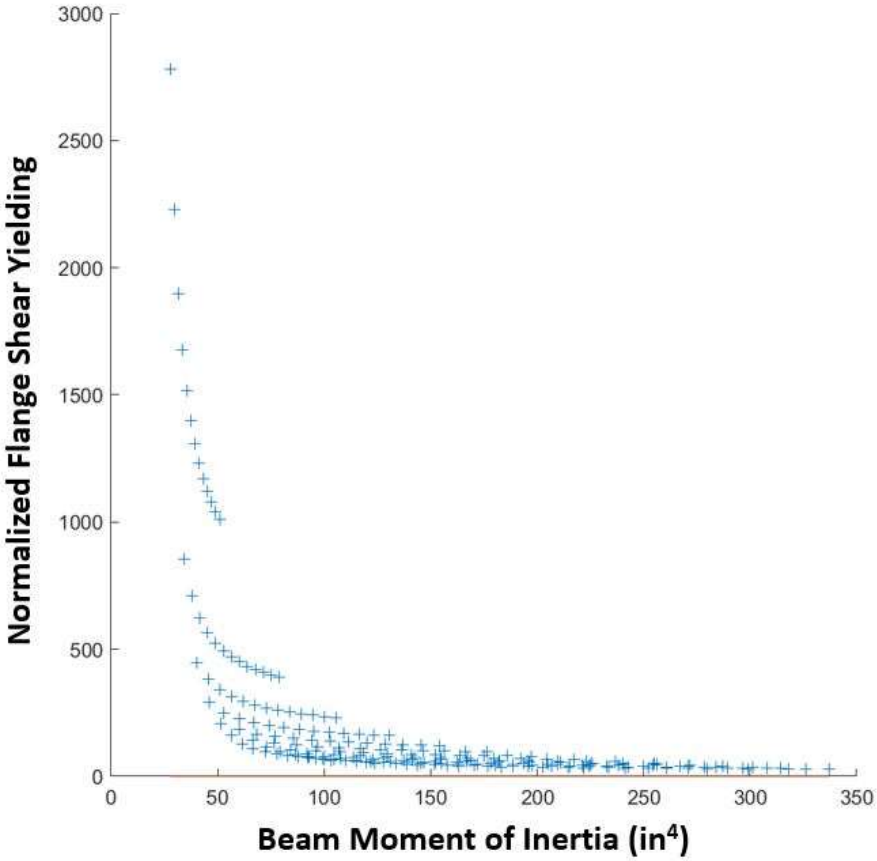

Figure 227: Scenario I: Normalized flange shear yielding vs moment of inertia (I_x)

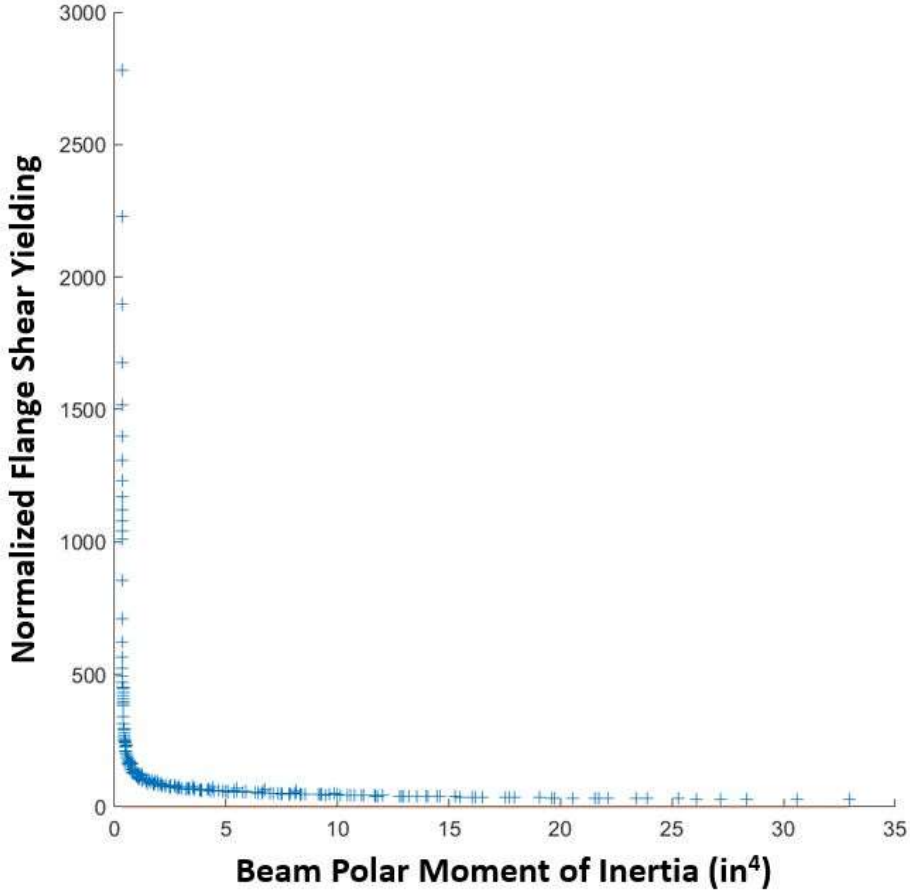

Figure 228: Scenario I: Normalized flange shear yielding vs polar moment of inertia (*J*)

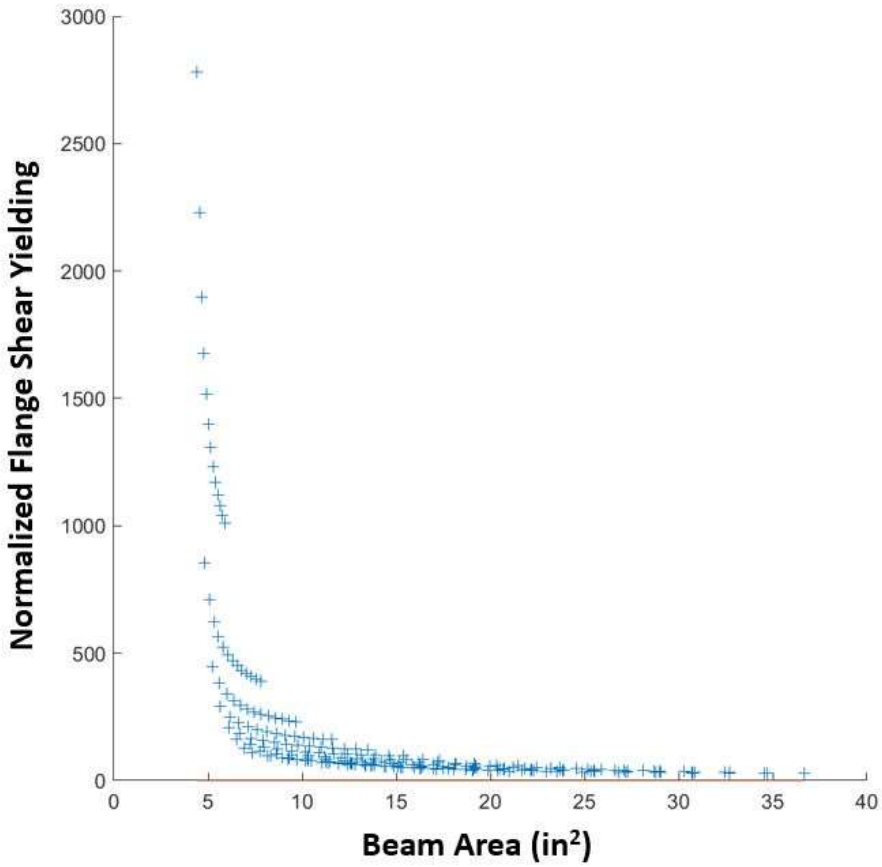

Figure 229: Scenario I: Normalized flange shear yielding vs cross-sectional area

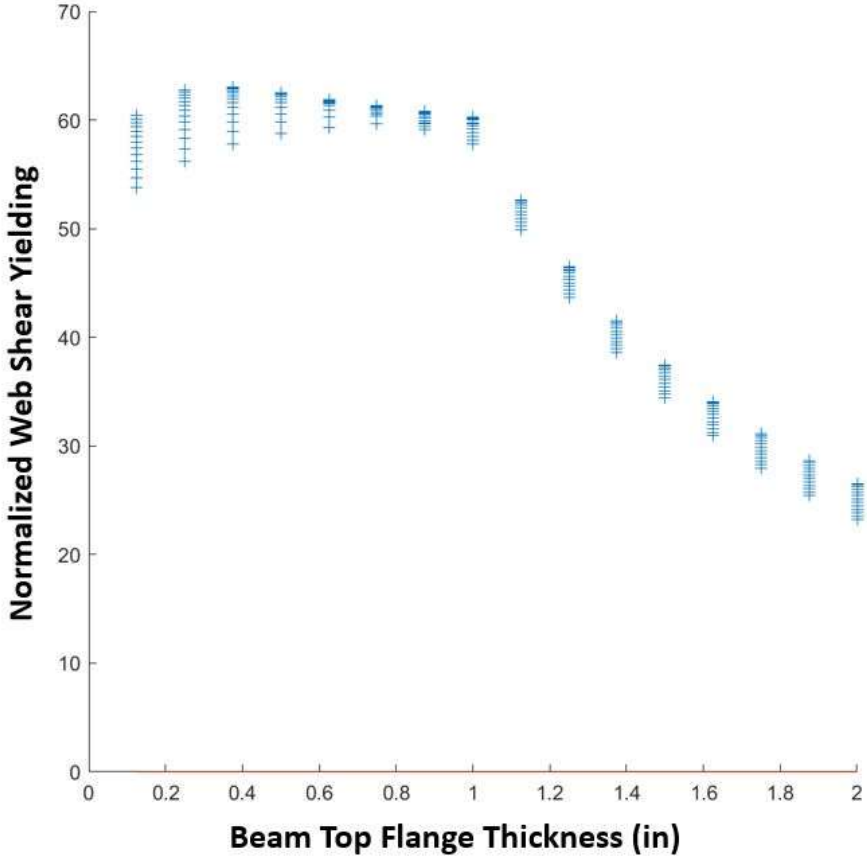

Figure 230: Scenario I: Normalized web shear yielding vs top flange thickness (t_{ft})

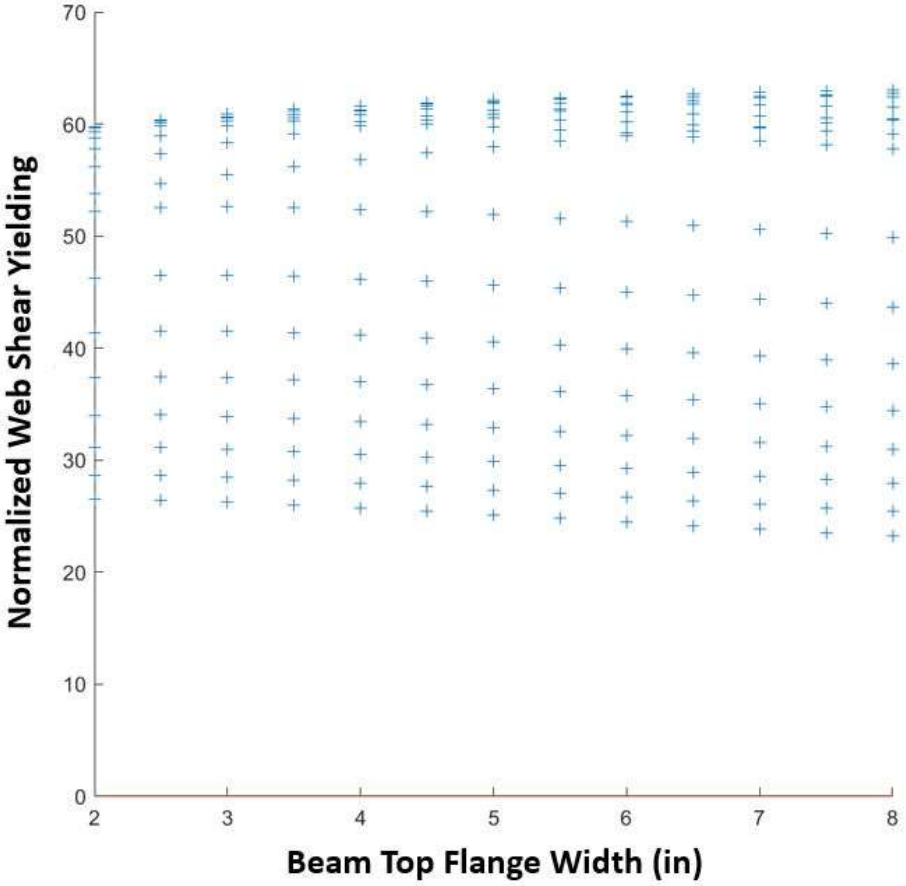

Figure 231: Scenario I: Normalized web shear yielding vs top flange width (b_{ft})

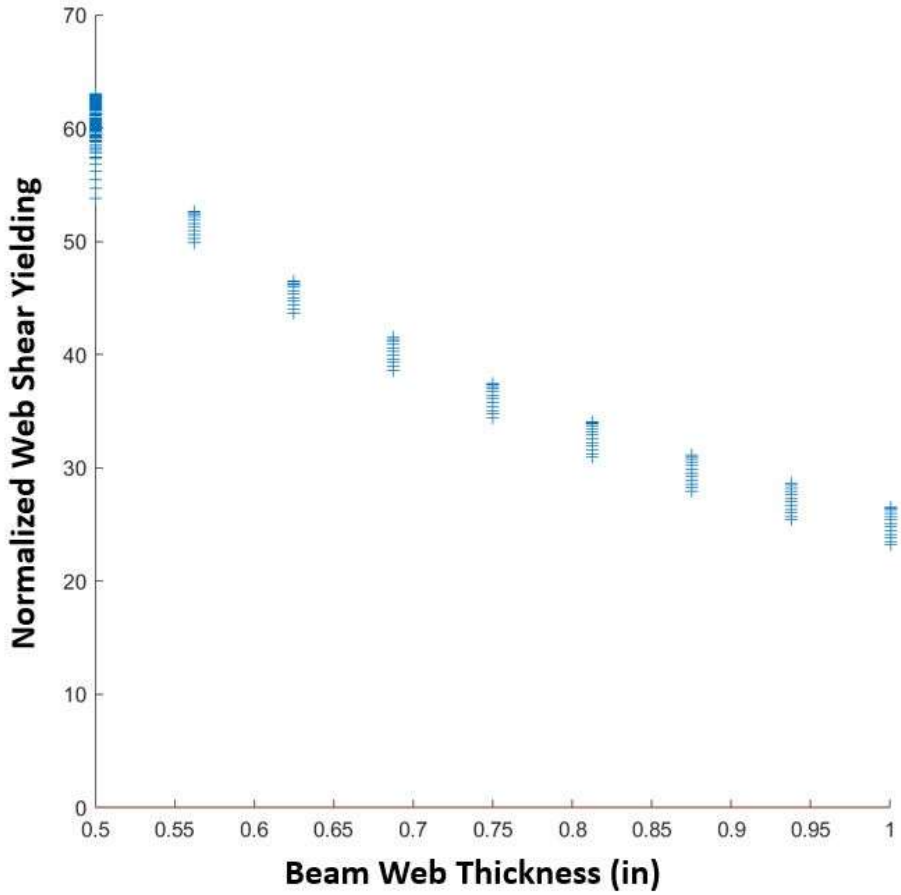

Figure 232: Scenario I: Normalized web shear yielding vs web thickness (t_w)

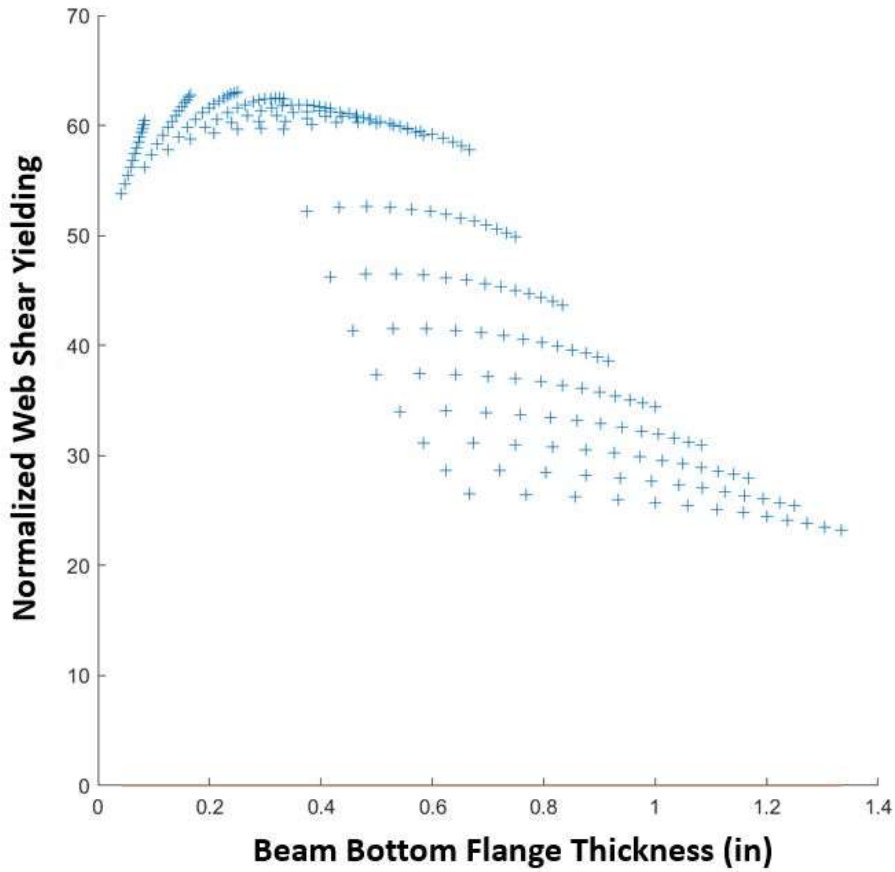

Figure 233: Scenario I: Normalized web shear yielding vs bottom flange thickness (t_{fb})

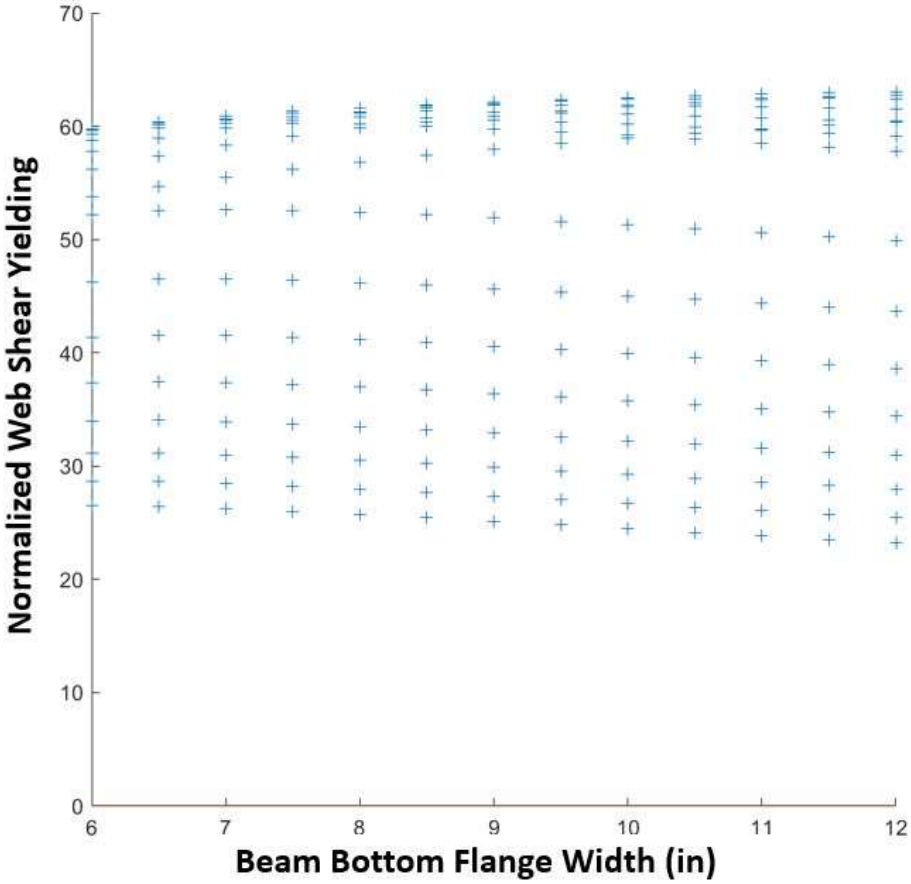

Figure 234: Scenario I: Normalized web shear yielding vs bottom flange width (b_{fb})

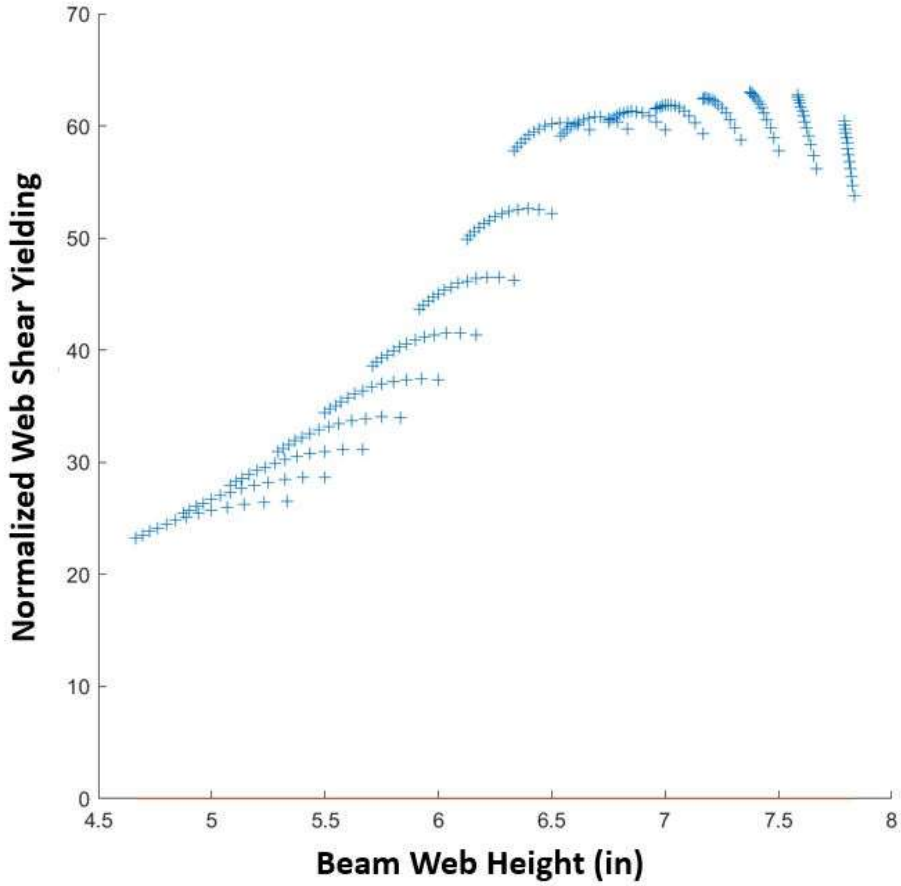

Figure 235: Scenario I: Normalized web shear yielding vs web height

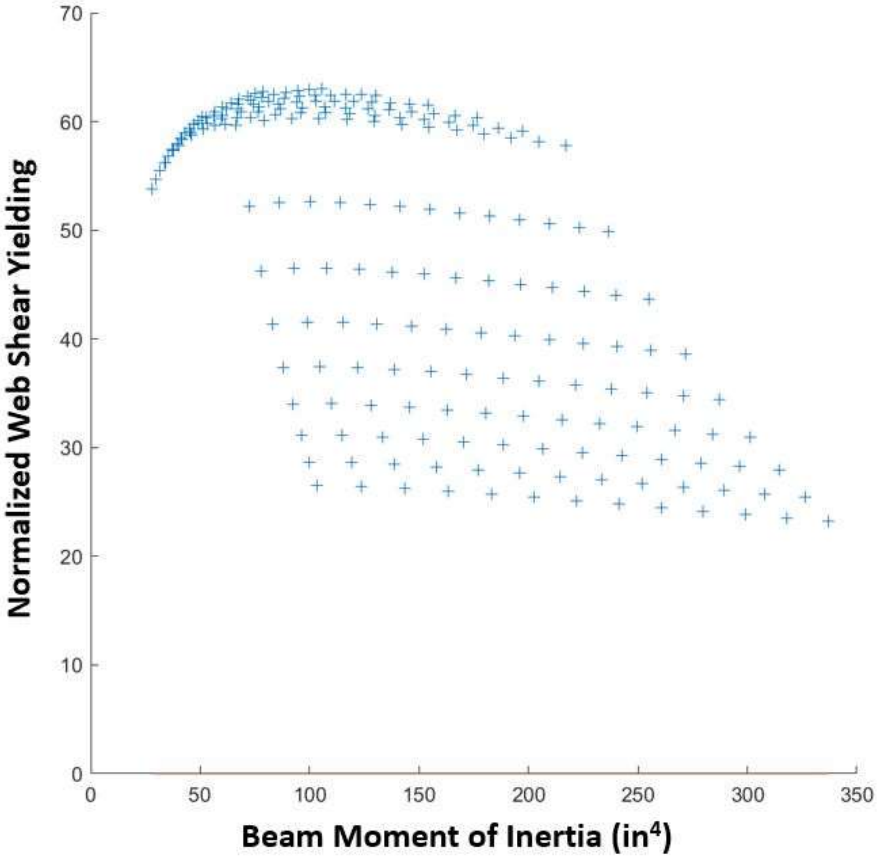

Figure 236: Scenario I: Normalized web shear yielding vs moment of inertia (I_x)

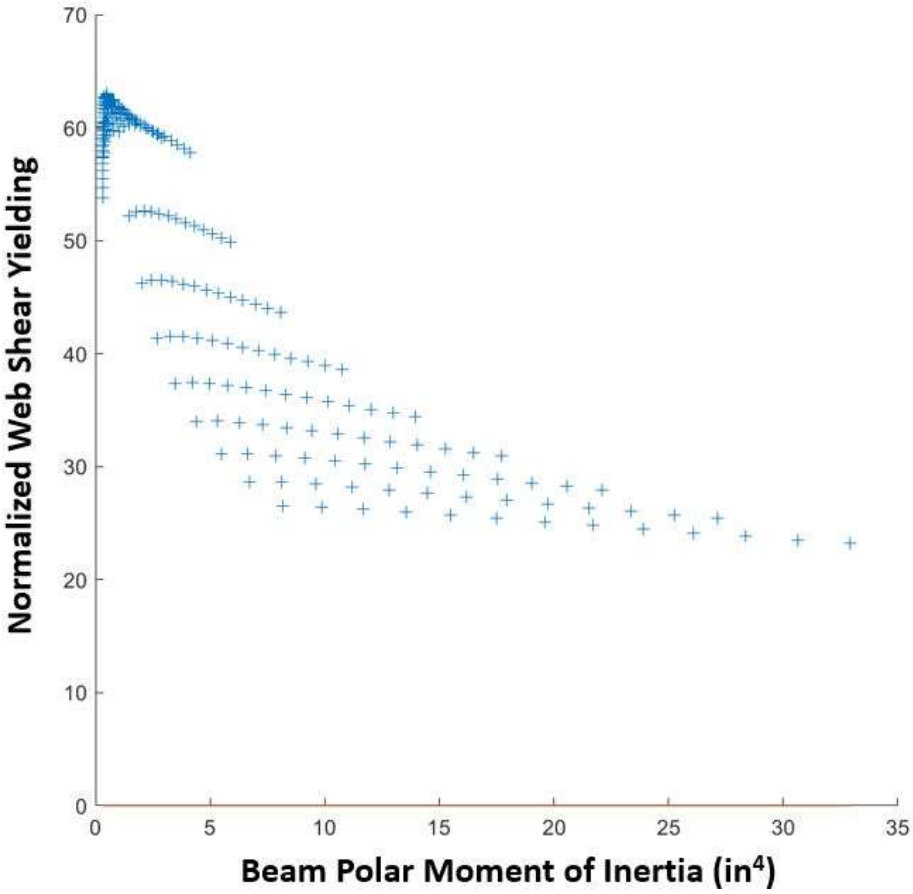

Figure 237: Scenario I: Normalized web shear yielding vs polar moment of inertia (*J*)

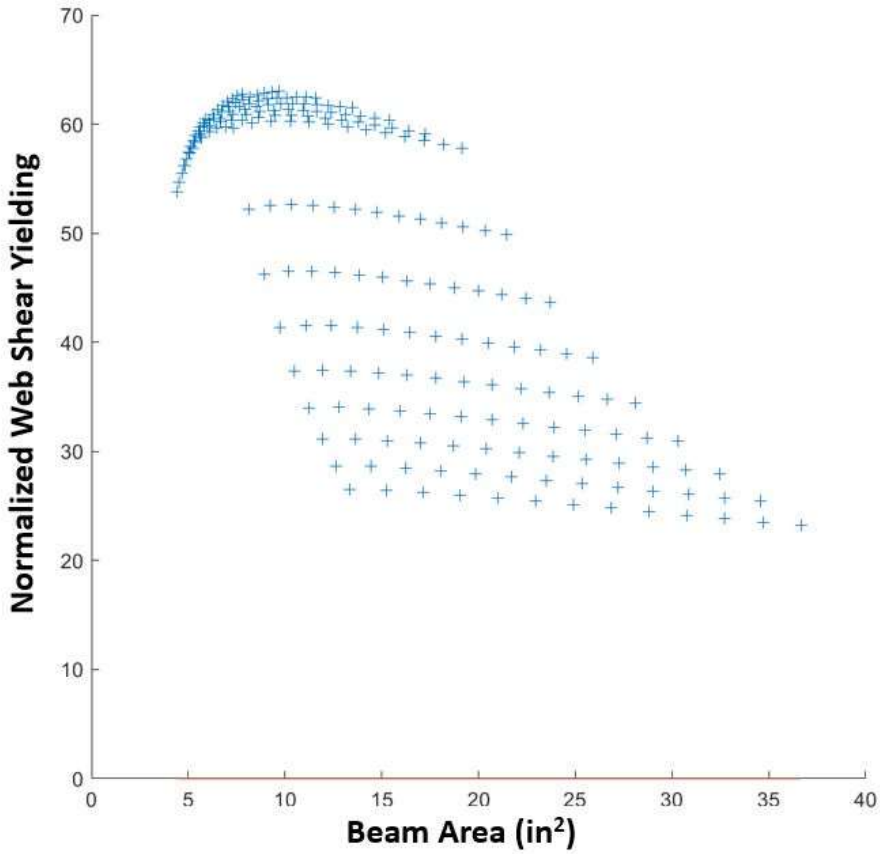

Figure 238: Scenario I: Normalized web shear yielding vs cross-sectional area

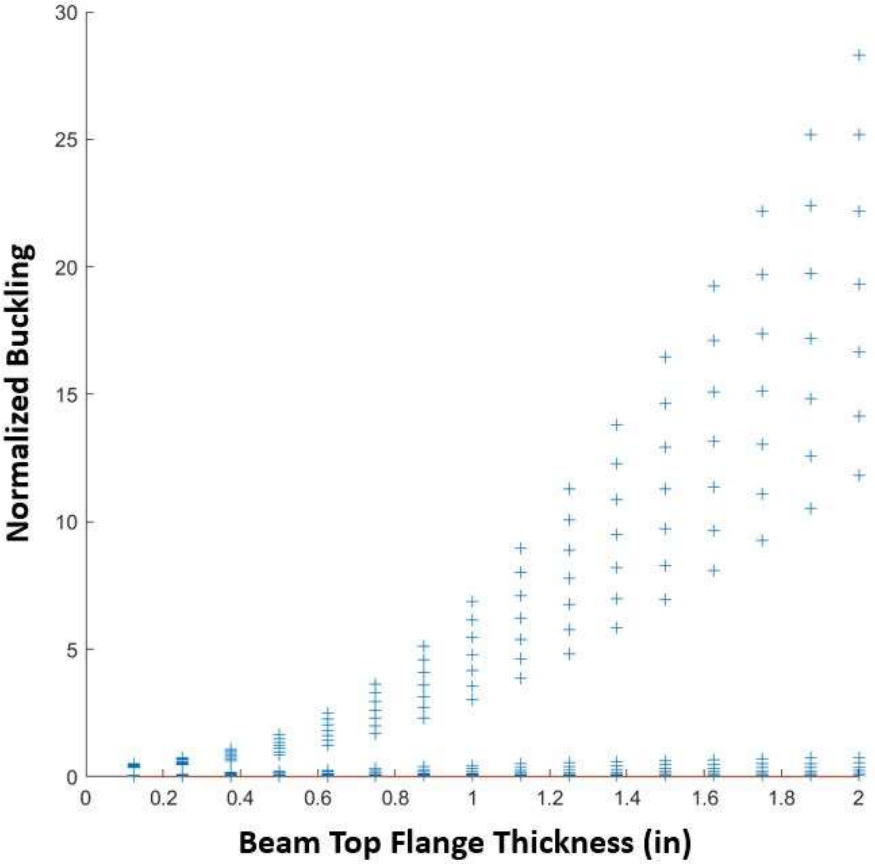

Figure 239: Scenario I: Normalized buckling vs top flange thickness (t_{ft})

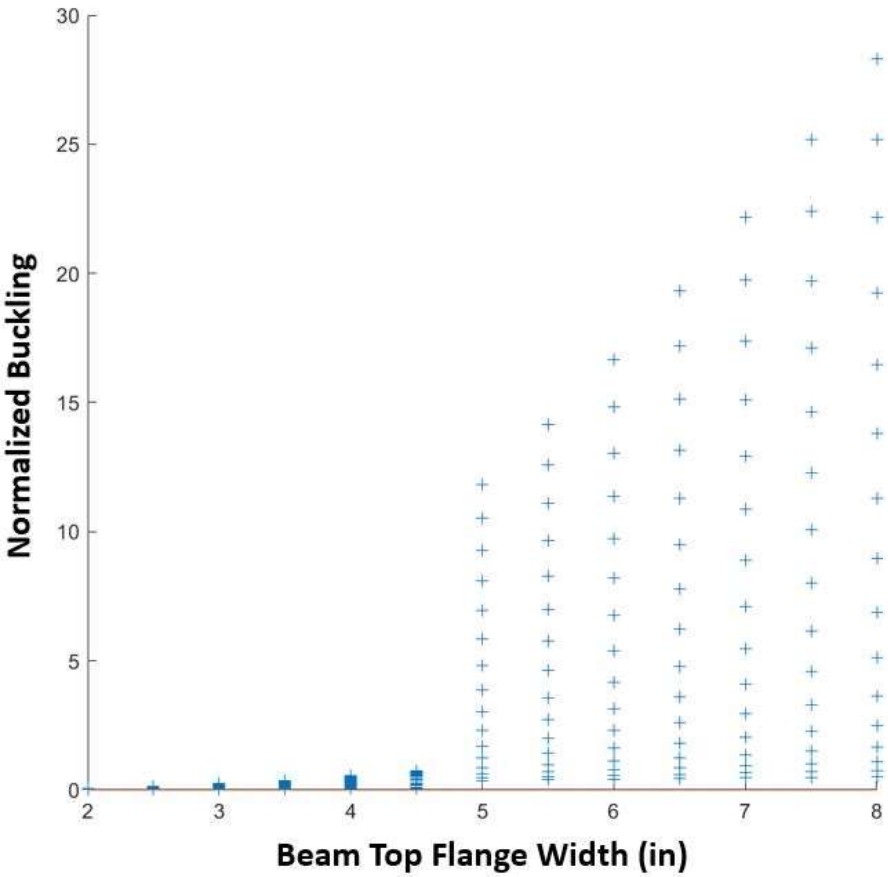

Figure 240: Scenario I: Normalized buckling vs top flange width (b_{ft})

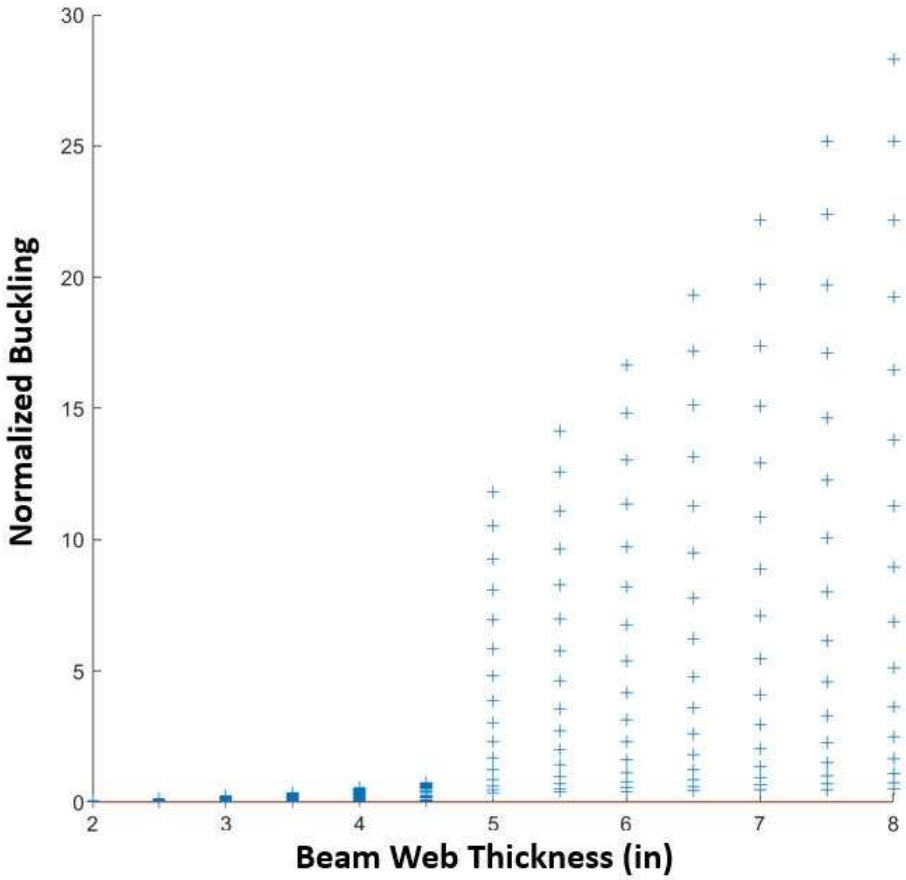

Figure 241: Scenario I: Normalized buckling vs web thickness (t_w)

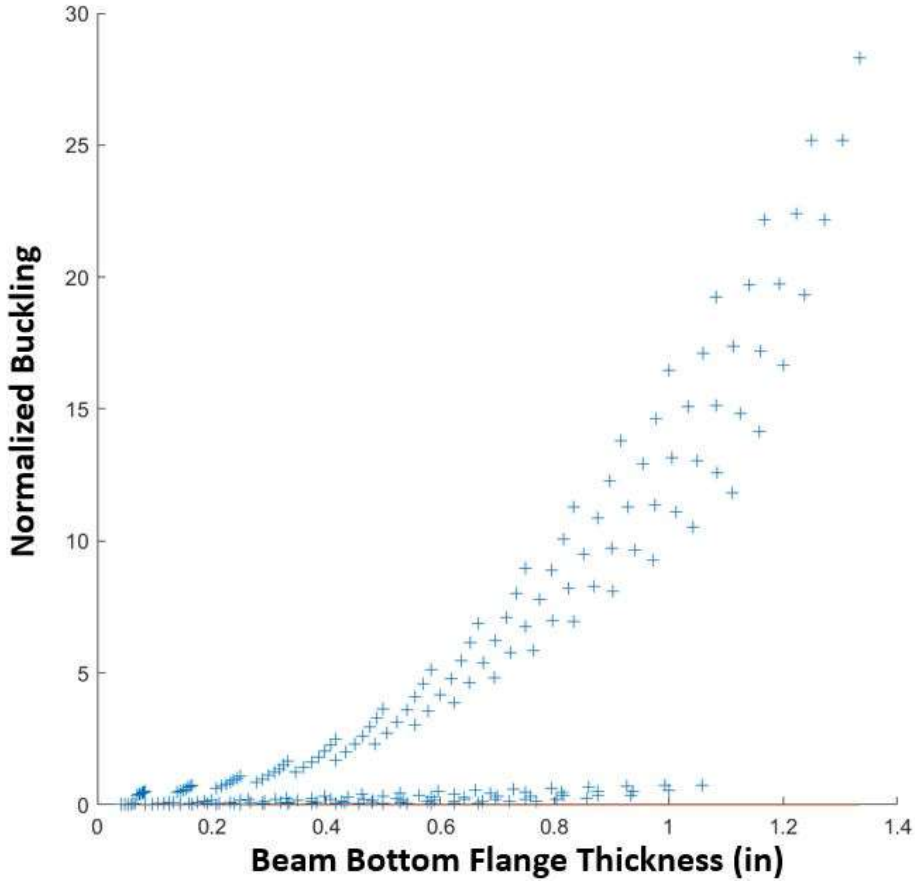

Figure 242: Scenario I: Normalized buckling vs bottom flange thickness (t_{fb})

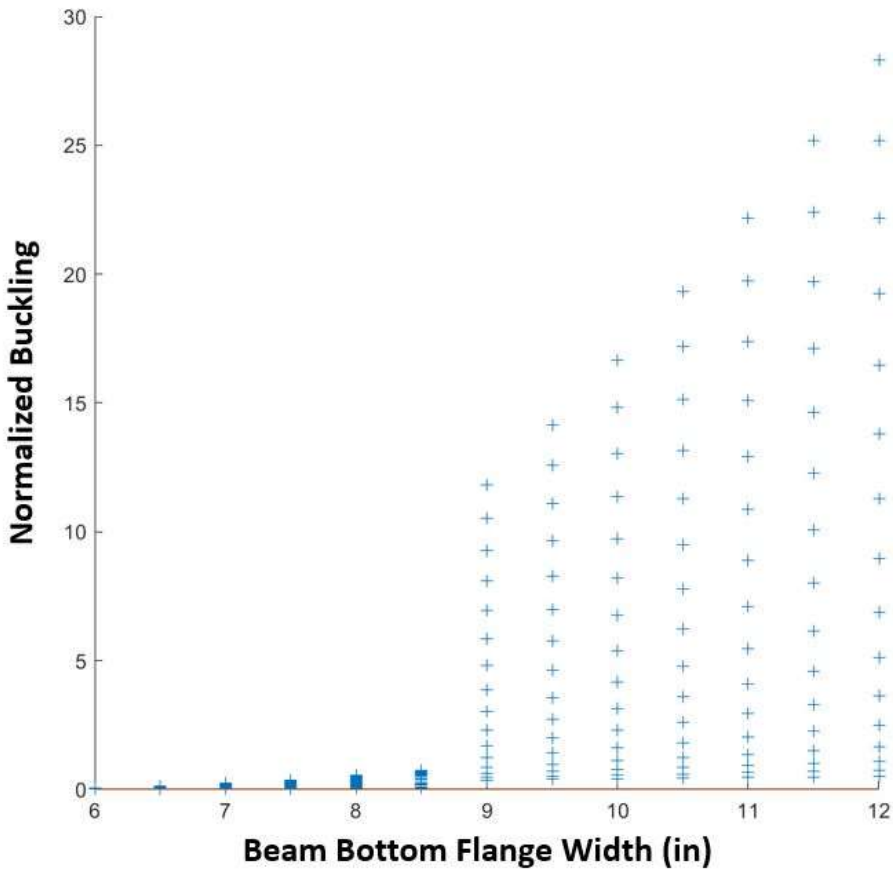

Figure 243: Scenario I: Normalized buckling vs bottom flange width (b_{fb})

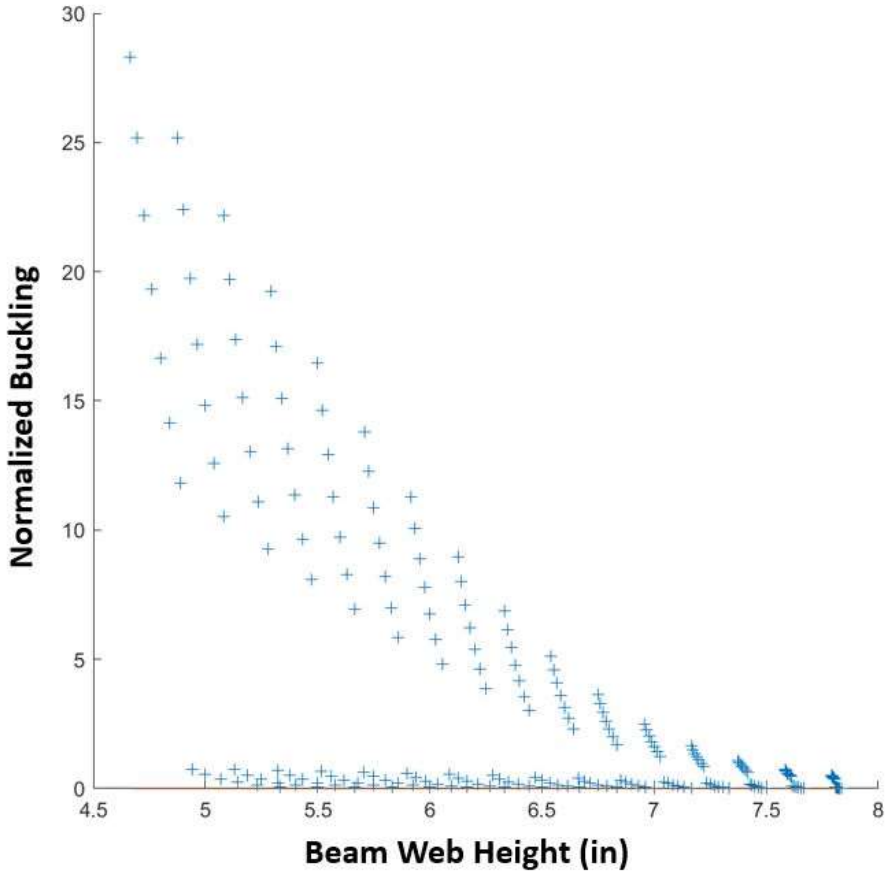

Figure 244: Scenario I: Normalized buckling vs web height

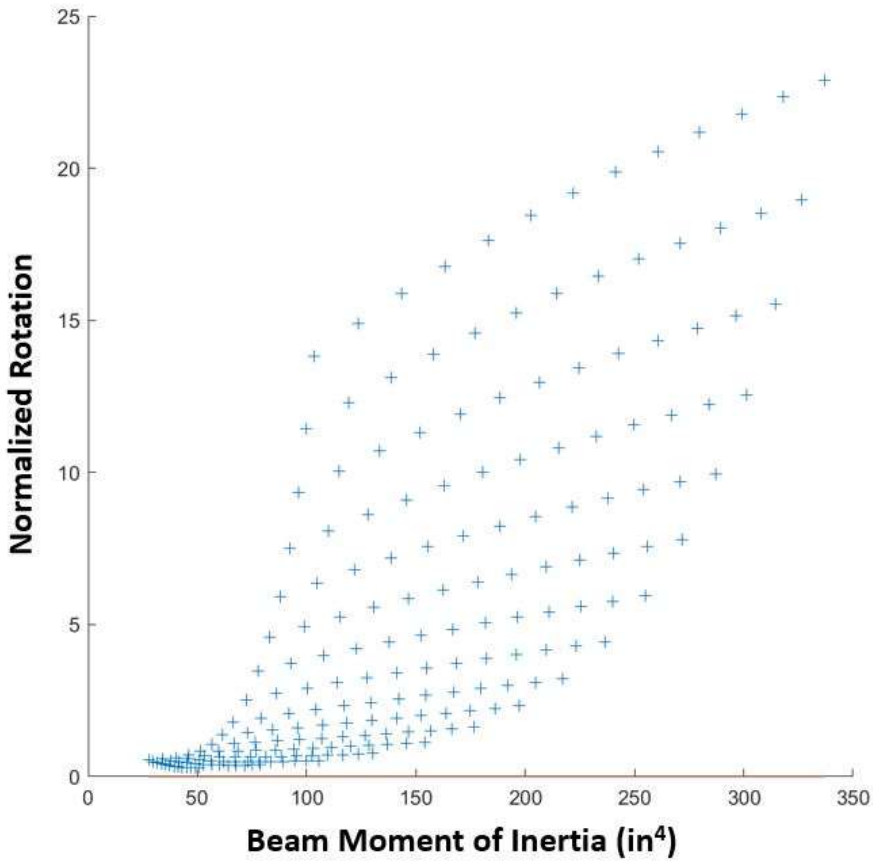

Figure 245: Scenario I: Normalized buckling vs moment of inertia (I_x)

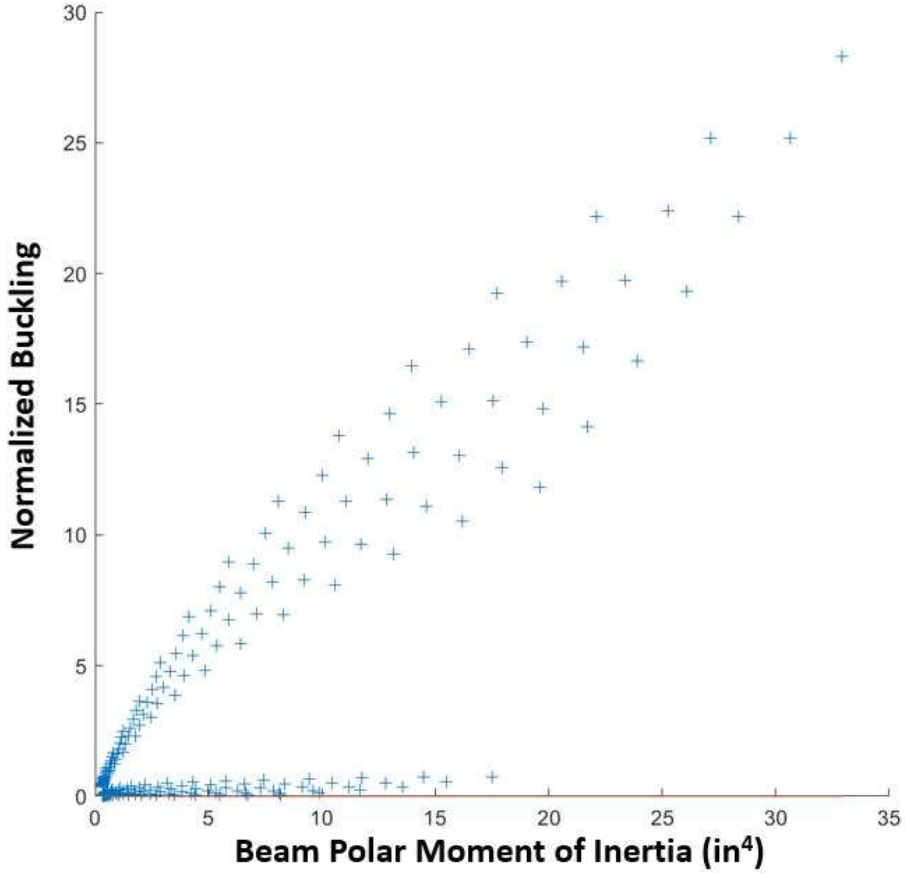

Figure 246: Scenario I: Normalized flange shear yielding vs polar moment of inertia (*J*)

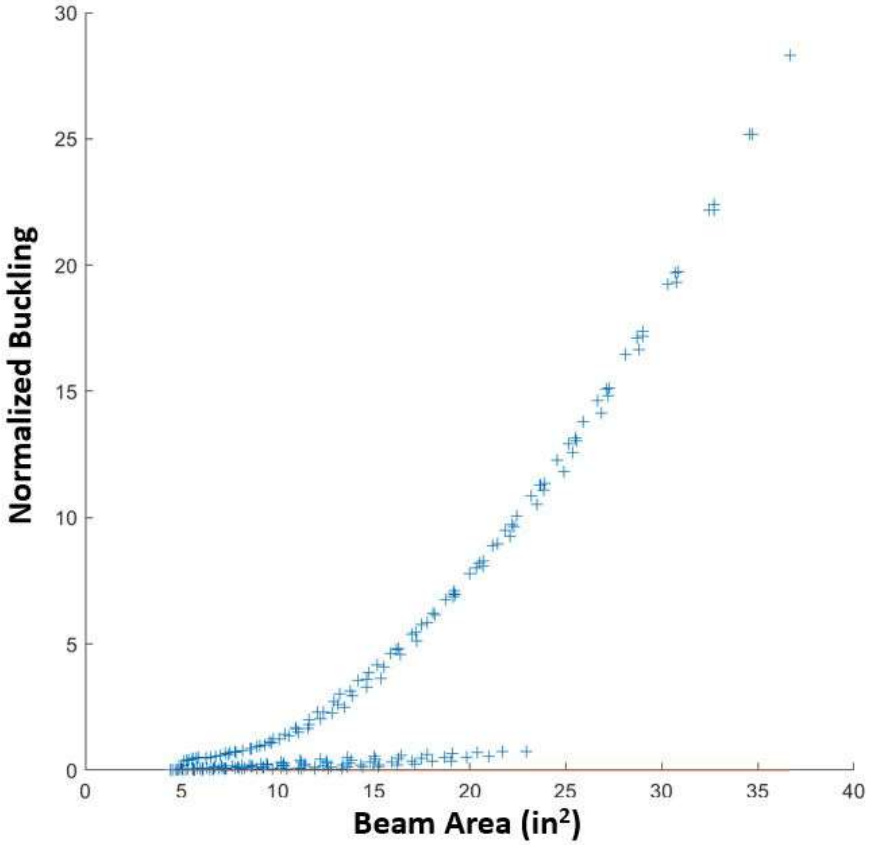

Figure 247: Scenario I: Normalized buckling vs cross-sectional area

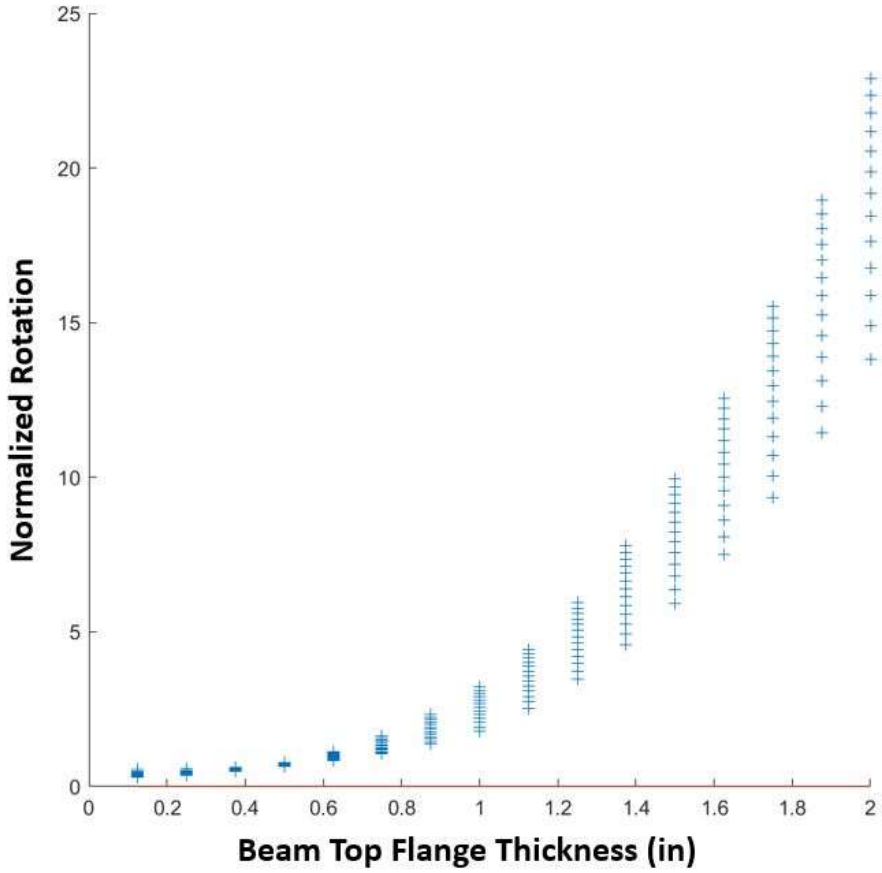

Figure 248: Scenario I: Normalized rotation vs top flange thickness (t_{ft})

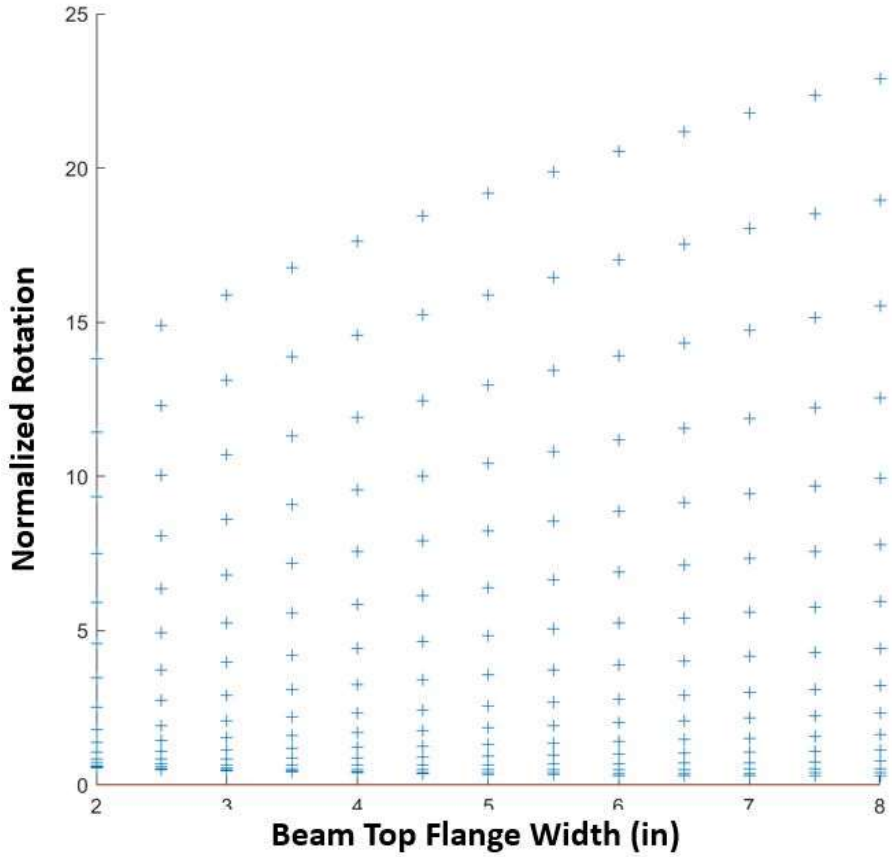

Figure 249: Scenario I: Normalized rotation vs top flange width (b_{ft})

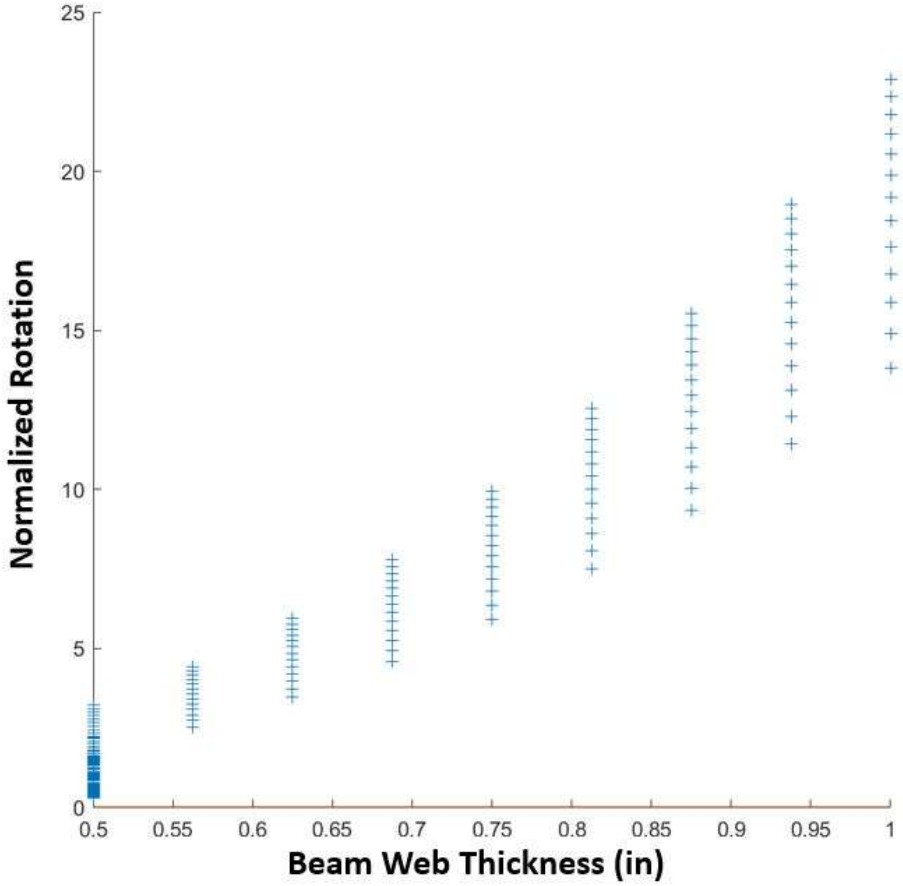

Figure 250: Scenario I: Normalized rotation vs web thickness (t_w)

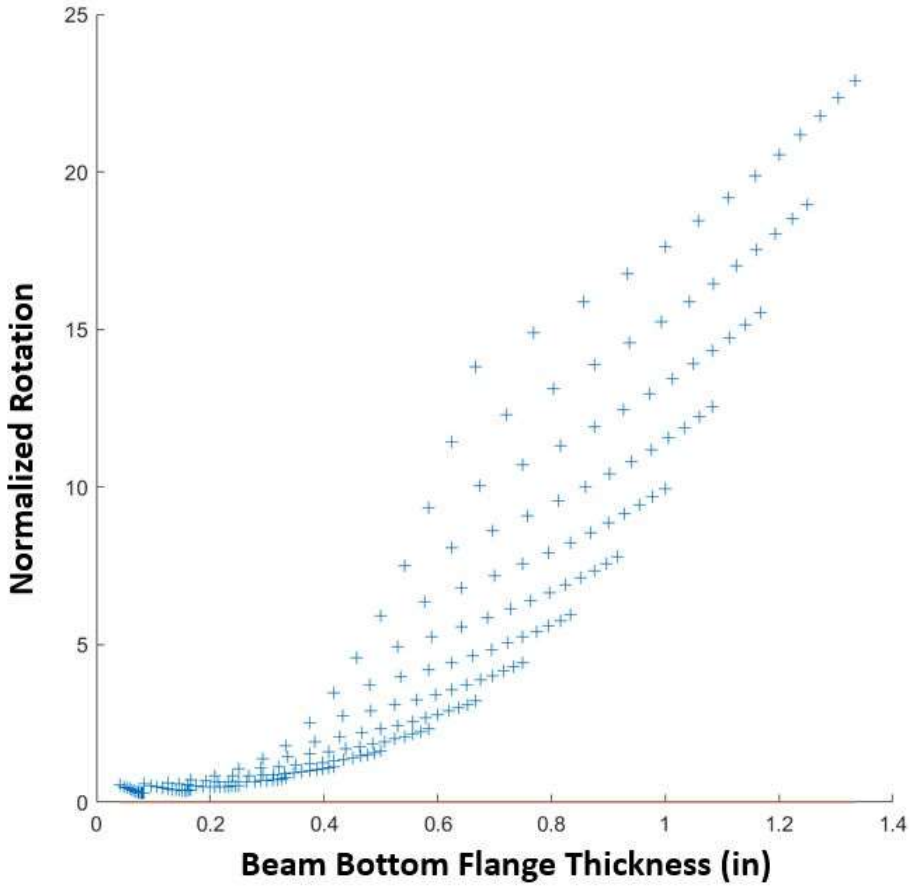

Figure 251: Scenario I: Normalized rotation vs bottom flange thickness (t_{fb})

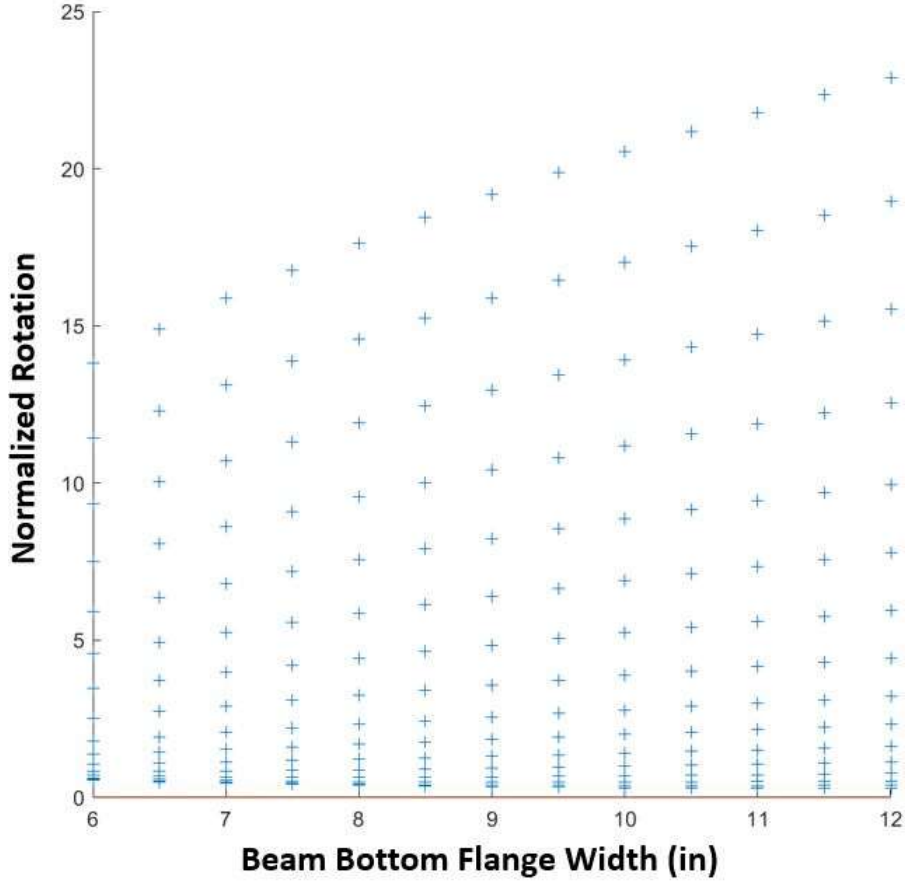

Figure 252: Scenario I: Normalized rotation vs bottom flange width (b_{fb})

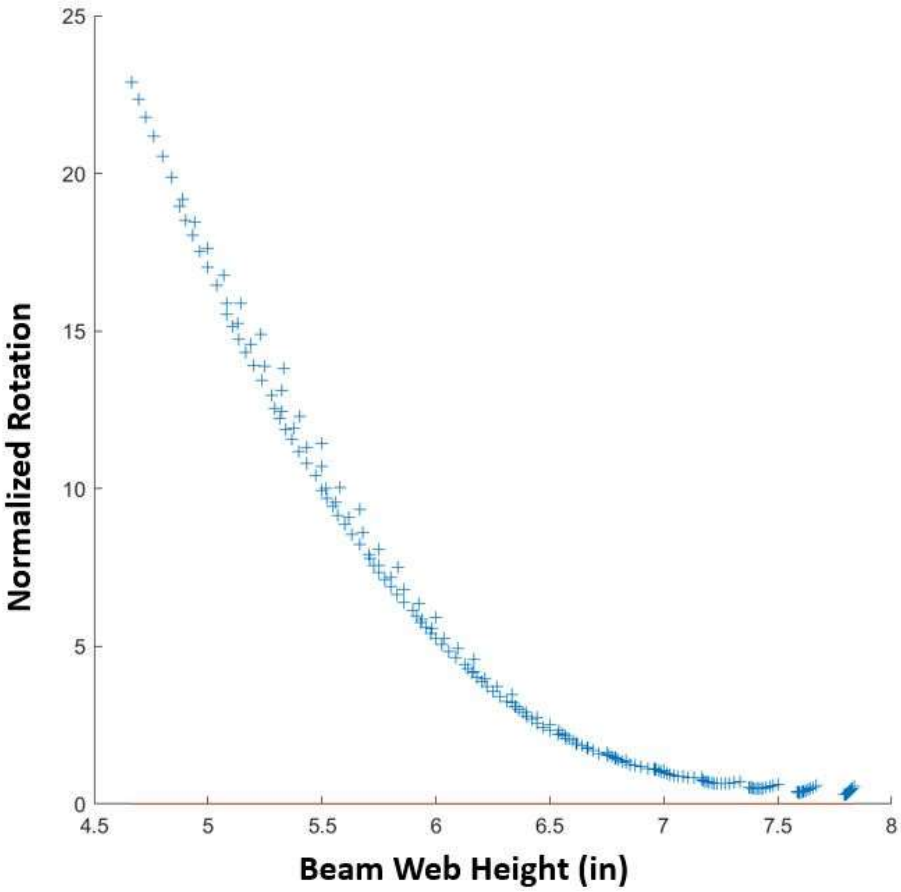

Figure 253: Scenario I: Normalized rotation vs web height

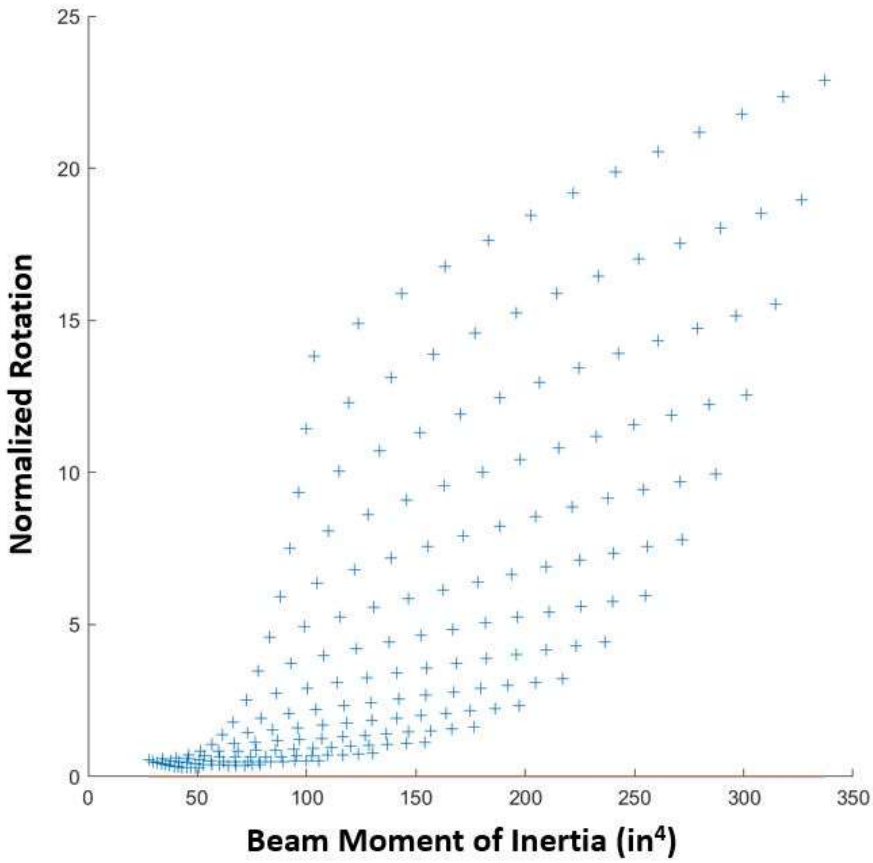

Figure 254: Scenario I: Normalized rotation vs moment of inertia (I_x)

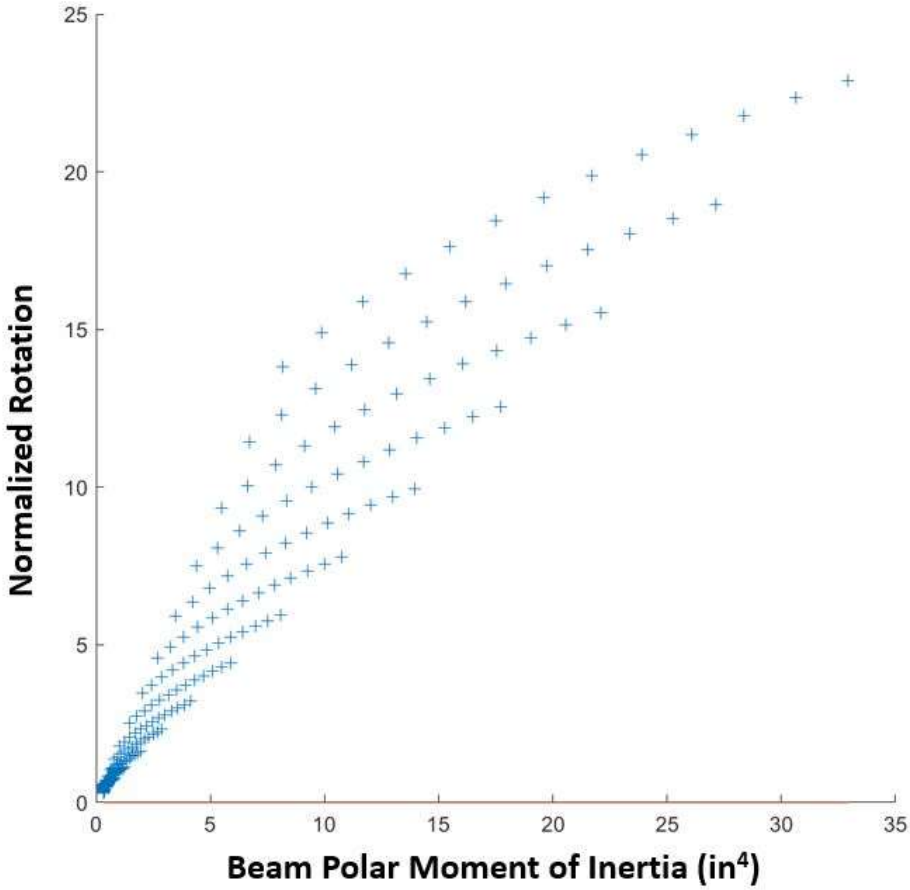

Figure 255: Scenario I: Normalized rotation vs polar moment of inertia (*J*)

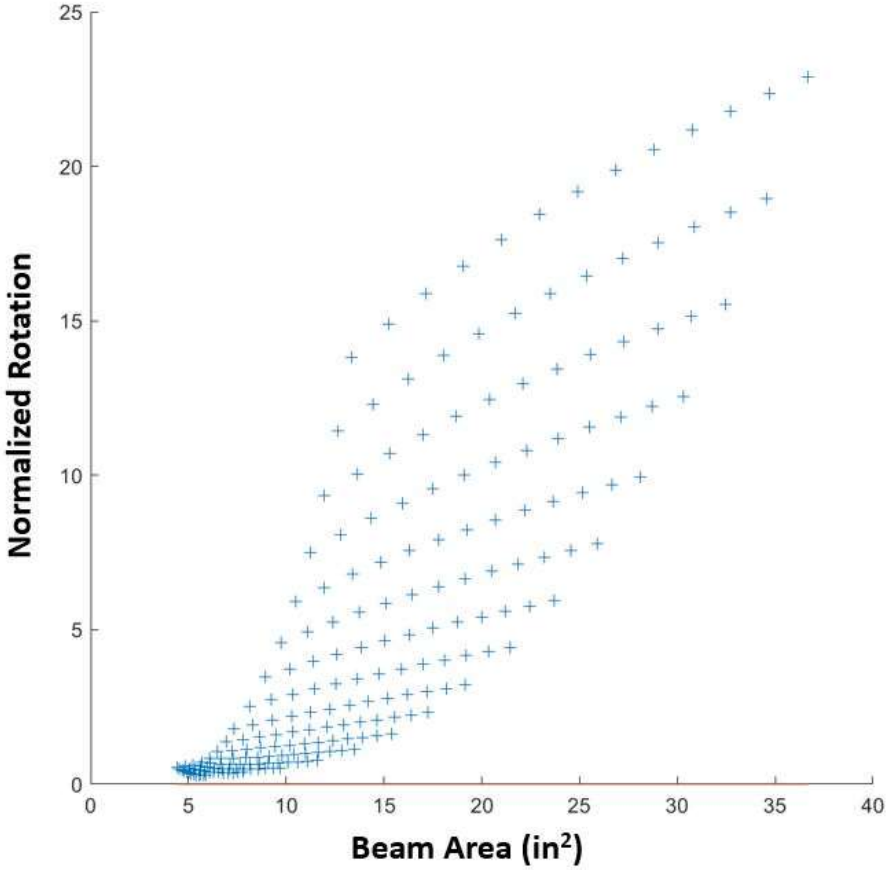

Figure 256: Scenario I: Normalized rotation vs cross-sectional area

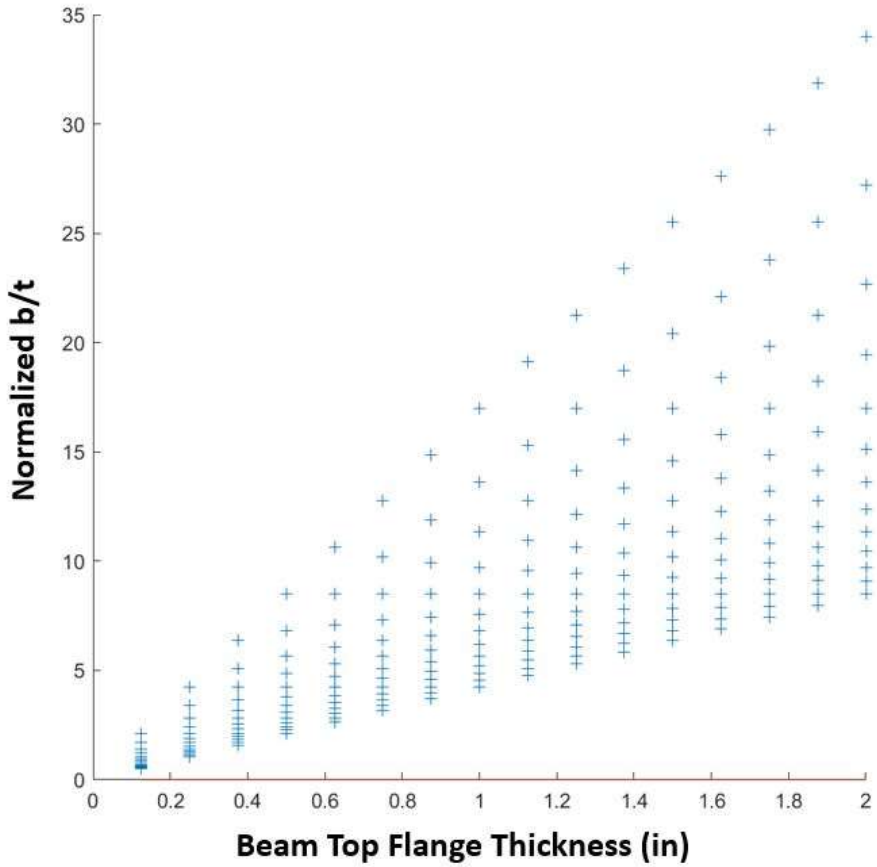

Figure 257: Scenario I: Normalized b/t vs top flange thickness (t_{ft})

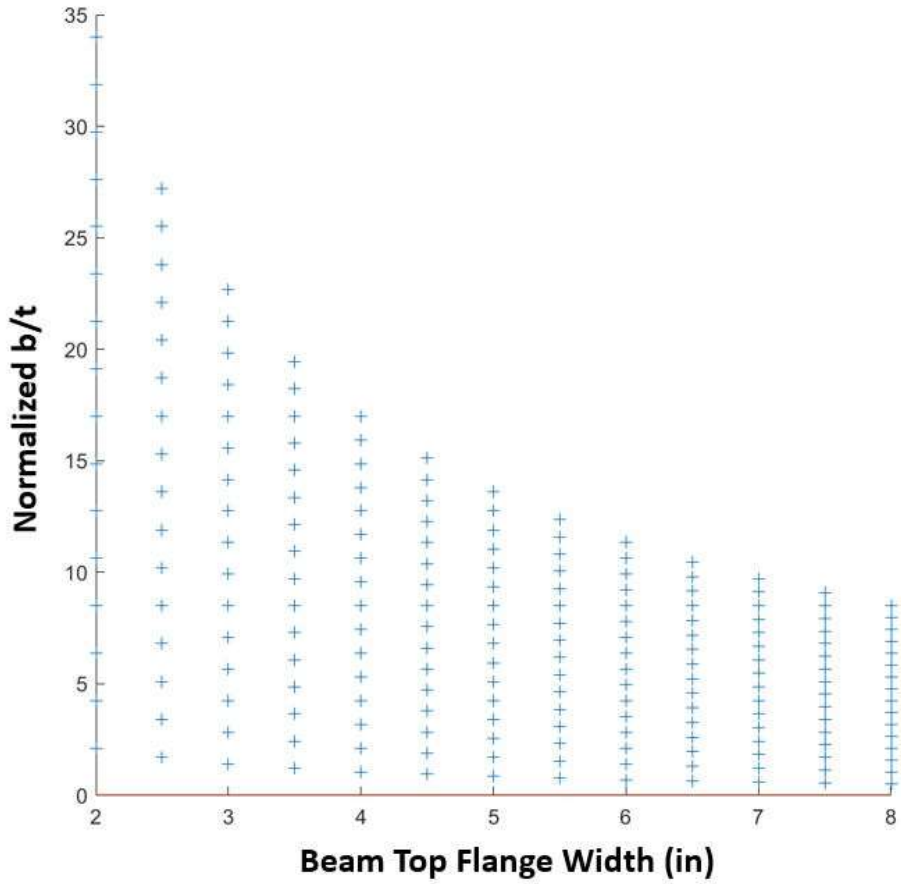

Figure 258: Scenario I: Normalized b/t vs top flange width (b_{ft})

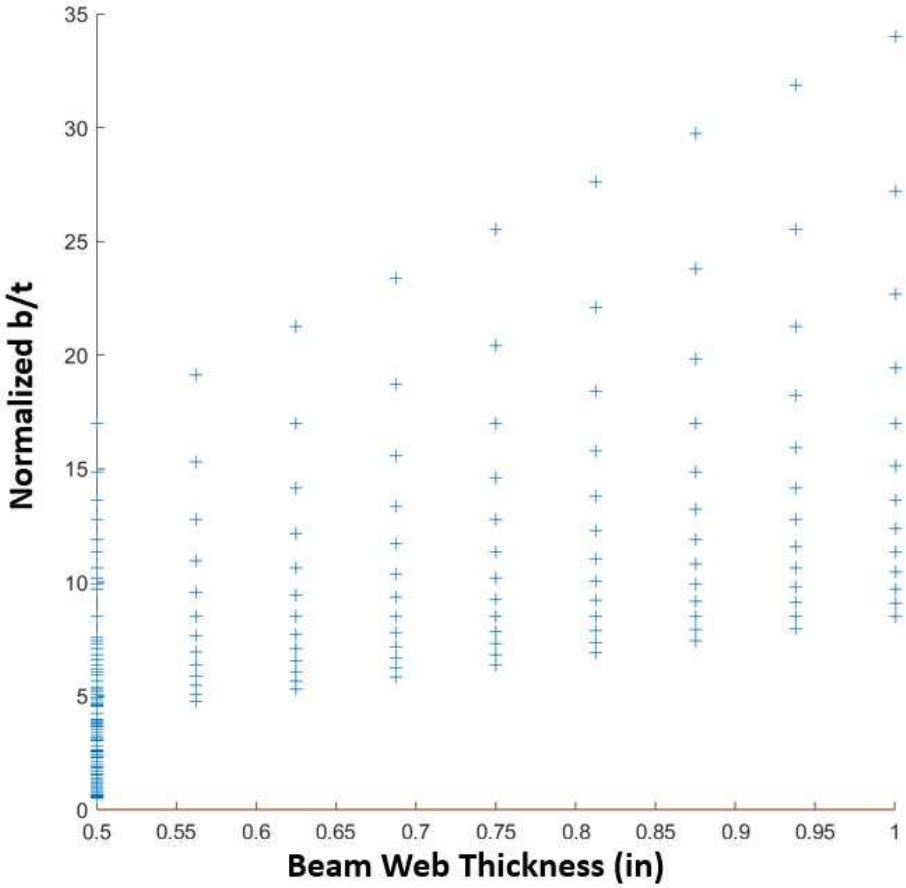

Figure 259: Scenario I: Normalized b/t vs web thickness (t_w)

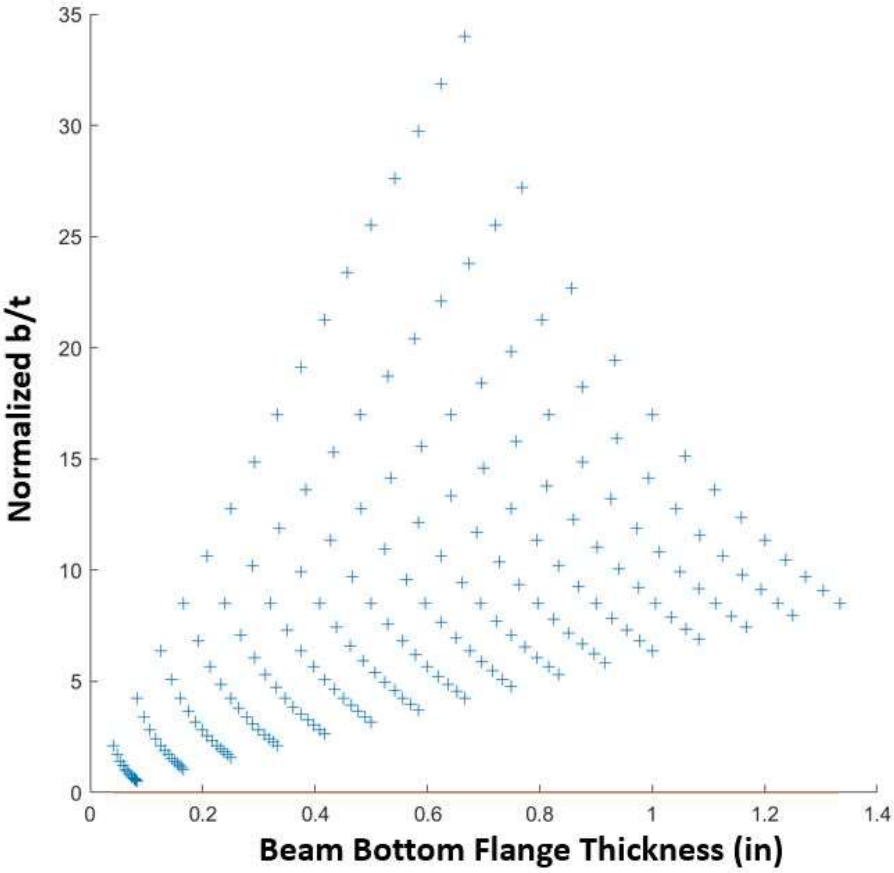

Figure 260: Scenario I: Normalized b/t vs bottom flange thickness (t_{fb})

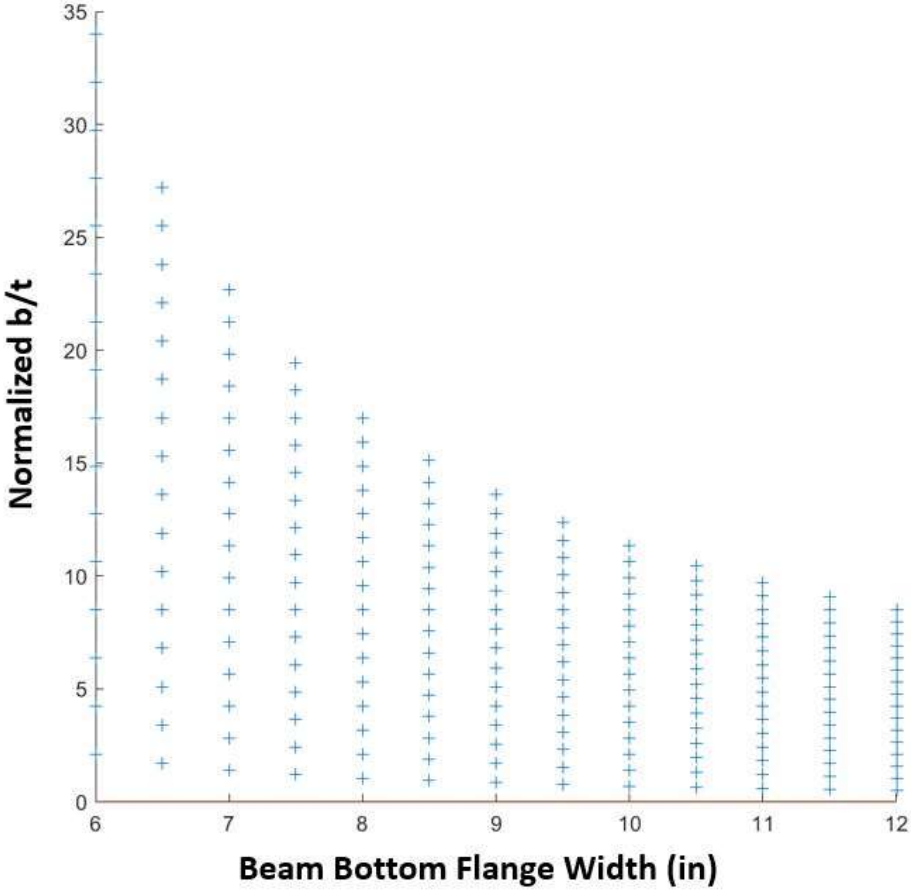

Figure 261: Scenario I: Normalized b/t vs bottom flange width (b_{fb})

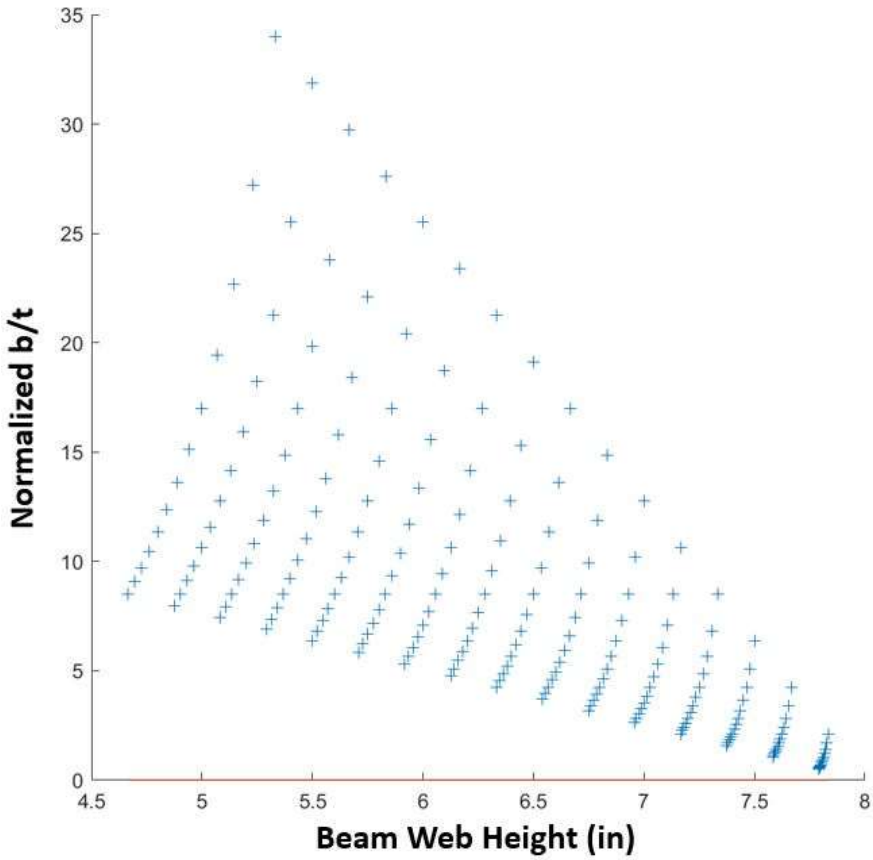

Figure 262: Scenario I: Normalized b/t vs web height

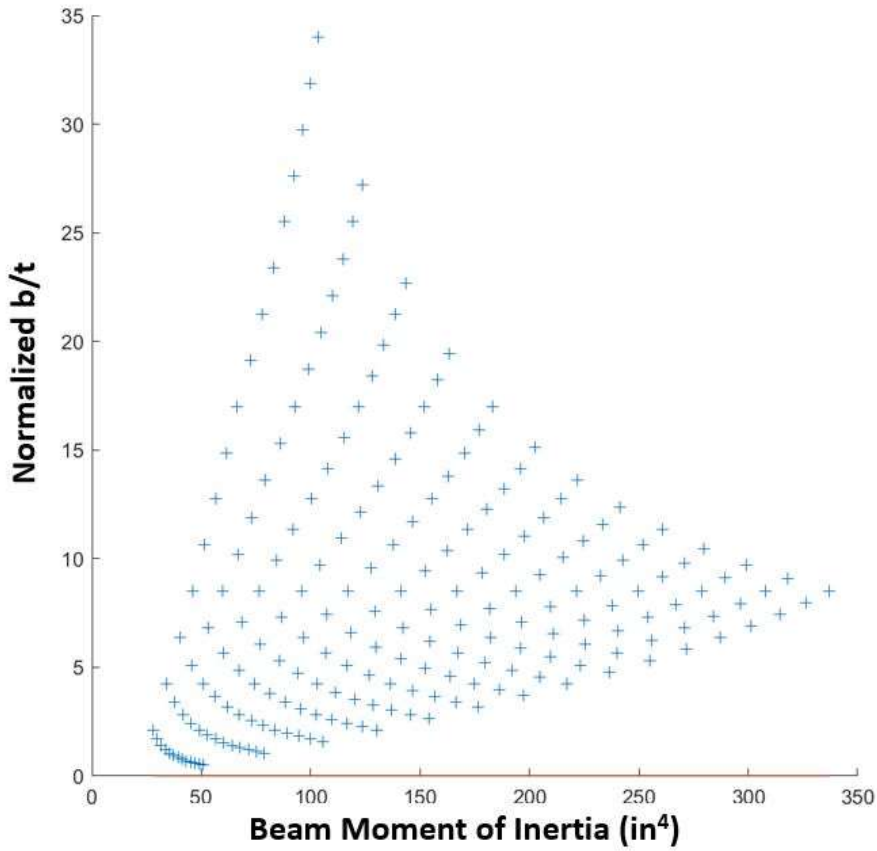

Figure 263: Scenario I: Normalized flange shear yielding vs moment of inertia (I_x)

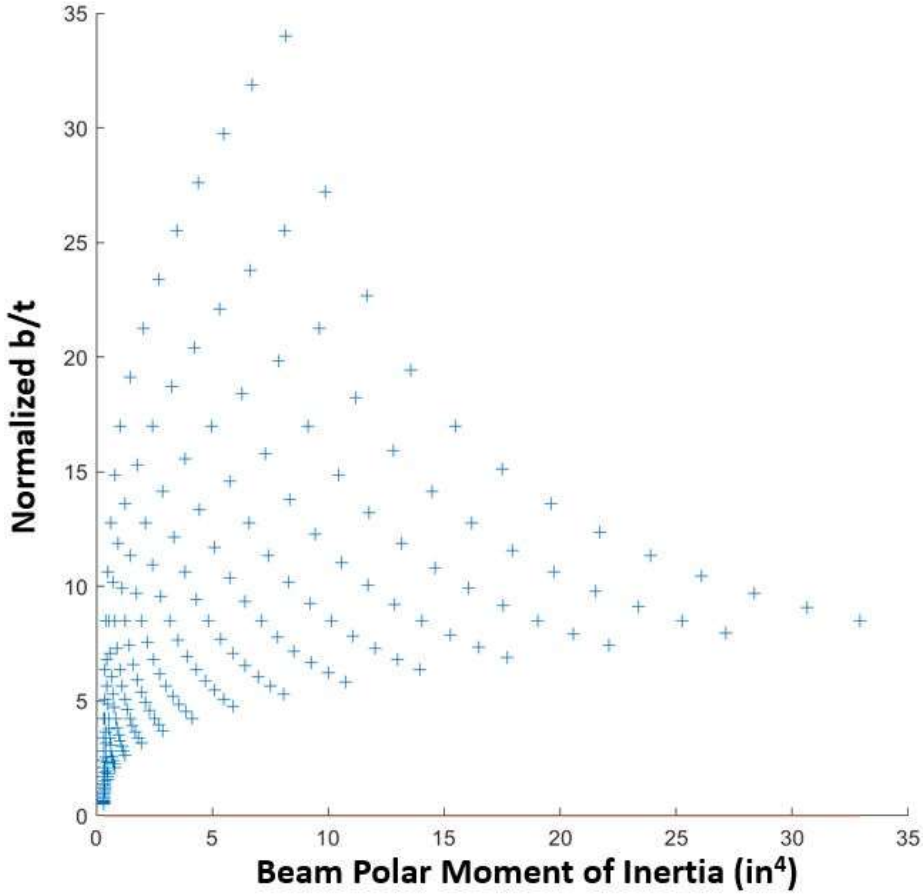

Figure 264: Scenario I: Normalized b/t vs polar moment of inertia (*J*)

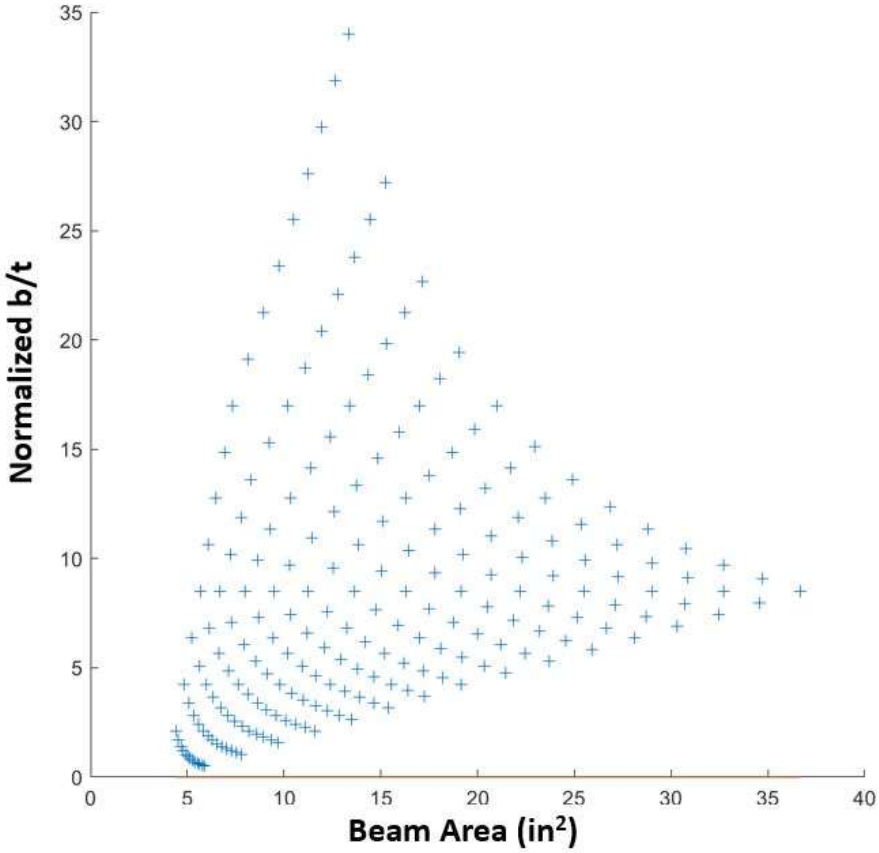

Figure 265: Scenario I: Normalized b/t vs cross-sectional area

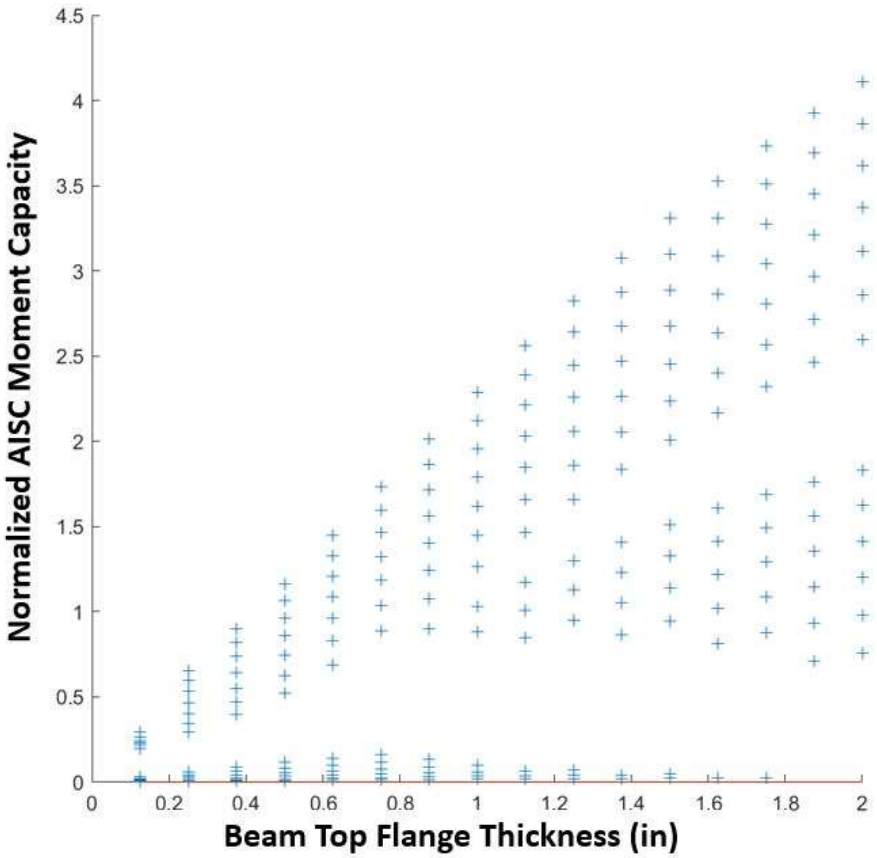

Figure 266: Scenario II: Normalized AISC Moment Capacity vs Top Flange Thickness (t_{ft})

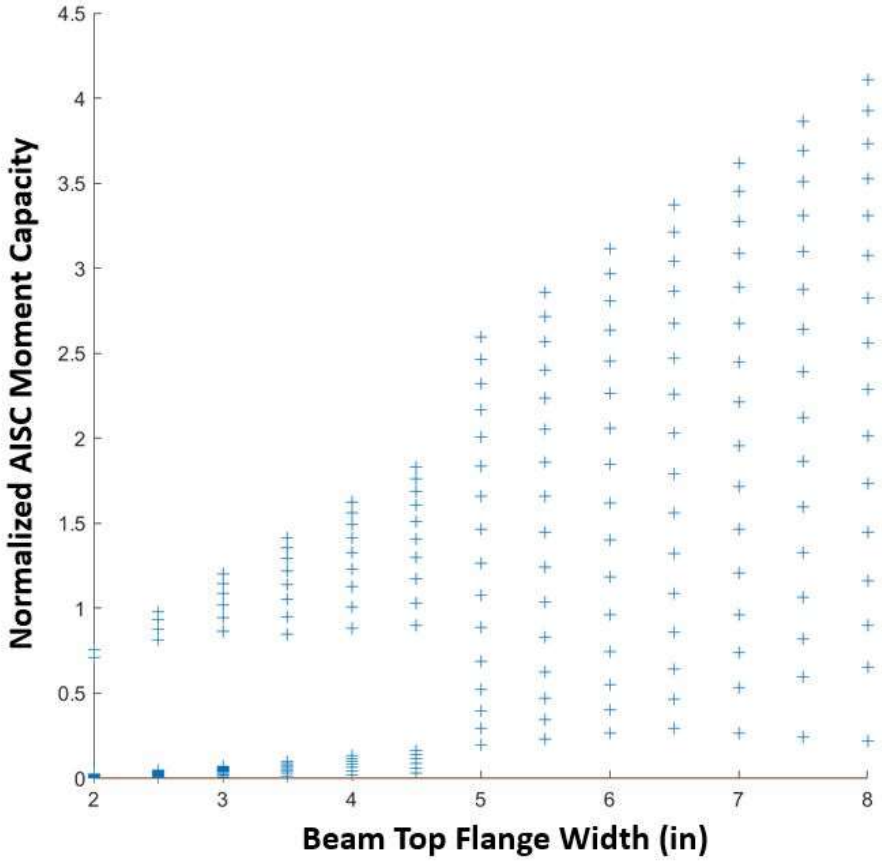

Figure 267: Scenario II: Normalized AISC moment capacity vs top flange width (b_{ft})

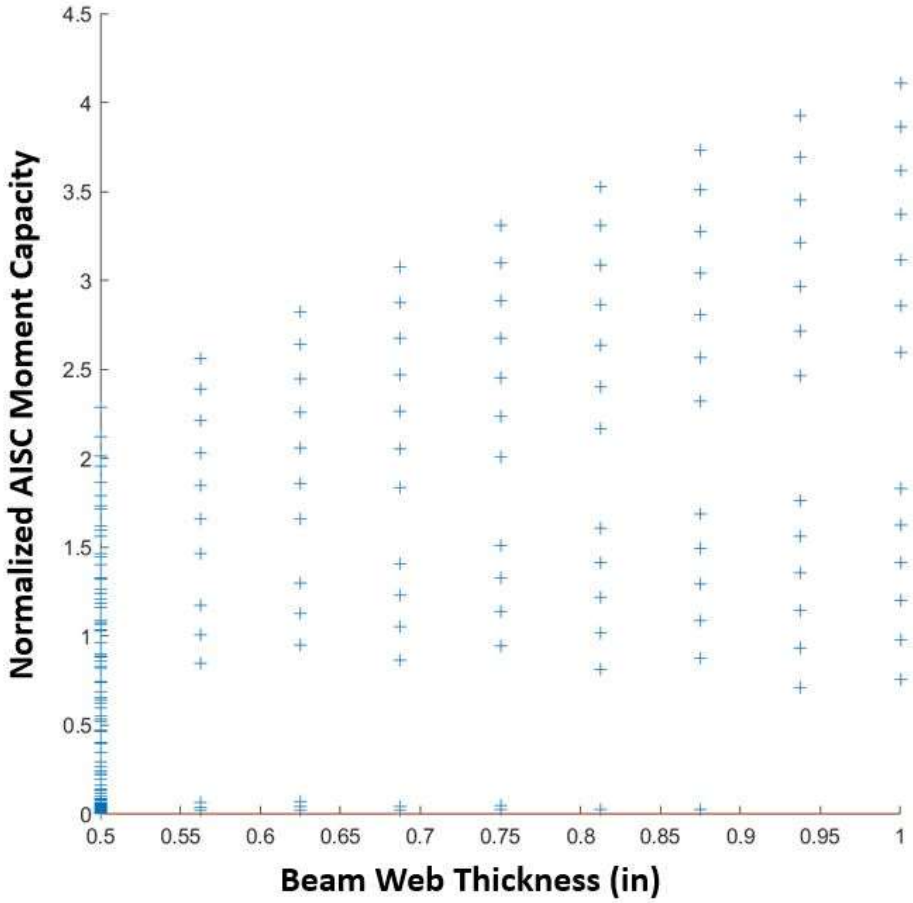

Figure 268: Scenario II: Normalized AISC moment capacity vs web thickness (t_w)

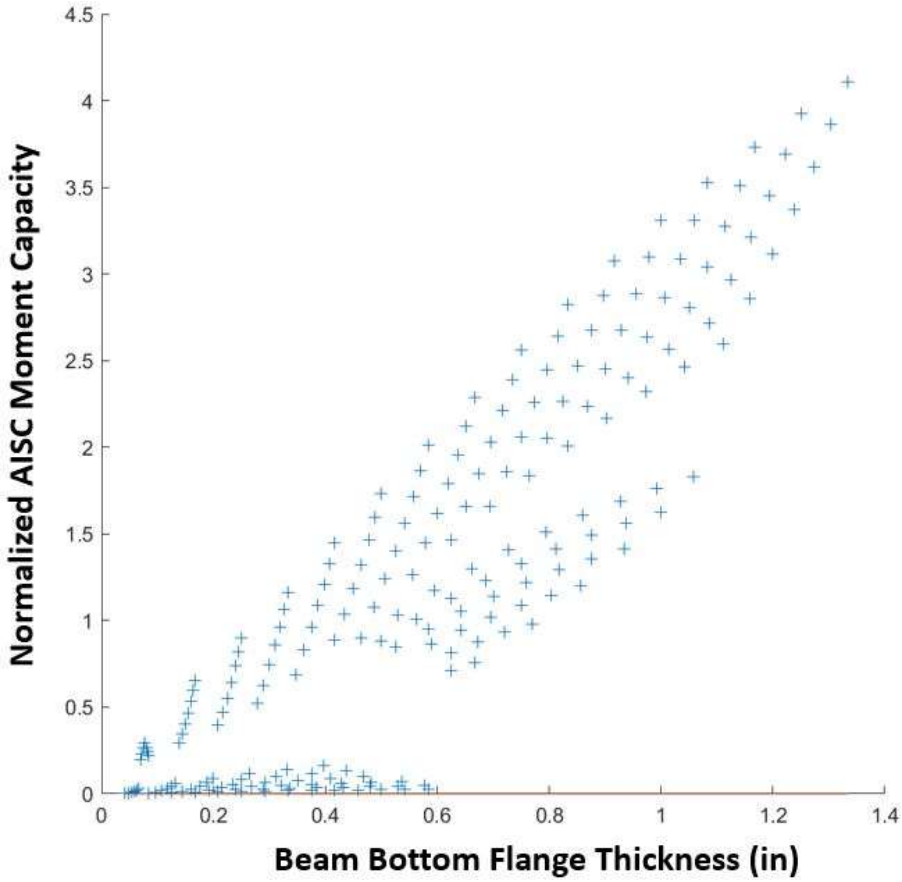

Figure 269: Scenario II: Normalized AISC moment capacity vs bottom flange thickness (t_{fb})

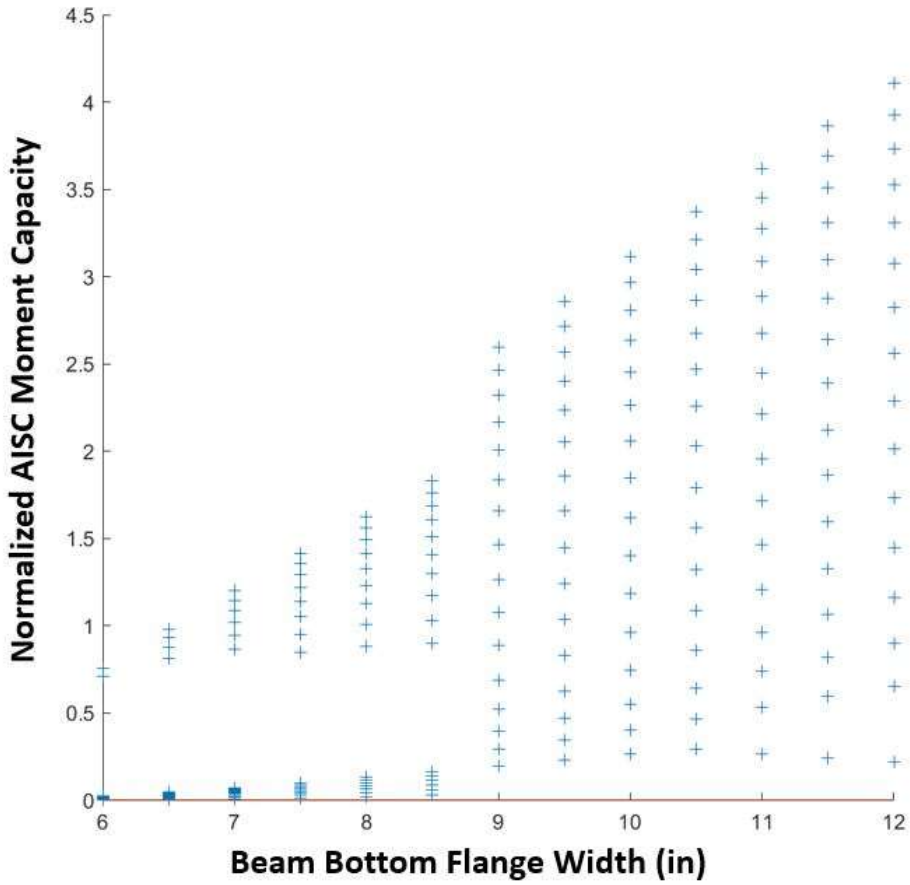

Figure 270: Scenario II: Normalized AISC moment capacity vs bottom flange width (b_{fb})

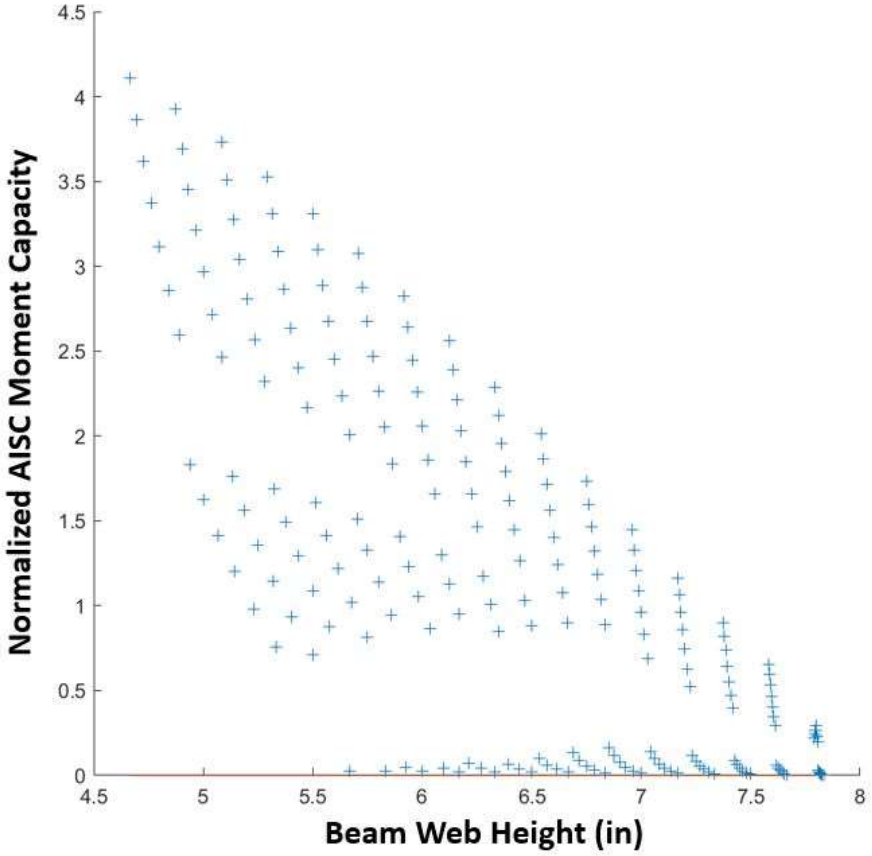

Figure 271: Scenario II: Normalized AISC moment capacity vs web height

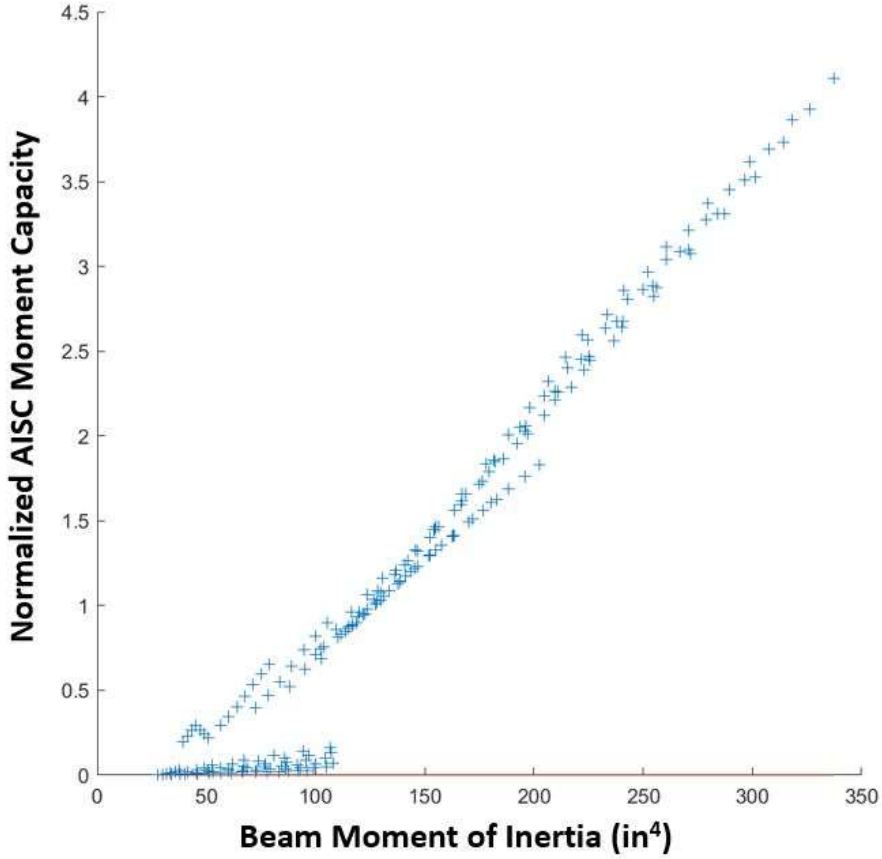

Figure 272: Scenario II: Normalized AISC moment capacity vs moment of inertia (I_x)

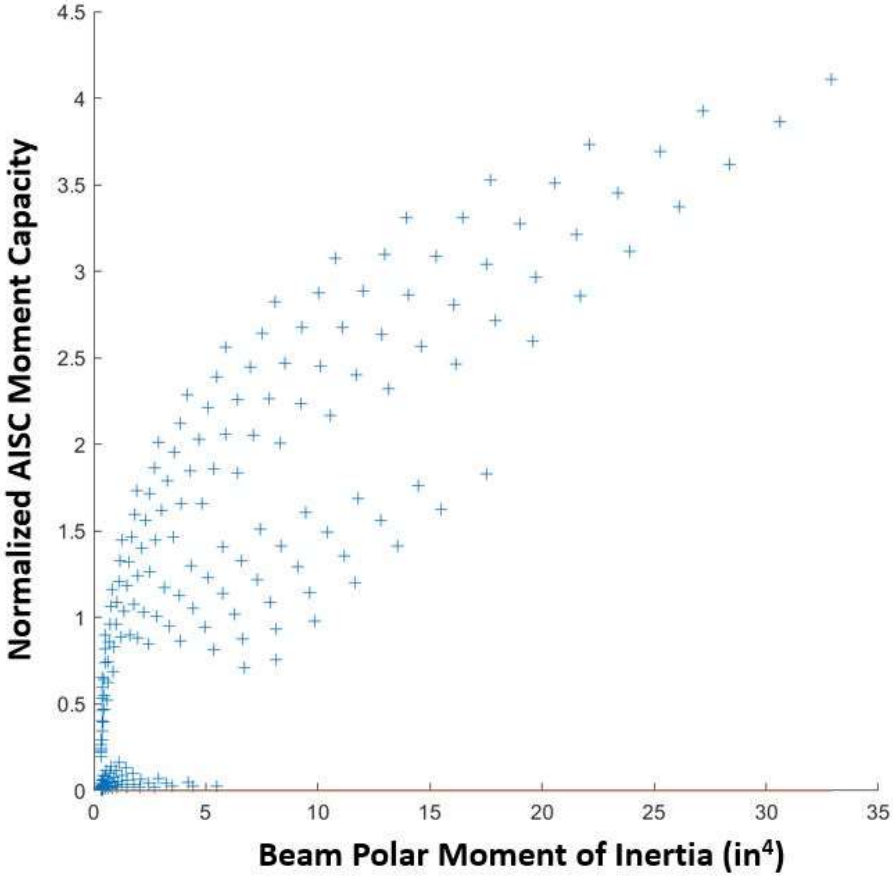

Figure 273: Scenario II: Normalized AISC moment capacity vs polar moment of inertia (*J*)

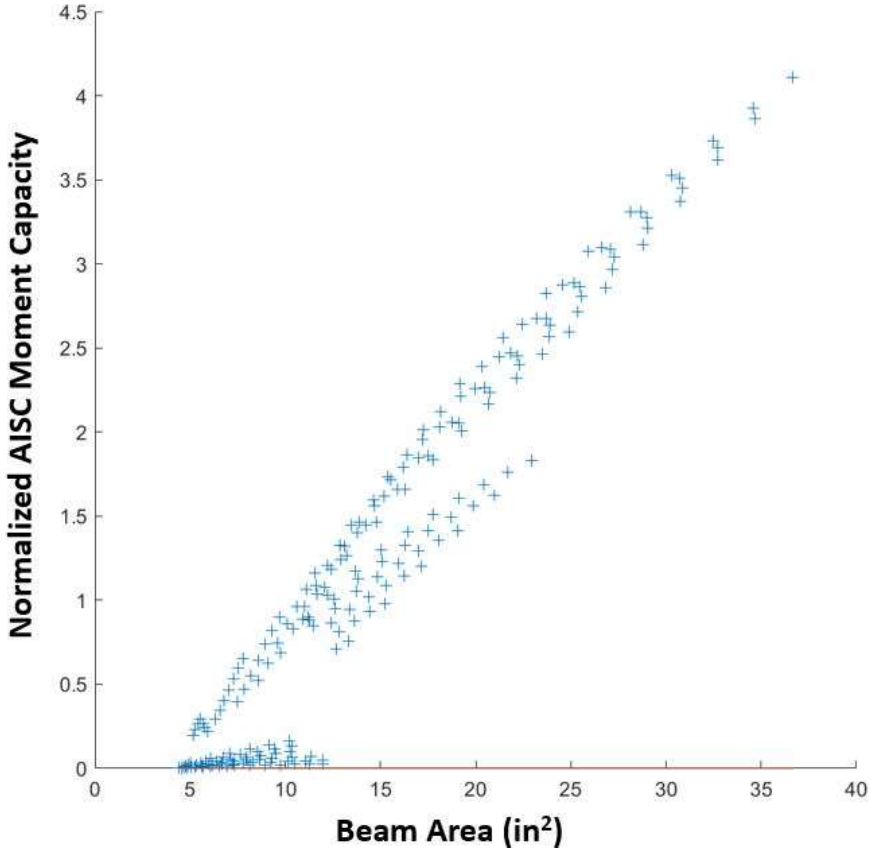

Figure 274: Scenario II: Normalized AISC moment capacity vs cross-sectional area

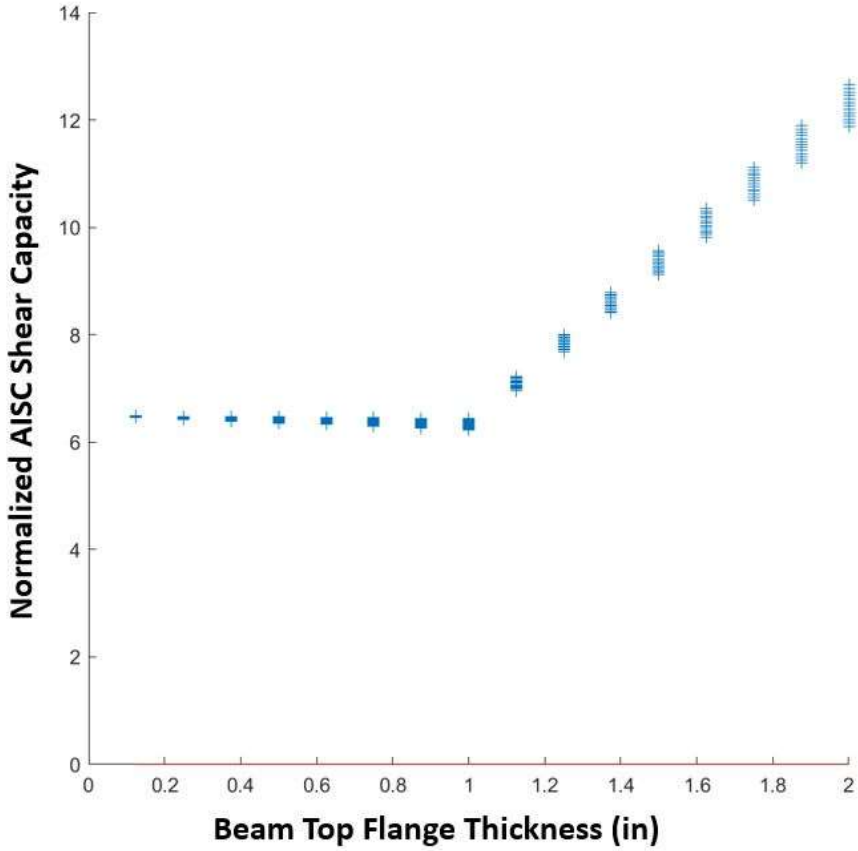

Figure 275: Scenario II: Normalized AISC shear capacity vs top flange thickness (t_{ft})

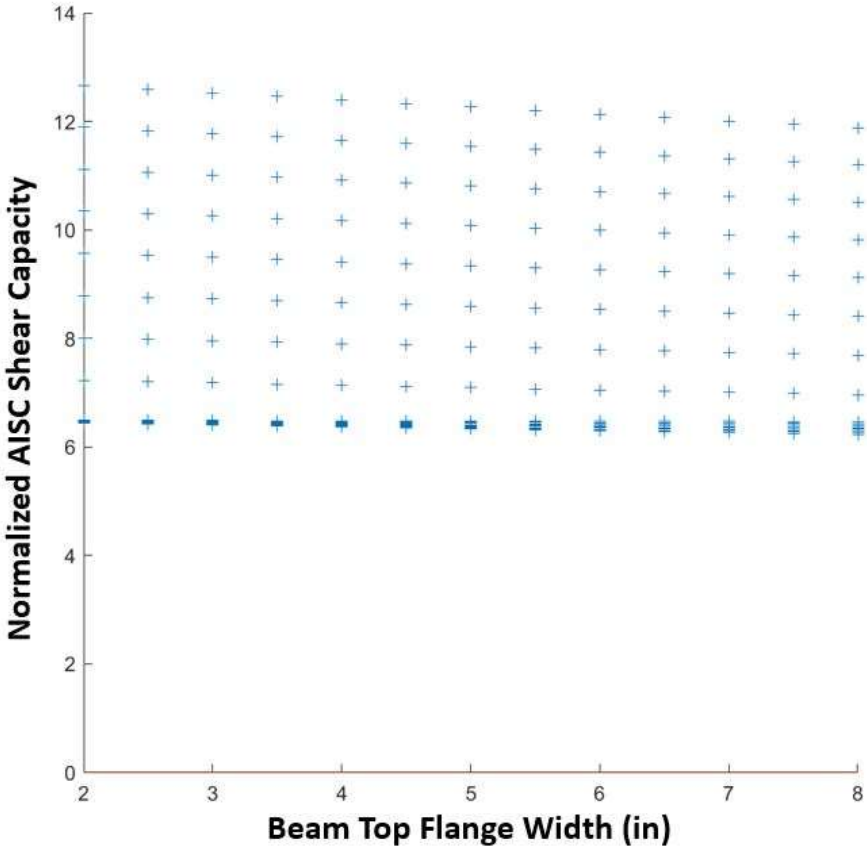

Figure 276: Scenario II: Normalized AISC shear capacity vs top flange width (b_{ft})

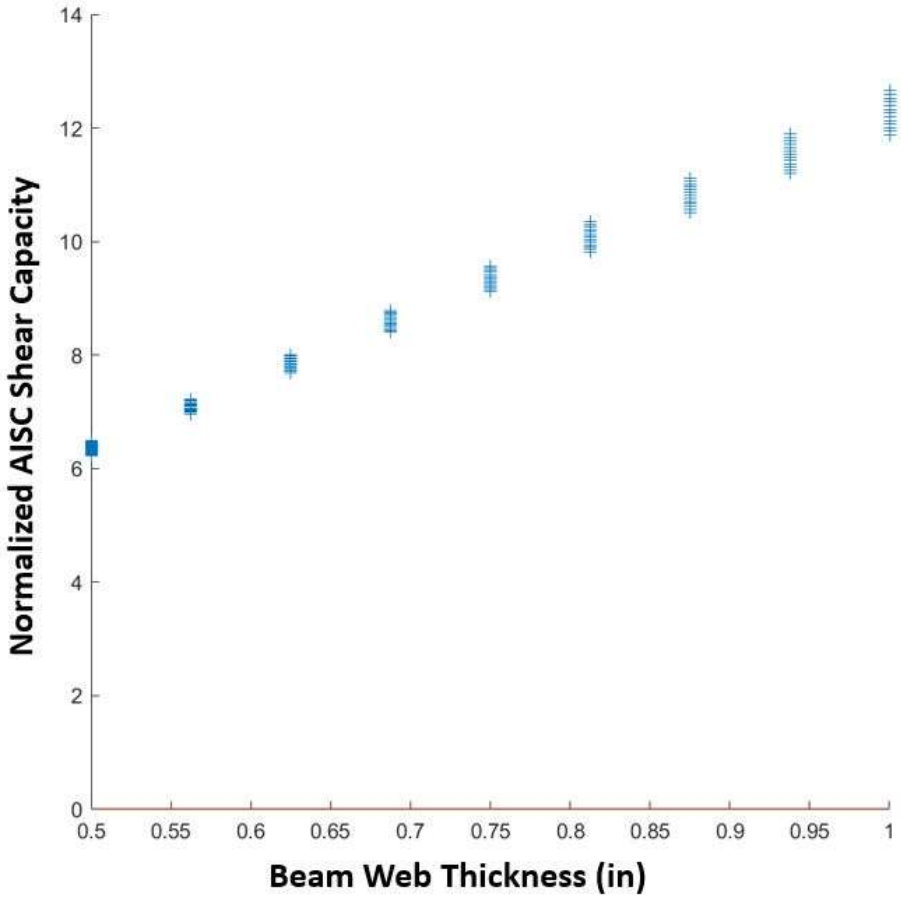

Figure 277: Scenario II: Normalized AISC shear capacity vs web thickness (t_w)

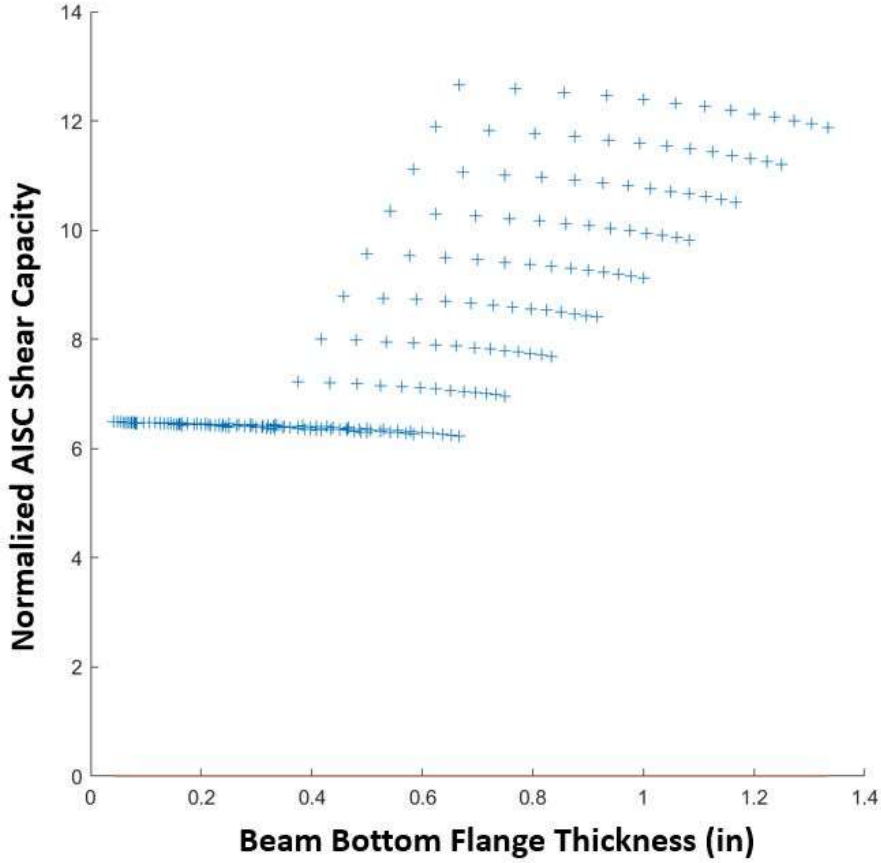

Figure 278: Scenario II: Normalized AISC shear capacity vs bottom flange thickness (t_{fb})

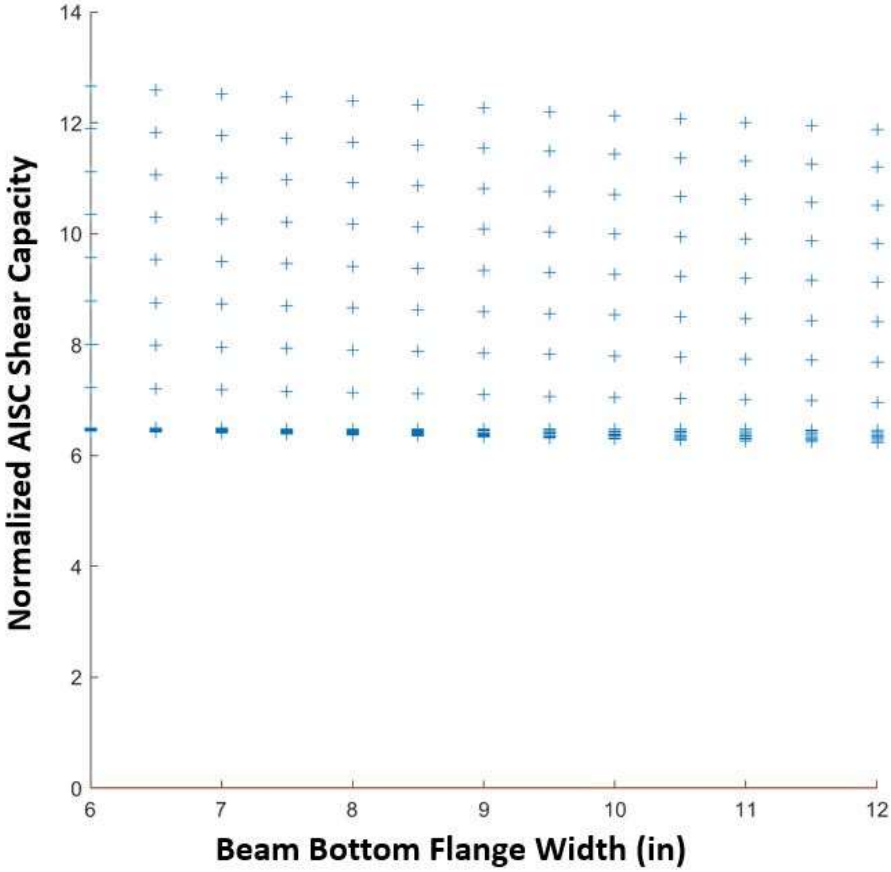

Figure 279: Scenario II: Normalized AISC shear capacity vs bottom flange width (b_{fb})

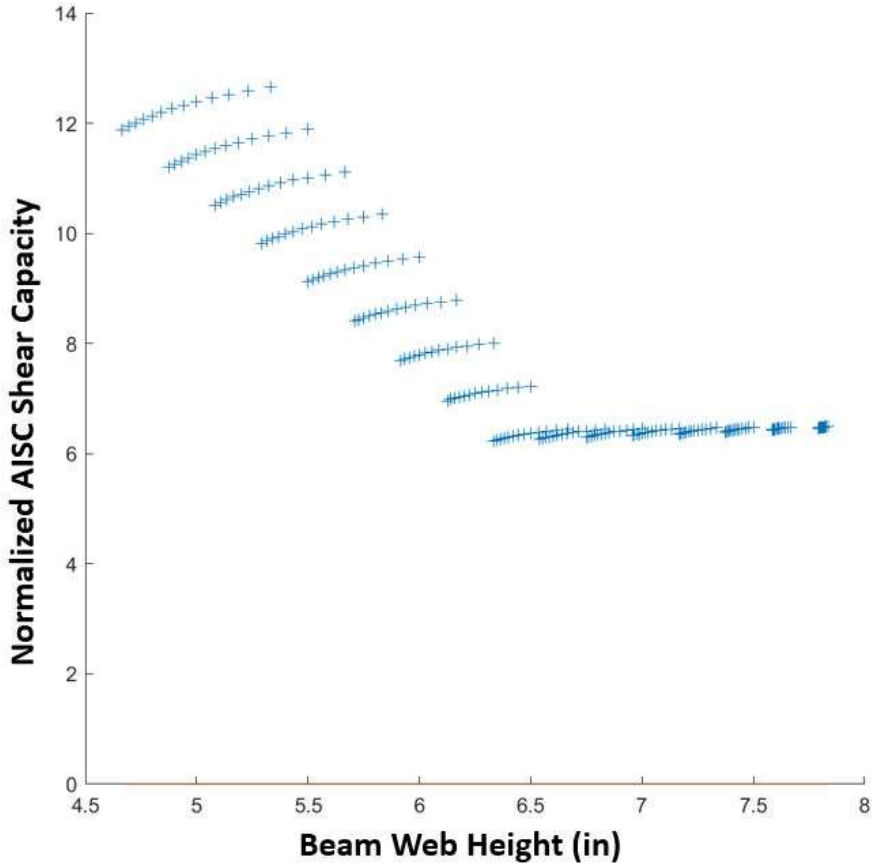

Figure 280: Scenario II: Normalized AISC shear capacity vs web height

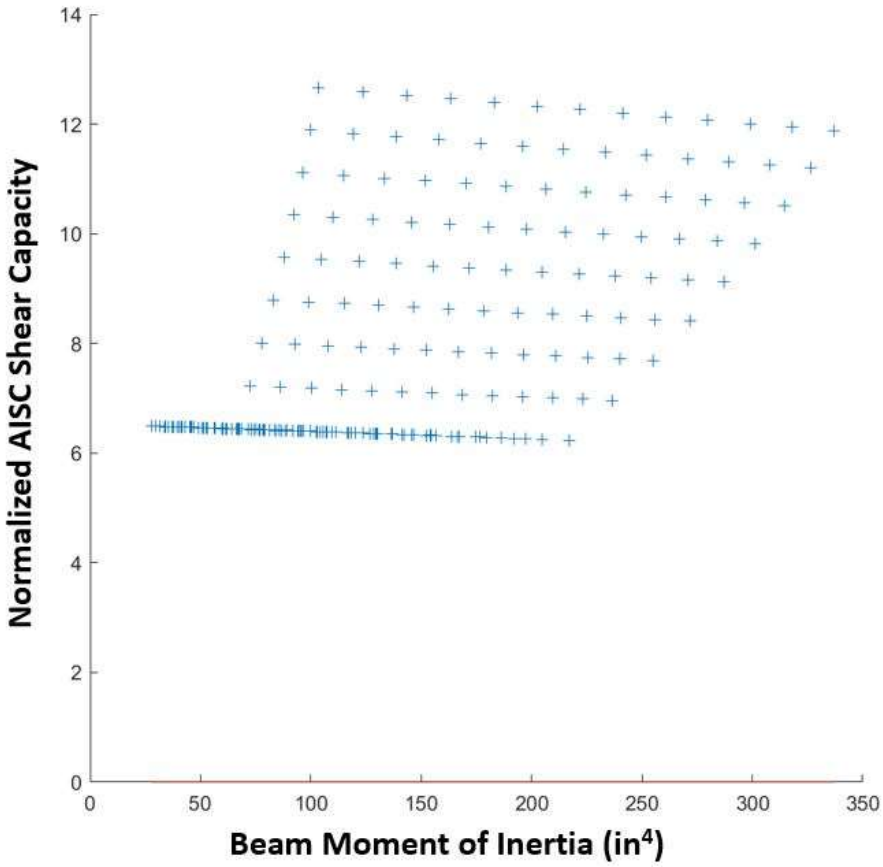

Figure 281: Scenario II: Normalized AISC shear capacity vs moment of inertia (I_x)

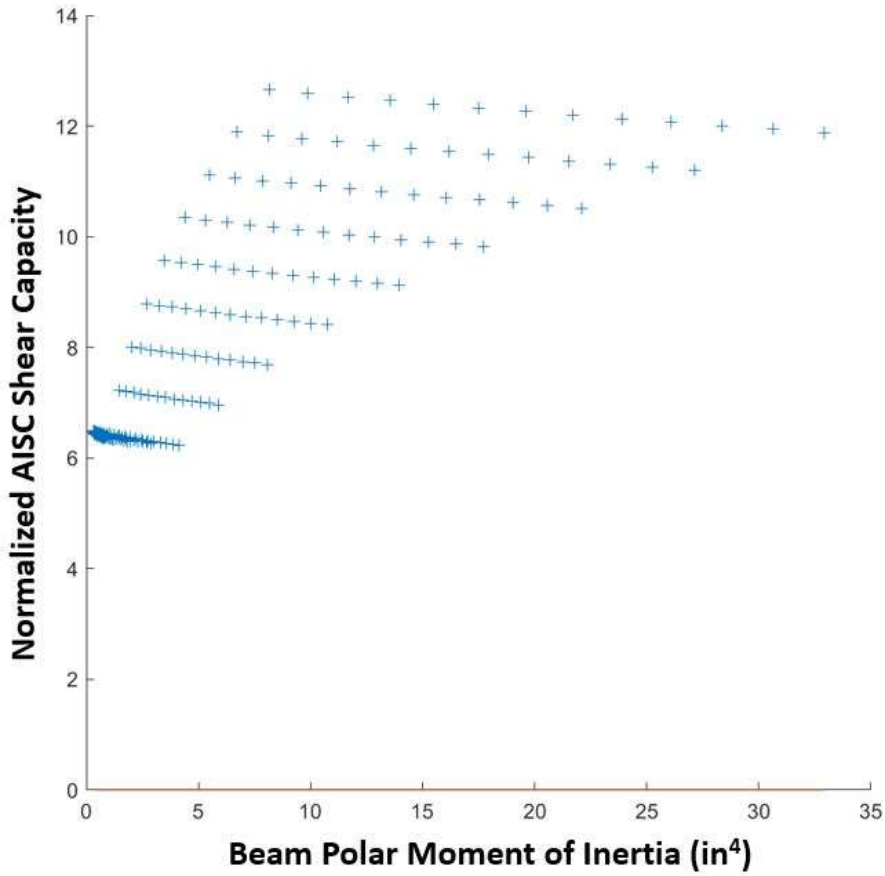

Figure 282: Scenario II: Normalized AISC shear capacity vs polar moment of inertia (*J*)

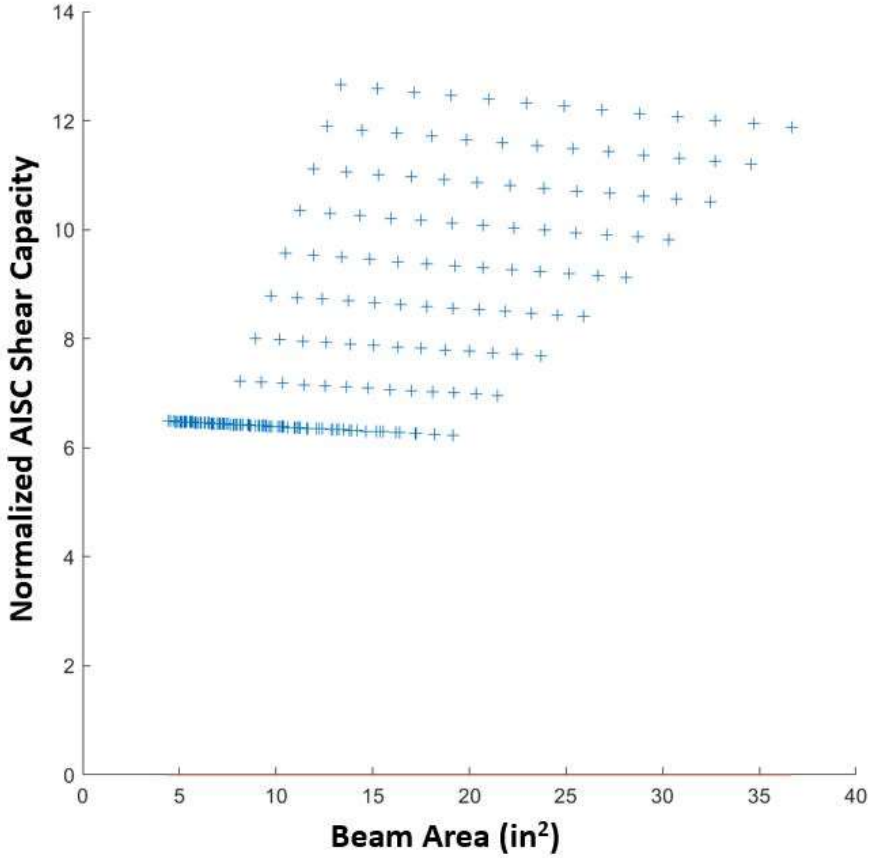

Figure 283: Scenario II: Normalized AISC shear capacity vs cross-sectional area

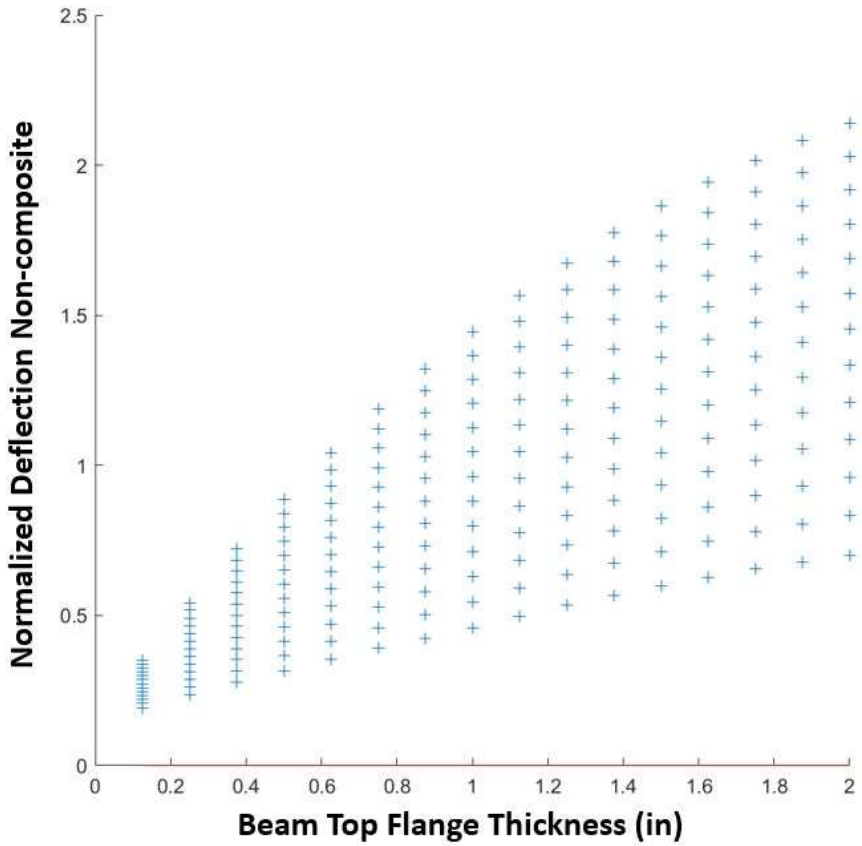

Figure 284: Scenario II: Normalized deflection non-composite vs top flange thickness (t_{ft})

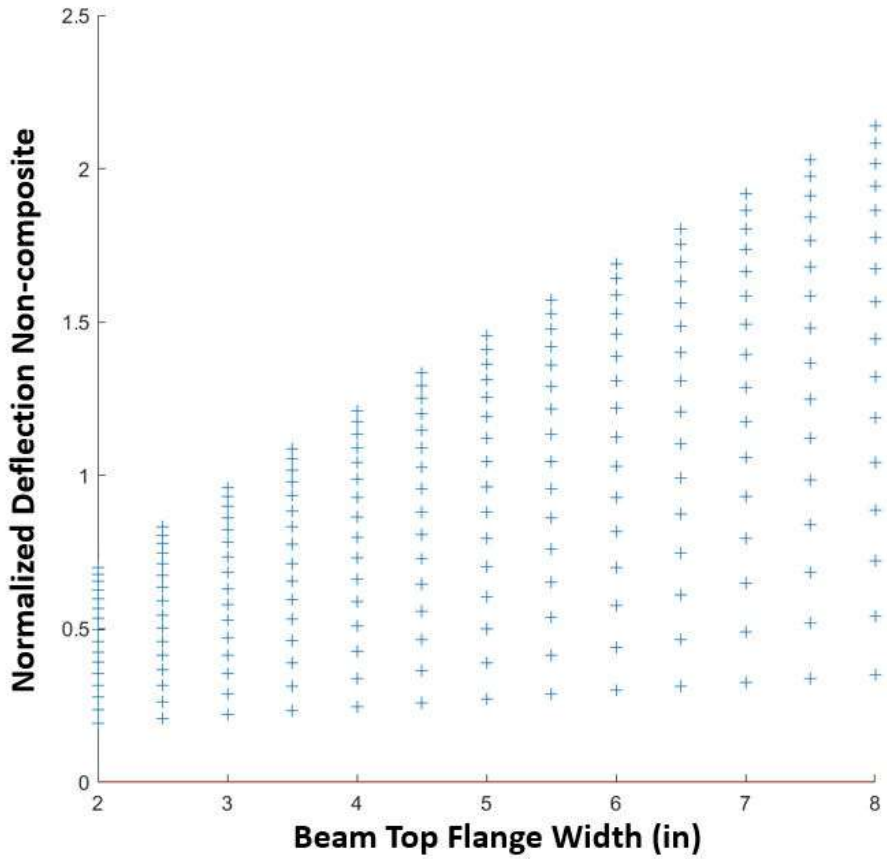

Figure 285: Scenario II: Normalized deflection non-composite vs top flange width (b_{ft})

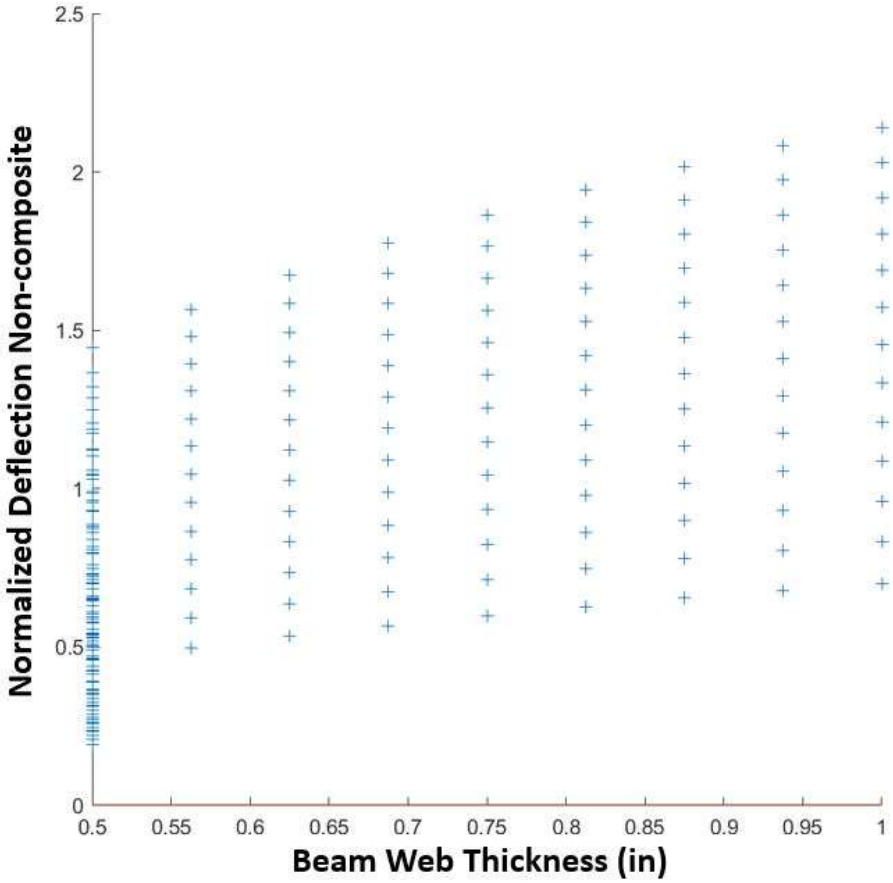

Figure 286: Scenario II: Normalized deflection non-composite vs web thickness (t_w)

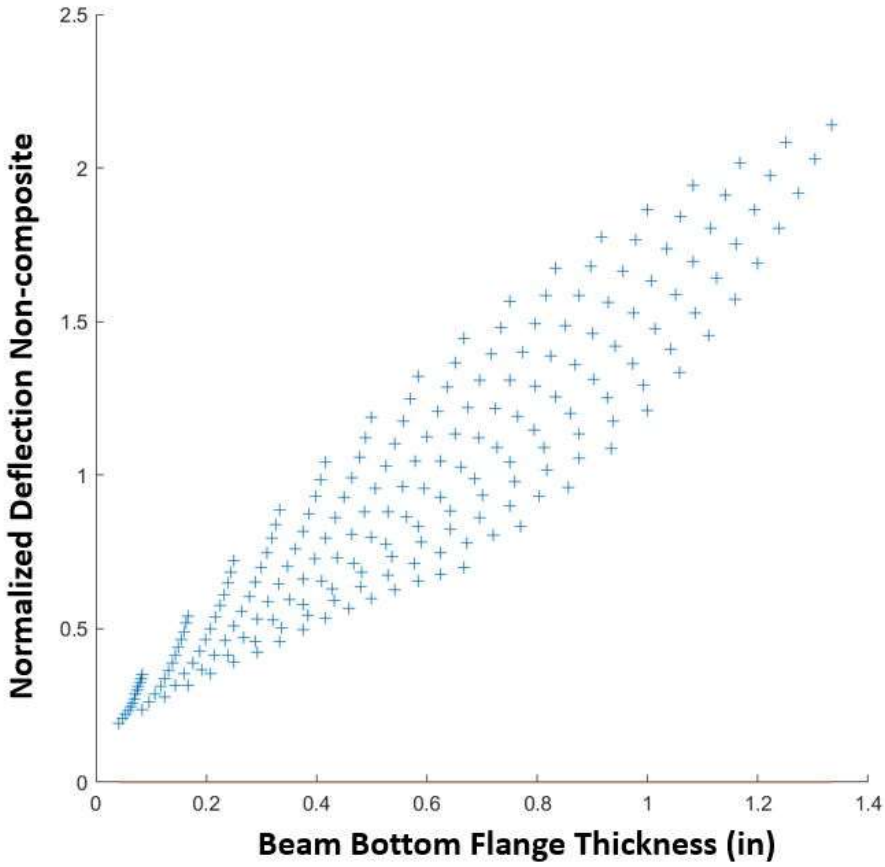

Figure 287: Scenario II: Normalized deflection non-composite vs bottom flange thickness (t_{fb})

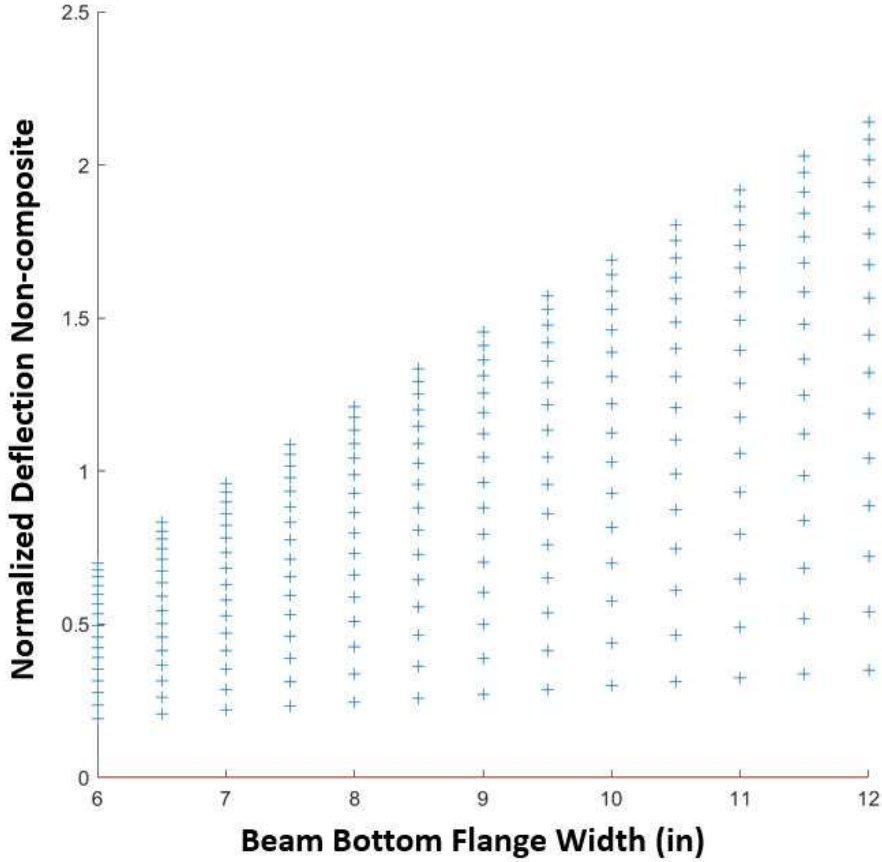

Figure 288: Scenario II: Normalized deflection non-composite vs bottom flange width (b_{fb})

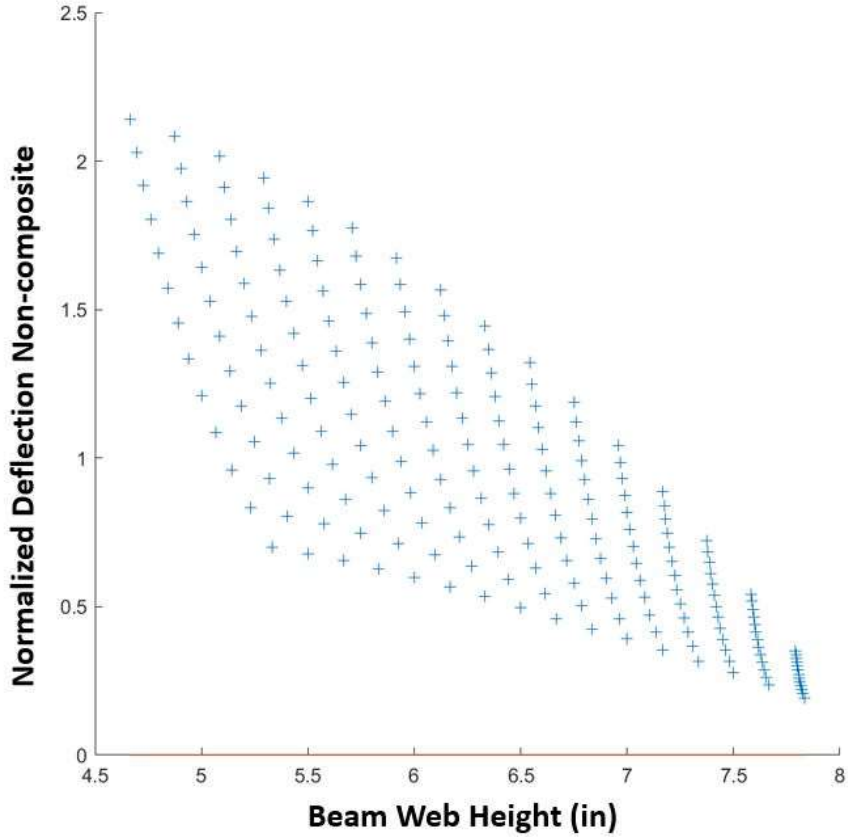

Figure 289: Scenario II: Normalized deflection non-composite vs web height

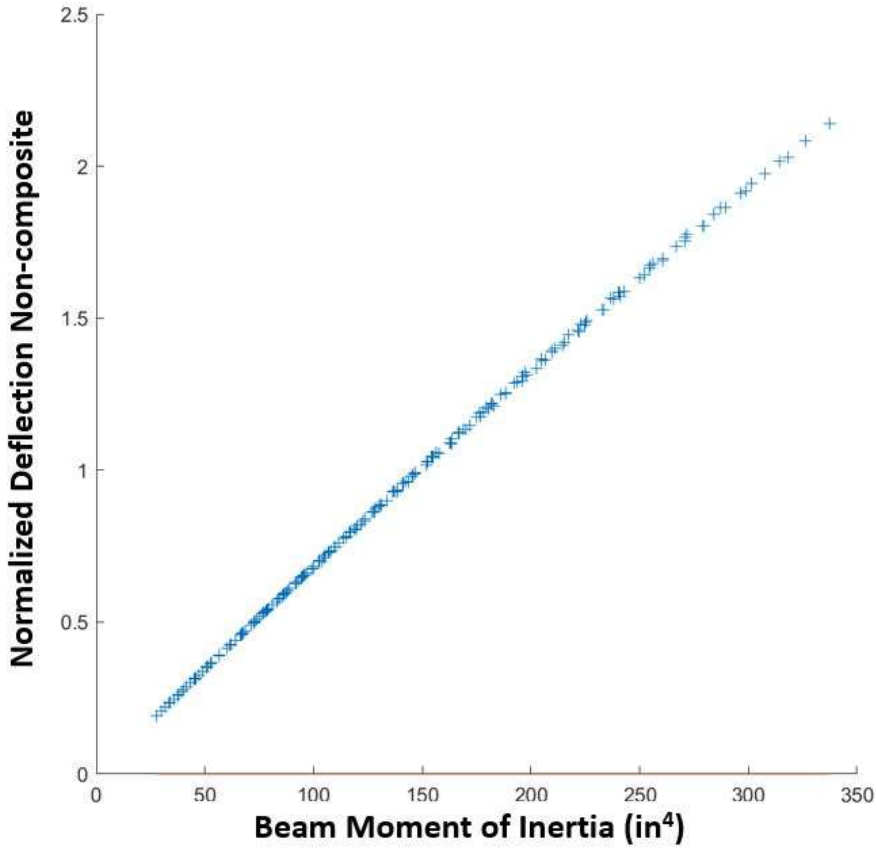

Figure 290: Scenario II: Normalized deflection non-composite vs moment of inertia (I_x)

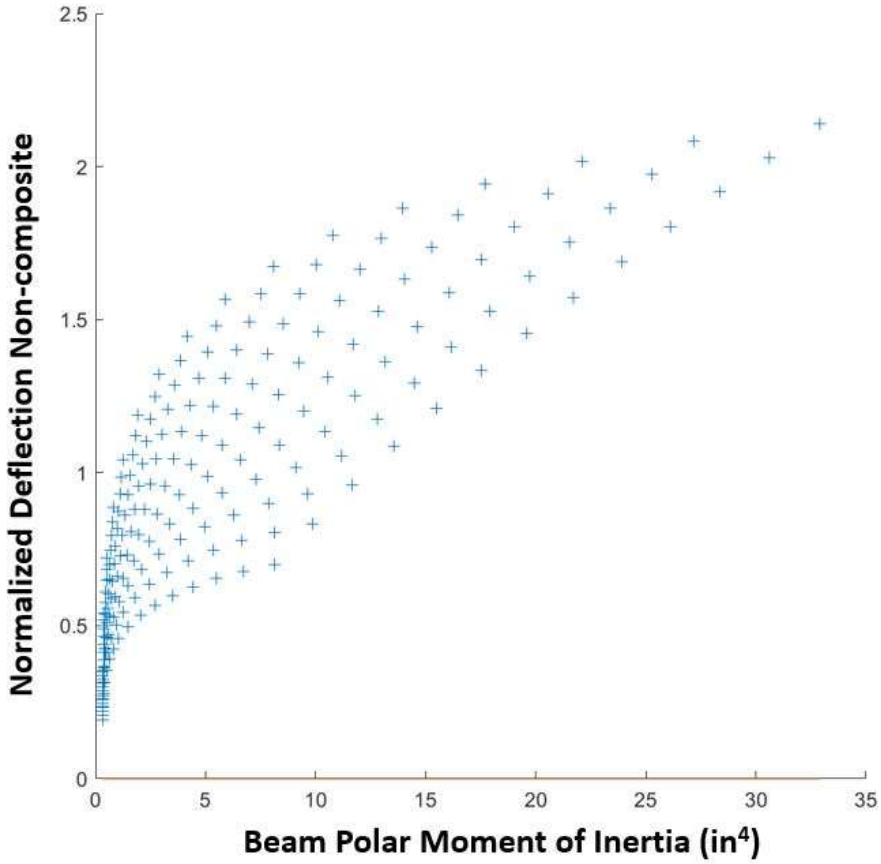

Figure 291: Scenario II: Normalized deflection non-composite vs polar moment of inertia (*J*)

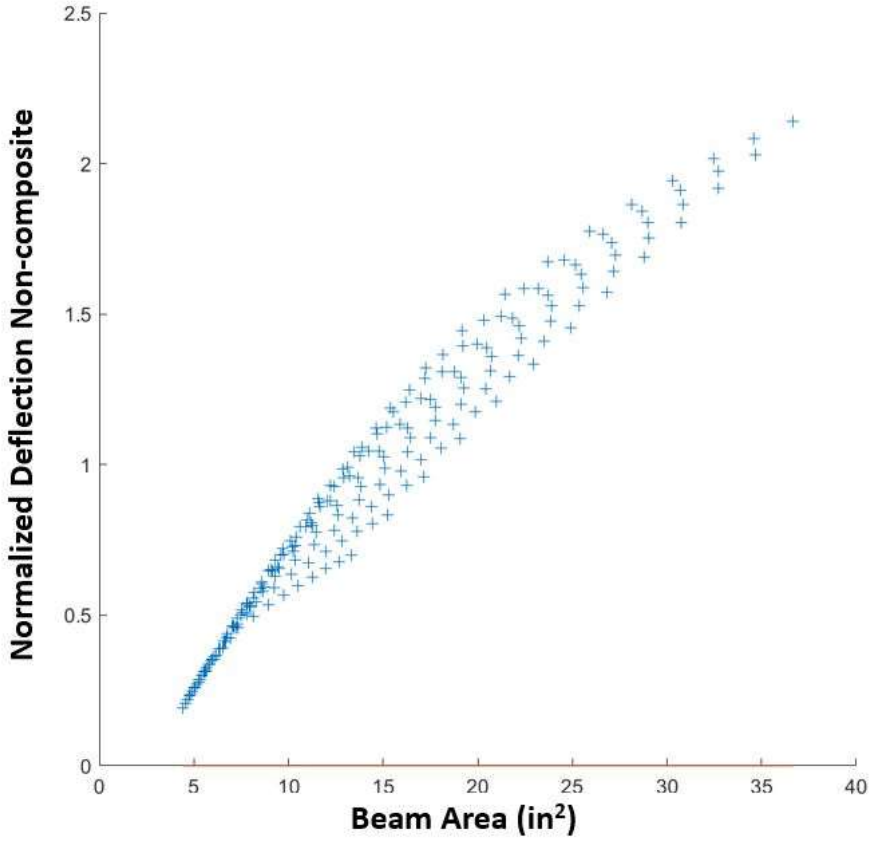

Figure 292: Scenario II: Normalized deflection non-composite vs cross-sectional area

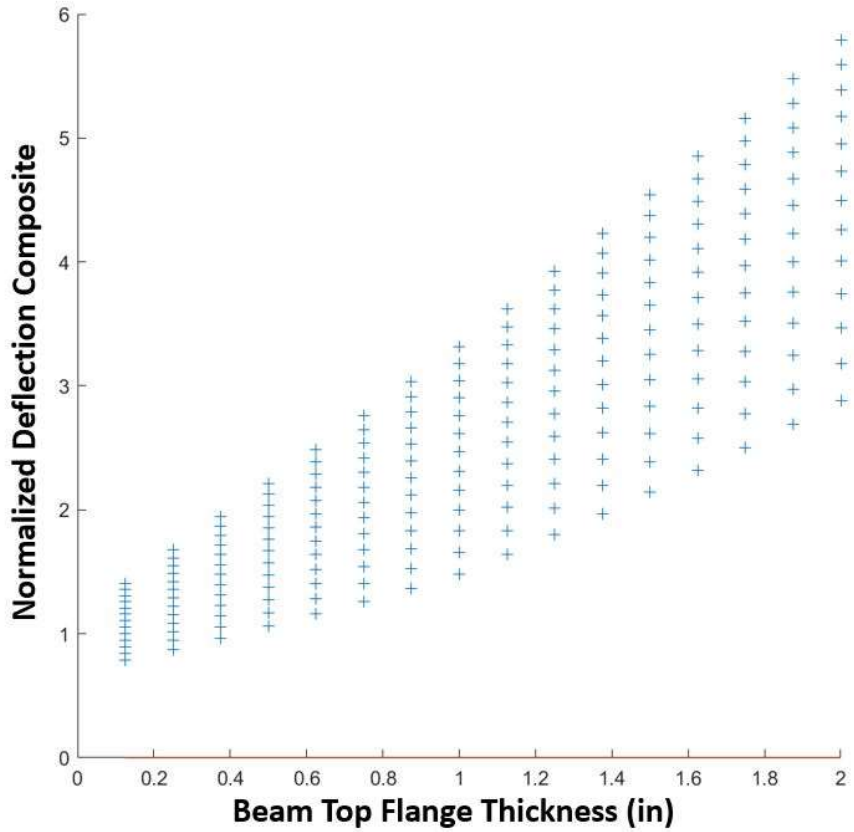

Figure 293: Scenario III: Normalized deflection composite vs top flange thickness (t_{ft})

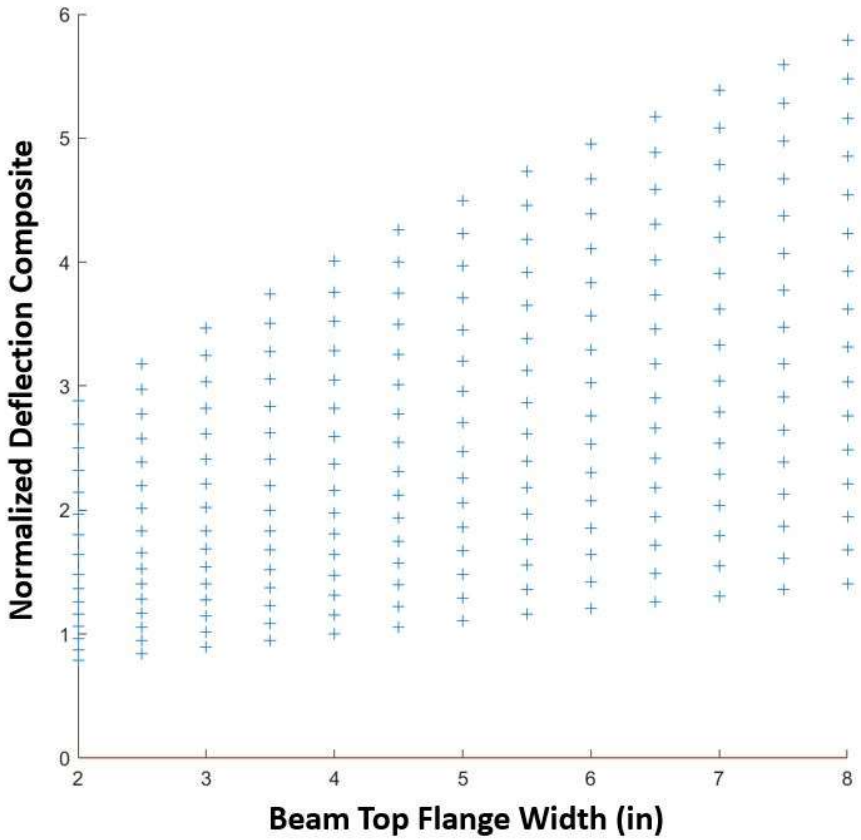

Figure 294: Scenario III: Normalized deflection composite vs top flange width (b_{ft})

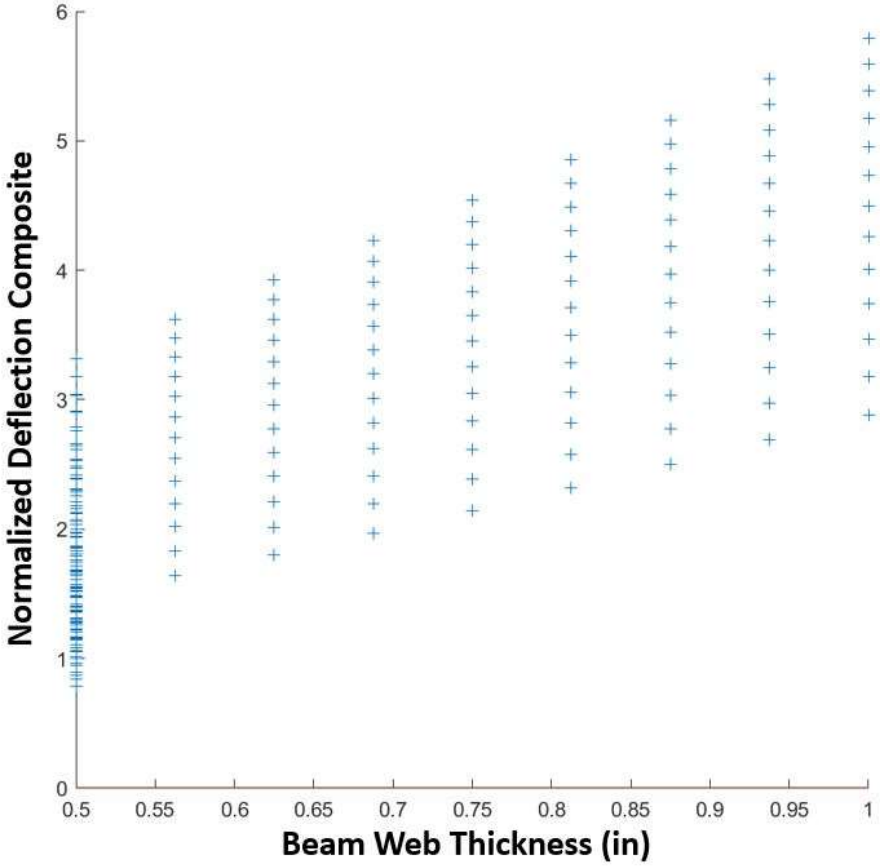

Figure 295: Scenario III: Normalized deflection composite vs web thickness (t_w)

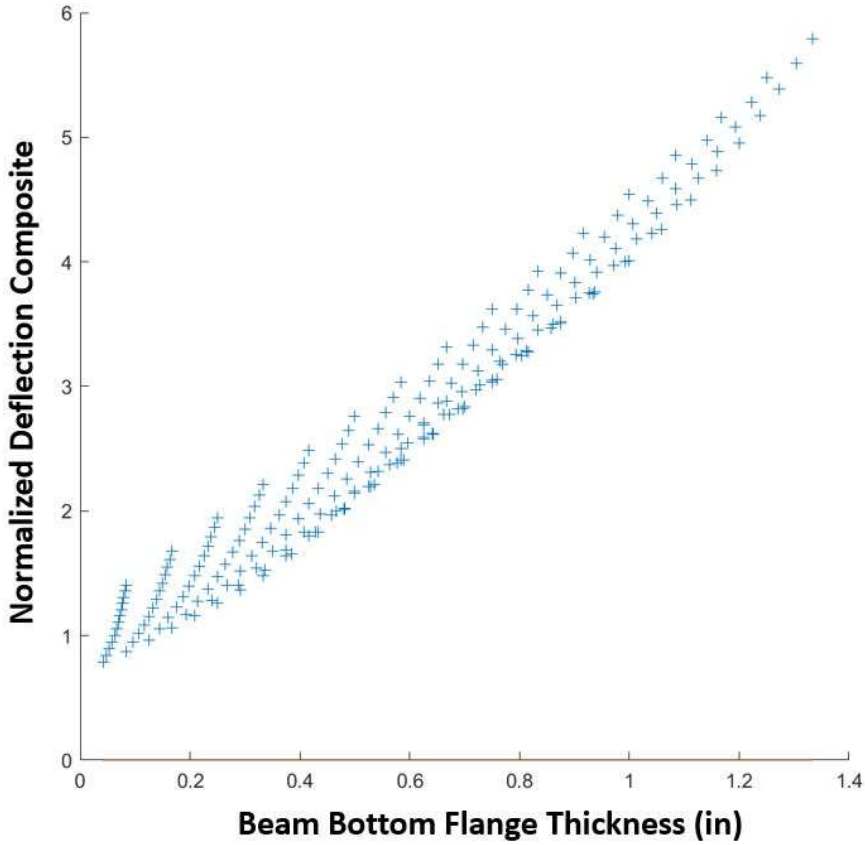

Figure 296: Scenario III: Normalized deflection composite vs bottom flange thickness (t_{fb})

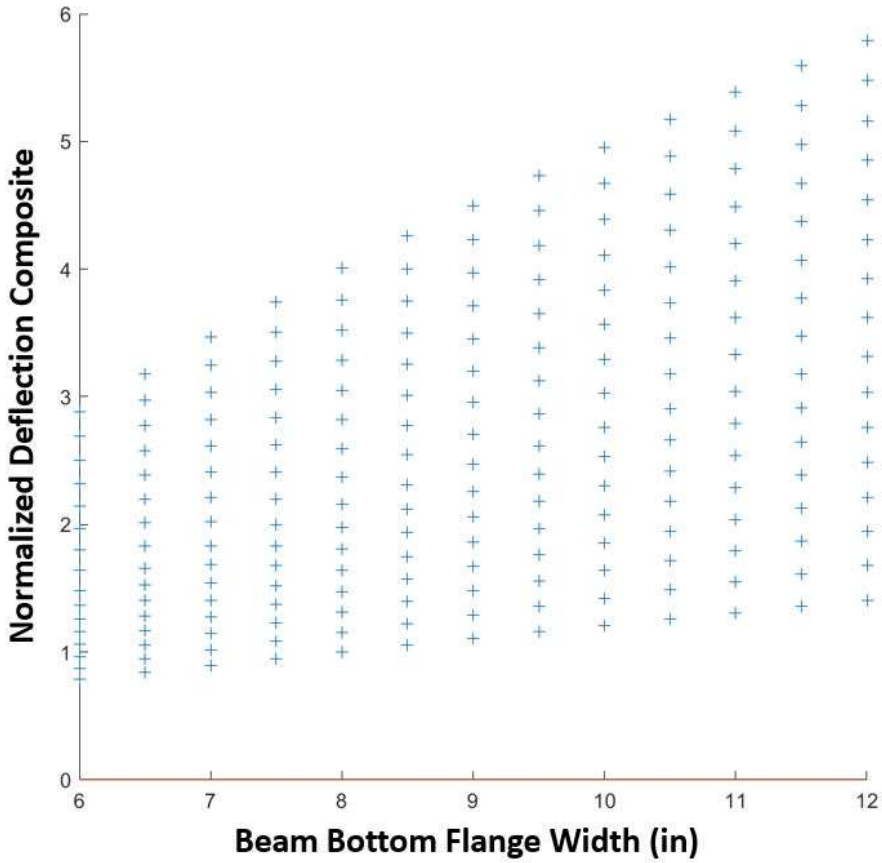

Figure 297: Scenario III: Normalized deflection composite vs bottom flange width (b_{fb})

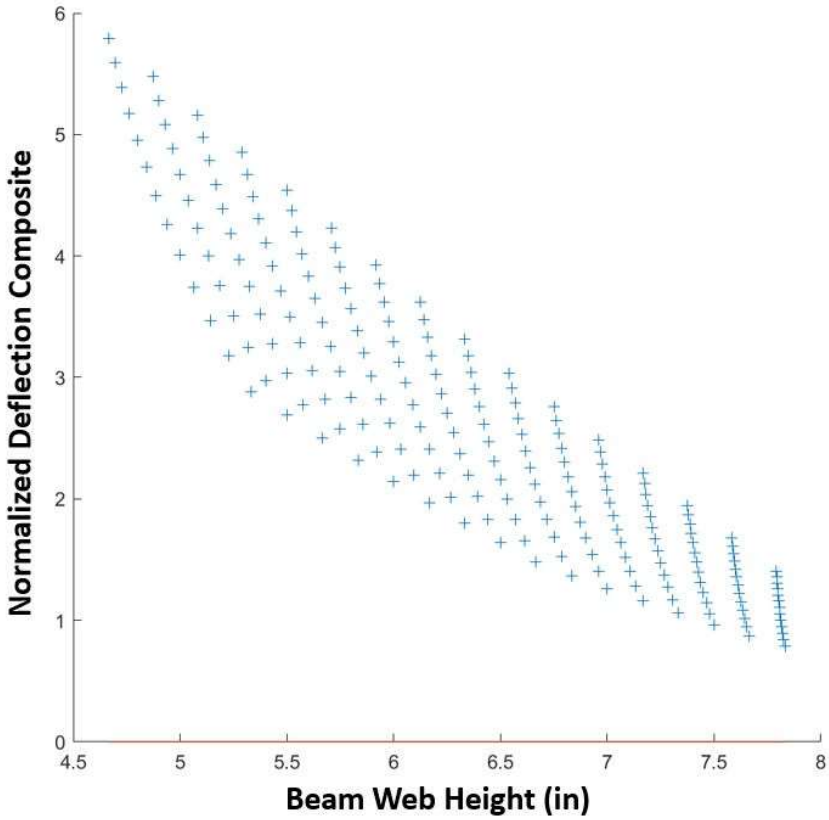

Figure 298: Scenario III: Normalized deflection composite vs web height

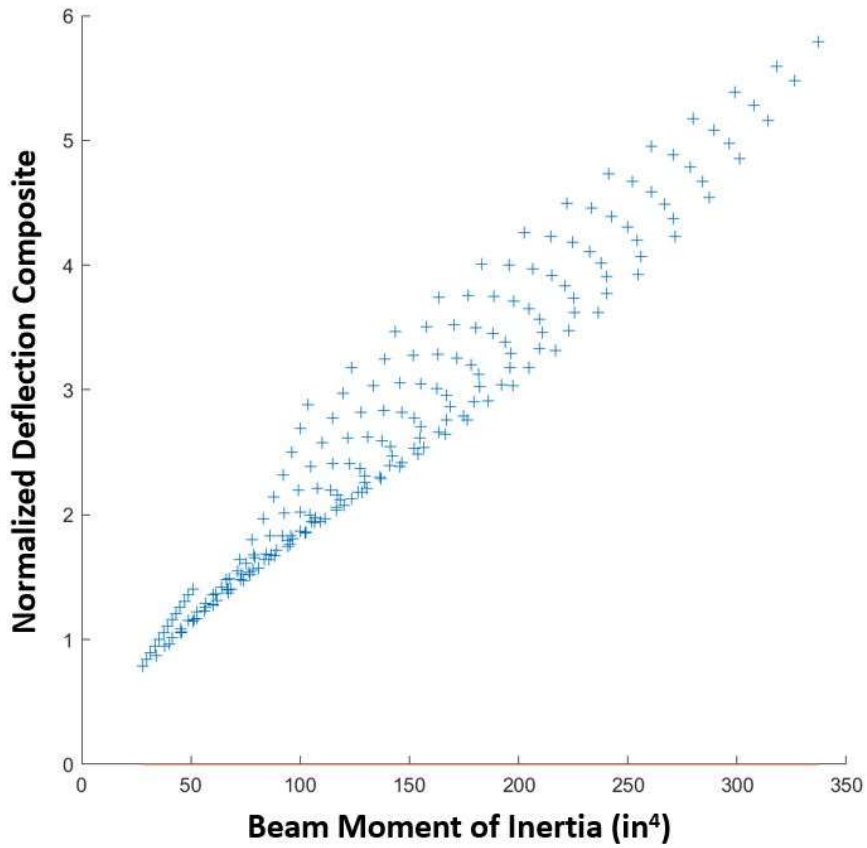

Figure 299: Scenario III: Normalized deflection composite vs moment of inertia (I_x)

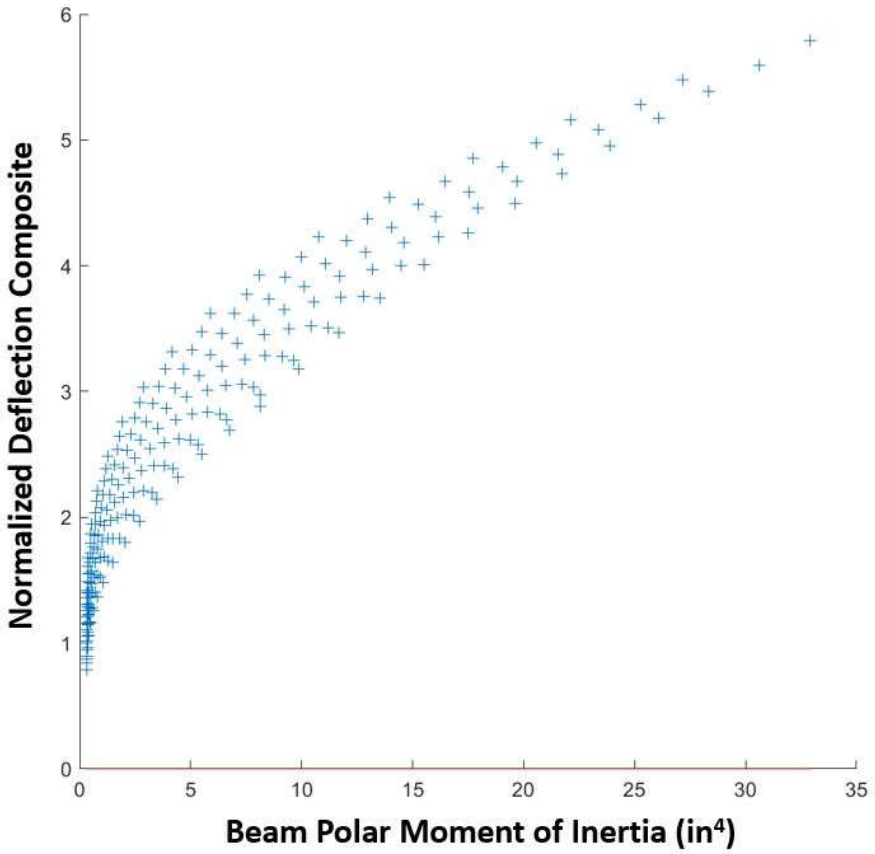

Figure 300: Scenario III: Normalized deflection composite vs polar moment of inertia (*J*)

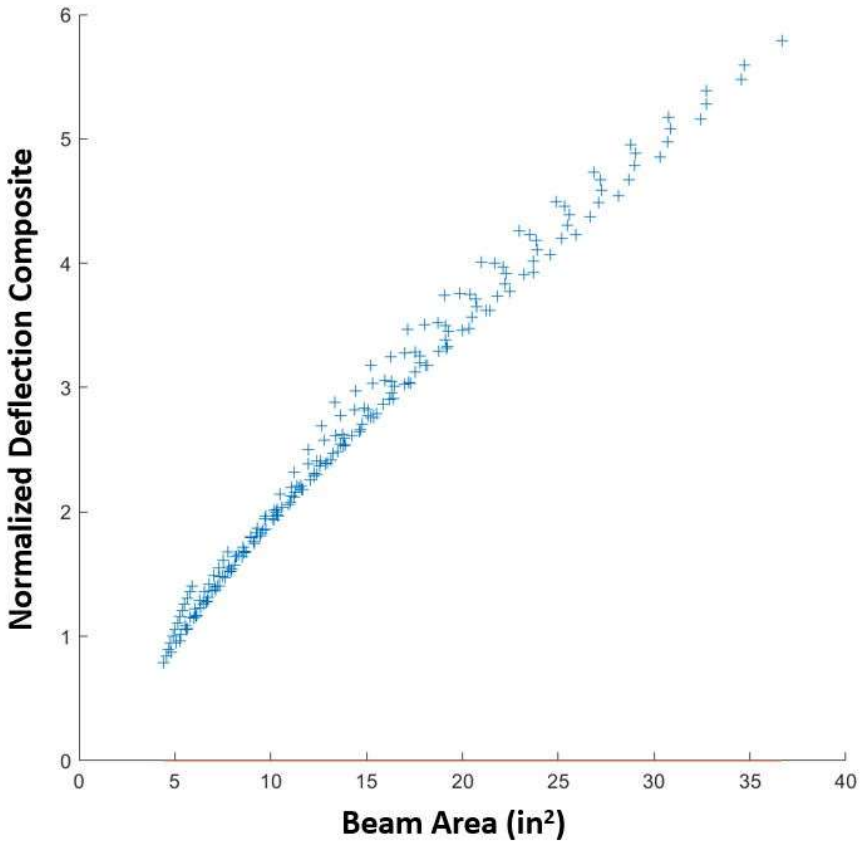

Figure 301: Scenario III: Normalized deflection composite vs cross-sectional area

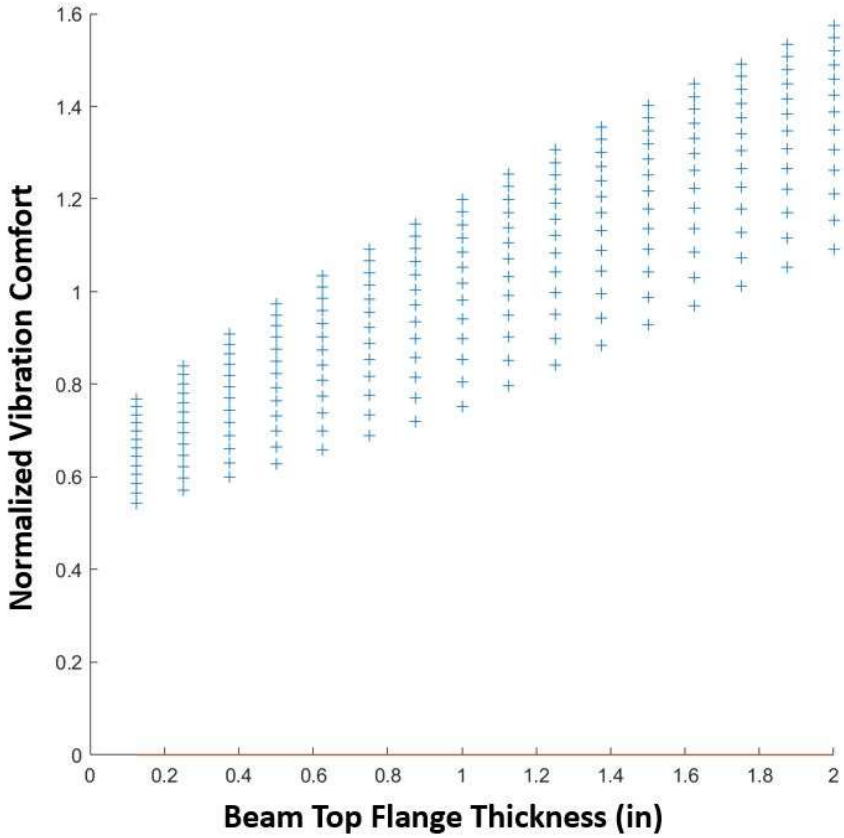

Figure 302: Scenario III: Normalized vibration comfort vs top flange thickness (t_{ft})

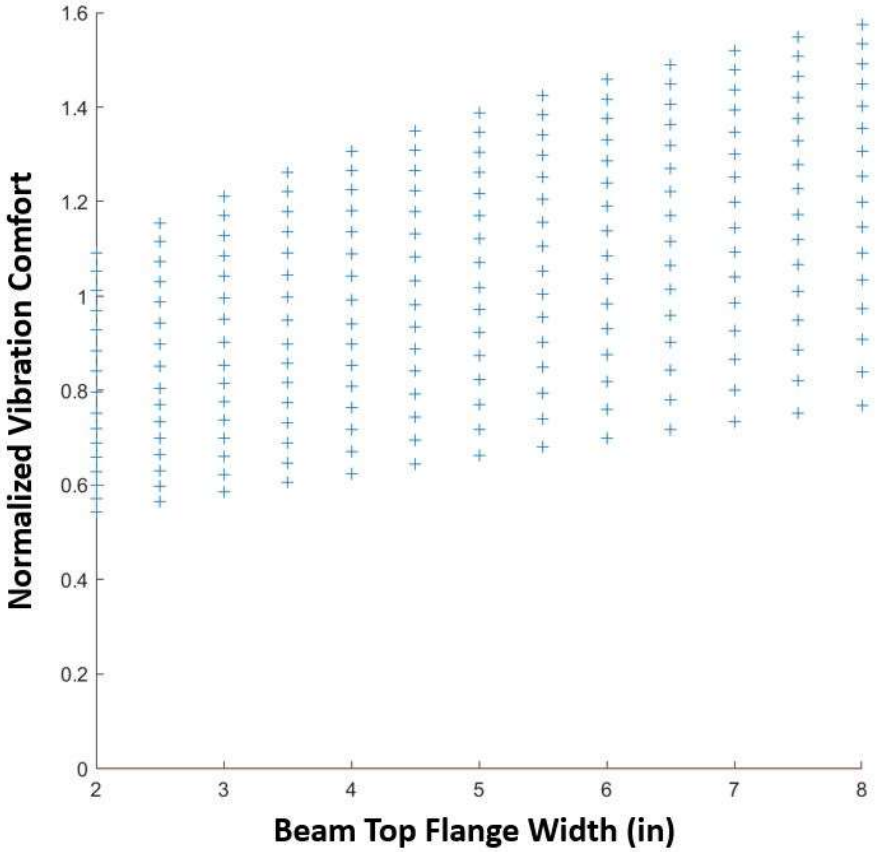

Figure 303: Scenario III: Normalized vibration comfort vs top flange width (b_{ft})

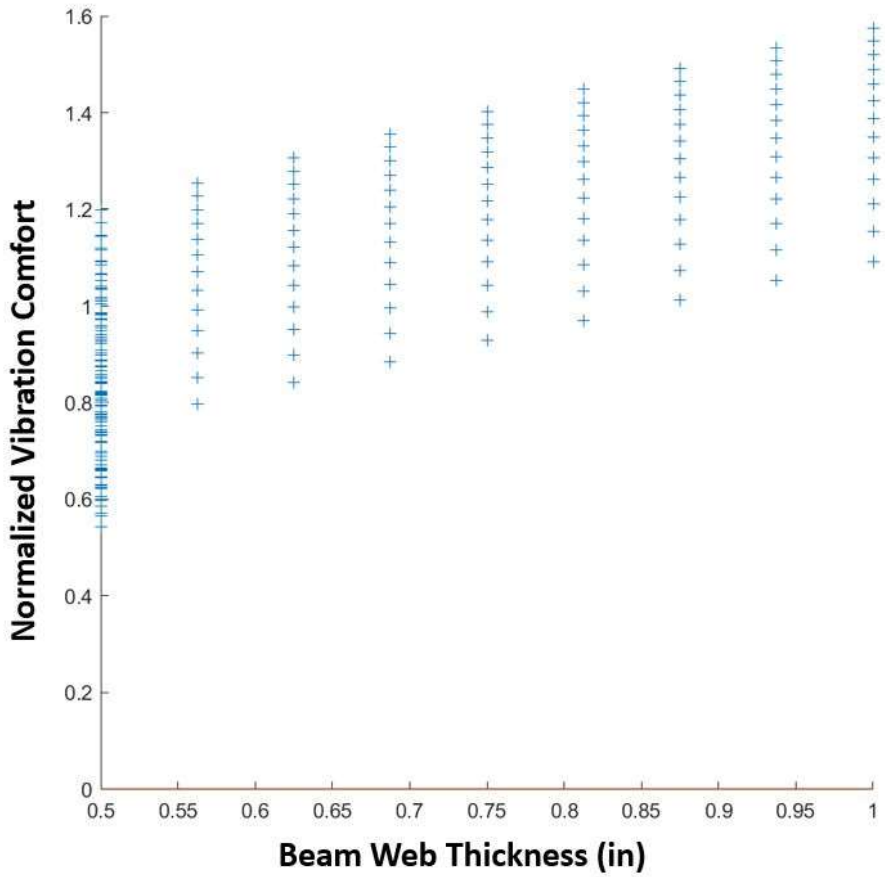

Figure 304: Scenario III: Normalized vibration comfort vs web thickness (t_w)

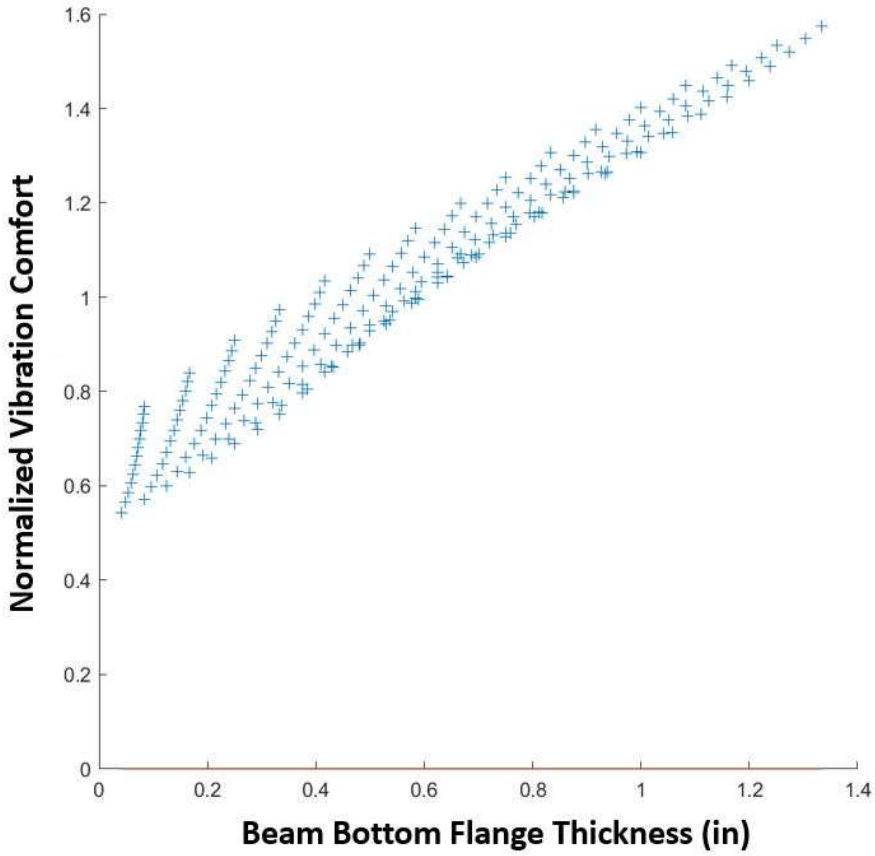

Figure 305: Scenario III: Normalized vibration comfort vs bottom flange thickness (t_{fb})

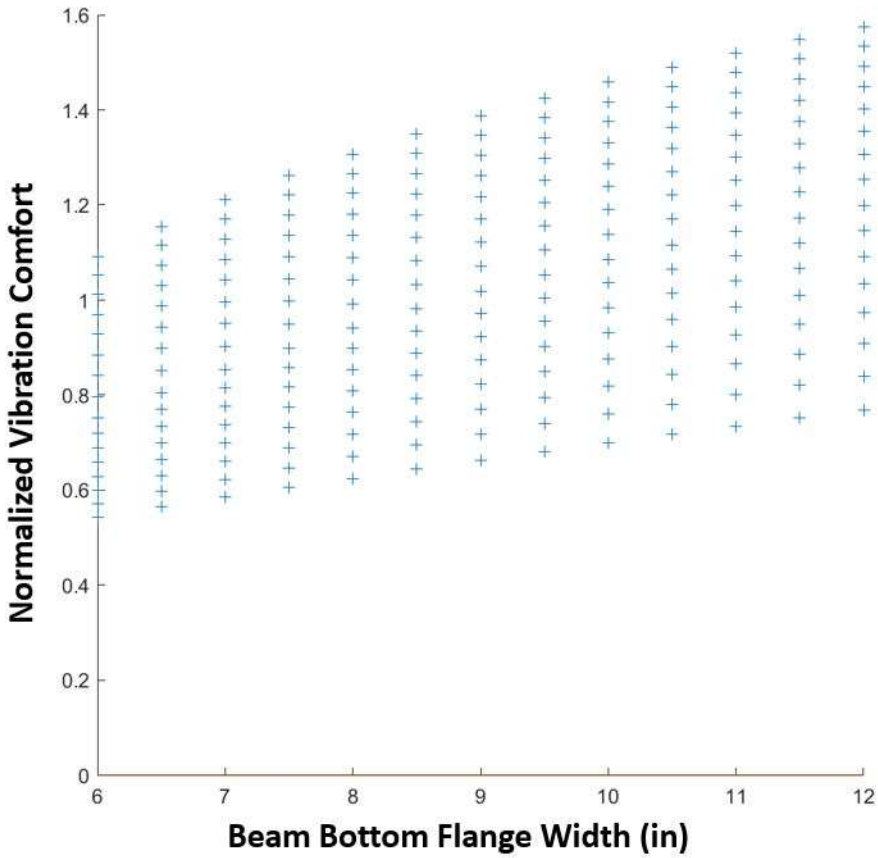

Figure 306: Scenario III: Normalized vibration comfort vs bottom flange width (b_{fb})

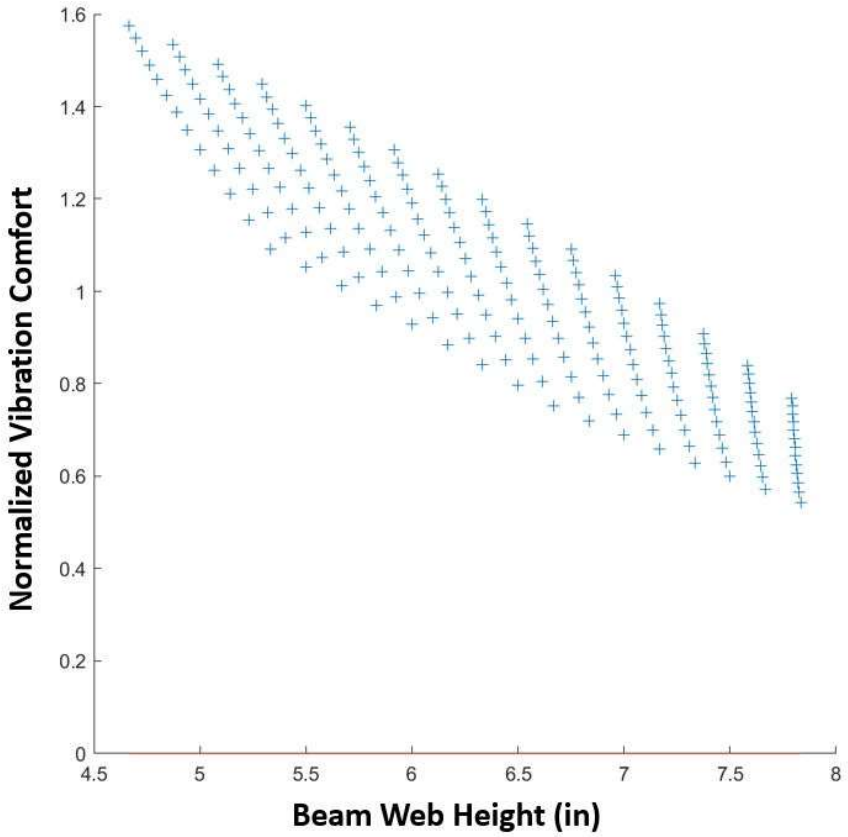

Figure 307: Scenario III: Normalized vibration comfort vs web height

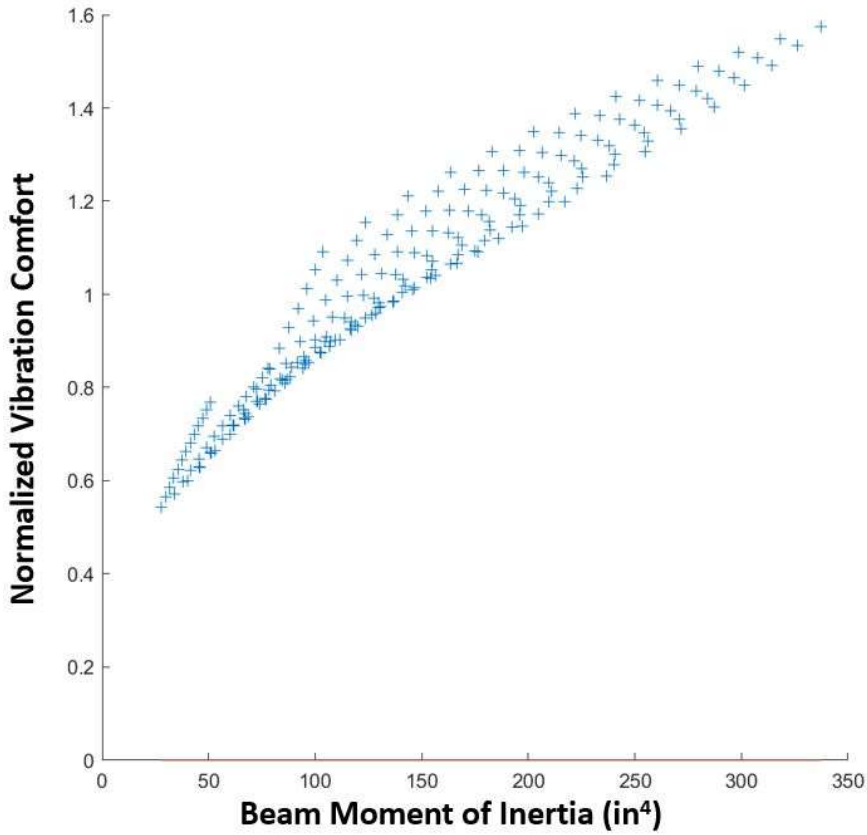

Figure 308: Scenario III: Normalized vibration comfort vs moment of inertia (I_x)

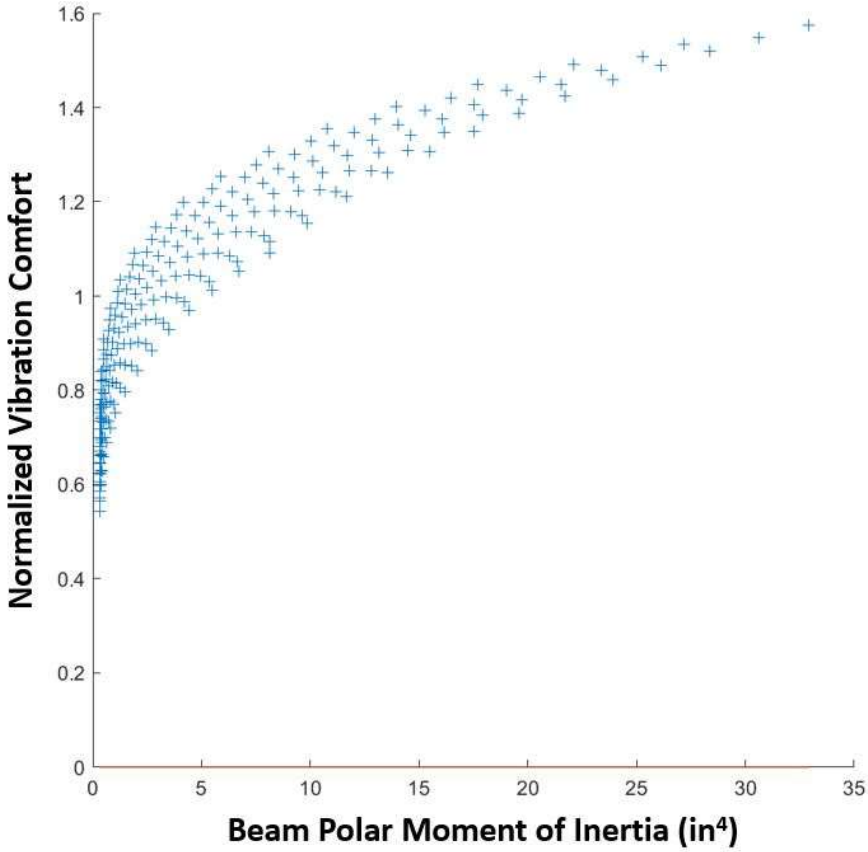

Figure 309: Scenario III: Normalized vibration comfort vs polar moment of inertia (*J*)

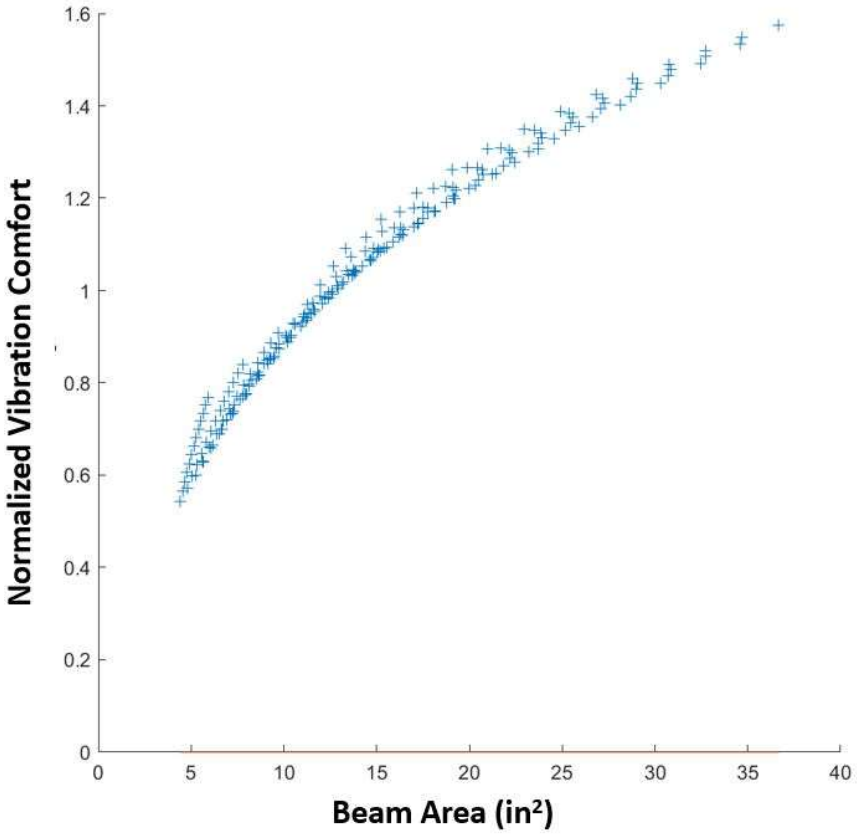

Figure 310: Scenario III: Normalized vibration comfort vs cross-sectional area

APPENDIX C

ANALYTICAL STUDY MATLAB CODE

Analytical study MATLAB input file.

```
close all; clear all ; clc;
% close all; clc;
global Fy E G Lb Cb Case Final Final_Pass;

% Add to driver file
Fy = 50;
E = 29000;
G = 11200;
Cb = 1;
Case = 10;
steel_weight = 490;   % pounds per cubic foot of steel
concrete_weight = 150; %pounds per cubic foot of concrete


%*********************************************************************
%******************** Beam Parameters ******************************
%*********************************************************************

d = 8;                   % section depth
    %***Top Flange Thickness***
tft_min  = 0.125  ;      % Top Flange Thickness Minimum value
tft_max  = 2   ;      % Top Flange Thickness Maximum value
tft_step = 0.125   ;      % Top Flange Thickness Iteration Step Value
    %***Top Flange Width***
bft_min  = 2   ;      % Top Flange Width Minimum value
bft_max  = 8  ;      % Top Flange Width Maximum value
bft_step = .5   ;      % Top Flange Width Iteration Step Value
   %***Web Thickness***
tw_min   = 0.5  ;      % Web Width Minimum value
%***currently not used, tw is calculated as bft/2 > tw_min
%    tw_max   = 0.5625   ;      % Web Width Maximum value
%    tw_step  = 0.125   ;      % Web Width Iteration Step Value
    %***Bottom Flange Width***
%***currently not used, bfb is calculated using bft and seat_width
%     bfb_min  = 8.0   ;      % Bottom Flange Width Minimum value
%     bfb_max  = 8.0  ;      % Bottom Flange Width Maximum value
%     bfb_step = 0.5   ;      % Bottom Flange Width Iteration Step
Value
seat_width = 4; %Total seat width gross(in.) (bfb=bft+seat_width)
 %***Bottom Flange Thickness***
     % Bottom Flange Thickness is equal to top flange thickness or
alpha
```

```
     % factor below controls check lines 177 and 178 for correct
     % application
       % the alpha factor below
alpha = (50/50)^-1;            % Ratio of upper flange area to lower
flange area
                       % example (0.9) is small lower flange area
                       %      Area_Top = 0.9*Area_Bottom
                       % example (1.1) is larger lower flange area
                       %      Area_Top = 1.1*Area_Bottom
Depth = 6;           % Depth of precast panels (inches)
Topping_Slab_Thickness = 3; % Depth of topping slab over precast
panel(inches)
Spacing = 10;           % Beam Spacing for panel placement (feet)
Length = 20;           % Length of Beam (feet)
l = Length*12;           % Beam length units (inches)
Lb = Length*12;
% 2018 IBC Chapter 16 Table 1604.3 Floor member deflection limit //360
D_factor = 240  ;      % Maximum allowed deflection L/(??)
Dc_factor = 360;       %Compostire Maximum deflections L/(???)
b_t_limit = 17 ;

%*********************************************************************
%******************** Scenario 1 Loading ****************************
%*********************************************************************

% ******* Service Loading Section (SL_1)*******
    %ASCE 7-10 2.3.2 Load case (4) 1.4D+1.6L(Cr) LRFD
Factor_SL_1_L = 1.6    ;  % Live Loading factor
Load_SL_1_L = 20;         % Live load given in (psf)

Factor_SL_1_D = 1.4    ;  % Dead Loading factor
Load_SL_1_D = 57;         % Superimposed Dead load given in (psf)
    % Beam Weight is calculated below and changes per section
Trib_SL_1 = Spacing/2;            % Tributary width of load (feet)
e = 1;                    % Eccentricity for Dg9 (inches)
Theta_allow = 3   ;       % Allowable Rotation in (degrees)

%*********************************************************************
%******************** Scenario 2a Loading ***************************
%*********************************************************************

% ******* Service Loading Section (SL_2)*******

Factor_SL_2a_L = 1.6    ;   % Live Loading factor
Load_SL_2a_L = 20;         % Live load given in (psf)
    % Weight of Concrete Panels per psf

Factor_SL_2a_D = 1.4    ;   % Dead Loading factor
Load_SL_2a_D1 = 57;         % Superimposed Dead load given in (psf) 67
Topping_Slab_Thickness_2a = Topping_Slab_Thickness; % thickness of
topping slab in (inches)
    % Beam Weight is calculated below and changes per section change
```

```
Trib_SL_2a = Spacing;           % Tributary width of load (feet)

%*******************************************************************
%******************** Scenario 2b Loading ****************************
%*******************************************************************

% ******* Service Loading Section (SL_1)*******
    %ASCE 7-10 2.3.2 Load case (4) 1.2D+1.6L LRFD
Factor_SL_2b_L = 1.6    ;  % Live Loading factor
    %uses Trib_SL_2b (same as the panels)
Load_SL_2b_L = 20;         % Live load given in (psf)(concentric)

Factor_SL_2b_D = 1.4    ;  % Dead Loading factor
    % Weight of Concrete Panels per psf
Load_SL_2b_D = 57;         % Superimposed Dead load given in
(psf)(concentric)
Trib_SL_2b = Spacing;            % Tributary width of load
(feet)(concentric)


Topping_Slab_Thickness_2b = Topping_Slab_Thickness; % thickness of
topping slab in (inches)(eccentric)
    % Usually would be half of trib above
Trib_SL_2b_e = Spacing/2;            % Tributary width of load
(feet)(eccentric)
e_2b = 1;                     % Eccentricty (in)(eccentric)

    % Beam Weight is calculated below and changes per section

%*******************************************************************
%******************** Senerio 3 Loading ******************************
%*******************************************************************

% ******* Service Loading Section (SL_3)*******
Factor_3_Composite = 1;
Load_3_Composite = 100;
Trib_3 = Spacing;            % Tributary width of load
(feet)(concentric)

F_prime_c= 4.0;   %Concrete strength in ksi
b_e= min(l/4,Spacing);        %effective width
Topping_Slab_Thickness_3 = Topping_Slab_Thickness; % thickness of
topping slab in (inches)

%********Vibration inputs Design Guide 11********
%Girder Specs
%W12x65
Ag = 17    ; % Area of girder (in^2)
Ixg = 833  ; % Moment of inertia of girder (in%4)
Lg = 30 ; % Girder Length in feet
dg = 12 ; %Girder depth in inches
```

```
wgirder =  65 ;  %Girder weight (plf)
%AISC DG11 Table 4-2, the estimated damping ratio is determined as
follows:
%? = 0.01(structural system)+0.01(ceiling and ductwork)+0.01(paper
office fit-out)
Beta = 0.03;
%AISC DG11 equation 4.3 Cj = 2.0 for joist or beams in most areas
Cj = 2.0;
%1.8 for girders supporting beams connected to the girder web
Cg = 1.8;
 % Weight of Concrete Panels per psf
Load_SL_3_D = 57;         % Superimposed Dead load given in (psf)
Load_LL_3 = 8;
Load_DL_3 = 4;
%Walking Evaluation
Po = 65 ; %lb

%*********************************************************************
%*********************************************************************
%*********************************************************************
%*******************OUTPUT INFORMATION*****************************
%ALL MOMENTS AND SHEARS ARE OUTPUTED IN KIP-IN AND KIPS RESPECTFULLY
%*********************************************************************
%*********************************************************************
%*********************************************************************
%*********************************************************************



Max_Deflection = l/D_factor ;
Maxc_Deflection = l/Dc_factor ;



i=0;
for bft = bft_min:bft_step:bft_max
    for tft = tft_min:tft_step:tft_max
%         for bfb = bfb_min:bfb_step:bfb_max
        for bfb=bft+seat_width
            %for tw = tw_min:tw_step:tw_max
            tw = max(tw_min,tft/2);
            i=i+1;

%     tfb =  tft;
    tfb = alpha * bft * tft / bfb;

    [h,At,Ab,Aw,ybar_bottom,ybar_top,Ixt,Ixb,Ixw,Ix,Iy,Iyt,...
    Sx_top,Sx_bottom,yp,Zx,J,ho,a2,Wno_top,Wno_bottom,Sw_top,...
    Sw_bottom,Qf_top,Qf_bottom,Qw,Aw_s,e_shear,Cw]...
    = Function_Section_parameters(d,bft,tft,bfb,tfb,tw);
```

```
    Atot = At+Ab+Aw;

    %pounds per linear foot (plf)
    beam_weight = Atot/144*steel_weight ;

    Beam(i,:)=[tft bft tw tfb bfb Atot Ix J beam_weight d];

    Section(i,:)=[h At Ab Aw ybar_bottom Ixt Ixb Ixw Ix Iy Iyt ...
    Sx_top Sx_bottom yp Zx J ho a2 Wno_top Wno_bottom Sw_top ...
    Sw_bottom Qf_top Qf_bottom Qw Aw_s e_shear Cw];

%******************* Scenario 1 Loading ******************************

  % Distributed load units (kips/inches)
    w_Factor = (Factor_SL_1_L*(Load_SL_1_L*Trib_SL_1)+Factor_SL_1_D*...
        (Load_SL_1_D*Trib_SL_1+beam_weight))/12/1000;

  % Distributed load units (kips/inches)
    w_Service = ((Load_SL_1_L*Trib_SL_1)+...
        (Load_SL_1_D*Trib_SL_1+beam_weight))/12/1000;

  % Torsional load units (kips-in /inches)
    t_Factor =((Factor_SL_1_L*(Load_SL_1_L*Trib_SL_1)+Factor_SL_1_D*...
        (Load_SL_1_D*Trib_SL_1))/12/1000)*(bfb/2-e);

  % Torsional load units (kips-in /inches)
    t_Service = (((Load_SL_1_L*Trib_SL_1)+...
        (Load_SL_1_D*Trib_SL_1))/12/1000)*(bfb/2-e);

  %****** Find Service Deflection, Moment and Shears **********
        [Delta,Mu_Service,Mu_Factor,Vu_Service,...
    Vu_Factor] = Function_Deflection(w_Service,w_Factor,...
    l,Ix);

   %****** Find Torsional Stresses DG9 **********
    [Sigma_w_top_flange_midspan,Sigma_b_top_flange_midspan,...
    Sigma_w_bottom_flange_midspan,Sigma_b_bottom_flange_midspan,...
    tau_t_flange__support,tau_w_flange_support,tau_b_flange_support,...
    tau_t_web_support,tau_b_web_support,rotation]...
    = Function_AISC_dg9_case4(t_Factor,t_Service,l,a2,J,Mu_Factor,...
    Vu_Factor,Sx_top,Sx_bottom,Ix,tft,tfb,tw,Wno_top,Wno_bottom,...
    Sw_top,Sw_bottom,Qf_top,Qf_bottom,Qw);

   %****** Calculate Max Torsional Stresses**********
    fun_c = (abs(Sigma_b_top_flange_midspan)+abs...
        (Sigma_w_top_flange_midspan));
    fun_t = (abs(Sigma_b_bottom_flange_midspan)+abs...
        (Sigma_w_bottom_flange_midspan));
    fuv_f = abs(tau_t_flange__support)+abs(tau_w_flange_support)...
        +abs(tau_b_flange_support);
    fuv_w = abs(tau_t_web_support)+abs(tau_b_web_support);
```

```
   %****** Find Shear AISC G2 **********
    [phiVn] = Function_AISC_15ed_G2(h,tw,Aw_s);

   %****** Find Moment AISC F4 F5 **********
    [phiMn,Top_Flange,Web,Fcr,AISC_results] = ...

Function_AISC_15ed_F4F5(d,h,bft,tft,bfb,tfb,tw,ybar_bottom,yp,Sx_bottom
,...
    Sx_top,Zx,Iyt,Iy,Ix,J,ho,e_shear,l,Cw,Atot);

   %****** Save Loading 1 Matrix **********
    Load_1(i,:)=[w_Factor w_Service t_Factor t_Service Delta
Mu_Service...
    Mu_Factor Vu_Service Vu_Factor fun_c fun_t fuv_f fuv_w rotation...
    phiVn phiMn Top_Flange Web Fcr];

    Checks_1(i,:)=[0.9*Fy/fun_t 0.9*Fy/fun_c ...
        0.9*0.6*Fy/fuv_f 0.9*0.6*Fy/fuv_w 0.85*Fcr/fun_c ...
        Theta_allow/rotation b_t_limit/(bft/2/tft) phiMn/Mu_Factor...
        phiVn/Vu_Factor Max_Deflection/Delta];

%******************* Scenario 2a Loading ******************************

    % Distributed load units (kips/inches)
    w_Factor =
(Factor_SL_2a_L*(Load_SL_2a_L*Trib_SL_2a)+Factor_SL_2a_D*...
        (Load_SL_2a_D1*Trib_SL_2a+beam_weight+(Trib_SL_2a*...
        (Topping_Slab_Thickness_2a/12)*concrete_weight)))/12/1000;

    % Distributed load units (kips/inches)
    w_Service = ((Load_SL_2a_L*Trib_SL_2a)+...
        (Load_SL_2a_D1*Trib_SL_2a+beam_weight+(Trib_SL_2a*...
        (Topping_Slab_Thickness_2a/12)*concrete_weight)))/12/1000;

   %****** Find Service Deflection, Moment and Shears **********
    [Delta,Mu_Service,Mu_Factor,Vu_Service,...
    Vu_Factor] = Function_Deflection(w_Service,w_Factor,...
    l,Ix);
   %****** Find Shear AISC G2 **********
    [phiVn] = Function_AISC_15ed_G2(h,tw,Aw_s);

   %****** Find Moment AISC F4 F5 **********
    [phiMn,Top_Flange,Web,Fcr,AISC_results] = ...

Function_AISC_15ed_F4F5(d,h,bft,tft,bfb,tfb,tw,ybar_bottom,yp,Sx_bottom
,...
    Sx_top,Zx,Iyt,Iy,Ix,J,ho,e_shear,l,Cw,Atot);

   %****** Save Loading 2a Matrix **********
    Load_2a(i,:)=[w_Factor w_Service Delta Mu_Service...
```

```
    Mu_Factor Vu_Service Vu_Factor fun_c fun_t fuv_f fuv_w rotation...
    phiVn phiMn Top_Flange Web Fcr];

    Checks_2a(i,:)=[phiMn/Mu_Factor phiVn/Vu_Factor ...
    Max_Deflection/Delta];


%******************* Scenario 2b Loading ******************************

   % Distributed load units (kips/inches)
    w_Factor =
(Factor_SL_2b_L*(Load_SL_2b_L*Trib_SL_2b)+Factor_SL_2b_D*...
        (Load_SL_2b_D*Trib_SL_2b+beam_weight))/12/1000;

   % Distributed load units (kips/inches)
    w_Service = ((Load_SL_2b_L*Trib_SL_2b)+...
        (Load_SL_2b_D*Trib_SL_2b+beam_weight))/12/1000;

   % Torsional load units (kips-in /inches)
    t_Factor
=((Factor_SL_2b_L*Load_SL_2b_L*Trib_SL_2b_e+Factor_SL_2b_D*...
        (Trib_SL_2b_e*(Topping_Slab_Thickness_2b/12)*...
        concrete_weight))/12/1000)*(bfb/2-e_2b);

   % Torsional load units (kips-in /inches)
    t_Service = ((Load_SL_2b_L*Trib_SL_2b_e+...
        (Trib_SL_2b_e*(Topping_Slab_Thickness_2b/12)*...
        concrete_weight))/12/1000)*(bfb/2-e_2b);

   %****** Find Service Deflection, Moment and Shears **********
        [Delta,Mu_Service,Mu_Factor,Vu_Service,...
    Vu_Factor] = Function_Deflection(w_Service,w_Factor,...
    l,Ix);

   %****** Find Torsional Stresses DG9 **********
    [Sigma_w_top_flange_midspan,Sigma_b_top_flange_midspan,...
    Sigma_w_bottom_flange_midspan,Sigma_b_bottom_flange_midspan,...
    tau_t_flange__support,tau_w_flange_support,tau_b_flange_support,...
    tau_t_web_support,tau_b_web_support,rotation]...
    = Function_AISC_dg9_case4(t_Factor,t_Service,l,a2,J,Mu_Factor,...
    Vu_Factor,Sx_top,Sx_bottom,Ix,tft,tfb,tw,Wno_top,Wno_bottom,...
    Sw_top,Sw_bottom,Qf_top,Qf_bottom,Qw);

   %****** Calculate Max Torsional Stresses**********
    fun_c = (abs(Sigma_b_top_flange_midspan)+abs...
        (Sigma_w_top_flange_midspan));
    fun_t = (abs(Sigma_b_bottom_flange_midspan)+abs...
        (Sigma_w_bottom_flange_midspan));
    fuv_f = abs(tau_t_flange__support)+abs(tau_w_flange_support)...
        +abs(tau_b_flange_support);
    fuv_w = abs(tau_t_web_support)+abs(tau_b_web_support);
```

```
   %****** Find Shear AISC G2 **********
    [phiVn] = Function_AISC_15ed_G2(h,tw,Aw_s);

   %****** Find Moment AISC F4 F5 **********
    [phiMn,Top_Flange,Web,Fcr,AISC_resultse] = ...

Function_AISC_15ed_F4F5(d,h,bft,tft,bfb,tfb,tw,ybar_bottom,yp,Sx_bottom
,...
    Sx_top,Zx,Iyt,Iy,Ix,J,ho,e_shear,l,Cw,Atot);

   %****** Save Loading 2b Matrix **********
    Load_2b(i,:)=[w_Factor w_Service t_Factor t_Service Delta
Mu_Service...
    Mu_Factor Vu_Service Vu_Factor fun_c fun_t fuv_f fuv_w rotation...
    phiVn phiMn Top_Flange Web Fcr];

    Checks_2b(i,:)=[0.9*Fy/fun_t 0.9*Fy/fun_c ...
    0.9*0.6*Fy/fuv_f 0.9*0.6*Fy/fuv_w 0.85*Fcr/fun_c ...
    Theta_allow/rotation b_t_limit/(bft/2/tft) phiMn/Mu_Factor...
    phiVn/Vu_Factor Max_Deflection/Delta];

%******************* Scenario 3 Loading ******************************

    w_Composite = (Load_3_Composite*Trib_3*Factor_3_Composite)/12/1000;

    [Composite_Delta,Ic_dg11] =
Function_Composite_Deflection(w_Composite,F_prime_c,...

b_e,Topping_Slab_Thickness_3,d,ybar_bottom,Ix,Atot,l,Depth,seat_width,t
fb,bfb,h);

    [fj,fg,fn,ap_g]...
    =
Function_AISC_dg11(concrete_weight,F_prime_c,Topping_Slab_Thickness,Bet
a,...
    Spacing,Atot,ybar_top,Ix,Load_LL_3,Load_DL_3,Load_SL_3_D,...
    beam_weight,l,Cj,Length,Lg,dg,Ag,Ixg,wgirder,Cg,Po,Ic_dg11);

    Composite_vector(i,:)=[Composite_Delta fj fg fn ap_g];



    Checks_3(i,:)=[Maxc_Deflection/Composite_Delta 0.51/ap_g];


    AISC_output(i,:) = [i AISC_results];

    count(i,:)=i;
```

```
        end
    end
end


Final=[count Beam(:,1) Beam(:,2) Beam(:,3) Beam(:,4) Beam(:,5) ...
       Beam(:,6) Beam(:,7) Beam(:,8)...
       Checks_1(:,1) Checks_1(:,2) Checks_1(:,3) Checks_1(:,4) ...
       Checks_1(:,5) Checks_1(:,6) Checks_1(:,7) Checks_1(:,8) ...
       Checks_1(:,9) Checks_1(:,10) Checks_2a(:,1) Checks_2a(:,2)...
       Checks_2a(:,3) Checks_2b(:,1) Checks_2b(:,2) Checks_2b(:,3)...
       Checks_2b(:,4) Checks_2b(:,5) Checks_2b(:,6) Checks_2b(:,7)...
       Checks_2b(:,8) Checks_2b(:,9) Checks_2b(:,10) Checks_3(:,1)...
       Checks_3(:,2) Beam(:,10)];
Final_Checks = Final;
Final_Checks(:,[1,2,3,4,5,6,7,8,9]) = [] ;
min_value_vector = min(Final_Checks,[],2);
[M,I]= min(Final_Checks,[],2);
Final_Min_Matrix = [count Beam(:,6) min_value_vector I];
Final_Min_Matrix_Sort = Final_Min_Matrix;


save Output_Final_1.mat Final
save Output_Beam.mat d
save Output_Final_Min Final_Min_Matrix_Sort
save Output_AISC.mat AISC_output
% Remove Failed Criteria
Final_Pass=Final;
Final_Pass(Final(:, 9)<= 1, :)= [];

for zz=10:18

Final_Pass(Final_Pass(:, zz)<= 1, :)= [];

end



run('Output_Application.mlapp');

fprintf('Section height is %f inches\n', d);
fprintf('Top Flange thickess range is %f inches to %f inches with %f
size steps.\n', tft_min, tft_max,tft_step);
fprintf('Top Flange width range is %f inches to %f inches with %f size
steps.\n', bft_min, bft_max,bft_step);
fprintf('Bottom flange width is top flange width plus seat width of %f
inches.\n', seat_width);
fprintf('Bottom flange thickness is calculated to proportion top and
bottom flange area  %f was used.\n', alpha);
```

Analytical study MATLAB function file: Function_Section_parameters.m.

```
function [h,At,Ab,Aw,ybar_bottom,ybar_top,Ixt,Ixb,Ixw,Ix,Iy,Iyt,...

Sx_top,Sx_bottom,yp,Zx,J,ho,a2,Wno_top,Wno_bottom,Sw_top,Sw_bottom,Qf_t
op,Qf_bottom,Qw,Aw_s,e_shear,Cw]...
    = Function_Section_parameters(d,bft,tft,bfb,tfb,tw)
global E G;
%*********************************************************
%*******************Section Properties******************
%*********************************************************
%****Calculate the depth of the web****
h = d-tft-tfb ;
h_t = d-tft ;
h_b = d-tfb ;
%****Find area of flanges and web****
% Top flange area
At = bft*tft;
% Bottom flange area
Ab = bfb*tfb;
% Web area
Aw = h*tw;
% Web area for shear
Aw_s = d *tw;
% Total area of the Section
Atotal = At + Ab + Aw;


%****Find moment of inertia (Ix) of the flanges and web****
% Top flange moment of inertia
Ixt = bft*tft^3/12;
% Bottom flange moment of inertia
Ixb = bfb*tfb^3/12;
% Web moment of inertia
Ixw = tw*h^3/12;
% Sum all moment of Inertias
Ix1 = Ixt + Ixb + Ixw;

%****Find moment of inertia (Iy) of the flanges and web****
% Top flange moment of inertia
Iyt = bft^3*tft/12;
% Bottom flange moment of inertia
Iyb = bfb^3*tfb/12;
% Web moment of inertia
Iyw = tw^3*h/12;
% Sum all moment of Inertias
Iy = Iyt + Iyb + Iyw;

%****Find rotational center of the flanges and web (y)****
%****Referenced from bottom of section****
```

```
% Top flange y
yt = d-tft/2;
% Bottom flange y
yb = tfb/2;
% Web y
yw = tfb+h/2;
%****Find rotational center of the flanges and web (x)****
%****Section is symetric in weak axis****
xt = 0;
xb = 0;
xw = 0;

%****Calculate Ay for moment of inertia parallel axis theorem
calculation****
% Top flange Ay
Ayt = At*yt;
% Bottom flange Ay
Ayb = Ab*yb;
% Web Ay
Ayw = Aw*yw;

%****Calculate ybar Top for moment of inertia parallel axis theorem
calculation****
ybar_bottom = (Ayt + Ayb + Ayw)/(At + Ab + Aw);
ybar_top = d-ybar_bottom;


%****Calculate y-ybar for moment of inertia parallel axis theorem
calculation****
% Top flange y-ybar
yt2 = yt-ybar_bottom;
% Bottom flange y-ybar
yb2 = yb-ybar_bottom;
% Web y-ybar
yw2 = yw-ybar_bottom;

%****Calculate A(y-ybar)^2 for moment of inertia parallel axis theorem
calculation****
% Top flange parallel axis theorem A(y-ybar)^2
PAt = At*(yt2)^2;
% Bottom flange parallel axis theorem A(y-ybar)^2
PAb = Ab*(yb2)^2;
% WEb parallel axis theorem A(y-ybar)^2
PAw = Aw*(yw2)^2;
% Sum all A(y-ybar)^2
PAsum = PAt + PAb + PAw;

% Combine calcuations to find moment of inertia of the section
Ix = Ix1 + PAsum;
% Due to symmetric section in the x direction
Iy = Iy;
```

```
% Calcualte Section Modulus
Sx_top = Ix/ybar_top;
Sx_bottom = Ix/ybar_bottom;

%*******************************************************
%**********Calculations for Torsional properties*********
%*******************************************************
%Parameter taken from (SSRC 1998, Picard and Beaulieu 1991)
d_prime = d-(tft+tfb)/2;

alpha = 1/(1+(bft/bfb)^3*(tft/tfb));

J = (bft*tft^3 + bfb*tfb^3 + d_prime*tw^3)/3;

ho = d-tft/2-tfb/2;

% Steel Structures 5th edition Salmon, Johnson, Malhas
% Appendix Table A2 Cw
Cw = ho^2*((Iyt*Iyb)/(Iyt+Iyb));

% SSRC Picard and Beaulieu check of Cw
% alpha3 = 1/(1+(bft/bfb)^3*(tft/tfb))
% Cw = ho^2*bft^3*tft*alpha3/(12)

% Appendix Table A2 e
 e_shear = ho*(Iyt/(Iyt+Iyb));
%Design Guide 9 Parameters
a2 = E*Cw/(G*J);

alpha2 = (bfb^3*tfb/(bft^3*tft+bfb^3*tfb))*ho;  %Heins: Bending and
Torisonal Desing (7.29)

%Wno_top = h_t*bft/4;                  %DG9 (3.7)
%Wno_bottom = h_b*bfb/4               %DG9 (3.7)

Wno_top = (alpha2*bft)/2;            %Heins: Bending and Torisonal
Desing (7.30)
Wno_bottom = (ho-alpha2)/2*bfb;      %Heins: Bending and Torisonal
Desing (7.31)

Sw_top = Wno_top*bft*tft/4;         %DG9 (3.8)
Sw_bottom = Wno_bottom*bfb*tfb/4;   %DG9 (3.8)

%Qf = h*tft*(bft-tw)/4 %DG9 (3.9)
% Design of Members Subject to Combined Bending and ...
% Torsion, Nethercot, Salter, Malik 1989
% Qf (Statical moments for top flange)
yf_top = ybar_top-(tft/2);
Af_top = (bft-tw)/2*tft;
Qf_top = Af_top * yf_top;
% Qf (Statical moments for bottom flange)
```

```
yf_bottom = ybar_bottom-(tfb/2);
Af_bottom = (bfb-tw)/2*tfb;
Qf_bottom = Af_bottom * yf_bottom;
% Qw (Statical moments for web)
Aw_2 = (ybar_top-tft)*tw;
A_Qw = At+Aw_2;
yw = ((At*(ybar_top-tft/2)+Aw_2*((ybar_top-tft)/2))/(A_Qw));
Qw = A_Qw * yw;
%Qw = (h*bft*tft)/2+((h-tft)^2*tw)/8

%*******************************************************
%***********Calculations for plasic y_bar (yp)***********
%*******************************************************
A_half = Atotal/2;
%plasic y_bar is assuming bottom flange is large enough to move yp into
%section web or section lower flange ***can not be in top flange)***
if At>A_half
        yp = d-A_half/bft;
        Plastic = "top flange";

elseif A_half > Ab
        yp = (A_half-Ab)/tw+tfb;
        Plastic = "web";
else
        yp = A_half/bfb;
        Plastic = "bottom flange";
end

if Plastic == "web"
    UPWA = (d-tft-yp)*tw ;  % upper plastic web area
    LPWA = Aw - UPWA   ;    % lower plastic web area

    AC = At + UPWA ;%Area of plastic section in compression
    yC = (((UPWA)*UPWA/tw/2)+(At*(d-tft/2-yp)))/AC; %centroid of
compression area

    AT = Ab + LPWA ;%Area of plastic section in tension
    yT = (LPWA*(LPWA/tw/2)+(Ab*(yp-tfb/2)))/AT; %centroid of tension
area

    Zx =  AC * yC + AT * yT; %Plastic Modulus
elseif Plastic == "bottom flange"
    LPFA = yp*bfb   ;    % lower plastic flange area
    UPFA =  Ab-LPFA;  % upper plastic flange area

    AC = At + Aw + UPFA  ;  %Area of plastic section in compression
    yC = ((At*(d-tft/2-yp)+(Aw*(tfb-yp+h/2))+((UPFA)*(tfb-yp)/2)))/AC;
%centroid of compression area

    AT = LPFA ;  %Area of plastic section in tension
    yT = yp/2 ;   %centroid of tension area
```

```
    Zx =  AC * yC + AT * yT ;%Plastic Modulus
else

    UPFA = (d-yp)*bft;
    LPFA = At-UPFA;

    AC = UPFA;
    yC = (h-yp)/2;

    AT = LPFA + Ab + Aw;
    yT = (Ab*(yp-tfb/2)+Aw*(yp-tfb-
h/2)+LPFA*(LPFA/(2*bft)))/(Ab+Aw+LPFA);

    Zx =  AC * yC + AT * yT; %Plastic Modulus

end
end
```

Analytical study MATLAB function file: Function_AISC_15ed_F4F5.m.

```
function [phiMn,Top_Flange,Web,Fcr,AISC_results] = ...

Function_AISC_15ed_F4F5(d,h,bft,tft,bfb,tfb,tw,ybar_bottom,yp,Sx_bottom
,...
    Sx_top,Zx,Iyt,Iy,Ix,J,ho,e_shear,l,Cw,Atot)
global Fy E G Lb Cb Case;
%format long
tol = .01 ; %Floating number tolerance for >= and <= comparisons
%*******************************************************
%**************     AISC 15th Edition      **************
%*******************************************************

%*******************************************************************
%*****Limiting Width-to-Thickness Ratio (lambda p and lambda r)*****
%**************FLANGE FLANGE FLANGE FLANGE FLANGE******************
%*******************************************************************
%taken from Table B4.1b (16.1-18)
%subnote (a)
kc = 4/sqrt(h/tw);
kc_ul = 0.76;
kc_ll = 0.35;

if kc > kc_ul
    kc = kc_ul;
elseif kc<kc_ll
    kc = kc_ll;
else
```

```
    kc = kc;
end
%subnote (b)
%Find Sx_tension/Sx_compression ratio
Sx_ratio = Sx_bottom/Sx_top;

%flange limiting W-to-T ratios
%lambda p (compact/noncompact) limit
lp_flange = 0.38*sqrt(E/Fy);

if Sx_ratio >= 0.7
    Fl = 0.7*Fy            ;%(F4-6a)
else
        Fl = Fy*Sx_ratio   ;%(F4-6b)
            if Fl>0.5*Fy
                Fl = 0.5*Fy   ;%(F4-6b)
            end
end
Fl_check = Fl;
%lambda r (noncompact/slender) limit
if Case==10
    %case 10 Table B4.1b (page 16.1-18)
    lr_flange = 1.0*sqrt(E/Fy);
else
    %case 11 Table B4.1b (page 16.1-18)
 lr_flange = 0.95*sqrt(kc*E/Fl) ;
end

%**************   Find hc off the elastic neutral axis AISC 15th
%           Table B4.1b case 16**********************

hc = 2* (d-tft-ybar_bottom);
hp = 2* (d-tft-yp);

%**************   ELastic Yield Moment**********************
Myc = Fy * Sx_top ;% (F4-4) ---(kip-in)
%**************   ELastic Yield Moment**********************
Myt = Fy * Sx_bottom; % (F4-4) ---(kip-in)
%*************   Plastic Bending Moment********************
Mpc = Fy * Zx;% equation not numbered page (16.1-19)---(kip-in)

MPYR = Mpc/Myc; % Moment Plastic/Yield Ratio
%*****************************************************************
%*****Limiting Width-to-Thickness Ratio (lambda p and lambda r)*****
%***************WEB WEB WEB WEB WEB WEB WEB WEB*******************
%*****************************************************************

%web limiting W-to-T ratios
%lambda p (compact/noncompact) limit
lp_web = ((hc/hp)*sqrt(E/Fy))/((0.54*MPYR-0.09)^2);
lr_web = 5.70*sqrt(E/Fy);
```

```
%*****************************************************************
%*Classification of Web and Flange (compact, noncompact, or slender*
%*****************************************************************


b_t_top = bft/2/tft ;   %top flange b/t
b_t_bottom = bfb/2/tfb; %bottom flange b/t
hc_tw = hc/tw    ;      %web hc/tw

if b_t_top < lp_flange
    Top_Flange = "compact";
elseif b_t_top > lr_flange
    Top_Flange = "slender";
else
    Top_Flange = "non-compact";
end

if b_t_bottom < lp_flange
    Bottom_Flange = "compact";
elseif b_t_top > lr_flange
    Bottom_Flange = "slender";
else
    Bottom_Flange = "non-compact";
end

if hc_tw < lp_web
    Web = "compact";
elseif hc_tw > lr_web
    Web = "slender";
else
    Web = "non-compact";
end

% Moment of inertia of the compression flange (top) about the y-axis
Iyc = Iyt;
WPFR = Iyc/Iy;  %Web Plasifiation Factor Ratio
%***********   effective radius of gyration F4.2(c)(6)  ***********
aw = hc*tw/(bft*tft); %(F4-12)
rt = bft/(sqrt(12*(1+aw/6))); %(F4-11)

%*********   Nominal Compression Flange Stress F4.2(c)(2)  *********
if WPFR > 0.23

    Fcr_F4 =
Cb*pi^2*E/(Lb/rt)^2*sqrt(1+0.078*(J/(Sx_top*ho))*(Lb/rt)^2);
else
    J2 = 0;
    Fcr_F4 =
Cb*pi^2*E/(Lb/rt)^2*sqrt(1+0.078*(J2/(Sx_top*ho))*(Lb/rt)^2);
end
%*********   Nominal Compression Flange Stress F4.2(c)(3)  *********
```

```
%*************   Web Plastification F4.2(c)(6)  *************
% Rpc, the web plasification factor Section F4.2(c)(6)

if WPFR > 0.23

    if hc_tw > lp_web

        Rpc1 = ((MPYR)-(MPYR-1)*((hc_tw-lp_web)/(lr_web-lp_web)));
       %(F4-9b)

            if Rpc1 > MPYR
                Rpc = MPYR ; %(F4-9a)
            else
                Rpc = Rpc1;
            end

    else
        Rpc = MPYR;
    end

else
    Rpc = 1.0   ;       %(F4-10)
end

Rpc_4_2 = Rpc;

% 4.1 Compression Flange Yielding (F4.1)

MnF4_1 = Rpc * Myc; %kip-in          %Equation (F4-1)


JShr = J/(Sx_top*ho) ; % J/Sx ho ratio

Lp = 1.1*rt*sqrt(E/Fy); %(F4-7)
%Lr = 1.95*rt*(E/Fl)*(sqrt(JShr+(sqrt(JShr^2+(6.76*(Fl/E)^2))))) %(F4-
8)
Lr = 1.95*rt*E/Fl*sqrt((JShr+sqrt(JShr^2+6.76*(Fl/E)^2)));
Lp_4_2 = Lp;
Lr_4_2 = Lr;
% 4.2 Lateral-Torsional Buckling (F4.2)

if Lb <= Lp
    MnF4_2 = "does not apply";

elseif Lb > Lr
    MnF4_2 = Fcr_F4 *Sx_top  ;   %Equation (F4-3)
```

```
else
    MnF4_2 = Cb*(Rpc*Myc-(Rpc*Myc-Fl*Sx_top)*((Lb-Lp)/(Lr-Lp)));
end

if isnumeric(MnF4_2)

    if MnF4_2 > MnF4_1
        MnF4_2 = MnF4_1  ;%(F4-2) and (F4-3)
    end
else
  MnF4_2 = "does not apply";
end


% 4.3 Compression Flange Local Buckling (F4.2)

if Top_Flange == "compact"
    MnF4_3 = "does not apply";

elseif Top_Flange == "non-compact"
    MnF4_3 = Rpc*Myc-(Rpc*Myc-Fl*Sx_top)*...
        ((b_t_top-lp_flange)-(lr_flange-lp_flange));

else Top_Flange == "slender";
    MnF4_3 = 0.9*E*kc*Sx_top/((b_t_top)^2);

end

% 4.4 Tension Flange Yielding (F4.2)
% Round Sx top and bottom to remove floating point for "if" statement
Sx_bottom_round = round(Sx_bottom,3);
Sx_top_round = round(Sx_top,3);

if Sx_bottom_round >= Sx_top_round
    MnF4_4 =  "does not apply";

elseif Sx_bottom < Sx_top
        if Iyc/Iy > 0.23
            if hc/tw <= lp_web
                Rpt = Mpc/Myt;
            else
                Rpt = (Mpc/Myt)-(Mpc/Myt-1)*...
                    ((hc_tw-lp_web)-(lr_web-lp_web));

                if Rpt > Mpc/Myt
                Rpt = Mpc/Myt;
                end
            end
        else
            Rpt = 1.0;
        end
```

```
    MnF4_4 = Rpt*Myt;


end

%**************** F5 Spec ***************

Rpg = 1-(aw/(1200+300*aw))*(hc/tw-5.7*sqrt(E/Fy)); %Equation (F5-6)

if Rpg>1
    Rpg = 1.0;
end

% 5.1 Compression Flange Yielding (F5.1)

MnF5_1 = Rpg * Fy * Sx_top ; %kip-in         %Equation (F5-1)

% 5.2 Lateral-Torsional Buckling (F5.2)

Lr = pi*rt*sqrt(E/(0.7*Fy));                 %Equation (F5-5)


if Lb < Lp
    MnF5_2 = "does not apply" ;

elseif Lb > Lr
    Fcr_F5 = Cb*pi^2*E/(Lb/rt)^2 ;           %Equation (F5-4)

    if Fcr_F5 >Fy
        Fcr_F5 = Fy;
    end

    MnF5_2 = Rpg * Fcr_F5 *Sx_top    ;            %Equation (F5-2)

else
    Fcr_F5 = Cb*(Fy-(0.3*Fy)*((Lb-Lp)/(Lr-Lp)));%Equation (F5-3)

    if Fcr_F5 >Fy
        Fcr_F5 = Fy;
    end
    MnF5_2 = Rpg * Fcr_F5 * Sx_top      ;         %Equation (F5-2)
end

% 5.3 Compression Flange Local Buckling (F5.3)

if Top_Flange == "compact"
    MnF5_3 = "does not apply";
```

```
elseif Top_Flange == "non-compact"
    Fcr_F5 = Fy-(0.3*Fy)*...
        ((b_t_top-lp_flange)-(lr_flange-lp_flange)); %Equation (F5-8)
    MnF5_3 = Rpg * Fcr_F5 * Sx_top      ;         %Equation (F5-7)

else Top_Flange == "slender";
    Fcr_F5 = 0.9*E*kc/(bft/(2*tft))^2  ;        %Equation (F5-9)
    MnF5_3 = Rpg * Fcr_F5 * Sx_top     ;         %Equation (F5-7)

end

% 5.4 Tension Flange Yielding (F5.4)

if Sx_bottom_round >= Sx_top_round

    MnF5_4 = "does not apply";

else
    MnF5_4 = Fy *Sx_top    ;    %Equation (F5-10)

end


%**************** E3-E4 Spec ****************
%*******Determine Fcr for Design Guide 9*****
%Coordinate of shear center with respect to the centroid
y0 = ybar_bottom-e_shear;
x0 = 0;
%Calculations of radius of gyration
rx = sqrt(Ix/Atot);
ry = sqrt(Iy/Atot);
ro_2 = x0^2 + y0^2 + (Ix+Iy)/Atot;   %(E4-9)
H = 1-(x0^2+y0^2)/ro_2;           %(E4-8)
% effective length factors for buckling
Kx = 1.0;
Ky = 1.0;
Kz = 1.0;
% effective length K*Lc
Lcx = Kx*l;
Lcy = Ky*l;
Lcz = Kz*l;
%Sub calculations for Fe E4.b
Fex = pi^2*E/((Lcx/rx)^2) ;  %(E4-5)
Fey = pi^2*E/((Lcy/ry)^2) ;  %(E4-6)
Fez = ((pi^2*E*Cw)/(Lcz^2)+G*J)*(1/(Atot*ro_2));   %(E4-7)

Fe = ((Fey + Fez)/2*H)*(1-(sqrt(1-((4*Fey*Fez*H)/((Fey+Fez)^2)))));
%(E4-3)

slender_crit = min(Lcx/rx,Lcy/ry);
```

```
% if slender_crit > 4.71*sqrt(E/Fy)
%
%         Fcr_E = 0.877*Fe;
% else
%
%         Fcr_E = (0.658^(Fy/Fe))*Fy;
% end




MomentF4=["F4-1" "F4-2" "F4-3" "F4-4"];
ResultsF4=[MnF4_1 MnF4_2 MnF4_3 MnF4_4 "does not apply"];
ResultsF4F=ResultsF4;
ResultsF4(ResultsF4=="does not apply")=[];
ResultsF4=double(ResultsF4);
ResultsF4(ResultsF4<=0)=[];
minResultsF4=min(ResultsF4);
F4casefind=find(ResultsF4==minResultsF4);
F4case=MomentF4(1,F4casefind);

MomentF5=["F5-1" "F5-2" "F5-3" "F5-4"];
ResultsF5=[MnF5_1 MnF5_2 MnF5_3 MnF5_4 "does not apply"];
ResultsF5F=ResultsF5;
ResultsF5(ResultsF5=="does not apply")=[];
ResultsF5=double(ResultsF5);
ResultsF5(ResultsF5<=0)=[];
minResultsF5=min(ResultsF5);
F5casefind=find(ResultsF5==minResultsF5);
F5case=MomentF5(1,F5casefind);

if  Web == "slender"
    Result = ResultsF5;
    Fcr_cal = Fcr_F5;
    AISCcase = F5case;
else
    Result = ResultsF4;
    Fcr_cal = Fcr_F4;
    AISCcase = F4case;
end

Fcr = Fcr_cal;
phiMn = 0.90 * min(Result);
AISC_results =
[AISCcase,Top_Flange,Web,Bottom_Flange,Lp_4_2,Lr_4_2,Rpc_4_2,Fl_check,S
x_ratio,phiMn];
```

Analytical study MATLAB function file: Function_AISC_15ed_G2.m.

```
function [phiVn] = Function_AISC_15ed_G2(h,tw,Aw_s)
```

```
global Fy E;

%*******************************************************
%**************     AISC 15th Edition      **************
%**************    Design of Shear (G2)    **************
%*******************************************************

% Shear Strength of Webs without Tension Field Action
% Phi factor place in under G2-3 and G2-4 of 0.9
% Phi factor for G2-2 is 1.0
kv = 5.34;                                    %(G.2.1.b.2.i)

if h/tw <= 2.24*sqrt(E/Fy)                    %(G2.1.a)
    Cv1 = 1.0;                                %(G2-2)
else                                          %(G2.1.b)
    if h/tw > 1.10 * sqrt(kv*E/Fy)            %(G.2.1.b.1.ii)
        Cv1 = 0.9 * 1.1*sqrt(kv*E/Fy)/(h/tw); %(G2-4)
    else                                      %(G.2.1.b.1.i)
        Cv1 = 0.9 * 1.0;                      %(G2-3)
    end
end

Vn =  0.6 * Fy * Aw_s * Cv1;                    %(G2-1)

phiVn = 0.90 * Vn;
end
```

Analytical study MATLAB function file: Function_AISC_dg9.m.

```
function [Sigma_w_top_flange_midspan,Sigma_b_top_flange_midspan,...
    Sigma_w_bottom_flange_midspan,Sigma_b_bottom_flange_midspan,...
    tau_t_flange__support,tau_w_flange_support,tau_b_flange_support,...
    tau_t_web_support,tau_b_web_support,rotation]...
    = Function_AISC_dg9_case4(t_Factor,t_Service,l,a2,J,Mu_Factor,...
    Vu_Factor,Sx_top,Sx_bottom,Ix,tft,tfb,tw,Wno_top,Wno_bottom,...
    Sw_top,Sw_bottom,Qf_top,Qf_bottom,Qw)
global E G;
%*******************************************************
%*************     AISC Design Guide 9      *************
%*******************************************************

%*****************************************************************
%*****Limiting Width-to-Thickness Ratio (lambda p and lambda r)*****
%**************FLANGE FLANGE FLANGE FLANGE FLANGE******************
%*****************************************************************
t = t_Factor;
t_s = t_Service;
```

```
a = sqrt(a2);

%Theta calculated in center of beam
z_c = l/2;

Theta_c = t_s*a^2/(G*J)*((l^2/(2*a^2))*((z_c/l)-(z_c^2/l^2))+...
    cosh(z_c/a)-tanh(l/(2*a))*sinh(z_c/a)-1.0);

Theta_c_prime = -(a^2*t*((l^2*((2*z_c)/l^2 - 1/l))/(2*a^2) -...
    sinh(z_c/a)/a + (tanh(l/(2*a))*cosh(z_c/a))/a))/(G*J);

Theta_c_prime2 = -(a^2*t*(1/a^2 - cosh(z_c/a)/a^2 + (tanh(l/(2*a))...
    *sinh(z_c/a))/a^2))/(G*J);

Theta_c_prime3 = (a^2*t*(sinh(z_c/a)/a^3 - (tanh(l/(2*a))...
    *cosh(z_c/a))/a^3))/(G*J);

%Theta calculated at support
z_e = 0;

Theta_e = t*a^2/(G*J)*((l^2/(2*a^2))*((z_c/l)-(z_c^2/l^2))+...
    cosh(z_c/a)-tanh(l/(2*a))*sinh(z_c/a)-1.0);

Theta_e_prime = -(a^2*t*((l^2*((2*z_c)/l^2 - 1/l))/(2*a^2) -...
    sinh(z_c/a)/a + (tanh(l/(2*a))*cosh(z_c/a))/a))/(G*J);

Theta_e_prime2 = -(a^2*t*(1/a^2 - cosh(z_c/a)/a^2 + (tanh(l/(2*a))...
    *sinh(z_c/a))/a^2))/(G*J);

Theta_e_prime3 = (a^2*t*(sinh(z_c/a)/a^3 - (tanh(l/(2*a))...
    *cosh(z_c/a))/a^3))/(G*J);



%****************************************
% *****     Midspan Calcuations     *****
%****************************************

% *****  Flange Normal Stresses    *****
%********  Top Flange ********
% The normal stress due to warping
Sigma_w_top_flange_midspan = E*Wno_top*Theta_c_prime2  ;      % (4.3a)
% The normal stress due to bending
Sigma_b_top_flange_midspan = Mu_Factor/Sx_top;           % (4.5)
%********  Bottom Flange ********
% The normal stress due to warping
Sigma_w_bottom_flange_midspan = E*Wno_bottom*Theta_c_prime2;  % (4.3a)
% The normal stress due to bending
Sigma_b_bottom_flange_midspan = Mu_Factor/Sx_bottom;     % (4.5)
```

```
% *****  Flange Shear Stresses    *****
%********  Top Flange ********
% The shear stress due to pure torsion
tau_t_top_flange_midspan_ = G*t*Theta_c_prime;        % (4.1)
% The shear stress due to warping
tau_w_top_flange_midspan = -E*Sw_top*Theta_c_prime3/tft;  %(4.2a)
% The shear stress due to bending
tau_b_top_flange_midspan = Vu_Factor*Qf_top/Ix*tft; % (4.6)
%********  Bottom Flange ********
% The shear stress due to pure torsion
tau_t_bottom_flange_midspan_ = G*t*Theta_c_prime;        % (4.1)
% The shear stress due to warping
tau_w_bottom_flange_midspan = -E*Sw_bottom*Theta_c_prime3/tfb;  %(4.2a)
% The shear stress due to bending
tau_b_bottom_flange_midspan = Vu_Factor*Qf_bottom/Ix*tfb;  % (4.6)


% *****  Web Shear Stresses    *****
tau_t_web_midspan = G*t*Theta_c_prime;            % (4.1)
% The shear stress due to bending
tau_b_web_midspan = Vu_Factor*Qw/Ix*tw;     % (4.6)

rotation = Theta_c*180/pi();

%****************************************
% *****     Support Calcuations     *****
%****************************************

% *****  Flange Normal Stresses    *****
%********  Top Flange ********
% The normal stress due to warping
Sigma_w_top_flange_support = E*Wno_top*Theta_e_prime2;        % (4.3a)
% The normal stress due to bending
Sigma_b_top_flange_support = 0;                               % (4.5)
%********  Bottom Flange ********
% The normal stress due to warping
Sigma_w_bottom_flange_support = E*Wno_bottom*Theta_e_prime2;  % (4.3a)
% The normal stress due to bending
Sigma_b_bottom_flange_support = 0;                            % (4.5)

% *****  Flange Shear Stresses    *****
%********  Top Flange ********
% The shear stress due to pure torsion
tau_t_flange__support = G*t*Theta_e_prime;        % (4.1)
% The shear stress due to warping
tau_w_flange_support = -E*Sw_top*Theta_e_prime3/tft;  %(4.2a)
% The shear stress due to bending
tau_b_flange_support = Vu_Factor*Qf_top/Ix*tft; % (4.6)

tau_w_flange_support_bottom = -E*Sw_top*Theta_e_prime3/tfb;  %(4.2a)
% The shear stress due to bending
tau_b_flange_support_bottom = Vu_Factor*Qf_bottom/Ix*tfb; % (4.6)
```

```
% *****  Web Shear Stresses    *****
tau_t_web_support = G*t*Theta_e_prime;            % (4.1)
% The shear stress due to bending
tau_b_web_support = Vu_Factor*Qw/Ix*tw;     % (4.6)

end
```

Analytical study MATLAB function file: Function_AISC_dg11.m.

```
function [fj,fg,fn,ap_g]...
    =
Function_AISC_dg11(concrete_weight,F_prime_c,Topping_Slab_Thickness,Bet
a,...
    Spacing,Atot,ybar_top,Ix,Load_LL_3,Load_DL_3,Load_SL_3_D,...
    beam_weight,l,Cj,Length,Lg,dg,Ag,Ixg,wgirder,Cg,Po,Ic_dg11)
global E;

%gravity in/s^2
g=386.089;

d_slab = Topping_Slab_Thickness;

Ec=concrete_weight^(1.5)*sqrt(F_prime_c);

slab_deck_weight=d_slab/12*concrete_weight+Load_SL_3_D;

% Modular ratio with 35% increase in Ec per AISC D11 Section 3.2
n=(E)/(1.35*Ec);

%Effective Concrete Slab Width with conversion from ft. to in.
Eff_csw = Spacing*12;
%Transformed Concrete Slab Width
Eff_Tcsw = Eff_csw/n;
%Transformed Concrete Slab Area
Eff_TcsA = d_slab*Eff_Tcsw;
%Composite Transformed Moment
y_bar=(Eff_TcsA*(ybar_top+d_slab/2))/(Eff_TcsA+Atot);

Icomp_slab = Eff_Tcsw*d_slab^3/12+Eff_TcsA*(ybar_top+d_slab/2-y_bar)^2;
Icomp_joist = Ix+Atot*ybar_top^2;
Ij = Icomp_slab + Icomp_joist;

% A more "exact" Composite moment on inertia ***if you need the
capacity***
Ij=Ic_dg11;

%Loading per Joist
```

```
wj = (beam_weight+(Spacing*(Load_LL_3+Load_DL_3+slab_deck_weight)));

%Deflection per joist
Delta_j = 5*wj/1000/12*l^4/(384*E*Ij);

%Joist Fundamental Frequency
fj = 0.18*sqrt(g/Delta_j);

%Transformed Moment of inertia per unit width in slab span direction
%(in^4/ft)
Ds = d_slab^3/n;

%Transformed Moment of inertia per unit width in joist span direction
%(in^4/ft)
Dj = Ij/Spacing;

%Effective beam panel width
Bj = Cj*(Ds/Dj)^0.25*Length;

%Beam panel weight
Wj = (wj/Spacing)*Bj*Length;

%Girder Transformed Effective Moment of Inertia
%Effective concrete slab width
Eff_TcswG = 0.2*Lg+0.2*Lg;

%Transformed Concrete Slab Width
Eff_TCSW = Eff_TcswG*12/n;

%Effective width of the slab in the deck
Eff_WSD = Spacing*12/n;

%Transformed Concrete Slab Area
Eff_TCSA = Eff_TCSW*d_slab;

%Fully composite transformed moment of inertia
y_bar2 = (Eff_TCSA*(dg/2+d_slab/2))/(Eff_TCSA+Ag);

Icomp_slab_transformed = Eff_TCSW*d_slab^3/12+Eff_TCSA*(dg/2+d_slab/2-
y_bar2)^2;
Icomp_girder=Ixg+Ag*y_bar2^2;
Ig = Icomp_slab_transformed + Icomp_girder;

%Girder equivalend uniform loading
wg = Length*(wj/Spacing)+wgirder;

%Deflection per girder
Delta_g = 5*wg/12/1000*(Lg*12)^4/(384*E*Ig);

%Joist Fundamental Frequency
```

```
fg = 0.18*sqrt(g/Delta_g);

Dg = Ig/Length;

%Effective girder panel width
Bg = Cg*(Dj/Dg)^0.25*Lg;

Wg = (wg/Length)*Bg*Lg;

fn = 0.18*sqrt(g/(Delta_g+Delta_j));

Delta_g_prime = Length/Bj*Delta_g;

W = (Delta_j/(Delta_j+Delta_g_prime)*Wj) +
((Delta_g_prime/(Delta_j+Delta_g_prime))*Wg);

ap_g = 100*(Po*exp(-0.35*fn))/(Beta*W);
```

Analytical study MATLAB function file: Function_Deflection.m.

```
function [Delta,Mu_Service,Mu_Factor,Vu_Service,...
    Vu_Factor] = Function_Deflection(w_Service,w_Factor,...
    l,Ix)
global E;
%*******************************************************
%*************       AISC Deflection        *************
%*******************************************************

%*****************************************************************
%********     Simple Beam - Uniformly Distributed Load      ********
%********    Table 3-23 Shears, Moments and Deflections     ********
%*****************************************************************


% Max Vertical deflection in center of beam due to Service Load 1
(SL_1)
Delta = 5*w_Service*l^4/(384*E*Ix);
% Max Moment in center of beam SL_1
Mu_Service = w_Service*l^2/8;
Mu_Factor = w_Factor*l^2/8;
% Calculate
Vu_Service = w_Service*l/2;
Vu_Factor = w_Factor*l/2;

end
```

Analytical study MATLAB function file: Function_Composite_Deflection.m.

```
function [Composite_Delta,Ic_dg11] =
Function_Composite_Deflection(w_Composite,F_prime_c,...

b_e,Topping_Slab_Thickness_3,d,ybar_bottom,Ix,Atot,l,Depth,seat_width,t
fb,bfb,h)
global E;
%*******************************************************
%*************       SCI Deflection        *************
%*******************************************************

%*****************************************************************
%********     Simple Beam - Uniformly Distributed Load      ********
%********          The Steel Construction Institute         ********
%*****************************************************************
Ec=57000*sqrt(F_prime_c*1000);

alpha_e = E*1000/Ec;
n=(E*1000)/(1.35*Ec);

ye = d-ybar_bottom;

A = Atot;

Ac1 = (bfb-seat_width)*Depth;

D = d;

Dd = Depth;

Tb = tfb;

Be = b_e*12;

Ds = Topping_Slab_Thickness_3;

Ac = Ds * Be;

Dc = Dd + Ds - Tb - h;

yec = (A*ye + ((Ac1/alpha_e)*(D-(0.5*Dd)-Tb))+(Ac/alpha_e)*((0.5*Ds)-
Dc))/...
    (A+((Ac+Ac1)/alpha_e)); %Appendix B1.2 equation (18)

Ic = Ix + A*((ye-yec)^2) + (Ac/alpha_e)*(((0.5*Ds)-Dc-
yec)^2)+(Ac/alpha_e)*...
```

```
    ((Ds^2)/12)+(Ac1/alpha_e)*((D-(0.5*Dd)-Tb-
yec)^2)+(Ac1/alpha_e)*((Dd^2)/12);
                            %Appendix B1.2 equation (19)
yec_dg11 = (A*ye + ((Ac1/n)*(D-(0.5*Dd)-Tb))+(Ac/n)*((0.5*Ds)-Dc))/...
    (A+((Ac+Ac1)/n));        %Appendix B1.2 equation (18)

Ic_dg11 = Ix + A*((ye-yec_dg11)^2) + (Ac/n)*(((0.5*Ds)-Dc-
yec_dg11)^2)+(Ac/n)*...
    ((Ds^2)/12)+(Ac1/n)*((D-(0.5*Dd)-Tb-
yec_dg11)^2)+(Ac1/n)*((Dd^2)/12);
                            %Appendix B1.2 equation (19)

% Max Vertical deflection in center of beam due to Service Load 1
(SL_1)
Composite_Delta = 5*w_Composite*l^4/(384*E*Ic);
```

Analytical study MATLAB function file: Output_Application.mlapp.

```
classdef Output_Application < matlab.apps.AppBase


% Properties that correspond to app components
properties (Access = public)
UIFigure matlab.ui.Figure
HeightEditField matlab.ui.control.EditField
TextArea matlab.ui.control.TextArea
AISCCaseEditFieldLabel matlab.ui.control.Label
AISCCaseEditField matlab.ui.control.EditField
WebEditFieldLabel matlab.ui.control.Label
WebEditField matlab.ui.control.EditField
BottomFlangeEditFieldLabel matlab.ui.control.Label
BottomFlangeEditField matlab.ui.control.EditField
TopFlangeEditFieldLabel matlab.ui.control.Label
TopFlangeEditField matlab.ui.control.EditField
WeightperFootEditField matlab.ui.control.NumericEditField
WeightperFootEditFieldLabel matlab.ui.control.Label
LimitLineEditField matlab.ui.control.NumericEditField
LimitLineEditFieldLabel matlab.ui.control.Label
Image2 matlab.ui.control.Image
MomentofInertiaEditField matlab.ui.control.NumericEditField
MomentofInertiaEditFieldLabel matlab.ui.control.Label
SectionAreaEditField matlab.ui.control.NumericEditField
SectionAreaEditFieldLabel matlab.ui.control.Label
BottomFlangebfEditField matlab.ui.control.NumericEditField
BottomFlangebfEditFieldLabel matlab.ui.control.Label
BottomFlangetfEditField matlab.ui.control.NumericEditField
```

```
BottomFlangetfEditFieldLabel matlab.ui.control.Label
WebtwEditField matlab.ui.control.NumericEditField
WebtwEditFieldLabel matlab.ui.control.Label
TopFlangebfEditField matlab.ui.control.NumericEditField
TopFlangebfEditFieldLabel matlab.ui.control.Label
TopFlangetfEditField matlab.ui.control.NumericEditField
TopFlangetfEditFieldLabel matlab.ui.control.Label
RunBeamButton matlab.ui.control.Button
BeamNumberEditFieldLabel matlab.ui.control.Label
BeamNumberEditField matlab.ui.control.NumericEditField
PlotButton matlab.ui.control.Button
Parameters matlab.ui.container.ButtonGroup
webheightinButton matlab.ui.control.RadioButton
Jin4Button matlab.ui.control.RadioButton
Ixin4Button matlab.ui.control.RadioButton
Areain2Button matlab.ui.control.RadioButton
bfbottominButton matlab.ui.control.RadioButton
tfbottominButton matlab.ui.control.RadioButton
twinButton matlab.ui.control.RadioButton
bftopinButton matlab.ui.control.RadioButton
tftopinButton matlab.ui.control.RadioButton
Parameters_2 matlab.ui.container.ButtonGroup
MinimumforalllimitstatesyaxisLabel matlab.ui.control.Label
CompositeDeflectionL360C3aButton matlab.ui.control.RadioButton
Vibration050C3bButton matlab.ui.control.RadioButton
MinimumPlotButton matlab.ui.control.RadioButton
RotationC2bButton matlab.ui.control.RadioButton
BucklingC2bButton matlab.ui.control.RadioButton
WebShearYieldingC2bButton matlab.ui.control.RadioButton
FlangeShearYieldingC2bButton matlab.ui.control.RadioButton
CompressionFlangeYieldingC2bButton matlab.ui.control.RadioButton
TensionFlangeYieldingC2bButton matlab.ui.control.RadioButton
DeflectionL240C2aButton matlab.ui.control.RadioButton
thAISCShearC2aButton matlab.ui.control.RadioButton
thAISCMomentC2aButton matlab.ui.control.RadioButton
btButton matlab.ui.control.RadioButton
RotationC1Button matlab.ui.control.RadioButton
BucklingC1Button matlab.ui.control.RadioButton
WebShearYieldingC1Button matlab.ui.control.RadioButton
FlangeShearYieldingC1Button matlab.ui.control.RadioButton
CompressionFlangeYieldingC1Button matlab.ui.control.RadioButton
TensionFlangeYieldingC1Button matlab.ui.control.RadioButton
Image matlab.ui.control.Image
UIAxes2 matlab.ui.control.UIAxes
UIAxes matlab.ui.control.UIAxes
end
```

```
% Callbacks that handle component events
methods (Access = private)


% Button pushed function: PlotButton
function PlotButtonPushed(app, event)
%load data
global Final
Final=[];
load Output_Final_1.mat;
load Output_Final_Min.mat;
load Output_Beam.mat;
row = dataTipTextRow('Beam Number',Final(:,1) );
row2 = dataTipTextRow('**N/A**',Final(:,1));
if app.tftopinButton.Value==true
x=Final(:,2);
elseif app.bftopinButton.Value==true
x=Final(:,3);
elseif app.twinButton.Value==true
x=Final(:,4);
elseif app.tfbottominButton.Value==true
x=Final(:,5);
elseif app.bfbottominButton.Value==true
x=Final(:,6);
elseif app.Areain2Button.Value==true
x=Final(:,7);
elseif app.Ixin4Button.Value==true
x=Final(:,8);
elseif app.Jin4Button.Value==true
x=Final(:,9);
elseif app.webheightinButton.Value==true
x=d-Final(:,2)-Final(:,5);
end
if app.TensionFlangeYieldingC1Button.Value==true
y=Final(:,10); % (1)
elseif app.CompressionFlangeYieldingC1Button.Value==true
y=Final(:,11);% (2)
elseif app.FlangeShearYieldingC1Button.Value==true
y=Final(:,12);% (3)
elseif app.WebShearYieldingC1Button.Value==true
y=Final(:,13);% (4)
elseif app.BucklingC1Button.Value==true
y=Final(:,14);% (5)
elseif app.RotationC1Button.Value==true
y=Final(:,15);% (6)
elseif app.btButton.Value==true
y=Final(:,16);% (7)
```

```
elseif app.thAISCMomentC2aButton.Value==true
y=Final(:,20);% (11)
elseif app.thAISCShearC2aButton.Value==true
y=Final(:,21);% (12)
elseif app.DeflectionL240C2aButton.Value==true
y=Final(:,22);% (13)
elseif app.TensionFlangeYieldingC2bButton.Value==true
y = Final(:,23);% (14)
elseif app.CompressionFlangeYieldingC2bButton.Value==true
y=Final(:,24);% (15)
elseif app.FlangeShearYieldingC2bButton.Value==true
y=Final(:,25);% (16)
elseif app.WebShearYieldingC2bButton.Value==true
y=Final(:,26); % (17)
elseif app.BucklingC2bButton.Value==true
y=Final(:,27); % (18)
elseif app.RotationC2bButton.Value==true
y=Final(:,28); % (19)
elseif app.CompositeDeflectionL360C3aButton.Value==true
y=Final(:,33); % (24)
elseif app.Vibration050C3bButton.Value==true
y=Final(:,34); % (25)
elseif app.MinimumPlotButton.Value==true
y=Final_Min_Matrix_Sort(:,3);
x = Final_Min_Matrix_Sort(:,2);
row2 = dataTipTextRow('Min Plot Case Number',Final_Min_Matrix_Sort(:,4));
end
XLMin = min(x);
XLMax = max(x);
LL=app.LimitLineEditField.Value;
Limit_vector = [LL LL];
s=scatter(app.UIAxes,x,y,'+');
hold(app.UIAxes,'on');
plot(app.UIAxes,[XLMin XLMax],Limit_vector);
hold(app.UIAxes,'off');
% row2 = dataTipTextRow('Min Beam Number',Final_Min_Matrix_Sort(:,1));
s.DataTipTemplate.DataTipRows(end+1) = row;
s.DataTipTemplate.DataTipRows(end+1) = row2;


% datacursormode(app.UIAxes,'on')
end


% Button pushed function: RunBeamButton
function RunBeamButtonPushed(app, event)
Final=[];
```

```
load Output_Final_1.mat;
load Output_Beam.mat;
load Output_AISC.mat;


RN = app.BeamNumberEditField.Value;


P1 = -1*Final(RN,3)/2;
P2 = Final(RN,3)/2;
P3 = Final(RN,2);
P4 = -1*Final(RN,4)/2;
P5 = Final(RN,4)/2;
P6=Final(RN,5);
P7=-1*Final(RN,6)/2;
P8=Final(RN,6)/2;





plot(app.UIAxes2,[P1 P2],[d d],'color','black','LineWidth',1)
hold(app.UIAxes2,'on');
plot(app.UIAxes2,[P1 P1],[d d-P3],'color','black','LineWidth',1)
plot(app.UIAxes2,[P2 P2],[d-P3 d],'color','black','LineWidth',1)
plot(app.UIAxes2,[P1 P4],[d-P3 d-P3],'color','black','LineWidth',1)
plot(app.UIAxes2,[P5 P2],[d-P3 d-P3],'color','black','LineWidth',1)
plot(app.UIAxes2,[P5 P5],[P6 d-P3],'color','black','LineWidth',1)
plot(app.UIAxes2,[P4 P4],[P6 d-P3],'color','black','LineWidth',1)
plot(app.UIAxes2,[P5 P8],[P6 P6],'color','black','LineWidth',1)
plot(app.UIAxes2,[P7 P4],[P6 P6],'color','black','LineWidth',1)
plot(app.UIAxes2,[P7 P7],[0 P6],'color','black','LineWidth',1)
plot(app.UIAxes2,[P8 P8],[0 P6],'color','black','LineWidth',1)
plot(app.UIAxes2,[P7 P8],[0 0],'color','black','LineWidth',1)
%I have set the Axis to 12"x12" for 8" beams
L1 = (d+4)/2;
L2 = d+4;
xlim(app.UIAxes2,[-L1 L1]);
ylim(app.UIAxes2,[0 L2]);
hold(app.UIAxes2,'off');
axis(app.UIAxes2,'off');
title(app.UIAxes2,'');


app.HeightEditField.Value = num2str(d);
app.TopFlangetfEditField.Value = double(Final(RN,2));
```

```
app.TopFlangebfEditField.Value = double(Final(RN,3));
app.WebtwEditField.Value = double(Final(RN,4));
app.BottomFlangetfEditField.Value = double(Final(RN,5));
app.BottomFlangebfEditField.Value = double(Final(RN,6));
app.SectionAreaEditField.Value = double(Final(RN,7));
app.MomentofInertiaEditField.Value = double(Final(RN,8));
app.WeightperFootEditField.Value = double(Final(RN,7))*12*.28356;
app.TopFlangeEditField.Value = (AISC_output(RN,3));
app.WebEditField.Value = (AISC_output(RN,4));
app.BottomFlangeEditField.Value = (AISC_output(RN,5));
app.AISCCaseEditField.Value = (AISC_output(RN,2));
clear
end
end


% Component initialization
methods (Access = private)


% Create UIFigure and components
function createComponents(app)


% Create UIFigure and hide until all components are created
app.UIFigure = uifigure('Visible', 'off');
app.UIFigure.Position = [100 100 1276 676];
app.UIFigure.Name = 'UI Figure';


% Create UIAxes
app.UIAxes = uiaxes(app.UIFigure);
xlabel(app.UIAxes, 'Beam Parameters (in., in.^2, or in.^4)')
ylabel(app.UIAxes, 'Normalized Design Criteria')
app.UIAxes.Position = [298 102 563 559];


% Create UIAxes2
app.UIAxes2 = uiaxes(app.UIFigure);
zlabel(app.UIAxes2, 'Z')
app.UIAxes2.XLim = [0 1];
app.UIAxes2.XColor = [1 1 1];
app.UIAxes2.XTick = [];
app.UIAxes2.YColor = [1 1 1];
app.UIAxes2.YTick = [];
app.UIAxes2.ZColor = [1 1 1];
app.UIAxes2.Position = [932 13 302 297];
```

```
% Create Image
app.Image = uiimage(app.UIFigure);
app.Image.Position = [1086 587 82 82];
app.Image.ImageSource = 'AISC.png';


% Create Parameters_2
app.Parameters_2 = uibuttongroup(app.UIFigure);
app.Parameters_2.Title = 'Criteria for y-axis ';
app.Parameters_2.Position = [11 111 262 550];


% Create TensionFlangeYieldingC1Button
app.TensionFlangeYieldingC1Button = uiradiobutton(app.Parameters_2);
app.TensionFlangeYieldingC1Button.Text = '(1) Tension Flange Yielding (C-
1)';
app.TensionFlangeYieldingC1Button.Position = [4 504 198 22];
app.TensionFlangeYieldingC1Button.Value = true;


% Create CompressionFlangeYieldingC1Button
app.CompressionFlangeYieldingC1Button = uiradiobutton(app.Parameters_2);
app.CompressionFlangeYieldingC1Button.Text = '(2) Compression Flange
Yielding (C-1)';
app.CompressionFlangeYieldingC1Button.Position = [4 483 229 22];


% Create FlangeShearYieldingC1Button
app.FlangeShearYieldingC1Button = uiradiobutton(app.Parameters_2);
app.FlangeShearYieldingC1Button.Text = '(3) Flange Shear Yielding (C-1)';
app.FlangeShearYieldingC1Button.Position = [4 462 188 22];


% Create WebShearYieldingC1Button
app.WebShearYieldingC1Button = uiradiobutton(app.Parameters_2);
app.WebShearYieldingC1Button.Text = '(4) Web Shear Yielding (C-1)';
app.WebShearYieldingC1Button.Position = [4 441 176 22];


% Create BucklingC1Button
app.BucklingC1Button = uiradiobutton(app.Parameters_2);
app.BucklingC1Button.Text = '(5) Buckling (C-1)';
app.BucklingC1Button.Position = [4 420 116 22];
```

```
% Create RotationC1Button
app.RotationC1Button = uiradiobutton(app.Parameters_2);
app.RotationC1Button.Text = '(6) Rotation (C-1)';
app.RotationC1Button.Position = [4 399 115 22];


% Create btButton
app.btButton = uiradiobutton(app.Parameters_2);
app.btButton.Text = '(7) b/t';
app.btButton.Position = [5 362 53 22];


% Create thAISCMomentC2aButton
app.thAISCMomentC2aButton = uiradiobutton(app.Parameters_2);
app.thAISCMomentC2aButton.Text = '(11) 15th AISC Moment (C-2a)';
app.thAISCMomentC2aButton.Position = [5 323 184 22];


% Create thAISCShearC2aButton
app.thAISCShearC2aButton = uiradiobutton(app.Parameters_2);
app.thAISCShearC2aButton.Text = '(12) 15th AISC Shear (C-2a)';
app.thAISCShearC2aButton.Position = [5 302 173 22];


% Create DeflectionL240C2aButton
app.DeflectionL240C2aButton = uiradiobutton(app.Parameters_2);
app.DeflectionL240C2aButton.Text = '(13) Deflection (L/240) (C-2a)';
app.DeflectionL240C2aButton.Position = [5 281 179 22];


% Create TensionFlangeYieldingC2bButton
app.TensionFlangeYieldingC2bButton = uiradiobutton(app.Parameters_2);
app.TensionFlangeYieldingC2bButton.Text = '(14) Tension Flange Yielding
(C-2b)';
app.TensionFlangeYieldingC2bButton.Position = [5 238 212 22];


% Create CompressionFlangeYieldingC2bButton
app.CompressionFlangeYieldingC2bButton = uiradiobutton(app.Parameters_2);
app.CompressionFlangeYieldingC2bButton.Text = '(15) Compression Flange
Yielding (C-2b';
app.CompressionFlangeYieldingC2bButton.Position = [5 217 238 22];


% Create FlangeShearYieldingC2bButton
app.FlangeShearYieldingC2bButton = uiradiobutton(app.Parameters_2);
```

```
app.FlangeShearYieldingC2bButton.Text = '(16) Flange Shear Yielding (C-
2b)';
app.FlangeShearYieldingC2bButton.Position = [5 196 202 22];


% Create WebShearYieldingC2bButton
app.WebShearYieldingC2bButton = uiradiobutton(app.Parameters_2);
app.WebShearYieldingC2bButton.Text = '(17) Web Shear Yielding (C-2b)';
app.WebShearYieldingC2bButton.Position = [5 175 190 22];


% Create BucklingC2bButton
app.BucklingC2bButton = uiradiobutton(app.Parameters_2);
app.BucklingC2bButton.Text = '(18) Buckling (C-2b)';
app.BucklingC2bButton.Position = [5 154 129 22];


% Create RotationC2bButton
app.RotationC2bButton = uiradiobutton(app.Parameters_2);
app.RotationC2bButton.Text = '(19) Rotation (C-2b)';
app.RotationC2bButton.Position = [5 133 129 22];


% Create MinimumPlotButton
app.MinimumPlotButton = uiradiobutton(app.Parameters_2);
app.MinimumPlotButton.Text = 'Minimum Plot ';
app.MinimumPlotButton.Position = [75 4 127 26];


% Create Vibration050C3bButton
app.Vibration050C3bButton = uiradiobutton(app.Parameters_2);
app.Vibration050C3bButton.Text = '(25) Vibration (0.50%) (C-3b)';
app.Vibration050C3bButton.Position = [4 68 177 22];


% Create CompositeDeflectionL360C3aButton
app.CompositeDeflectionL360C3aButton = uiradiobutton(app.Parameters_2);
app.CompositeDeflectionL360C3aButton.Text = '(24) Composite Deflection
(L/360) (C-3a)';
app.CompositeDeflectionL360C3aButton.Position = [4 89 241 22];


% Create MinimumforalllimitstatesyaxisLabel
app.MinimumforalllimitstatesyaxisLabel = uilabel(app.Parameters_2);
app.MinimumforalllimitstatesyaxisLabel.HorizontalAlignment = 'center';
app.MinimumforalllimitstatesyaxisLabel.FontAngle = 'italic';
app.MinimumforalllimitstatesyaxisLabel.Position = [4 29 267 40];
```

```
app.MinimumforalllimitstatesyaxisLabel.Text = {'Minimum for all limit
states (y-axis)'; 'auto Area (x-axis) use Min Beam for selection'};


% Create Parameters
app.Parameters = uibuttongroup(app.UIFigure);
app.Parameters.Title = 'Parameters for x-axis';
app.Parameters.Position = [329 11 523 90];


% Create tftopinButton
app.tftopinButton = uiradiobutton(app.Parameters);
app.tftopinButton.Text = 'tf (top) (in.)';
app.tftopinButton.Position = [11 43 171 22];


% Create bftopinButton
app.bftopinButton = uiradiobutton(app.Parameters);
app.bftopinButton.Text = 'bf (top) (in.)';
app.bftopinButton.Position = [10 22 172 22];


% Create twinButton
app.twinButton = uiradiobutton(app.Parameters);
app.twinButton.Text = 'tw (in.)';
app.twinButton.Position = [11 1 171 22];


% Create tfbottominButton
app.tfbottominButton = uiradiobutton(app.Parameters);
app.tfbottominButton.Text = 'tf (bottom) (in.)';
app.tfbottominButton.Position = [166 46 171 22];


% Create bfbottominButton
app.bfbottominButton = uiradiobutton(app.Parameters);
app.bfbottominButton.Text = 'bf (bottom) (in.)';
app.bfbottominButton.Position = [166 25 171 22];


% Create Areain2Button
app.Areain2Button = uiradiobutton(app.Parameters);
app.Areain2Button.Text = 'Area (in.^2)';
app.Areain2Button.Position = [336 3 171 22];
app.Areain2Button.Value = true;
```

```
% Create Ixin4Button
app.Ixin4Button = uiradiobutton(app.Parameters);
app.Ixin4Button.Text = 'Ix (in.^4)';
app.Ixin4Button.Position = [338 45 171 22];


% Create Jin4Button
app.Jin4Button = uiradiobutton(app.Parameters);
app.Jin4Button.Text = 'J (in.^4)';
app.Jin4Button.Position = [338 24 171 22];


% Create webheightinButton
app.webheightinButton = uiradiobutton(app.Parameters);
app.webheightinButton.Text = 'web height (in.)';
app.webheightinButton.Position = [166 4 171 22];


% Create PlotButton
app.PlotButton = uibutton(app.UIFigure, 'push');
app.PlotButton.ButtonPushedFcn = createCallbackFcn(app, @PlotButtonPushed,
true);
app.PlotButton.FontSize = 16;
app.PlotButton.FontWeight = 'bold';
app.PlotButton.Position = [17 45 255 56];
app.PlotButton.Text = 'Plot';


% Create BeamNumberEditField
app.BeamNumberEditField = uieditfield(app.UIFigure, 'numeric');
app.BeamNumberEditField.Position = [981 559 263 22];


% Create BeamNumberEditFieldLabel
app.BeamNumberEditFieldLabel = uilabel(app.UIFigure);
app.BeamNumberEditFieldLabel.HorizontalAlignment = 'right';
app.BeamNumberEditFieldLabel.Position = [886 559 85 22];
app.BeamNumberEditFieldLabel.Text = 'Beam Number';


% Create RunBeamButton
app.RunBeamButton = uibutton(app.UIFigure, 'push');
app.RunBeamButton.ButtonPushedFcn = createCallbackFcn(app,
@RunBeamButtonPushed, true);
app.RunBeamButton.Position = [896 528 346 23];
app.RunBeamButton.Text = 'Run Beam';
```

```
% Create TopFlangetfEditFieldLabel
app.TopFlangetfEditFieldLabel = uilabel(app.UIFigure);
app.TopFlangetfEditFieldLabel.HorizontalAlignment = 'right';
app.TopFlangetfEditFieldLabel.Position = [926 499 93 22];
app.TopFlangetfEditFieldLabel.Text = 'Top Flange (tf) =';


% Create TopFlangetfEditField
app.TopFlangetfEditField = uieditfield(app.UIFigure, 'numeric');
app.TopFlangetfEditField.Position = [1034 499 82 22];


% Create TopFlangebfEditFieldLabel
app.TopFlangebfEditFieldLabel = uilabel(app.UIFigure);
app.TopFlangebfEditFieldLabel.HorizontalAlignment = 'right';
app.TopFlangebfEditFieldLabel.Position = [923 469 97 22];
app.TopFlangebfEditFieldLabel.Text = 'Top Flange (bf) =';


% Create TopFlangebfEditField
app.TopFlangebfEditField = uieditfield(app.UIFigure, 'numeric');
app.TopFlangebfEditField.Position = [1035 469 82 22];


% Create WebtwEditFieldLabel
app.WebtwEditFieldLabel = uilabel(app.UIFigure);
app.WebtwEditFieldLabel.HorizontalAlignment = 'right';
app.WebtwEditFieldLabel.Position = [955 439 64 22];
app.WebtwEditFieldLabel.Text = 'Web (tw) =';


% Create WebtwEditField
app.WebtwEditField = uieditfield(app.UIFigure, 'numeric');
app.WebtwEditField.Position = [1034 439 82 22];


% Create BottomFlangetfEditFieldLabel
app.BottomFlangetfEditFieldLabel = uilabel(app.UIFigure);
app.BottomFlangetfEditFieldLabel.HorizontalAlignment = 'right';
app.BottomFlangetfEditFieldLabel.Position = [907 409 112 22];
app.BottomFlangetfEditFieldLabel.Text = 'Bottom Flange (tf) =';


% Create BottomFlangetfEditField
app.BottomFlangetfEditField = uieditfield(app.UIFigure, 'numeric');
app.BottomFlangetfEditField.Position = [1034 409 82 22];
```

```
% Create BottomFlangebfEditFieldLabel
app.BottomFlangebfEditFieldLabel = uilabel(app.UIFigure);
app.BottomFlangebfEditFieldLabel.HorizontalAlignment = 'right';
app.BottomFlangebfEditFieldLabel.Position = [904 379 115 22];
app.BottomFlangebfEditFieldLabel.Text = 'Bottom Flange (bf) =';


% Create BottomFlangebfEditField
app.BottomFlangebfEditField = uieditfield(app.UIFigure, 'numeric');
app.BottomFlangebfEditField.Position = [1034 379 82 22];


% Create SectionAreaEditFieldLabel
app.SectionAreaEditFieldLabel = uilabel(app.UIFigure);
app.SectionAreaEditFieldLabel.HorizontalAlignment = 'right';
app.SectionAreaEditFieldLabel.Position = [935 349 84 22];
app.SectionAreaEditFieldLabel.Text = 'Section Area =';


% Create SectionAreaEditField
app.SectionAreaEditField = uieditfield(app.UIFigure, 'numeric');
app.SectionAreaEditField.Position = [1034 349 82 22];


% Create MomentofInertiaEditFieldLabel
app.MomentofInertiaEditFieldLabel = uilabel(app.UIFigure);
app.MomentofInertiaEditFieldLabel.HorizontalAlignment = 'right';
app.MomentofInertiaEditFieldLabel.Position = [910 319 109 22];
app.MomentofInertiaEditFieldLabel.Text = 'Moment of Inertia =';


% Create MomentofInertiaEditField
app.MomentofInertiaEditField = uieditfield(app.UIFigure, 'numeric');
app.MomentofInertiaEditField.Position = [1034 319 82 22];


% Create Image2
app.Image2 = uiimage(app.UIFigure);
app.Image2.Position = [1179 593 81 72];
app.Image2.ImageSource = 'A&M_logo.png';


% Create LimitLineEditFieldLabel
app.LimitLineEditFieldLabel = uilabel(app.UIFigure);
app.LimitLineEditFieldLabel.HorizontalAlignment = 'right';
app.LimitLineEditFieldLabel.Position = [20 12 96 22];
app.LimitLineEditFieldLabel.Text = 'Limit Line';
```

```
% Create LimitLineEditField
app.LimitLineEditField = uieditfield(app.UIFigure, 'numeric');
app.LimitLineEditField.Position = [144 12 84 22];
app.LimitLineEditField.Value = 1;


% Create WeightperFootEditFieldLabel
app.WeightperFootEditFieldLabel = uilabel(app.UIFigure);
app.WeightperFootEditFieldLabel.HorizontalAlignment = 'right';
app.WeightperFootEditFieldLabel.Position = [914 289 104 22];
app.WeightperFootEditFieldLabel.Text = 'Weight per Foot = ';


% Create WeightperFootEditField
app.WeightperFootEditField = uieditfield(app.UIFigure, 'numeric');
app.WeightperFootEditField.Position = [1033 289 82 22];


% Create TopFlangeEditField
            app.TopFlangeEditField = uieditfield(app.UIFigure, 'text');
            app.TopFlangeEditField.HorizontalAlignment = 'center';
            app.TopFlangeEditField.Position = [1145 481 100 22];


            % Create TopFlangeEditFieldLabel
            app.TopFlangeEditFieldLabel = uilabel(app.UIFigure);
            app.TopFlangeEditFieldLabel.HorizontalAlignment = 'right';
            app.TopFlangeEditFieldLabel.Position = [1157 506 65 22];
            app.TopFlangeEditFieldLabel.Text = 'Top Flange';


            % Create BottomFlangeEditField
            app.BottomFlangeEditField = uieditfield(app.UIFigure, 'text');
            app.BottomFlangeEditField.HorizontalAlignment = 'center';
            app.BottomFlangeEditField.Position = [1149 381 100 22];


            % Create BottomFlangeEditFieldLabel
            app.BottomFlangeEditFieldLabel = uilabel(app.UIFigure);
            app.BottomFlangeEditFieldLabel.HorizontalAlignment = 'right';
            app.BottomFlangeEditFieldLabel.Position = [1157 406 84 22];
            app.BottomFlangeEditFieldLabel.Text = 'Bottom Flange';


            % Create WebEditField
```

```
        app.WebEditField = uieditfield(app.UIFigure, 'text');
        app.WebEditField.HorizontalAlignment = 'center';
        app.WebEditField.Position = [1147 431 100 22];

        % Create WebEditFieldLabel
        app.WebEditFieldLabel = uilabel(app.UIFigure);
        app.WebEditFieldLabel.HorizontalAlignment = 'right';
        app.WebEditFieldLabel.Position = [1180 454 30 22];
        app.WebEditFieldLabel.Text = 'Web';

        % Create AISCCaseEditField
        app.AISCCaseEditField = uieditfield(app.UIFigure, 'text');
        app.AISCCaseEditField.HorizontalAlignment = 'center';
        app.AISCCaseEditField.Position = [1151 288 100 22];

        % Create AISCCaseEditFieldLabel
        app.AISCCaseEditFieldLabel = uilabel(app.UIFigure);
        app.AISCCaseEditFieldLabel.HorizontalAlignment = 'right';
        app.AISCCaseEditFieldLabel.Position = [1169 313 65 22];
        app.AISCCaseEditFieldLabel.Text = 'AISC Case';

        % Create TextArea
        app.TextArea = uitextarea(app.UIFigure);
        app.TextArea.FontSize = 48;
        app.TextArea.BackgroundColor = [0.9412 0.9412 0.9412];
        app.TextArea.Position = [896 587 105 68];
        app.TextArea.Value = {'A'};

        % Create HeightEditField
        app.HeightEditField = uieditfield(app.UIFigure, 'text');
        app.HeightEditField.HorizontalAlignment = 'center';
        app.HeightEditField.FontSize = 48;
        app.HeightEditField.BackgroundColor = [0.9412 0.9412 0.9412];
        app.HeightEditField.Position = [937 591 64 60];

        % Show the figure after all components are created
        app.UIFigure.Visible = 'on';
    end
end
```

```
    % App creation and deletion
    methods (Access = public)

        % Construct app
        function app = Output_Application

            % Create UIFigure and components
            createComponents(app)

            % Register the app with App Designer
            registerApp(app, app.UIFigure)

            if nargout == 0
                clear app
            end
        end

        % Code that executes before app deletion
        function delete(app)

            % Delete UIFigure when app is deleted
            delete(app.UIFigure)
        end
    end
end
```

APPENDIX D

ABAQUS PARAMETRIC STUDY BEAM TABLE

Table 12: Abaqus Parametric Study Beam Table

Designation:	Top flange width (b_{ft}):	Top flange thickness (t_{ft}):	Bottom flange width (b_{fb}):	Bottom flange thickness (t_{fb}):	Web thickness (t_w):		Kg/m and *lbs/ft*
W8x31 0.25 b_f	50.8	11.05	203.2	11.05	7.24	(mm)	34.4
	2	0.435	8	0.435	0.285	(in.)	*23.1*
W8x31 0.50 b_f	101.6	11.05	203.2	11.05	7.24	(mm)	38.8
	4	0.435	8	0.435	0.285	(in.)	*26.1*
W8x31 0.75 b_f	152.4	11.05	203.2	11.05	7.24	(mm)	43.3
	6	0.435	8	0.435	0.285	(in.)	*29.1*
W8x31 1.00 b_f	203.2	11.05	203.2	11.05	7.24	(mm)	47.7
	8	0.435	8	0.435	0.285	(in.)	*32*
W8x31 1.25 b_f	254	11.05	203.2	11.05	7.24	(mm)	52.1
	10	0.435	8	0.435	0.285	(in.)	*35*
W8x31 1.50 b_f	304.8	11.05	203.2	11.05	7.24	(mm)	56.5
	12	0.435	8	0.435	0.285	(in.)	*38*
W8x31 1.75 b_f	355.6	11.05	203.2	11.05	7.24	(mm)	60.9
	14	0.435	8	0.435	0.285	(in.)	*40.9*
W8x31 2.00 b_f	406.4	11.05	203.2	11.05	7.24	(mm)	65.3
	16	0.435	8	0.435	0.285	(in.)	*43.9*
W8x31 0.25 t_f	203.2	2.76	203.2	11.05	7.24	(mm)	34.4
	8	0.109	8	0.435	0.285	(in.)	*23..1*
W8x31 0.50 t_f	203.2	5.52	203.2	11.05	7.24	(mm)	38.8
	8	0.218	8	0.435	0.285	(in.)	*26.1*
W8x31 0.75 t_f	203.2	8.29	203.2	11.05	7.24	(mm)	43.3
	8	0.326	8	0.435	0.285	(in.)	*29.1*
W8x31 1.00 t_f	203.2	11.05	203.2	11.05	7.24	(mm)	47.7
	8	0.435	8	0.435	0.285	(in.)	*32*
W8x31 1.25 t_f	203.2	13.81	203.2	11.05	7.24	(mm)	52.1
	8	0.544	8	0.435	0.285	(in.)	*35*
W8x31 1.50 t_f	203.2	16.57	203.2	11.05	7.24	(mm)	56.5
	8	0.653	8	0.435	0.285	(in.)	*38*

W8x31 1.75 t_f	203.2	19.34	203.2	11.05	7.24	(mm)	60.9
	8	0.761	8	0.435	0.285	(in.)	*40.9*
W8x31 2.00 t_f	203.2	22.1	203.2	11.05	7.24	(mm)	65.3
	8	0.87	8	0.435	0.285	(in.)	*43.9*
W18x76 0.25 b_f	69.85	17.27	279.4	17.27	10.8	(mm)	87.2
	2.75	0.68	11	0.68	0.425	(in.)	*58.6*
W18x76 0.50 b_f	139.7	17.27	279.4	17.27	10.8	(mm)	96.7
	5.5	0.68	11	0.68	0.425	(in.)	*65*
W18x76 0.75 b_f	209.55	17.27	279.4	17.27	10.8	(mm)	106.1
	8.25	0.68	11	0.68	0.425	(in.)	*71.3*
W18x76 1.00 b_f	279.4	17.27	279.4	17.27	10.8	(mm)	115.6
	11	0.68	11	0.68	0.425	(in.)	*77.7*
W18x76 1.25 b_f	349.25	17.27	279.4	17.27	10.8	(mm)	125.1
	13.75	0.68	11	0.68	0.425	(in.)	*84.1*
W18x76 1.50 b_f	419.1	17.27	279.4	17.27	10.8	(mm)	134.6
	16.5	0.68	11	0.68	0.425	(in.)	*90.4*
W18x76 1.75 b_f	488.95	17.27	279.4	17.27	10.8	(mm)	144.1
	19.25	0.68	11	0.68	0.425	(in.)	*96.8*
W18x76 2.00 b_f	558.8	17.27	279.4	17.27	10.8	(mm)	153.6
	22	0.68	11	0.68	0.425	(in.)	*103.2*
W18x76 0.25 t_f	279.4	4.32	279.4	17.27	10.8	(mm)	87.2
	11	0.17	11	0.68	0.425	(in.)	*58.6*
W18x76 0.50 t_f	279.4	8.64	279.4	17.27	10.8	(mm)	96.7
	11	0.34	11	0.68	0.425	(in.)	*65*
W18x76 0.75 t_f	279.4	12.95	279.4	17.27	10.8	(mm)	106.1
	11	0.51	11	0.68	0.425	(in.)	*71.3*
W18x76 1.00 t_f	279.4	17.27	279.4	17.27	10.8	(mm)	115.6
	11	0.68	11	0.68	0.425	(in.)	*77.7*
W18x76 1.25 t_f	279.4	21.59	279.4	17.27	10.8	(mm)	125.1
	11	0.85	11	0.68	0.425	(in.)	*84.1*
W18x76 1.50 t_f	279.4	25.91	279.4	17.27	10.8	(mm)	134.6
	11	1.02	11	0.68	0.425	(in.)	*90.4*
W18x76 1.75 t_f	279.4	30.23	279.4	17.27	10.8	(mm)	144.1
	11	1.19	11	0.68	0.425	(in.)	*96.8*
W8x31 2.00 t_f	279.4	34.54	279.4	17.27	10.8	(mm)	153.6
	11	1.36	11	0.68	0.425	(in.)	*103.2*

APPENDIX E

ANALYTICAL STUDY BEAM TABLE

Table 13: Analytical Study Beam Table

Beam Number:	Top flange width (b_{ft}):	Top flange thickness (t_{ft}):	Bottom flange width (b_{fb}):	Bottom flange thickness (t_{fb}):	Web thickness (t_w):		Kg/m and *lbs/ft*
1	50.8	3.2	152.4	1.1	12.7	(mm)	22.4
	2	0.125	6	0.042	0.5	(in.)	*15.1*
2	50.8	6.4	152.4	2.1	12.7	(mm)	24.5
	2	0.25	6	0.083	0.5	(in.)	*16.5*
3	50.8	9.5	152.4	3.2	12.7	(mm)	26.6
	2	0.375	6	0.125	0.5	(in.)	*17.9*
4	50.8	12.7	152.4	4.2	12.7	(mm)	28.7
	2	0.5	6	0.167	0.5	(in.)	*19.3*
5	50.8	15.9	152.4	5.3	12.7	(mm)	30.9
	2	0.625	6	0.208	0.5	(in.)	*20.7*
6	50.8	19.1	152.4	6.4	12.7	(mm)	33.0
	2	0.75	6	0.250	0.5	(in.)	*22.2*
7	50.8	22.2	152.4	7.4	12.7	(mm)	35.1
	2	0.875	6	0.292	0.5	(in.)	*23.6*
8	50.8	25.4	152.4	8.5	12.7	(mm)	37.2
	2	1	6	0.333	0.500	(in.)	*25.0*
9	50.8	28.6	152.4	9.5	14.3	(mm)	41.4
	2	1.125	6	0.375	0.563	(in.)	*27.8*
10	50.8	31.8	152.4	10.6	15.9	(mm)	45.4
	2	1.25	6	0.417	0.625	(in.)	*30.5*
11	50.8	34.9	152.4	11.6	17.5	(mm)	49.4
	2	1.375	6	0.458	0.688	(in.)	*33.2*
12	50.8	38.1	152.4	12.7	19.1	(mm)	53.3
	2	1.5	6	0.500	0.750	(in.)	*35.8*
13	50.8	41.3	152.4	13.8	20.6	(mm)	57.0
	2	1.625	6	0.542	0.813	(in.)	*38.3*
14	50.8	44.5	152.4	14.8	22.2	(mm)	60.6
	2	1.75	6	0.583	0.875	(in.)	*40.8*
15	50.8	47.6	152.4	15.9	23.8	(mm)	64.2
	2	1.875	6	0.625	0.938	(in.)	*43.1*

16	50.8	50.8	152.4	16.9	25.4	(mm)	67.6
	2	2	6	0.667	1	(in.)	*45.4*
17	63.5	3.2	165.1	1.2	12.7	(mm)	23.0
	2.5	0.125	6.5	0.048	0.5	(in.)	*15.5*
18	63.5	6.4	165.1	2.4	12.7	(mm)	25.7
	2.5	0.25	6.5	0.096	0.5	(in.)	*17.3*
19	63.5	9.5	165.1	3.7	12.7	(mm)	28.5
	2.5	0.375	6.5	0.144	0.5	(in.)	*19.1*
20	63.5	12.7	165.1	4.9	12.7	(mm)	31.2
	2.5	0.5	6.5	0.192	0.5	(in.)	*21.0*
21	63.5	15.9	165.1	6.1	12.7	(mm)	33.9
	2.5	0.625	6.5	0.240	0.5	(in.)	*22.8*
22	63.5	19.1	165.1	7.3	12.7	(mm)	36.7
	2.5	0.75	6.5	0.288	0.5	(in.)	*24.6*
23	63.5	22.2	165.1	8.5	12.7	(mm)	39.4
	2.5	0.875	6.5	0.337	0.5	(in.)	*26.5*
24	63.5	25.4	165.1	9.8	12.7	(mm)	42.1
	2.5	1	6.5	0.385	0.5	(in.)	*28.3*
25	63.5	28.6	165.1	11.0	14.3	(mm)	46.9
	2.5	1.125	6.5	0.433	0.563	(in.)	*31.5*
26	63.5	31.8	165.1	12.2	15.9	(mm)	51.6
	2.5	1.25	6.5	0.481	0.625	(in.)	*34.7*
27	63.5	34.9	165.1	13.4	17.5	(mm)	56.1
	2.5	1.375	6.5	0.529	0.688	(in.)	*37.7*
28	63.5	38.1	165.1	14.7	19.1	(mm)	60.6
	2.5	1.5	6.5	0.577	0.750	(in.)	*40.7*
29	63.5	41.3	165.1	15.9	20.6	(mm)	64.9
	2.5	1.625	6.5	0.625	0.813	(in.)	*43.6*
30	63.5	44.5	165.1	17.1	22.2	(mm)	69.1
	2.5	1.75	6.5	0.673	0.875	(in.)	*46.5*
31	63.5	47.6	165.1	18.3	23.8	(mm)	73.2
	2.5	1.875	6.5	0.721	0.938	(in.)	*49.2*
32	63.5	50.8	165.1	19.5	25.4	(mm)	77.2
	2.5	2	6.5	0.769	1	(in.)	*51.9*
33	76.2	3.2	177.8	1.4	12.7	(mm)	23.6
	3	0.125	7	0.054	0.5	(in.)	*15.9*

34	76.2	6.4	177.8	2.7	12.7	(mm)	27.0
	3	0.25	7	0.107	0.5	(in.)	*18.1*
35	76.2	9.5	177.8	4.1	12.7	(mm)	30.3
	3	0.375	7	0.161	0.5	(in.)	*20.4*
36	76.2	12.7	177.8	5.4	12.7	(mm)	33.7
	3	0.5	7	0.214	0.5	(in.)	*22.6*
37	76.2	15.9	177.8	6.8	12.7	(mm)	37.0
	3	0.625	7	0.268	0.5	(in.)	*24.9*
38	76.2	19.1	177.8	8.2	12.7	(mm)	40.4
	3	0.75	7	0.321	0.5	(in.)	*27.1*
39	76.2	22.2	177.8	9.5	12.7	(mm)	43.7
	3	0.875	7	0.375	0.5	(in.)	*29.4*
40	76.2	25.4	177.8	10.9	12.7	(mm)	47.1
	3	1	7	0.429	0.5	(in.)	*31.6*
41	76.2	28.6	177.8	12.2	14.3	(mm)	52.5
	3	1.125	7	0.482	0.563	(in.)	*35.3*
42	76.2	31.8	177.8	13.6	15.9	(mm)	57.7
	3	1.25	7	0.536	0.625	(in.)	*38.8*
43	76.2	34.9	177.8	15.0	17.5	(mm)	62.9
	3	1.375	7	0.589	0.688	(in.)	*42.3*
44	76.2	38.1	177.8	16.3	19.1	(mm)	67.9
	3	1.5	7	0.643	0.750	(in.)	*45.6*
45	76.2	41.3	177.8	17.7	20.6	(mm)	72.8
	3	1.625	7	0.696	0.813	(in.)	*49.0*
46	76.2	44.5	177.8	19.1	22.2	(mm)	77.7
	3	1.75	7	0.750	0.875	(in.)	*52.2*
47	76.2	47.6	177.8	20.4	23.8	(mm)	82.4
	3	1.875	7	0.804	0.938	(in.)	*55.3*
48	76.2	50.8	177.8	21.8	25.4	(mm)	86.9
	3	2	7	0.857	1	(in.)	*58.4*
49	88.9	3.2	190.5	1.5	12.7	(mm)	24.3
	3.5	0.125	7.5	0.058	0.5	(in.)	*16.3*
50	88.9	6.4	190.5	3.0	12.7	(mm)	28.2
	3.5	0.25	7.5	0.117	0.5	(in.)	*19.0*
51	88.9	9.5	190.5	4.4	12.7	(mm)	32.2
	3.5	0.375	7.5	0.175	0.5	(in.)	*21.6*

52	88.9	12.7	190.5	5.9	12.7	(mm)	36.2
	3.5	0.5	7.5	0.233	0.5	(in.)	*24.3*
53	88.9	15.9	190.5	7.4	12.7	(mm)	40.2
	3.5	0.625	7.5	0.292	0.5	(in.)	*27.0*
54	88.9	19.1	190.5	8.9	12.7	(mm)	44.1
	3.5	0.75	7.5	0.350	0.5	(in.)	*29.6*
55	88.9	22.2	190.5	10.4	12.7	(mm)	48.1
	3.5	0.875	7.5	0.408	0.5	(in.)	*32.3*
56	88.9	25.4	190.5	11.9	12.7	(mm)	52.1
	3.5	1	7.5	0.467	0.5	(in.)	*35.0*
57	88.9	28.6	190.5	13.3	14.3	(mm)	58.1
	3.5	1.125	7.5	0.525	0.563	(in.)	*39.0*
58	88.9	31.8	190.5	14.8	15.9	(mm)	63.9
	3.5	1.25	7.5	0.583	0.625	(in.)	*43.0*
59	88.9	34.9	190.5	16.3	17.5	(mm)	69.7
	3.5	1.375	7.5	0.642	0.688	(in.)	*46.8*
60	88.9	38.1	190.5	17.8	19.1	(mm)	75.3
	3.5	1.5	7.5	0.700	0.750	(in.)	*50.6*
61	88.9	41.3	190.5	19.3	20.6	(mm)	80.8
	3.5	1.625	7.5	0.758	0.813	(in.)	*54.3*
62	88.9	44.5	190.5	20.7	22.2	(mm)	86.2
	3.5	1.75	7.5	0.817	0.875	(in.)	*58.0*
63	88.9	47.6	190.5	22.2	23.8	(mm)	91.5
	3.5	1.875	7.5	0.875	0.938	(in.)	*61.5*
64	88.9	50.8	190.5	23.7	25.4	(mm)	96.7
	3.5	2	7.5	0.933	1	(in.)	*65.0*
65	101.6	3.2	203.2	1.6	12.7	(mm)	24.9
	4	0.125	8	0.063	0.5	(in.)	*16.7*
66	101.6	6.4	203.2	3.2	12.7	(mm)	29.5
	4	0.25	8	0.125	0.5	(in.)	*19.8*
67	101.6	9.5	203.2	4.8	12.7	(mm)	34.1
	4	0.375	8	0.188	0.5	(in.)	*22.9*
68	101.6	12.7	203.2	6.4	12.7	(mm)	38.7
	4	0.5	8	0.250	0.5	(in.)	*26.0*
69	101.6	15.9	203.2	7.9	12.7	(mm)	43.3
	4	0.625	8	0.313	0.5	(in.)	*29.1*

70	101.6	19.1	203.2	9.5	12.7	(mm)	47.9
	4	0.75	8	0.375	0.5	(in.)	*32.2*
71	101.6	22.2	203.2	11.1	12.7	(mm)	52.5
	4	0.875	8	0.438	0.5	(in.)	*35.3*
72	101.6	25.4	203.2	12.7	12.7	(mm)	57.1
	4	1	8	0.500	0.5	(in.)	*38.3*
73	101.6	28.6	203.2	14.3	14.3	(mm)	63.7
	4	1.125	8	0.563	0.563	(in.)	*42.8*
74	101.6	31.8	203.2	15.9	15.9	(mm)	70.1
	4	1.25	8	0.625	0.625	(in.)	*47.1*
75	101.6	34.9	203.2	17.5	17.5	(mm)	76.5
	4	1.375	8	0.688	0.688	(in.)	*51.4*
76	101.6	38.1	203.2	19.1	19.1	(mm)	82.7
	4	1.5	8	0.750	0.750	(in.)	*55.6*
77	101.6	41.3	203.2	20.6	20.6	(mm)	88.9
	4	1.625	8	0.813	0.813	(in.)	*59.7*
78	101.6	44.5	203.2	22.2	22.2	(mm)	94.9
	4	1.75	8	0.875	0.875	(in.)	*63.7*
79	101.6	47.6	203.2	23.8	23.8	(mm)	100.7
	4	1.875	8	0.938	0.938	(in.)	*67.7*
80	101.6	50.8	203.2	25.4	25.4	(mm)	106.5
	4	2	8	1	1	(in.)	*71.6*
81	114.3	3.2	215.9	1.7	12.7	(mm)	25.5
	4.5	0.125	8.5	0.066	0.5	(in.)	*17.1*
82	114.3	6.4	215.9	3.4	12.7	(mm)	30.7
	4.5	0.25	8.5	0.132	0.5	(in.)	*20.6*
83	114.3	9.5	215.9	5.0	12.7	(mm)	35.9
	4.5	0.375	8.5	0.199	0.5	(in.)	*24.2*
84	114.3	12.7	215.9	6.7	12.7	(mm)	41.2
	4.5	0.5	8.5	0.265	0.5	(in.)	*27.7*
85	114.3	15.9	215.9	8.4	12.7	(mm)	46.4
	4.5	0.625	8.5	0.331	0.5	(in.)	*31.2*
86	114.3	19.1	215.9	10.1	12.7	(mm)	51.6
	4.5	0.75	8.5	0.397	0.5	(in.)	*34.7*
87	114.3	22.2	215.9	11.8	12.7	(mm)	56.8
	4.5	0.875	8.5	0.463	0.5	(in.)	*38.2*

88	114.3	25.4	215.9	13.4	12.7	(mm)	62.1
	4.5	1	8.5	0.529	0.5	(in.)	*41.7*
89	114.3	28.6	215.9	15.1	14.3	(mm)	69.3
	4.5	1.125	8.5	0.596	0.563	(in.)	*46.5*
90	114.3	31.8	215.9	16.8	15.9	(mm)	76.4
	4.5	1.25	8.5	0.662	0.625	(in.)	*51.3*
91	114.3	34.9	215.9	18.5	17.5	(mm)	83.3
	4.5	1.375	8.5	0.728	0.688	(in.)	*56.0*
92	114.3	38.1	215.9	20.2	19.1	(mm)	90.2
	4.5	1.5	8.5	0.794	0.750	(in.)	*60.6*
93	114.3	41.3	215.9	21.9	20.6	(mm)	96.9
	4.5	1.625	8.5	0.860	0.813	(in.)	*65.1*
94	114.3	44.5	215.9	23.5	22.2	(mm)	103.5
	4.5	1.75	8.5	0.926	0.875	(in.)	*69.6*
95	114.3	47.6	215.9	25.2	23.8	(mm)	110.0
	4.5	1.875	8.5	0.993	0.938	(in.)	*73.9*
96	114.3	50.8	215.9	26.9	25.4	(mm)	116.3
	4.5	2	8.5	1.059	1	(in.)	*78.2*
97	127.0	3.2	228.6	1.8	12.7	(mm)	26.1
	5	0.125	9	0.069	0.5	(in.)	*17.6*
98	127.0	6.4	228.6	3.5	12.7	(mm)	32.0
	5	0.25	9	0.139	0.5	(in.)	*21.5*
99	127.0	9.5	228.6	5.3	12.7	(mm)	37.8
	5	0.375	9	0.208	0.5	(in.)	*25.4*
100	127.0	12.7	228.6	7.1	12.7	(mm)	43.7
	5	0.5	9	0.278	0.5	(in.)	*29.3*
101	127.0	15.9	228.6	8.8	12.7	(mm)	49.5
	5	0.625	9	0.347	0.5	(in.)	*33.3*
102	127.0	19.1	228.6	10.6	12.7	(mm)	55.4
	5	0.75	9	0.417	0.5	(in.)	*37.2*
103	127.0	22.2	228.6	12.3	12.7	(mm)	61.2
	5	0.875	9	0.486	0.5	(in.)	*41.1*
104	127.0	25.4	228.6	14.1	12.7	(mm)	67.1
	5	1	9	0.556	0.5	(in.)	*45.1*
105	127.0	28.6	228.6	15.9	14.3	(mm)	74.9
	5	1.125	9	0.625	0.563	(in.)	*50.3*

106	127.0	31.8	228.6	17.6	15.9	(mm)	82.6
	5	1.25	9	0.694	0.625	(in.)	*55.5*
107	127.0	34.9	228.6	19.4	17.5	(mm)	90.2
	5	1.375	9	0.764	0.688	(in.)	*60.6*
108	127.0	38.1	228.6	21.2	19.1	(mm)	97.6
	5	1.5	9	0.833	0.750	(in.)	*65.6*
109	127.0	41.3	228.6	22.9	20.6	(mm)	105.0
	5	1.625	9	0.903	0.813	(in.)	*70.5*
110	127.0	44.5	228.6	24.7	22.2	(mm)	112.2
	5	1.75	9	0.972	0.875	(in.)	*75.4*
111	127.0	47.6	228.6	26.5	23.8	(mm)	119.3
	5	1.875	9	1.042	0.938	(in.)	*80.1*
112	127.0	50.8	228.6	28.2	25.4	(mm)	126.2
	5	2	9	1.111	1	(in.)	*84.8*
113	139.7	3.2	241.3	1.8	12.7	(mm)	26.8
	5.5	0.125	9.5	0.072	0.5	(in.)	*18.0*
114	139.7	6.4	241.3	3.7	12.7	(mm)	33.2
	5.5	0.25	9.5	0.145	0.5	(in.)	*22.3*
115	139.7	9.5	241.3	5.5	12.7	(mm)	39.7
	5.5	0.375	9.5	0.217	0.5	(in.)	*26.7*
116	139.7	12.7	241.3	7.4	12.7	(mm)	46.2
	5.5	0.5	9.5	0.289	0.5	(in.)	*31.0*
117	139.7	15.9	241.3	9.2	12.7	(mm)	52.7
	5.5	0.625	9.5	0.362	0.5	(in.)	*35.4*
118	139.7	19.1	241.3	11.0	12.7	(mm)	59.1
	5.5	0.75	9.5	0.434	0.5	(in.)	*39.7*
119	139.7	22.2	241.3	12.9	12.7	(mm)	65.6
	5.5	0.875	9.5	0.507	0.5	(in.)	*44.1*
120	139.7	25.4	241.3	14.7	12.7	(mm)	72.1
	5.5	1	9.5	0.579	0.5	(in.)	*48.4*
121	139.7	28.6	241.3	16.5	14.3	(mm)	80.5
	5.5	1.125	9.5	0.651	0.563	(in.)	*54.1*
122	139.7	31.8	241.3	18.4	15.9	(mm)	88.8
	5.5	1.25	9.5	0.724	0.625	(in.)	*59.7*
123	139.7	34.9	241.3	20.2	17.5	(mm)	97.0
	5.5	1.375	9.5	0.796	0.688	(in.)	*65.2*

124	139.7	38.1	241.3	22.1	19.1	(mm)	105.1
	5.5	1.5	9.5	0.868	0.750	(in.)	*70.6*
125	139.7	41.3	241.3	23.9	20.6	(mm)	113.0
	5.5	1.625	9.5	0.941	0.813	(in.)	*76.0*
126	139.7	44.5	241.3	25.7	22.2	(mm)	120.9
	5.5	1.75	9.5	1.013	0.875	(in.)	*81.2*
127	139.7	47.6	241.3	27.6	23.8	(mm)	128.6
	5.5	1.875	9.5	1.086	0.938	(in.)	*86.4*
128	139.7	50.8	241.3	29.4	25.4	(mm)	136.1
	5.5	2	9.5	1.158	1	(in.)	*91.5*
129	152.4	3.2	254.0	1.9	12.7	(mm)	27.4
	6	0.125	10	0.075	0.5	(in.)	*18.4*
130	152.4	6.4	254.0	3.8	12.7	(mm)	34.5
	6	0.25	10	0.150	0.5	(in.)	*23.2*
131	152.4	9.5	254.0	5.7	12.7	(mm)	41.6
	6	0.375	10	0.225	0.5	(in.)	*27.9*
132	152.4	12.7	254.0	7.6	12.7	(mm)	48.7
	6	0.5	10	0.300	0.5	(in.)	*32.7*
133	152.4	15.9	254.0	9.5	12.7	(mm)	55.8
	6	0.625	10	0.375	0.5	(in.)	*37.5*
134	152.4	19.1	254.0	11.4	12.7	(mm)	62.9
	6	0.75	10	0.450	0.5	(in.)	*42.3*
135	152.4	22.2	254.0	13.3	12.7	(mm)	70.0
	6	0.875	10	0.525	0.5	(in.)	*47.0*
136	152.4	25.4	254.0	15.2	12.7	(mm)	77.1
	6	1	10	0.600	0.5	(in.)	*51.8*
137	152.4	28.6	254.0	17.1	14.3	(mm)	86.2
	6	1.125	10	0.675	0.563	(in.)	*57.9*
138	152.4	31.8	254.0	19.1	15.9	(mm)	95.1
	6	1.25	10	0.750	0.625	(in.)	*63.9*
139	152.4	34.9	254.0	21.0	17.5	(mm)	103.9
	6	1.375	10	0.825	0.688	(in.)	*69.8*
140	152.4	38.1	254.0	22.9	19.1	(mm)	112.6
	6	1.5	10	0.900	0.750	(in.)	*75.7*
141	152.4	41.3	254.0	24.8	20.6	(mm)	121.1
	6	1.625	10	0.975	0.813	(in.)	*81.4*

142	152.4	44.5	254.0	26.7	22.2	(mm)	129.6
	6	1.75	10	1.050	0.875	(in.)	*87.1*
143	152.4	47.6	254.0	28.6	23.8	(mm)	137.9
	6	1.875	10	1.125	0.938	(in.)	*92.7*
144	152.4	50.8	254.0	30.5	25.4	(mm)	146.1
	6	2	10	1.200	1	(in.)	*98.2*
145	165.1	3.2	266.7	2.0	12.7	(mm)	28.0
	6.5	0.125	10.5	0.077	0.5	(in.)	*18.8*
146	165.1	6.4	266.7	3.9	12.7	(mm)	35.7
	6.5	0.25	10.5	0.155	0.5	(in.)	*24.0*
147	165.1	9.5	266.7	5.9	12.7	(mm)	43.5
	6.5	0.375	10.5	0.232	0.5	(in.)	*29.2*
148	165.1	12.7	266.7	7.9	12.7	(mm)	51.2
	6.5	0.5	10.5	0.310	0.5	(in.)	*34.4*
149	165.1	15.9	266.7	9.8	12.7	(mm)	58.9
	6.5	0.625	10.5	0.387	0.5	(in.)	*39.6*
150	165.1	19.1	266.7	11.8	12.7	(mm)	66.7
	6.5	0.75	10.5	0.464	0.5	(in.)	*44.8*
151	165.1	22.2	266.7	13.8	12.7	(mm)	74.4
	6.5	0.875	10.5	0.542	0.5	(in.)	*50.0*
152	165.1	25.4	266.7	15.7	12.7	(mm)	82.1
	6.5	1	10.5	0.619	0.5	(in.)	*55.2*
153	165.1	28.6	266.7	17.7	14.3	(mm)	91.8
	6.5	1.125	10.5	0.696	0.563	(in.)	*61.7*
154	165.1	31.8	266.7	19.7	15.9	(mm)	101.4
	6.5	1.25	10.5	0.774	0.625	(in.)	*68.1*
155	165.1	34.9	266.7	21.6	17.5	(mm)	110.8
	6.5	1.375	10.5	0.851	0.688	(in.)	*74.4*
156	165.1	38.1	266.7	23.6	19.1	(mm)	120.1
	6.5	1.5	10.5	0.929	0.750	(in.)	*80.7*
157	165.1	41.3	266.7	25.6	20.6	(mm)	129.3
	6.5	1.625	10.5	1.006	0.813	(in.)	*86.9*
158	165.1	44.5	266.7	27.5	22.2	(mm)	138.3
	6.5	1.75	10.5	1.083	0.875	(in.)	*92.9*
159	165.1	47.6	266.7	29.5	23.8	(mm)	147.2
	6.5	1.875	10.5	1.161	0.938	(in.)	*98.9*

160	165.1	50.8	266.7	31.4	25.4	(mm)	156.0
	6.5	2	10.5	1.238	1	(in.)	*104.8*
161	177.8	3.2	279.4	2.0	12.7	(mm)	28.6
	7	0.125	11	0.080	0.5	(in.)	*19.2*
162	177.8	6.4	279.4	4.0	12.7	(mm)	37.0
	7	0.25	11	0.159	0.5	(in.)	*24.9*
163	177.8	9.5	279.4	6.1	12.7	(mm)	45.4
	7	0.375	11	0.239	0.5	(in.)	*30.5*
164	177.8	12.7	279.4	8.1	12.7	(mm)	53.7
	7	0.5	11	0.318	0.5	(in.)	*36.1*
165	177.8	15.9	279.4	10.1	12.7	(mm)	62.1
	7	0.625	11	0.398	0.5	(in.)	*41.7*
166	177.8	19.1	279.4	12.1	12.7	(mm)	70.4
	7	0.75	11	0.477	0.5	(in.)	*47.3*
167	177.8	22.2	279.4	14.1	12.7	(mm)	78.8
	7	0.875	11	0.557	0.5	(in.)	*52.9*
168	177.8	25.4	279.4	16.2	12.7	(mm)	87.1
	7	1	11	0.636	0.5	(in.)	*58.6*
169	177.8	28.6	279.4	18.2	14.3	(mm)	97.4
	7	1.125	11	0.716	0.563	(in.)	*65.5*
170	177.8	31.8	279.4	20.2	15.9	(mm)	107.6
	7	1.25	11	0.795	0.625	(in.)	*72.3*
171	177.8	34.9	279.4	22.2	17.5	(mm)	117.7
	7	1.375	11	0.875	0.688	(in.)	*79.1*
172	177.8	38.1	279.4	24.2	19.1	(mm)	127.6
	7	1.5	11	0.955	0.75	(in.)	*85.7*
173	177.8	41.3	279.4	26.3	20.6	(mm)	137.4
	7	1.625	11	1.034	0.813	(in.)	*92.3*
174	177.8	44.5	279.4	28.3	22.2	(mm)	147.0
	7	1.75	11	1.114	0.875	(in.)	*98.8*
175	177.8	47.6	279.4	30.3	23.8	(mm)	156.6
	7	1.875	11	1.193	0.938	(in.)	*105.2*
176	177.8	50.8	279.4	32.3	25.4	(mm)	166.0
	7	2	11	1.273	1	(in.)	*111.5*
177	190.5	3.2	292.1	2.1	12.7	(mm)	29.3
	7.5	0.125	11.5	0.082	0.5	(in.)	*19.7*

178	190.5	6.4	292.1	4.1	12.7	(mm)	38.3
	7.5	0.25	11.5	0.163	0.5	(in.)	*25.7*
179	190.5	9.5	292.1	6.2	12.7	(mm)	47.2
	7.5	0.375	11.5	0.245	0.5	(in.)	*31.7*
180	190.5	12.7	292.1	8.3	12.7	(mm)	56.2
	7.5	0.5	11.5	0.326	0.5	(in.)	*37.8*
181	190.5	15.9	292.1	10.4	12.7	(mm)	65.2
	7.5	0.625	11.5	0.408	0.5	(in.)	*43.8*
182	190.5	19.1	292.1	12.4	12.7	(mm)	74.2
	7.5	0.75	11.5	0.489	0.5	(in.)	*49.9*
183	190.5	22.2	292.1	14.5	12.7	(mm)	83.2
	7.5	0.875	11.5	0.571	0.5	(in.)	*55.9*
184	190.5	25.4	292.1	16.6	12.7	(mm)	92.2
	7.5	1	11.5	0.652	0.5	(in.)	*61.9*
185	190.5	28.6	292.1	18.6	14.3	(mm)	103.1
	7.5	1.125	11.5	0.734	0.563	(in.)	*69.3*
186	190.5	31.8	292.1	20.7	15.9	(mm)	113.9
	7.5	1.25	11.5	0.815	0.625	(in.)	*76.5*
187	190.5	34.9	292.1	22.8	17.5	(mm)	124.6
	7.5	1.375	11.5	0.897	0.688	(in.)	*83.7*
188	190.5	38.1	292.1	24.8	19.1	(mm)	135.1
	7.5	1.5	11.5	0.978	0.750	(in.)	*90.8*
189	190.5	41.3	292.1	26.9	20.6	(mm)	145.5
	7.5	1.625	11.5	1.060	0.813	(in.)	*97.8*
190	190.5	44.5	292.1	29.0	22.2	(mm)	155.8
	7.5	1.75	11.5	1.141	0.875	(in.)	*104.7*
191	190.5	47.6	292.1	31.1	23.8	(mm)	165.9
	7.5	1.875	11.5	1.223	0.938	(in.)	*111.5*
192	190.5	50.8	292.1	33.1	25.4	(mm)	176.0
	7.5	2	11.5	1.304	1	(in.)	*118.2*
193	203.2	3.2	304.8	2.1	12.7	(mm)	29.9
	8	0.125	12	0.083	0.5	(in.)	*20.1*
194	203.2	6.4	304.8	4.2	12.7	(mm)	39.5
	8	0.25	12	0.167	0.5	(in.)	*26.6*
195	203.2	9.5	304.8	6.4	12.7	(mm)	49.1
	8	0.375	12	0.250	0.5	(in.)	*33.0*

196	203.2	12.7	304.8	8.5	12.7	(mm)	58.7
	8	0.5	12	0.333	0.5	(in.)	*39.5*
197	203.2	15.9	304.8	10.6	12.7	(mm)	68.4
	8	0.625	12	0.417	0.5	(in.)	*45.9*
198	203.2	19.1	304.8	12.7	12.7	(mm)	78.0
	8	0.75	12	0.500	0.5	(in.)	*52.4*
199	203.2	22.2	304.8	14.8	12.7	(mm)	87.6
	8	0.875	12	0.583	0.5	(in.)	*58.9*
200	203.2	25.4	304.8	16.9	12.7	(mm)	97.2
	8	1	12	0.667	0.5	(in.)	*65.3*
201	203.2	28.6	304.8	19.1	14.3	(mm)	108.8
	8	1.125	12	0.750	0.563	(in.)	*73.1*
202	203.2	31.8	304.8	21.2	15.9	(mm)	120.2
	8	1.25	12	0.833	0.625	(in.)	*80.8*
203	203.2	34.9	304.8	23.3	17.5	(mm)	131.5
	8	1.375	12	0.917	0.688	(in.)	*88.4*
204	203.2	38.1	304.8	25.4	19.1	(mm)	142.6
	8	1.5	12	1	0.750	(in.)	*95.9*
205	203.2	41.3	304.8	27.5	20.6	(mm)	153.7
	8	1.625	12	1.083	0.813	(in.)	*103.3*
206	203.2	44.5	304.8	29.6	22.2	(mm)	164.6
	8	1.75	12	1.167	0.875	(in.)	*110.6*
207	203.2	47.6	304.8	31.8	23.8	(mm)	175.3
	8	1.875	12	1.25	0.938	(in.)	*117.8*
208	203.2	50.8	304.8	33.9	25.4	(mm)	186.0
	8	2	12	1.333	1	(in.)	*125.0*